Universitat Autònoma de Barcelona

Development of novel biobased thermoplastic polyurethanes containing 2,5-furandicarboxylic acid polyesters

Daniel Garcia Martos

Universitat Autònoma de Barcelona

Development of novel biobased thermoplastic polyurethanes containing 2,5-furandicarboxylic acid polyesters

Daniel Garcia Martos

Tesis Doctoral

Programa de Doctorat en Química

Prof. Dr. Joan Carles Bayón Rueda

Departament de Química

Facultat de Ciències

2022

Manuscript presented to obtain the PhD Degree by Daniel Garcia Martos

GARCIA MARTOS, DANIEL (FIRMA)

Firmado digitalmente por GARCIA MARTOS, DANIEL (FIRMA)
Fecha: 2022.09.27 13:03:51 +02'00'

Daniel Garcia Martos

With the approval of Prof. Dr. Joan Carles Bayón Rueda

JUAN CARLOS BAYON RUEDA - DNI 38481842J

Signat digitalment per JUAN CARLOS BAYON RUEDA - DNI 38481842J
Data: 2022.09.27 16:11:17 +02'00'

Prof. Dr. Joan Carles Bayón Rueda

Departament de Química

Facultat de Ciències

Universitat Autònoma de Barcelona

Agradecimientos

Ahora llega la parte más difícil de cualquier tesis, aquella que siempre se deja para el final, escribir los agradecimientos.

Todo este trabajo no habría sido posible sin el apoyo de muchísima gente, tanto a nivel científico como personal.

En primer lugar, me gustaría dar gracias a mi director de tesis. Joan Carles, muchísimas gracias por haberme acogido en tu grupo de investigación aquel verano hace ya 8 años a pesar de apenas conocerme. Has sido un gran mentor para mí todos estos años y claramente, no podría haber llegado a aprender ni la mitad de lo que he hecho sin tu ayuda. Siempre te tendré como referente sobre como un investigador debe ser y trabajar. Gracias por haberme dado la libertad para explorar todos los temas que de repente me surgían como interés y por pararme los pies cuando mis elucubraciones dejaban de tener sentido, que ha pasado bastante. Gracias por haber tenido siempre la puerta abierta, o el móvil encendido, cada vez que necesitaba ayuda con cualquier problema o discutir alguna parte de los resultados que no entendía.

También me gustaría agradecer a Lubrizol, tanto por el soporte económico que ha permitido el desarrollo de este trabajo, como por el apoyo de el personal. En especial me gustaría agradecer a Maria Josep y Nikola. Muchas gracias a ambos por el apoyo que habéis dado durante la elaboración de este trabajo y por haber aguantado esas reuniones con presentaciones que parecían no acabar nunca.

Muchas gracias a toda mi familia. Creo que no hace falta decir que no habría llegado hasta aquí sin vuestro apoyo. Aunque todo no haya sido siempre fácil, y estos últimos días de escritura y corrección menos conmigo encerrado en la “cueva”, papa, mama, Jaume, gracias por haber estado siempre allí. A los primos, tanto viejos como nuevos, muchas gracias por todos los días de meriendas, salidas, y gin-tonics (aunque sean falsos).

Y ahora llega el momento que estabais esperando, el de la otra familia, la de inorgánica, esa que he encontrado en el transcurso de la tesis y que ira directamente a leer esta parte en cuanto puedan poner las manos en el librito (¡os he pillado eh!). Miriam, o quizás debería llamarte por tu titulo oficial, Mama Pato, muchas gracias por estar allí cuando se me iba la cabeza y me expandía ocupando 4 vitrinas y un taburete porque no tenia suficiente espacio para hacerlo todo a la vez. Gracias por haber intentado ser la voz de la razón, aunque a veces te escuchara poco. A la persona con el nombre más guachi que existe en este mundo, Mario Emilio Garcia-Risco Aguado de todos los santos amen y a aquel que, aun después de haber

hecho parte de la carrera y del máster juntos, no me conocía hasta llegar al doctorado y que aun no ha aprendido a pronunciar mi nombre bien, Francisco. Muchas gracias por esos momentos en el SAF de desconexión y por haberme animado cuando la presión de todo aumentaba demasiado. Mariona, lo siento por haberte animado a que vinieras con nosotros ese día cuando Emi estaba en Inglaterra y haberte introducido en el grupo, entiendo que me odies, pero ahora eres demasiado importante para nosotros así que ya no tienes escapatoria. Gloria, aunque seas la única persona de inorgánica que no tiene un apodo porque tu dedo nos da miedo, muchas gracias por los ánimos durante todo este tiempo. A las chicas del ICMAB, Lavi y Diana, muchas gracias por los momentos de café, aunque yo no bebiera y por haber estado allí cuando se os necesitara. Y por último los "niños", esos que llegasteis más tarde que el resto (y no hablo de vuestro retrasito), gracias por haber dado algo de vidilla a los muermos octogenarios. Dani, te dejo en herencia lo más importante, el maldito nombre por el que me llamáis. A partir de ahora, tú eres Danieée, y no, no puedes devolverlo. Marcus, nuestra tira palos profesional, aunque está muy feo que presentes el mismo día que yo para no tener que venirme a ver, gracias por haber estado allí para lo que necesitara. Hactor, esa persona un poco ida de la cabeza (pero no tanto como yo) que entro en el laboratorio un día y se ha hecho indispensable, gracias por haberme animado ni que sea un poco la vida. Abel aka Tomas aka Tommy, creo que no hace falta que te diga por qué (momento tembleque), pero muchas gracias por aguantar mis desvaríos.

A los orgánicos/analíticos, esos aliens que pululan por las otras plantas, Arnau, Judit, Mariona, Laura, muchas gracias por las quedadas de sushi y por. Marta, mi compañera de atasco de la C58 que ya ha escapado de UAB, muchas gracias por inyectar un poco de locura a cada día con los bailes en el coche, gracias a ti no podré escuchar las canciones de la Señora Tomasa sin que se me venga una sonrisa a la cara.

Por último, pero no menos importante, Valentina y Jordi. Valen, muchas gracias por todos los momentos y desvaríos juntos desde hace ya diez años. Jordi, la cosa valenciana que apareció un día por clase y que, por alguna razón, decidió hablarme, gracias por haber estado siempre allí.

“Hear, feel, think.”

Venat

Preface

This work has been carried out in collaboration with Lubrizol Advances Materials S.L. Consequently, some information regarding the employed processes, catalysts and additives will not be disclosed due to a confidentiality agreement. The polyurethanes reported in this work are protected under the preliminary patent EP 22382851.8.[1]

Abstract

The ever-increasing demand for polymeric materials entails that, if no significant changes are made in the plastics industry, by 2050 polymer production will account for 20 % of the global oil use and 15% of the greenhouse gas emission budget stipulated by the Paris Agreement. Therefore, a switch to a more sustainable production model is crucial to avoid the disasters brought up by man-made climate change. The development of biorenewable monomers has emerged as one of the most important tools to minimise both the oil dependence and the greenhouse gas emissions linked to the production of polymers. It enables the use of biofeedstocks, rather than crude oil, to generate monomers. This approach not only eliminates the dependency on crude oil but also minimises the greenhouse gas emissions associated with this industry. From the existing biobased monomers, 2,5-furandicarboxylic acid has emerged as an excellent choice to develop novel, greener plastic materials, since it can be obtained from many easily accessible biofeedstocks, like glucose, fructose or lignocellulose, and its production presents a low carbon footprint.

This PhD dissertation details the synthesis and characterisation of a new family of biobased thermoplastic polyurethanes based on 2,5-furandicarboxylic acid polyesters to generate materials with a reduced carbon footprint. Moreover, their petrochemical isophthalate analogous were developed to compare and assess the differences in reactivity and properties induced by the two different aromatic diacids. The synthesis of the polyesters was carried out with two different diols, 1,3-propanediol and 1,6-hexanediol, and a variety of different molecular weights, in the range of 1000-2000 g/mol. These polyesters were then introduced into a large number of polyurethane formulations, consisting of two different diisocyanates, methylene diphenyl diisocyanate and hexamethylene diisocyanate and hard segment contents (10, 30 and 50% molar fraction). This large formulation domain has enabled us to gain a deep insight into the effect that the aromatic polyesters have on the morphology and mechanical properties of these new thermoplastic polyurethanes. To gather the information about how the different diacids affect the morphology of the polyurethanes, and how that impacts their mechanical properties, a large array of different techniques was employed. Differential scanning calorimetry, small-angle X-ray scattering and wide-angle X-ray scattering were selected to gain an insight into the chain mobility, phase segregation and crystallinity of the materials. Moreover, the hardness, tensile strength and shape memory properties of the studied materials were measured and correlated with the variations in morphology between the different polyurethane formulations.

The materials synthesised in this work exhibit exceptional mechanical properties, achieving polymers with high hardness at low diisocyanate contents and shape memory polymers with outstanding actuation strength, overcoming those of the current state-of-the-art.

Overall, the properties of the studied polyurethanes depend on just one factor, the supramolecular interactions present in the materials. These supramolecular interactions govern all of their characteristics, from their microphase morphology and chain mobility to their mechanical and shape memory properties. These supramolecular interactions can be divided into two groups, the cohesion forces within each of the domains, hard segment and soft segment, and the interactions between them. As a general trend, strong cohesion forces result in polymers with a high segregation and crystallisation capability, while strong interactions between the phases inhibit the segregation process, limiting the crystallinity of the materials. The degree of phase segregation of the materials is responsible for many of their mechanical properties and therefore, the factors that reduce this phase segregation produce materials with the worst mechanical properties. Accordingly, the low interaction of the aliphatic hexamethylene diisocyanate moieties from the hard segment, with the highly aromatic soft segment domains, results in materials with a high phase segregation and therefore, excellent mechanical properties, namely, tensile strength, and actuation strength. Likewise, the high cohesion forces of the soft segment containing 2,5-furandicarboxylate moieties induce the segregation of the polymers, resulting in polymers with outstanding mechanical properties.

Abbreviations

ACN	Acetonitrile
AN	Annealed
BDO	1,4-butanediol
CE	Chain extender
CO_{2e}	Carbon dioxide equivalents
CP	Chain packing
d	HS interdomain distance
DCM	Dichloromethane
DFT	Density functional theory
DMSO	Dimethyl sulfoxide
DOE	Design of experiments
DSC	Differential scanning calorimetry
E	Young's modulus
EoL	End-of-life
E_ρ	Energy density of the shape memory process
FDCA	2,5-furandicarboxylic acid
FDCAHDO	Polyhexamethylene furandicarboxylate
FDCAME	Methyl 2,5-furandicarboxylate
FDCAPDO	Polypropylene furandicarboxylate
GC-MS	Gas-chromatography mass-spectroscopy
GHG	Greenhouse gas

GPC	Gel permeation chromatography
h	Width of the shell surrounding the HS domains
HDO	1,6-hexanediol
HS	Hard segment
IA	Acidity index
IOH	Hydroxyl index
IOMe	Methyl ester index
IPHTA	Isophthalic acid
IPHTABDO	Polybutylene isophthalate
IPHTAHDO	Polyhexamethylene isophthalate
IPHTAME	Dimethyl isophthalate
IPHTAPDO	Polypropylene isophthalate
IR	Infrared
LCA	Lifecycle assessment
M_n	Molecular number
MST	Microphase separation transition
M_w	Molecular weight
M_z	Z average molecular weight
N_D	Critical sequence length
NMR	Nuclear magnetic resonance
P(q)	Form factor
PDO	1,3-propanediol

PE	Polyethylene
PET	Polyethylene theraphtalate
PP	Polypropylene
R	HS radius
R_f	Shape fixity
R_h	Radius of the HS domains and their surrounding shell
R_r	Shape recovery
S(q)	Structure factor
SAXS	Small-angle X-ray scattering
SMP	Shape memory polymer
SS	Soft segment
T_b	Brittle-ductile transition temperature
T_c	Crystallisation temperature
T_{CC}	Cold crystallisation temperature
T_g	Glass transition temperature
THF	Tetrahydrofuran
T_m	Melting temperature
TPA	Terephthalic acid
TPU	Thermoplastic polyurethane
UnAN	Unannealed
WAXS	Wide-angle X-ray scattering
ε	Elongation or strain

ε_b	Elongation or strain at break
ε_r	Shape memory recovery strain
ε_Y	Elongation at yield point
θ	X-ray incidence angle
σ	Stress
σ_b	Stress at break
σ_d	Standard deviation of the HS interdomain distances.
σ_r	Shape memory stress recovery
σ_R	Standard deviation of the HS radius
σ_Y	Yield point
Φ	Volume fraction of the HS domains
Φ_C	Degree of crystallinity

Formulation Summary

The nomenclature employed for the polyesters and the thermoplastic polyurethanes synthesised during this work can be found hereinafter.

Polyesters

In this dissertation, polyesters made out of two different dicarboxylic acids, isophthalic acid (IPHTA) and 2,5-furandicarboxylic acid (FDCA) and three different diols, 1,3-propanediol (PDO), 1,4-butanediol (BDO) and 1,6-hexanediol (HDO) have been synthesised and given the following codes.

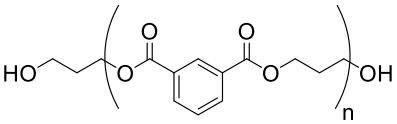

Polypropylene isophthalate
(IPHTAPDO)

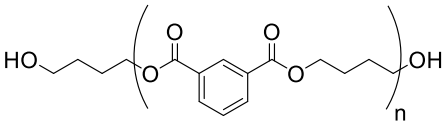

Polybutylene isophthalate
(IPHTABDO)

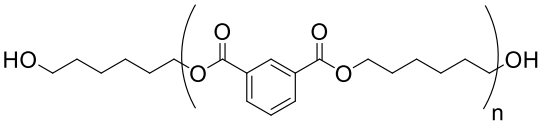

Polyhexamethylene isophthalate
(IPHTAHDO)

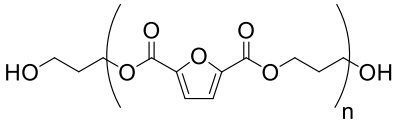

Polypropylene 2,5-furandicarboxylate
(FDCAPDO)

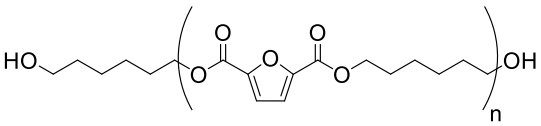

Polyhexamethylene 2,5-furandicarboxylate
(FDCAHDO)

Polyesters with different molecular weights have been prepared during this study. To ease the comprehension of the results, a simplified nomenclature, in which the target molecular weight, rather than its actual value was employed. The simplified nomenclature is as follows: **DiacidDiol Target molecular weight** (Example: IPHTAPDO 1000, meaning an isophthalic polyester diol of 1,3-propanediol with a M_n around 1000). Note that this simplification of the polyester molecular weight is only applied to facilitate the reading and understanding of the results. Any calculations or parameterisations concerning the materials were carried out employing the actual molecular weight of the polyesters, not their simplified values.

Thermoplastic polyurethanes

The thermoplastic polyurethanes synthesised within this work were prepared from the aforementioned polyesters, two different diisocyanates, methylene diphenyl diisocyanate (MDI) and hexamethylene diisocyanate (HDI), 1,4-butanediol (BDO) as chain extender and three different hard segments (HS) contents.

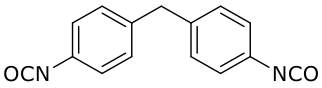

4,4-diphenylmethylene diisocyanate (MDI)

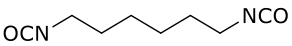

Hexamethylene diisocyanate (HDI)

As in the polyesters, a simplified nomenclature, employing the target polyester molecular weight rather than its actual value has been developed to ease the comprehension of the results. Hence, the TPUs' nomenclature follows the pattern **DiacidDiol Target molecular weight HS content (%) Diisocyanate** (Example: IPHTAPDO 1000 10% MDI).

Table of contents

Chapter 1: Introduction

This chapter serves as a collection of the basic foundations of polymer chemistry and their environmental impact necessary to comprehend the objectives and results of this thesis.
A special focus will be given to polyurethanes and their properties.

1.1 Polymers and global warming

Global warming is one of the most pressing issues our current society needs to tackle. Most studies place the current increase in temperature caused by manmade global warming at around 1 °C and, if there is not a significant reduction to the global greenhouse gas (GHG) emissions, temperatures are expected to increase by 0.2 ºC per decade.[2–4] The effects of global warming, namely shrinkage of glaciers, an increase in sea levels, droughts, changes in plant patterns… are already noticeable and would prove disastrous if temperatures are allowed to continue rising. To restrain the effects of global warming, the Paris agreement signed by 196 members of the United Nations council aims to limit global warming to well below 1.5 ºC, just 0.5 ºC above its current value.[5] As a tool to determine the environmental impact of the different greenhouse gasses, a parameter, called CO_2 equivalents (CO_{2e}) has been developed. CO_{2e} is defined as "a measure of how much energy the emissions of 1 ton of a gas will absorb over a given period, relative to the emissions of 1 ton of carbon dioxide".[6] To limit the global temperature increase below 1.5 ºC these CO_{2e} emissions need to be kept under 120 Gt CO_{2e}.[7,8] To reach this goal, all industries need to significantly reduce their GHG emissions.

In 2019, the polymer industry alone generated 0.86 Gt of CO_{2e}, which accounted for 2% of the global GHG emissions. These values are expected to increase to 1.34 Gt CO_{2e} by 2030 and to 2.8 Gt CO_{2e} by 2050 as the demand for polymeric materials grows. This would amount to 10-15% of the GHG emission budget stipulated in the Paris Agreement.[9–11] Moreover polymers are expected to consume around 20% of the yearly oil production by 2050.[12] Therefore new processes and technologies aimed at reducing the carbon footprint of polymeric materials are required to meet the goals set by the Paris agreement.

1.1.1 Strategies to reduce greenhouse gas emissions from polymers

If one thinks about ways to reduce the GHG emissions caused by polymers, the first idea that comes to mind is to just stop using plastics altogether. However, contrary to general belief, the use of plastics indirectly reduces global GHG emissions. This is due to one of the properties of polymers, their low density, which is highly beneficial for many of their applications, like automotive parts or packaging. Even though the generation and end-of-life (EoL) stages of many alternative materials to plastics, such as aluminium, ceramics, steel, etc. produce less CO_{2e} emissions than polymers, their increased weight means that, during their use, they generate higher emissions than plastics, offsetting this positive balance. If a full life-cycle assessment (LCA) accounting for the GHG emissions of different materials is carried out, including not only their preparation and EoL stages but also the amount of CO_{2e} produced during their use, plastics exhibit the lowest GHG emissions (**Figure 1.1**).[13–16]

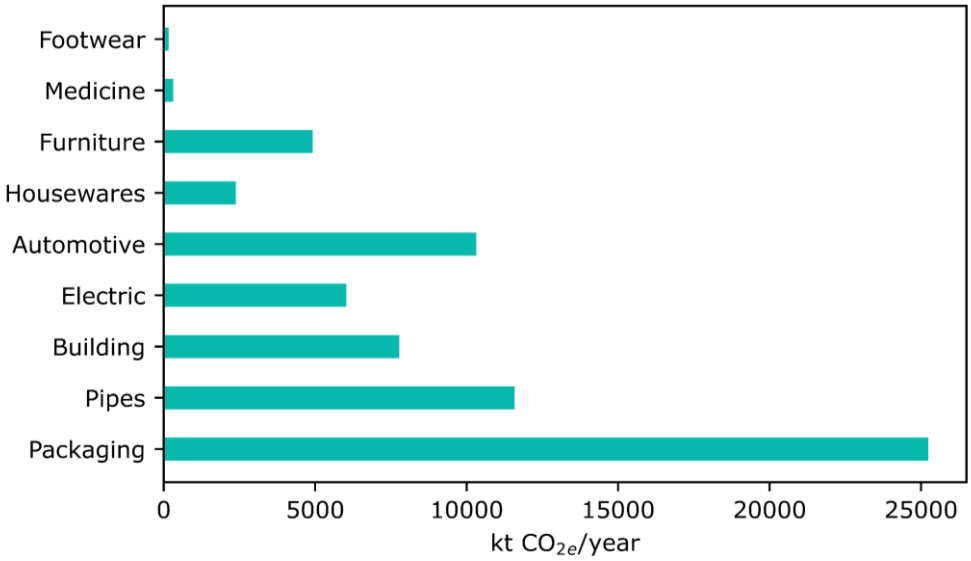

Figure 1.1: kt CO_{2e}/year savings of plastic products compared to alternative materials. Adapted from[15].

This clearly shows that the complete elimination of polymeric materials is not the solution to the GHG emissions issue. Rather, a combination of many different strategies is required to reduce the GHG emissions derived from the polymer industry.

1.1.1.1 Reduction of single-use plastics

Single-use plastics account for 40% of the overall demand for polymeric materials. Although these products tend to be made of as little material as possible, thus producing very low GHG emissions per piece, they need to be continuously generated and disposed of, leading to an immense generation of CO_{2e}. Moreover, vast amounts of the residues arising from single-use plastics are incinerated, further exacerbating this issue.[17] By substituting these single-use products with reusable ones, the impact of polymer chemistry on climate change could be reduced to a great extent. Reusable products tend to be thicker than single-use ones, so per unit, their environmental impact is higher. However, given enough uses, this higher generation of CO_{2e} during their production is offset, leading to overall lower GHG emissions. On top of that, the number of waste materials generated can be greatly decreased.[9,12,17] A single-use item that perfectly exemplifies the previous fact is plastic bags. In several LCA studies it has been found that, by using reusable plastic bags just 6-11 times, the increase in GHG emissions from their generation and disposal can be compensated in comparison with their single-use analogues. In these same studies, the generally considered greener option, cotton bags, were also analysed. These cotton bags require 131-149 uses to compensate for the higher GHG emissions of their production than single-use plastics.[18,19] This drives the point even further that the solution to this issue is not eliminating plastic materials but rather redesigning their use.

1.1.1.2 Recycling

The EoL stage of polymers accounts for 9% of all the GHG emissions caused by polymers, so improvements in these processes could significantly reduce the GHG emissions of the plastics industry (**Figure 1.2)**.[9] From the three main disposal processes: incineration, landfill disposal and recycling, the former is by far the most damaging, producing around 60% of all CO_{2e} emitted during the EoL processes, equivalent to 3 t CO_{2e}/t polymer.[10] Even if all the energy produced by the incineration of the polymers was to be recovered, the GHG emissions would amount to 0.9 t CO_{2e}/t polymer. Although polymer recycling is an energy-intensive process that generates about 0.7 t CO_{2e}/t polymer, it is still the most attractive solution towards reducing the GHG emissions of the EoL stage. That is because the process with the highest carbon footprint of the plastics industry is polymer production (**Figure 1.2**).[9] The low CO_{2e} emissions of the recycling process compared to those of polymer production means that substituting the so-called virgin polymers with recycled ones leads to a great offset on the GHG emissions,[18,19] resulting in a decrease of the carbon emissions of around 1.4 kg CO_{2e}/t polymer compared to their current value.[10]

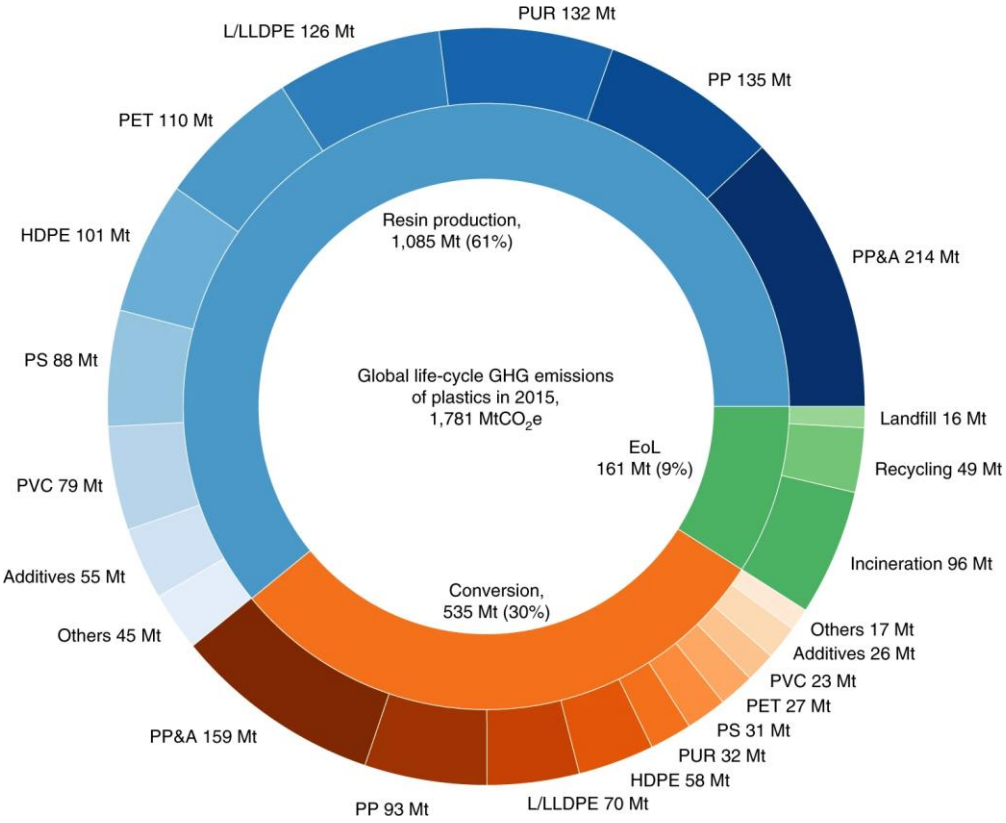

Figure 1.2: Global lifecycle GHG emissions of polymer industries in 2015 by lifecycle stage and plastic type. The different lifecycle stages are divided into resin production (blue), conversion of materials into products (orange) and EoL stages (green). Plastic types: polyphthalamide (PP&A), polypropylene (PP), polyurethane (PUR), low-density polyethylene (L/LLDPE), polyethylene terephthalate (PET), high-density polyethylene (HDPE), polystyrene (PS), polyvinyl chloride (PVC). Image reproduced with permission of Springer.[9]

Despite the highly beneficial contribution that polymer recycling has towards the reduction of GHG emissions, only 30-33% of plastics are recycled.[10,17,22] These low recycling volumes are derived from the limitations of the predominant process, mechanical recycling. In mechanical recycling, polymers are separated into different types depending on their chemical structure and then, shredded, melted, and directly formed into new products. Hence, only thermoplastic materials, which melt without excessive degradation, can be recycled by this process. Moreover, the mixing of products made with the same base polymer but with different formulations (additives, molecular weight, initiators…) inhibits their mechanical recycling, as the newly formed materials lose many of the original properties. This limits the recyclable products to mostly clear polyethene terephthalate (PET) bottles, clear polyethylene (PE) packaging and

white polypropylene (PP) bottles.[22] Moreover, although these materials show little degradation when melted, it is still not zero. Hence the number of cycles that the polymers can be recycled is limited and either some virgin polymer needs to be added to the waste feed to obtain materials with the appropriate properties or the waste products are downsised rather than recycled.[23–26] All these drawbacks restrict the volume of polymers that can be recycled.

To overcome the limitations of mechanical recycling, new processes which solve the issues of thermal degradation and formulation incompatibility are currently being explored. These new processes are usually referred to as chemical recycling as they involve the use of chemical reactions to revert polymers to their monomeric components or to crude oil and gas. The strategies to depolymerise polymers into their monomers are currently only applicable for condensation polymers like polyesters, polyamides, polyethers or polyurethanes, and they involve the use of catalysts to cleave and revert the bonds formed through the condensation reaction usually by hydrolysis.[27] Additionally, crude oil and gas can be obtained from all polymer types by means of three different methodologies: pyrolysis, gasification, and hydrothermal treatment. In both pyrolysis and gasification, the waste materials are heated to high temperatures (≈1000-1500 °C) where they decompose into crude oil. The only difference between both processes is whether they are carried out under O_2 (gasification) or not (pyrolysis). The hydrothermal treatment requires lower temperatures than the previous two processes. Instead, high pressures are used to treat the waste materials with supercritical H_2O.[28–30] Although these chemical recycling strategies are highly efficient at reducing plastic waste, they are not so in terms of GHG emissions. Unlike in mechanical recycling, to generate polymers from chemically recycled monomers, both purification and repolymerisation processes are required. On top of that, all these processes, especially pyrolysis and gasification, demand large amounts of energy.

1.1.1.3 Bio-based polymers

More than 60% of the GHG emissions derived from polymer production are a direct result of the generation of monomers from crude oil.[9,31–33] Therefore, changing crude oil for other more ecological feedstock sources would greatly decrease the GHG emissions of the polymer industry. Accordingly, there is a large interest in the development of biobased alternatives to existing plastics. Biobased polymers are compounds derived from natural products obtained from either plants or bioreactors. For them to be viable their extraction, synthesis and purification need to generate significantly lower GHG emissions than petrochemical monomers. Products that require extensive derivatisation of the biofeedstocks or which involve processes

with high energetic demand are not appropriate for industrial production.[9,34] Although biobased polymers can have a positive impact on the reduction of climate change, they can also harm the environment, as the production of biofeedstocks requires extensive land and water use. With no control over the conditions in which the different crops are grown and harvested, several environmental issues such as soil acidification, eutrophication, or pesticide pollution can occur.[35,36] On top of these environmental issues, the mass production of these biofeedstock crops can also lead to food shortages due to the replacement of vital foodstuff crops.[37] As such, special consideration should be given to the origin and growth conditions of the feedstock crops selected for polymer production.

Biobased polymers can be classified into three different groups: natural polymers, bioengineered polymers and synthetic biopolymers.[38]

1.1.1.3.1 Natural polymers

Both naturally occurring polymers such as cellulose or silk or modifications of them like rayon or cellulose acetate are classified as natural polymers. The GHG emissions from this class of materials are extremely low as there is no need for any polymerisation processes, all that is required is their extraction and, in some cases, derivatisation. Moreover, most of them are highly efficient carbon fixing systems and biodegradable.[39] However, their limited chemical composition restricts their use to just a few applications.

1.1.1.3.2 Bioengineered polymers

Bioengineered polymers are produced by genetically modified microorganisms or transgenic plants. As in the case of natural polymers, they present low GHG emissions as the polymerisation process is carried out by the organisms themselves. However, they exhibit the same drawback as natural polymers, their low versatility. Currently, bioengineered polymers are limited to bacterial celluloses, poly(3-hydroxyalkanoates) (PHA) and polyglutamic acid (**Figure 1.3**).[40]

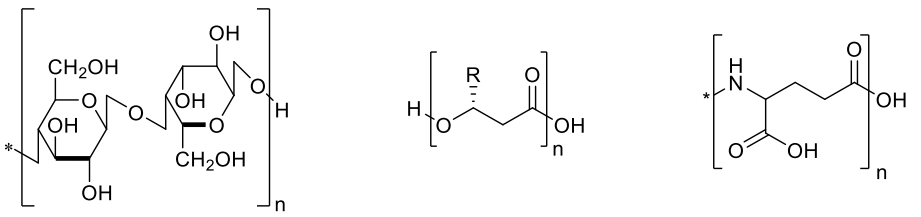

Figure 1.3: Bio-engineered polymers.

1.1.1.3.3 Synthetic biopolymers

Unlike in the two previous classes, synthetic biopolymers are not directly produced by living organisms but rather by standard polymerisation processes in chemical reactors. The difference between synthetic biopolymers and petrochemical polymers lays in the origin of their monomers. On the former, the required building blocks are obtained from natural feedstocks rather than petrochemical sources. This bypasses the need for crude oil extraction and purification, reducing the overall GHG emissions of polymer production. The main advantage of synthetic biopolymers in front of the other two classes is that there is a large number and variety of polymers accessible. On top of that, some of the most produced petrochemical monomers, such as ethylene or terephthalic acid, can be obtained from biofeedstocks (**Figure** 1.4).[35,38,40] As such, most of the efforts of the plastics industry to develop biobased polymers have been centred on the development of biobased monomers.

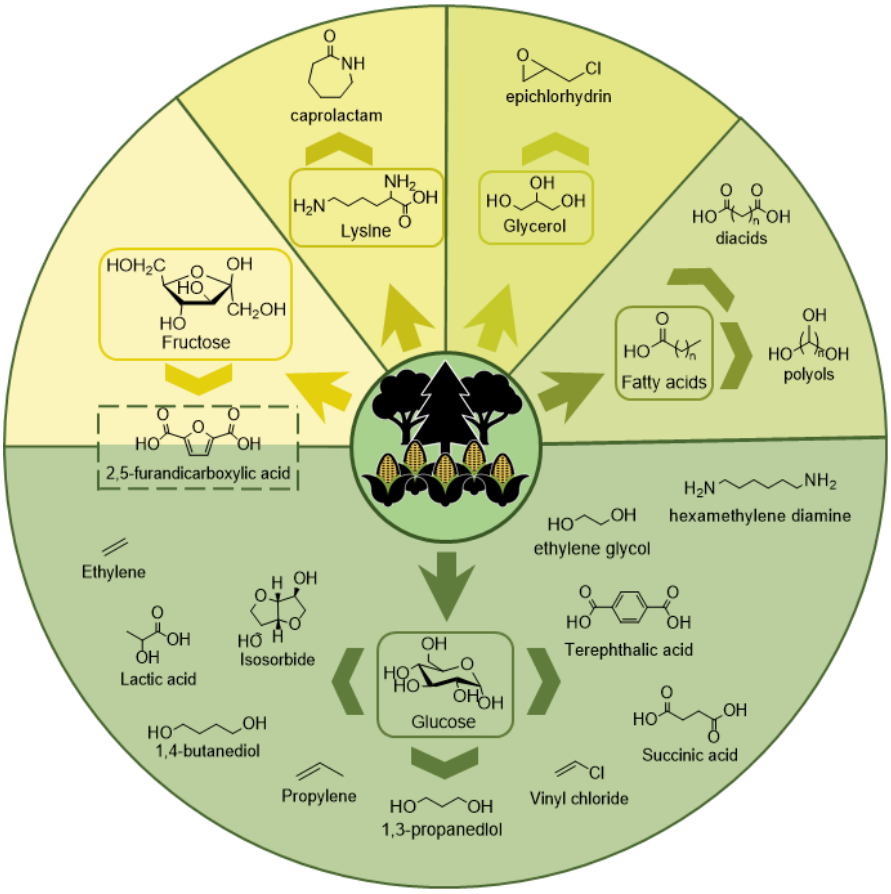

Figure 1.4: Common biobased monomers and their origin.

The exact reduction in GHG emissions when substituting petrochemical monomers with biobased ones differs for each compound, with values that can range from just a 10% reduction to more than 200% (**Figure 1.5**). In some cases, such as polypropylene (PP) or polyethylene (PE), even negative GHG emissions could be obtained, owing to the carbon capture carried out by the crops employed to develop the monomers.[41]

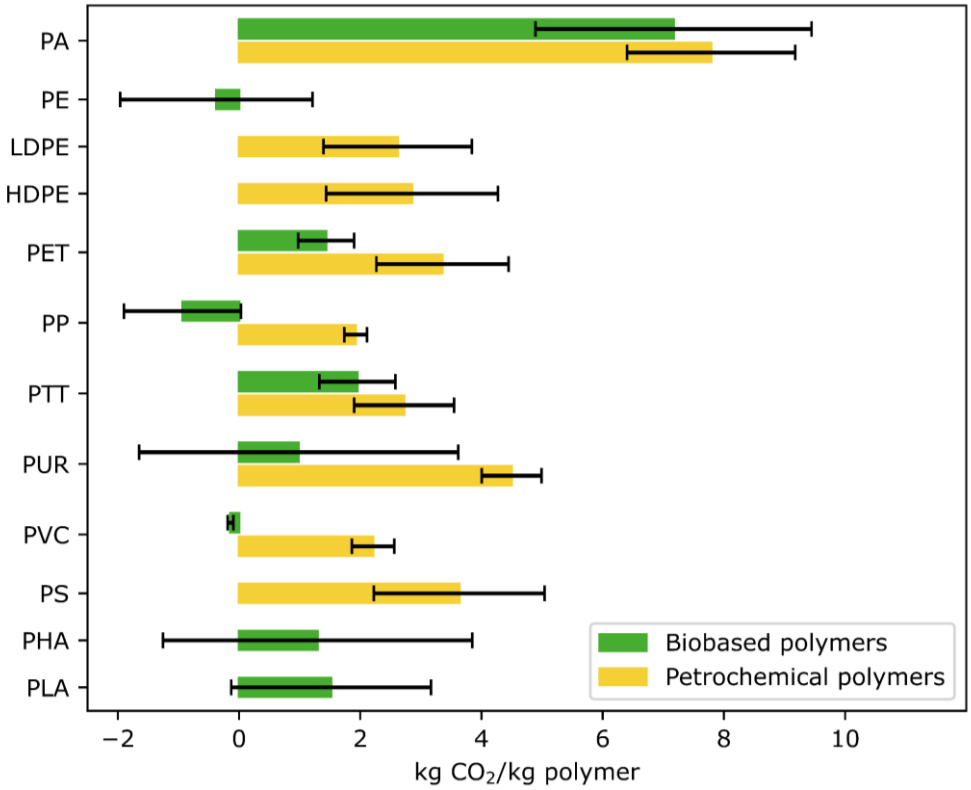

Figure 1.5: Comparison of GHG emissions of some biobased (green) and petrochemical (yellow) polymers. Data extracted from [41]. PA (polyamide), PE (polyethylene), LDPE (low-density polyethylene), HDPE (high-density polyethylene), PET (polyethylene terephthalate), PP (polypropylene), PTT (polytrimethylene terephthalate), PUR (polyurethane), PVC (polyvinyl chloride), PS (polystyrene), PHA (poly(3-hydroxyalkanoate)), PLA (polylactide). Error bars indicate the minimum and maximum global warming potential of each polymer.

These large differences in GHG emissions between the different synthetic biopolymers can be mainly attributed to the diverse synthetic routes used for the biobased monomer synthesis. Some compounds, such as bioethylene require just one synthetic step, while others such as bioterephthalic acid can require up to 5 steps. As such, a proper selection of the synthetic route and the appropriate biobased monomer can lead to huge reductions in carbon emissions.

1.1.1.3.3.1 2,5-furandicarboxylic acid

Although the obtention of 2,5-furandicarboxylic acid (FDCA) from fructose has been known since the early 20th century,[42,43] it has started to gain both industrial and academic interest in the last decade (**Figure 1.6**). This sudden rise in interest has been spearheaded by the investment of the Coca-Cola Company to produce greener plastic bottles.[44]

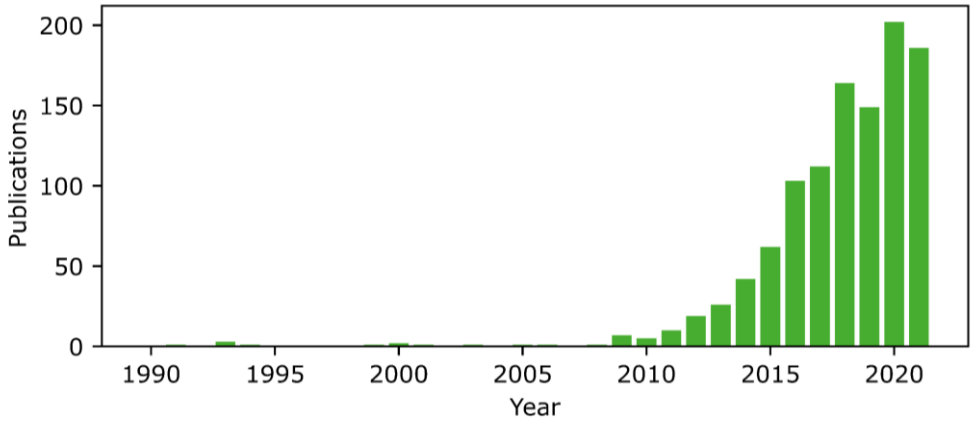

Figure 1.6: Publications containing FDCA by year. Data obtained from WebOfScience. Accessed on September 18th 2022.

FDCA can be used as a substitute for terephthalic acid (TPA) in polyethylene terephthalate (PET). Although TPA has already several synthetic routes from biofeedstocks, its production involves a large number of steps (**Figure 1.7**).[45–49]

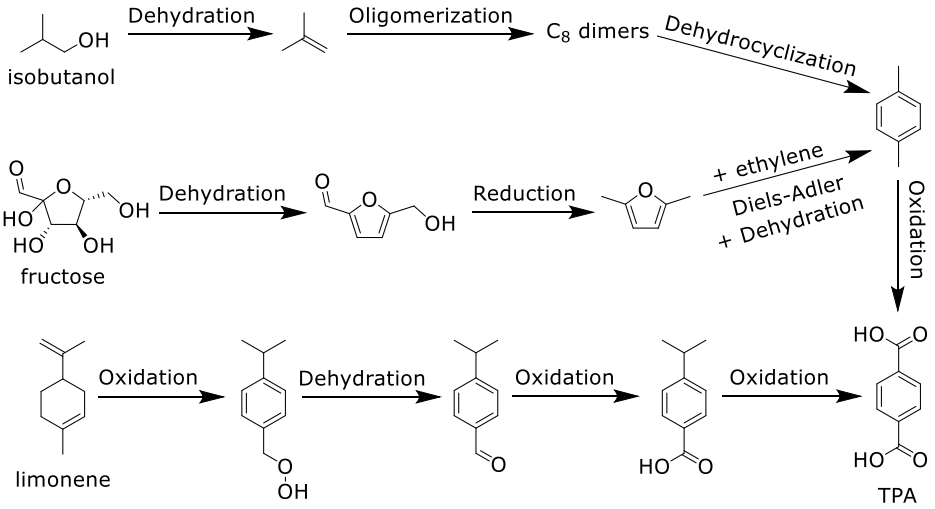

Figure 1.7: Synthetic routes to obtain TPA from biofeedstocks.

On the other hand, the synthesis of FDCA from biofeedstocks requires just 2-3 steps depending on whether the starting material is glucose or fructose (**Figure 1.8**).[50,51] Although the exact amount of CO_{2e} emissions varies greatly between studies, cradle-to-grate LCA studies of bio-FDCA production place their carbon emissions at around 0.5-2.5 $kgCO_{2e}$/eq, 10-50% less than bioPTA.[50–52] Moreover FDCA could be achieved not only from glucose or fructose but also from their complex carbohydrates, like lignin or cellulose.[53,54] This opens the door to a potential use of biomass waste as the origin for the FDCA precursors, which would remove the need of growing crops specifically for the production of the biomonomer, one of the main drawbacks of synthetic biopolymers.

The low GHG emissions of the FDCA synthesis, which could be reduced even further by industrial optimisation of the different steps of the process, coupled with the possibility of employing waste biomass for their development, turn FDCA into an optimal monomer to produce several types of polymers such as polyesters or polyurethanes. This work will be focused on the development of polyester polyurethanes containing FDCA.

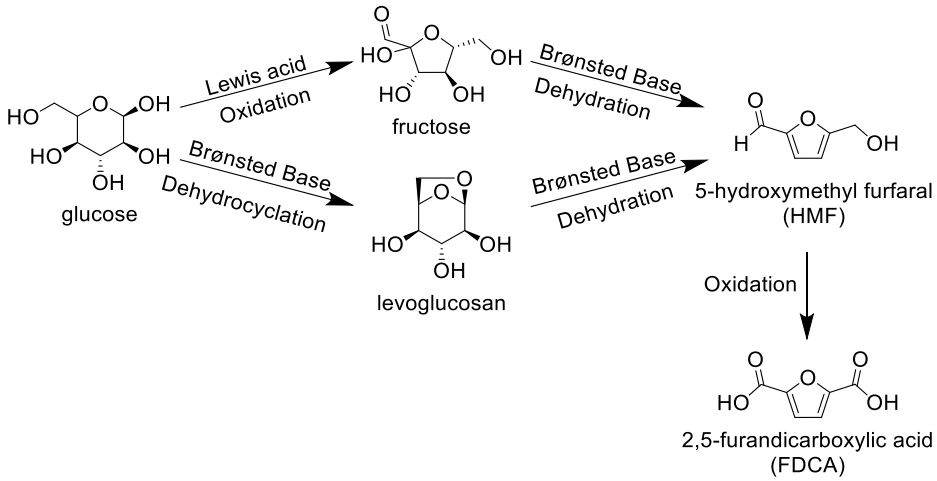

Figure 1.8: Synthetic routes to obtain FDCA from glucose and fructose as biofeedstocks.

1.2 Thermoplastic polyurethanes

Polyurethanes are a highly versatile group of speciality polymers. Traditionally, they are obtained by the reaction of polyisocyanates with polyols through an addition reaction that generates carbamate linkages (**Figure 1.9**). Recently, so-called non-isocyanate polyurethanes, in which the isocyanates are substituted by less toxic compounds have started to be developed.[55] Depending on the nature of polyisocyanate and polyol, elastomers, coatings, adhesives, sealants, shape memory polymers and rigid or flexible foams, can be obtained, with their most extensive application being the latter.[56]

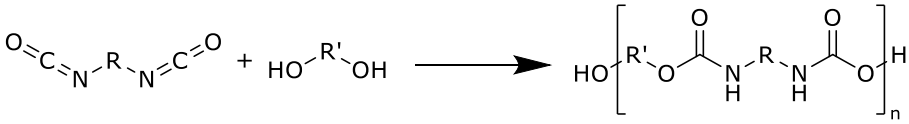

Figure 1.9: Schematic representation of a polyurethane synthesis.

Thermoplastic polyurethanes (TPUs) are a subcategory of random linear polyurethanes typically obtained by the reaction of low molecular weight diols (40-200 g/mol) and high molecular weight diols (>1000 g/mol) with a diisocyanate. The low molecular weight diols, which are referred to as chain extenders (CE), are usually C1-C12 linear or branched alcohols, while the high molecular weight diols can be either polyesters, polyethers or polycarbonates.[57] The presence of both short and long chain alcohols provides TPUs with their most influential characteristic, phase segregation. Phase segregation is the ability of TPUs to form two distinct phases, one called hard segment (HS) and another one named soft segment (SS) (**Figure** 1.10). These two phases are mainly differentiated by one factor, their diisocyanate content. The HS phase is essentially constituted of chain fragments enriched in diisocyanate and CE. Hence, this phase contains an elevated concentration of carbamate moieties. These carbamate groups act as both H-bond donors and acceptors, and as such induce order onto the HS chain fragments, producing a highly crystalline domain. On the other hand, the SS phase is enriched in polyol. Therefore, it tends to be less ordered as its chain packing is governed by relatively weak Van der Waals interactions. Nevertheless, its crystallinity is highly dependent on the nature of the chosen polyol.[58,59]

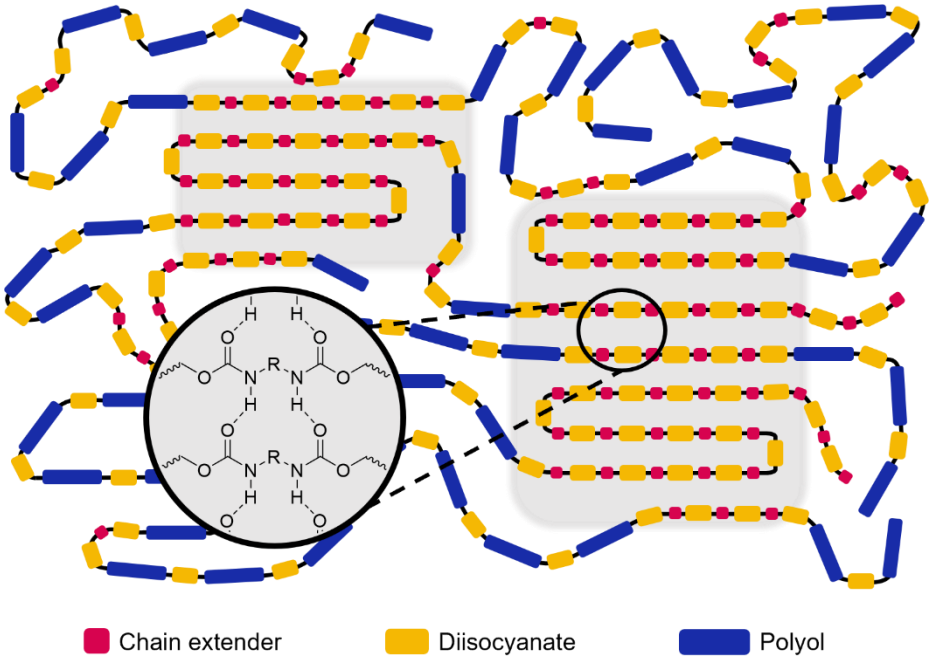

Figure 1.10: Representation of phase segregation on TPUs. HS in grey, SS in white.

The phase segregation, as well as the morphology and crystallinity of each phase, plays a crucial role in determining the properties of the materials. Hence, to understand and correlate changes in composition or processing of the material with its final properties, it is crucial to discern how each factor affects the microstructure of TPUs.[60–63]

1.2.1 Hard segment

The HS is composed of two different components, the diisocyanate and the CE. However, not all the diisocyanate and CE moieties are part of the HS phase. Rather, a crucial distinction needs to be made between HS domains and HS content. HS domains comprise the portion of CE-diisocyanate chain fragments that are ordered by H-bonds and thus, form a distinct phase. However, this definition is not the one usually employed when talking about which is the HS content of the material. As the degree of phase segregation of TPUs is impossible to predict before their synthesis, HS content values obtained from the composition of the polymer are used. Depending on the case, HS content is referred to as the total weight percentage of diisocyanate and CE in the material, the weight percentage of the CE and its equivalent diisocyanate, or as the molar percentage of CE and its equivalent diisocyanate. In this work,

the latter definition, called from now on HS (mol%), will be used (**Equation 1.1**).[56] When a 1:1 NCO:OH ratio is employed, this expression can be simplified to HS (mol%) = mol CE/mol DI.

$$\text{HS (mol\%)} = \frac{\text{mol CE} + \text{mol DI}_{\text{CEeq}}}{\text{mol CE} + \text{mol Polyol} + \text{mol DI}}$$

Equation 1.1: Definition of HS comtent (mol%). DI: diisocyanate, DI_{CEeq}: diisocyanate equivalents to CE.

Owing to its high crystallinity and strong supramolecular interactions, the HS phase has a very high influence over the hardness and tensile strength of the material. As a rule of thumb, high HS contents result in hard materials with a high modulus, but low maximum elongations. Moreover, changes in HS content also modify the morphology of the phases. Similarly to other block copolymers, the system evolves from a micellar-like dispersion when there is a large proportion of one of the two components to a lamellar morphology when both phases are present in similar volume fractions (**Figure 1.11**).[64,65] This difference in morphology affects the properties of the final polymers. Materials in which the HS phase is continuous show better tensile properties but lower elastic recoveries than those with disperse HS domains.[66,67]

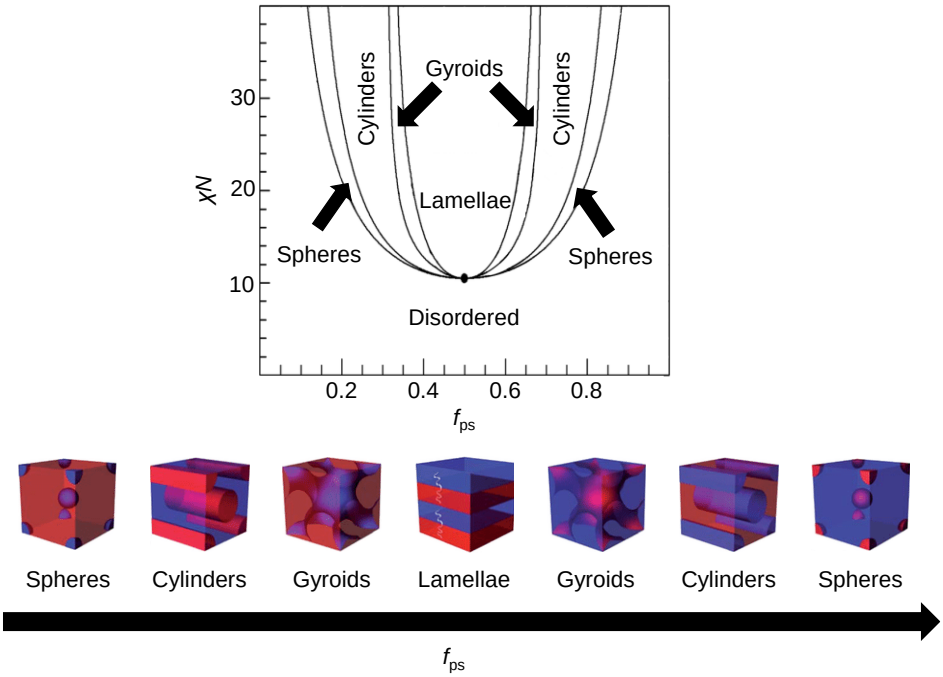

Figure 1.11: Phase diagram of linear diblock copolymers as predicted by self-consistent mean-field theory. χN=degree of phase segregation, f_{ps}= volume fraction of one block. Adapted with permission of RSC.[68]

Furthermore, the chemical nature of each of the HS components and their distinct interaction with the SS can change the overall phase segregation and morphology of the TPU, leading to many effects on the final properties of the material.

1.2.1.1 Diisocyanate

The diisocyanates employed on TPUs can mostly be split into two different families, aliphatic or aromatic (**Figure 1.12**). Generally, aromatic diisocyanates produce stiffer, harder, more crystalline polyurethanes. This is due to two factors: their lower flexibility and their ability to form not only H-bonds but also π-π stacking interactions, leading to a tighter HS chain packing. In contrast, aliphatic diisocyanates generate softer polyurethanes with lower crystallinity. Moreover, aliphatic polyurethanes tend to be transparent as they do not form big crystalline structures capable of interacting with light. This lower crystallinity is even greater in the case of isophorone diisocyanate and 4,4'-dicyclohexilmethane diisocyanate as their steric hindrance inhibits segment packing.[69–73] Another factor that contributes to the crystallinity of the HS domains is the linearity of the diisocyanate. It has been observed that linear diisocyanates enhance the phase segregation of the material as they can achieve a high HS domain aggregation owing to their high symmetry.[74]

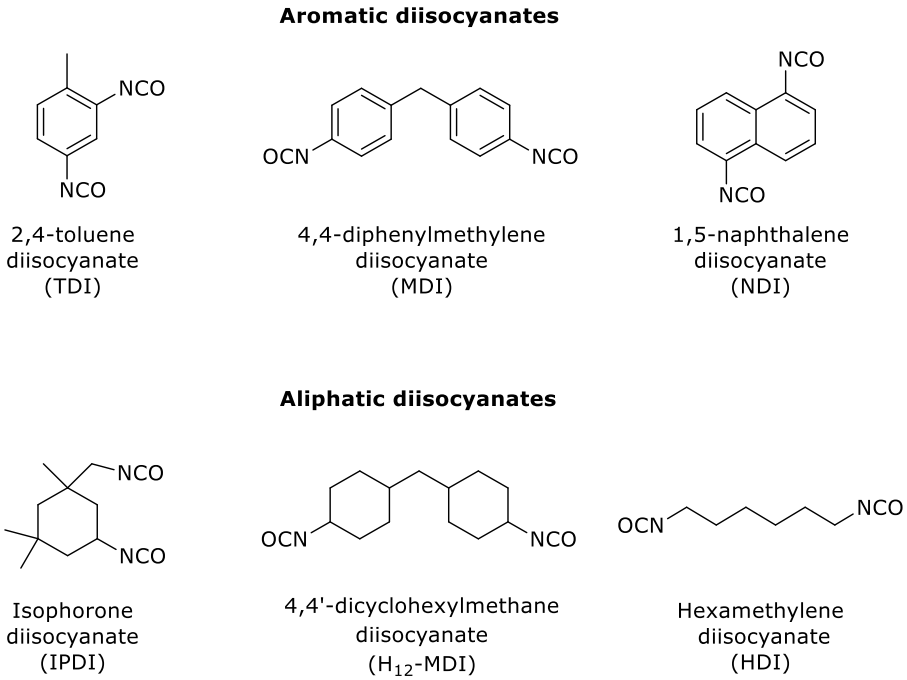

Figure 1.12: Most common diisocyanates used on industrial TPUs.

Thermodynamically, the phase segregation in aromatic diisocyanate TPUs should be higher than that of the aliphatic monomers owing to their stronger supramolecular interactions. However, if the kinetics of the phase segregation process are considered, an inversion of this behaviour can occur. Their stronger supramolecular interactions of the aromatic HS than those of their aliphatic counterpart, coupled with their high rigidity hinder the movement of the HS chain fragments inside the polymeric matrix. This entails that the phase segregation of aliphatic diisocyanates can be in some cases, higher than that of the aromatic ones, especially when chain mobility is the limiting factor.[75] Nonetheless, regardless of the nature of the TPUs' HS, the higher the degree of phase segregation, the higher the tensile strength and hardness of the materials.[76] Additionally, the stronger supramolecular interactions and rigidity of aromatic diisocyanate TPUs in comparison with the aliphatic ones, also influence the melting temperature (T_m) and glass transition temperature (T_g) of the HS phase, increasing the energy required to achieve said phase transitions.[72,77]

To sum up, aromatic diisocyanates lead to stiffer polyurethanes with higher tensile strength, HS T_m and T_g, and lower maximum strains than aliphatic diisocyanates. However, all of this can be inverted depending on the nature of the SS phase, its compatibility with the HS phase and the overall chain mobility of the system.[78,79]

Setting aside the mechanical and thermal properties of the materials, another key difference between aromatic and aliphatic diisocyanate TPUs is their chemical stability and resistance to UV radiation. Aliphatic TPUs are the clear winners regarding stability. Their carbamate bonds are way more resistant to nucleophilic attacks owing to the lower electrophilicity of their sp^2 carbon. This lower electrophilicity is derived from the superior capabilities of the carbamate's nitrogen to act as an electron donor (**Figure 1.13, red**). On aromatic polyurethanes, the aromatic moieties act as electronsinks, reducing the electron density of this nitrogen by resonance (**Figure 1.13, blue**), something that cannot happen on aliphatic diisocyanates.[80]

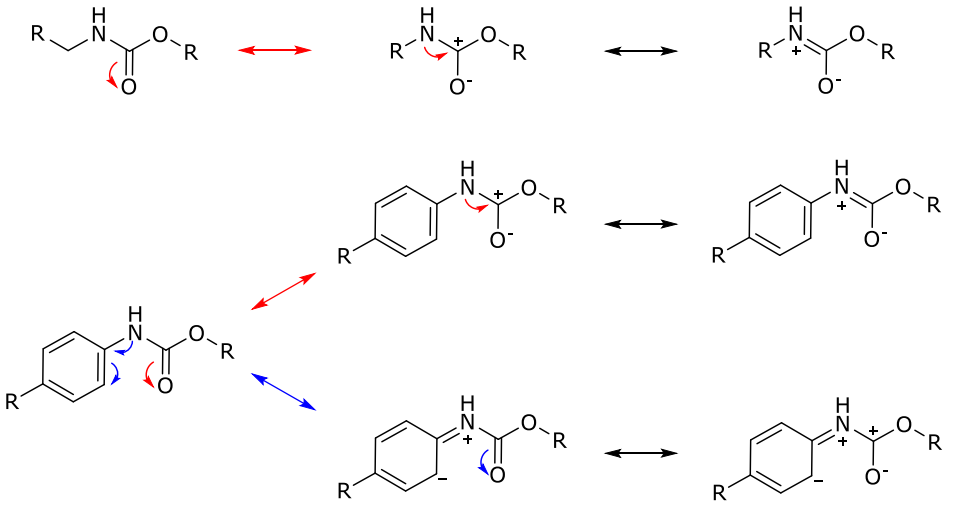

Figure 1.13: Difference in nucleophilicity due to resonant effects on aromatic *vs* aliphatic diisocyanates.

Likewise, aliphatic diisocyanates are more stable under UV radiation. The first step in the UV degradation pathway involves the generation of free radicals. These free radicals are usually generated from π electrons and as such, they are more easily obtained on aromatic than on aliphatic polyurethanes.[81] Moreover, the photodegradation of aromatic diisocyanates generates quinonoid structures, which induce a yellowing of the material. Thus, aromatic polyurethanes are unsuitable for applications in which prolonged sun exposure is required.[82]

1.2.1.2 Chain extender

Chain extenders (CE) can also be classified into two different classes: linear and ramified diols (**Figure 1.14**).[83–85] As expected, the latter hinders the chain packing of the HS phase due to their steric hindrance, producing less crystalline HS than linear diols. The reduction in crystallinity results in softer materials with lower HS T_m and T_g and tensile strengths.[86]

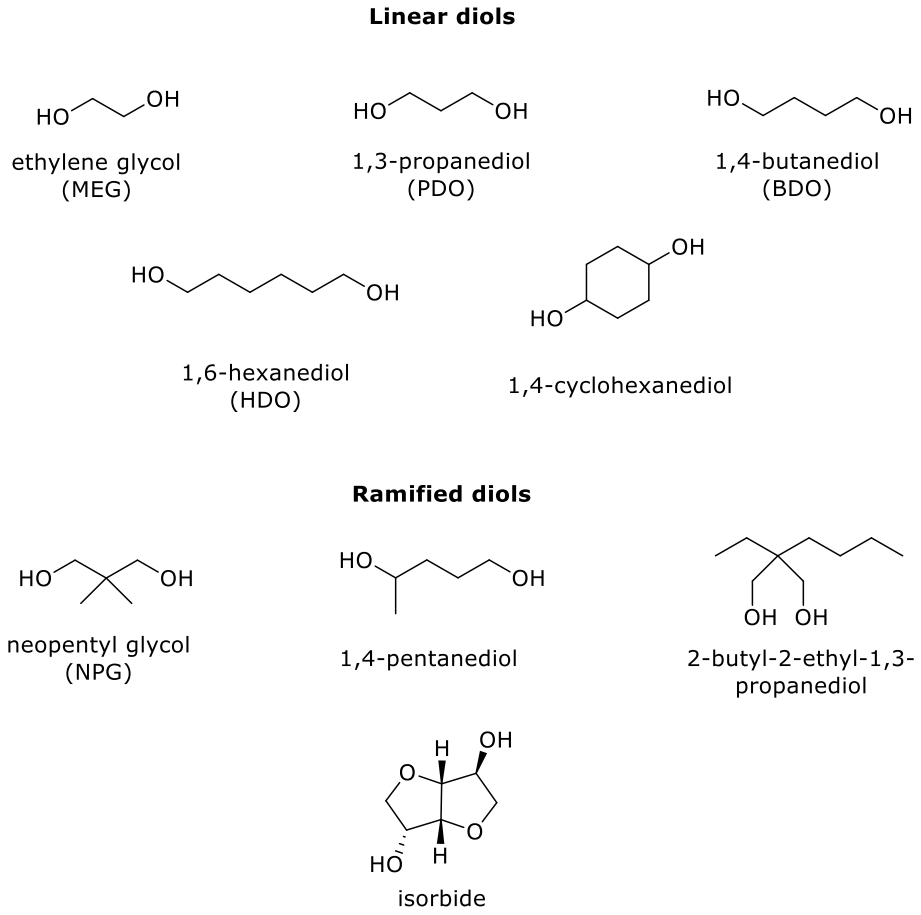

Figure 1.14: List of most common CE used industrially.

A less obvious parameter that affects the final crystallinity of the HS is whether the number of atoms between the alcohol groups on the CE is odd (odd-CE) or even (even-CE). In 1981, a study by Blackwell *et al.* [87] observed by X-ray measurements that on MDI TPUs even-CE could adopt their fully extended conformation while odd-CE adopted a contracted conformation. This difference in morphology is produced by the restrictions to the CE conformation required for the formation of the H-bonds from the two carbamate groups the CE is linked to. For even-CE, both carbamate groups can form H-bonding interactions with another chain fragment with the diol fragment fully extended in *anti*-conformation. Contrarily on odd-CE, the diol chain needs to adopt a *gauche*-conformation so that these two carbamate groups can interact appropriately to form both H-bonds (**Figure 1.15**).[88] Consequently, even-CEs produce HS with a higher

crystallinity than odd-CEs, giving rise to products with higher tensile strength, hardness, and HS T_m and T_g values.[89,90]

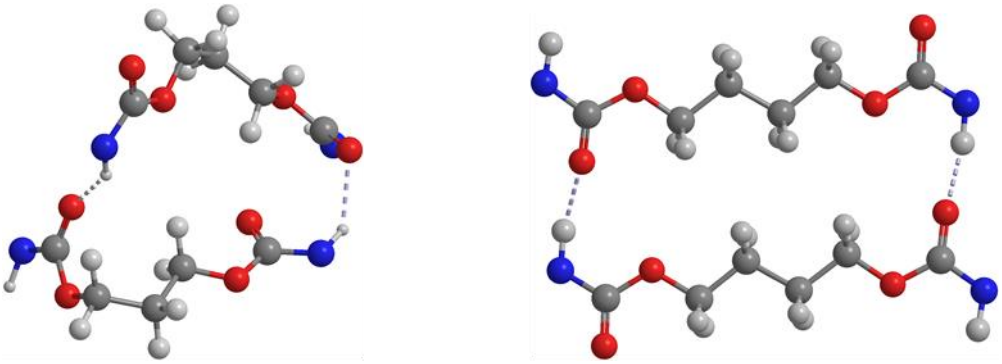

Figure 1.15: Diol conformations of odd-diol HS (*anti-gauche-gauche-anti*) and even-diol HS (*anti*).

1.2.2 Soft segment

The soft segment (SS) phase constitutes the bulk of the material and is predominantly composed of long-chain diols linked by diisocyanates. Its main role is to act as a disordered rubbery matrix between HS phases, decreasing the overall crystallinity of the polymer. Hence, TPUs usually are softer and more elastic the higher SS content they have.[91] Additionally, as the SS phase comprises the most abundant component of the polymer, it is responsible to determine the main T_g of the material. The value of this transition temperature is highly influenced by the morphology of the polyol. As can be expected, ramified polyols difficult the chain packing of the SS, reducing to a great extent its interaction capabilities, thus decreasing T_g. For this reason, ramified polyols are used when soft flexible materials are desired.[56] The T_m of the SS is modified in the same manner, with ramified polyols producing lower T_m than the linear ones.

SS and HS cannot be considered in a vacuum, as the nature of the SS phase plays a huge role in the phase segregation of the system and in the crystallinity of the HS. Just as in the case of the CE, the odd-even effect of the polyol affects the packing of both the HS and SS. Following the same trend as in the CE, when the repeated unit of the polyol consists of an even linear atomic length, the crystallinity of both HS and SS is enhanced as the maximum chain packing is achieved.[92] This is boosted even further by the fact that the polyols by themselves already show odd-even effect following the same trend as TPUs. The crystallinity of the polyol is enhanced when the atomic length of the monomeric unit (the diacid-diol/diol-diol pair in the case

of polyesters/ polycarbonates) is even.[93,94] This increase in chain packing leads to higher T_m and T_g of both HS and SS phases and to stiffer polymers with higher tensile strength and lower maximum strains.

The degree of phase segregation of the system is also affected by the molecular weight of the chosen polyol. Generally, the higher the molecular weight of the polyol is, the higher phase segregation is obtained. This is caused by a reduction of the entropy of mixing between the HS and SS domains when the polyol length increases.[95]

The chemical nature of the SS can also affect the chain mobility of TPUs. SS phases with restricted chain mobility act as barriers to the formation of HS crystallites as they inhibit the movement required by the HS chain fragments to interact and order themselves.[96,97] Additionally, depending on the miscibility between both domains, higher or lower degrees of phase segregation can be obtained. If the energetic difference between the HS-HS and HS-SS interactions is not high enough, the phase segregation phenomenon might be prevented or limited in some manner. Therefore, polyols with different chemical makeups will induce striking changes to the internal structure of the TPUs.[98,99]

The SS phase is usually divided into three categories according to the nature of their polyol: polyethers, polyesters and polycarbonates.[56,91] Each type can interact differently with the HS phase, leading to differences in phase segregation.

1.2.2.1 Polyethers

Polyethers are one of the polyols families employed on SS. The most common type of polyethers used in polyurethanes are branched or linear aliphatic polyether-diols with a molecular weight of 1000-3000 g/mol (**Figure 1.16**).[56]

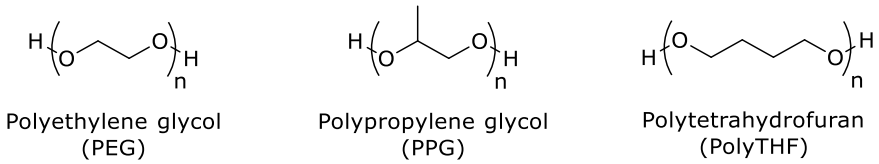

Figure 1.16: Common polyethers used on TPUs.

These polyethers are usually generated by the ring-opening polymerisation of cyclic ethers, typically tetrahydrofuran or epoxide derivatives, by using a difunctional diol as an initiator (**Figure 1.17**).[80]

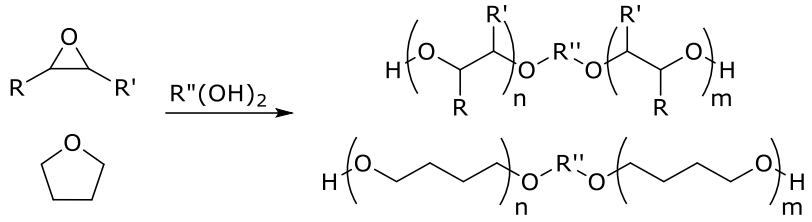

Figure 1.17: Polyether synthesis by ring-opening polymerisation of cyclic ethers.

Polyether SS generally produce polyurethanes with high degrees of phase segregation. The ether group is a poor H-bond acceptor and thus, mainly weak Van der Waals interactions are generated between the HS and SS phases, which leads to a low phase miscibility.[79,101,102] Moreover, the weak dipole moments on the polyethers cause a poor packing of the SS, inducing a highly disordered SS structure. This is correlated with materials with a very low T_g, which accordingly remain flexible at very low temperatures.[78] Furthermore, the amorphous nature of the SS provides the materials with good rebound resilience properties as they can act as ideal elastomers without storing much of the induced deformation as new supramolecular interactions.[103–105] This comes at a cost of the maximum strains the material can withstand, as the cohesion interactions among the SS chains are weak.[79] Their low tensile strength is in contrast with their high phase segregation, by which the materials should have a high modulus. This shows that phase segregation is not the only factor needed to understand the mechanical properties of TPUs. Although the rule of higher phase segregation leads to higher maximum modulus still applies within the polyether family,[106] the disordered nature of the SS offsets this behaviour when comparing polyethers with the other SS types.

One of the main advantages of polyether polyurethanes is their chemical stability. The low polarisation of the ether linkages means that they are resistant to both electrophilic and nucleophilic attacks. For this reason, these kinds of polymers are usually selected for biomedical applications as they will not experience a fast degradation under physiological conditions. However, polyether polyurethanes perform badly when in contact with organic solvents. The poor supramolecular interactions and chain packing of their SS entails that they swell or dissolve easily with organic solvents, oils, or vapours, losing many of their properties in the process.[107]

1.2.2.2 Polyester

The second big family of macrodiols employed in the SS are polyesters. This group of compounds includes both products obtained from direct condensation reactions of dicarboxylic acid derivatives and diols as well as the ring-opening polymerisation of lactones (**Figure** 1.18).[108,109] Although these structures can present a great deal of variability, as there is a large library of available dicarboxylic acid derivatives and diols, the most common are those obtained from the polymerisation of C2-C12 aliphatic dicarboxylic acid derivatives with C2-C12 aliphatic linear or branched diols.[56,78,79]

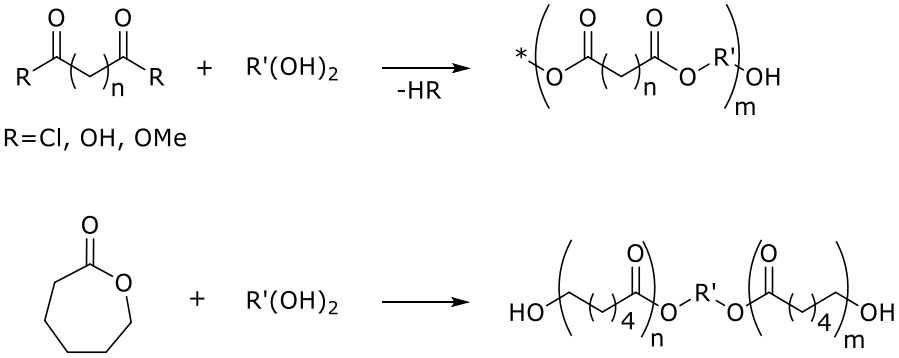

Figure 1.18: Common synthetic routes for the obtention of polyesters.

Unlike as in polyether polyurethanes, the interaction between HS and SS in polyester polyurethanes is not limited to weak dipole-dipole interactions but rather H-bonds can be generated between the carbonyl of the esters and the carbamates on the HS.[109] Therefore, phase segregation is lower for polyester than polyether polyurethanes, as the miscibility between the HS and SS domains is greater for the polyester-based TPUs than the polyether-based ones.[79,96,101] Additionally, the higher dipolar moment of the ester groups compared with that of ethers also entails that the cohesion forces and interactions among SS chains are stronger, promoting their crystallisation.[78] For these reasons polyester polyurethanes are the go-to TPU materials when high tensile strength and abrasion resistance are required. Moreover, the high HS-SS miscibility and cohesion strength of the polyester SS results in materials with high T_g and T_m.[78,79] However, the high polarisation of the carbonyl bond leads to one of the biggest drawbacks of polyester SS, their poor hydrolytic resistance. The carbonyl group is a relatively good electrophile, especially if compared to the ether moiety, and can be cleaved under mild conditions. Moreover, the presence of esterases in biological systems limits their use as medical implants as the lifetimes of the materials are highly reduced

by the enzymatic activity.[110,111] All these properties tend to increase the more ester moieties are present on the polymer structure, as the polarity and crystallinity of the SS phase increase.[112]

1.2.2.3 Polycarbonates

Polycarbonates complete the list of compounds typically employed as polyols on SS. Although the most common polycarbonates in the polymer industry are those based on bisphenol A, on polyurethanes, their use is limited. Rather, aliphatic polycarbonates derived from 1,4-butanediol or 1,6-hexanediol are the most employed. Polycarbonates were traditionally obtained from the reaction of alcohols with phosgene or dialkyl or diphenyl carbonates derived from phosgene (**Figure 1.19**).[113]

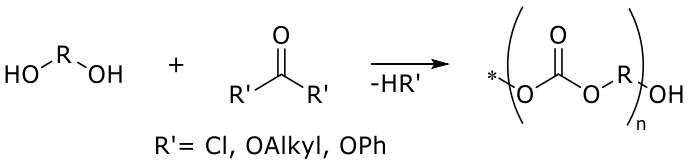

Figure 1.19: Synthesis of polycarbonates from phosgene.

However, in 1995, the Asahi Kasei Corporation developed a new synthetic route in which diphenyl carbonate is generated from CO_2 and ethylene oxide, removing the need for the highly toxic phosgene (**Figure 1.20**).[114,115]

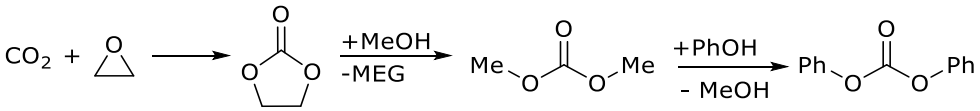

Figure 1.20: Asahi Kasei Corporation route to diphenyl carbonate from CO_2.

Polycarbonates show the lesser phase segregation and HS crystallinity of all typical SS structures since the carbonate moiety is the strongest H-bond acceptor from the different polyol types previously discussed.[116,117] Moreover, polycarbonate SS show poor crystallisation abilities due to the repulsion of the big electron-rich region generated by the three oxygen atoms of the carbonate.[86] This leads to a highly disordered system in which few SS or HS crystallites are formed. The lack of crystalline structures grants them high transparency since visible-light radiation does not get dispersed when traversing the material.[116] In addition, the weak cohesion forces of the SS domains concede poor abrasion resistance to the material,[118] while their strong H-bonding interactions grant them high tensile strength.[104] Likewise, the strong SS-HS

interactions produce materials with high T_g, as expected for materials with low phase segregation.[120]

1.2.3 Synthetic procedure

Chemical composition is not the only factor that determines the microstructure and properties of TPUs. A proper selection of the synthetic procedure can aid in either increasing or diminishing the phase segregation and crystallinity of the material, leading to polymers with different properties but with the same chemical composition.[121,122]

Depending on the order in which the reagents are added, all at once (one-step polymerisation) or sequentially (two-step polymerisation) two synthetic procedures arise.

1.2.3.1 Two-step polymerisation

In the two-step polymerisation or prepolymer synthesis of polyurethanes, first, a diisocyanate end-capped prepolymer is obtained from the reaction of the polyol with an excess of diisocyanate either in bulk or dissolved in a polar non-protic solvent. Afterwards, a fraction of the prepolymer is titrated with di-*n*-butylamine using bromophenol blue as an indicator following the ASTM D2572-19 standardised procedure to obtain the molal percentage of unreacted isocyanate groups.[123] Finally, during the so-called chain extension step, the corresponding CE and in some cases, extra diisocyanate, are added to the reaction mixture to generate the final polymer.[78]

The stepwise addition of the reagents leads to the formation of HS segments with low molecular weight, including a large proportion of fragments containing a single CE unit. The generation of these short HS chain fragments is driven by the elevated concentration of the prepolymer units compared to that of free diisocyanate at the beginning of the chain extension step.[122] Short HS fragments have a higher miscibility with the SS matrix than larger ones, to the point where HS chain fragments with a single diisocyanate-CE unit are unable to segregate.[63] Hence, the two-step polymerisation process generates polymers with a low degree of phase segregation and a poor HS domain crystallinity.[95,122]

In addition to the HS length, another factor that depends on the synthesis procedure is the polydispersity of the HS fragments. This attribute can be modified by changes in the chain extension step. If no additional diisocyanate is incorporated, the system evolves towards a more monodisperse distribution of the HS chain fragments, while the addition of diisocyanate leads to higher polydispersities. As high HS polydispersities result in products with a low HS

crystallinity, the amount of diisocyanate added during the chain extension step can be employed to fine-tune the desired properties of the materials. [122,124]

Overall, the two-step polymerisation process produces TPUs with low phase segregation and poor HS crystallinity which can be slightly modified depending on the chain extension step.

1.2.3.2 One-step polymerisation

The one-step or one-shot synthetic procedure consists of the addition of all reagents: polyol, CE, diisocyanate and additives, at once into the reaction vessel, usually under solvent-free conditions.[125] Therefore, the reaction is controlled by the diffusion of the species in the media and by their differences in reactivity. Opposite to the prepolymer process, the formation of mono-diisocyanate HS fragments is not favoured. On the contrary, the formation of large HS fragments is favoured since the initial reaction rates of the CE with the diisocyanate are higher than those of the polyol. This is a consequence of the higher mobility of the CE within the reaction mixture and its higher miscibility with the diisocyanate than that of the polyol.[122,126,127] As discussed before, longer HS chain fragments generate materials with higher phase segregations hence, the one-step polymerisation method produces TPUs with high crystallinity and phase segregation.[63,95,122]

1.2.4 Thermal treatment

As aforementioned, although phase segregation is a thermodynamically favourable process, the restricted chain mobility of the TPUs can inhibit it due to kinetic effects. This kinetic obstruction is especially relevant in the most common TPU processing methods, injection, extrusion and 3D printing.[128–130] During these procedures, first the materials are melted, obtaining a homogeneous mixture without any kind of segregated microstructure.[131–133] Then, they are cooled down in the shape of the corresponding product, which results in phase segregation and the formation of the HS crystallites.[134,135] This decrease in temperature is usually accomplished in the range of seconds to maximise product production, which stunts phase segregation of the material and the growth of crystallites. Although TPUs can, given enough time, evolve by themselves and increase their phase segregation and crystallinity to reach a more stable state, this process can be slow, especially in materials with low chain mobility. Hence, the application of an elevated temperature during a given time, called thermal annealing, can aid in reaching the segregated, more stable state. The effectivity of the thermal treatment is highly dependent on the selected temperature as strikingly different phase morphologies can be obtained depending on the conditions. When annealing is performed just

above the T_g of the materials, chain mobility is enough to induce phase segregation, which rapidly increases. However, no changes in the crystallisation of the HS are observed, as the chains are too restricted to properly align themselves in an ordered manner. As annealing temperature rises, phase segregation starts to diminish as the miscibility between the HS domains in the SS matrix increases. Phase segregation decreases until the microphase transition temperature (MST) is reached, upon which, all of the HS chain fragments become mixed with the SS regardless of their size. The first HS chain fragments that become soluble within the SS matrix during the annealing procedure are those of smaller size, and as temperature rises, bigger and bigger fragments are dissolved until the MST is reached. This size-dependent solubilisation generates a new value, the critical sequence length (N_D), which is the lowest HS size that is capable of remaining segregated from the SS at a given temperature. The rise in annealing temperature not only decreases phase segregation but also increases HS crystallinity and crystallite size. Following a process reminiscent to the Ostwald ripening, the smaller, less crystalline HS crystallites and paracrystals unravel, and their HS chain fragment with a size higher than N_D, and that therefore are not miscible with the SS, get incorporated into already existing crystalline HS fragments, which act as nucleation sites. In disperse HS systems, this process is carried out in an anisotropic manner, as crystallite growth is favoured in one axis of the crystal, the direction of the H-bonding interactions. This means that spherical HS domains grow into elliptical ones and that elliptical systems grow in length, but not much in width. In addition to reducing the number of HS domains, the employment of high temperatures during the annealing process also enhances the crystallinity of the HS domains, as the increase in chain mobility enables their ordering.[134,136–138] These characteristics of thermal annealing give rise to two different property optimisations. To increase the ultimate tensile strength of the materials, annealing at low temperatures can be applied to increase phase segregation. On the other hand, high temperatures can be applied to the system to increase their crystallinity and thus, the resilience of their mechanical properties to temperatures, albeit at a cost of the maximum tensile strength and strain of the material.[61]

1.3 Characterisation techniques

The extraordinary complexity of TPUs requires the employment of a great number of different characterisation techniques to understand their chemical structure, supramolecular organisation, phase morphology, crystallinity, and mechanical properties.

Hereinafter, an introductory look into the techniques employed during this work will be presented, focusing on their specific application in the TPU field and the related polymeric systems.

1.3.1 Infrared spectroscopy

Infrared (IR) spectroscopy is a class of vibrational spectroscopy that employs the vibration modes of functional groups to extract information about the composition and structure of the analysed sample. Specifically, IR spectroscopy is capable of extracting information from vibration modes in which there is a change in the dipolar moment. Although IR radiation ranges from 14000-10 cm^{-1}, most standard IR analyses are performed in the mid-IR region of 4000-400 cm^{-1}, where the fundamental vibrations and rotation-vibrations are located.[139,140]

The main use of IR spectroscopy in the polyurethane field is to control the evolution of the condensation reaction and ensure that no free diisocyanate is present in the final product. This is achieved by monitoring the signal corresponding to the unreacted N=C=O stretching absorption at 2300-2200 cm^{-1} (**Figure 1.21**). Moreover, by observing the presence or lack thereof of the O-H stretching band between 3200-3400 cm^{-1} the consumption of both polyol and CE can be ascertained.

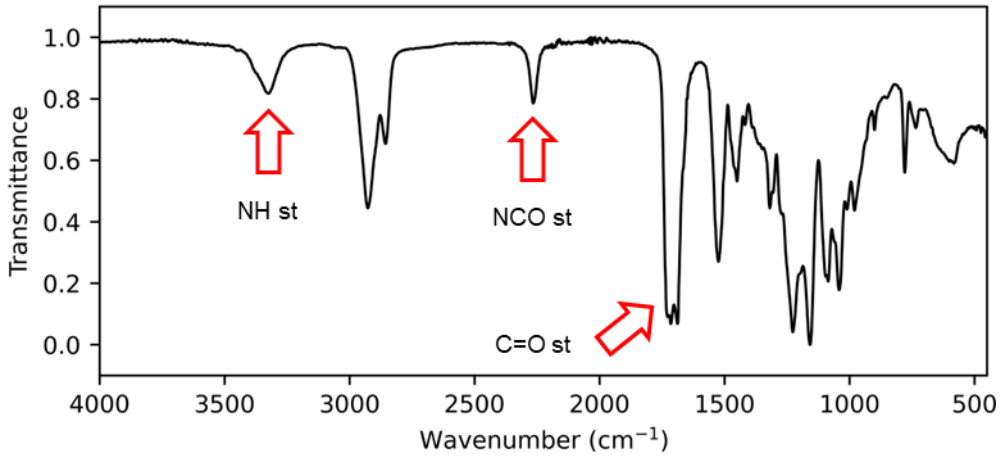

Figure 1.21: Most significant bands of a polyurethane IR spectrum.

Some authors propose IR spectroscopy as a fitting technique to analyse the degree of phase segregation of TPUs through the deconvolution of the region attributed to the C=O stretching around 1700 cm^{-1}. It has been proposed that the peaks from the H-bonded and non-H-bonded carbonyl groups can be identified and accurately integrated by the deconvolution of the region. This would allow the quantification of the carbamates that are interacting with one another through H-bonds. As most of the carbamate H-bond interactions take place on the HS, the ratio between the areas of the H-bonded and non H-bonded C=O deconvoluted peaks could be employed as an estimation of the degree of phase segregation of the TPUs. In the most straightforward case, where polyethers are employed as polyol, there is only one kind of carbonyl group present, the carbamates. Therefore, the deconvolution of the C=O band is quite simple, yielding only two peaks.[118,141] When polyester or polycarbonate polyols are employed, the complexity of the deconvolution increases, as two different types of carbonyl groups, carbamates and esters or carbonates, each one with their respective H-bonded and non-H-bonded forms are present in the structure.[142,143] Moreover, there is not a clear consensus about how many forms each carbonyl group presents. Although some authors propose the presence of two distinct peaks, the already mentioned H-bonded and non-bonded C=O st, others suggest the existence of three different forms, non-bonded, disordered H-bonded and ordered H-bonded C=O st (**Figure 1.22**).[144–147] The discrepancies between authors and the finicky nature of the line-base selection and deconvolution process has made us discard the use of IR spectroscopy as a tool for the quantification of the phase segregation of the system.

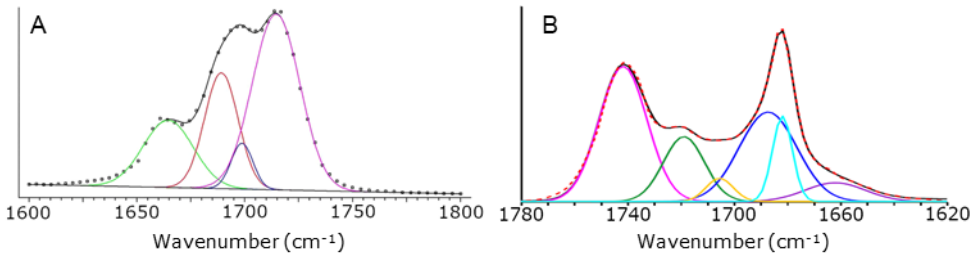

Figure 1.22: Examples of the deconvolution of the carbonyl region of IR spectra from TPUs. A. Deconvolution of a C=O stretching region with 2 peaks by each carbonyl type, H-bonded and non-H-bonded.[143] B. Deconvolution with 3 peaks by each carbonyl type, ordered H-bonded, disordered H-bonded and non-H-bonded.[144]

1.3.2 Gel permeation chromatography

Gel permeation chromatography (GPC) is one of the most used techniques for the determination of the molecular weight and polydispersity of macromolecular compounds. As all chromatographic techniques, it consists of the interaction of the sample dissolved in a mobile phase with a stationary phase. In the case of GPC, the stationary phase is a size-exclusion column made out of a mesoporous gel capable of separating compounds by their size, more specifically by their radius of gyration, which is related to the molecular weight of the compounds. Small species have an increased residence time inside the column as they are capable of diffusing deeper into the gel pores. As such, big compounds will be eluted first and the smallest ones last (**Figure 1.23**).[148,149]

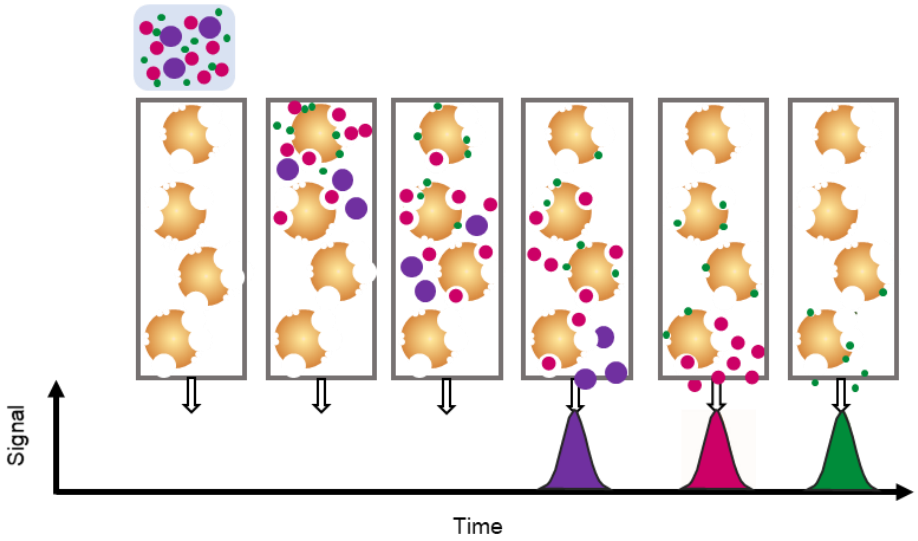

Figure 1.23: Representation of GPC working mechanism. Image reproduced with permission from the authors.[150]

GPC allows the determination of all three types of molecular weight: number average molecular weight (M_n), weight average molecular weight (M_w) and Z average molecular weight (M_z) (**Equation 1.2**).

$$M_n = \frac{\sum_{i=1}^{\infty} N_i M_i}{\sum_{i=1}^{\infty} N_i} \qquad M_w = \frac{\sum_{i=1}^{\infty} N_i M_i^2}{\sum_{i=1}^{\infty} N_i M_i} \qquad M_z = \frac{\sum_{i=1}^{\infty} N_i M_i^3}{\sum_{i=1}^{\infty} N_i M_i^2}$$

Equation 1.2: Formulas for Mn, Mw and Mz. N_i = number of chains, M_i = weight of the chain.

M_n corresponds to the average weight of the different polymeric chains divided between the total number of chains, while M_w and M_z give more weight to the heavier chains than to the

lighter ones and are employed for some simulations of the properties of polymeric materials (**Figure 1.24**).[148]

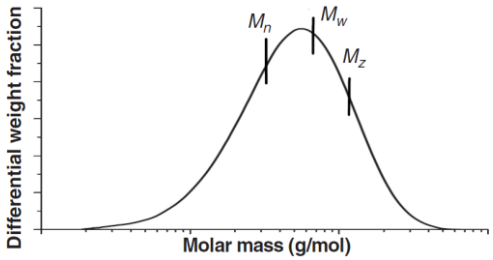

Figure 1.24: Graphical representation of M_n, M_w and M_z.

1.3.3 Acid Index

The acid index (IA) is a titration technique employed to determine the content of carboxylic acid in resins. This is achieved by the direct titration of a polymer dissolved in an aprotic solvent with phenolphthalein and a standardised basic solution, usually a methanolic KOH solution. In the case of polyesters arising from the reaction of a carboxylic acid and a diol, this value can be employed to measure the consumption of the carboxylic acid and therefore, of the evolution of the reaction.[151] The IA value is usually given as mg KOH/g polymer.

1.3.4 Hydroxyl index.

The hydroxyl index (IOH), just like IA, is a titration technique used to determine the content of hydroxylic groups in resins. Unlike IA, the process does not consist of a direct titration of the polymers, but rather, of an indirect titration of the reaction between acetic anhydride and the polymer. During this procedure, first, the hydroxyls of the polymer are acetylated with acetic anhydride with the aid of a catalyst, usually 1-methylimidazole (**Figure 1.25**). Then, water is added and the carboxylic acids resulting from both the hydrolysis of the acetic anhydride and acetylation of the alcohols are titrated employing a standardised methanolic KOH solution and phenolphthalein.[152] Finally, by comparison with a blank in which no polymer has been added, the number of alcohol terminations can be determined. The IOH value is usually given as equivalent mg KOH/g polymer.

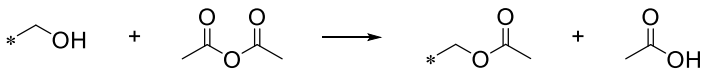

Figure 1.25: Acetylation of alcohols with acetic anhydride

On polyesters synthesised from carboxylic acids, IA and IOH allow the determination of the number of total terminations by gram of polymer. Hence, the molecular number (M_n) of the polymers can be obtained by following **Equation 1.3.**

$$M_n = \frac{\text{Polyester functionality} \times M_w \text{ KOH} \times 1000}{\text{IOH} + \text{IA}}$$

Equation 1.3: Obtention of M_n from IA and IOH.

1.3.5 Nuclear magnetic resonance spectroscopy

Nuclear magnetic resonance (NMR) spectroscopy is a widely employed non-destructive technique for the elucidation of molecular structures. It consists of the application of a strong magnetic field to the sample followed by its irradiation with radiowaves. The magnetic field splits the degenerate nuclear spin energy levels and allows their interactions with the incident radiation (**Figure 1.26**). However, this can only be achieved by nuclei with a non-zero nuclear spin. The magnetic field observed by each atom and hence, the energy gap between the split energy levels is not only dependent on the nature of the nuclei but also its electronic environment. Electrons generate a magnetic field when moving, which interacts with the one produced by the equipment, decreasing it through a process called shielding. Therefore, atoms surrounded with a higher electron density have a smaller energy gap and appear at lower fields. As electron density is dependent on the environment each nucleus is in, this technique reveals the connectivity of each atom, which leads to the elucidation of the molecular structure of the studied sample.

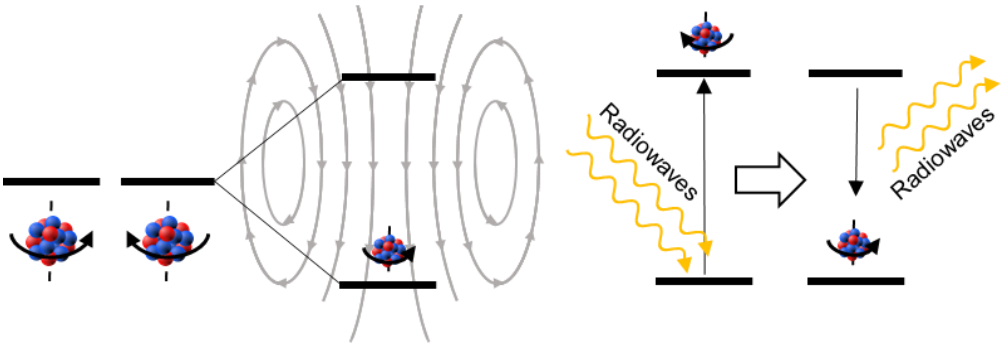

Figure 1.26: Representation of NMR working mechanism.

NMR spectroscopy not only provides knowledge about the structure of polymers but, for compounds with a relatively low molecular weight, it can also be employed to determine their M_n by so-called end-group analysis. If distinct signals for the terminal and internal groups of a polymer can be identified on the NMR spectra, the ratio between their integrals can be

employed to extract the average number of monomers by chain and consequently, the M_n of the polymer. Note however that only the M_n can be obtained through this technique, not the M_w nor M_z.

1.3.6 Density measurement by buoyancy

The density of solids can be measured by many different techniques but perhaps the most straightforward and widely used is buoyancy. It employs Archimedes' principle, which states that a body immersed in a fluid experiences an upward force equal to the weight of the fluid that is displaced.[153] Hence, by measuring the difference in weight of a sample in air and in a liquid of known density, it is possible to know the volume of displaced liquid and in turn, the volume of the sample, allowing the determination of the density of the material (**Equation 1.4**).[154,155]

$$\rho = \frac{W_A}{W_A - W_L} \times \rho_L$$

Equation 1.4: Determination of the density of a material (ρ) from buoyancy measurements. W_A=weight of sample on air, W_L=weight of sample in a liquid, ρ_L=density of the employed liquid.

1.3.7 Differential scanning calorimetry

Differential scanning calorimetry (DSC) is a technique employed to study the thermal transitions of materials. This is achieved by monitoring the heat required to modify the temperature of a sample at a specified heating or cooling rate and comparing it with that of an empty crucible. Both cooling and heating ramps are applied to the system, so the thermal transitions during both processes can be obtained.[156]

On TPUs and most polymers, the main transitions studied on DSC are the glass transition, crystallisation and melting of the materials.[157] Melting transitions are characterised by an absorption of energy by the system, while the contrary is true for crystallisation processes, so endothermic peaks are observed for the former while exothermic peaks are attributed to the latter (**Figure 1.27**). During glass transition processes, no energy is released nor absorbed by the material, rather a change in its specific heat capacity (C_p) is produced which is observed as an S-shaped curve, the inflexion point of which marks the glass transition temperature (T_g) (**Figure 1.27**).[156]

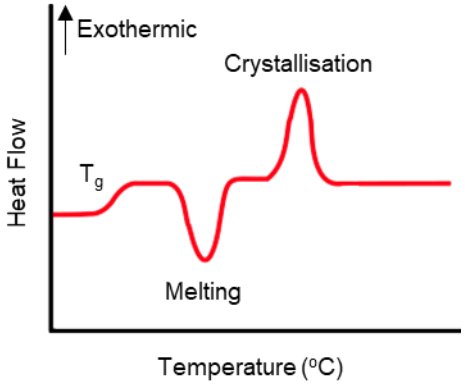

Figure 1.27: Representation of the standard DSC peaks of polymers.

DSC can also be employed to study the degree of crystallinity of polymeric systems. The crystallisation and melting enthalpies are proportional to the weight fraction of crystallised or melted material. Therefore, these values can be employed for the quantification of the degree of crystallinity of the material. However, to obtain this parameter, it is necessary to know the enthalpy of a 100% crystalline sample (**Equation 1.5**).[158] The attainment of completely crystalline polymeric materials is very complex, especially in the case of block copolymers. Hence, the use of DSC to quantify the crystallinity of TPUs is ill-suited and in most cases, it is merely employed to compare the crystallinity between similar samples.

$$\alpha = \frac{\Delta H}{\Delta H_c} \times 100$$

Equation 1.5: Crystallinity of a material (α) from DSC data. ΔH = experimental enthalpy, ΔH_c = enthalpy of the 100% crystalline material.

1.3.8 Tensile testing

Tensile testing is the fundamental technique to study the deformation of materials. It consists of the deformation of a material under either controlled strain (ε) or stress (σ) during which, both parameters are carefully measured. Through this analysis, several parameters related to the σ and ε behaviours of materials, like their elongation at break (ε_b) or stress at break (σ_b) can be measured (**Figure 1.28**).

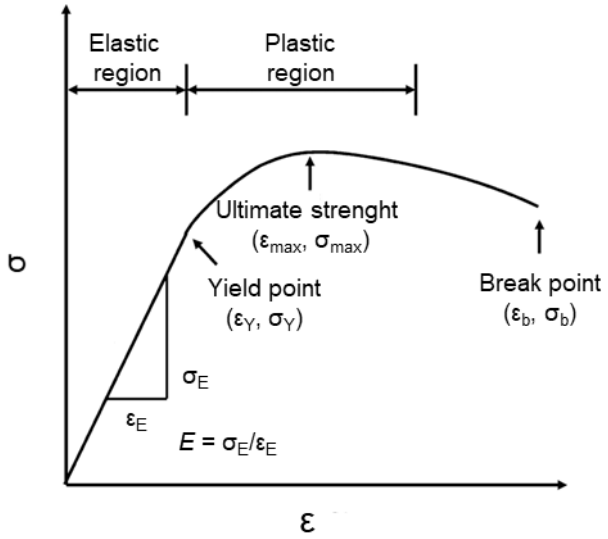

Figure 1.28: Stress-strain curve with most relevant regions indicated.

Moreover, tensile testing allows the distinction between the conditions under which the material displays an elastic or plastic behaviour. In the initial steps of the deformation of any material, the process is elastic, meaning that all the strain the polymers have sustained will revert once the stress is released. The elastic behaviour of materials can be identified by Hooke's law which states that the relationship between σ and ε during elastic deformation is linear. This linearity generates one of the parameters used for the characterisation of such behaviour, Young's module (*E*), which corresponds to the slope of the σ/ε line. Once deformation increases, the system might switch to a plastic behaviour where the deformation the system suffers is not recovered after the stress is released. This is observed in the strain-stress curve as a change in the slope and a loss in its linearity, which gives rise to the yield stress (σ_Y) and strain (ε_Y) (**Figure 1.28**).[159]

In the polymer field, the tensile test of materials is usually analysed following ISO 37.[160] This standard regulates the use of dumbbell-shaped samples. The dumbbell samples can be divided into two sections, the grip section (A), and the reduced material (D). The former is used to anchor the material to the dynamometer while the latter is where the test is effectuated. Moreover, the elongation of the sample is measured with reference to the gage length of the material (E). Different sample sizes can be utilised. In our case, type 2 dumbbells will be employed (**Figure 1.29, Table 1.1**).

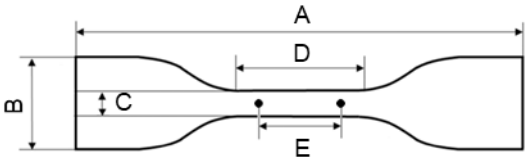

Figure 1.29: Representation of a dumbbell sample following ISO 37 regulations**.**

Table 1.1: Dumbbell dimensions by ISO37.

Dimension (mm)	Type 1	Type 1A	Type 2	Type 3	Type 4
Overall length (A)	115	100	75	50	35
Width of grip section (B)	25 ± 1	25 ± 1	12.5 ± 1	8.5 ± 1	6 ± 0.5
Length of reduced section (C)	33 ± 2	21 ± 1	25 ± 1	16 ± 1	12 ± 0.5
Width of reduced section (D)	6.2 ± 0.2	5 ± 0.1	4 ± 0.1	4 ± 0.1	2 ± 0.1
Gage length (E)	25 ± 0.5	20 ± 0.5	20 ± 0.5	10 ± 0.5	10 ± 0.5

1.3.9 Durometer hardness

The hardness of rubbers, plastics and soft gels is usually measured through indentation in the Shore Hardness scale (ISO 48).[161] The equipment, called durometer, employs a thin needle to measure the resistance to indentation of the material under a specified load. This resistance is then correlated to a value within the Shore hardness scale. There are two main Shore scales for the analysis of polymers which differ in the applied force, Shore A used for soft materials and Shore D is employed for hard materials.

1.3.10 X-ray scattering

X-ray scattering techniques are a set of procedures that allow the characterisation of the morphological characteristics of a diverse array of compounds. They are based on the elastic scattering of X-ray radiation by the electrons present in the sample. Once an electron is impacted by an X-ray beam, it will start oscillating, becoming a dipole which generates an omnidirectional wave with the same wavelength (λ) as the incident radiation (**Figure 1.30**).[162]

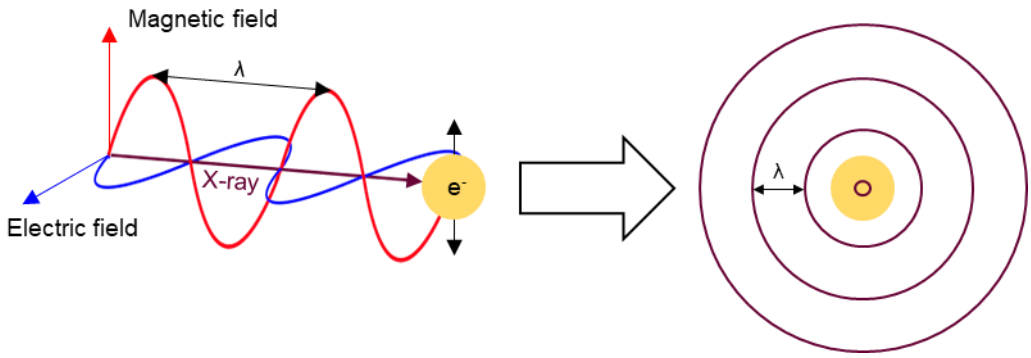

Figure 1.30: Interaction and scattering of X-ray radiation by an electron.

The generated X-ray waves will propagate and interact with the radiation created by other electrons, generating a diffraction pattern (**Figure 1.31**).

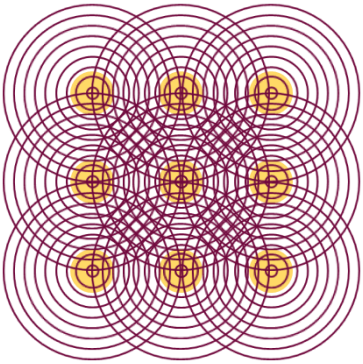

Figure 1.31: Representation of a diffraction pattern of different X-ray waves scattered by electrons.

This diffraction pattern is collected as a function of the angle between the incident radiation and the scattered X-rays (θ), usually employing a 2D detector that allows the recording over a broad range of θ. The incidence angle is related to the real space distances (d) of the structures present in the material by Bragg's Law (**Equation 1.6)** and therefore can be used to determine the morphological characteristics of the sample.[162]

$$\lambda = \frac{2d}{\sin\theta}$$

Equation 1.6: Bragg's law.

The diffraction pattern depends on both θ and the frequency of the employed X-ray radiation. Hence, to facilitate the comparison between spectra recorded at different equipments with

different X-ray sources, a variable known as q has been established which normalizes θ with respect to λ (**Equation 1.7**).

$$q = \frac{4\sin\theta}{\lambda}$$

Equation 1.7: Normalisation of θ with respect to λ.

Depending on the ranges of θ, two different techniques can be differentiated, small-angle X-ray scattering (SAXS) and wide-angle X-ray scattering (WAXS).

1.3.10.1 Small-angle X-ray scattering

As its name itself implies, on SAXS the diffraction pattern obtained at low θ values, from 0.1° to 10°, is analysed. As θ is inversely proportional to d, SAXS allows the determination of electron-density differences on the sample at the nanometric scale. For the specific case of TPUs, SAXS is an excellent technique to study their microphase segregation, as the size of the HS domains is usually found in the nanometre range. As aforementioned, the diffraction pattern of any object is dependent on the number and position of its electrons. Accordingly, the intensity of the diffraction at each q value, I(q), is proportional to the electron density of the sample at each point of space (**Equation 1.8**). [163]

$$I(q) = \iiint \rho^2(r) e^{-iqr} dV$$

Equation 1.8: Scattering intensity over all the reciprocal space as a function of the electron density (ρ) at each position within the material (r).

The previous expression shows the main limitation of SAXS. If there is no difference in electron density throughout the material, no data about the sample can be extracted. Moreover, it is an impossible task to obtain the electron density at each space point within the material. Therefore, to extract information from SAXS data, a set of different relationships needs to be applied depending on the characteristics of the sample and the q range explored.

SAXS's q range can be divided into three different zones, named the Guinier, Fourier and Porod regions (**Figure 1.32**).

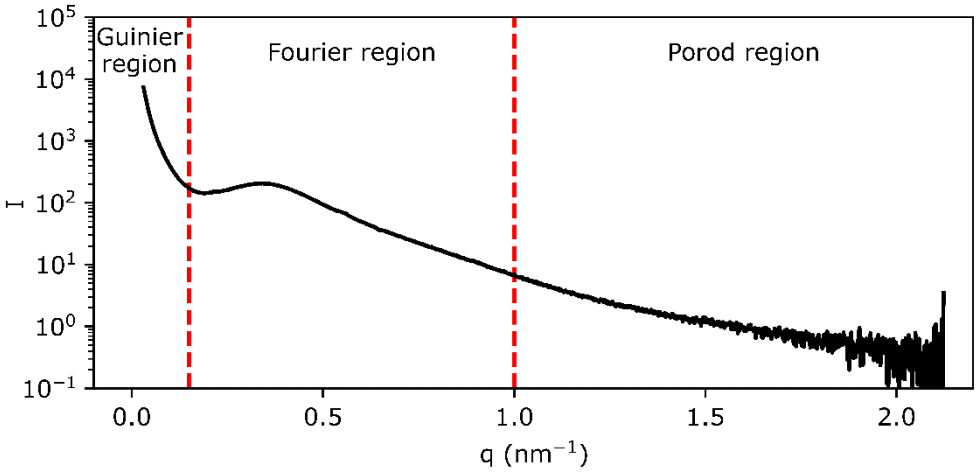

Figure 1.32: Representation of a 1D SAXS spectrum and its different regions.

The Guinier region is where the maximum intensity of a SAXS spectrum is found and it is characterised by an exponential decay produced by intraparticle scattering. There are two main points of interest in this region, the intensity at q = 0, I(0), which corresponds to the maximum in the spectra and the rate of the decay. The former is produced by all emitted waves being on phase, which only can happen when θ=0º. Accordingly, the minimum will correspond to the angle at which all the scattered waves are out of phase. The slope between this maximum and minimum intensity is dependent on the radius of gyration (R_g) of the scatterer. Hence, by following Guinier's equation, R_g can be obtained, allowing the determination of the particle's size (**Equation 1.9**). Unfortunately, this relationship is only true at very low q values and for compounds with a highly diluted particle concentration. As q increases, interparticle wave interference effects start to appear, which modifies the decay rate of the signal. These effects will appear at lower q values as the particle concentration increases. Consequently, the analysis of the Guinier region is often restricted to the evaluation of solutions containing a low concentration of dispersed particles.[163–168]

$$\lim_{q\to\infty} I = I_o e^{\frac{-q^2R_g^2}{3}}$$

Equation 1.9: Guinier equation.

The Fourier region contains the scattering interactions produced by a long-range order on the dispersed scatterers. Unlike the Guinier region, the analysis of this area allows the assessment

of samples with an elevated concentration of particles in which the interparticle interaction is not negligible. Hence, it is the most adequate region to gain information about the morphology of block copolymers, nanocomposite materials or highly concentrated dispersions. To extract the information stored in this area, the use of models is required. These models correspond to expressions that consider the form of the scattering pattern with respect to the size, shape and polydispersity of the scatterers. These expressions can be divided into two types, form factors, P(q), and structure factors, S(q). P(q) depends on the shape and size of the scatterer, while S(q) depends on the interaction between the scattered waves of the particles. The intensity in this area can be regarded as **Equation 1.10**. Hence, to correctly extract the information contained in the Fourier region, a proper selection of the two fitting models is required.[169–174]

$$I(q) = Scale \times P(q) \times S(q)$$

Equation 1.10: Description of I(q) in the Fourier region.

Finally, the Porod region corresponds to the area of the spectrum where the data about the surface of the scatterer is located. This region could be used to obtain the surface/volume ratios of the HS domains.[163] However, this is of little interest for TPU materials, hence, the analysis and properties of this region will be omitted.

1.3.10.2 Wide-angle X-ray scattering

Contrary to SAXS, WAXS is a scattering technique centred on the analysis of the scattering pattern obtained at high θ, allowing the study of short distances corresponding to the interatomic or interplanar distances of crystallites.

In the specific case of polymers, WAXS is an excellent technique to explore the internal order and the degree of crystallinity of the semicrystalline domains. This can be achieved in quite a straightforward way by deconvoluting the WAXS spectra. This deconvolution allows the differentiation between wide peaks, which correspond to the amorphous domains of the materials and narrow peaks, which pertain to a more ordered, crystalline domain. By employing the areas of these different peaks, the degree of crystallinity can be calculated from the direct relationship between the area of the crystalline peaks and the total intensity of the spectra, which contains the area of the amorphous and crystalline bands (**Equation 1.11**).[175–180]

$$\text{Degree of crystallinity} = \frac{\text{Area crystalline peaks}}{\text{Area crystalline peaks} + \text{Area amorphous peaks}}$$

Equation 1.11: Determination of the degree of crystallinity by WAXS data.

Chapter 2: Objectives and experimental design

This chapter establishes the objectives of this PhD thesis and the initial experimental approach employed to reach them.

This work aims to develop and study the properties of thermoplastic polyurethanes containing 2,5-furandicarboxylic acid (FDCA) as a biobased monomer to produce materials with a low environmental footprint. To incorporate FDCA into the TPU structure, the biomonomer will be introduced into an alcohol-terminated polyester, which will then be reacted with a diisocyanate (DI) and a chain extender (CE) to generate the desired TPU (**Figure 2.1**).

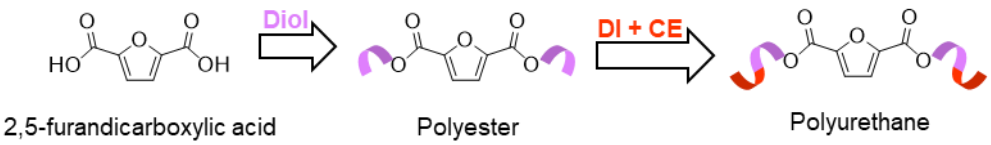

Figure 2.1: Schematic representation of TPU development process.

Accordingly, the first objective of this work is to develop FDCA polyesters suitable for TPU production. Is during this step that the first issue of the project arises. Currently, the price of FDCA is extremely elevated, as it is in the early stages of industrial pilot plant production. Hence, a cheaper alternative that could be employed as a model for the optimisation of the synthesis procedure and exploration of the material's properties has been sought out. To that avail, isophthalic acid (IPHTA) has been selected as model compound, as likewise to FDCA, it is an aromatic diacid in which the carboxylate moieties are in *meta* position (**Figure 2.2**). With this model compound, the best diacid derivative and polycondensation conditions will be explored and once optimised, exported to FDCA.

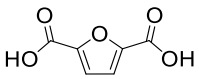

2,5-furandicarboxylic acid
(FDCA)

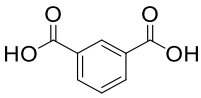

Isophthalic acid
(IPHTA)

Figure 2.2: Structures of FDCA and IPHTA.

Once the polyesters have been developed, the second objective of the thesis, the development and characterisation of the TPUs will be explored. This will be carried out initially with the IPHTA polyesters, to ensure the compatibility between the selected formulations with the aromatic diacid polyesters, and afterwards with the FDCA polyesters. To gain an understanding of the impact that the aromatic monomers have in different formulations, different diisocyanates (methylene diphenyl diisocyanate and hexamethylene diisocyanate), HS contents (10, 30, 50 mol%), polyester compositions (polypropylene, polybutylene and polyhexamethylene polyesters) and polyester M_n (1000-2000 g/mol range) will be assessed to obtain a clear representation of the material's behaviour. Special emphasis will be given to exploring the relationship between the composition, morphology, and mechanical properties of the produced polymers.

Chapter 3: Polyester development and characterisation

The optimisation of the synthetic procedure of polyesters containing isophthalate and furandicarboxylate moieties in their structure is discussed in this chapter. In addition, the characterisation of their thermal transitions is also assessed in this chapter and employed to get an initial picture of the supramolecular interactions present in the aromatic polymers.

3.1 Isophthalate polyesters synthesis

The first step towards the development of biobased 2,5-furandicarboxylate TPUs is the synthesis of their corresponding polyesters. However, as aforementioned, owing to its excessive price, rather than starting with the biomonomer, a cheaper more available petrochemical monomer family, isophthalates, were selected as models for the optimisation of the synthetic procedure. During this work, two different isophthalic monomers were employed, dimethyl isophthalate (IPHTME) and isophthalic acid (IPHTA) (**Figure 3.1**).

Dimethyl isophthalate (IPHTME) | Isophthalic acid (IPHTA)

Figure 3.1: Isophthalate monomers.

For the polyester to be suitable for mass-scale TPU production it must be obtained under solvent-free conditions in less than 120 h and without any purification processes. Moreover, its number of non-hydroxyl terminations must be lower than 0.008 mmol/g polymer. The non-alcohol terminations that can be present in the target polyesters can be either methyl esters or carboxylic acids. The latter will be quantified by Acidity Index (IA) (**Experimental section 6.2.1**)[151], while for the former ^{1}H NMR spectroscopy will be employed (**Experimental section 6.2.3**). In order to compare the evolution of the reactions from the diacid and methyl ester monomers, a new expression, called Methyl Ester Index (IOMe), was defined. This value

is related to the number of unreacted methyl ester moieties arising from the IPHTME monomer remaining in the polymer and it is based on the results of a hypothetical titration of the unreacted methyl ester groups with KOH. Both values, IA and IOMe need to be lower than 0.5 mg KOH/g polymer to reach the required polyester specifications.

To gather information about the behaviour of TPUs containing odd and even atomic lengths, two different diols will be initially explored, 1,4-butanediol (BDO) and 1,3-propanediol (PDO) producing respectively odd, polybutylene isophthalate (IPHTABDO) and even, polypropylene isophthalate (IPHTAPDO) (**Figure 3.2**).

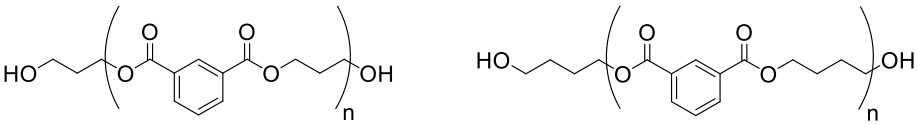

Polypropylene isophthalate (IPHTAPDO)

Polybutylene isophthalate (IPHTABDO)

Figure 3.2: Target isophthalate polyesters.

The molecular weight of the polyesters will be analysed, when possible, by both hydroxyl index (IOH) (**Experimental section 6.2.4**) and ^{1}H NMR end-group analysis (**Experimental section 6.2.5**).

3.1.1 Dimethyl isophthalate as diacid

The first attempts to obtain the desired polyesters were carried out with IPHTAME and a target M_n of 1000 g/mol (**Figure 3.3**). Although employing the dimethyl ester instead of the dicarboxylic acid increases the environmental impact of the process, as methanol rather than water is generated as by-product, the dimethyl ester can be easily purified by distillation, which ensures monomers with a suitable purity for polycondensation. This could be particularly relevant in the posterior synthesis of the FDCA polyester since the purification of this monomer in its diacid form is not completely established at the industrial scale yet. Nonetheless, the produced methanol can be collected after the reaction and recycled for other processes, reducing the environmental impact of employing the methyl ester monomer.

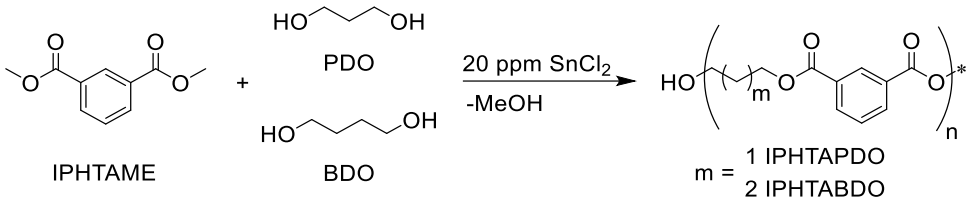

Figure 3.3: First polycondensation attempts with IPHTAME.

The reaction was carried out under standard polycondensation conditions previously developed in our group for the synthesis of aliphatic polyesters (**Experimental Section 6.2.6**) and monitored by observing the disappearance of the methyl ester signal and the appearance of the new ester by ^{1}H NMR spectroscopy (**Figure 3.4**). First, a transesterification step is carried out at 180 °C under N_2 at atmospheric pressure. In this step, a substitution of the methyl esters by diol ones (PDO or BDO) takes place, generating isophthalate-diol oligomers. Once the reaction has evolved and barely any free diol is present in the mixture, vacuum is applied to drive the elimination of the more volatile alcohol, in this case, methanol, and induce chain growth.

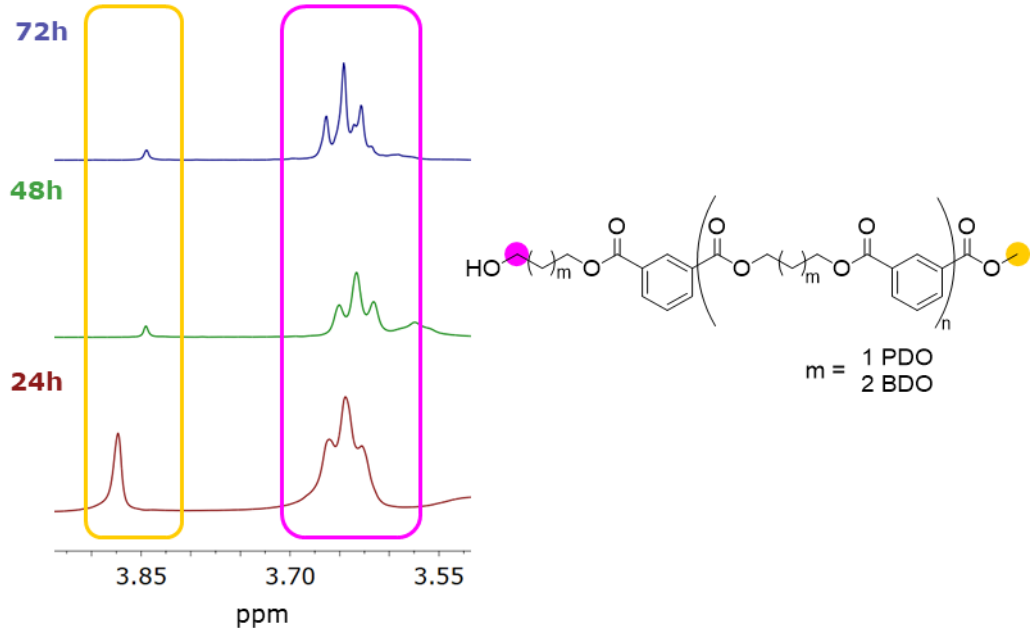

Figure 3.4: Example of the evolution of the IPHTAME polycondensation reaction by ^{1}H NMR spectroscopy (400 MHz) over time. Solvent $CDCl_3$.

As commented above, for the synthetic procedure to be suitable for our purposes, an IOMe value lower than 0.5 mg KOH/g polymer needs to be reached in less than 120 h. However, the route starting from the methyl ester proved to be quite slow, reaching only IOME values of 13.4-7.5 mg KOH/g polymer after 144 h of reaction, even after incorporating additional diol and applying vacuum (**Experimental Section 13.6.1**). Moreover, an additional issue was observed when employing BDO as diol. The rate of the polycondensation reaction for this monomer, especially once conversion advanced above 90% was extremely slow. This was attributed to the so-called backbiting reaction of BDO.[181] This side-reaction corresponds to the cyclisation of BDO to tetrahydrofuran (THF) through an intramolecular attack, which produces a new acid termination (**Figure 3.5**). This process was identified by the presence of THF mixed with the methanol distilled during the reaction (**Figure 3.6**). The presence of this side-reaction not only reduces the speed of the polycondensation reaction but also generates new non-hydroxyl terminations (carboxylic acids). Therefore, the target of 0.008 mmol non-hydroxyl terminations/g polymer cannot be reached. The presence of the side-reaction required an extensive addition of BDO to displace the equilibrium of the reaction and decrease the IA and IOMe values of the polymer, which in turn increases the amount of by-products generated in the reaction.

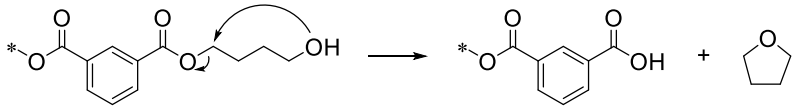

Figure 3.5: Backbiting reaction of BDO.

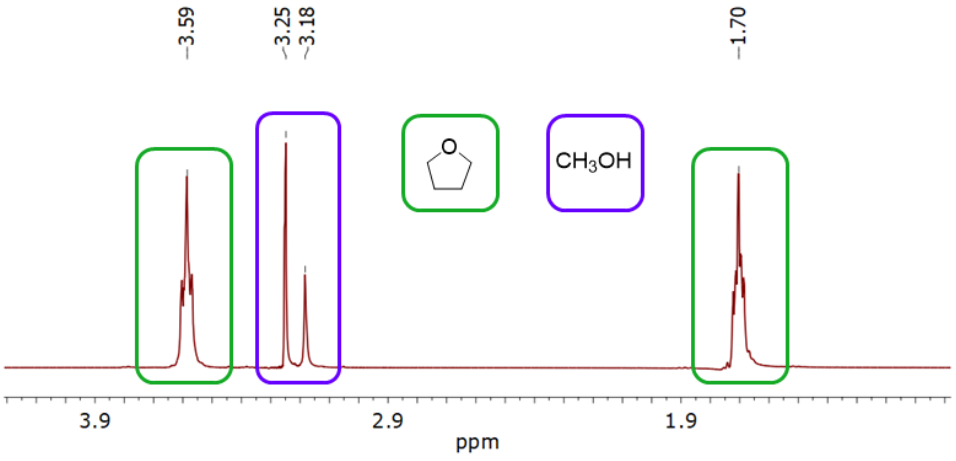

Figure 3.6: Fragment of a ^{1}H NMR spectrum (400 MHz) of the collected distillate of the reaction between IPHTME and BDO. Solvent $CDCl_3$.

Owing to the low polycondensation rates obtained during this procedure, the use of IPHTME as starting material was discarded and isophthalic acid (IPHTA) was selected to continue the exploration of the reaction.

3.1.2 Isophthalic acid as monomer

Following the unsuccessful attempts to obtain polyesters fulfilling the required specifications with IPHTME, the use of isophthalic acid (IPHTA) as monomer was assessed. For the first essays, PDO was selected as diol as it does not exhibit the backbiting side reaction (**Figure** 3.7).

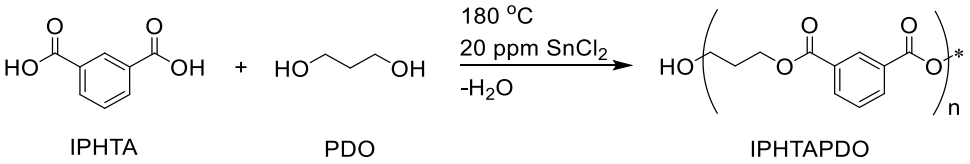

Figure 3.7: Reaction of IPHTA with PDO.

The reaction was essayed under the previously established polycondensation conditions (**Experimental Section 6.2.6**). However, taking advantage of the change in monomer, this time its evolution was monitored by IA titration.

Just as in the previous attempt, a target polyester with a 1000 g/mol M_n was selected to allow the direct comparison with the previous IPHTAME PDO reaction (**Experimental Section 13.6.3**). Compared with IPHTME, the use of IPHTA increased the reaction rates to a great extent, allowing the generation of a polyester with the required characteristics in less than 120 h (**Figure 3.8**).

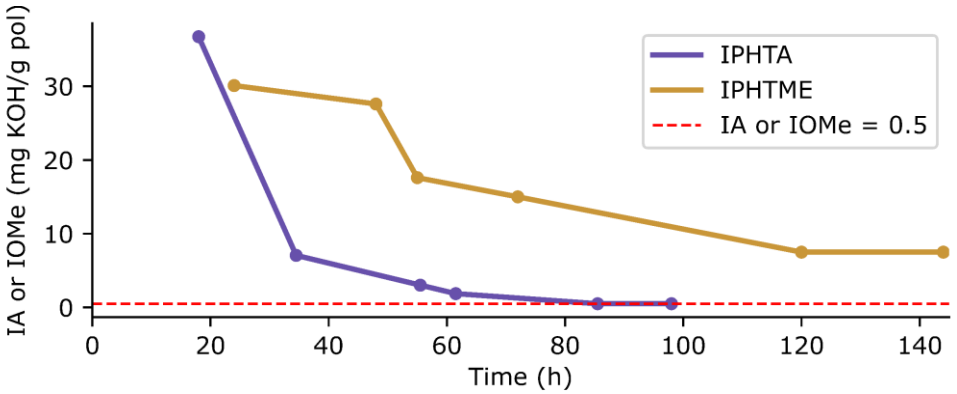

Figure 3.8: Non-hydroxyl termination evolution comparison of IPHTA (IA) vs IPHTAME (IOMe) of the polycondensation reaction with PDO.

As the evolution of the reaction proceeded quite rapidly, the omission of the catalyst was assessed to determine if a greener, metal-free process could be developed (**Experimental Section 13.6.4)**. Although in the first stages the catalysed and non-catalysed reactions proceeded at comparable rates, once IA dropped below 30 mg KOH/g pol, the speed of the uncatalysed reaction declined (**Figure 3.9**), requiring 143 h to reach an IA value lower than 0.5 mg KOH/g polymer. Hence, the removal of the catalyst was discarded. Moreover, as the initial catalysed conditions allowed the generation of polyesters within the required specifications, no further optimisation was performed on the IPHTAPDO synthesis.

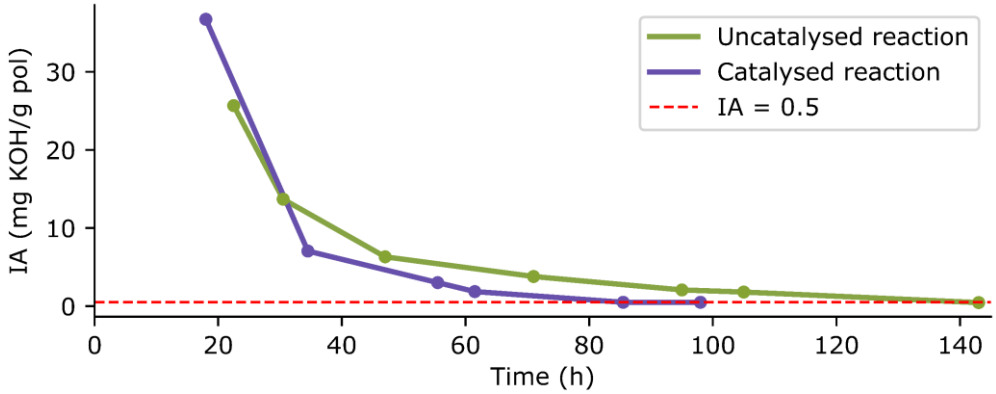

Figure 3.9: Evolution of the reaction between IPHTA and PDO catalysed and uncatalysed by IA.

Next, the BDO polyesters, which have the additional complexity of the backbiting reaction, were evaluated (**Figure 3.10**).

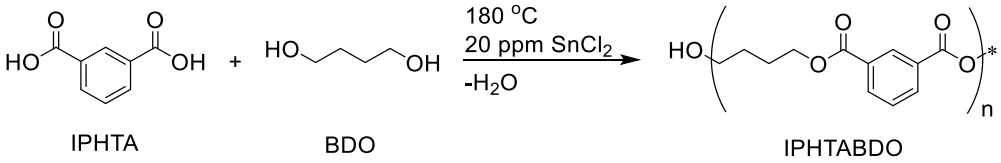

Figure 3.10: Reaction of IPHTA with BDO.

The first essay was performed with a target M_n of 1000 g/mol employing an initial excess of diol to force the esterification of the acid terminations (**Experimental Section 13.6.5**). During this test, although a fast decrease of the IA was obtained at the beginning of the reaction, it became stagnated at an IA value of around 2 mg KOH/g polymer and could not be decreased even after extensive addition of BDO during the reaction (**Figure 3.11**).

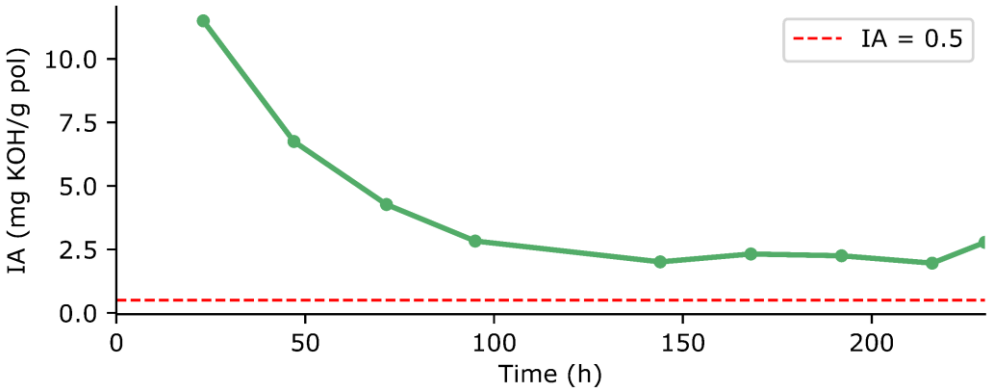

Figure 3.11: Evolution of the reaction between IPHTA and BDO by IA.

This suggests that the backbiting reaction reaches an equilibrium with the esterification of the acid terminations of the polymer, hindering the obtention of polyesters with the desired IA values.

Although the backbiting reaction is also observed with aliphatic diacids, its rate is noticeably slower and does not prevent the obtention of polyesters with low IA values. Hence, there must be some difference in the reactivity of the aliphatic and aromatic diacids that accelerates the side-reaction.

The first step in the formation of THF from a BDO ester consists in the generation of an intramolecular H-bond between the carbonyl's ester and its alcohol (**Figure 3.12**).[182] Therefore, the stronger the affinity towards the generation of said interactions the carbonyl has, the faster the backbiting reaction will be.

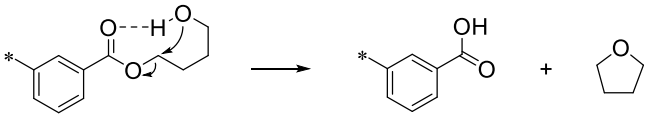

IPHTABDO

Figure 3.12: BDO backbiting mechanism through intramolecular H-bonding.

Owing to resonant effects, the electron density of the aromatic carbonyl is higher than the aliphatic ones (**Figure 3.13**). Thus, the formation of the H-bonds is favoured in the former, leading to a faster reaction rate for the backbiting process.

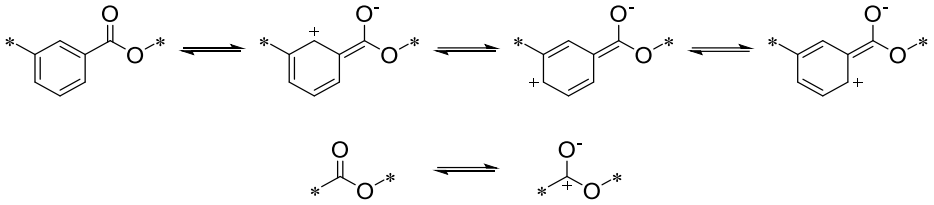

Figure 3.13: Resonant structures of aromatic *vs*. aliphatic esters.

The high affinity of aromatic carbonyls to form intramolecular H-bonds is made manifest by ^{1}H NMR spectroscopy. On standard aliphatic polyester diols, only one signal for the ester O-CH_2 protons is observed, as the terminal and internal esters have almost the same chemical environment.[183] However, on the IPHTA polyesters, two different signals are distinguishable, one arising from the internal ester O-CH_2 protons and another from the terminal ones (**Figure** 3.14). This proves that the electron density on the aromatic carbonyl and its affinity towards the formation of H-bonds is higher than that of their aliphatic counterpart and that this parameter is quite probably behind their different backbiting reactivity.

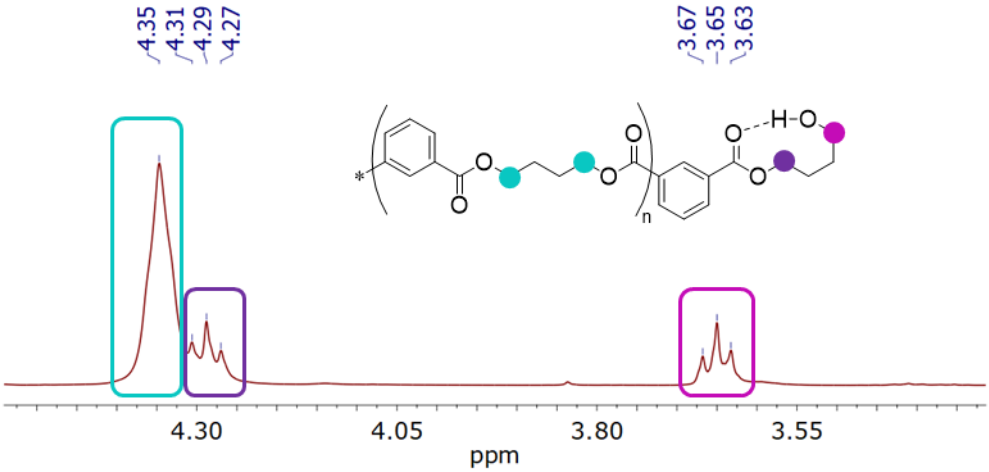

Figure 3.14: Proof of intramolecular H-bonding by ^{1}H NMR spectroscopy (360 MHz) in a IPHTABDO polyester. Solvent $CDCl_3$.

Since the same conditions employed for the synthesis of the IPHTAPDO polyesters could not be used to obtain IPHTABDO polymers with the required specifications, two different tests, one increasing the temperature of the reaction to 230 °C (**Experimental Section 13.6.6**) and another one decreasing it to 160 °C (**Experimental Section 13.6.7**) were assessed. At 230 °C, the generation of the diol terminated polyester was highly diminished, which demonstrates that

the backbiting reaction is favoured at high temperatures (**Figure 3.15**). However, when the temperature was reduced to 160 °C, the IA values of the polymer did not improve compared to the test performed under the standard temperature of 180 °C (**Figure 3.15)**. Although initially the evolution of the reaction at 160 °C was lower than that at 180 °C, once relatively low IA values were achieved, the reaction at 160 °C converged to almost the same rates and IA values as the reaction at 180 °C. The observed tendency implies that, just as the backbiting reaction, the polycondensation reaction is also favoured by the increase of temperature, and that, once the reaction has advanced enough, the esterification of the diacid end-groups and the backbiting processes enter an equilibrium, inhibiting the obtention of polyesters with the desired IA values.

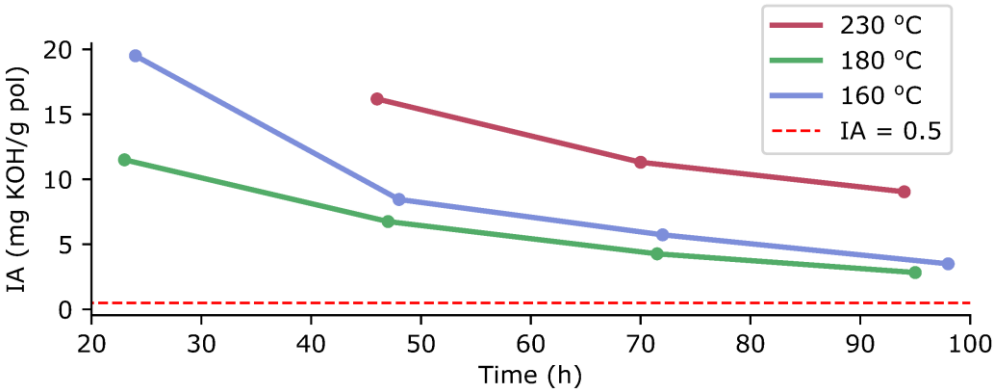

Figure 3.15: Evolution of the reaction between IPHTA and BDO at different temperatures by IA.

As BDO polyesters following the required specifications could not be reached, to assess the properties of materials with an odd chain length the synthesis of polyesters containing 1,6-hexanediol (HDO) to generate polyhexamethylene isophthalate (IPHTAHDO) was assessed (**Figure 3.16**).

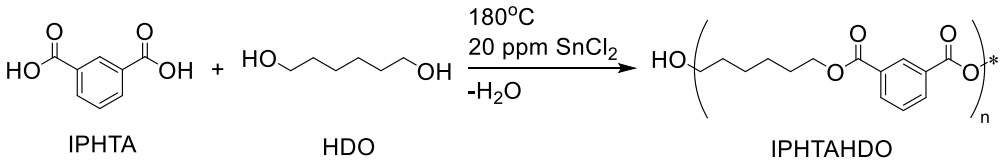

Figure 3.16: Reaction of IPHTA with HDO.

Compared with the PDO polyesters, the reaction rates of the polycondensation with HDO are significantly higher, reaching the desired IA values in under 40 h (**Figure 3.17, Experimental Section 13.6.8**).

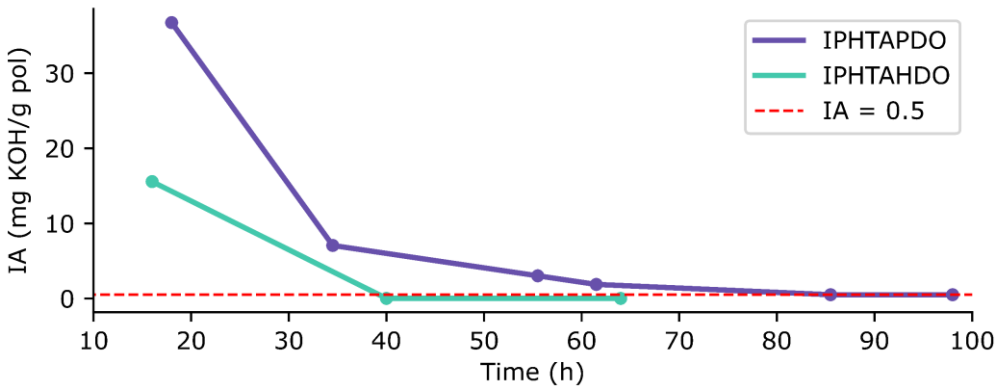

Figure 3.17: Evolution of the reaction of IPHTA with PDO and HDO by IA.

This increase in reactivity might be caused by the lower viscosity of the IPHTAHDO melt compared with that of IPHTAPDO (2027.23 mPa·s *vs*. 3704.44 mPa·s at 140 °C). As the reaction is carried out under solvent-free conditions, higher media viscosity results in a lower chain mobility of the system, which in turn might difficult the evolution of the process. Moreover, the higher viscosity of the reaction crude might also hinder the elimination of water required to complete the polymerisation and reach the desired IA values, lowering the effectivity of the vacuum.

Employing these conditions, different batches of PDO and HDO polyesters with a target M_n of either 1000 or 2000 g/mol were produced at various scales (**Experimental section 13.6.9-13.6.12**) and characterised by ^{1}H NMR, $^{13}C\{^{1}H\}$ NMR and IR spectroscopy (**Annex A1.1**, **A2.1**) for their posterior use in the synthesis of TPUs.

3.2 Furandicarboxylate polyester synthesis

Following the synthesis of the isophthalate polyesters, the production of the furandicarboxylate polyesters was assessed, starting from the same conditions obtained for the development of the IPHTA polyesters. The polymer synthesis was attempted with PDO and HDO as diols, generating polypropylene furandicarboxylate (FDCAPDO) and polyhexamethylene furandicarboxylate (FDCAHDO), while BDO was discarded due to its backbiting side reaction (**Figure 3.18**). However, this time, three different target molecular weights were assessed, 1000, 1500, and 2000 g/mol.

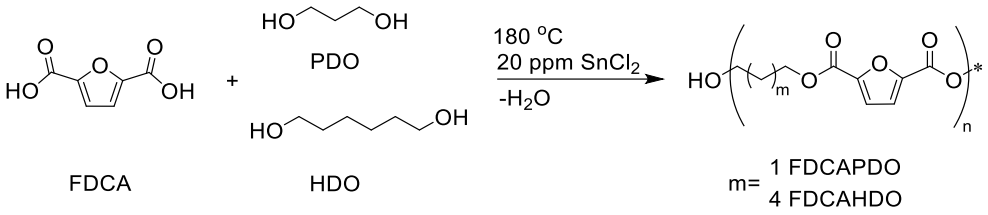

Figure 3.18: Polyester synthesis of FDCAPDO and FDCAHDO.

Before any polymerisation test, a purity assessment of the different FDCA batches was performed. This was carried out to ensure that no by-products from the extraction or derivatisation of sugars which could hinder the polycondensation reaction were present on the monomer. These tests were performed for all the batches of FDCA employed during this work. First, the purity of the diacid was assessed by ^{1}H NMR and $^{13}C\{^{1}H\}$ NMR spectroscopy, where no signals corresponding to impurities were observed (**Figure 3.19, Figure 3.20**), suggesting an extremely low concentration of the impurities if any.

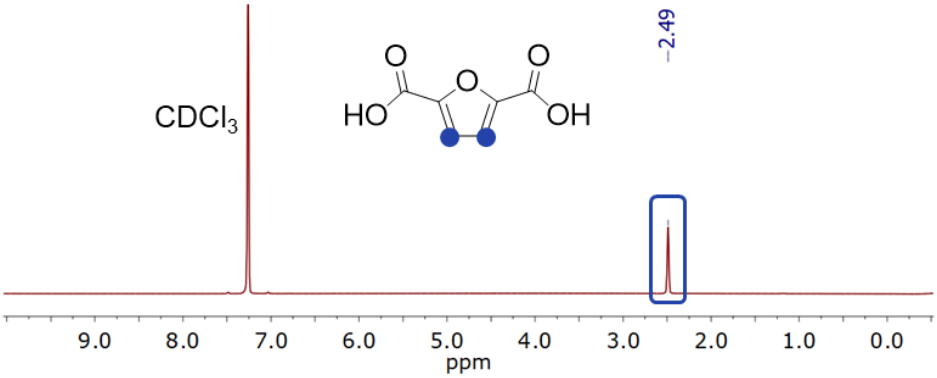

Figure 3.19: Purity analysis of FDCA batch 1 by ^{1}H NMR spectroscopy (400 MHz). Solvent $CDCl_3$.

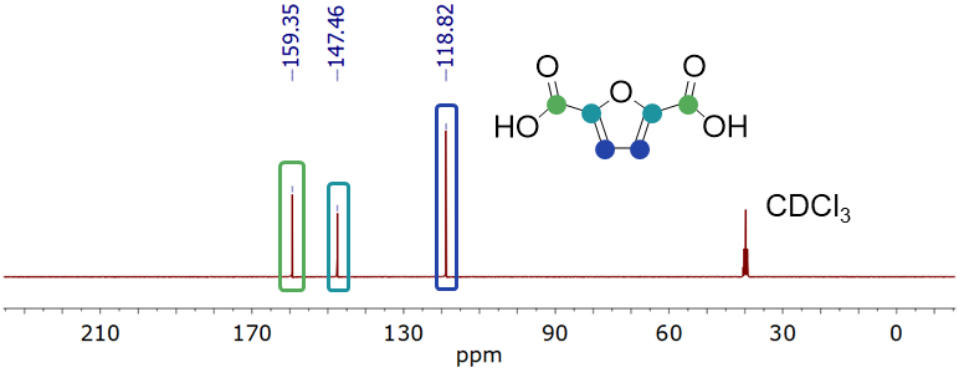

Figure 3.20: Purity analysis of FDCA batch 1 by $^{13}C\{^{1}H\}$ NMR spectroscopy (400 MHz). Solvent $CDCl_3$.

Afterwards, a technique with a lower detection limit, gas-chromatography mass-spectrometry (GC-MS), was employed to ensure that indeed, no impurities were present in the diacid and they were suitable for polymerisation. However, direct application of GC-MS is not possible, as FDCA and other carboxylic acids that might act as impurities and hamper chain growth are non-volatile and cannot be detected by this technique. For that reason, a previous derivatisation of all the carboxylic acids present in the sample to their corresponding methyl esters was performed by employing BF_3·MeOH (**Figure 3.21, Experimental Section 6.2.8**).

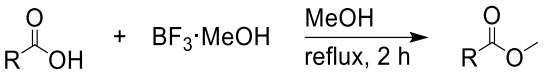

Figure 3.21: Derivatisation of carboxylic acids with BF_3·MeOH.

On all samples, other than the mono and diesterified FDCA, sub-ppm amounts of two antioxidants, 2,4-di-tert-butylphenol and 4-methylbiphenyl, and of some plasticisers, pentadecane, heptadecane, and the esterified octadodecanoic acid and pentadecanoic acid were present (**Annex A3.1**). These impurities were attributed to additives contained in the plastic bags where the monomer was transported and stored, as all of them are well-known plastic additives. Although the presence of the two monocarboxylic acid components could hinder the polymerisation reaction, their low concentration was deemed innocuous enough to allow the production of polyesters with the desired M_n.

Before any large-scale synthesis of the polymers was attempted, a small-scale reactivity comparison was performed between FDCA and IPHTA with HDO as diol (**Figure 3.22, Experimental Section 6.2.7)**.

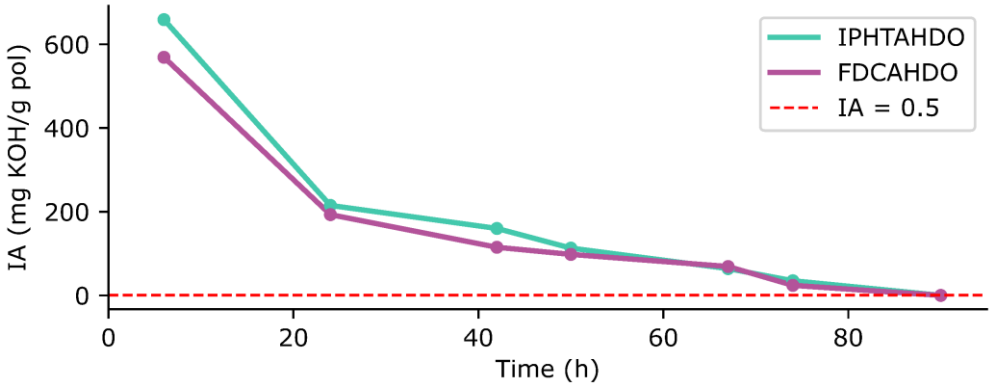

Figure 3.22: Reactivity comparison between FDCA and IPHTA with HDO monitored by IA at a small-scale.

Reactivity-wise both the IPHTA and FDCA diacids behaved similarly. This proves that the choice of IPHTA as model compound for the reactivity of FDCA was appropriate and that the conditions determined for the development of the IPHTA polyesters could be extrapolated to FDCA. Surprisingly, a disparity between the reactivity of the IPHTA resins at this small-scale test with those of the synthesis conducted at, at least, a 1 kg scale was observed. The small-scale process took 90 h to reach an IA below 0.5 mg KOH/g polymer while the large-scale synthesis required just around 40 h. This was attributed, on one part, to the lower amount of water vapour produced during the reaction, which lengthens the time required to heat the distillation column to the appropriate temperature for water distillation, and to the poorer stirring of magnetic systems employed in the small-scale tests compared to the mechanical ones used on the large-scale synthesis.

As the same reactivity was observed between the IPHTA and FDCA monomers at a small scale, the large-scale synthesis of FDCA polyesters was attempted following the identical as those of the model diacid. The first attempt was performed on a 1 kg scale with PDO as diol and a target M_n of 1000 g/mol (**Figure 3.23, Experimental section 13.6.13**).

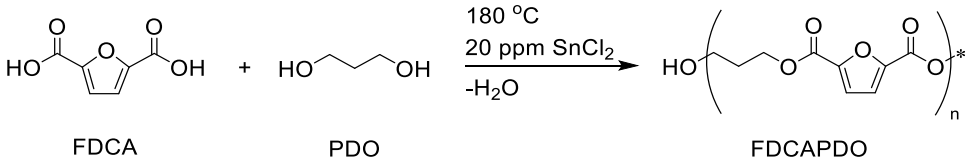

Figure 3.23: 1 kg scale reaction of FDCA with PDO.

Unlike what happened at a small scale, the reactivity of FDCA was higher than that of IPHTA (**Figure 3.24**). This disparity between the behaviour at the two different scales might be caused by the previously discussed poorer mechanical stirring and low water vapour formation, which might have masked the difference in reactivity between the diacids. From this test, it seems like FDCA has the highest reactivity of the two diacids, which could be caused by the presence of the oxygen in the aromatic ring, which decreases the electron density around the carbonyl's carbon, increasing its electrophilic nature.

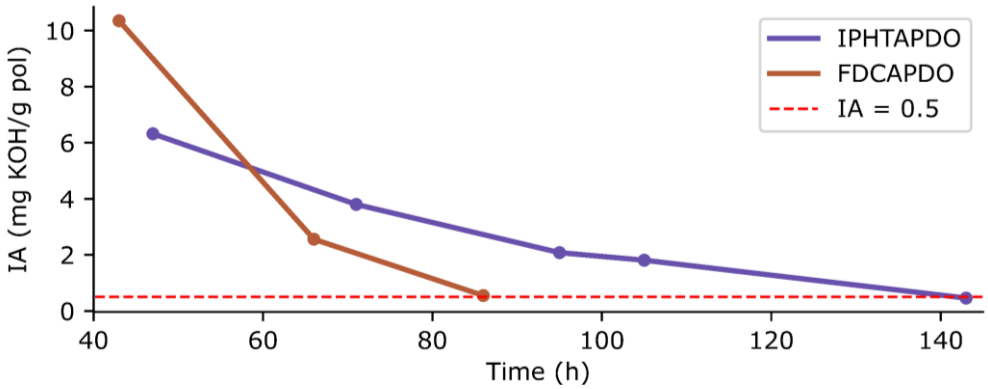

Figure 3.24: Reactivity comparison between IPHTA and FDCA and with PDO at a 1 kg scale.

Besides the increased reaction rates, two further differences were observed between the FDCAPDO and IPHTAPDO polyesters. The solubility of the FDCAPDO resin was significantly lower than that of its IPHTA counterpart and could only be dissolved in dimethyl sulfoxide (DMSO) above 120 °C, rather than at room temperature dichloromethane (DCM). This implied that the IA measurement had to be done employing this solvent and that, the determination of the molecular weight by IOH could not be performed. Hence, to determine the M_n of the polymer, ^{1}H NMR end group analysis in DMSO-d_6 at 120 °C was employed. Moreover, rather than being white or having a slight yellow hue like the IPHTA polyesters, the FDCA polymers display a deep brown colour (**Figure 3.25**).

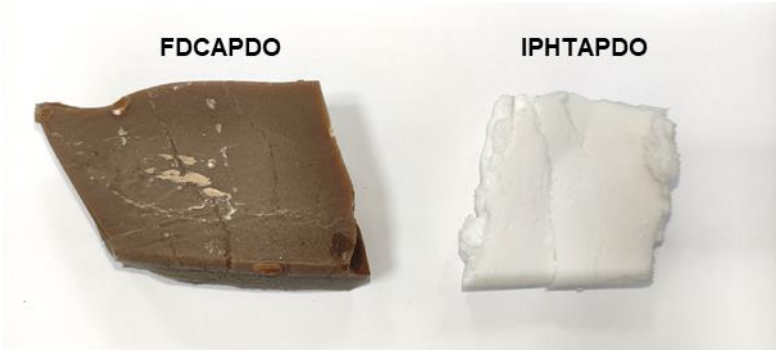

Figure 3.25: Colour difference between FDCAPDO (left) and IPHTAPDO (right).

To ensure that the colour of the product did not appear due to an incorrect deoxygenation during the reaction, the synthesis was repeated (**Experimental Section 13.6.14**). On this test, the same behaviour was observed regarding reactivity, solubility, and colour. This indicates that the colouration problem is not generated by any incorrect deoxygenation, but rather that it is

derived from the thermal degradation of some impurity present on FDCA. The impurity was not observed in the previous purity analysis; hence, it should be present in extremely low concentrations on the FDCA monomer. As an attempt to isolate the contaminant, some cleaning tests of FDCA employing several solvents were performed. To identify if any of the solvents were able to remove the colour, first, the monomer was subjected to a solid-liquid extraction with the chosen solvent. This process was performed three times for each solvent, by stirring the FDCA powder suspension for 1h and then filtering it. Subsequently, the cleaned FDCA fractions were subjected to the same conditions as during the polymerisation process (addition of PDO and 160 °C for 2h), and the colour of each mixture was assessed (**Figure 3.26, Experimental Section 6.2.9**).

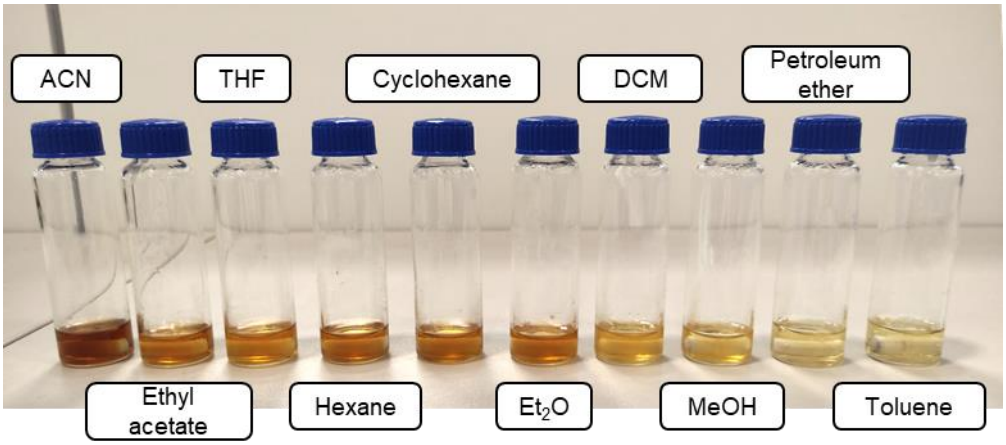

Figure 3.26: Assessment of the colour of cleaned FDCAPDO samples. Acetonitrile (ACN), tetrahydrofuran (THF), dichloromethane (DCM).

The cleaning tests show that toluene, petroleum ether and, to a lesser extent, dichloromethane (DCM) and MeOH can remove the colour arising from the polymerisation process. This ratifies that the colour was derived from an impurity, and not from FDCA itself. Surprisingly, the ability of solvents to reduce the colouration does not follow any kind of polarity trend, as both apolar solvents such as toluene and polar solvents like MeOH can reduce the formation of colour while other solvents with similar polarities like acetonitrile (ACN) or hexane do not.

To elucidate the nature of the impurity, the solvents employed for the extractions that resulted in a significant decrease of the colour, DCM, MeOH, petroleum ether and toluene, were evaporated under reduced pressure to isolate the impurity and analyse it by NMR spectroscopy. However, after the evaporation of the solvent, no residue was observed. This agrees with our previous FDCA purity assessments, as this means that the impurity is present in extremely low

concentrations in the diacid. To obtain a higher quantity of the impurity and enable its identification, the extraction with petroleum ether of 1 kg of FDCA followed by the analysis of the residue by ^{1}H, $^{13}C\{^{1}H\}$, NOESY and HSQC NMR spectroscopy was carried out (**Annex A3.2**). In these extractions, just a couple milligrams of the residue were identified. Unfortunately, it was impossible to discern if said impurities arose from the monomer or from the 2L of petroleum ether employed for the extraction. Hence, the elucidation of the impurity was not possible.

As the elimination of the colour of the polyester requires impossibly large quantities of solvent, the production of the desired FDCA polyesters with the target M_n of 1000, 1500 and 2000 g/mol has been carried out without any purification of the monomer (**Experimental Section 13.6.15-13.6.20**). The resulting polyesters have been characterised by ^{1}H NMR, $^{13}C\{^{1}H\}$ NMR and IR spectroscopy before their use for the synthesis of the TPUs (**Annex A1.1**, **A2.1**).

3.3 Polyester thermal behaviour

To gain an understanding of how the polyesters will behave on the TPU and which effect the aromatic monomers have on the structure of the polymers, DSC was employed to explore their crystallinity and the nature of their supramolecular interactions. To simplify the comprehension of the results, the following nomenclature will be used for all the polyesters, in which the target M_n rather than their real one is employed: **DiacidDiol TargetM$_n$** (Example: IPHTAPDO 1000). Notice that this is just a notation to simplify the discussion of the results. For further calculations, like the synthesis of the TPUs, the real M_n value of the polyesters, which can be found in **Experimental Section 6.2.12.1-6.2.12.8** was employed. The polyesters have been analysed by employing a two-cycle process. In the first cycle, the thermal history of the compounds is removed by heating them well above their melting temperature. In the second cycle, the materials are cooled and heated again to record the thermal transitions inherent to the polymers (**Experimental Section 6.1.9**). In this section, only their 2nd heating and cooling cycles will be shown, as they do not include the thermal history of the material and therefore, enable direct their comparison.

On the IPHTA family of polyesters, a clear lack of crystallinity on all of the polymers can be observed from the DSC thermograms as only the glass transition of the resins can be identified, and no crystallisation nor melting peak is present (**Figure 3.27**).

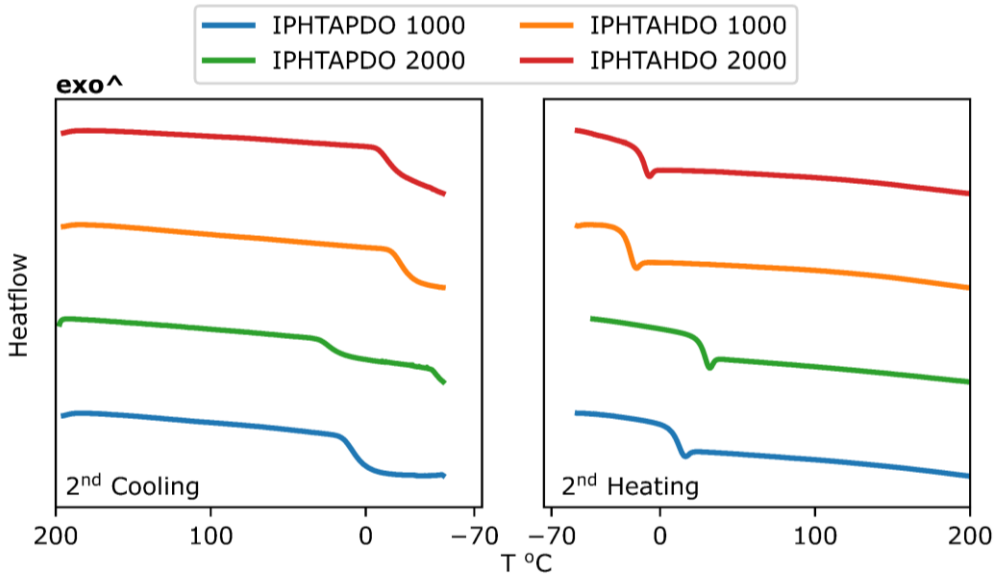

Figure 3.27: DSC thermograms of the IPHTA polyesters. Left: 2nd cooling. Right: 2nd heating.

Despite the lack of crystalline transitions, the temperature corresponding to the glass transition (T_g) allows the determination of some of the characteristics of the materials. The T_g of the aromatic polyesters is higher than that of standard aliphatic polyesters, which are usually in the range of -70 to -40 °C (**Table 3.1**).[184] The higher the T_g, the more thermal energy the polymeric chains require to gain enough mobility so that the material enters its rubbery state. Thus, the introduction of aromatic moieties in the polyesters reduces their chain mobility, probably through the formation of π-π stacking interactions and the restriction to bond rotation arising from the aromatic fragments. This agrees with the fact that the T_g of IPHTAPDO polyesters is higher than that of the IPHTAHDO ones. The PDO polyesters have a higher diacid density than their HDO counterpart, and therefore, their capability to generate π-π interactions is greater, decreasing the chain mobility of the polymers and increasing T_g. The T_g of the materials also increases with the M_n of the polyester, which could be explained by the higher number of supramolecular interactions by chain fragment that longer polymers can produce.

Table 3.1: T_g of the IPHTA polyesters by DSC

	T_g 2nd Cooling (°C)	T_g 2nd Heating (°C)
IPHTAPDO 1000	12.3	8.9
IPHTAPDO 2000	24.9	24.4
IPHTAHDO 1000	-21.6	-19.0
IPHTAHDO 2000	-13.8	-9.9

On the FDCA polyesters, in addition to glass transitions, meltings, crystallisations and cold crystallisations could be also observed (**Figure 3.28**). Moreover, within this family, there is a clear difference between the PDO and HDO polyesters, which is especially noticeable in the 2nd cooling cycle. During their cooling, the FDCAPDO polymers act similarly to their IPHTA counterpart, showing only a glass transition, while the HDO resins exhibit just crystallisations. This indicates that the capability of the FDCAHDO polymers to generate ordered structures is quite elevated and that most of the material crystallises within the timespan of the cooling process. This difference in trend might be produced by the higher chain mobility of the HDO polymers, which can aid in the generation of the ordered structures.

In the 2nd heating, all similarities between the FDCAPDO and IPHTAPDO polyesters disappear. Rather than displaying exclusively a glass transition, on the FDCAPDO polyesters, both cold crystallisation and melting transitions are present. The presence of a cold crystallisation process, which consists of an ordering of the polymer chains upon heating, reveals that the FDCAPDO polyesters require additional energy to achieve the chain mobility necessary to crystallise. Likewise, the FDCAHDO polyesters show a cold crystallisation and melting transition. However, the enthalpy associated with their cold crystallisation process is quite small (**Table 3.2**), which is understandable since the polymers have already crystallised during the cooling process and such a small fraction of the material remains in an amorphous state that no T_g is observed.

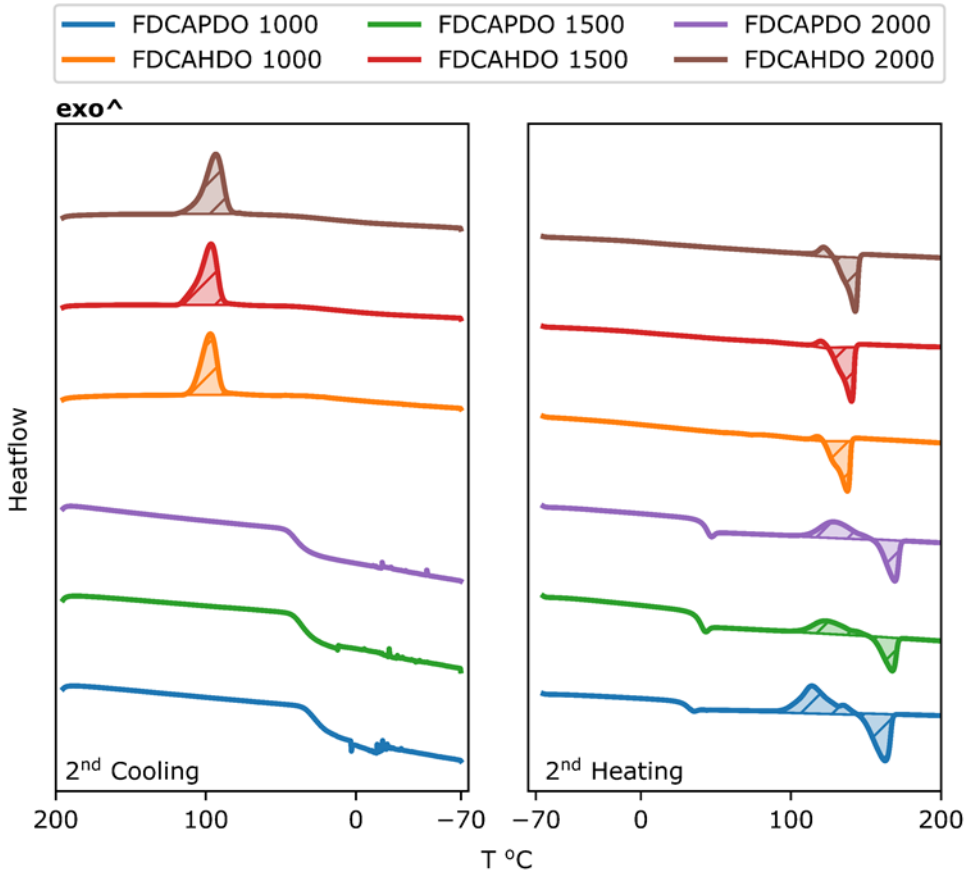

Figure 3.28: DSC thermograms of the FDCA polyesters. Left: 2nd cooling. Right: 2nd heating.

Although the FDCA polyesters cannot be compared with one another by their T_g, as some of the materials have no T_g, their melting temperatures (T_m) can be employed for their comparison (**Table 3.2**). Just as in the case of the T_g of the IPHTA polyesters, the T_m of the FDCA polyesters is higher for the PDO than HDO resins. This can be attributed, once more, to the higher density of aromatic moieties, which results in a more elevated number of π-π stacking interactions and a higher restriction to bond rotation. Moreover, the T_m slightly increases as the M_n of the polymers does, which might indicate that more stable crystallites are formed when the length of the polymeric chains grows.

Table 3.2: Transition temperatures and enthalpies of the FDCA polyesters by DSC.

	T_g 2nd Cooling (°C)	T_c (°C)	ΔH_c (J/g)	T_g 2nd Heating (°C)	T_{cc} (°C)	ΔH_{cc} (J/g)	T_m (°C)	ΔH_m (J/g)
FDCAPDO 1000	27.9	–	–	31.9	114.0	-30.3	162.6	29.2
FDCAPDO 1500	36.4	–	–	40.4	123.4	-8.6	167.3	8.0
FDCAPDO 2000	40.7	–	–	44.2	128.1	-11.0	169.0	12.2
FDCAHDO 1000	–	97.4	-61.8	–	112.5	-1.42	142.2	59.2
FDCAHDO 1500	–	96.9	-60.0	–	119.5	-1.85	139.7	55.6
FDCAHDO 2000	–	93.7	-59.2	–	121.4	-4.13	142.2	59.2

From the studies of both polyester families, IPHTA and FDCA, it can clearly be observed that, while the IPHTA resins are mostly amorphous, the FDCA polymers are either semi (PDO) or highly crystalline (HDO). This difference could be explained by two factors, kinetics, or thermodynamics. If the chain mobility of the FDCA polyesters is substantially higher than that of the IPHTA ones, their crystallisation would be favoured. On the other hand, if the supramolecular interactions on the FDCA polyesters are stronger than those formed by the IPHTA polymers, their crystallisation would be thermodynamically favoured, inducing a higher degree of crystallinity of the FDCA resins.

To elucidate which of the two factors is at play, firstly the T_g of the PDO polymers from both polyester families, FDCA and IPHTA, were compared. From these values, it is quite clear that the IPHTA polymers have higher chain mobility than the FDCA ones since their T_g are significantly lower, in the range of 8-25°C than the FDCA ones, with T_g in the range of 28-44 °C. This disagrees with the kinetic hindrance theory, as, according to kinetics, the FDCA polyesters should be just as amorphous as the IPHTA polymers.

To gain some insight into the differences in the strength of the supramolecular interactions generated by the IPHTA and FDCA moieties, density functional theory (DFT) calculations were employed to assess the strength of the π-π stacking interactions arising from both monomers. For this purpose, the energy of dimerisation of both molecules was calculated and compared

between both species (**Experimental section 6.2.10**). To simplify the model, as the main supramolecular interactions expected in the systems are those arising from the aromatic moieties, dimethyl isophthalate (IPHTAME) and dimethyl furan-2,5-dicarboxylate (FDCAME) have been employed for the calculations. For each diacid derivative, two dispositions of the two molecules forming the dimer have been considered. In one of them, the carbonyl groups are facing the same direction (C1) while in the other, the carbonyl groups are pointing opposite directions (C2) (**Figure 3.29**).

The strength of the supramolecular interactions has been evaluated by subtracting the Gibbs free energy of the monomers from that of the dimeric structures (**Equation 3.1**).

$$\Delta G_{dimerisation} = \Delta G_{dimer} - 2 \times \Delta G_{monomer}$$

Equation 3.1: Obtention of the supramolecular interaction strength by DFT calculations.

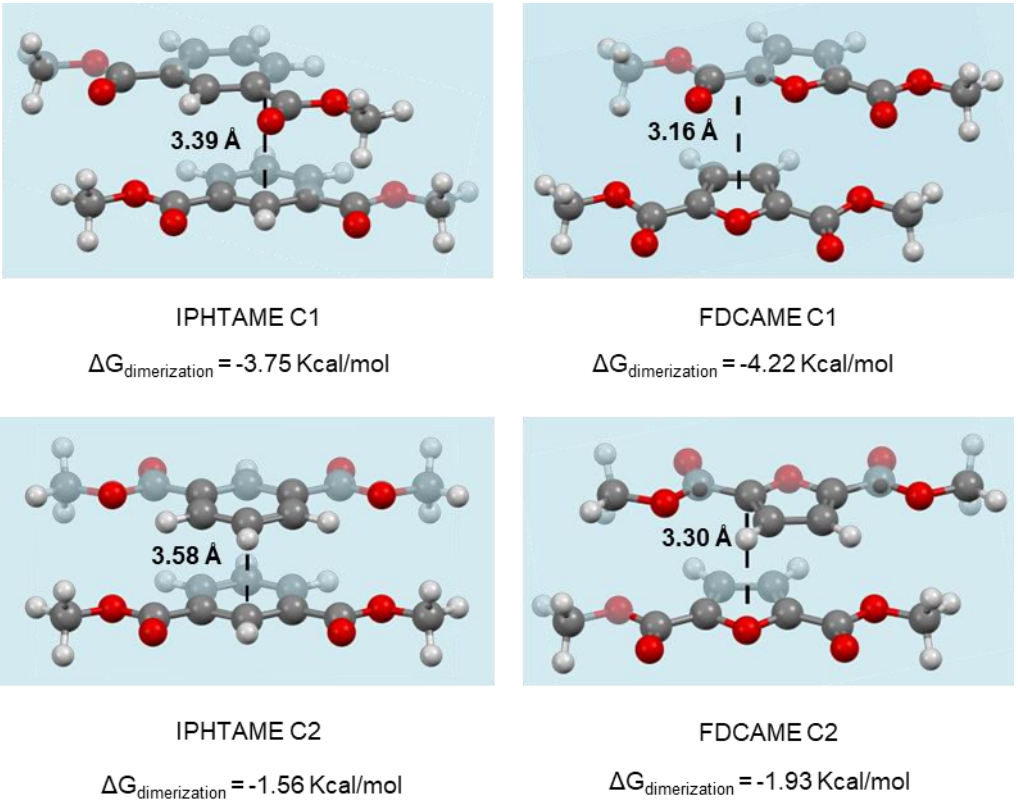

Figure 3.29: Optimised structures and Gibbs free energy of the IPHTA and FDCA methyl esters dimers.

According to the dimerisation calculations, FDCA creates more stable dimers than IPHTA. This would explain the variations in the crystallinity of their respective polyesters. As the supramolecular interactions generated by FDCA are stronger than those of IPHTA, the cohesion between the polymeric chains and therefore, their capability for forming ordered structures is favoured in the FDCA than in the IPHTA polymers. Moreover, this difference in thermodynamic stabilisation is relevant enough that it overcomes the lower chain mobility of the FDCA polymers (i.e. the kinetic effect above mentioned).

In addition to the factor behind the different crystallinity of the polymers, another somewhat unexpected result was observed in the DFT calculations. As the carbonyl groups have a high electron density, it could be forecasted that they would prefer to be as far away as possible to minimise their repulsion. Nonetheless, this is not the case, rather conformation C1, in which the carbonyl groups of the two molecules are relatively close to one another, is the disposition that forms more stable dimers. This can be understood by looking at the electron density profile of both monomers (**Figure 3.30**).

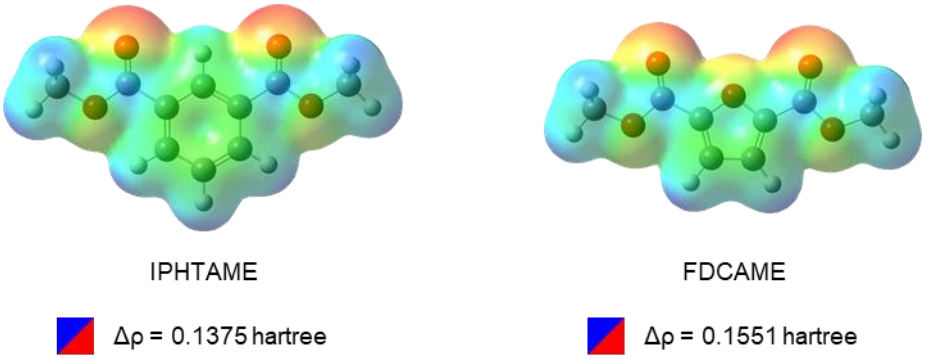

Figure 3.30: Calculated electron density profiles of IPHTAME and FDCAME. Δρ = electron density difference. Higher electron density red, lower electron density blue.

The electron density profiles show that the highest electron density areas are those around the oxygen of the carbonyl group, while the most electron-positive areas are the carbon atoms directly linked to the oxygens. The structures with the stronger supramolecular interactions would be those in which the most electronegative region of a molecule overlaps with the most electropositive zone of the other, and vice versa. By comparing these electron density profiles with the optimised dimer structures, C1 and C2, the stacking of electron-rich and electron-poor areas is only achieved in C1, while in C2 this alignment is not possible. This explains the stronger supramolecular interactions obtained in the C1 disposition. Moreover, this electron density profiles also give further insight into the stronger supramolecular interactions of the

FDCA monomer in comparison to those of IPHTA. The difference in electron density from the most electropositive region (blue) to the most electronegative (red) is bigger in FDCAME than in IPHTAME. This means that the dipolar moment of the furanic monomer is higher, resulting in the formation of stronger dipole-dipole interactions for the FDCA monomers than the IPHTA ones.

Overall, it looks like the supramolecular interactions governing the aggregation of the aromatic dimers, π-π stacking and dipole-dipole interactions, are stronger for the FDCA than the IPHTA monomers. Accordingly, the higher crystallisation capabilities of the FDCA polyesters in comparison with the IPHTA ones seem to be originated from the difference in strength of the supramolecular interactions generated by their aromatic moieties.

Chapter 4: Polyurethane development and characterisation

The synthesis of the thermoplastic polyurethanes containing furandicarboxylate and isophthalate polyesters is contained within this chapter. Moreover, the characterisation of the morphology of the polymers by differential scanning calorimetry (DSC), small-angle X-ray scattering (SAXS) and wide-angle X-ray scattering (WAXS) is discussed within. The results from this morphological assessment are then employed to rationalise the hardness, tensile strength, and shape memory behaviour of the materials.

4.1 Polyurethane synthesis

After the synthesis of the polyesters, the production of TPUs containing two different diisocyanates, methylene diphenyl diisocyanate (MDI) and hexamethylene diisocyanate (HDI) was assessed. The synthetic procedure will follow the previously discussed one step methodology, in which no solvent is employed, and which yields products with a high degree of phase segregation, resulting in materials with excellent mechanical properties. Since our aim is to understand the effect that the aromatic monomers have on the properties of the TPUs in a wide composition range, a design of experiment (DOE) approach was used.[185] The TPUs discussed in this work are protected under the preliminary patent EP 22382851.8.[1]

In the case of the IPHTA-polyester TPUs (IPHTA TPUs), a full factorial design of 12 different TPUs with three different hard segment (HS) contents, 10, 30 and 50 mol%, two different diisocyanates, the aromatic MDI and the aliphatic HDI and polyesters with two different molecular weights, 1000 and 2000 g/mol has been targeted (**Figure 4.1**). This will allow to simultaneously understand the effect that increasing the polyol M_n, rising the HS content, and modifying the nature of the diisocyanate have on the material.

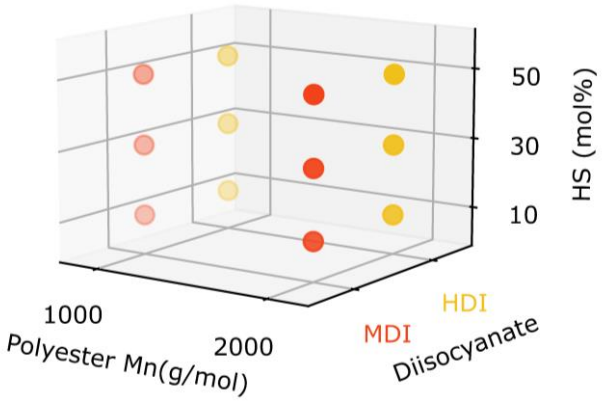

Figure 4.1: Design of the IPHTA-polyol TPUs.

For the case of the FDCA-polyester TPUs (FDCA TPUs), the approach was slightly adapted to decrease the amount of expensive FDCA used. Hence a Box-Behnken-like approach[185] was employed to reduce the number of TPUs by two while conserving the range of the studied domain. This was achieved by introducing a third molecular weight (1500 g/mol) into the polyol families, resulting in 10 distinct TPUs (**Figure 4.2**).

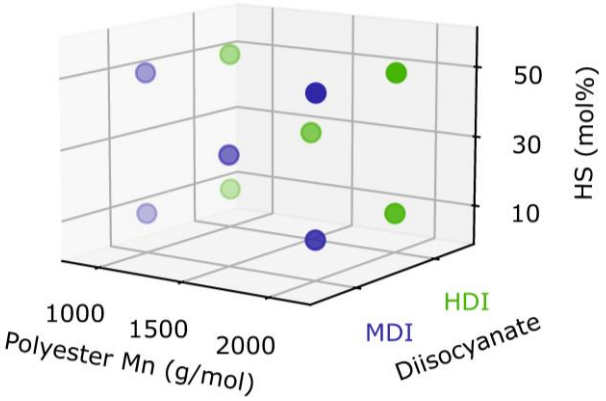

Figure 4.2: Design of the FDCA-polyol TPUs.

Before any large-scale synthesis, a reactivity test of the polyesters was performed to ensure that their reaction with the diisocyanates would occur smoothly. As model systems, the tests were performed with the IPHTA polyesters and MDI in the presence of a catalyst, the specific nature of which will not be disclosed due to the confidentiality agreement with Lubrizol (**Figure** 4.3, **Experimental Section 6.2.11**). The essay was performed by observing the time required to reach a maximum in temperature caused by the exothermy of the reaction.

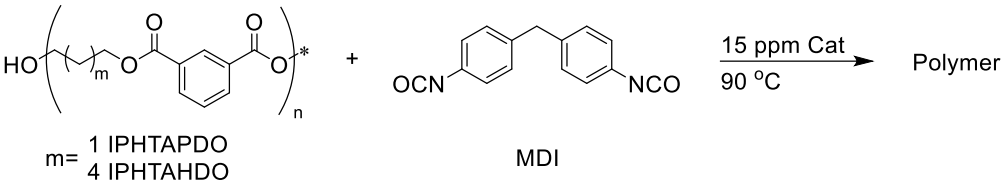

Figure 4.3: Conditions of the reactivity test of IPHTA polyesters and MDI.

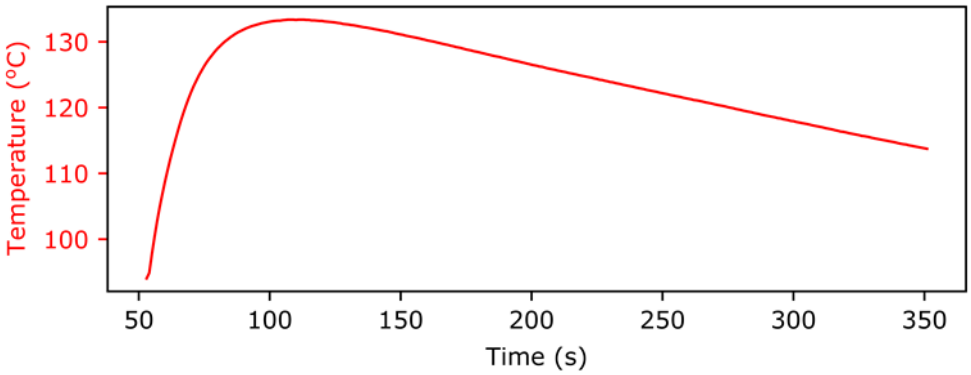

Figure 4.4: Reactivity test of an IPHTAHDO 1000 polyester and MDI.

The results show that the completion of the reaction occurs between 2-3 minutes, which is a standard value to produce TPUs (**Figure 4.4**, **Table 4.1**). Accordingly, the catalyst loading employed was deemed as correct. However, the starting temperature of the reaction was deemed unsuitable. At 90 °C, the reaction mixture was extremely viscous, and the homogenisation of the components was quite difficult to achieve. Hence, in the synthesis of each of the TPU formulations, the starting temperature will be qualitatively assessed by slowly increasing the temperature of the molten polyesters until a liquid with the appropriate viscosity was achieved.

Table 4.1: Results from the reactivity test between IPHTA polyesters and MDI.

	Reaction time (s)
IPHTAHDO 1000	110
IPHTAHDO 2000	216
IPHTAPDO 1000	150
IPHTAPDO 2000	160

With this data in hand, the synthesis of TPUs following the previous DOE was explored. Just as in the case of the polyesters, for simplicity's sake, the different polymers will be coded employing the target molecular weight of the polyester, rather than their true M_n. Hence, the TPUs' nomenclature will follow the pattern **DiacidDiol TargetMn HS (mol%) Diisocyanate** (Example: IPHTAPDO 1000 10% MDI). The exact molecular weight of the polyols employed for the synthesis of each TPU can be found in **Experimental Section 6.2.12.1-6.2.12.8**. The different materials were developed employing a standard Lubrizol formulation with 1,4-butanediol (BDO) as CE. Moreover, two additives, an antioxidant and a wax were added to ensure the processability of the TPUs. Due to the confidentiality agreement, the nature of both additives will not be disclosed under this work. The synthesis was carried out with the one-step procedure, in which first, the polyester is melted and heated to the starting temperature of the reaction, and then, all the reagents, catalysts, and additives are added to the melt (**Figure 4.5, Experimental Section 6.2.12**). Due to the difference in viscosity between the IPHTA and FDCA polyesters, the starting temperature for the former was selected as 160 °C while for the latter 180 °C was employed.

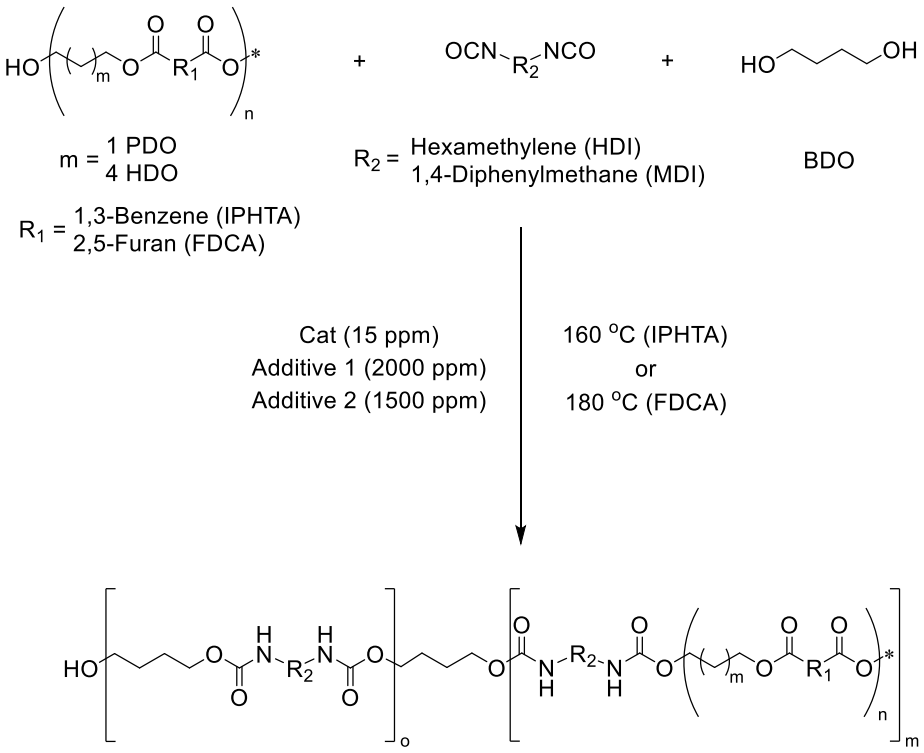

Figure 4.5: Synthetic conditions for the synthesis of the TPUs.

To ensure that all of the diisocyanate is consumed during the reaction, IR spectroscopy has been employed. By observing the presence or lack thereof of the peaks corresponding to unreacted NCO and OH, the completion of the reaction could be ensured (**Figure 4.6)**. In all cases, the full consumption of the diisocyanate and the hydroxyl groups could be observed as well as the appearance of the bands corresponding to the carbamate's NH (**Annex A1.2**). In addition to IR spectroscopy, when soluble materials were obtained, ^{1}H and $^{13}C\{^{1}H\}$ NMR and GPC have been employed for the chemical characterisation of the materials, showing that, indeed, the desired polymers were obtained with a M_n between 28000-80000g/mol (**Annex A2.2**, **A4**).

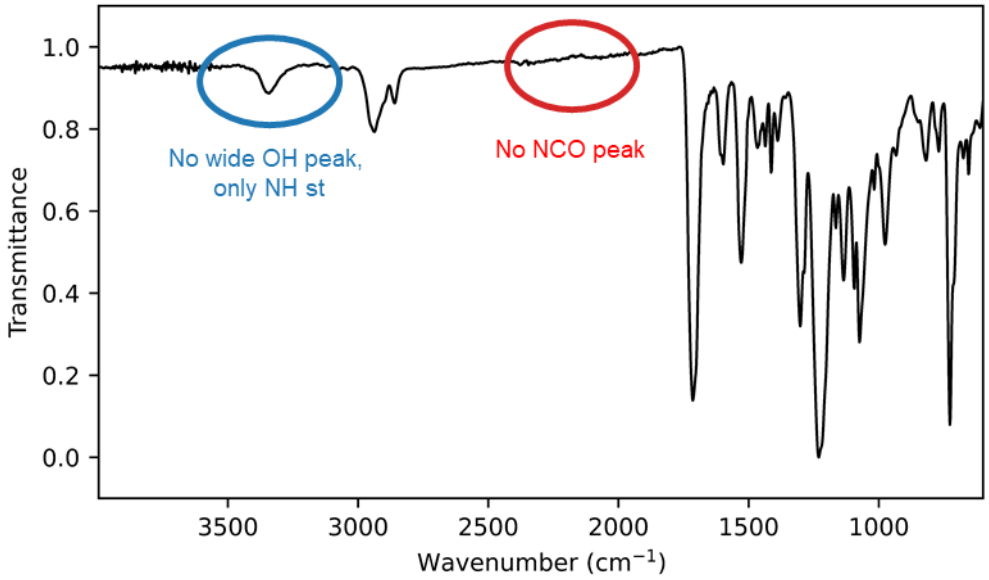

Figure 4.6: IR sample spectra of a properly polymerised TPU.

Before their thermal and mechanical characterisation, the TPUs were shredded into small pieces of approximately 1 cm (**Figure 4.7 left**, **Experimental Section 6.1.5**) and afterwards, injected into 8 x 9 x 0.25 cm plates (**Figure 4.7 right**, **Experimental Section 6.1.6**).

Figure 4.7: Left: Shredded polymer. Right: Injected plate.

4.2 Polyurethane morphological characterisation

Most of the mechanical properties of TPU materials are linked to their phase morphology, with phase segregation and crystallinity playing the biggest role in determining the mechanical behaviour of the materials. Therefore, to understand the mechanical properties of the materials, an assessment of their morphology needs to be carried out.

4.2.1 Differential scanning calorimetry

One of the techniques that has been employed to obtain information about the phase morphology of the materials is differential scanning calorimetry (DSC). DSC allows the determination of the phase transitions in the materials. Hence, information concerning the crystallinity and glass transition of the TPUs can be extracted by this technique. The analysis of the T_g can be employed to shed a light on the chain mobility of the polymers, while the melting and crystallisation of the hard segment (HS) and soft segment (SS) gives information about the degree of phase segregation and relative order of each domain. However, the melting and crystallisation processes only give information about the crystalline phases. Therefore, they cannot be used to get the whole image of the phase segregation of the TPUs, since disordered HS and SS domains, which do not give rise to a melting or crystallisation peak, can exist within the TPU structure.

A 2-cycle process will be employed to analyse the thermal transitions of the TPUs. In the first cycle, the materials are brought to the initial essay temperature (-70 or -50 °C) and heated to a temperature well above their glass transition and melting temperatures (T_g and T_m). In this first

step, referred from here on out as 1st heating cycle, the effect that the injection process and storage of the materials have on its microstructure can be gathered. On a second cooling and heating cycle, the material will be cooled back to the initial temperature and heated once more above its T_m. These cooling and heating processes will be referred to as 2nd cooling and heating cycles. This 2nd cycle contains only the morphological information inherent to the material, erasing the effect that their storage and injection process have on the morphology (**Experimental Section 6.1.9**).

Initially, the 2nd heating and cooling cycles of the different materials will be assessed, as they enable the comparison of the materials under the exact same conditions, without taking into consideration their thermal history. The morphology inferred from these two cycles will be employed to determine the relative chain mobility and crystallisation capabilities of the TPUs with regard to one another. Moreover, this data will be employed to find, if any, the existing relationships between the different composition parameters, namely the HS content (10, 30, 50%), diacid (FDCA and IPHTA), diol (PDO or HDO), and polyester M_n (1000-2000 g/mol), and the morphology and chain mobility of the materials. In addition to the analysis of the 2nd heating and cooling cycles, the 1st heating cycle will be employed to determine the effects that the injection process and storage of the materials have on the chain mobility and morphology of the TPUs. The mechanical properties of the materials will not be measured right after their injection, but rather, they will be stored for at least a week at 21 °C before their analysis. Therefore, knowing the morphological characteristics of the materials including their thermal history, which is produced by both their storage and injection process, is crucial to understand the variations in the mechanical properties of the different formulations. Accordingly, the data obtained from the 1st heating cycle will be used in a posterior section to analyse how the differences in morphology between the TPUs affect their mechanical properties.

4.2.1.1 IPHTA MDI TPUs

In the IPHTA MDI TPUs, no melting nor crystallisation peak could be observed on the 2nd cooling or heating cycle of either the IPHTAPDO or IPHTAHDO formulations, with only glass transitions being detectable in the thermograms (**Figure 4.8**, **Figure 4.9**). This is the same behaviour that was observed in their corresponding polyesters, in which, likewise, only glass transitions could be observed. The lack of transitions related to any crystalline structure indicates that the polymers are amorphous. Although the amorphous nature of the SS could be expected, as the corresponding polyesters also lack any crystallinity, the absence of crystallinity on the HS is more unexpected. This lack of crystalline domains could be originated from two

different factors, a high miscibility between the SS and HS chain fragments and/or a highly restricted chain mobility. As the HS and SS domains have a high density of aromatic moieties, π-π stacking interactions can be formed between them, leading to an elevated SS-HS miscibility and therefore, to low phase segregations. Likewise, a low chain mobility would result in the lack of HS and SS domains, since chain mobility is required for the polymeric chains to segregate, and form ordered structures.

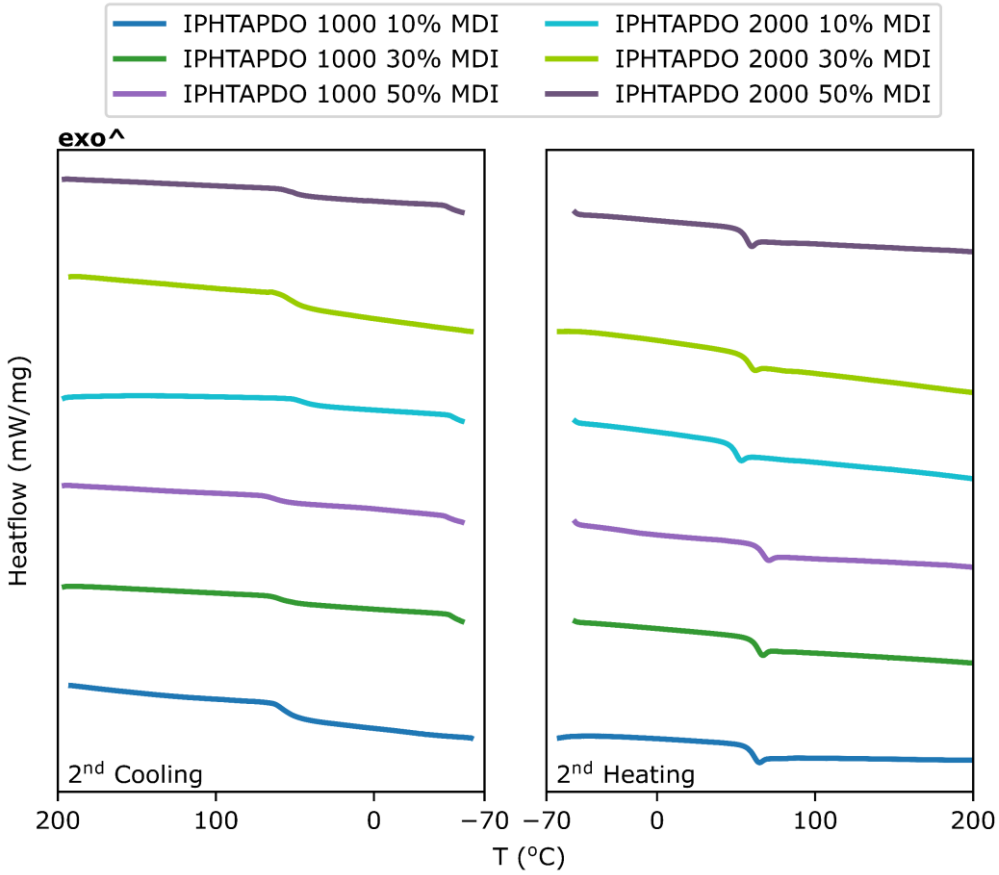

Figure 4.8: Thermograms of the IPHTAPDO MDI TPUs. Left: 2nd cooling cycle. Right: 2nd heating cycle.

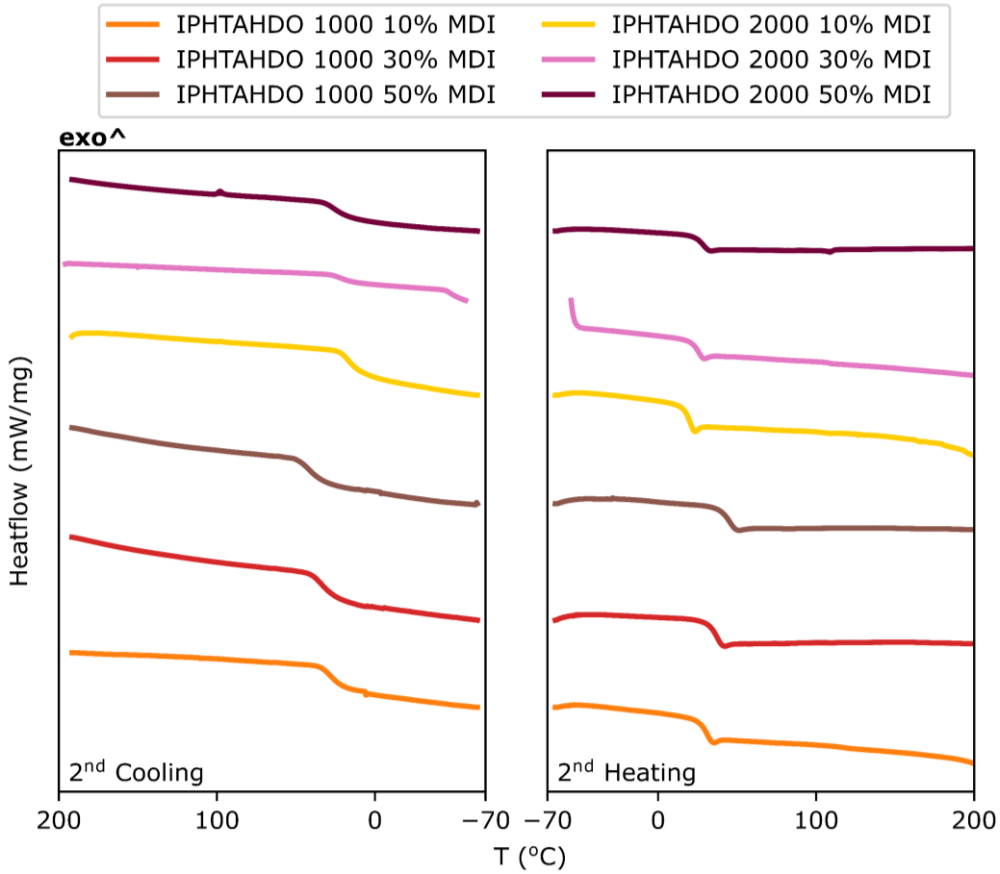

Figure 4.9: Thermograms of the IPHTAHDO MDI TPUs. Left: 2nd cooling cycle. Right: 2nd heating cycle.

Further information can be extracted by analysing the relationship between the T_g and composition of the materials (**Table 4.2**). The first noticeable trend that can be observed is that the PDO TPUs have a higher T_g than their HDO counterpart. This is the same behaviour found in their corresponding polyesters and can be explained by the same phenomenon. The higher concentration of aromatic monomers in the SS of the PDO TPUs in comparison with those of the HDO materials allows the formation of a greater number of supramolecular interactions, reducing the chain mobility of the PDO formulations. Two additional trends can be extracted from the T_g data. Firstly, the T_g of the materials increases with the HS content. This is standard for most TPUs, as unless complete phase segregation is achieved, the highest the HS content, the more HS chain fragments become mixed with the SS. As the HS chain fragments are capable of forming H-bonds, which are the strongest supramolecular interactions that can be formed in these materials, the mixing of the HS within the SS leads to an increase in the T_g.

The second observed trend is that as the polyester M_n increases, the T_g of the material decreases. This can be likewise explained by the change in HS concentration in the system. As the M_n of the polyester increases, to maintain the HS molar fraction, HS (mol%), less diisocyanate and chain extender (CE) by weight % have to be added in order to reach the desired formulation. Consequently, an increase in the polyester M_n leads to a decrease in the molal concentration of the two HS monomers, while that of the polyol increases. Therefore, the number of H-bonding interactions, which require diisocyanate moieties to be generated, decreases. The reduction in the number of H-bonding interactions results in a decrease of the T_g, which the increase in the number of π-π stacking interactions from the higher IPHTA concentration are not able to compensate. The effect of MDI in the T_g of the TPUs is so big that, the introduction of a single mole of MDI can compensate for the loss of a mole of polyester, which contains between 3.6-10.6 IPHTA units per chain.

Table 4.2: T_g of the IPHTA MDI TPUs 2nd cooling and heating cycles.

	T_g (°C)[a]		T_g (°C)[a]
IPHTAPDO 1000 10% MDI	60.0 ± 0.3	**IPHTAHDO 1000 10% MDI**	29.7 ± 0.8
IPHTAPDO 1000 30% MDI	61.4 ± 0.1	**IPHTAHDO 1000 30% MDI**	35.4 ± 0.7
IPHTAPDO 1000 50% MDI	64.6 ± 0.2	**IPHTAHDO 1000 50% MDI**	42.9 ± 0.5
IPHTAPDO 2000 10% MDI	50.2 ± 0.7	**IPHTAHDO 2000 10% MDI**	20.0 ± 0.1
IPHTAPDO 2000 30% MDI	52.8 ± 0.2	**IPHTAHDO 2000 30% MDI**	23.5 ± 0.6
IPHTAPDO 2000 50% MDI	53.9 ± 0.2	**IPHTAHDO 2000 50% MDI**	27.8 ± 0.2

[a] Calculated as the mean of the T_g obtained from the 2nd cooling and heating cycles from three different injected plates.

After the analysis of the 2nd cooling and heating cycles of the IPHTA MDI TPUs, their 1st heating cycle has been assessed. The study of the 1st heating cycle will allow the determination of any changes in phase morphology induced by the injection process or by the evolution of the materials with time during their storage.

Just as in the 2nd heating process, on the 1st heating cycle no melting transition was observed for any of the materials, just glass transitions arise from the DSC (**Figure 4.10**). However, unlike during the 2nd cycle, a large hysteresis was observed on the T_g transitions, especially on the PDO TPUs. This hysteresis is observed as an endothermic peak right at the high temperature end of the T_g and is related to the structural relaxation of the polymers when transitioning from the glassy to the rubbery state. From the presence of this hysteresis process it can be inferred that during the cooling process of the material to room temperature after its injection process,

the structure of the polymer is frozen in a constrained state, which is released once the material gains enough chain mobility.[186,187]

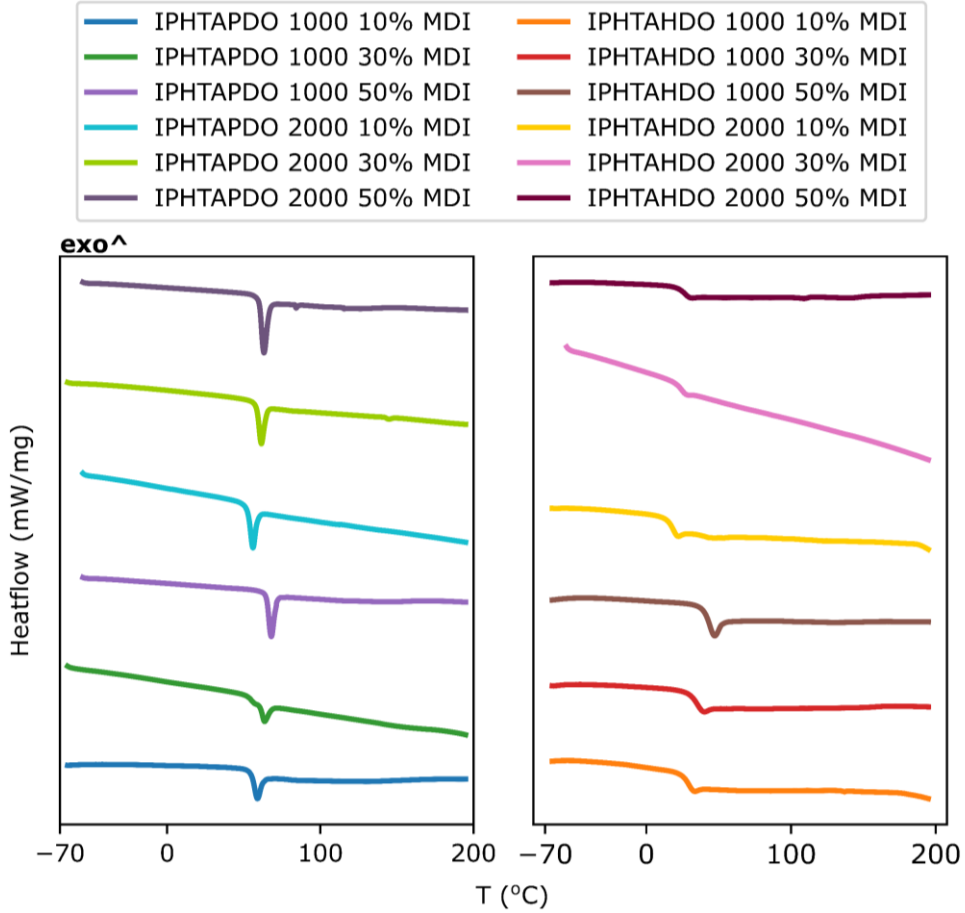

Figure 4.10: Thermograms of the IPHTA MDI TPUs 1st heating cycle.

The analysis of the relationships between composition and T_g of the materials during their 1st heating process yields the same trends as those observed during the 2nd heating cycle. The T_g of the PDO polymers is higher than that of the HDO ones and it increases as the HS content increases and the polyester M_n decreases (**Table 4.3**). Moreover, the T_g obtained from the 1st heating process were 0.3-4 °C lower than those of the 2nd cycle. This might be an indication that the phase segregation of the polymers in their injected state is ever so slightly higher than after their 2nd cooling and heating cycles. Nonetheless, the phase segregation of the materials seems to be low, with no ordered HS or SS domains being formed.

Table 4.3: T_g of the IPHTA MDI TPUs 1st heating cycle.

	T_g (°C)[a]		T_g (°C)[a]
IPHTAPDO 1000 10% MDI	60.7 ± 2.6	**IPHTAHDO 1000 10% MDI**	30.2 ± 0.7
IPHTAPDO 1000 30% MDI	58.0 ± 2.8	**IPHTAHDO 1000 30% MDI**	35.8 ± 0.4
IPHTAPDO 1000 50% MDI	67.4 ± 0.9	**IPHTAHDO 1000 50% MDI**	45.0 ± 0.9
IPHTAPDO 2000 10% MDI	48.6 ± 3.9	**IPHTAHDO 2000 10% MDI**	20.2 ± 0.2
IPHTAPDO 2000 30% MDI	51.5 ± 0.8	**IPHTAHDO 2000 30% MDI**	24.6 ± 0.4
IPHTAPDO 2000 50% MDI	61.0 ± 1.6	**IPHTAHDO 2000 50% MDI**	25.3 ± 0.0

[a] Calculated as the mean of the T_g obtained from the 1st heating cycle from three different injected plates.

4.2.1.2 IPHTA HDI TPUs

The analysis of the thermograms from the 2nd heating and cooling cycles of the IPHTAPDO HDI TPUs leads to the same observations as their MDI counterpart. All of the IPHTAPDO HDI TPUs are amorphous materials, exhibiting only a glass transition, with no crystallisation nor melting transition being discernible (**Figure 4.11**).

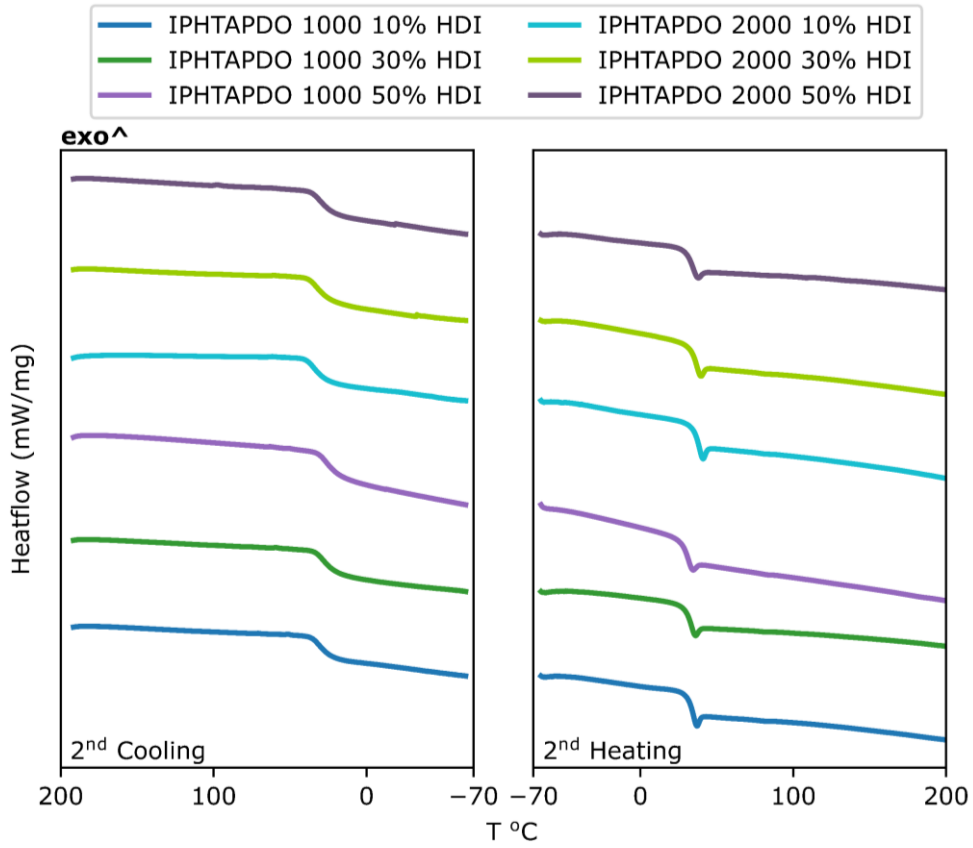

Figure 4.11: Thermograms of the IPHTAHDO HDI TPUs. Left: 2nd cooling cycle. Right: 2nd heating cycle.

In the IPHTAHDO HDI materials, a deviation from the amorphous nature of the IPHTAHDO MDI TPUs can be observed (**Figure 4.12**). Although most of the IPHTAHDO HDI formulations are amorphous, just as in the previous materials, in the two TPUs with the highest HS content, **IPHTAHDO 1000 50%** and **FDCAHDO 2000 50% HDI**, transitions associated with the presence of crystalline structures can be noted. The fact that the presence of crystallites is only detected on the TPUs with the highest HS content seems to indicate the presence of ordered HS domains, rather than crystalline SS structures. In both polymers, in addition to melting transitions, a cold crystallisation process could be observed during the 2nd heating cycle. The presence of cold crystallisation indicates that the materials require additional energy to achieve an ordered structure, as the chain mobility of the polymers is too low to enable their crystallisation without the introduction of thermal energy into the TPUs. Therefore, the presence of cold crystallisations indicates that one of the parameters that is inhibiting the segregation and

crystallisation of the HS domains is the poor chain mobility of the materials, generated by the abundant supramolecular interactions present in the polymers.

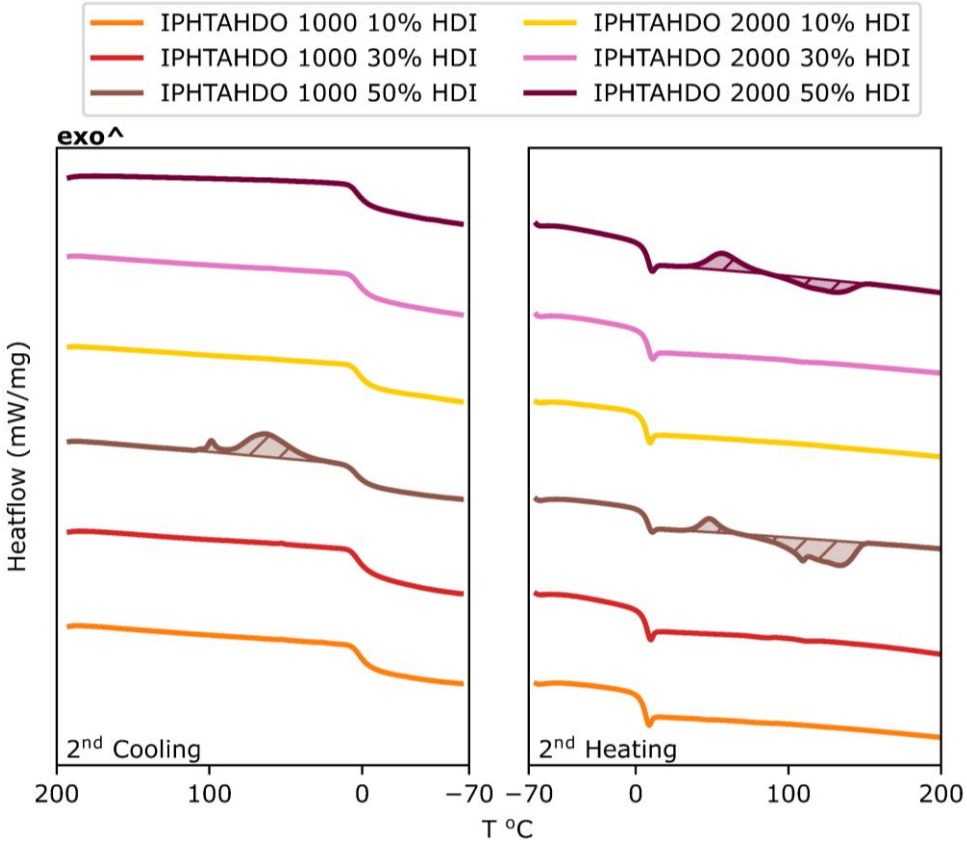

Figure 4.12: Thermograms of the IPHTAHDO HDI TPUs. Left: 2nd cooling cycle. Right: 2nd heating cycle.

In addition to cold crystallisations and melting transitions, a crystallisation of the material could be observed on the 2nd cooling of the **IPHTAHDO 1000 50% HDI**. The fact that the **IPHTAHDO 1000 50% HDI** sample can crystallise during the 2nd cooling process while the **2000 50% HDI** formulation cannot indicates that the ability of the HS domains to segregate and form ordered structures is higher the lower the polyester M_n is. This agrees with the values obtained for the enthalpy of the melting process, which were higher for **IPHTAHDO 1000 50% HDI** than **IPHTAHDO 2000 50% MDI**, confirming the higher crystallinity of the former (**Table 4.4**).

Table 4.4: Temperatures and enthalpies of the IPHTA HDI TPUs 2nd cooling and heating cycles.

	T_g (°C)[a]	T_{cryst} (°C)[b]	ΔH_{cryst} (J/g)[c]	T_{CC} (°C)[b]	ΔH_{cc} (J/g)[c]	T_m (°C)[b]	ΔH_m (J/g)[c]
IPHTAPDO 1000 10% HDI	32.9 ± 0.2	–	–	–	–	–	–
IPHTAPDO 1000 30% HDI	31.1 ± 0.2	–	–	–	–	–	–
IPHTAPDO 1000 50% HDI	28.6 ± 0.1	–	–	–	–	–	–
IPHTAPDO 2000 10% HDI	36.6 ± 0.2	–	–	–	–	–	–
IPHTAPDO 2000 30% HDI	34.7 ± 0.5	–	–	–	–	–	–
IPHTAPDO 2000 50% HDI	32.4 ± 0.1	–	–	–	–	–	–
IPHTAHDO 1000 10% HDI	3.2 ± 0.9	–	–	–	–	–	–
IPHTAHDO 1000 30% HDI	5.4 ± 0.3	–	–	–	–	–	–
IPHTAHDO 1000 50% HDI	6.0 ± 0.4	63.2 ± 0.7	-13.5 ± 2.5	48.5 ± 0.1	-5.9 ± 1.7	133.3 ± 0.0	12.8 ± 4.9
IPHTAHDO 2000 10% HDI	4.6 ± 0.4	–	–	–	–	–	–
IPHTAHDO 2000 30% HDI	5.3 ± 0.4	–	–	–	–	–	–
IPHTAHDO 2000 50% HDI	4.8 ± 1.3	–	–	57.1 ± 0.2	-7.3 ± 0.6	130.1 ± 2.0	7.1 ± 0.8

[a] Calculated as the mean of the T_g obtained from the 2nd cooling and heating cycles from three different injected plates.
[b] Calculated as the mean of the maximums of the corresponding peaks from three different injected plates, cryst=crystallisation, CC=cold crystallisation, m=melting.
[c] Calculated as the mean of the enthalpies of the corresponding peaks from three different injected plates.

The analysis of the T_g of the materials yields information about how the chain mobility of the polymers affects their crystallinity. Just as on the IPHTA MDI formulations, the IPHTAPDO HDI polymers have a higher T_g than the HDO ones. This can be attributed, once more, to the higher number of supramolecular interactions present in the PDO formulations owing to their higher IPHTA concentration in comparison with the HDO TPUs. The differences in chain mobility

between both HDO and PDO formulations seem to be the root of their different crystallinity. The formation of HS ordered domains on the IPHTAHDO HDI materials is already restricted by their low chain mobility, as evidenced by the presence of a cold crystallisation process. Therefore, in the IPHTAPDO HDI TPUs, which have a higher T_g than their HDO counterpart, this chain mobility restriction is even higher, inhibiting the formation of any ordered HS domains even in polymers with a high HS content.

Additional information on the effect that each of the TPU components has on the structure of the materials can be extracted by the comparison between the T_g of the IPHTA MDI and HDI TPUs. In all cases, the T_g of the MDI polymers is higher than that of their HDI analogous (**Figure** 4.13). This indicates that MDI has a greater impact on the chain mobility of the materials than HDI. The difference in chain mobility between the MDI and HDI materials can be attributed to the same phenomenon, the aromatic or aliphatic nature of the diisocyanate. Owing to its aromatic nature, MDI has higher rigidity and forms stronger supramolecular interactions than the aliphatic HDI, as MDI is not only capable of generating H-bonding interactions, just as HDI, but also π-π stacking interactions. Moreover, the capability of MDI of generating π-π stacking interactions also increases its HS-SS miscibility, as π-π stacking interactions can be generated between the aromatic IPHTA and MDI. Since low phase segregations result in elevated T_g values, as the interactions generated between the HS and SS restrict the mobility of the polymers, the high miscibility between HS and SS domains generated by MDI further decreases the chain mobility of their corresponding TPUs. The stronger supramolecular interactions of MDI coupled with the lower phase segregation it produces in comparison with HDI induces a lower chain mobility in the MDI materials.

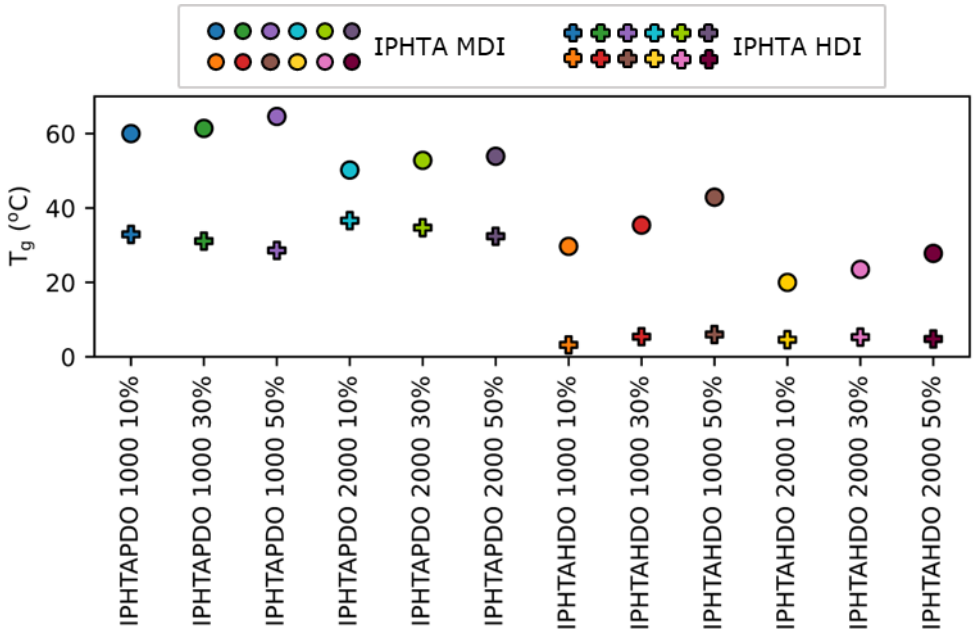

Figure 4.13: T_g comparison of IPHTA MDI and IPHTA HDI TPUs.

Once all the information contained within the 2nd cooling and heating cycles was extracted, the data collected from the 1st heating process has been interpreted. By just an initial glance at the thermograms, a striking difference between the 1st and 2nd heating cycles can be noted (**Figure** 4.14). The crystallinity of the materials during the 1st heating process is notably higher than that during the 2nd heating cycle, with all of the IPHTAHDO formulations and two IPHTAPDO TPUs showing some kind of melting transition. The higher crystallinity of the materials during the 1st heating process agrees with the previous hypothesis, which stated that the crystallinity of the TPUs is restricted due to their low chain mobility. The crystallisation time given to the materials after injection is higher than the one the materials have during the 2nd cooling and heating process. This higher crystallisation time allows for the formation of a higher number of ordered structures, as the chain fragments have enough time to rearrange themselves into more stable crystalline structures. The fact that all of the HDO materials are semicrystalline while only two of the PDO formulations show any crystalline structure proves, once more, the great impact that the chain mobility of the TPUs has on their crystallinity since the PDO formulations have a lower chain mobility than their HDO counterparts.

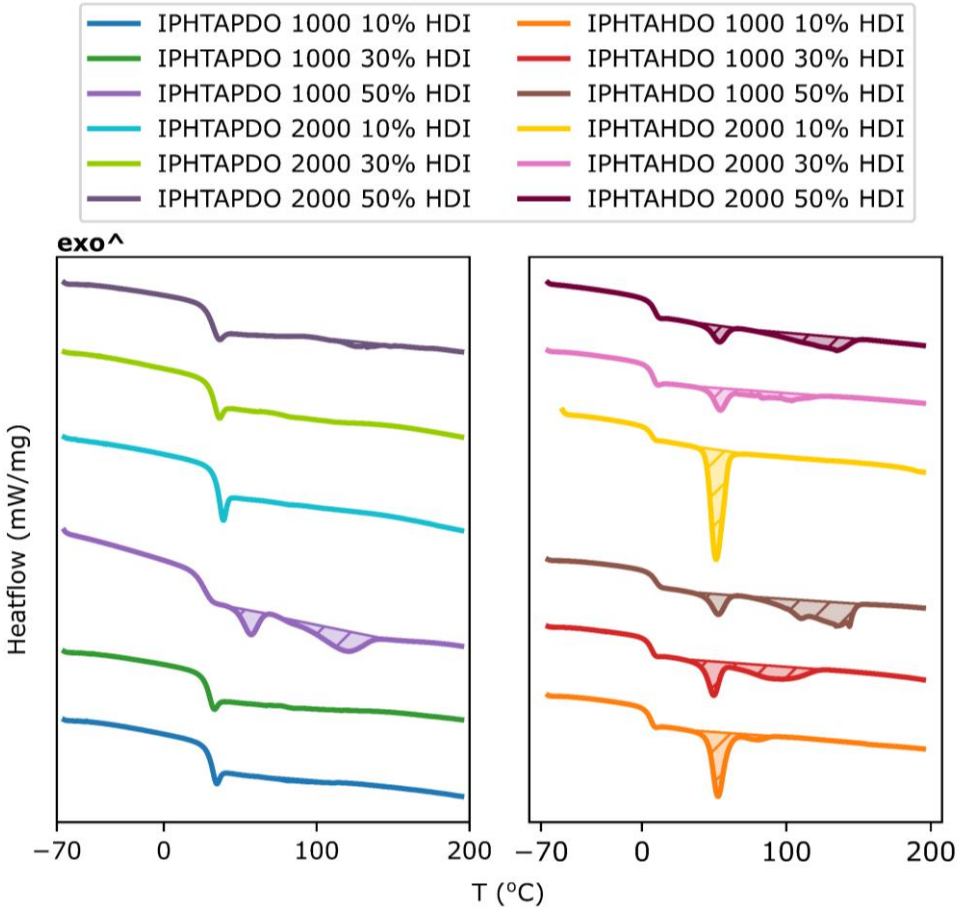

Figure 4.14: Thermograms of the IPHTA HDI TPUs 1st heating cycle.

In addition to the higher number of semicrystalline materials observed during the 1st heating process in comparison to the 2nd heating cycle, an additional difference can be noted between the thermograms of both cycles. On the 2nd heating cycle of the semicrystalline materials, only one melting peak, at around 130 °C assigned to the formation of ordered HS domains could be identified, while on the 1st heating cycle, two different melting processes are present, one at 47-72 °C and another one at 79-134 °C (**Table 4.5**).

Table 4.5: Temperatures and enthalpies of the IPHTA HDI TPUs 1st heating cycle.

	T_g (°C)[a]	T_m, Peak 1 (°C)[b]	ΔH_m, Peak 1 (J/g)[c]	T_m, Peak 2 (°C)[b]	ΔH_m, Peak 2 (J/g)[c]
IPHTAPDO 1000 10% HDI	28.3 ± 1.0	–	–	–	–
IPHTAPDO 1000 30% HDI	28.1 ± 1.4	–	–	–	–
IPHTAPDO 1000 50% HDI	27.3 ± 0.9	57.1 ± 0.2	3.7 ± 0.2	119.4 ± 0.8	9.9 ± 1.6
IPHTAPDO 2000 10% HDI	35.3 ± 1.1	–	–	–	–
IPHTAPDO 2000 30% HDI	31.0 ± 0.5	–	–	–	–
IPHTAPDO 2000 50% HDI	32.3 ± 04	72.2 ± 0.2	1.5 ± 0.2	117.1 ± 3.1	1.7 ± 0.1
IPHTAHDO 1000 10% HDI	5.0 ± 0.9	53.9 ± 0.6	14.5 ± 0.6	79.7 ± 1.2	2.7 ± 0.7
IPHTAHDO 1000 30% HDI	7.0 ± 0.3	54.7 ± 0.6	8.3 ± 0.6	97.1 ± 5.4	9.9 ± 1.3
IPHTAHDO 1000 50% HDI	6.3 ± 2.4	53.6 ± 0.4	5.4 ± 0.4	134.1 ± 0.8	16.9 ± 3.0
IPHTAHDO 2000 10% HDI	6.8 ± 0.1	47.8 ± 0.3	21.8 ± 0.3	–	–
IPHTAHDO 2000 30% HDI	6.9 ± 0.7	53.6 ± 1.4	6.5 ± 1.4	100.2 ± 3.5	6.4 ± 1.9
IPHTAHDO 2000 50% HDI	7.6 ± 1.1	49.9 ± 0.9	3.2 ± 0.9	96.3 ± 28	9.3 ± 3.4

[a] Calculated as the mean of the T_g obtained from the 1st heating cycle from three different injected plates.
[b] Calculated as the mean of the maximums of the corresponding peaks from three different injected plates. m=melting.
[c] Calculated as the mean of the enthalpies of the corresponding peaks from three different injected plates.

The existence of two distinct melting bands seems to indicate that both HS and SS ordered domains are present within the materials. Each of the peaks could be assigned to one of the two domains by analysing their variation with the HS and SS content. The peak located at the lowest temperature (47-72 °C), which will be referred from now on as peak 1 can be attributed to the SS domains, since the enthalpies associated with this melting process increase hand in hand with the SS content. The peak located at higher temperatures, from now on referred to as

peak 2, shows the exact inverse trend, increasing in intensity alongside the HS content (**Table 4.5**). Therefore, peak 2 can be assigned to the existence of ordered HS domains. The lack of SS crystallites during the 2nd heating cycle, in contrast to their presence in the 1st heating process, indicates that crystallisation of the SS domains is more restricted than that of the HS crystallites and that they require more time in order to orient themselves into ordered structures.

Further information about the crystalline structure of the HS domains can be obtained by comparing the temperatures and enthalpies of the different transitions of the 1st heating process. The temperature associated with the melting of the HS domains increases with the HS content (**Table 4.5**). This might indicate that, as the HS content increases, the order and therefore the stability of the HS domains grows, producing structures that require more energy in order to melt.

4.2.1.3 FDCA MDI TPUs

The 2nd cooling and heating cycles of the FDCA MDI TPUs exhibit the same behaviour as that of their IPHTA MDI analogous. The materials are completely amorphous showing only a T_g with no melting or crystallisation transition being present (**Figure 4.15**, **Figure 4.16**). This proves that just as in the IPHTA MDI TPUs, the crystallinity of the FDCA MDI formulations is hindered.

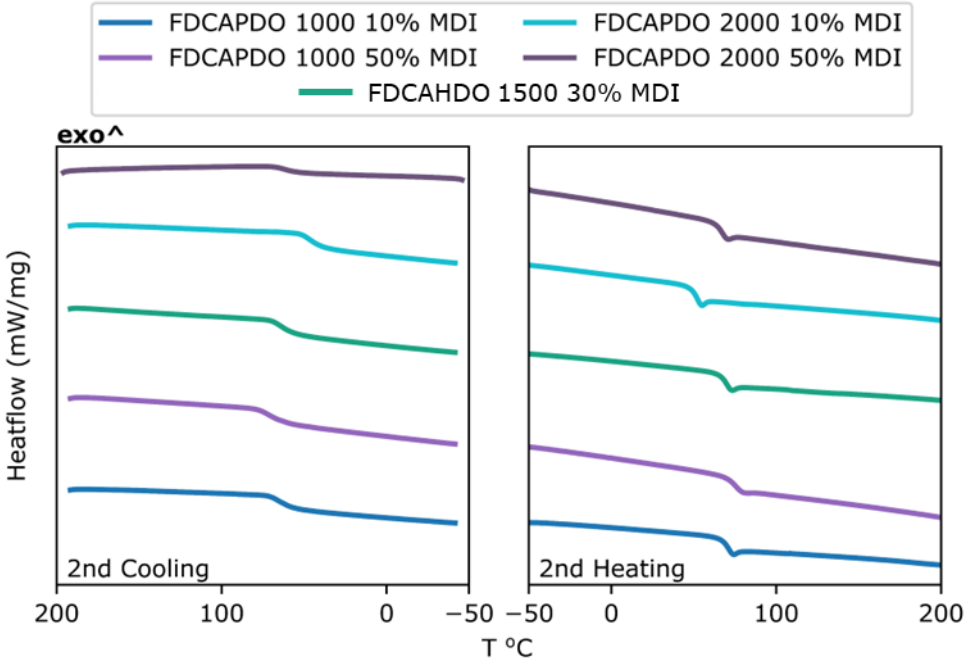

Figure 4.15: Thermograms of the FDCAPDO MDI TPUs. Left: 2nd cooling cycle. Right: 2nd heating cycle.

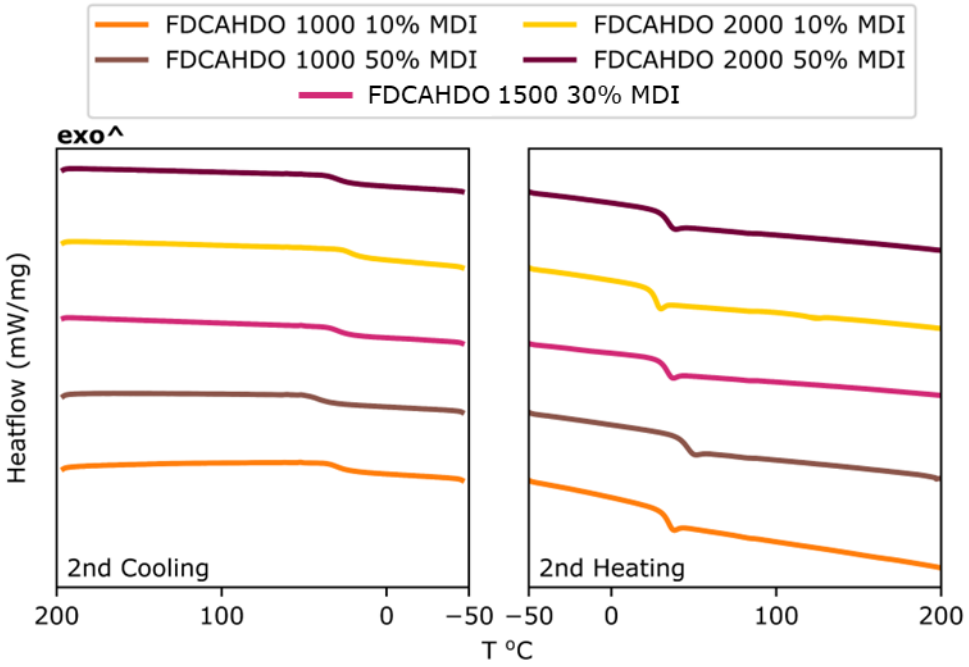

Figure 4.16: Thermograms of the FDCAHDO MDI TPUs. Left: 2nd cooling cycle. Right: 2nd heating cycle.

In addition to the FDCA MDI TPUs presenting the same amorphous character as their IPHTA counterpart, the same trends involving T_g and composition can be observed in both formulations. In the FDCA MDI materials, just as in their IPHTA analogous, T_g increases with the diisocyanate concentration. Therefore, a higher HS content and a lower polyester M_n are translated into a higher T_g of the FDCA MDI TPUs (**Table 4.6**). Nonetheless, the fact that the same trends regarding T_g are followed for the IPHTA and FDCA materials does not mean that the change in diacid does not have any effect on the T_g. The T_g of the FDCA TPUs is slightly higher than that of their IPHTA counterpart (**Figure 4.17**). According to the previous DFT calculations, the dimerisation strength of the FDCA moieties is approximately 1.1-1.2 times higher than that of IPHTA. The stronger supramolecular interactions generated by the FDCA SS in comparison to those of the IPHTA SS domains produce a decrease in the chain mobility of the material resulting in a lower chain mobility for the former.

Table 4.6: T_g of the IPHTA MDI TPUs 2nd cooling and heating.

	T_g (°C)[a]		T_g (°C)[a]
FDCAPDO 1000 10% MDI	69.8 ± 0.8	FDCAHDO 1000 10% MDI	32.4 ± 0.5
FDCAPDO 1000 50% MDI	73.1 ± 0.3	FDCAHDO 1000 50% MDI	43.8 ± 0.4
FDCAPDO 1500 30% MDI	67.1 ± 0.1	FDCAHDO 1500 30% MDI	31.2 ± 0.9
FDCAPDO 2000 10% MDI	49.4 ± 0.2	FDCAHDO 2000 10% MDI	24.3 ± 0.2
FDCAPDO 2000 50% MDI	64.6 ± 0.5	FDCAHDO 2000 50% MDI	32.1 ± 0.5

[a] Calculated as the mean of the T_g obtained from the 2nd cooling and heating cycles from three different injected plates.

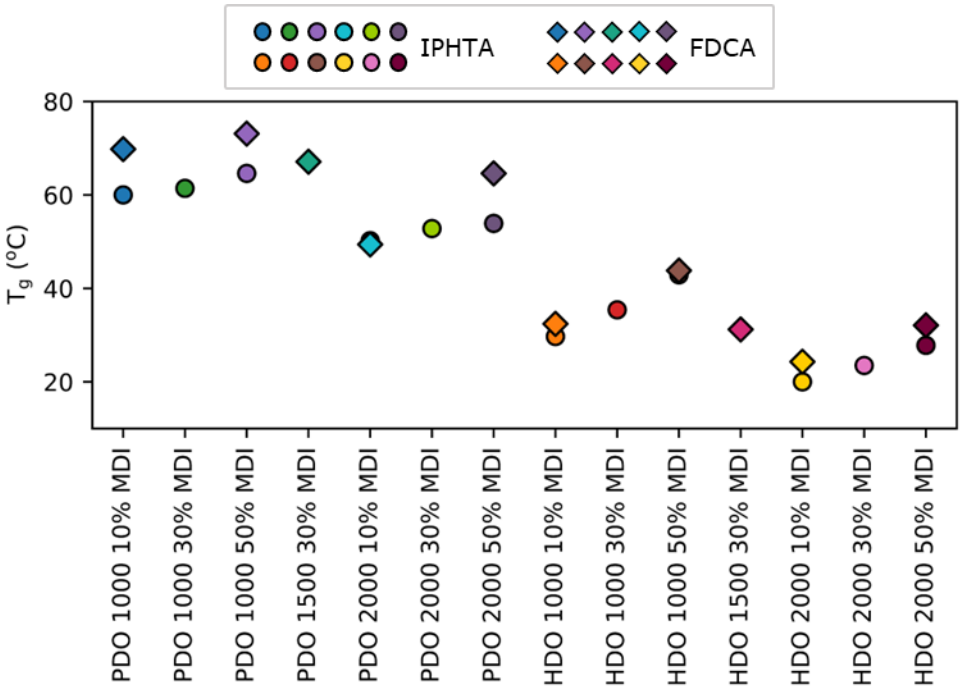

Figure 4.17: Tg comparison of IPHTA MDI and FDCA MDI TPUs.

Unlike during the 2nd heating cycle of the FDCA MDI TPUs, in which only amorphous materials could be found, some thermal transitions associated with the existence of crystalline structures could be observed in the 1st heating process of the FDCAHDO MDI formulations (**Figure 4.18**). On most of the HDO polymers, low-intensity melting transitions could be noted, with one remarkable exception, **FDCAHDO 2000 10% MDI**, which exhibits a highly intense cold

crystallisation and melting transition. The existence of melting transitions in the 1st heating process but not the 2nd shows that, given enough time, some of the materials can segregate and form ordered structures. This serves as proof, once more, of the great influence that the kinetics of the segregation and crystallisation processes have on the structure of these aromatic polyol TPUs. In addition to the existence of some crystalline transitions, a big hysteresis in the T_g of the FDCAPDO materials could be noted, similar to what was observed on the IPHTA MDI materials. This high hysteresis is associated, as previously discussed, with a relaxation of the structure of the materials and indicates that during their cooling process after injection, their structure is frozen in a constrained state.

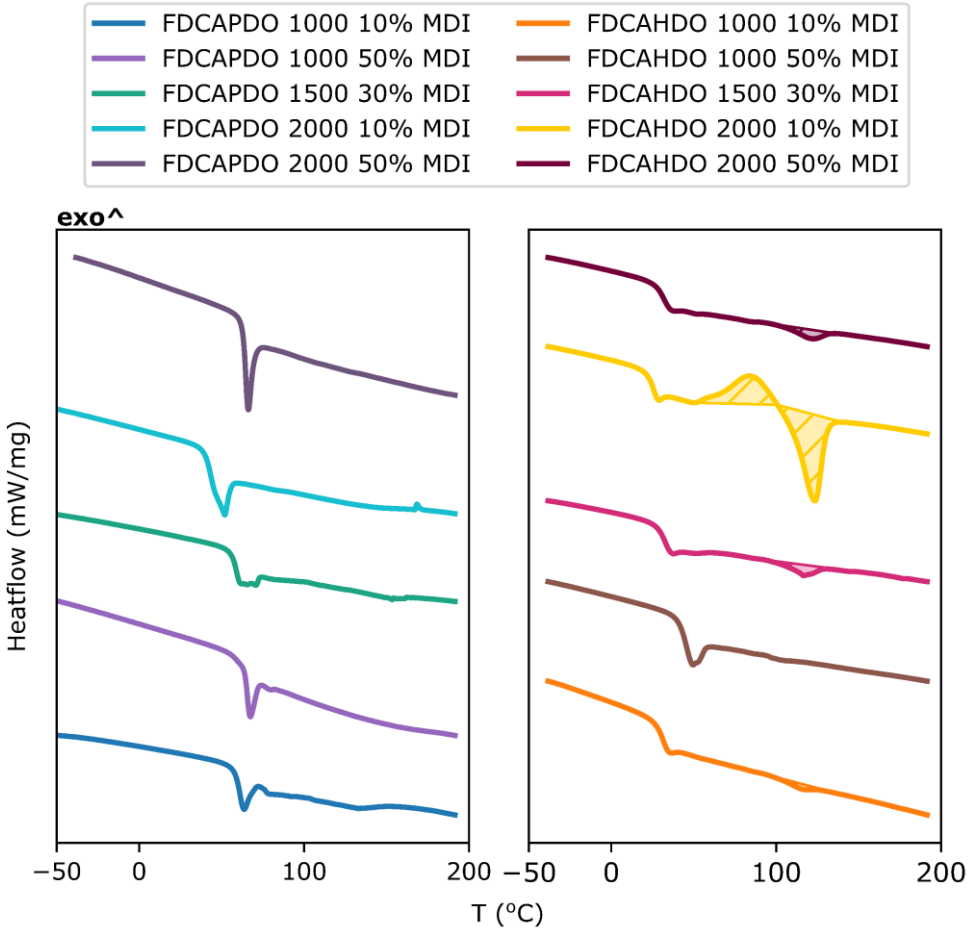

Figure 4.18: Thermograms of the FDCA MDI TPUs 1st heating cycle.

The assignation of the crystalline transitions of the FDCAHDO MDI TPUs observed on the 1st heating thermograms proved more complex than those of the IPHTA formulations, as the trends related to the relationship between composition and crystallinity are less clear (**Table 4.7**).

Table 4.7: Temperatures and enthalpies of the FDCA MDI TPUs 1st heating cycle.

	T_g (°C)[a]	T_{cc} (°C)[b]	ΔH_{cc} (J/g)[c]	T_m (°C)[b]	ΔH_m (J/g)[c]
FDCAPDO 1000 10% MDI	65.6 ± 1.7	–	–	–	–
FDCAPDO 1000 50% MDI	61.4 ± 3.0	–	–	–	–
FDCAPDO 1500 30% MDI	57.5 ± 1.0	–	–	–	–
FDCAPDO 2000 10% MDI	43.5 ± 1.1	–	–	–	–
FDCAPDO 2000 50% MDI	64.4 ± 0.1	–	–	–	–
FDCAHDO 1000 10% MDI	31.3 ± 0.2	–	–	115.0 ± 0.3	2.2 ± 1.7
FDCAHDO 1000 50% MDI	45.5 ± 0.3	–	–	–	–
FDCAHDO 1500 30% MDI	31.8 ± 0.7	–	–	116.7 ± 0.7	4.9 ± 1.5
FDCAHDO 2000 10% MDI	28.3 ± 1.8	71.9 ± 8.9	-9.9 ± 2.9	122.7 ± 0.6	18.9 ± 2.0
FDCAHDO 2000 50% MDI	30.8 ± 0.7	–	–	120.5 ± 0.4	5.8 ± 2.5

[a] Calculated as the mean of the T_g obtained from the 1st heating cycle from three different injected plates.
[b] Calculated as the mean of the maximums of the corresponding peaks from three different injected plates, CC=cold crystallisation, m=melting.
[c] Calculated as the mean of the enthalpies of the corresponding peaks from three different injected plates.

As an attempt to establish the origin of the crystalline structures, polymers containing exclusively SS (pure SS polymers) have been synthesised and analysed by DSC (**Figure 4.19**, **Experimental section 6.2.13**).

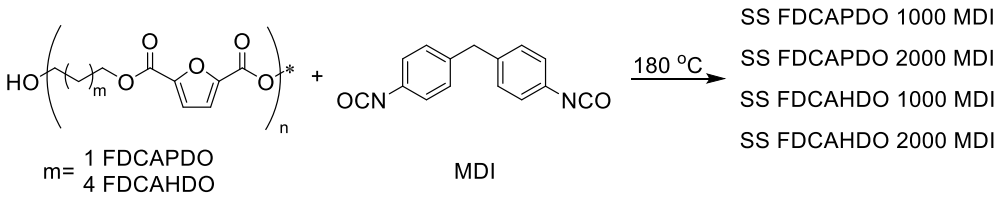

Figure 4.19: Synthesis of the FDCAPDO and HDO MDI SS.

The DSC from the pure SS materials shows two distinct behaviours depending on whether the material contains a PDO or HDO polyester (**Figure 4.20**). The pure SS FDCAHDO MDI polymers are semicrystalline, exhibiting crystallisation, cold crystallisation and melting transitions, while the pure SS FDCAPDO MDI samples are amorphous, exhibiting only a glass transition, just like their respective TPUs. The temperature of the melting peaks observed on the pure SS FDCAHDO MDI samples matches those observed on the 1st heating cycle of the TPUs. Moreover, the temperature of the cold crystallisation process of the pure SS samples matches the one observed for **FDCAHDO 2000 10% MDI**, demonstrating that the crystalline structures exhibited by the TPU materials correspond to the crystallisation of their SS (**Table 4.7**, **Table 4.6**).

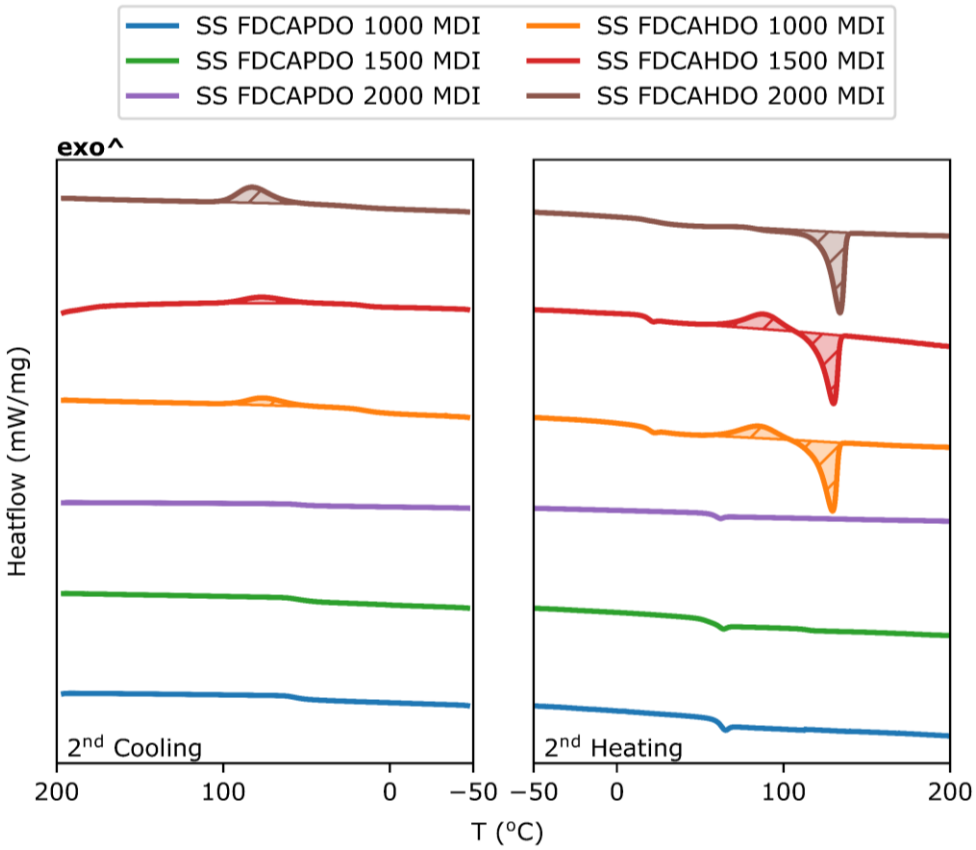

Figure 4.20: Thermograms of the pure SS FDCA MDI polymers. Left: 2nd cooling cycle. Right: 2nd heating cycle.

Some information about the effects that the presence of FDCA has on the morphology of the polymers can be extracted by comparing the crystallinity of the FDCA MDI and IPHTA MDI TPUs. On the IPHTA MDI formulations, no crystalline structure could be identified by DSC, owing to the low chain mobility and high compatibility between their HS and SS phases. Contrarily, on the FDCA MDI TPUs, the formation of SS crystallites is observed by DSC. This dichotomy between the IPHTA and FDCA materials seems to be determined by the difference in interaction strength of their corresponding aromatic SS monomers. The higher cohesion forces of the FDCA SS in comparison to those of the IPHTA SS seem to drive their segregation and enable the formation of ordered structures. Moreover, the difference in interaction strength has such a great impact that can overcome the lower chain mobility that the FDCA MDI TPUs have in comparison with their IPHTA analogues. If the only factor determining the crystallinity

of the TPUs was their chain mobility, the FDCAMDI TPUs should present the same amorphous nature as their IPHTA analogous, as their T_g is higher.

4.2.1.4 FDCA HDI TPUs

In the 2nd heating and cooling cycles of the FDCAPDO HDI materials, no crystalline structure could be identified, with the thermograms showing only a glass transition (**Figure 4.21**). In contrast, all of the FDCAHDO HDI materials exhibit some sort of crystalline structure, as evidenced by the presence of crystallisation, cold crystallisation and melting transitions in the thermograms (**Figure 4.22**). The difference in crystallinity between the FDCAPDO and FDCAHDO HDI materials mirrors the one observed for the IPHTA HDI formulations, for which crystalline structures were also observed in the HDO polymers while none could be identified on the PDO materials. However, only two of the IPHTAHDO HDI polymers showed any crystalline structure, while all of the FDCAHDO HDI materials do, proving once more that the segregation and crystallisation capabilities of the FDCA TPUs are greater than those of the IPHTA formulations.

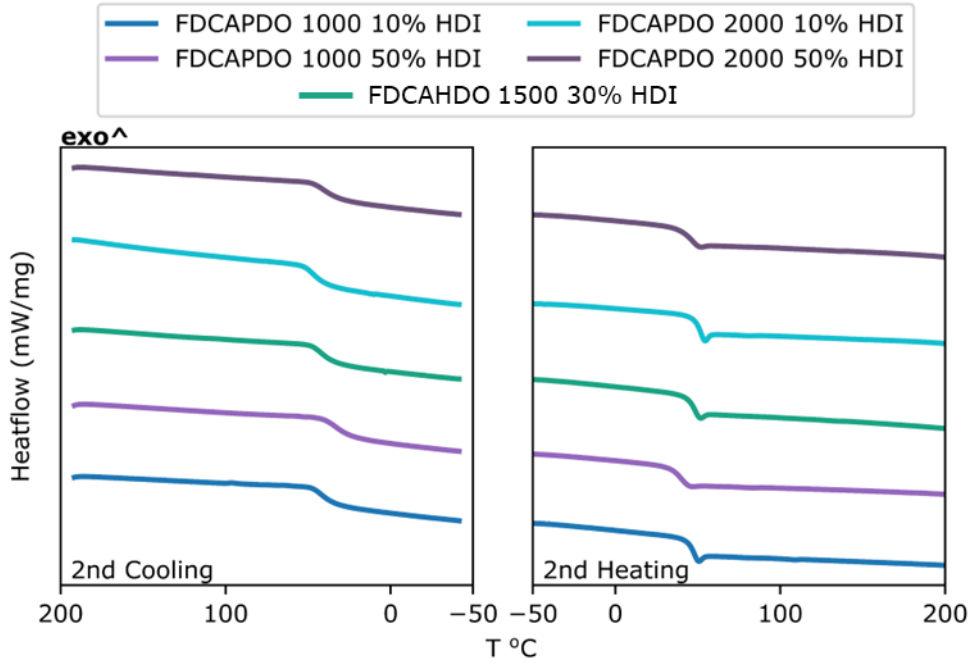

Figure 4.21: Thermograms of the FDCAPDO HDI TPUs. Left: 2nd cooling cycle. Right: 2nd heating cycle.

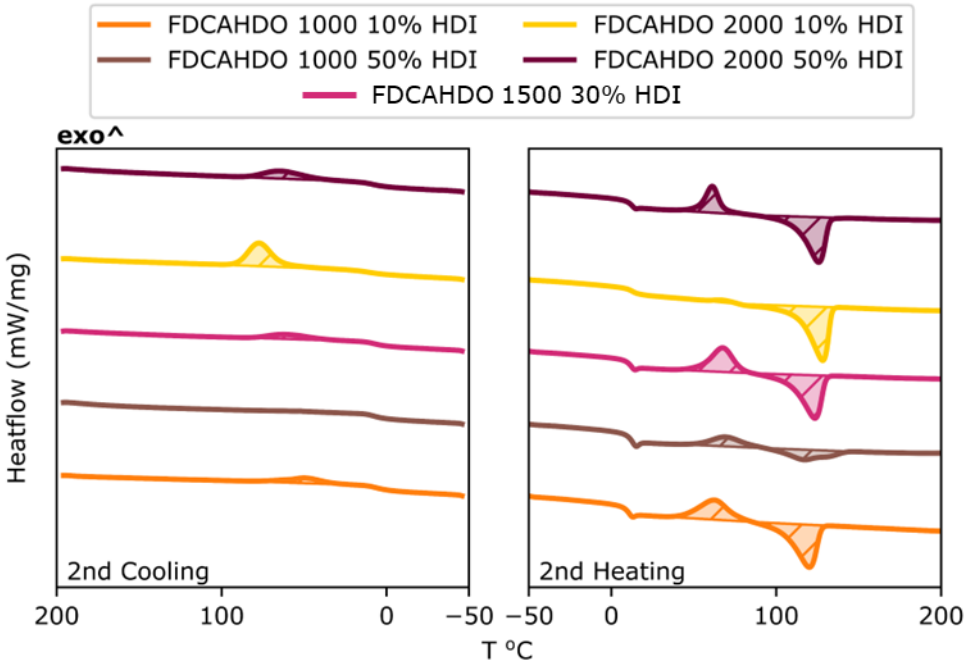

Figure 4.22: Thermograms of the FDCAHDO HDI TPUs. Left: 2nd cooling cycle. Right: 2nd heating cycle.

Following the same behaviour as the rest of the studied polymers, the T_g of the FDCAPDO HDI materials is higher than that of their HDO counterpart, which once more, can be explained by the higher concentration of aromatic moieties in the FDCAPDO formulations (**Table 4.8**). Consequently, the variations in crystallinity between the FDCAPDO and FDCAHDO materials can be attributed to the lower chain mobility of the PDO polymers in comparison to that of the HDO materials. Moreover, the analysis of the relationship between T_g and composition from the FDCA HDI materials yields the same trends as those obtained for the IPHTA HDI TPUs. Overall, the T_g of the FDCA HDI formulations increases with the polyester M_n and decreases with the HS content, indicating that the T_g of the FDCA HDI TPUs increases as the concentration of FDCA increases (**Table 4.8**).

Table 4.8: Temperatures and enthalpies of the FDCA MDI TPUs 2nd heating and cooling cycles.

	T_g (°C)[a]	T_{cryst} (°C)[b]	ΔH_{cryst} (J/g)[c]	T_{CC} (°C)[b]	ΔH_{CC} (J/g)[c]	T_m (°C)[b]	ΔH_m (J/g)[c]
FDCAPDO 1000 10% HDI	44.6 ± 0.5	–	–	–	–	–	–
FDCAPDO 1000 50% HDI	36.9 ± 0.5	–	–	–	–	–	–
FDCAPDO 1500 30% HDI	45.9 ± 0.4	–	–	–	–	–	–
FDCAPDO 2000 10% HDI	49.6 ± 0.2	–	–	–	–	–	–
FDCAPDO 2000 50% HDI	43.8 ± 0.4	–	–	–	–	–	–
FDCAHDO 1000 10% HDI	8.9 ± 0.4	50.6 ± 1.3	-6.1 ± 3.9	67.7 ± 4.0	-18.6 ± 1.3	118.2 ± 1.6	24.2 ± 4.2
FDCAHDO 1000 50% HDI	11.0 ± 0.3	52.5 ± 0.1	-6.1 ± 5.1	68.5 ± 0.9	-9.6 ± 1.0	117.1 ± 15.0	12.1 ± 1.5
FDCAHDO 1500 30% HDI	10.4 ± 0.4	59.9 ± 0.9	-9.2 ± 1.8	67.9 ± 0.8	-18.5 ± 1.5	122.8 ± 0.3	27.5 ± 0.6
FDCAHDO 2000 10% HDI	11.5 ± 1.1	75.9 ± 0.9	-35.5 ± 0.7	65.8 ± 2.0	-0.6 ± 0.5	128.3 ± 0.3	34.6 ± 1.1
FDCAHDO 2000 50% HDI	10.5 ± 0.2	64.7 ± 0.6	-19.7 ± 1.5	60.9 ± 0.4	-11.1 ± 1.5	126.0 ± 0.5	28.9 ± 0.5

[a] Calculated as the mean of the T_g obtained from the 1st heating cycle from three different injected plates.
[b] Calculated as the mean of the maximums of the corresponding peaks from three different injected plates, CC=cold crystallisation, m=melting.
[c] Calculated as the mean of the enthalpies of the corresponding peaks from three different injected plates.

The assignation of the thermal transitions corresponding to the presence of crystalline structures on the FDCA HDI TPUs proved to be quite complex, just as in the previous FDCA MDI formulations. Although the temperature associated with the crystallisation, cold crystallisation and melting transitions observed in the FDCA HDI TPUs match with the HS of the IPHTA HDI TPUs, which were observed to be at around 63, 55 and 130 °C respectively, the enthalpies of the melting processes are not in agreement with this assignation. The enthalpy of the HS domains should increase as the HS content increases. However, the enthalpy of the melting processes arising from the FDCA HDI TPUs increase as the SS content increases, which would indicate the presence of SS crystallites (**Table 4.8**). These results could only be explained if the melting temperatures of the FDCA HDI SS and HS crystallites share the same range. Therefore, to enable the assignation of the crystalline structures on the FDCA HDI TPUs,

polymers containing only FDCA HDI SS (pure SS polymers) have been synthesised and analysed by DSC, to determine the temperature associated with their melting transition (**Figure** 4.23**, Experimental section 6.2.13**).

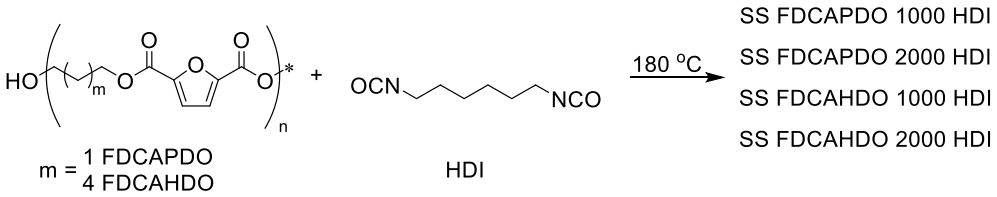

Figure 4.23: Synthesis of the FDCAPDO and HDO HDI SS.

The pure SS FDCAHDO samples exhibit crystallisation and melting transitions in the range of 79-96 °C and 129-136 °C respectively (**Figure 4.24, Table 4.9**). These temperatures match with those observed on the corresponding FDCAHDO HDI TPUs, which indicates the presence of SS crystallites in these formulations.

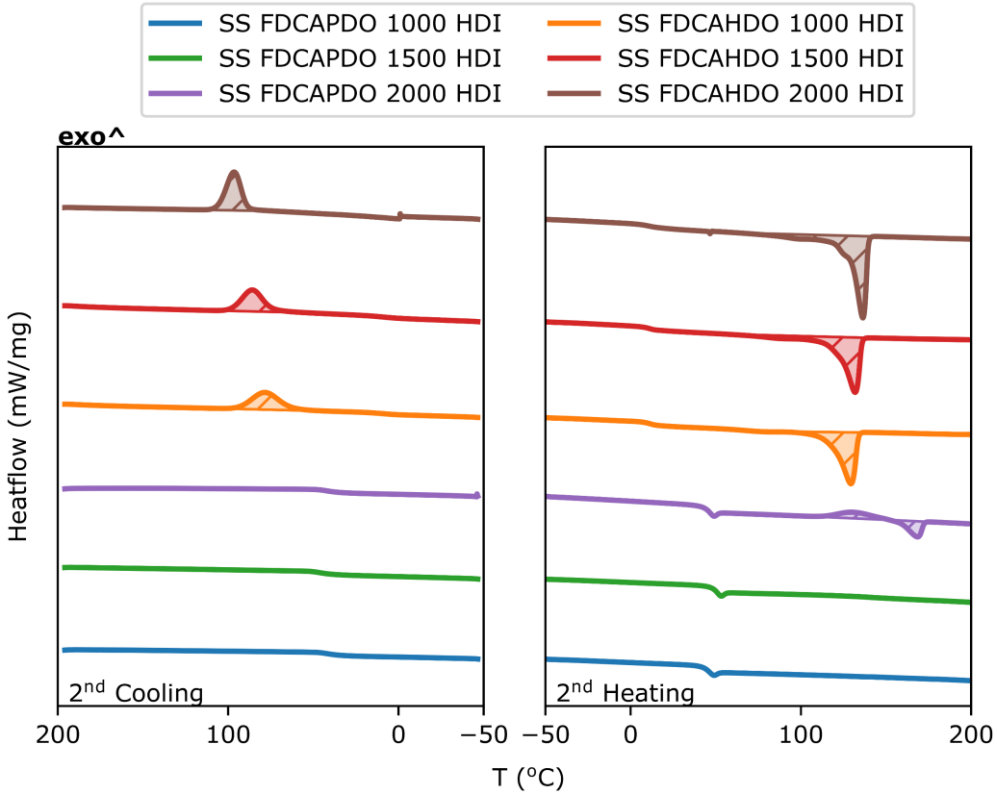

Figure 4.24: Thermograms of the FDCA HDI SS. Left: 2nd cooling cycle. Right: 2nd heating cycle.

Table 4.9: Temperatures and enthalpies of the pure SS FDCA HDI 2nd heating and cooling cycles.

	T_g (°C)[a]	T_{cryst} (°C)[b]	ΔH_{cryst} (J/g)[c]	T_{CC} (°C)[b]	ΔH_{CC} (J/g)[c]	T_m (°C)[b]	ΔH_m (J/g)[c]
SS FDCAPDO 1000 HDI	44.2	–	–	–	–	–	–
SS FDCAPDO 1500 HDI	48.7	–	–	–	–	–	–
SS FDCAPDO 2000 HDI	44.6	–	–	130.4	-8.5	168.3	8.6
SS FDCAHDO 1000 HDI	10.5	78.5	-40.7	–	–	129.1	36.7
SS FDCAHDO 1500 HDI	12.9	85.8	-39.7	–	–	131.7	43.5
SS FDCAHDO 2000 HDI	8.4	96.6	-49.6	–	–	136.2	52.8

[a] Calculated as the mean of the T_g inflexion point obtained from the 2nd cooling and heating cycles.
[b] Calculated as the maximums of the corresponding peaks, CC=cold crystallisation, m=melting.
[c] Calculated as the enthalpies of the corresponding peaks.

Although the existence of SS crystallites in the FDCAHDO HDI TPUs is made clear from both the match between their crystallisation and melting temperatures with those of the pure SS samples and from the relationship between SS content and melting enthalpies, the existence of HS domains cannot be discarded. As the HS and SS crystallisation and melting temperatures appear to share the temperature range, it is plausible that the transitions from both structures overlap with one another, showing only one crystallisation and melting band. No clear peak overlapping was observed on the DSC of the TPUs besides on **FDCAHDO 1000 50% HDI**, where a small shoulder can be observed. However, based on the previous data obtained from the HDI materials, the bands have been attributed to the presence of both HS and SS crystallites. On the IPHTAHDI TPUs, the crystallisation ability of the HS surpasses that of the SS. Therefore, it is difficult to accept that on the FDCAHDI polymers, which show greater segregation capabilities than the IPHTA ones, SS crystalline structures are generated without the existence of HS crystalline domains.

To finish with the interpretation of the DSC data from the FDCA HDI TPUs, their 1st heating has been assessed. Unsurprisingly, the FDCA HDI TPUs materials are the most crystalline

materials among all of the studied TPUs, with all of the formulations showing some sort of crystalline structure (**Figure 4.25**).

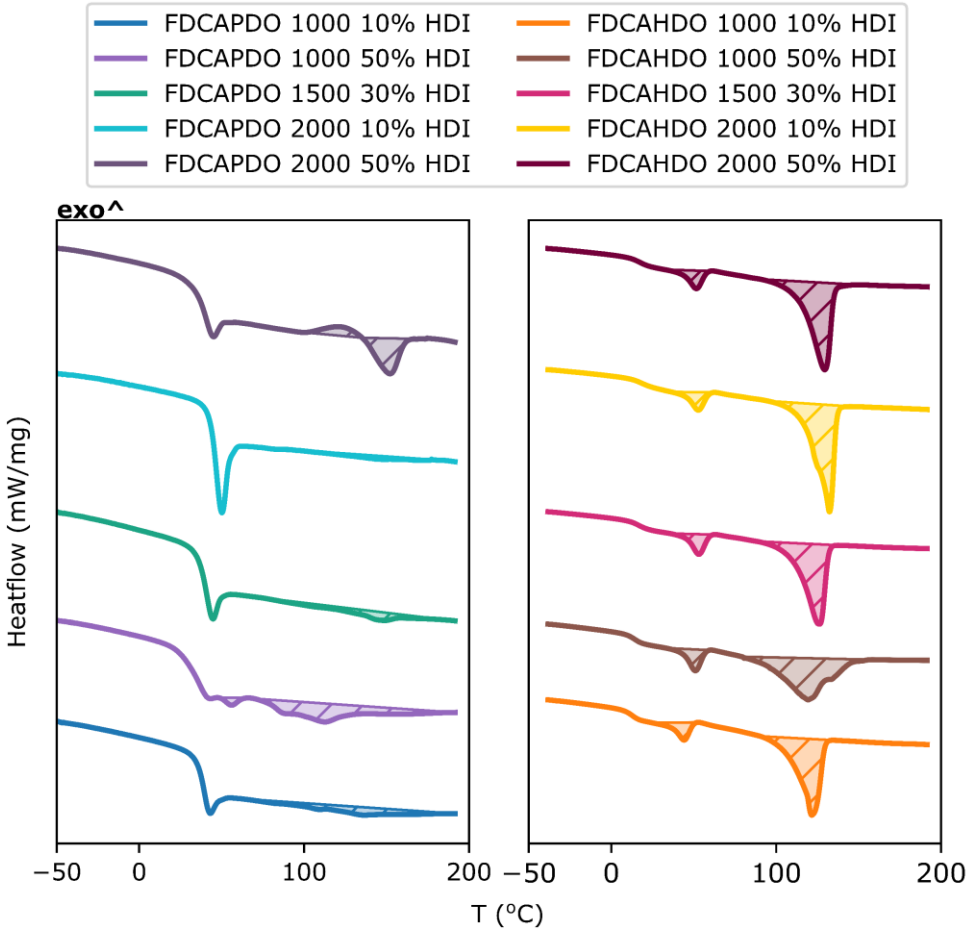

Figure 4.25: Thermograms of the FDCA MDI SS 1st heating cycle.

The FDCAHDO HDI TPUs exhibit two different crystallisation peaks, one that matches the bands observed on their 2nd heating and that could be attributed to the same mixture of SS and HS crystalline structures, and another one at a significantly lower temperature (**Figure 4.25**). The low temperature peak can be easily assigned if the storage temperature of the TPUs, which was 21 °C, is taken into consideration. It is well known that TPU materials that are stored or annealed at a temperature above their T_g can originate a melting transition at 20-30 °C above their storage or annealing temperature which is associated with an internal reorganisation of the HS domains.[188] This is the same behaviour as observed for this low temperature peak,

which is located at 46-52 °C, exactly 20-30 °C above the storage temperature of the TPUs (**Table 4.10**). The presence of a peak corresponding to the reorganisation of the HS domains validates our previous assumption that the melting and crystallisation transitions observed on the FDCAHDO HDI TPUs are generated by both HS and SS ordered structures as, if there were no HS crystallites, their reorganisation would not be observed.

The FDCAPDO HDI materials show a more complex melting profile, with a higher variability between the different formulations (**Figure 4.25**). Nonetheless, by careful analysis and comparison between the different polymers, some information about the origin of their crystallites can be drawn. In the three formulations showing the simplest melting profiles, **FDCAPDO 1500 30% HDI, FDCAPDO 2000 10% HDI** and **FDCAPDO 2000 50% HDI**, a melting transition located between 143 and 151 °C can be observed (**Table 4.10**). The temperature of these transitions is approximately 20 °C higher than those observed on the FDCAHDO HDI materials and matches quite closely with the melting transition observed on the FDCAPDO 2000 HDI SS sample, which exhibited a melting at 168 °C. Moreover, the cold crystallisation observed on the **FDCAPDO 2000 50% HDI** TPU is also in agreement with that found in the pure SS FDCAPDO 2000 HDI polymer. Therefore, the melting and cold crystallisation transitions of the three **FDCAPDO 1500 30% HDI, FDCAPDO 2000 10% HDI** and **FDCAPDO 2000 50% HDI** formulations can be attributed to the presence of SS crystallites. Surprisingly, the SS melting enthalpy of **FDCAPDO 2000 50% HDI** is higher than those of **FDCAPDO 2000 10% HDI**. Usually, the inverse behaviour was observed, with the enthalpies of the SS crystallites increasing in intensity the highest the SS content and, therefore, the lower the HS content is. This inversion of the previously observed trends can be explained by the difference in chain mobility between the two formulations. The T_g of the **FDCAPDO 2000 10% HDI** is significantly higher than that of **FDCAPDO 2000 50% HDI**, being 46.8 and 41.1 °C respectively, which indicates that the chain mobility of the **FDCAPDO 2000 10%** formulation is lower than that of the higher HS content material. This low chain mobility restricts the crystallisation of the SS, producing the observed trend.

The interpretation of the data from the two formulations with the lowest polyester M_n, **FDCAPDO 1000 10% HDI** and **FDCAPDO 1000 50% HDI** is more complex, owing to the presence of overlapping peaks. In the **FDCAPDO 1000 50% HDI** polymer, the same low temperature peak located at 20-30 °C above the storage temperature that in the FDCAHDO HDI materials was assigned to the reorganisation of the HS domains could be observed (**Figure 4.25**). The existence of this peak implies that in **FDCAPDO 1000 50% HDI,** crystalline HS domains exist. Therefore, the presence of overlapping bands on that formulation can be attributed to the

existence of both HS and SS ordered domains. On the **FDCAPDO 1000 10% HDI** formulation, only a very wide band can be observed on the thermograms (**Figure 4.25**). Despite the absence of the HS reorganisation peak, the high width of the observed melting transition seems to indicate the presence of both HS and SS crystallites in the **FDCAPDO 1000 50% HDI** polymer.

Table 4.10: Temperatures and enthalpies of the FDCA HDI TPUs 1st heating cycle.

	T_g (°C)[a]	T_{CC} (°C)[b]	ΔH_{CC} (J/g)[c]	T_m 1 (°C)[b]	ΔH_m 1 (J/g)[c]	T_m 2 (°C)[b]	ΔH_m 1 (J/g)[c]
FDCAPDO 1000 10% HDI	40.0 ± 0.7	–	–	133.5 ± 2.0	4.5 ± 0.9	–	–
FDCAPDO 1000 50% HDI	36.3 ± 0.2	–	–	55.0 ± 0.7	0.5 ± 0.0	109.1 ± 2.0	9.8 ± 0.6
FDCAPDO 1500 30% HDI	40.9 ± 0.1	–	–	143.6 ± 1.4	3.5 ± 0.1	–	–
FDCAPDO 2000 10% HDI	46.8 ± 0.1	–	–	145.1± 1.9	2.7 ± 1.0	–	–
FDCAPDO 2000 50% HDI	41.1 ± 0.2	119.7 ± 2.2	-3.4 ± 1.0	150.9 ± 0.8	4.7 ± 0.7	–	–
FDCAHDO 1000 10% HDI	13.4 ± 0.6	–	–	46.9 ± 2.2	5.0 ± 0.1	122.3 ± 1.0	31.1 ± 0.9
FDCAHDO 1000 50% HDI	14.1 ± 0.1	–	–	50.9 ± 0.1	5.5 ± 0.1	119.2 ± 0.6	31.0 ± 2.6
FDCAHDO 1500 30% HDI	16.3 ± 0.5	–	–	52.8 ± 0.2	5.3 ± 0.1	125.1 ± 0.6	33.0 ± 0.8
FDCAHDO 2000 10% HDI	18.3 ± 0.5	–	–	52.6 ± 0.2	4.9 ± 0.1	130.8 ± 1.1	37.3 ± 0.5
FDCAHDO 2000 50% HDI	17.0 ± 0.1	–	–	51.9 ± 0.2	5.1 ± 0.3	129.3 ± 0.9	35.4 ± 0.5

[a] Calculated as the mean of the T_g inflexion point obtained from the 1st heating cycle from three different injected plates.
[b] Calculated as the mean of the maximums of the corresponding peaks from three different injected plates, CC=cold crystallisation, m=melting.
[c] Calculated as the mean of the enthalpies of the corresponding peaks from three different injected plates.

4.2.1.5 T_g parametrisation

To obtain further insights into the relationship between the composition of the polymers and their chain mobility, a modelling of the variation of the T_g with different composition parameters has been carried out. This parametrisation of the T_g would serve two functions. First, it would enable the obtention of quantifiable data regarding the effect that each variation in composition has on the chain mobility of the TPUs. In addition, the derived equations would allow the development of a T_g prediction model, opening the door to the generation of materials with tailor-made T_g.

To build the different models, first, the composition parameters that affect the T_g of the materials need to be established. From the previous analysis, it is clear that the concentration of diisocyanate and diacid, which are dependent on the HS content, and polyester M_n are two of the parameters that influence to a greater extent the T_g of the materials. Therefore, an initial parametrisation of T_g with the HS (mol%) and polyester M_n as fitting variables has been carried out, using the IPHTA MDI formulation as the model for the behaviour of the other formulations. The fitting has been performed using the linear regression tool of Excel, using three T_g replicates of each TPU as input to account for the experimental error of the measure, and the actual polyester M_n of the TPUs rather than the simplified target values (**Experimental Section 6.2.13**).

A good fitting of the experimental T_g data to the two composition variables, HS (mol%) and polyester M_n was obtained demonstrating that their relationship with T_g is linear (**Figure 4.26**, **Equation 4.1**, **Equation 4.2**).

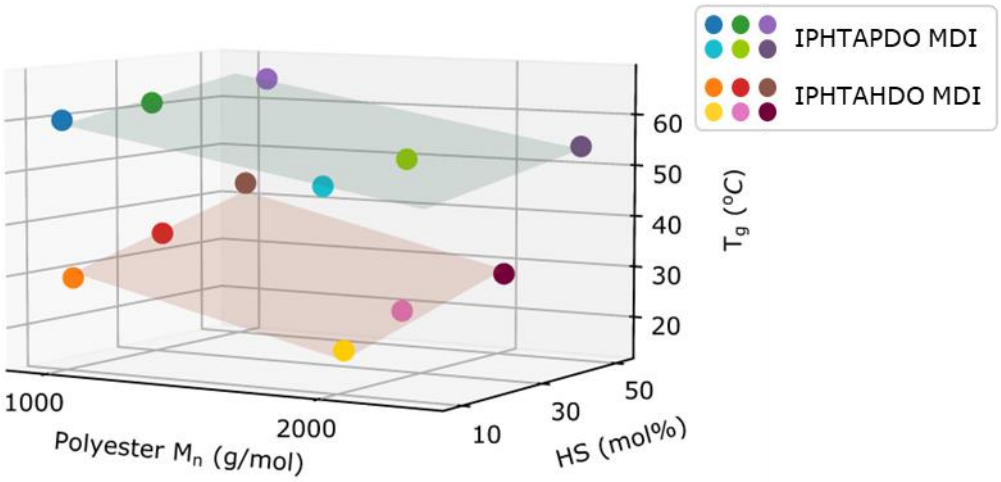

Figure 4.26: IPHTA MDI T_g *vs* Polyester M_n and HS (mol%) linear regression plots.

IPHTAPDO MDI: $T_g = 0.16 \times HS(mol\%) - 0.010 \times Polyester\ M_n + 67.24,\ R^2 = 0.9861$

Equation 4.1: T_g *vs* Polyester M_n and HS (mol%) linear regression of the IPHTAPDO MDI TPUs**.** T_g domain: 40.2-64.6 °C. Residual standard deviation: $T_g \pm 0.6$ °C.

IPHTAHDO MDI: $T_g = 0.25 \times HS(mol\%) - 0.013 \times Polyester\ M_n + 42.68,\ R^2 = 0.9747$

Equation 4.2: T_g *vs* Polyester M_n and HS (mol%) linear regression of the IPHTAHDO MDI TPUs. T_g domain: 20.0-42.9 °C. Residual standard deviation: $T_g \pm 1.2$ °C.

Two different linear regressions arise from the modelling of T_g, one corresponding to the PDO materials, and another one to the HDO polymers. The different behaviour regarding T_g between the PDO and HDO formulations had been already established and attributed to their difference in diacid concentration. To test if indeed, this was the case, and the only difference between the chain mobility of the PDO and HDO materials is derived from their different diacid concentration, an additional linear regression model, this time employing the molal IPHTA concentration as fitting variable, was assessed. If just one equation capable of describing the variation of T_g for both the PDO and HDO TPUs results from this model, the differences between the T_g of both materials could be attributed just to their different IPHTA concentration. Instead, the T_g modelling yielded two different linear regressions, one for PDO and another one for HDO, which demonstrates that, although the concentration of IPHTA in the materials has some effect on their chain mobility, it is not the only factor differentiating the PDO and HDO formulations (**Figure 4.27**, **Equation 4.3**, **Equation 4.4**).

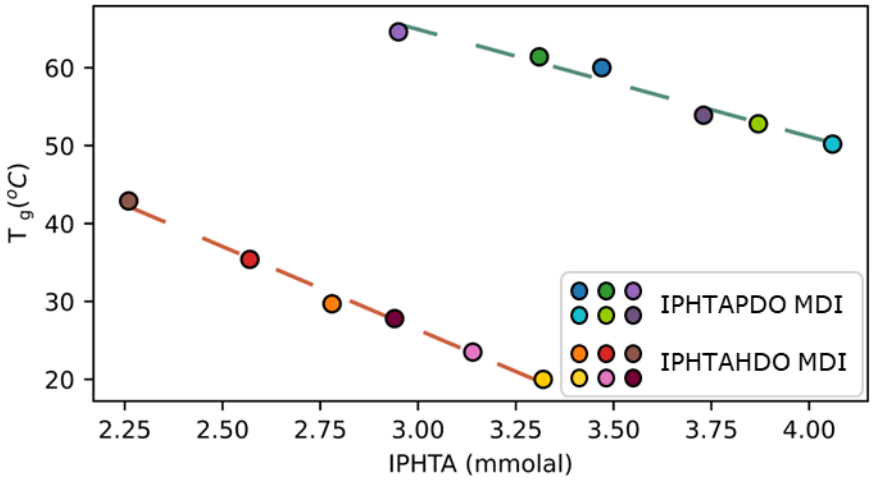

Figure 4.27: IPHTA MDI T_g *vs* IPHTA molality regression plots.

IPHTAPDO MDI: T_g = -13.74 IPHTA (mmolal) + 106.12, R^2= 0.9650

Equation 4.3: T_g *vs* IPHTA (mmolal) linear regression of the IPHTAPDO MDI TPUs**.** T_g domain: 40.2-64.6 °C. Residual standard deviation: T_g ± 1.0 °C.

IPHTAHDO MDI: T_g = -22.16 IPHTA (mmolal) + 93.07, R^2= 0.9917

Equation 4.4: T_g *vs* IPHTA (mmolal) linear regression of the IPHTAHDO MDI TPUs. T_g domain: 20.0-42.9 °C. Residual standard deviation: T_g ± 1.7 °C.

In addition to their different diacid concentration, the other main disparity between the PDO and HDO formulations is the odd-even length of their respective polyester. As previously explained, even chain polyols enhance the chain packing of the TPU structure, as they can adopt an *anti*-conformation rather than a *gauche* one.[87] This difference in chain packing usually results in a higher T_g for the even chain length polyols in comparison with the odd ones. This matches the observed results, as the PDO TPUs, which have an even polyol length, are the ones with the highest T_g. To test if indeed, a closer chain packing is obtained for the PDO than for the HDO materials, density measurements have been employed. The density of the different TPUs has been measured by determining their buoyancy, employing 5 different replicates selected from 3 different injected plates for each formulation (**Experimental Section 6.1.8**). The exact density values and their associated standard deviations can be found in **Annex A5**. If, as theorised, the PDO materials have a better chain packing than their HDO counterpart, they should exhibit a higher density. Indeed, a clear difference between the density of the PDO and HDO TPUs can be observed, with the PDO polymers showing the highest values (**Figure 4.28**). This agrees with the theoretical chain packing effects and explains why the difference in IPHTA content is not enough to describe the highest T_g of the PDO materials. Due to the odd-even effect, the PDO polymers have a tighter chain packing than their HDO counterpart, leading to a higher restriction to their chain mobility.

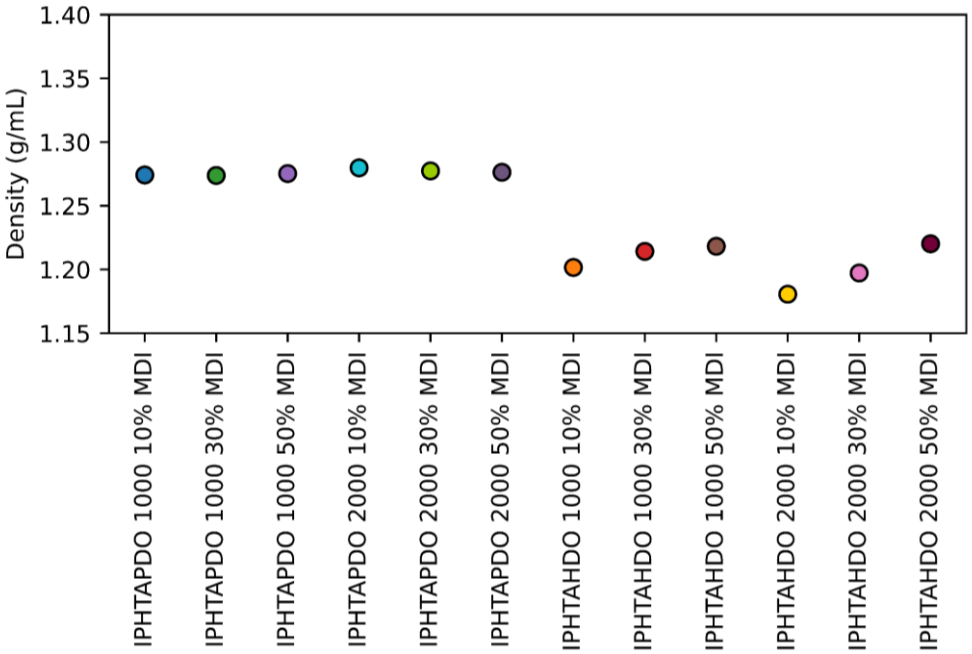

Figure 4.28: Density values of the IPHTA MDI TPUs measured by buoyancy. Average standard deviation of the density measurements ± 0.004 g/mL.

To determine if indeed the variations in chain packing between the PDO and HDO TPUs, in addition to their difference in IPHTA concentration, are the factor that differentiates the chain mobility of the PDO and HDO TPUs, an additional linear regression analysis has been carried out. This time, chain packing has been added as a fitting variable into the modelling of the experimental data as a new parameter, CP, which has been given a value of 1 for PDO TPUs and 2 for HDO TPUs. With the addition of the new CP parameter, a single linear regression including the HDO and PDO formulations has been reached (**Equation 4.5**). The good fit of the regression indicates that, as theorised, the differences in chain packing and IPHTA concentration are what differentiates the T_g of the PDO and HDO materials. Hence, the parameters that affect the T_g of the IPHTA TPUs are their diisocyanate and diacid concentration and their chain packing structure, which are dependent on the HS (mol%), polyester M_n, and the diol employed on the polyesters.

$$T_g = 0.22 \times HS(mol\%) - 0.012 \times Polyester\ M_n - 27.70 \times CP + 96.41,\ R^2 = 0.9901$$

Equation 4.5: T_g *vs* Polyester M_n, HS (mol%) and CP linear regression of the IPHTA MDI TPUs. CP: PDO=1, HDO=2. T_g domain: 20.0-64.6 °C. Residual standard deviation: T_g ± 1.5 °C.

Once the parameters that affect the T_g of the TPUs have been determined, the modelling of the other TPU families, IPHTA HDI, FDCA MDI and FDCA HDI, has been assessed. However, before their fitting, their density has been measured to determine if the same difference in chain packing caused by the odd-even effect is followed outside of the IPHTA MDI formulations. The density of the materials has been obtained employing the same procedure as for the IPHTA MDI formulations (**Experimental Section 6.1.8**). The exact density values and their associated standard deviations can be found in **Annex A5**.

In all three TPU families, the same relationship between density and composition can be observed, with the PDO materials exhibiting, in all cases, higher densities than their HDO counterparts (**Figure 4.29**, **Figure 4.30**, **Figure 4.31**). This indicates that the variations in chain packing generated by the odd-even effect are maintained on all of the TPU formulations, no matter which is their diisocyanate or diacid.

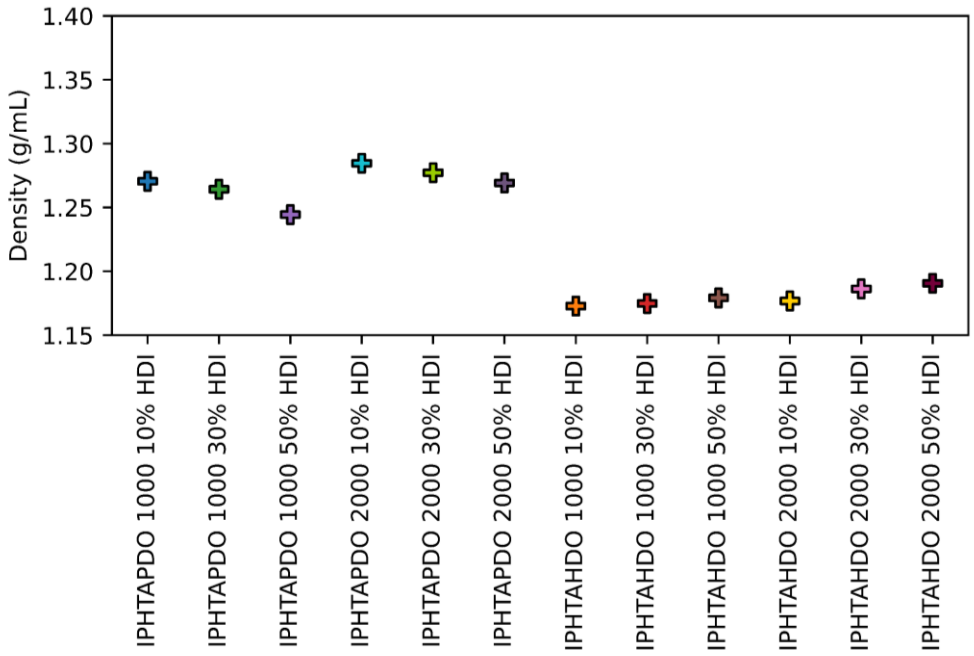

Figure 4.29: Density values of the IPHTA HDI TPUs measured by buoyancy. Average standard deviation of the density measurements ± 0.007 g/mL.

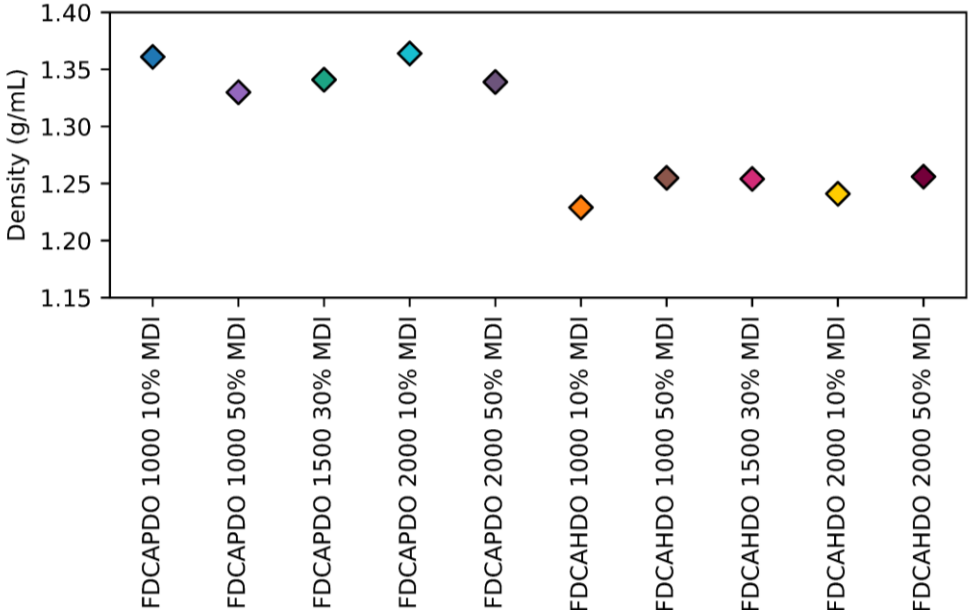

Figure 4.30: Density values of the FDCA MDI TPUs measured by buoyancy. Average standard deviation of the density measurements ± 0.010 g/mL.

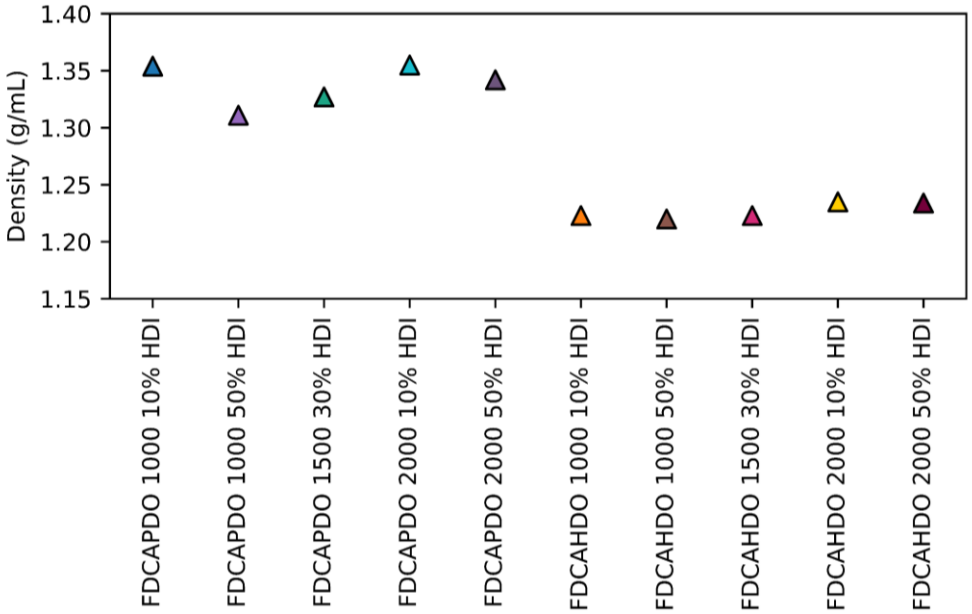

Figure 4.31: Density values of the FDCA HDI TPUs measured by buoyancy. Average standard deviation of the density measurements ± 0.007 g/mL.

In addition to the tighter chain packing that the PDO polymers have in comparison to the HDO TPUs, another interesting point arises by comparing the densities of the IPHTA and FDCA formulations. The density of the IPHTA polymers is significantly lower than that of their FDCA counterpart (**Table 4.11**). This variation in density can be attributed to the differences in stacking distance between the IPHTA and FDCA moieties. According to the previously discussed DFT calculations, the interplanar ring distance of the IPHTA dimers is in the order of 3.39-3.58 Å, while that of the FDCA moieties ranges from 3.16-3.3 Å. These will not be the same distances that the aromatic fragments of the SS chains adopt since the restrictions to chain mobility and the steric hindrance of the chains would disrupt this ideal packing of the aromatic monomers. Nonetheless, the polymeric chain distances should follow the same trends as those of their respective monomers, resulting in the closer packing of the FDCA than the IPHTA SS.

Table 4.11: Density ranges of the different TPUs categorised according to the diacid and diol of their polyesters.

	PDO	**HDO**
IPHTA	1.244 - 1.285 g/mL	1.173 - 1.214 g/mL
FDCA	1.311 - 1.364 g/mL	1.220 - 1.256 g/mL

Given that the same influence of the odd-even effect on the chain packing of the TPUs as that of the IPHTA MDI TPUs has been observed for the IPHTA HDI, FDCA MDI and FDCA HDI formulations, the parametrisation of their T_g including the CP parameter has been assessed. The modelling of the experimental data from those TPUs has been developed following the same procedure as for the IPHTA MDI formulations (**Experimental Section 6.2.13**, **Equation** 4.6, **Equation 4.7**, **Equation 4.8**). An acceptable fitting of the linear regression model was found for the three TPU formulations, which indicates that the three composition parameters, HS (mol%), polyester M_n and CP have been properly selected and that they are the three variables that influence the chain mobility of the materials.

$$T_g = -0.04 \times HS(mol\%) + 0.002 \times \text{Polyester } M_n - 27.18 \times CP + 57.38, \quad R^2 = 0.9886$$

Equation 4.6: T_g *vs* Polyester Mn, HS (mol%) and CP linear regression of the IPHTA HDI TPUs. CP: PDO=1, HDO=2. T_g domain: 3.2-36.6 °C. Residual standard deviation: $T_g \pm 1.5$ °C.

$$T_g = 0.26 \times HS(mol\%) - 0.012 \times Polyester\ M_n - 31.14 \times CP + 106.62,\ R^2 = 0.9590$$

Equation 4.7: T_g *vs* Polyester Mn, HS (mol%) and CP linear regression of the FDCA MDI TPUs. CP: PDO=1, HDO=2. T_g domain: 24.3-73.1 °C. Residual standard deviation: $T_g \pm 2.0$ °C.

$$T_g = -0.08 \times HS(mol\%) + 0.004 \times Polyester\ M_n - 33.74 \times CP + 74.31,\ R^2 = 0.9811$$

Equation 4.8: T_g *vs* Polyester Mn, HS (mol%) and CP linear regression of the FDCA HDI TPUs. CP: PDO=1, HDO=2. T_g domain: 8.9-49.6 °C. Residual standard deviation: $T_g \pm 1.8$ °C.

Just from observing the coefficients from the equations of the four different TPU families, a distinction between the MDI and HDI formulations can already be inferred. However, each of the composition variables, HS (mol%), polyester M_n and CP have different orders of magnitude. Therefore, to accurately compare the different coefficients with one another, a normalisation needs to be performed. To that avail, the median of the different variables (30 for the HS (mol%), 1500 for the polyester M_n, and 1.5 for CP and DA) has been employed for recalculating a new set of normalised coefficients (**Table 4.12**).

Table 4.12: Normalised coefficients linear regression of T_g *vs* composition for all the TPU formulations.

	HS (mol%)	**Polyester M_n**	**CP**
IPHTA MDI	6.62	-17.42	-41.56
FDCA MDI	7.85	-17.60	-46.70
IPHTA HDI	-1.21	3.17	-40.76
FDCA HDI	-2.33	5.84	-50.60

The different effect that the two diisocyanates, HDI and MDI, have on the chain mobility of the TPUs is displayed in the signs of the HS (mol%) and polyester M_n coefficients (**Table 4.12**). On the MDI TPUs, a positive and negative contribution can be found respectively for the HS (mol%) and polyester M_n variables. Since the diisocyanate concentration is proportional to the HS (mol%) and inversely proportional to the polyester M_n, the sign of the coefficients indicates that the T_g of the MDI TPUs increases hand in hand with the concentration of diisocyanate. Moreover, to increase the molar fraction of diisocyanate in the materials, that of the polyester has to decrease, which indicates that the T_g of the MDI TPUs increases as the concentration of diacid decreases. On the HDI TPUs, the inverse trend can be observed, with the T_g of the materials increasing altogether with the concentration of diacid and therefore, decreasing as the diisocyanate concentration increases. This dichotomy can be explained by the distinct HS

cohesion forces and SS-HS interactions generated by the two diisocyanates. Owing to its aromatic nature, MDI is capable of generating both π-π stacking and H-bond interactions, while HDI is only capable of producing the latter. Therefore, the strength of the supramolecular interactions generated by MDI are higher than those produced by HDI. Moreover, the MDI HS chain fragments have a higher compatibility with the SS than the HDI HS domains, as their ability to generate π-π stacking enables their interaction with the aromatic diacids of the SS. The stronger supramolecular interactions and higher phase miscibility generated by MDI entail that this diisocyanate is capable of restricting the chain mobility of the TPUs to a greater extent than HDI. Nevertheless, contrary to the observed results, an increase in HDI concentration should still induce an increase in the T_g of the TPUs, since the H-bonds that the HDI moieties generate are the strongest supramolecular interactions present in the materials. To understand the negative contribution that the HDI concentration has upon the T_g, an additional parameter needs to be considered. As previously stated, since the molar fraction of the polyesters and diisocyanate are inversely proportional to one another, an increase in the diisocyanate concentration results in a decrease in the number of diacid units in the TPUs, with each addition of a mol of diisocyanate resulting in the loss of between 3.60-10.89 diacid units. In the case of MDI, this decrease in the total number of supramolecular interactions arising from the decrease in diacid units is overcome by the high strength of the interactions generated by MDI and by the high HS-SS miscibility it induces. However, the aliphatic HDI is incapable of counterbalancing the drop in the number of diacid moieties, since it generates weaker supramolecular interactions and a lower HS-SS mixing than MDI. Ultimately, this effect is observed as the different signs of the HS (mol%) and polyester M_n coefficients between HDI and MDI.

Despite the differences in the HS (mol%) and polyester M_n coefficients, those belonging to the CP variable remain quite constant on all four TPUs, with just a slight increase in their absolute value being appreciated for the FDCA materials when compared to their IPHTA analogues. This might be a result of the tighter chain packing of the FDCA materials in comparison with that of the IPHTA TPUs generated by their smaller stacking distances.

Surprisingly, the relative value of each of the coefficients in the FDCA and IPHTA models is quite similar. This might indicate that, as in the case of the two different diols, the introduction of a new fitting parameter related to the diacid might enable the merger of the four models into just two, one for the MDI and another one for the HDI TPUs. Therefore, a new parameter for the diacids, called DA, with a value of 1 for IPHTA and 2 for FDCA has been generated and introduced into the models. The fitting of the experimental T_g data to the four variables, HS (mol%), polyester M_n, CP and DA resulted in two linear regressions with a fit just as good as

those of the initial model in which the contributions from the different diacids were split (**Equation 4.9**, **Equation 4.10**, **Experimental Section 6.2.13**). This shows that the effect that the diacid has on the chain mobility of the TPUs is independent of the other variables. Moreover, the lower chain mobility of the FDCA TPUs in comparison with that of the IPHTA materials, owing to their stronger supramolecular interactions, can be inferred from the value of the coefficient.

$$T_g = 0.24 \times HS(mol\%) - 0.01 \times Polyester\ M_n - 29.18 \times CP + 6.01 \times DA + 92.32,\ R^2 = 0.9736$$

Equation 4.9: T_g *vs* Polyester Mn, HS (mol%), CP and DA linear regression of the MDI TPUs. CP: PDO=1, HDO=2. DA: IPHTA=1, FDCA=2. T_g domain: 20.0-73.1 °C. Residual standard deviation: $T_g \pm 2.0$ °C

$$T_g = -0.06 \times HS(mol\%) + 0.002 \times Polyester\ M_n - 30.15 \times CP + 8.70 \times DA + 53.59,\ R^2 = 0.9733$$

Equation 4.10: T_g *vs* Polyester Mn, HS (mol%), CP and DA linear regression of the HDI TPUs. CP: PDO=1, HDO=2. DA: IPHTA=1, FDCA=2. T_g domain: 3.2-73.1 °C. Residual standard deviation: $T_g \pm 2.2$ °C

4.2.1.6 Overview

From the data obtained from the four TPU families, some generalisations about the effect that each component of the materials has on their morphology can be extrapolated. Ultimately, phase morphology depends on how the difference in number and strength of the different supramolecular interactions affect three parameters, chain mobility, phase segregation, and SS domain cohesion. Components that limit the chain mobility of the materials inhibit their segregation and crystallisation. Similarly, monomers that induce a low phase segregation of the HS and SS domains by increasing the miscibility of the domains result in materials with poor segment crystallinity. Finally, the cohesion of the SS domains determines their crystallinity. The stronger the cohesion forces of the SS domains, the higher their crystallinity. These three parameters interact with one another, producing the final morphology of the material. Therefore, by understanding the effect that each of the components, diisocyanate, diacid and diol have on these three parameters, their effect on the morphology of the TPUs can be understood.

The MDI TPUs are overall amorphous materials, which show poor phase segregation and little to no HS crystallinity, as their high rigidity, strong supramolecular interactions, and high capability for generating interactions between the HS and SS domains induce low chain mobilities of the polymers and high miscibility amid the two domains. On the contrary, the HDI TPUs present higher crystallinities and phase segregation, as their weaker supramolecular interactions, lower miscibility between the HS and SS domains, and higher flexibility than their MDI counterpart allow the segregation and organisation of the different domains.

Owing to its stronger supramolecular interactions, FDCA generates materials with a lower chain mobility than IPHTA. However, this lower chain mobility is compensated by the high strength of said supramolecular interactions, which drives forward the segregation and crystallisation of the FDCA SS. In other words, the thermodynamic factor (supramolecular interactions) overcomes the kinetic one (chain mobility). Therefore, the FDCA TPUs present higher phase segregations and SS crystallinities than their IPHTA counterpart

Finally, the effect of the type of diol employed on the polyester can be associated with two factors. Their influence on the concentration of diacid and the chain packing of the SS. The PDO polyesters have a higher diacid concentration and tighter chain packing than their HDO counterparts owing to the odd-even effect. Accordingly, the chain mobility and therefore, phase segregation and crystallinity of the PDO TPUs is lower than the HDO formulations.

4.2.2 X-ray scattering

Continuing with the assessment of the morphological characteristics of the TPUs, small-angle X-ray scattering (SAXS) and wide-angle X-ray scattering (WAXS) were employed to supplement the data obtained by DSC. Both techniques allow the obtention of data from structures with a large range and short-range order, respectively. SAXS can be employed to study the segregation and size of the domains of the materials, while WAXS allows the exploration of their crystallinity.

Both SAXS and WAXS spectral data have been simultaneously collected at ALBA synchrotron, at the NCD-SWEET beamline (**Experimental Section 6.1.11**).

4.2.2.1 Small-angle x-ray scattering

SAXS is a useful tool to study and characterise differences in electron density of a sample at the nanometric scale. Owing to the different electron density of the HS and SS domains, this means that SAXS can be employed to examine the degree of phase segregation of the TPUs, even for amorphous domains, the data of which cannot be obtained from DSC measurements.

The first step in the interpretation of the SAXS spectra is to determine which is the region in which the information corresponding to the desired morphological characteristics is found. In the case of TPUs, the Fourier and Porod regions are the ones from which information relating to the phase segregation of the materials can be extracted (**Figure 4.32**). Although the Guinier region also contains data regarding the phase segregation of the TPUs, the high interparticle interactions derived from the relatively high concentration of HS domains render that area indecipherable unless highly complex mathematical models are employed. Several SAXS

studies of TPUs have already been reported in the literature, in which the peak found at the Fourier region is attributed to the HS domains.[172,189–194]

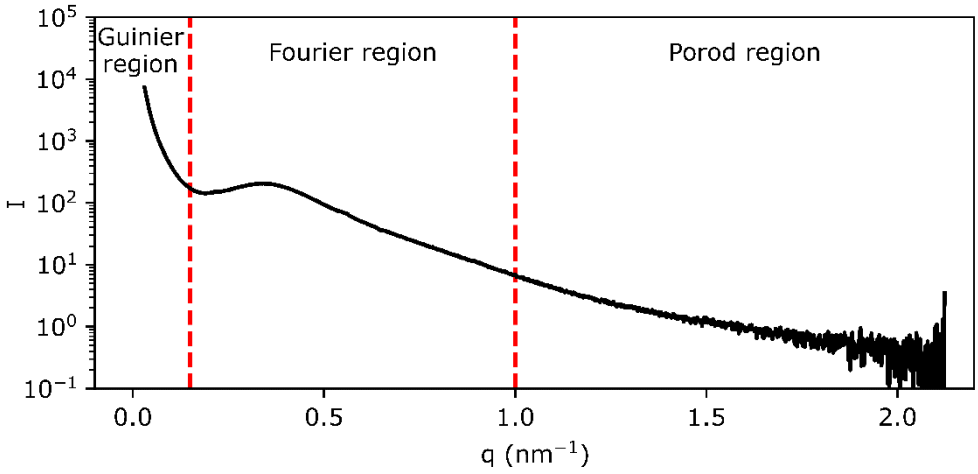

Figure 4.32: Representation of a 1D SAXS spectrum of a TPU.

In the TPUs reported in this work, the peak found in the Fourier region could be attributed to both the HS and SS domains, as SS and HS crystallites were identified by DSC. However, the analysis of samples made out of purely SS returned no signal in this region, even if SS melting peaks were observed by DSC (**Figure 4.33**). This indicates that the SS crystallites are either too big or too small to result in a peak in the Fourier region. Therefore, if any peak is found in the Fourier region of the TPUs it can be attributed to the HS domains.

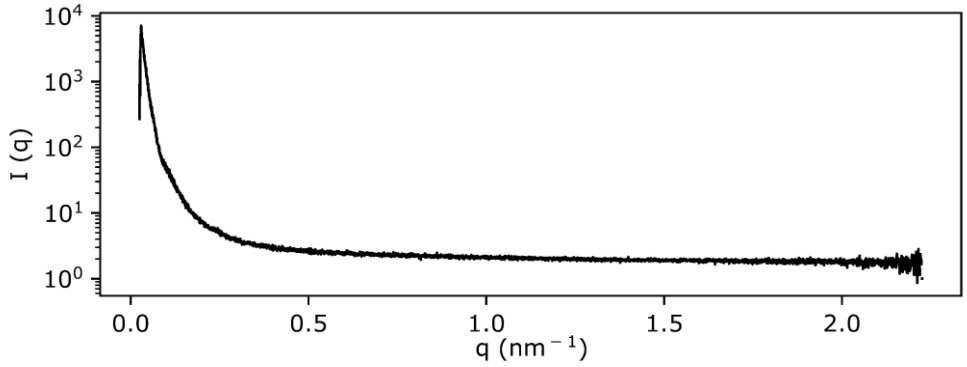

Figure 4.33: Example of the SAXS data from a SS sample.

First of all, the presence or lack thereof of a peak in the Fourier region of the SAXS spectra will be assessed for all the formulations. The presence of a peak indicates that segregated HS

domains are found in the sample, while the lack of a signal indicates that the polymer lacks any phase segregation, or that the number of HS domains is too low to be detected. No peak was observed on any of the IPHTA MDI TPUs, which confirms our previous findings, as those polymers have a high affinity between HS and SS and a low SS cohesion (**Annex A6**). Two different behaviours could be observed in the IPHTA HDI TPUs. All the IPHTAHDO HDI formulations exhibit a peak in the Fourier region, while none of the IPHTAPDO HDI TPUs show any signal. This is consistent with the DSC data, as on the IPHTAHDO HDI TPUs, a HS melting peak could be identified, while none was observed for the PDO materials, owing to their lower chain mobility, which hinders phase segregation. Continuing with the FDCA TPUs, similar findings could be observed. No peak was observed for any of the FDCA MDI TPUs materials, which then again, can be explained by the low chain mobility and high HS-SS compatibility of the MDI formulations. Finally, in the FDCA HDI TPUs, all of the HDO polymers exhibited a peak, just as on the IPHTA analogues. Moreover in two of the PDO samples, **FDCAPDO 1000 50% HDI** and **FDCAPDO 2000 50% HDI**, a peak could also be observed (**Annex A6**). The presence of phase segregation on the FDCAPDO HDI materials in contrast with the lack of any segregated domain on the IPHTAPDO HDI TPUs is proof, once more, of the stronger segregation capabilities of the FDCA polymers, owing to the stronger interaction strength of their SS.

Having identified the materials in which a peak at the Fourier region is present, the next step is to extract the morphological information contained within that band. To that avail, the spectral data has to be fitted to mathematical models. These models allow the determination of the size, polydispersity, and distribution of the HS domains in the TPUs.

The intensity of the signal in the Fourier region is defined by two parameters, the form factor, P(q), and the structure factor, S(q) (**Equation 4.11**). Therefore, to generate an accurate fitting of the data, a correct model for both parameters needs to be selected.

$$I(q) = Scale \times P(q) \times S(q)$$

Equation 4.11: Description of I(q) in the Fourier region.

P(q) depends on the shape of the HS domains, while S(q) depends on their interparticle interference. To select the appropriate factors, some approximations about the microphase morphology of the TPUs need to be done. The shape of the HS domains depends on two factors, their phase segregation, and their HS content. Usually, TPUs with a HS content (wt %) of 30-35% or less, are considered to contain spherical HS domains, although, on the larger limit of this range, the HS particles might start to deform, resembling elliptical particles rather than

spheres.[172,189–194] The aromatic polyol TPUs synthesised in this work contain between 7.7-36.5 HS wt %. Although in some of the studied TPUs, the HS content is outside the standard range considered for spherical particles, owing to the relatively low phase segregations observed by DSC, a spherical P(q) has been selected for the interpretation of the SAXS data. The spherical P(q) is only capable of describing an ideal model, in which the HS domains are monodisperse spheres. However, the HS domains are not monodisperse, but rather follow some kind of radius distribution. This size distribution does not follow a classical Gaussian distribution. The stability of the smallest HS domains is lower than that of the bigger ones, as they are usually made out of smaller chain fragments that can mix more easily with the SS matrix. Therefore, a Flory-Schulz size distribution, which gives a higher weight to the bigger particles has been selected.[195] Even accounting for the polydispersity of the HS domain size is not enough to fully describe the morphology of the materials. P(q) describes a system in which solid HS domains are homogeneously distributed throughout the SS matrix. This is far from the actual morphology of the TPUs. Rather, the segregated particles are made out of a solid core, which corresponds to the HS domain, and a secondary shell of polymeric chains surrounding the HS, which can be made out of either SS or HS chain fragments, covalently linked to the HS domain core. Moreover, the HS particles are not homogeneously distributed, but rather they present different spacings amongst them (**Figure 4.34**).[190,194] Therefore, to correctly represent the morphology of the TPUs, those characteristics need to be introduced into the model. This is achieved by adding said considerations into the S(q). To account for both, the core-shell-like structure of the particles, and their heterogeneous spacing, two different S(q) need to be employed, the Percus-Yevick and the Zernike-Prins models.[172,189–194]

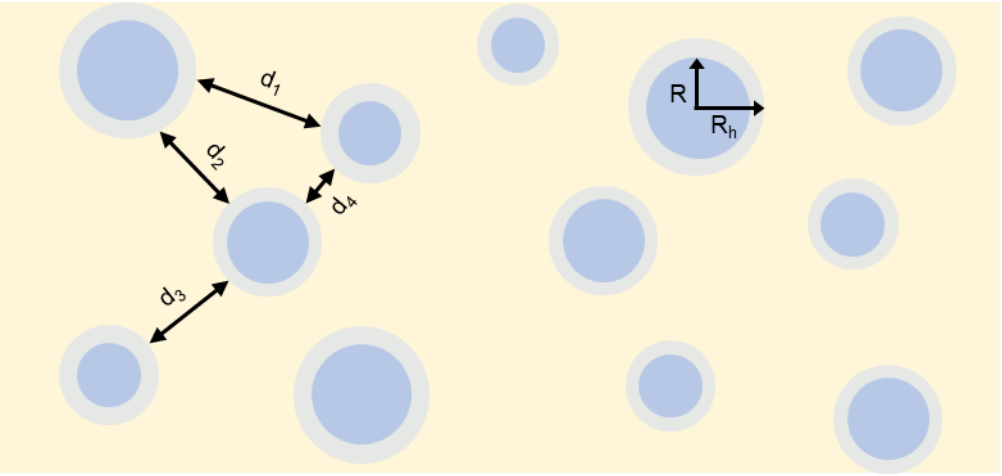

Figure 4.34: Representation of the TPUs morphology.

The Percus-Yevick model describes a system in which the HS particles are composed of a solid core, and a secondary shell, which is rigid enough to be impenetrable, but that has an electron density quite similar to the core of the particle (**Figure 4.35, left**). This describes the HS domains and their surrounding wrapping. However, this model considers all the particles to be equally spaced.[196,197] Therefore, to account for the heterogeneous distances between HS particles, a second fitting to the Zernike-Prins model needs to be performed. This model describes a system made of solid particles, which are heterogeneously dispersed in the SS matrix, allowing the computation of the different spacing between the HS domains (**Figure** 4.35**, right**).[197] Both models cannot be added to the same fitting equation, as the number of fitting variables would be too high. Therefore, two different fittings need to be employed, each of them with a different S(q). The use of both complementary S(q) models in addition to the spherical polydisperse P(q) allows the description of all the HS domain characteristics, with HS particles unequally spaced throughout the SS matrix with a radius the size of which follows a Flory-Schultz distribution and a surrounding shell made of chain fragments covalently linked to the HS.

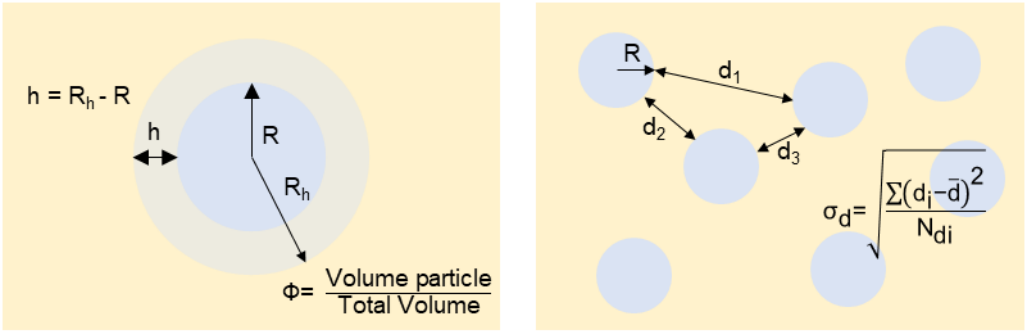

Figure 4.35: Graphical representation of the Percus-Yevick and Zernike-Prins models.

Each of the fitting parameters of the different models allows the determination of some of the morphological characteristics of the segregated particles, with some of those parameters being present in both of the models due to the employment of the same P(q) (**Table 4.13**).

Table 4.13: Fitting parameters of the chosen SAXS models.

Fitting Parameter	Factor	Model	Morphological characteristics
R	P(q)	Percus-Yevick and Zernike-Prins	Core radius
σ_R	P(q)	Percus-Yevick and Zernike-Prins	Standard deviation of R
R_h	S(q)	Percus-Yevick	Radius of the particle containing both the core and the shell.
Φ	S(q)	Percus-Yevick	Volume fraction of the particle
d	S(q)	Zernike-Prins	Mean distance between particles
σ_d	S(q)	Zernike-Prins	Standard deviation of d.

Once the appropriate models had been selected, the fitting of the experimental data to the corresponding equations was performed. The fitting was carried out by employing the corresponding analytical solutions of the P(q) (**Experimental Section 6.3.1**)[195] and S(q) (**Experimental Section 6.3.2, 6.3.3**)[193,196] equations, on Excel's solver tool (**Experimental Section 6.2.15**). Both the Percus-Yevick, and the Zernike-Prins models result in excellent fittings at both low, and high q values, even being capable of modelling the data up to the Porod region (**Figure 4.36**, **Annex A6**).

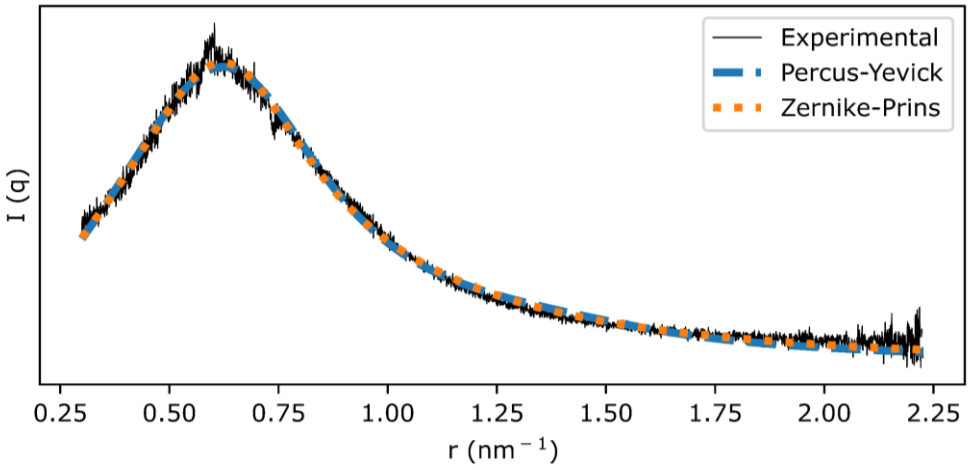

Figure 4.36: Example of the fitting of the experimental SAXS data to the Percus-Yevick and Zernike-Prins models.

Since a good fitting for both S(q) models was obtained, the morphological data extracted from both models was employed to compare the materials and observe, if any, the existing relationships between the different morphological characteristics and the composition of the materials.

On all the TPUs, a good agreement between the radius of the HS domain (R) obtained by the Percus-Yevick and Zernike-Prins models has been found, which agrees with the good fitting of both models (**Table 4.14**). The radius of the HS domains (R) would be expected to increase with the HS content. Although this is true for some formulations, in others, the contrary occurs. The same lack of any trends is echoed in the total radius of the particle (R_h). However, unlike on R, the differences in R_h between all the TPUs are quite small, albeit with one exception, **IPHTAHDO 2000 10% HDI**. Moreover, an unexpected finding could be extracted from the width of the shell surrounding the HS domains (h). This shell was bigger for the particles with smaller R, and vice versa, compensating for the higher differences in R of the polymers and leading to the relatively homogeneous distribution of R_h. This might indicate that the size of the segregated particles is limited by some unseen factor and is capped at just below 5 nm. The only exception to these trends is **IPHTAHDO 2000 10% HDI**, which exhibits a significantly higher h and therefore, R_h, producing particles bigger than 5 nm. The explanation for this behaviour might be given by the disordered nature of their HS domains. **IPHTAHDO 2000 10% HDI** is the only formulation on which HS domains could be observed by SAXS despite the lack of a HS melting peak on DSC. This indicates that the peak observed on SAXS corresponds to a disordered, segregated structure rather than to relatively ordered HS domains. The low order of the observed HS domains might be the root cause of their higher shell radius.

Table 4.14: Morphological data obtained from the fitting of the SAXS data.

	$R \pm \sigma_R$ (Percus-Yevick) (nm)	$R \pm \sigma_R$ (Zernike-Prins) (nm)	R_h (nm)	h (nm)[a]	Φ	$d \pm \sigma_d$ (nm)
IPHTAHDO 1000 10% HDI	3.6 ± 2.0	3.9 ± 2.2	4.7	1.1	0.10	8.1 ± 4.6
IPHTAHDO 1000 30% HDI	2.8 ± 1.6	3.1 ± 1.7	4.4	1.6	0.10	7.4 ± 4.3
IPHTAHDO 1000 50% HDI	1.9 ± 1.1	2.2 ± 1.3	4.2	2.3	0.13	7.2 ± 3.5
IPHTAHDO 2000 10% HDI	2.0 ± 1.5	2.1 ± 1.6	7.4	5.4	0.18	13.4 ± 5.5
IPHTAHDO 2000 30% HDI	2.9 ± 1.6	3.2 ± 1.8	4.3	1.4	0.11	7.6 ± 4.1
IPHTAHDO 2000 50% HDI	2.6 ± 1.4	3.0 ± 1.7	4.0	1.4	0.10	7.1 ± 3.7
FDCAHDO 1000 10% HDI	1.4 ± 0.9	1.5 ± 1.0	4.4	3.0	0.21	8.1 ± 3.1
FDCAHDO 1000 50% HDI	1.7 ± 1.0	1.9 ± 1.1	4.1	2.4	0.15	7.3 ± 3.3
FDCAHDO 1500 30% HDI	1.7 ± 1.0	2.0 ± 1.2	4.0	2.3	0.16	7.3 ± 3.2
FDCAHDO 2000 10% HDI	1.6 ± 1.0	1.9 ± 1.1	3.9	2.3	0.19	7.2 ± 2.9
FDCAHDO 2000 50% HDI	1.6 ± 1.0	1.8 ± 1.1	4.1	2.5	0.18	7.5 ± 3.1
FDCAHDO 2000 10% MDI	2.1 ± 1.2	2.3 ± 1.3	3.5	1.4	0.14	6.4 ± 3.0
FDCAPDO 1000 50% HDI	1.9 ± 1.2	2.0 ± 1.3	4.7	2.8	0.19	8.7 ± 3.5
FDCAPDO 2000 50% HDI	1.7 ± 1.1	1.9 ± 1.2	4.0	2.3	0.14	7.0 ± 3.5

[a]$h = R_h - R$ (Percus-Yevick)

Similar discrepancies between composition and morphology could be extracted from the volume fraction of the segregated particles (Φ). An increase in the HS content should result in a higher number of HS domains, and therefore, in higher Φ. However, this is not the case. Just as on R, no correlation between HS content and Φ could be observed. Moreover, a further

discrepancy related to Φ could be observed. TPUs with a larger HS particle radius (R_h) and with smaller HS domain distances (d), should have a higher Φ, as bigger HS domains placed closer to one another suggest that their concentration should be higher. However, this is not the case since no correlation between all three parameters can be drawn. Although this effect might seem erroneous, it can be understood if the IPHTA and FDCA Φ are compared. The Φ of the FDCA TPUs are, in general, higher than those of the IPHTA polymers. This is the expected behaviour since the DSC measurements demonstrate that the phase segregation of the FDCA polymers is higher than that of the IPHTA materials. However, this increase in Φ is not reflected in bigger R_h and smaller d for the FDCA than for the IPHTA TPUs. This can only indicate one thing, the HS domains are not scattered homogeneously throughout the SS matrix but rather, they are grouped into pockets. If the presence of SS crystals is taken into consideration, this behaviour can be more easily understood. According to DSC, the SS are capable of generating ordered structures since SS melting and crystallisation transitions could be identified on the thermograms. Moreover, given their lack of signal on SAX, coupled with the fact that in some cases, opaque materials are obtained, it can be concluded that the SS crystallites are quite big. The presence of SS crystallites entails that, in the areas where they are present, no segregated HS domains can be formed. Therefore, the HS domains will not be distributed through all of the SS matrix, but rather they will be located in the areas between the SS crystallites, where no crystalline structures are already present. As a result, Φ is not determined by how big and close together the HS domains are, but rather, by which is the concentration of the HS domain pockets. Although this explains why polymers with very similar R_h and d have different Φ, it does not explain why does Φ not increase as the HS content does. Although it is difficult to draw conclusions from the present data, seeing the high effect that the interactions between SS chains have on the distribution of the HS domains, they might also play some role in determining the size and availability of the HS domain pockets.

4.2.2.1.1 Overview

Overall, SAXS allows the obtention of a better mental image of which is the morphology of the HS domains on the polymeric structure. The particles formed by the HS domains and their surrounding polymeric shell seem to have their size restricted, with it being capped at around 5 nm. Moreover, rather than the particles being homogeneously distributed throughout the SS matrix, they exist in segregated pockets, with the space between them being filled by quite probably, SS lamellas.

The same relationships between phase segregation and composition as those observed by DSC could be obtained by SAXS. The HDI TPUs have higher phase segregation than their MDI

counterpart, owing to their lower HS-SS compatibility and higher chain mobility. Likewise, the stronger supramolecular interactions caused by the FDCA SS in comparison with those that the IPHTA moieties produce results in materials with a higher segregation ability.

4.2.2.2 Wide-angle x-ray scattering

WAXS is an ideal technique to study the crystallinity of polymers, as it allows the analysis of the electron density variations of a structure in the Å range.[198,199] Just as on SAXS, the first step in the extraction of the data encoded in the WAXS spectra is to assign the different observed bands. Two different kinds of peaks can be identified depending on their width. Wide peaks correspond to amorphous structures, while narrow peaks indicate the existence of more ordered, crystalline phases. In the case of semicrystalline polymeric materials, both, wide and narrow peaks are present, usually overlapping with one another. The presence of both peak types allows the determination of the degree of crystallinity of the material (Φ_C). According to the Hermans-Wedinger's definition,[200] the crystallinity of polymers corresponds on the ratio between the integrated area of the crystalline peaks (I_C) and that of the total scatter intensity, including both the amorphous (I_A) and crystalline bands (**Equation 4.12**). Therefore, if all the areas are known, it is possible to determine the Φ_C of the polymers. Owing to the overlap between the amorphous and crystalline bands, peak deconvolution is required to differentiate amongst the peaks arising from the amorphous and crystalline structures and obtain their respective areas.[198,199,201,202]

$$\Phi_C = \frac{\sum I_C}{\sum I_C + \sum I_A}$$

Equation 4.12: Determination of the degree of crystallinity (Φ_C) of a semicrystalline polymer by WAXS. I_C = integrated area of the crystalline peaks. I_A = Integrated area of the amorphous peaks.

4.2.2.2.1 IPHTA MDI TPUs

The assessment of the IPHTA MDI TPUs WAXS profile yields three different wide bands, located at q 14.1-14.4 nm^{-1}, 28.4-28.9 and 51.5-52.6 nm^{-1} (**Figure 4.37**, **Annex A7**). All three bands can be attributed to the same amorphous structure, as the two bands found at a higher q, 28.4-28.9 and 51.5-52.6 nm^{-1}, are positioned at approximately 2 and 4 times higher than the lowest q peak respectively. This relationship between the position of the different peaks indicates that the two peaks located at the highest q correspond to the 2nd and 3rd harmonics of the same base peak, that with q 14.1-14.4 nm^{-1}. In addition to the harmonic bands, a less intense, wide band seems to appear at low q values (7.0-8.0 nm^{-1}). However, owing to its overlap with the lower limit of the spectra and to the 1st harmonic band, it is difficult to guarantee

that the peak corresponds to some structural feature of the materials, and not to some artefact generated by the proximity to the borders of the detector.

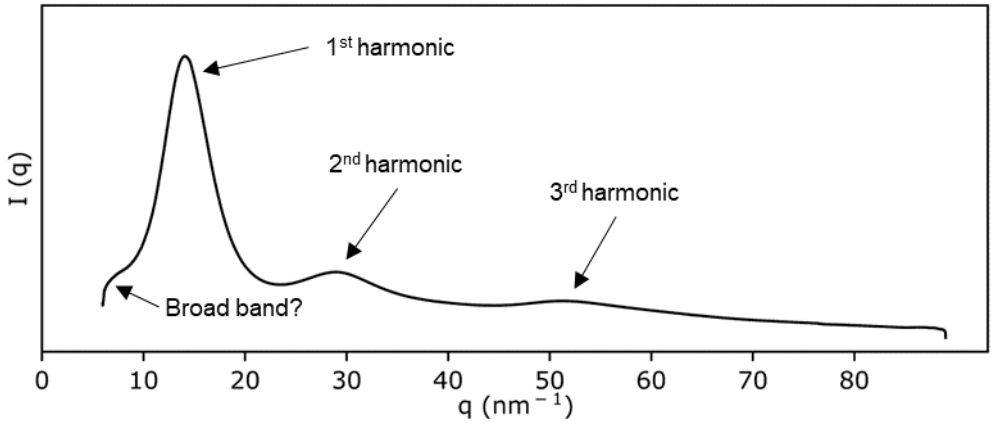

Figure 4.37: Example of a WAXS spectra from an IPHTA MDI TPU.

To ensure that no additional peaks are concealed under the wide, 1st harmonic band, peak deconvolution has been performed. This process was carried out on the Origin software, by fitting the spectra between 6 and 88 nm^{-1} to different Gaussian-Cauchy curves (**Experimental section 6.2.16**).[202–206] On all the materials, only the expected peaks; a broad band at 7.18-7.97 nm^{-1}, the 1st harmonic band at 14.1-14.4 nm^{-1} and its corresponding 2nd and 3rd harmonics could be identified (**Figure 4.38**, **Annex A7**). Therefore, it can be concluded that all of the IPHTA MDI TPUs are amorphous materials, containing a single amorphous phase. These findings agree with the previous results by both DSC and SAXS, which showed that the IPHTA MDI TPUs are completely amorphous and unsegregated.

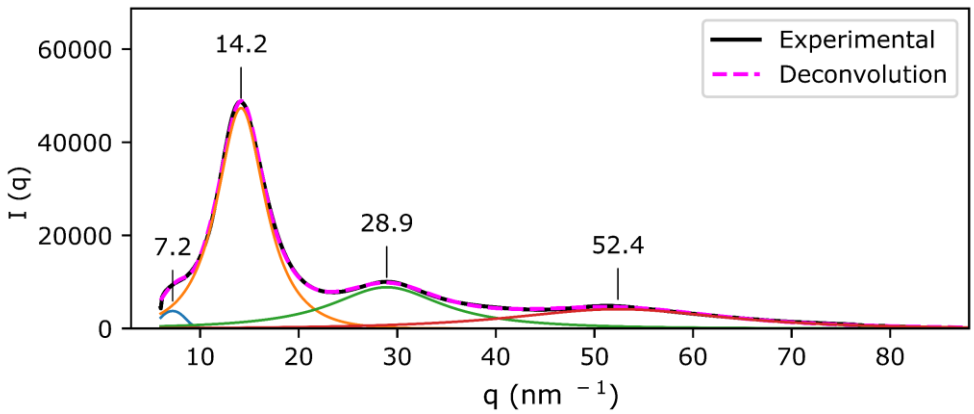

Figure 4.38: Example of the deconvolution of the IPHTA MDI TPUs.

4.2.2.2.2 IPHTA HDI TPUs

On the analysis of the WAXS spectra from the IPHTA HDI TPUs, a distinct behaviour was observed for the PDO and HDO formulations.

The IPHTAPDO HDI materials show the same profile as their MDI counterpart, yielding two wide bands, one at 7.9-8.1 nm^{-1} and another at 14.3-14.5 nm^{-1}, followed by the two harmonics at 28.4-28.9 and 51.0-52.6 nm^{-1} (**Annex A7**). Just as in the case of the IPHTA MDI materials, this agrees with the SAXS and DSC results, which showed no phase segregation nor crystallinity for the IPHTAPDO HDI TPUs.

The IPHTAHDO HDI TPUs present a different profile than all the previous materials, with all of the formulations showing some additional peak other than the wide bands corresponding to the amorphous phase. For most of the materials, this additional band is detected by the presence of a small shoulder at the high q area of the 1st harmonic peak (**Figure 4.39**, **left**). However, one of the materials, **IPHTAHDO 2000 10% HDI**, has a remarkably different profile than the rest, exhibiting a large number of well-defined peaks (**Figure 4.39**, **right**). The existence of narrow peaks in the IPHTAHDO HDI formulations agrees with the results obtained by DSC, on which melting transitions corresponding to the presence of crystallites could be noted. Moreover, on all of the IPHTAHDO HDI samples, the band at 7-8 nm^{-1}, which previously could not be assigned with certainty to either a peak or an artefact exhibits a better definition, indicating that that band is characteristic of the material, and not of any artefact of the detector.

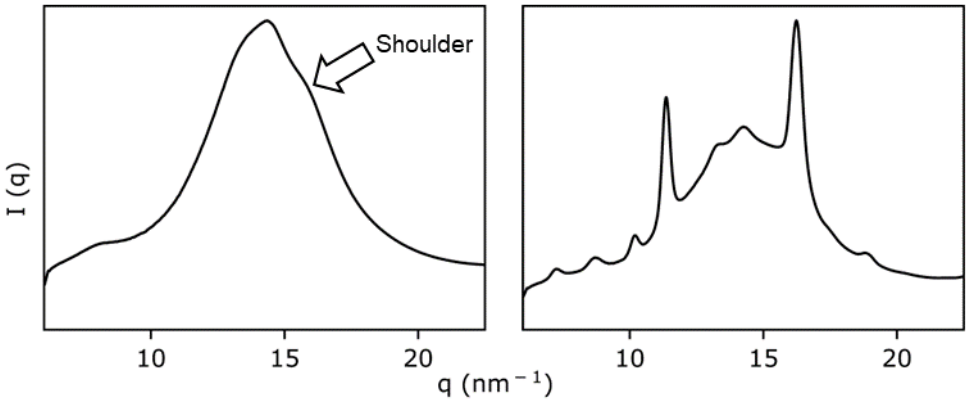

Figure 4.39: First band of the WAXS spectra from the IPHTA HDI TPUs. Right: IPHTAHDO 2000 10% HDI. Left: IPHTAHDO 1000 10% HDI.

To determine the origin of the different peaks observed in the spectra of the IPHTAHDO HDI TPUs, and their degree of crystallinity (Φ_C), peak deconvolution has been employed to obtain the number, areas and locations of the amorphous and crystalline peaks (**Experimental**

section 6.2.16). To simplify the visualisation of the peak deconvolution, the contributions from the 2nd and 3rd harmonic bands have been subtracted from the spectra (**Figure 4.40**). The full deconvoluted spectra can be found in **Annex A7**.

The deconvolution of the WAXS spectra from the five formulations in which only a shoulder can be observed, IPHTAHDO 1000 10-50% and 2000 30-50% HDI, yields either one or two peaks in addition to the wide bands associated with the amorphous phase of the TPUs (**Figure** 4.40, **top**). On most of the materials, just one band, which generates the shoulder appears at 15.9-16.2 nm^{-1}. However, on **IPHTAHDO 1000 10% HDI**, an additional peak at 14.5 nm^{-1} could also be detected. The existence of this additional peak in **IPHTAHDO 1000 10% HDI** can be attributed to its higher crystallinity in comparison with the other five formulations. Both peaks can be attributed to a crystalline phase, as they do not appear in the spectra of the amorphous formulations and their width is significantly lower than the bands arising from the amorphous structures. In the formulation in which well-defined peaks could be noted, **IPHTAHDO 2000 10% HDI**, 9 narrow, crystalline peaks resulted from the deconvolution, with two of them, located at 11.4 and 16.2 nm^{-1} being remarkably intense (**Figure 4.40**, **bottom**). This indicates that the structures found on **IPHTAHDO 2000 10% HDI** are more ordered than those of the other IPHTAHDO HDI materials. Despite the difference in order between the formulations, the two peaks that appear in the less ordered formulations at 14.5 and 15.9-16.2 nm^{-1} can also be observed in **IPHTAHDO 2000 10% HDI**, albeit with a lower width. This indicates that the same structures that give rise to both of those peaks can be found in all of the materials. Given that the same structures are present in all of the IPHTAHDI TPUs, the assignation of the narrow peaks to either HS or SS crystallines is quite straightforward. In the DSC of **IPHTAHDO 2000 10% HDI**, only a melting transition corresponding to SS crystallites could be identified, which implies that the peaks observed in WAXS belong to ordered SS domains, not HS crystallites. Therefore, given that the WAXS peaks are shared amongst all of the formulations, the narrow peaks can be assigned to the presence of SS crystalline domains. This is in agreement with the published results of WAXS studies from TPUs, in which no well-defined crystalline structure was observed for spherical HS domains.[191,207] Only when the HS have a big enough size and become either lamellar or cylindrical is some order observed.[208]

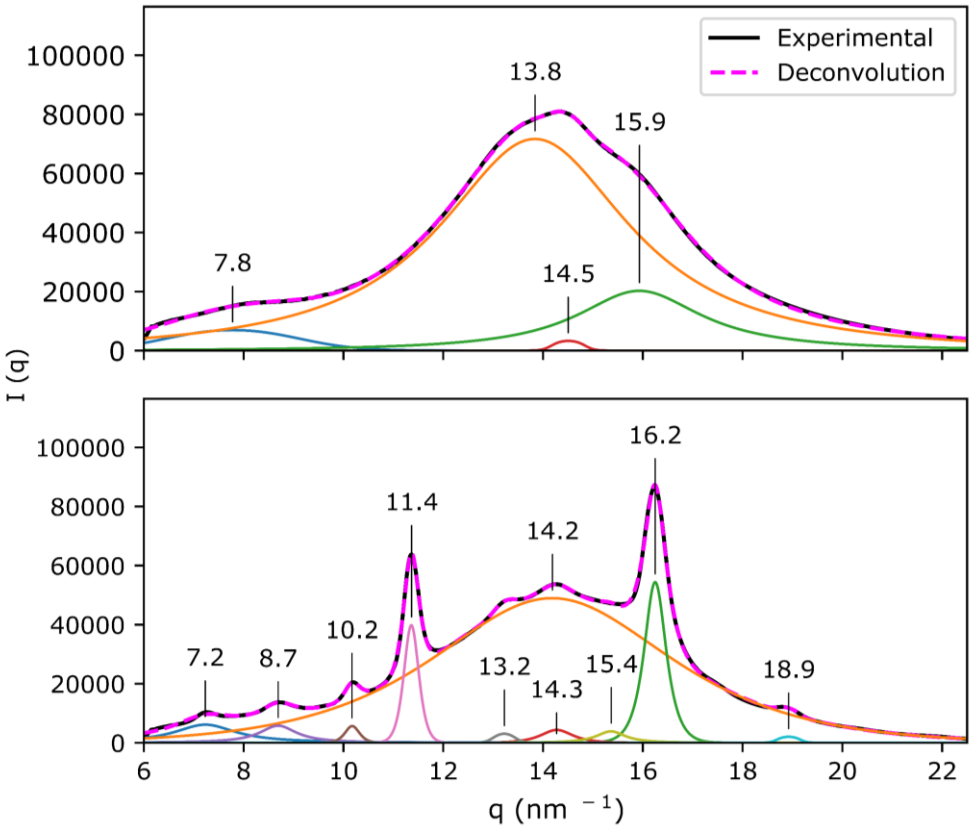

Figure 4.40: Example of the deconvolution of the two types of WAXS profiles from HDI samples.

After the deconvolution of the spectra and assignation of the resulting peaks to amorphous and crystalline structures, the areas for each band were obtained (**Annex A7**) and the degree of crystallinity of the materials (Φ_C) was calculated employing the previously discussed Hermans-Wedinger's definition (**Table 4.15**).[200] As all the crystalline peaks have been assigned to the SS, the Φ_C is expected to follow the same trends as those previously observed for the SS melting enthalpies on DSC. Indeed, if both values are compared, the same behaviour can be observed. The Φ_C decreases as the HS content increases, owing to both the lower SS content and the disruption of the SS crystallites by the higher concentration of HS. The fact that the same trends are observed for the DSC SS enthalpies and WAXS crystallinity corroborates that all of the crystalline peaks observed on WAXS correspond to the SS crystallites, not to HS domains.

Table 4.15: Degree of crystallinity of the IPHTAHDO HDI TPUs and SS melting enthalpy.

	Φ_C	SS ΔH_{melt} (J/g)
IPHTAHDO 1000 10% HDI	0.16	14.5 ± 0.6
IPHTAHDO 1000 30% HDI	0.07	8.3 ± 0.6
IPHTAHDO 1000 50% HDI	0.02	5.4 ± 0.4
IPHTAHDO 2000 10% HDI	0.20	21.8 ± 0.3
IPHTAHDO 2000 30% HDI	0.05	6.5 ± 1.4
IPHTAHDO 2000 50% HDI	0.02	3.2 ± 0.9

To elucidate the crystalline structure from the WAXS pattern, Rietveld refinement is usually employed. However, its application requires some prior information about the unit cell of the crystallites and therefore, could not be carried out on the TPUs developed during this work. Nonetheless, some information concerning the crystalline structure of the HS domains can be drawn by applying Bragg's law and observing the evolution of the two most intense crystalline peaks, those located at 11.4 nm^{-1} and 15.9-16.2 nm^{-1}, with Φ_C. According to Bragg's law, the real space distances between the polymeric chains of a material (d) and q are correlated by **Equation 4.13**. Therefore, the peaks at 15.9-16.2 nm^{-1} and 11.4 nm^{-1} correspond to a d of around 3.9 Å and 5.5 Å respectively. By exploring the evolution of the two peaks, it can be clearly observed that the one corresponding to the shortest d increases in intensity as Φ_C does, and that, only when a high enough order has been reached, does the peak corresponding to the longest distance appear (**Annex A7**). This seems to indicate that first, the polymeric chains of the SS start to organize themselves in the direction of the π-π stacking interaction, with a spacing between chains of 3.9 Å and that, once a high enough Φ_C is reached, a secondary alignment between groups of stacked chains starts to be formed through weaker interactions, which result in the apparition of the highest distance peak.

$$d = \frac{2\pi}{q}$$

Equation 4.13: Relationship between q and d according to Bragg's law.

4.2.2.2.3 FDCA MDI TPUs

The deconvolution of the WAXS spectra from many of the FDCA MDI formulations yields very similar results to their IPHTA analogous. On most of the formulations, only the two wide bands at 6.3-7.9 nm^{-1} and 14.1-14.4 nm^{-1}, and the corresponding two harmonics at 29.3-29.8 and 50.8-52.9 nm^{-1} are present in the spectra, indicating that most of the FDCA MDI TPUs are amorphous (**Annex A7**). However, in two of the formulations, **FDCAHDO 1000 10% MDI** and **FDCAHDO 2000 10% MDI** three additional, narrow peaks at 9.0, 11.5 and 16.3-16.4 nm^{-1}, corresponding to crystalline structures could be noted after the deconvolution of the spectra (**Figure 4.41**, **Annex A7**). The fact that SS crystallinity could be observed on the FDCA MDI TPUs but not on the IPHTA MDI formulations agrees with all of our previous observations, which attribute the highest crystallisation capability to the FDCA rather than to the IPHTA SS, owing to its stronger SS cohesion forces. Surprisingly, the position and relative intensity of the peaks arising from the FDCA formulations are very similar to those found in **IPHTAHDO 2000 10% HDI**, evidencing that the crystalline structure of the SS domains of the IPHTA and FDCA materials is very similar. This is in contradiction with the DFT and density measurements, which attributed a closer chain packing to the FDCA TPUs than to the IPHTA polymers. This might be an effect of the crystalline structure that the polymeric chains adapt, which might inhibit them from getting too close after crystallisation.

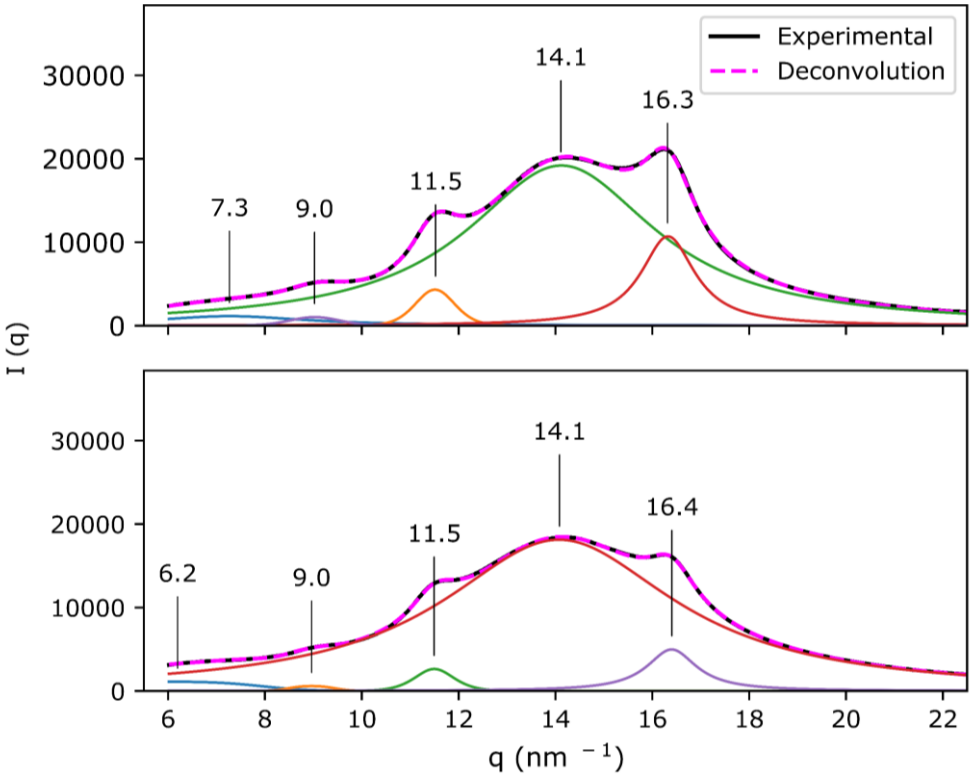

Figure 4.41: WAXS deconvoluted spectra of the semicrystalline FDCA MDI TPUs. Top: **FDCAHDO 1000 10% MDI**. Bottom: **FDCAHDO 2000 10% MDI**.

The same behaviour between the degree of crystallinity by WAXS of two semicrystalline FDCA MDI formulations, **FDCAHDO 1000 10% MDI** and **FDCAHDO 2000 10% MDI**, and DSC has been found, with the TPU with the lowest polyester M_n showing the highest Φ_C. (**Table 4.16**).

Table 4.16: Degree of crystallinity of the semicrystalline FDCAHDO MDI TPUs

	Φ_C
FDCAHDO 1000 10% MDI	0.17
FDCAHDO 2000 10% MDI	0.08

4.2.2.2.4 FDCA HDI TPUs

Finally, the FDCA HDI TPUs have been assessed. Similar to the IPHTA HDI materials, a clear distinction between the PDO and HDO formulations can be established. On the PDO materials, only the peaks corresponding to an amorphous structure could be observed after deconvolution (**Annex A7**). The lack of any SS crystallisation peak agrees with the DSC results, on which no SS crystalline structure was observed on the FDCAPDO materials. On the other hand, the HDO materials present a higher crystallinity, with narrow peaks being present in all of the formulations (**Figure 4.42**, **Annex A7**). This behaviour mirrors that of the IPHTA HDI TPUs, on which the PDO materials are amorphous while the HDO ones were semicrystalline. However, unlike in their IPHTAHDO HDI analogous, all of the FDCAHDO HDI materials show more than one well-defined, narrow peak, rather than just a shoulder (**Figure 4.42**, **Annex A7**). The presence of well-defined peaks rather than just a shoulder in the WAXS spectra of all the FDCA HDI materials agrees with the previous results of this work that state that the SS crystallinity of the FDCA materials is higher than that of the IPHTA ones.

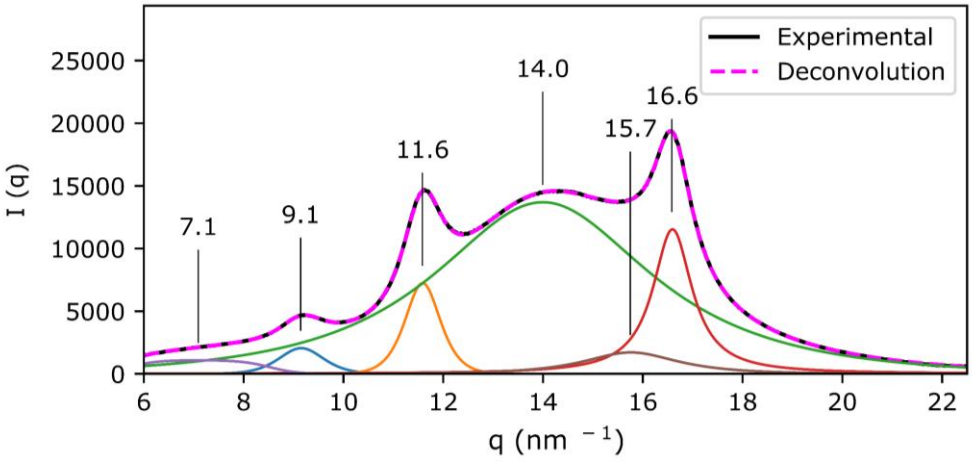

Figure 4.42: Example of the deconvolution of the FDCAHDO HDI TPUs. Sample: **FDCAHDO 1000 10% HDI**.

On the FDCAHDO TPU materials, the crystallinity of the SS could not be accurately quantified by DSC as the signals of the HS and SS melting overlapped. However, by WAXS, those values can be accurately quantified, as no HS peaks are present (**Table 4.17**). Despite their quantification, no relationship between Φ_C and composition could be found, indicating that the crystallinity of the FDCAHDO HDI TPUs is not directly determined by their composition.

Table 4.17: Degree of crystallinity of the FDCAHDO HDI TPUs

	Φ_C
FDCAHDO 1000 10% HDI	0.26
FDCAHDO 1000 50% HDI	0.10
FDCAHDO 1500 30% HDI	0.23
FDCAHDO 2000 10% HDI	0.18
FDCAHDO 2000 50% HDI	0.24

4.2.2.2.5 Overview

In WAXS, the effect that the different monomers have on the crystallinity of the SS mirrors the behaviours extrapolated from the DSC data. MDI generates TPUs with a lower crystallinity than their HDI counterparts, as its aromatic nature results in materials with poor chain mobility and high miscibility between SS and HS, both of which hinder the crystallisation of the material. Similarly, the crystallinity of the IPHTA TPUs is lower than that of their FDCA analogues, as the stronger supramolecular interactions that the latter is capable of generating drive forward the segregation and stacking of the SS chain fragments.

4.3 Polyurethane mechanical properties

After exploring the morphology and chain mobility of the TPUs by DSC, SAXS and WAXS, their hardness and tensile properties were assessed. The morphological data collected in the previous section will be employed to rationalise the variation in the mechanical properties of the different TPU formulations.

4.3.1 Hardness

The hardness of the materials was studied by measuring the resistance to indentation of the injected TPU plates according to ISO 49 on the Shore D scale. The analysis was carried out on ten different samples from three different plates per polymer at a temperature of 21 °C (**Experimental Section 6.1.7**).[161] The exact hardness values and their standard deviation can be found in **Annex A8**.

4.3.1.1 IPHTA MDI TPUs

The IPHTAHDO MDI TPUs, exhibit a lower hardness than the PDO ones (**Figure 4.43**). Moreover, a clear distinction between the hardness of the rubbery and glassy materials can be drawn. The rubbery materials, **IPHTAHDO 2000 10% MDI** and **IPHTAHDO 2000 30% MDI,** which have a T_g below or close to the essay temperature (21 ºC), exhibit a significantly lower hardness than the glassy materials. Nonetheless, both glassy and rubbery materials have exceptionally high hardness, especially when considering the low HS content of some of the formulations. Usually, to achieve materials with high hardness, elevated HS contents are required. For example, two commercial Lubrizol TPUs based on a polybutylene adipate polyester and an MDI/BDO HS, with a HS content of 50 and 88 mol% have a shore D hardness of just 33 and 60 respectively, lower than what is achieved with just a 10% HS in some of the IPHTA MDI TPUs. This is of high interest since diisocyanates are usually the most expensive, contaminant and hazardous monomers employed in TPU materials. Therefore, the capability of reaching high hardness TPUs with a reduced amount of diisocyanate could open the door to the generation of new more sustainable hard products. The higher hardness of the aromatic polyol TPUs in comparison with the standard, aliphatic polyol materials can be explained by the high cohesion strength of the aromatic SS. The aromatic SS have a higher cohesion strength than their aliphatic counterparts, as they are capable of generating π-π stacking interactions, stronger than the Van der Waals interactions formed on the aliphatic SS. The increase in cohesion strength leads to materials with a higher resistance to indentation, resulting in the high hardness of the IPHTA TPU materials.

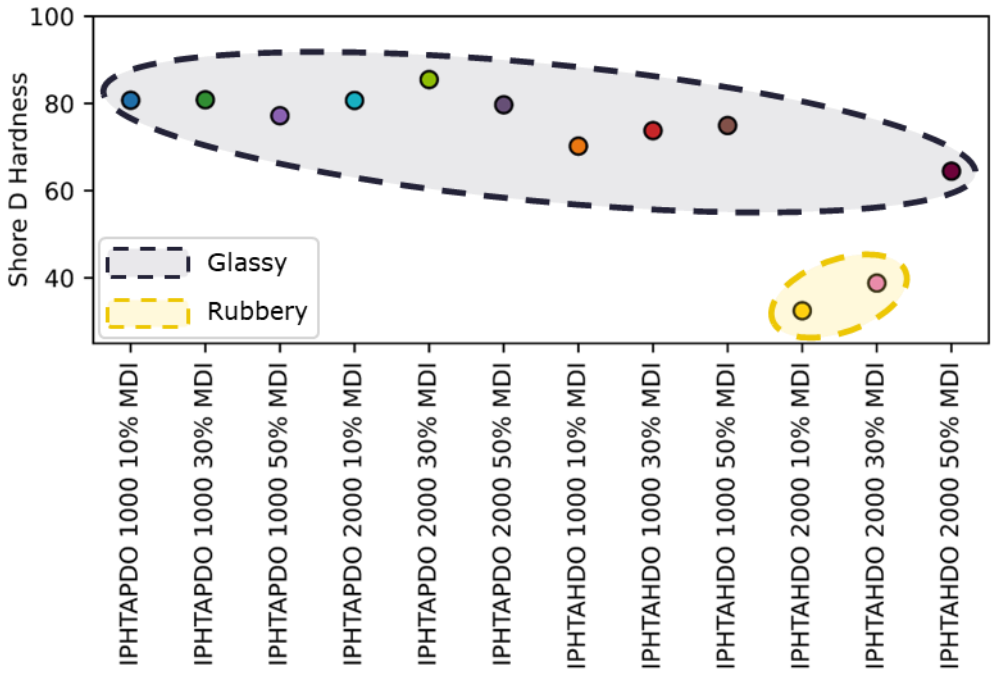

Figure 4.43: Shore D hardness of the IPHTA MDI TPUs. Average standard deviation ± 2.

4.3.1.2 IPHTA HDI TPUs

The IPHTA HDI TPUs exhibit the same behaviour as that of their MDI analogous, with the rubbery polymers (IPHTAHDO) having significantly lower hardness than the glassy ones (IPHTAPDO) (**Figure 4.44**). Despite them sharing the same behaviour, the hardness of the IPHTAHDI TPUs is slightly lower than that of the IPHTAMDI formulations, which can be attributed to the higher rigidity, HS-SS miscibility and stronger supramolecular interactions generated by MDI in comparison with HDI. Nonetheless, just as on the IPHTAMDI TPUs, the hardness of the IPHTAHDI formulations is remarkably higher than that of commercial aliphatic TPUs. The difference between the hardness of the standard aliphatic polyol HDI materials and the IPHTA formulations is even higher than on the MDI TPUs, as HDI TPUs tend to have a remarkably lower hardness than the MDI ones. Putting a commercial Lubrizol HDI TPU as example, the shore D hardness of a polycaprolactone-based polymer with a HS content of 60 mol % is of just 33, lower than any of the IPHTAHDI TPUs. The high hardness of the IPHTA HDI TPUs could open the door to the development of new products that require both high hardness and weatherability. MDI TPUs are inadequate for outdoor applications, even when high hardness are required since they turn yellow with exposure to solar radiation.

Although HDI TPUs do not suffer this issue, reaching formulations with high hardness employing this diisocyanate is complicated. Therefore, the introduction of aromatic polyols in the TPUs could aid in producing nonyellowing hard materials suitable for products which require both good weatherability and high hardness.

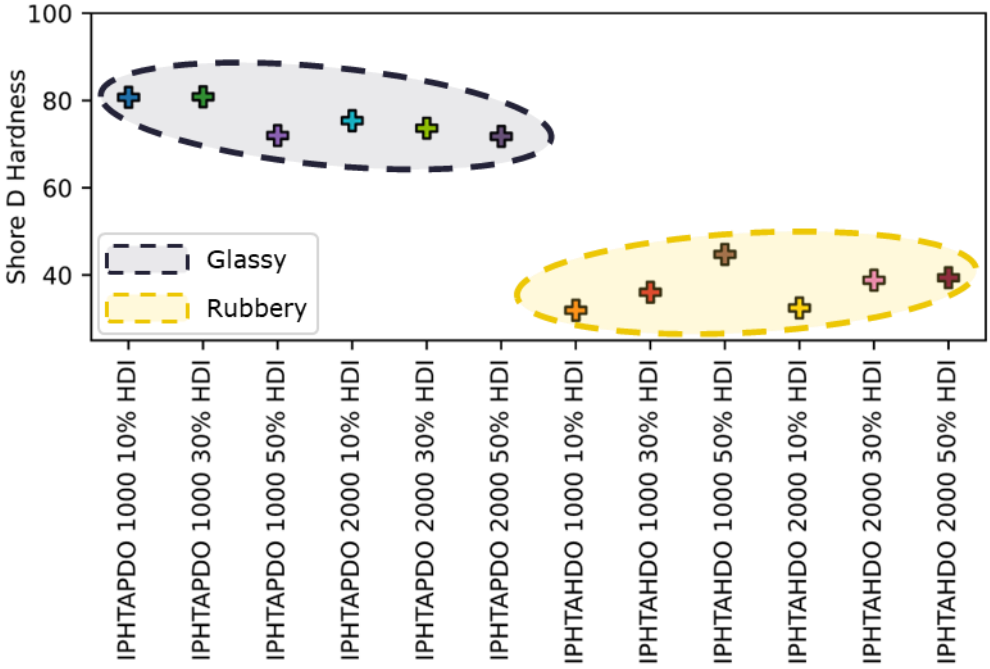

Figure 4.44: Shore D hardness of the IPHTA HDI TPUs. Average standard deviation ± 1.

The hardness of the rubbery TPUs increases with the HS content. However, the trend is not maintained in the glassy materials, which exhibit the opposite behaviour (**Figure 4.44**). Therefore, no generalisation can be drawn about the effect that the HS content has on hardness. Likewise, no trends could be extracted from the polyester M_n. Interestingly, this gives some information about the effect that the SS crystallinity has on hardness. As noted by DSC and WAXS, **IPHTAHDO 2000 10% HDI** has a significantly higher SS crystallinity than that of the other IPHTAHDO HDI polymers. However, this is not reflected in the hardness indicating that the SS crystallinity does not have a big effect on the hardness of the materials.

4.3.1.3 FDCA MDI TPUs

The FDCA MDI TPUs show higher hardness than their IPHTA homologues (**Figure 4.45**). The increase in hardness follows the same reasoning as stated when comparing aliphatic TPUs

with the IPHTA ones. The variations in SS cohesion strength, produced by the different strengths of the supramolecular interactions generated by the diacids, which follow the trend aliphatic < IPHTA < FDCA, result in the FDCA materials having the highest hardness. Unlike in the IPHTA materials, in which the hardness of the PDO TPUs was slightly higher than their HDO counterparts, no coherent trends could be observed in the FDCA MDI materials, with some HDO TPUs being harder than the PDO ones and *vice versa*. Nevertheless, the variations in hardness amongst the materials are quite low, with all of them presenting values above 90 shore D.

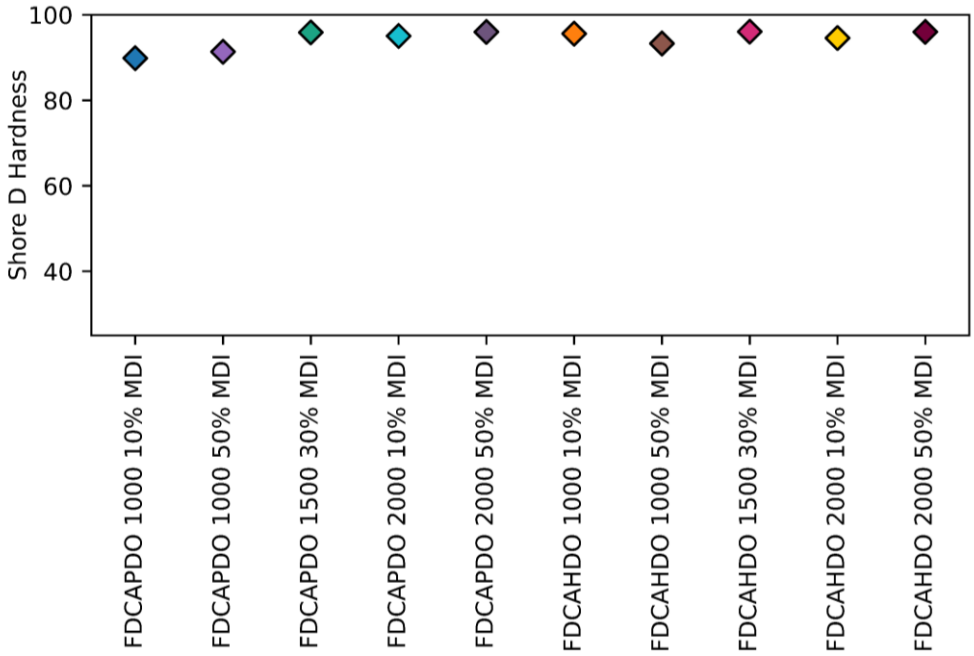

Figure 4.45: Shore D hardness of the FDCA MDI TPUs. Average standard deviation ± 2.

4.3.1.4 FDCA HDI TPUs

Following the same trends as those of the IPHTA materials, the hardness of the rubbery FDCA HDI TPUs are lower than those of the glassy formulations (**Figure 4.46**). Moreover, as in the MDI materials, the hardness of the FDCA HDI polymers is higher than that of the IPHTA HDI formulations. This is in agreement with the previous hypothesis stating that the stronger supramolecular interactions of FDCA in comparison to those of IPHTA result in materials with a higher hardness.

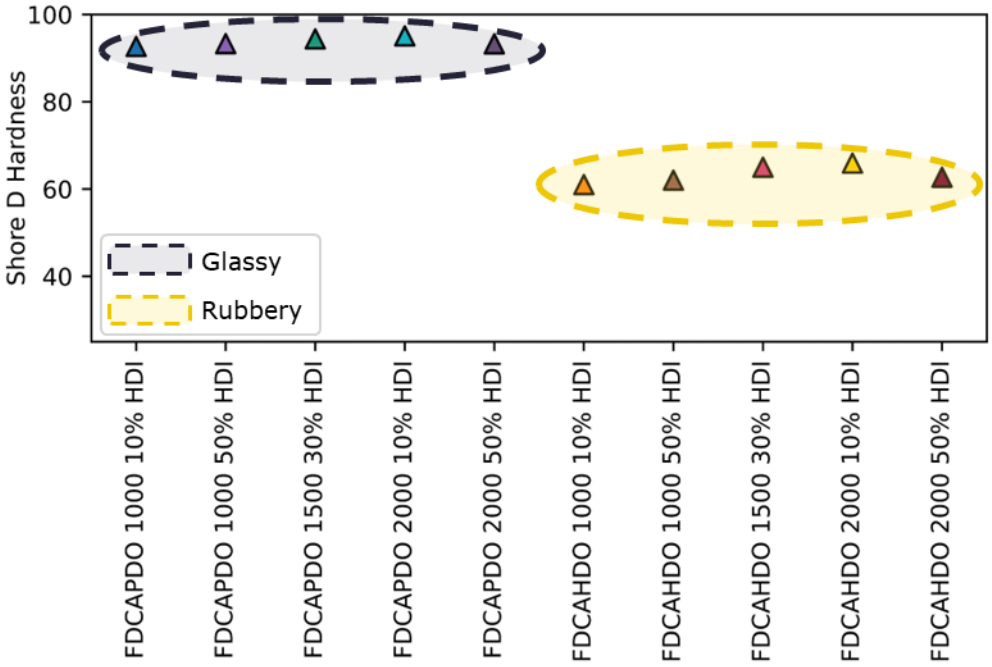

Figure 4.46: Shore D hardness of the FDCA HDI TPUs. Average standard deviation ± 2.

4.3.1.5 Overview

The two most influencing factors on the hardness of the studied TPUs are their glassy or rubbery state and the nature of the polyester. The effect of the polyester originates from the variations in supramolecular interaction strength of the SS, which increase when going from aliphatic diacids to IPHTA to FDCA. The stronger the supramolecular interactions, the highest the hardness, as the cohesion strength of the material and therefore, their resistance to indentation increases. Accordingly, the highest hardness are obtained for the FDCA TPUs, followed by the IPHTA polymers. The variations in hardness of the rubbery and glassy materials can be attributed to their differences in chain mobility. For the materials to suffer indentation, the polymeric chains need to reorganize themselves. Therefore, it is understandable that the less mobile the TPUs are, the lower their capability to accommodate indentation will be, resulting in harder materials.

4.3.2 Tensile properties

The tensile properties of the synthesised TPUs were evaluated by classical tensile testing. Tensile testing is based on the monitoring of the stress of the material during deformation, and enables, amongst others, the determination of the ductility and elastomeric behaviour of the materials. Furthermore, several key parameters concerning the mechanical performance of polymers, like their yield (σ_y) and ultimate stress (σ_{max}) or their elongation at break (ε_b), can be obtained from the tensile measurements. All of the tensile testing essays have been carried out in ISO 37 type 2 dumbbell samples cut from injected TPU plates, and the essays have been performed at a temperature of 21 °C (**Experimental Section 6.1.10.1**).

4.3.2.1 IPHTA MDI TPUs

The IPHTAMDI formulations have been employed to determine the conditions under which the tensile testing will be carried out. Initially, a standard elongation rate of 200 mm/min was selected for the assay. However, not all the materials could be analysed at such high elongation rates. The ε_b of some of the glassy IPHTAPDO MDI TPUs is so low that they yielded too fast for the equipment to register their stress under these deformation conditions. Therefore, the elongation rate was reduced to 5 mm/min to obtain comparable information for all the materials (**Experimental Section 6.1.10.1**).

The IPHTA MDI TPUs can be classified into four different categories according to their tensile behaviour: hard tough plastics, strong tough plastics, soft plastics, and ductile elastomers (**Figure 4.47**, **Annex A9**).[209] The four different behaviours can be identified by their characteristic stress *vs* strain profiles. Ductile elastomers are characterised by a mild initial increase in stress, which plateaus over a large period of strain until either the material breaks or the stress starts to increase back again. This increase in stress at high elongations is derived from the strain hardening or strain-induced crystallisation process, by which the polymeric chains order themselves in the direction of the strain, leading to an increase in stress. On the other hand, plastic materials are characterised by a steep increase in their stress at low elongations after which, depending on whether they are strong, hard or soft polymers, they will evolve differently. (**Figure 4.47**). The different plastic materials can be differentiated by two factors, their yield stress, and the presence or lack thereof of cold drawing.

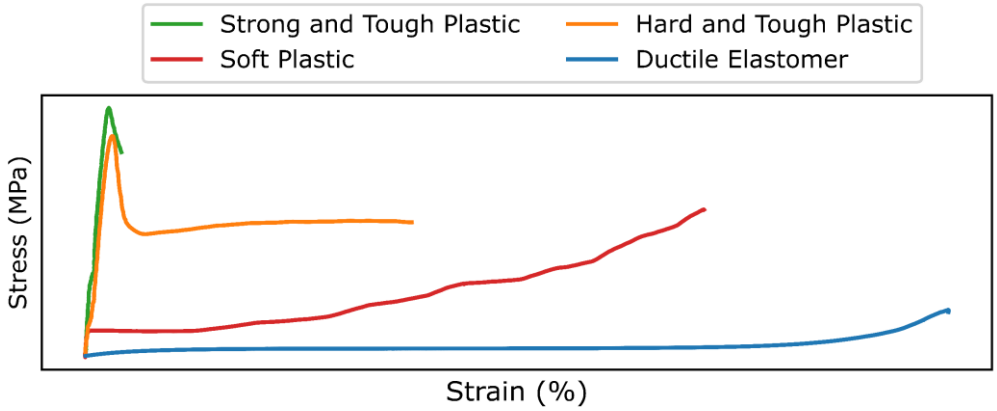

Figure 4.47: Different tensile behaviours of the IPHTA MDI TPUs.

Soft plastic polymers are characterised by the smallest yield stress of all the plastic materials, upon which they behave similarly to the elastomeric polymers, with their stress being stable until it starts to increase due to the strain hardening process. The strong tough and hard tough plastic materials exhibit greater yield stress than the soft plastic polymers. The main distinction between them is whether or not they exhibit cold drawing. During the cold drawing process, first, the material undergoes a necking process, in which a small cross-section of the dumbbell constricts, generating a region with a lower width. The lower area of the constricted region generates a decrease in the stress of the material. Afterwards, the constricted region starts to grow, as the polymeric chains rearrange to accommodate for the induced strain. Owing to the lower width of the cross-section during cold drawing, the process can be identified as a long region in elongation upon which the stress of the material is constant and lower than the yield stress (**Figure 4.48**).[210] The cold drawing process can evolve in two different manners. Either the material breaks during it, or the necking on the sample reaches the ends of the material. If the latter occurs, just as what occurred on the ductile materials, the chains can start to order due to the strain and crystallise, resulting in the strain hardening of the material.

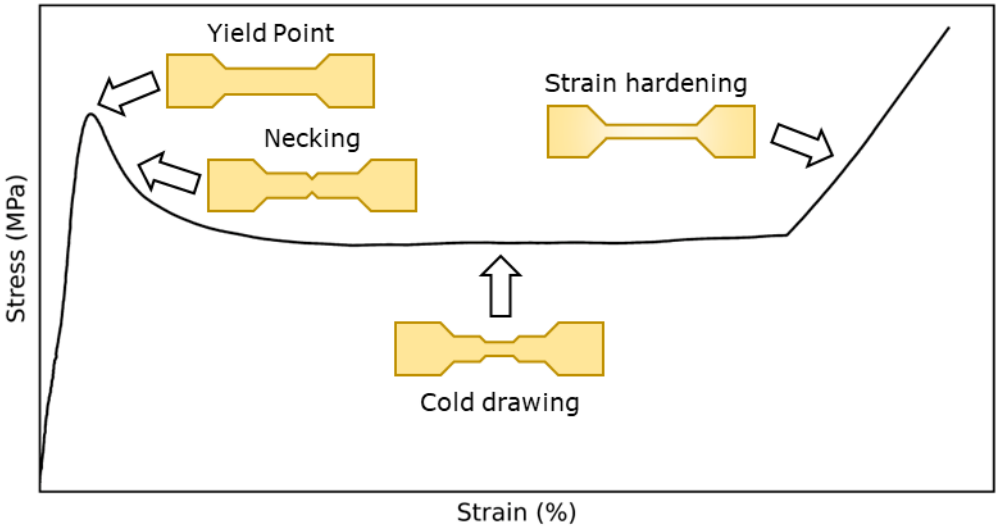

Figure 4.48: Possible stress-strain process features.

The difference in ductility between the ductile elastomers and soft plastics and the brittle strong and hard tough plastics can be attributed to the brittle-ductile transition temperature (T_b) of the TPUs. As the name implies, this is the temperature at which elastomeric materials turn from a brittle material to a ductile polymer. The materials that are assayed at a temperature above their T_b will be ductile, with ductility decreasing as this T_b is approached. This temperature can be equal to or lower than the T_g of the polymers depending on the nature of the material. Usually, polymers with bulky side groups are the ones in which T_b is equal to T_g, while high hardness materials have a T_b close to T_β. This T_β, which is lower than the T_g, is defined as the temperature at which localised chain movements, involving 4-8 carbon atoms, can occur.[211,212] In our case, the T_b has been observed to be around T_β, as some of the glassy materials behave as ductile soft plastics, not hard plastics (**Table 4.18**).

Table 4.18: Tensile properties of the IPHTA MDI TPUs.

	Elastomeric behaviour	Glassy or rubbery state [a]	σ_{max} (MPa) [b]	ε_b(%) [b]
IPHTAPDO 1000 10% MDI	Hard Tough Plastic	Glassy	70 ± 2	194 ± 58
IPHTAPDO 1000 30% MDI	Strong Tough Plastic	Glassy	77 ± 7	2 ± 1
IPHTAPDO 1000 50% MDI	Hard Tough Plastic	Glassy	62 ± 1	252 ± 14
IPHTAPDO 2000 10% MDI	Strong Tough Plastic	Glassy	62 ± 4	2 ± 2
IPHTAPDO 2000 30% MDI	Strong Tough Plastic	Glassy	74 ± 8	2 ± 1
IPHTAPDO 2000 50% MDI	Strong Tough Plastic	Glassy	75 ± 7	3 ± 0
IPHTAHDO 1000 10% MDI	Soft Plastic	Glassy	51 ± 1	330 ± 26
IPHTAHDO 1000 30% MDI	Hard Tough Plastic	Glassy	54 ± 2	279 ± 23
IPHTAHDO 1000 50% MDI	Hard Tough Plastic	Glassy	59 ± 2	215 ± 43
IPHTAHDO 2000 10% MDI	Ductile Elastomer	Rubbery	18 ± 3	424 ± 14
IPHTAHDO 2000 30% MDI	Ductile Elastomer	Glassy	20 ± 1	470 ± 21
IPHTAHDO 2000 50% MDI	Soft Plastic	Glassy	40 ± 5	360 ± 29

[a] Defined as whether the essay temperature (21 °C) is above (rubbery) or below (glassy) the T_g of the materials.
[b] Calculated as the mean of at least two different plates at 21 °C.

The IPHTA MDI TPUs are amorphous materials that do not exhibit phase segregation or crystallinity. Therefore, the effect that those two parameters have on the tensile properties of the materials can not be explored in these formulations. Nonetheless, the effect that the differences in chain mobility and composition between the IPHTA MDI formulations have on the tensile properties of the materials can be assessed.

A clear relationship between the ultimate stress (σ_{max}) and HS content of the IPHTA MDI formulations can be observed from the data. Overall, σ_{max} increases alongside the HS content, with one exception, **IPHTAPDO 1000 50% MDI** (**Figure 4.49**). Moreover, the TPUs with a polyester M_n of 1000 g/mol exhibit higher σ_{max} than those made out of the larger, 2000 g/mol polyester. These relationships between σ_{max} and composition are reminiscent of the trends between T_g and composition of the IPHTA MDI TPUs, which also increased with the HS content and decreased as the polyester M_n increased.

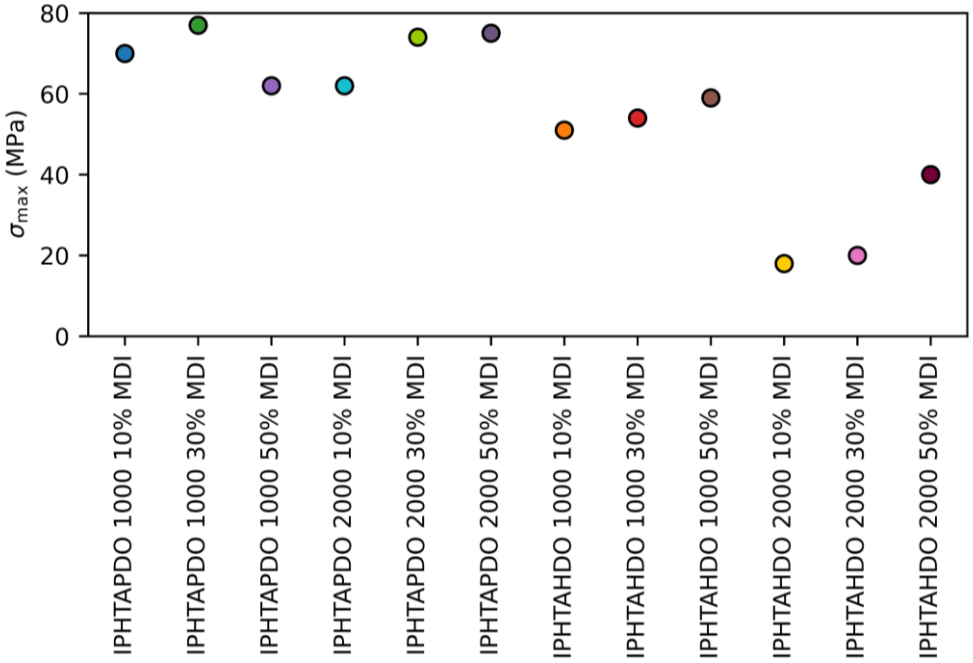

Figure 4.49: σ_{max} of the IPHTA MDI TPUs.

To assess, if indeed, a correlation between the chain mobility of the materials and their σ_{max} exists, a T_g *vs* σ_{max} plot has been drawn (**Figure 4.50**). The σ_{max} of the materials increases as the T_g does, until a plateau at around 60-75 MPa is reached, which indicates the chain mobility of the amorphous IPHTA MDI polymers is one of the main variables affecting their tensile strength. This is further highlighted by the presence of two different relationships between σ_{max} and T_g depending on whether the materials are ductile (elastomers and soft plastics) or brittle (strong or tough plastics). To understand the difference in behaviour between the ductile and brittle materials, a clear picture of how the mobility of linear polymeric systems varies with temperature is required. First of all, when the materials are at a temperature above their T_g, that is to say, in their rubbery state, the chains of the material are capable of effectuating large-scale

motions including above 50 atoms. As temperature decreases below T_g, these motions start to be inhibited, and, upon reaching T_β, the range of movement of the chains is restricted, with only localised chain movement involving 4-8 atoms being permitted. Finally, as temperature drops below T_β, the chains turn completely static, with only bond stretching and bending being permitted. Upon this point further decreasing the essay temperature has little effect on the mobility of the polymers, as the chains are completely static. Therefore a higher variability of the chain mobility with temperature is observed when the materials are essayed above their T_β than below it.[212–217] This is the same behaviour that is observed in the σ_{max} of the materials. The ductile materials, those which are essayed above their T_β, exhibit a larger variation in σ_{max} as their T_g and therefore their T_β increases than the brittle materials, which are essayed below their T_β and have their chain mobility inhibited.

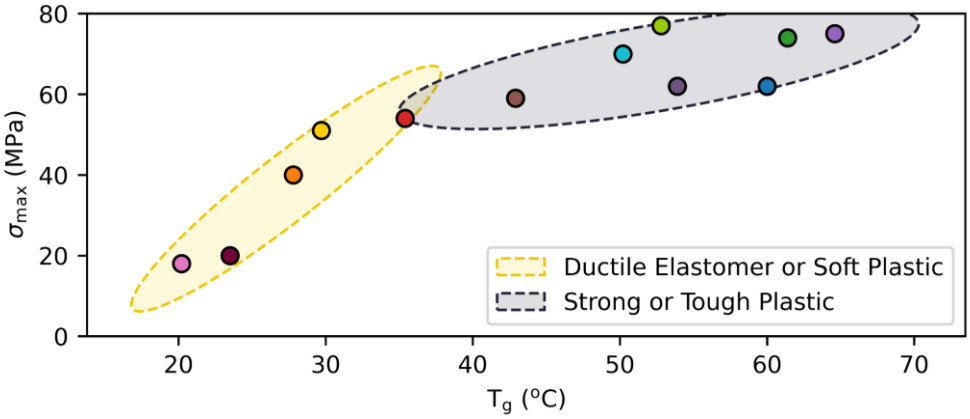

Figure 4.50: Correlation of the IPHTA MDI TPUs between $\boldsymbol{\sigma_{max}}$ and T_g.

Regarding the strain of the IPHTA MDI TPUs, a clear distinction can be observed between the strong tough plastics and the rest of the materials as, by definition, the strong tough materials exhibit very low elongation at break (ε_b), below 5%, while the rest of the materials are capable of deforming to a greater extent (**Figure 4.51**). The relationships between composition and ε_b are less clear than those found in tensile strength. Overall, the ε_b of the IPHTAHDO MDI TPUs seems to follow the inverse trend as that of tensile strength, with it increasing with the polyester M_n and decreasing as the HS content rises. However, an exception to this rule, **IPHTAHDO 2000 30% MDI**, can be noted. Since only two IPHTAPDO MDI TPUs showed any significant ε_b, no data can be extracted from just these two samples.

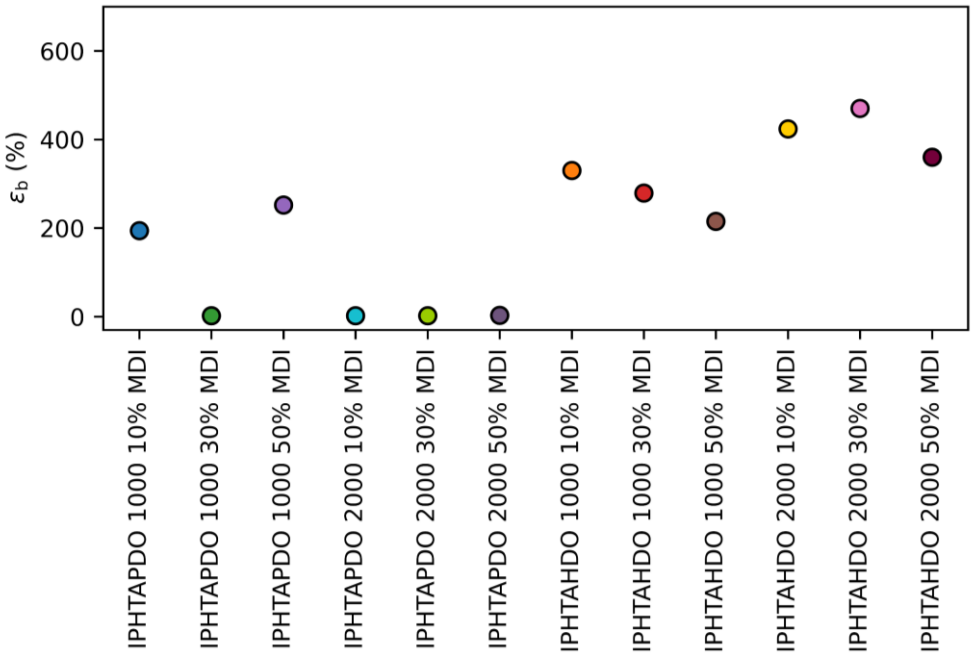

Figure 4.51: ε_b of the IPHTA MDI TPUs.

4.3.2.2 IPHTA HDI TPUs

Likewise to the IPHTA MDI TPUs, plastic and elastomeric materials are obtained from the IPHTA HDI formulations (**Table 4.19**, **Annex A9**). However, unlike in the MDI formulations, none of the plastic materials exhibit a tough plastics behaviour, rather, all of them act as soft plastics. This difference in behaviour can be attributed to the differences in T_g and therefore, in chain mobility between the MDI and HDI polymers. Tough plastics are achieved in materials with low chain mobilities, which hinder the displacement of the chains during deformation. Therefore, the higher chain mobility of the HDI TPUs in comparison with that of the MDI formulations results in the higher ductility of the HDI formulations than of their MDI analogues.

Table 4.19: Tensile properties of the IPHTA HDI TPUs.

	Elastomeric behaviour	Glassy or rubbery state [a]	σ_{max} (MPa) [b]	ε_b(%) [b]
IPHTAPDO 1000 10% HDI	Soft Plastic	Glassy	26 ± 4	371 ± 41
IPHTAPDO 1000 30% HDI	Soft Plastic	Glassy	24 ± 2	359 ± 60
IPHTAPDO 1000 50% HDI	Soft Plastic	Glassy	17 ± 5	263 ± 85
IPHTAPDO 2000 10% HDI	Soft Plastic	Glassy	38 ± 1	353 ± 40
IPHTAPDO 2000 30% HDI	Soft Plastic	Glassy	32 ± 2	342 ± 21
IPHTAPDO 2000 50% HDI	Soft Plastic	Glassy	27 ± 1	288 ± 18
IPHTAHDO 1000 10% HDI	Ductile Elastomer	Rubbery	21 ± 2	559 ± 17
IPHTAHDO 1000 30% HDI	Ductile Elastomer	Rubbery	41 ± 1	534 ± 2
IPHTAHDO 1000 50% HDI	Ductile Elastomer	Rubbery	25 ± 0	266 ± 20
IPHTAHDO 2000 10% HDI	Ductile Elastomer	Rubbery	5 ± 1	668 ± 62
IPHTAHDO 2000 30% HDI	Ductile Elastomer	Rubbery	30 ± 4	449 ± 36
IPHTAHDO 2000 50% HDI	Ductile Elastomer	Rubbery	35 ± 3	405 ± 3

[a] Defined as whether the essay temperature (21 °C) is above (rubbery) or below (glassy) the T_g of the materials.
[b] Calculated as the mean of at least three different plates at 21 °C.

Two different relationships between composition and σ_{max} were noted on the IPHTA HDI TPUs. The IPHTAPDO HDI formulations exhibit the inverse trends as those observed on their MDI analogues, with σ_{max} increasing as the polyester M_n increases and HS content decreases (**Figure 4.52**). Nonetheless, this does not imply that the relationship between the σ_{max} and the T_g of the IPHTAPDO HDI and MDI formulations differs. The T_g of the IPHTA HDI materials follows the inverse trends with composition as those of their MDI counterpart. Therefore, despite

the inverse relationship between σ_{max} and composition of the IPHTAPDO HDI and MDI materials, their correlation with chain mobility is the same, with σ_{max} being higher the more limited chain mobility is.

In the IPHTAHDO HDI TPUs, a less marked trend was observed (**Figure 4.52**). Although in most of the formulations, σ_{max} increases with the HS content, an outlier, **IPHTAHDO 1000 30% HDI**, can be found. Moreover, no relationship between polyester M_n and σ_{max} can be found. Therefore, no correlation between σ_{max} and T_g can be established for the IPHTAHDO HDI TPUs.

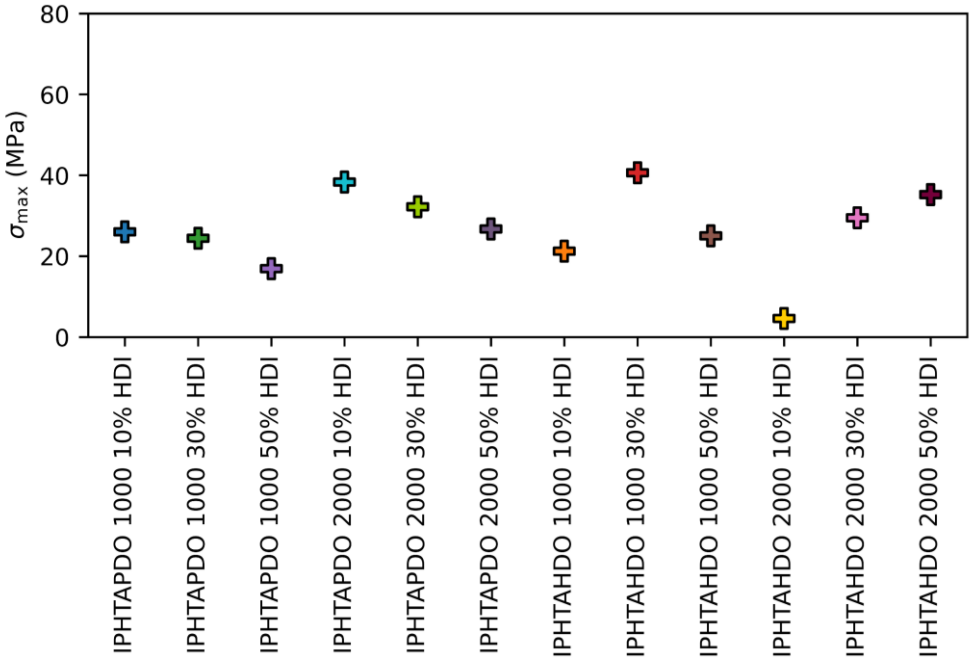

Figure 4.52: σ_{max} of the IPHTA HDI TPUs.

The differences between the IPHTAPDO and HDO HDI tensile behaviours become apparent by observing their T_g *vs* σ_{max} correlation plot (**Figure 4.53**). A clear linear relationship between T_g and σ_{max} can be found in the IPHTAPDO HDI formulations, while the IPHTAHDO HDI materials exhibit no such correlation. Therefore, there must be some parameter that is different for the PDO and HDO TPUs and that induces their difference in tensile behaviour.

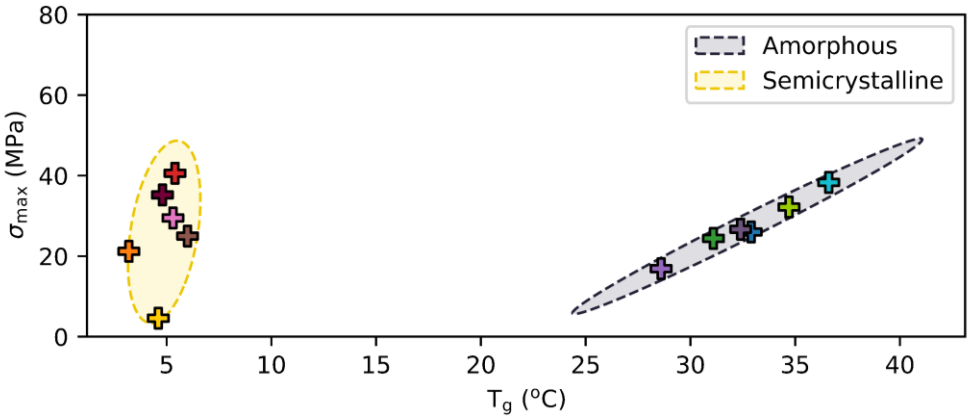

Figure 4.53: Correlation of the IPHTA HDI TPUs between $\boldsymbol{\sigma_{max}}$ and T_g.

By DSC, SAXS and WAXS, a clear distinction between the morphology of the IPHTAPDO and IPHTAHDO HDI TPUs could be identified. The IPHTAPDO HDI polymers are amorphous, unsegregated materials, while the IPHTAHDO HDI TPUs present both phase segregation and SS crystallinity. These segregated domains can act as physical crosslinks, modifying the deformation mechanism of the polymers. Therefore, the presence of segregated domains in the HDO formulations can explain the differences in tensile behaviour between the PDO and HDO TPUs. On non-crosslinked polymers, once strain is applied, the polymeric chains are capable of sliding by one another, reducing the tension that is experienced by the material (**Figure 4.54**, **right**).[218,219] The higher chain mobility is, the less strain is required to enable the sliding of the chains. Accordingly, the lower the T_g, the lower the stress experienced by the materials, as observed in the IPHTA MDI and IPHTAPDO HDI formulations.[219] On the other hand, in polymers with a significant crosslink density, the chains are anchored, meaning that they cannot slide. Consequently, when strain is applied to crosslinked materials, the chains experience a greater tension given their incapability to release the stress through chain slipping (**Figure 4.54**, **left**).[220–225] For that reason, on crosslinked polymers, the main factor that controls their σ_{max} is the cohesion strength of the crosslink and its concentration rather than their chain mobility.[226–231] The increase in the strain of the crosslinked polymers can be observed on the IPHTAHDO HDI TPUs, which have a higher σ_{max} than what would be expected given their high chain mobility.

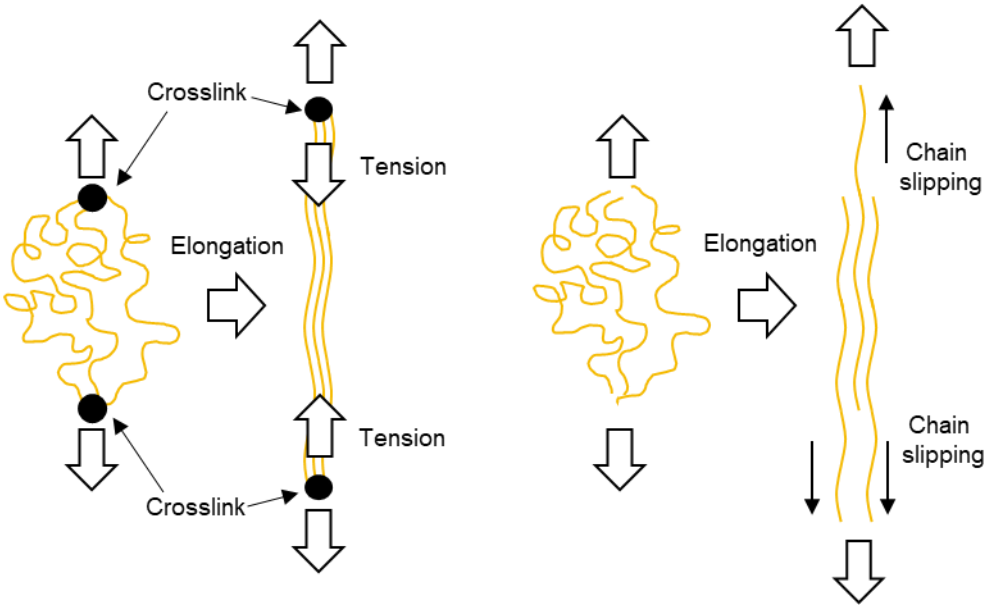

Figure 4.54: Representation of the elongation mechanism of a crosslinked polymer (left) and a non-crosslinked one (right).

Since both HS and SS segregated domains are found on the IPHTAHDO HDI materials, both structures could be acting as the physical crosslink inhibiting chain slipping. However, if the crystallinity of the SS obtained by WAXS and the variations in σ_{max} are compared, it is clear that the presence of SS crystallites does not influence to a great extent the σ_{max} of the materials. The highest SS crystallinity was observed for the TPUs with the lowest HS content, **IPHTAHDO 1000 10% HDI** and **IPHTAHDO 2000 10% HDI** which are the formulations with the lowest tensile strength, indicating that the SS crystallites are not capable of acting as effective physical crosslinks. This can be understood, once more, by the chain slipping process. Owing to their high aromatic content, the crystallisation of the SS will probably result in a lamellar ordering of the polymeric chains. The highly ordered domains will enable an easier chain slippage of the SS, as fewer defects, which hinder their gliding will be present.[232] This leaves the HS domains as the structures responsible for acting as physical crosslinks on the materials. Overall, an increase in σ_{max} is observed as the HS content increases, which is in agreement with the DSC results, in which an increase in the enthalpy of the melting of the HS domains is observed as HS content increases. However, one exception can be observed from the data, **IPHTAHDO 1000 30% HDI**, which has a higher σ_{max} than its **IPHTAHDO 1000 50% HDI** homologue. No clear reasoning can be found for the existence of this outlier, as both SAXS and DSC indicate

that the HS concentration of the **IPHTAHDO 1000 30% HDI** domains is lower than those of **IPHTAHDO 1000 50% HDI**.

The effect that the presence of HS domains and SS crystallites has on the tensile behaviour of the TPUs can also be observed in the ε_b of the materials (**Figure 4.55**, **Table 4.19**).[232] The ε_b of the IPHTAHDO HDI TPUs is lower the highest the HS concentration is. This can be attributed to the hindrance to the chain slipping process that the HS domains induce, which limits the ability of the material to deform without breaking. Interestingly, the same trends can be observed on the IPHTAPDO HDI TPUs. This indicates that contrarily to the IPHTAPDO MDI materials, the ε_b of the HDI formulations does not increase as their chain mobility increases. This inversion of the relationship between chain mobility and ε_b can be attributed to the hindrance to the chain slipping process of the HS chain fragments. The HS chain fragments, either segregated or mixed within the SS, act as imperfections in the SS structure, hindering the chain slipping process and therefore reducing the capability of the materials to elongate, inducing the faster failure of the materials. Moreover, this might indicate that the previously observed trend in strain from the IPHTA MDI TPUs is not caused by the decrease in chain mobility but rather, by the increase in HS content.

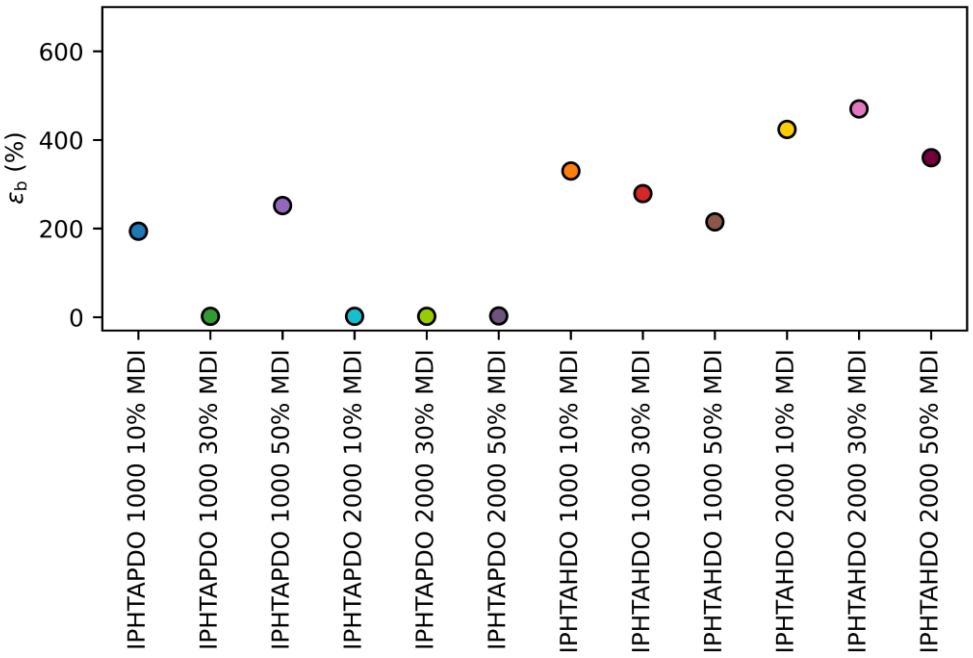

Figure 4.55: ε_b of the IPHTA HDI TPUs.

4.3.2.3 FDCA MDI TPUs

None of the FDCAMDI TPUs, are rubbery at room temperature and therefore, all of them act as plastic materials. Moreover, most of the polymers are brittle plastics, with only three of the formulations resulting in ductile, soft plastic materials (**Table 4.20, Annex A9**). This is consistent with the high T_g found for the FDCAMDI formulations, which limits their ductility.

Table 4.20: Tensile properties of the FDCA MDI TPUs.

	Elastomeric behaviour	**Glassy or rubbery state [a]**	**σ_{max} (MPa) [b]**	**ε_b(%) [b]**
FDCAPDO 1000 10% MDI	Hard Tough Plastic	Glassy	70 ± 1	141 ± 8
FDCAPDO 1000 50% MDI	Hard Tough Plastic	Glassy	71 ± 3	123 ± 17
FDCAPDO 1500 30% MDI	Strong Tough Plastic	Glassy	75 ± 5	11 ± 9
FDCAPDO 2000 10% MDI	Hard Tough Plastic	Glassy	68 ± 3	120 ± 26
FDCAPDO 2000 50% MDI	Strong Tough Plastic	Glassy	63 ± 1	39 ± 28
FDCAHDO 1000 10% MDI	Soft Plastic	Glassy	33 ± 2	247 ± 11
FDCAHDO 1000 50% MDI	Hard Tough Plastic	Glassy	53 ± 2	190 ± 18
FDCAHDO 1500 30% MDI	Soft Plastic	Glassy	43 ± 2	308 ± 2
FDCAHDO 2000 10% MDI	Soft Plastic	Glassy	36 ± 4	231 ± 16
FDCAHDO 2000 50% MDI	Hard Tough Plastic	Glassy	29 ± 5	159 ± 64

[a] Defined as whether the essay temperature (21 °C) is above (rubbery) or below (glassy) the T_g of the materials.
[b] Calculated as the mean of at least three different plates at 21 °C.

The σ_{max} of the FDCA MDI materials would be expected to follow the same relationship between composition and σ_{max} as their IPHTA MDI analogues since no phase segregation could be identified on any of the FDCA MDIformulations just as on the IPHTA MDI materials. However, the trends observed in the FDCA MDI TPUs are less marked than those of the IPHTA MDI

polymers (**Figure 4.56**). Overall, a decrease in the σ_{max} can be observed when moving from the PDO to the HDO polymers and as the polyester M_n decreases, albeit with one exception, the **PDO 1500 30% MDI** TPU, which shows a higher σ_{max} than their 1000 M_n counterparts. Regarding the HS content, a clear trend could not be found. In the 1000 M_n TPUs, the strength of the materials increases as the HS content does, while in the 2000 M_n TPUs, the inverse situation is observed.

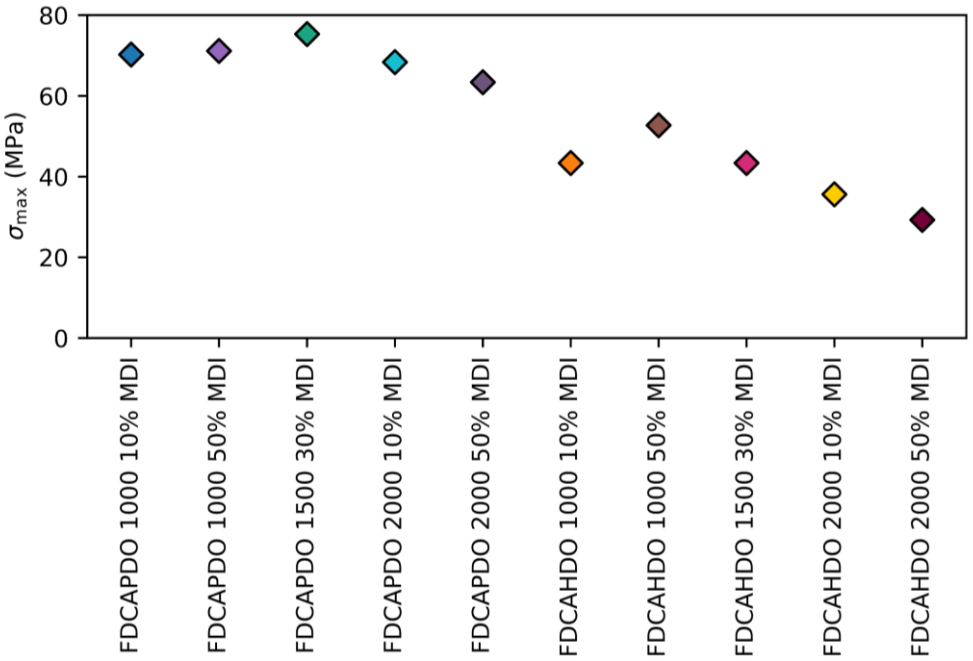

Figure 4.56: σ_{max} of the FDCA MDI TPUs.

The lack of a well-defined trend can likewise be observed on the σ_{max} *vs* T_g plot (**Figure 4.57**). Although overall an increase in the strength of the polymers with the T_g can be noted, several outliers, like **FDCAHDO 2000 10% MDI** or **FDCAHDO 2000 50% MDI** could be identified. The existence of the outliers could not be rationalised by any factor, as no strong difference in either HS or SS crystallinity was apparent from said samples. Additionally, also like on the IPHTA MDI TPUs, the σ_{max} of the materials plateaus at 60-75 MPa.

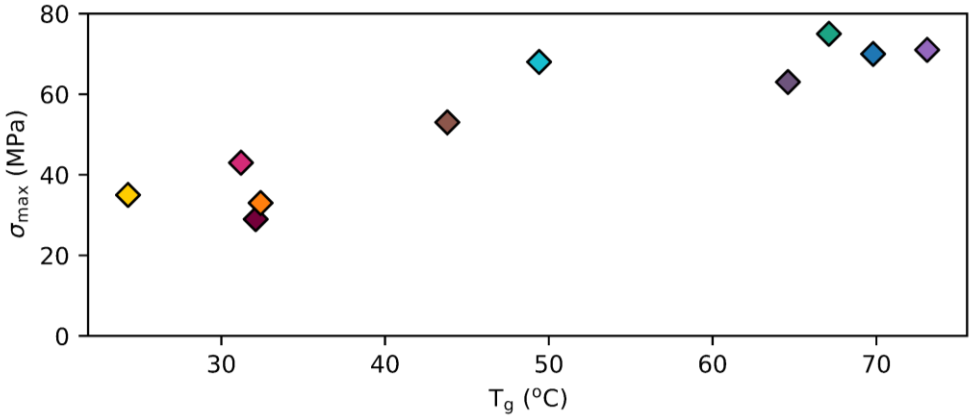

Figure 4.57: Correlation of the FDCA MDI TPUs between σ_{max} and T_g.

The FDCA MDI TPUs present the same relationship between composition and ε_b as all the previously discussed materials. The ε_b of the materials decreases as the HS content increases. This can be attributed, once more, to the higher number of HS defects on the SS structure, which hinder the chain slipping process. (**Figure 4.58**).

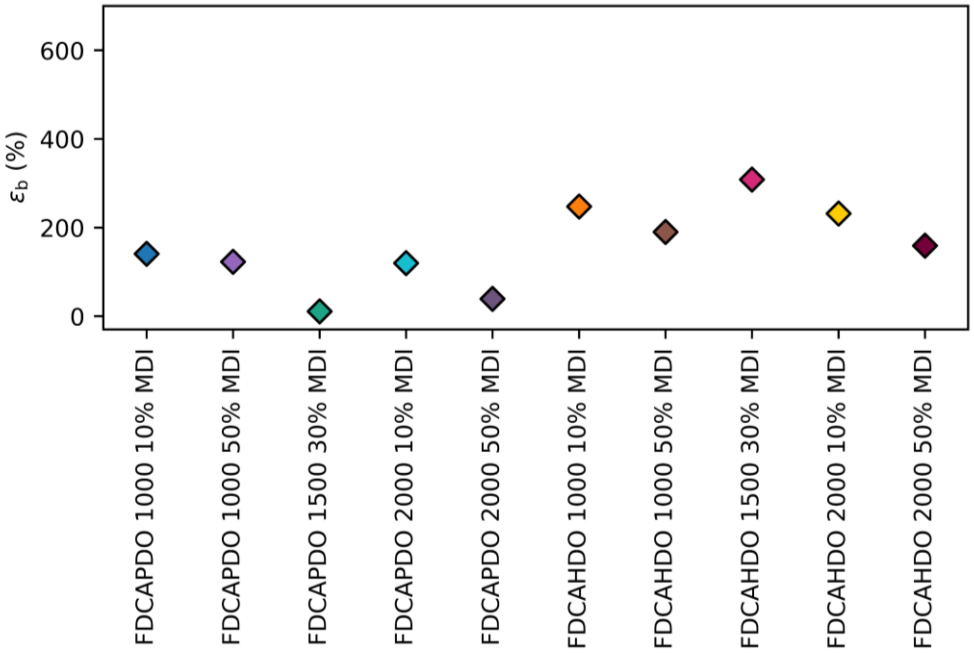

Figure 4.58: ε_b of the FDCA MDI TPUs.

4.3.2.4 FDCA HDI TPUs

Finally, the tensile properties of the FDCA HDI TPUs have been evaluated (**Table 4.21**). The higher T_g of the FDCAHDI materials in comparison with their IPHTA counterpart is reflected in their ductility, as all of the FDCA HDI materials exhibit a plastic deformation, in contrast with the elastic deformation of the IPHTAHDO HDI TPUs.

Table 4.21: Tensile properties of the FDCA HDI TPUs.

	Elastomeric behaviour	**Glassy or rubbery state** [a]	**σ_{max} (MPa)** [b]	**ε_b(%)** [b]
FDCAPDO 1000 10% HDI	Hard Tough Plastic	Glassy	50 ± 1	144 ± 46
FDCAPDO 1000 50% HDI	Hard Tough Plastic	Glassy	34 ± 0	175 ± 11
FDCAPDO 1500 30% HDI	Strong Tough Plastic	Glassy	65 ± 4	4 ± 3
FDCAPDO 2000 10% HDI	Strong Tough Plastic	Glassy	62 ± 7	4 ± 0
FDCAPDO 2000 50% HDI	Strong Tough Plastic	Glassy	63 ± 1	4 ± 0
FDCAHDO 1000 10% HDI	Soft Plastic	Rubbery	39 ± 4	283 ± 70
FDCAHDO 1000 50% HDI	Soft Plastic	Rubbery	34 ± 1	206 ± 16
FDCAHDO 1500 30% HDI	Soft Plastic	Rubbery	43 ± 2	411 ± 15
FDCAHDO 2000 10% HDI	Soft Plastic	Rubbery	47 ± 2	381 ± 6
FDCAHDO 2000 50% HDI	Soft Plastic	Rubbery	50 ± 1	437 ± 21

[a] Defined as whether the essay temperature (21 °C) is above (rubbery) or below (glassy) the T_g of the materials.

[b] Calculated as the mean of at least two different plates at 21 °C.

A similar morphology could be observed between the IPHTA and FDCA HDI TPUs. In both cases, the HDO TPUs exhibit phase segregation and SS crystallinity while the PDO materials are amorphous and do not show any segregation. Therefore, the tensile behaviour of the IPHTA and FDCA HDI TPUs should be similar. Indeed, just as in the IPHTA HDI TPUs, the FDCA HDI

TPUs exhibit two different relationships between σ_{max} and chain mobility depending on whether the materials are semicrystalline (HDO) or amorphous (PDO) (**Figure 4.59).** Moreover, also like their IPHTAPDO HDI analogues, the σ_{max} of the unsegregated FDCAPDO HDI polymers increases as the chain mobility of the materials is reduced, while no correlation between chain mobility and T_g could be extracted from the segregated FDCAHDO TPUs HDI.

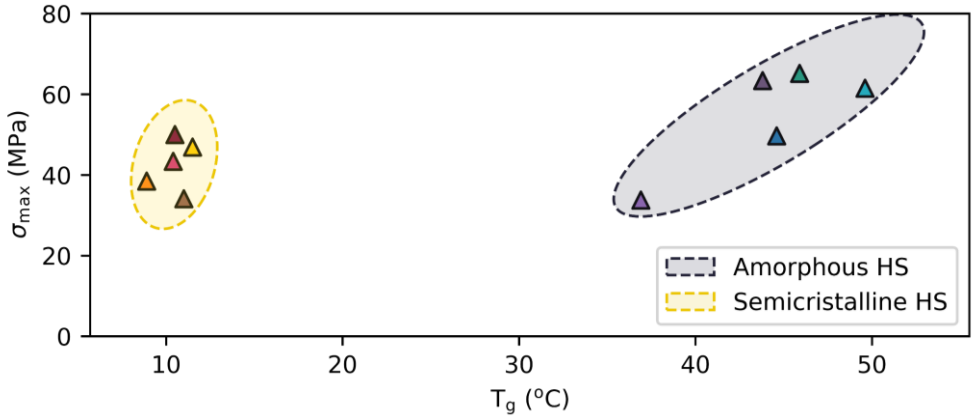

Figure 4.59: Correlation between $\boldsymbol{\sigma_{max}}$ and T_g of the FDCA HDI TPUs.

Although the relationships between σ_{max} and chain mobility were shared between the FDCA and IPHTA HDI materials, one striking difference appears between the HDO formulations of both types of TPU. Despite the FDCAHDO HDI TPUs being in their rubbery state, they show a plastic deformation, rather than behaving as elastomers, as happens with the rubbery IPHTAHDO HDI materials (**Table 4.21**). This indicates that, although the FDCAHDO HDI polymers have a high chain mobility, there is some kind of factor inhibiting their return to their initial shape after deformation. The only structural difference between the FDCAHDO HDI and the IPHTAHDO HDI TPUs lies in their SS. The crystallisation abilities of the FDCAHDO SS are higher than those of their IPHTA counterpart, as evidenced by the higher degree of crystallisation and SS melting enthalpies obtained by both WAXS and DSC for the FDCAHDO than for the IPHTAHDO polymers. Moreover, the SS crystallites formed on the FDCAHDO TPUs are more stable than those of the IPHTAHDO materials, as evidenced by their higher melting temperature (FDCA: 120-135 °C *vs* IPHTA: 47-72 °C). Both factors combined explain the change in elastomeric behaviour. During the elongation of the materials, strain-induced crystallisation takes place. This induced strain crystallisation generates structures that can act as physical crosslinks, inhibiting the elastic deformation of the materials by fixing the deformed structure. However, the low cohesion strength of the IPHTA crystallites hinders their ability to

form stable enough structures to store the stress induced into the polymers by their deformation. Furthermore, during the strain crystallisation process, the existing SS crystallites can act as nucleation sites, allowing the further growth of the crystalline structure. Therefore, the elastic deformation of the FDCA HDI TPUs is inhibited, owing to the higher number and stability of the crystallites in comparison with those of IPHTA.

To finish with the interpretation of the data obtained for the FDCA HDI TPUs, the trends regarding their strain behaviour were assessed (**Figure 4.60**). The analysis of the ε_b of the materials yielded no composition trends, as the strain of the material showed no correlation with either an increase or decrease of the HS content or the polyester M_n.

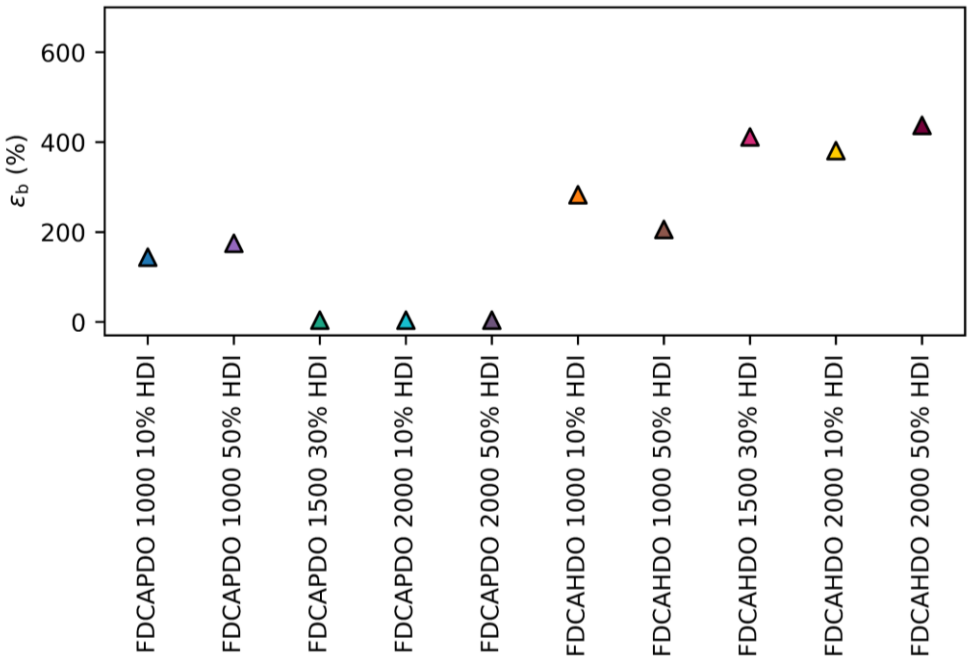

Figure 4.60: ε_b of the FDCA HDI TPUs.

4.3.2.5 Overview

Overall, two different tensile behaviours have been observed depending on whether the materials exhibit phase segregation or not.

The σ_{max} of the unsegregated materials is determined by their chain mobility. The highest the chain mobility, the lowest the σ_{max} of the materials since the chain slipping process is favoured. Contrarily, the ε_b of the unsegregated materials are not determined by their chain mobility, but

rather by their HS content. Higher HS content creates a larger number of defects in the SS structure, which hinders the chain slipping process and reduces the ε_b of the materials.

The σ_{max} of the segregated materials is not determined by their chain mobility but rather by the presence of HS domains. These HS domains act as physical crosslinks, inhibiting the capability of the chains to glide through the polymeric matrix, thus inducing stress in the materials.

During this work, the polymers have been classified as either plastics or elastomers. However, it was observed that, if the plastic materials are heated above their T_g after deformation, they recover their initial shape. This indicates that the studied materials present thermal-induced shape memory properties.

4.3.3 Shape memory

Shape memory polymers (SMPs) are a class of materials capable of changing their shape in response to an external stimulus. These materials can be processed into their so-called permanent shape by conventional processes (injection, extrusion, electrospinning, 3d printing…) and then programmed to a temporary shape, usually by deformation of the material. This temporary shape is metastable and, upon the application of an external stimulus, can be reverted to the permanent shape. This means that SMPs can be deformed, storing the stress induced into them as potential energy, and once a stimulus is applied, release said energy as mechanical work (**Figure 4.61**).[233,234]

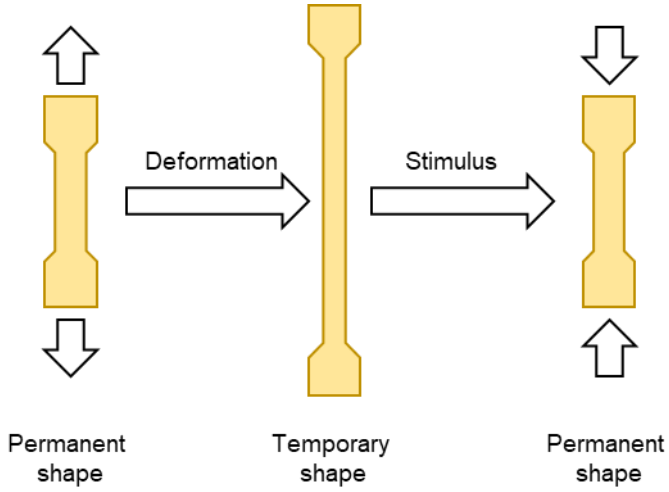

Figure 4.61: Representation of the shape memory process

The number of available stimuli is very varied, from the drying or addition of a solvent to heat, electricity, magnetic field, light or changes in pH. [235–239] Nonetheless, the most common mode of action is heat. This heat can be directly applied to the system, or indirectly.[240,241] For instance, photothermic, electrothermic or magnetothermal additives, like metallic nanoparticles or carbon-based nanomaterials, can be employed to increase the temperature of the polymeric matrix indirectly through the application of light, electricity or magnetic fields.[239,242–247] Despite their different modes of action, all of the thermal-induced SMPs require of at least two characteristics. A chemical or physical crosslink stable enough as to be unaffected by the deformation of the polymeric structure and weaker supramolecular interactions. These weak interactions act as the switch for the shape memory behaviour, restricting the chain mobility of the materials above the switching temperature (T_s). This chain mobility restriction is capable of overcoming the strain induced to the polymeric chains by the deformation, fixing the temporary shape. Once the temperature is increased above the T_s, the material regains enough chain mobility to return to its original, more stable permanent shape (**Figure 4.62**). Depending on the nature of the polymer, this T_s can be either the T_g or the T_m of one of the semicrystalline phases of the material.

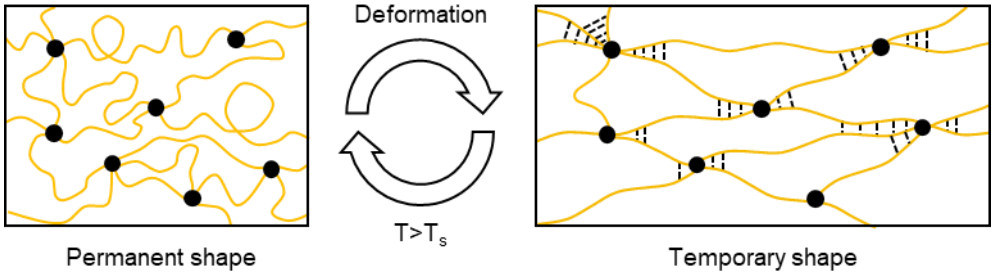

Figure 4.62: Shape memory mechanism of a temperature-induced SMP.

Owing to their interesting properties, SMPs have been gaining notoriety in the last 20 years, with the number of published articles exploding in the 2000s (**Figure 4.63**).

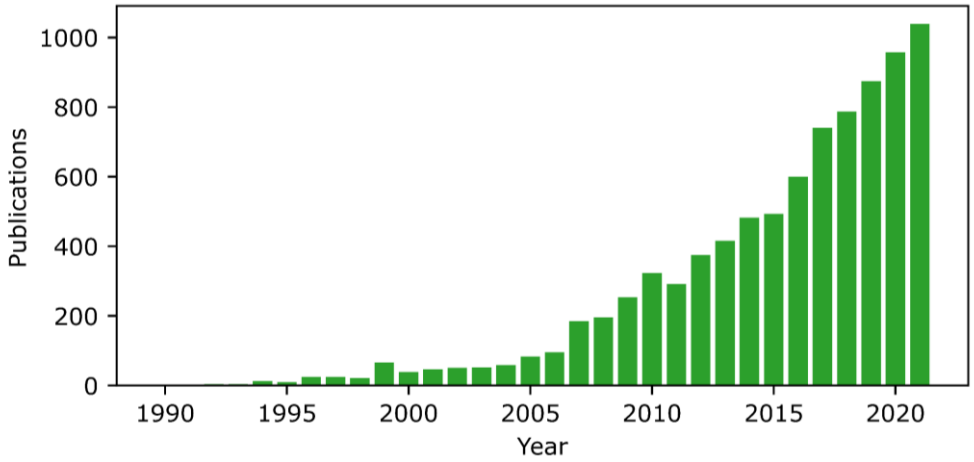

Figure 4.63: Publications containing shape memory polymers by year. Data obtained from WebOfScience. Accessed on September 18th 2022.

Many different applications have been proposed for SMPs, from self-expanding stents or self-knotting sutures in the medical field to mechanical actuators, artificial muscle fibres for prosthetics, or self-deploying structures for smart buildings or the aerospace field, like the deployment of solar sails or morphing wings (**Figure 4.64**).

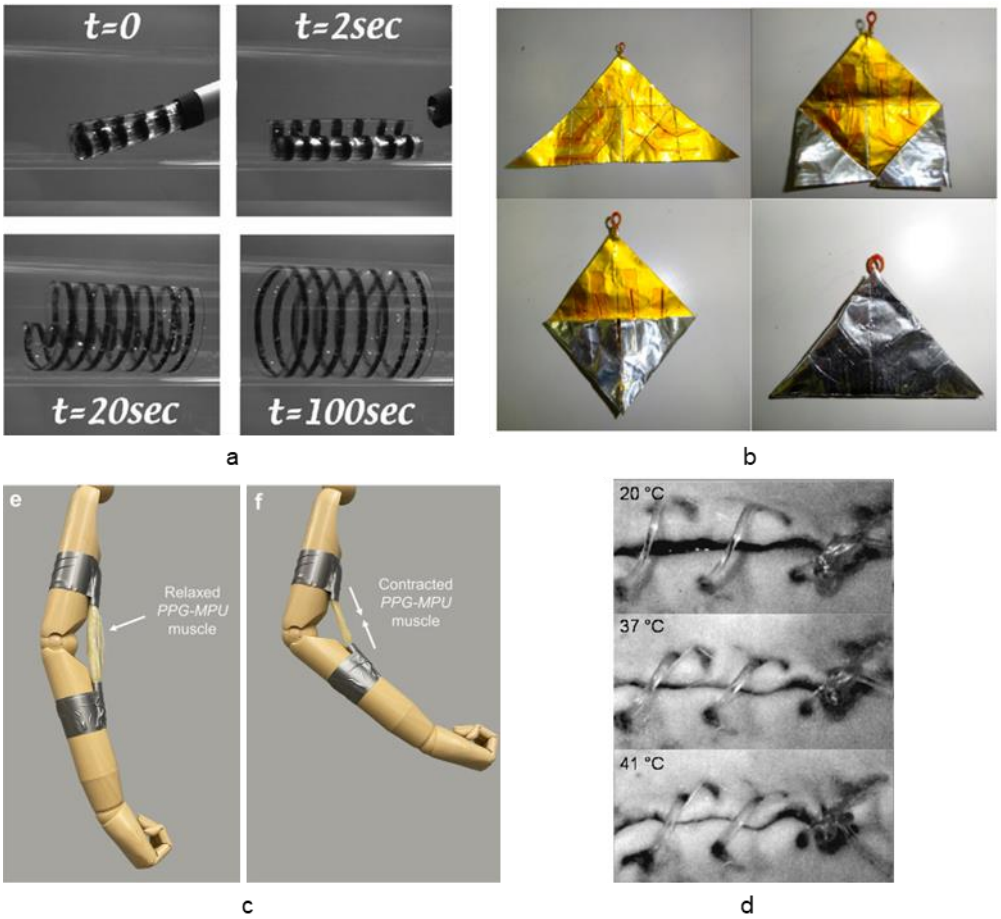

Figure 4.64: Examples of some shape memory devices. a. Shape memory stent. Image reproduced with permission from Elsevier.[248] b. Self-deployable solar sail. Image reproduced with permission from MDPI.[249] c. Artificial muscle fibre. Image reproduced under a Creative Commons Licence.[250] d. Self-knotting sutures. Image reproduced with permission from RSC.[251]

Several thermally-induced shape memory TPUs and TPU blends have been reported in the literature, made out of a wide variety of different polyols, chain extenders and diisocyanates.[252,253,262–270,254–261] Nonetheless, most of them are based on the same principle. They employ the HS domains as physical crosslink to drive the shape recovery and either the crystallisation or vitrification of the SS or of an additional blended polymer as the fixation agent for the temporary shape. In the case of the aromatic polyol TPUs studied in this work, it looks like the formation and breaking of the π-π stacking interactions from the aromatic diacids are the interactions responsible for the storage of the stress and fixation of the temporary shape, while the HS domains are the ones responsible for the shape recovery. Therefore, a mechanism

for the shape memory process of the studied TPUs could be proposed where, first, during their deformation, the weaker π-π interactions break and reform, while the H-bonds remain unaffected (**Figure 4.65**). These newly formed π-π stacking interactions would be capable of fixing the temporary shape despite the strain that is experienced by the structure. Then, once the temperature increases above T_g, the π-π interactions break, enabling the return of the structure to the permanent shape.

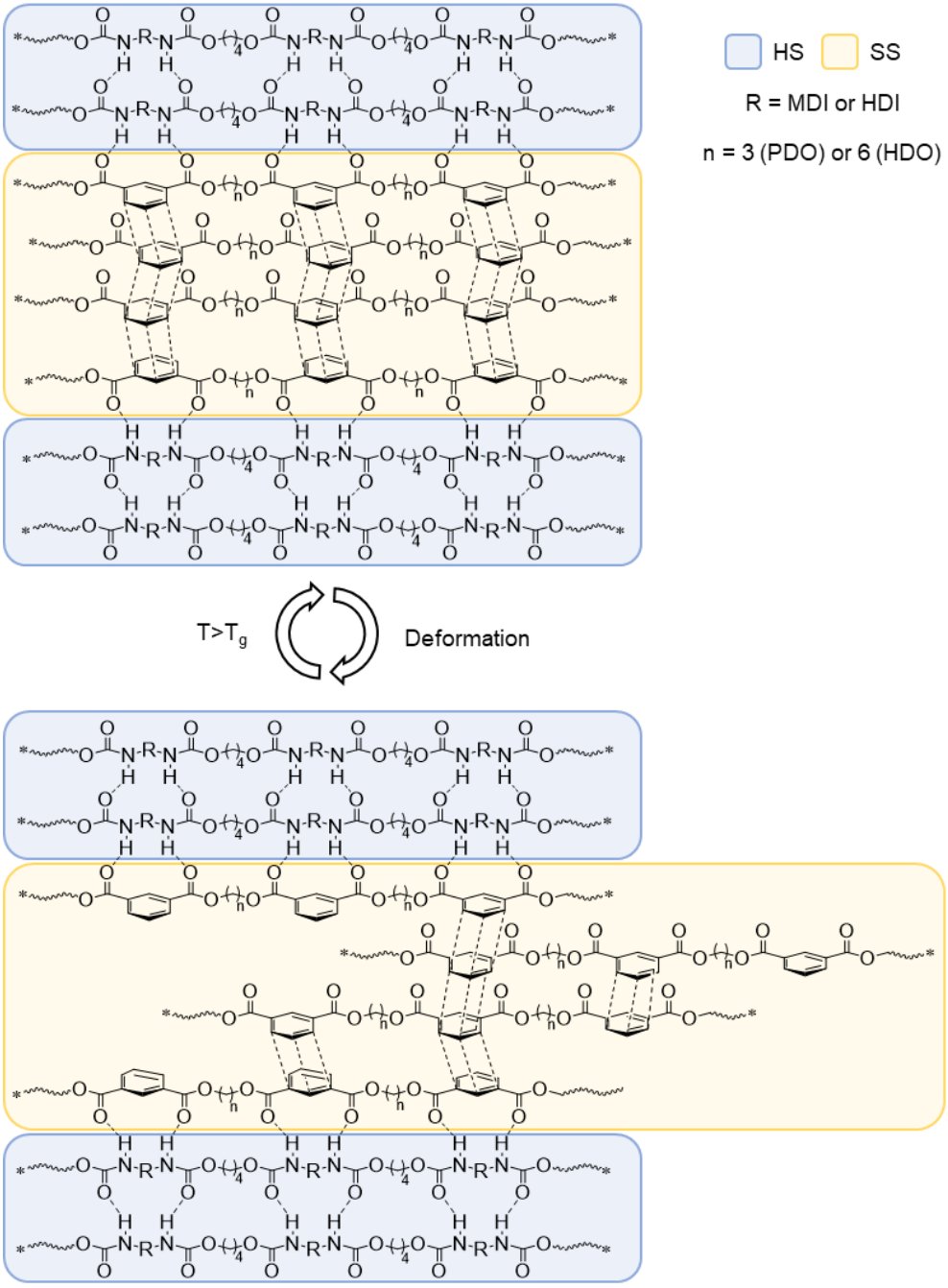

Figure 4.65: Proposed mechanism for the shape memory process on aromatic polyol TPUs.

To characterise the shape memory capabilities of SMPs, two parameters are commonly studied, their shape fixity (R_f) and shape recovery (R_r) indexes.

4.3.3.1 Shape fixity and recovery index

R_f and R_r are two parameters employed to determine respectively how good a SMP is at fixing the temporary shape induced by deformation and at returning to its permanent shape after the stimulus. To obtain both values, a single method was employed. First, the material is heated to 20 °C above its T_g, to ensure its ductility, and elongated to a 100% strain. At this point, the temperature is dropped to 20 °C below T_g to fix the elongated state of the sample as its temporary shape. Then the force of the equipment is set to 0 N and the material is allowed to equilibrate for 5 minutes. The difference between the strain before and after releasing the stress is measured as the R_f (**Equation 4.14**). Then, the material is heated again to 20 °C above its T_g and allowed to equilibrate for 30 minutes, with the value of elongation at this point serving as the parameter to determine the shape recovery of the sample (**Equation 4.15).** Afterwards, the cycle can be repeated to study the stability of the shape memory behaviour. In this study, three consecutive cycles were applied to each material (**Figure 4.66**, **Experimental Section 6.1.12**).

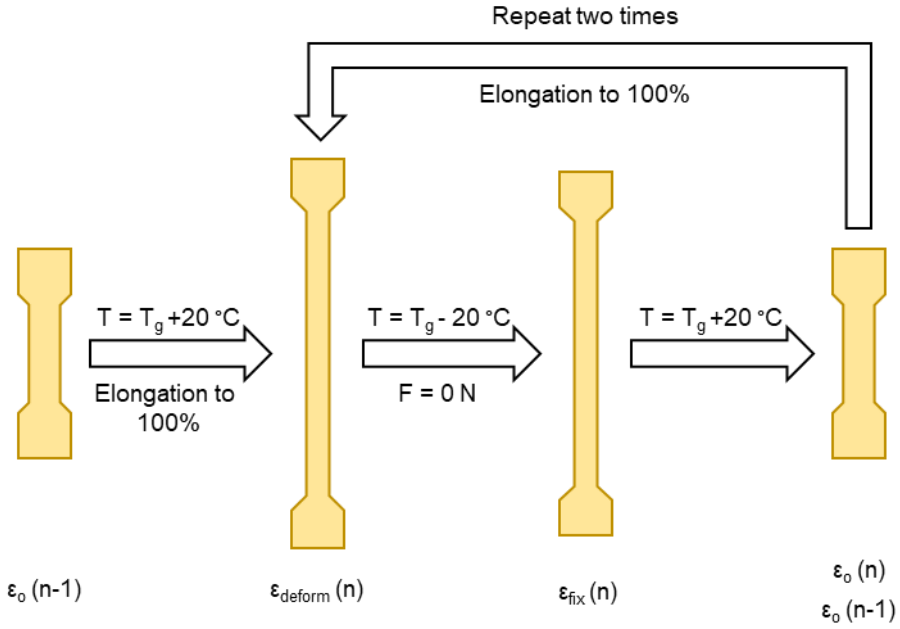

Figure 4.66: Method for the determination of the R_f and R_r.

$$R_f\,(\%) = \frac{\varepsilon_{fix}(n)}{\varepsilon_{deform}(n)} \times 100\%$$

Equation 4.14: Shape fixity ratio. ε_{fix} (n) = strain after the release of the stress and 5 min of equilibration of cycle n. ε_{deform} (n) = strain at which the material is elongated into of cycle n.

$$R_r\,(\%) = \frac{\varepsilon_{fix}(n)-\varepsilon_o(n)}{\varepsilon_{deform}(n)-\varepsilon_o(n-1)} \times 100\%$$

Equation 4.15: Shape recovery ratio. ε_{fix} (n) = strain after the release of the stress and 5 min of equilibration of cycle n. ε_{deform} (n) = strain at which the material is elongated into of cycle n. ε_o = strain of the sample after the recovery process and 30 min stabilisation of either the current (n) or the previous (n-1) cycle.

4.3.3.1.1 IPHTA MDI TPUs

The first polymers that have been evaluated are the IPHTA MDI TPUs. Their full shape memory cycle can be found in **Annex A10**.

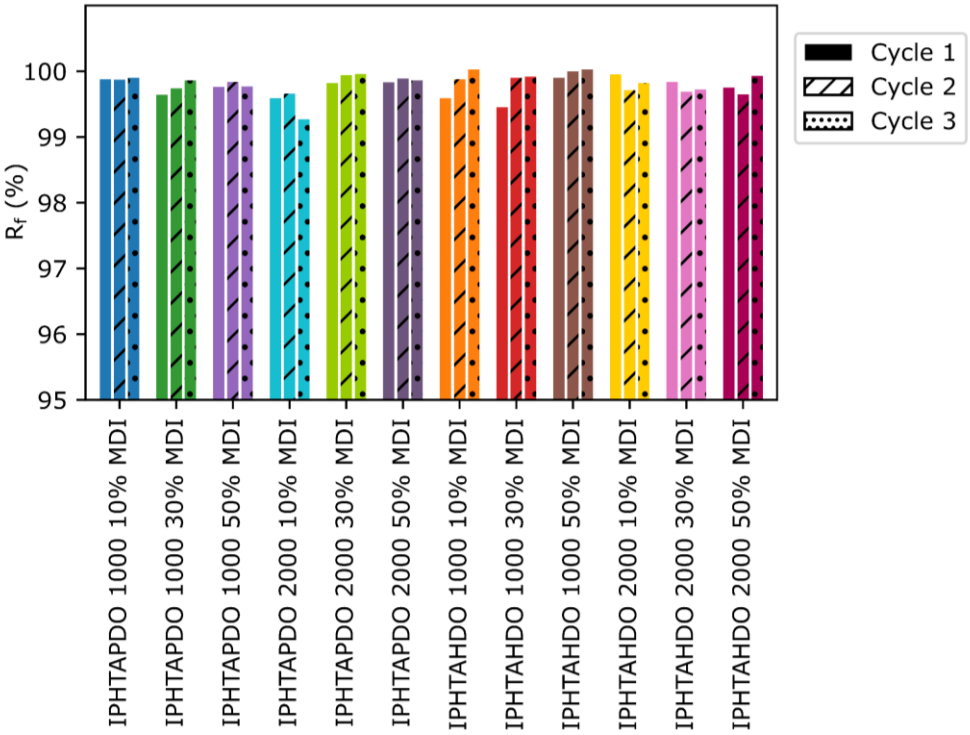

Figure 4.67: R_f of the IPHTA MDI TPUs.

From the R_f data, almost no difference amongst the IPHTA MDI formulations was observed, with all of the materials having fixity values above 99% and with the different cycles showing

little variation amongst them (**Figure 4.67**). The high R_f values demonstrate that the TPUs have a good capability for storing the stress applied by deformation through the fixation of the temporary shape. This can be attributed to the high number and strength of the supramolecular interactions generated by IPHTA. However in these polymers no phase segregation was observed, so it is not possible to disregard the contribution that the HS chain fragments dissolved into the SS matrix may have in determining the R_f of the materials.

Worst results were obtained than for the R_r of the IPHTA MDI formulations with, in one case, R_r being as low as 44% (**Figure 4.68**). Such low values could be understood by the low HS domain density of the materials, as observed by the lack of signal in both DSC and SAXS. As the HS domains are the physical crosslink that induces the return to the permanent shape after heating, a low concentration of said structures would lead to low R_r values. Nonetheless, the R_r values are not zero, reaching up to 80% during the first cycle in some formulations. This might indicate either the presence of a very low concentration of the HS domains, so low that they are unnoticeable by DSC and SAXS, or that the HS chain fragments dissolved within the SS are still capable of inducing, to some degree, the SMP process.

In general, R_r increases as the number of cycles does (**Figure 4.68**). This increase is common in several SMP and is referred to as a training of the material.[271] During this training step, the permanent shape of the material is transformed into a more stable structure by the repositioning of the polymeric chains through the deformation and recovery process, thus increasing the R_r of the system. No clear relationship between R_r and composition can be established. This indicates that the chain mobility of the TPUs has little effect on their R_r.

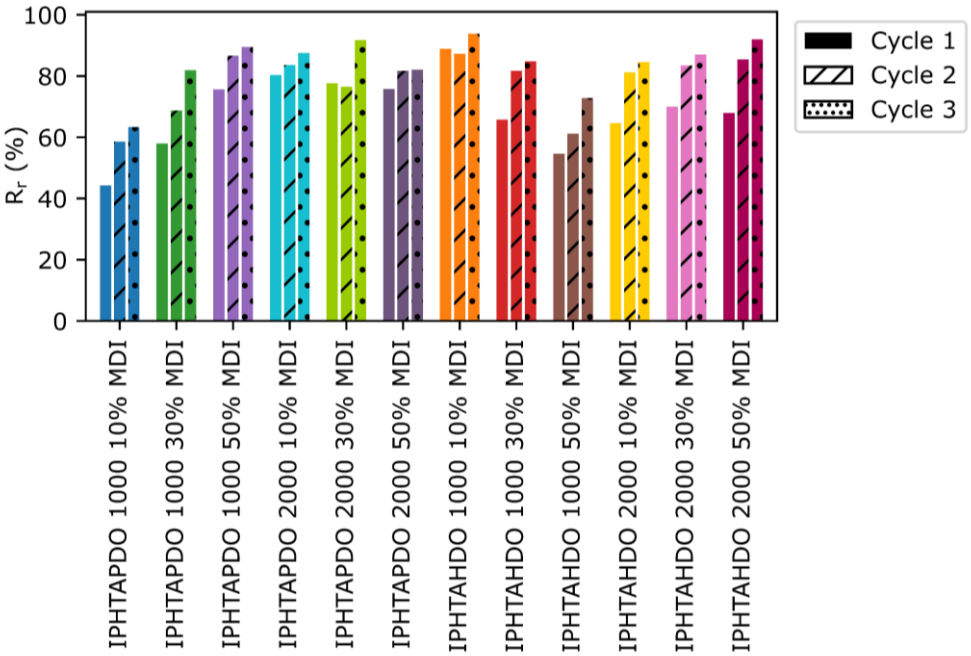

Figure 4.68: R_r of the IPHTA MDI TPUs.

4.3.3.1.2 IPHTA HDI TPUs

Next, the R_f and R_r of the IPHTA HDI TPUs were measured and evaluated (**Annex A10**).

Although the R_f values of the IPHTA HDI polymers are quite high, above 97%, they are slightly lower than those of their MDI analogous (**Figure 4.69**). This indicates that the sole responsible for the fixation of the temporary shape is not the supramolecular interactions generated by the IPHTA monomers, as they are shared in both TPU families. Rather, the supramolecular interactions of the diisocyanate must also play a small role in the fixation of the temporary shape. Moreover, a slight decrease in R_f as the HS content increases was observed, which might indicate that lower concentrations of the aromatic diacid result in a loss of the shape fixation capabilities of the HDI materials. By the same token, the overall lower R_f of the HDO TPUs could be explained by their lower IPHTA concentration in comparison to that of the PDO polymers.

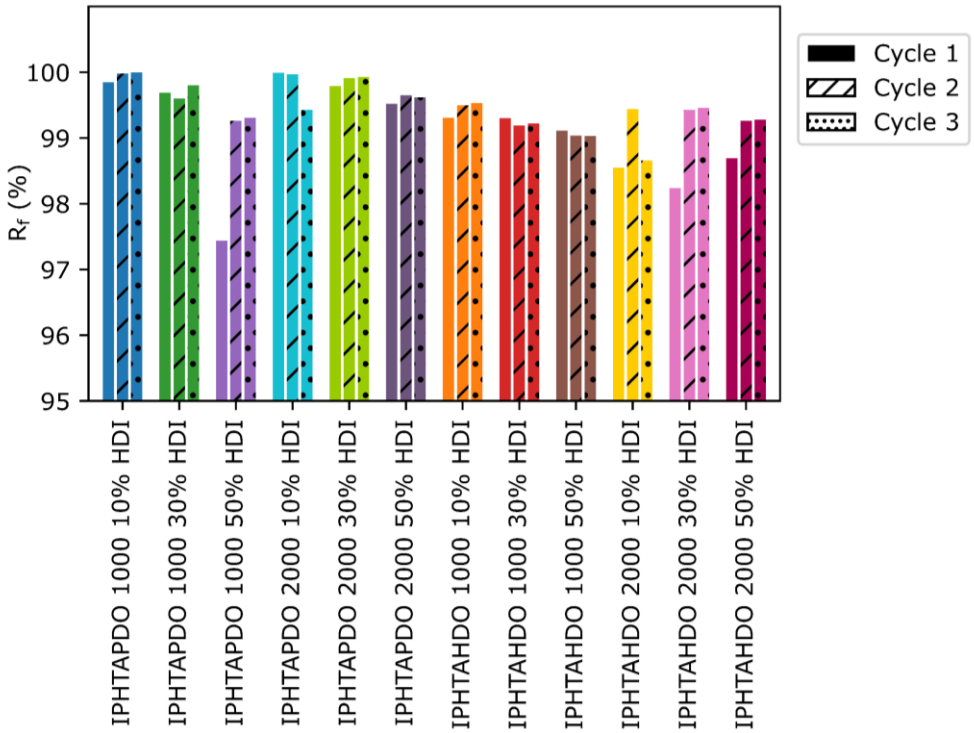

Figure 4.69: R_f of the IPHTA HDI TPUs.

On the other hand, the R_r values of IPHTAHDI TPUs are better than those of their MDI analogous, especially when comparing their first cycle (**Figure 4.70**). This is to be expected as the concentration of HS domains is higher in the IPHTA HDI TPUs than in their MDI counterpart, owing to their higher chain mobility and lower HS-SS compatibility. The higher HS domain density results in better R_r values, as they act as anchors for the permanent shape, inducing the shape recovery process. Moreover, the IPHTAHDO HDI TPUs exhibit higher R_r than their PDO analogues, which can be easily explained as the phase segregation and number of HS domains is greater in the HDO HDI formulations than in the PDO HDI ones, as evidenced by their respective DSC and SAXS data.

No relationships between R_r and the composition of the materials can be established. On both the IPHTAPDO and HDO HDI TPUs, the trends of R_r with composition seem to be completely random, and cannot be correlated with any morphological characteristic, not even if the degree of SS crystallinity, the degree of phase segregation, and HS domain size obtained by WAXS, SAXS and DSC are taken into account.

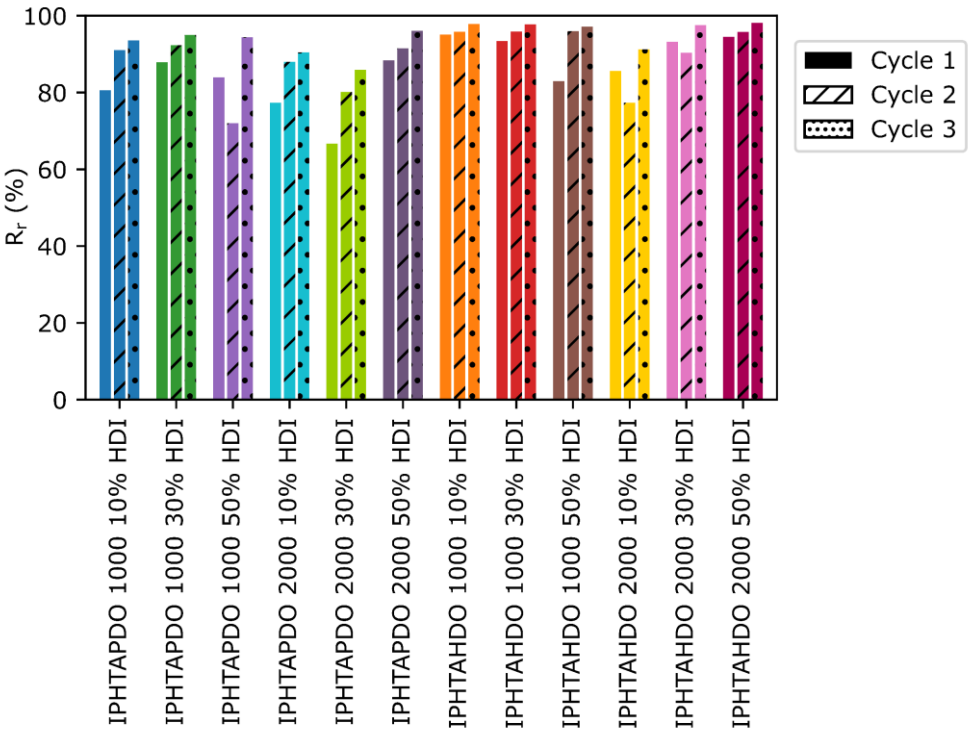

Figure 4.70: R_f of the IPHTA HDI TPUs.

4.3.3.1.3 FDCA MDI TPUs.

Owing to the stronger interactions formed by the FDCA monomer when compared to IPHTA, higher R_f should be expected for the TPUs of the former than the latter. However, the contrary was observed (**Figure 4.71**, **Annex A10**). The R_f of the FDCA MDI TPUs is lower than that of their IPHTA counterparts. This indicates that there must be some other factor, in addition to the strength of the supramolecular interactions that play some role in R_f. The other main difference between the IPHTA and FDCA TPUs is the crystallisation capability of their SS, with it being higher for the FDCA polymers than the IPHTA ones. Therefore, this parameter might affect in some manner the R_f of the materials. This agrees with the results observed for the FDCA MDI materials, as the two HDO materials with the lowest R_f, **FDCAHDO 1000 10% MDI** and **FDCAHDO 2000 10% MDI**, are the ones which exhibit SS crystallinity by WAXS. Moreover, their degree of crystallinity (Φ_C) shows the same trend as the R_f of the materials, with it being higher for **FDCAHDO 1000 10% MDI** (Φ_C = 0.17) than for **FDCAHDO 2000 10% MDI** (Φ_C = 0.08). One possible explanation behind this effect might be the strain-induced

crystallisation of the materials. This process could be favoured by the already existing SS crystallites acting as nucleating agents. The growth of these crystals would create new physical crosslinks on the structure, hindering the shape fixing capabilities of the materials.

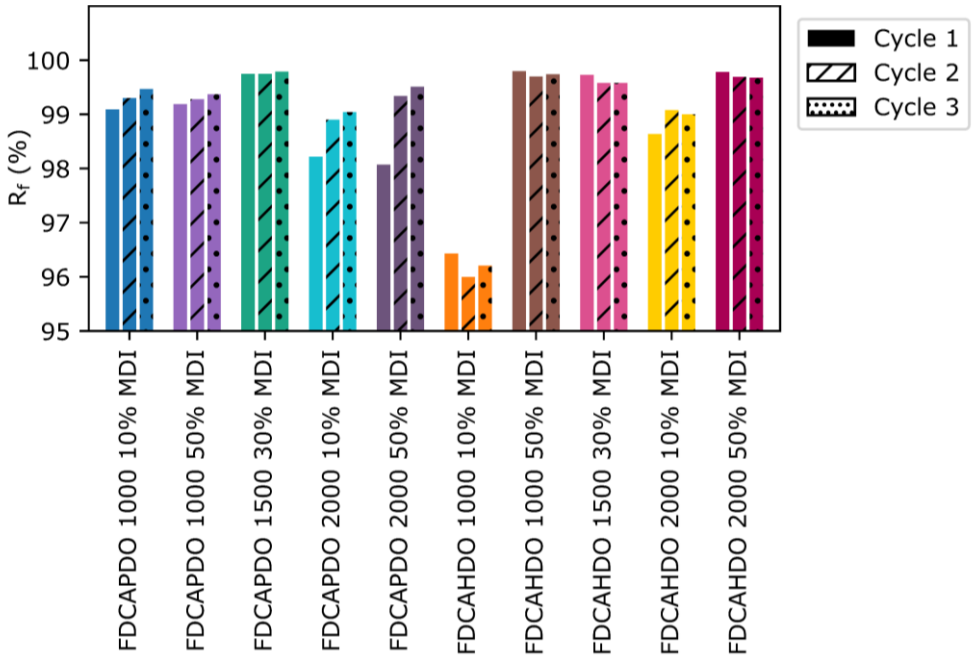

Figure 4.71: R_f of the FDCA MDI TPUs.

Two different behaviours were observed on the R_r of the FDCA MDI TPUs (**Figure 4.72**). The R_r of the PDO formulations is higher than that of their IPHTA counterpart, while on the HDO TPUs, lower R_r are found for the FDCA than for the IPHTA polymers. The origin of this disparity is located, quite probably, in the strain induced crystallisation of the SS. Owing to their greater chain mobility, the crystallisation of the FDCAHDO SS is more favoured than that of the PDO SS. The high capability of the FDCAHDO TPUs to form ordered structures could be verified by the appearance of the samples after the shape memory cycles. Before their assay, both the PDO and HDO samples are transparent. However, after the shape memory process, the HDO materials turn opaque, while the PDO ones remain transparent, evidencing the formation of crystalline structures capable of interacting with light through the strain crystallisation process in the FDCAHDO MDI formulations. The formation of these SS crystallites during the deformation of the materials would change their most stable morphology, leading to a modification of the permanent shape. Moreover, the two materials with the lowest R_r are those in which SS crystallites could be identified by WAXS, **FDCAHDO 1000 10% MDI** and

FDCAHDO 2000 10% MDI, with their R_r being consistent with their Φ_C, which is in agreement with our observations that the crystallinity of the SS is which limits their R_r.

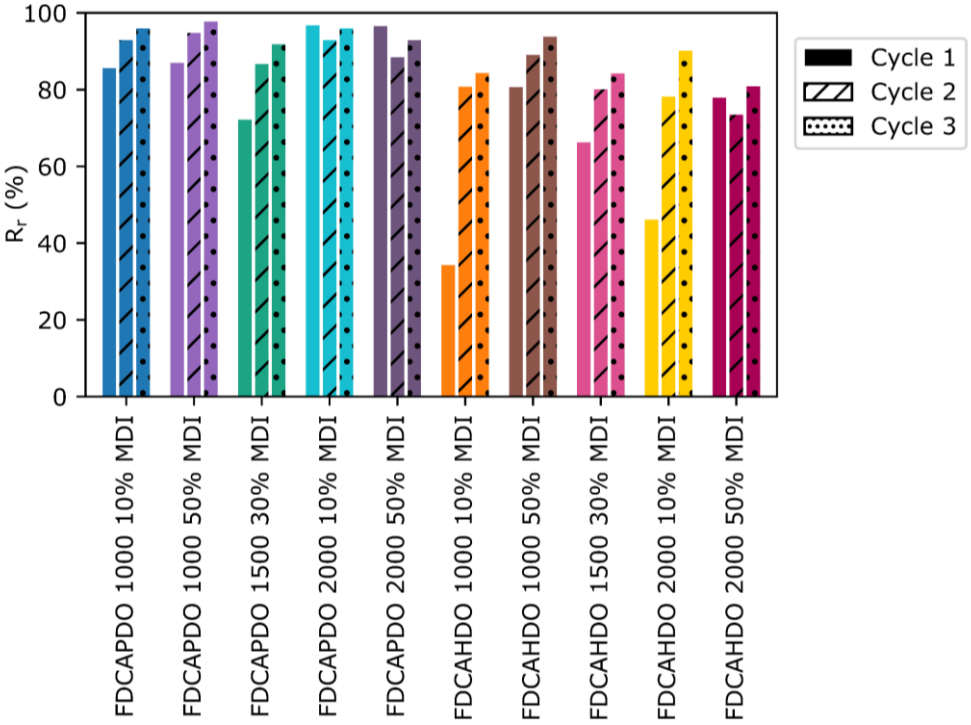

Figure 4.72: R_r of the FDCA MDI TPUs.

4.3.3.1.4 FDCA HDI TPUs

To finish the assessment of the R_f and R_r of the TPUs, the FDCA HDI formulations were assessed (**Annex A10**).

Just as in the previous MDI materials, lower R_f values were obtained for the FDCA HDI materials than for their IPHTA counterpart (**Figure 4.73**). This once more evidences the negative effect that the high capability of the FDCA materials to generate SS crystallites through strain crystallisation has on their R_f.

Overall, the FDCAHDO HDI materials show lower R_f than the FDCAPDO HDI ones. The leading cause behind this seems to be the presence of SS crystalline structures. All of the FDCAHDO HDI materials exhibit SS crystallisation, as observed by WAXS, while none of the PDO ones does. As previously discussed, the presence of crystallites can act as nucleation sites for the

further growth of the crystalline structures after strain, which seems to reduce the fixity capabilities of the materials.

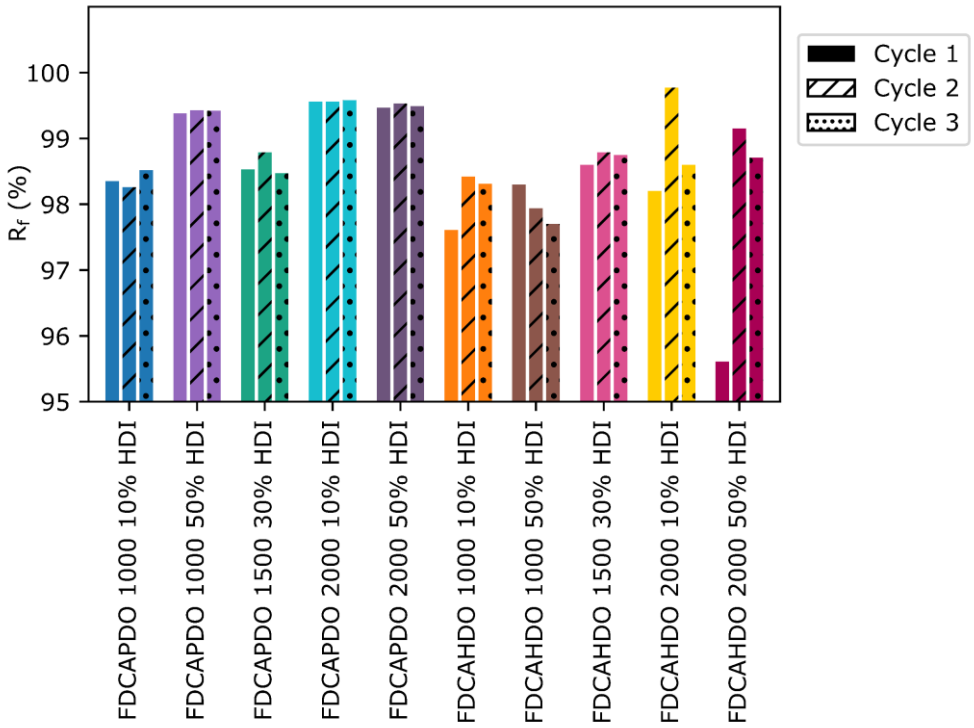

Figure 4.73: R_f of the FDCA HDI TPUs.

On R_r, similar trends as those followed by R_f could be identified (**Figure 4.74**). The R_r of the FDCAPDO HDI TPUs is significantly higher than that of the FDCAHDO HDI formulations. This can be explained, once more, by the negative effect that the presence of SS crystallites has on R_r, since the FDCAHDO polymers contain SS crystallites while the PDO materials do not.

Two different trends arise from the comparison of the R_r values from the FDCA HDI materials and their IPHTA analogous. On the PDO materials, the R_r of the FDCA and IPHTA materials is quite similar, while in the HDO formulations, higher R_r are obtained for the IPHTA than for the FDCA polymers. Then again, this is a result of the different SS crystallinity between the materials. Although both the IPHTA and FDCA HDO TPUs exhibit SS crystallisation, the stability of the crystallites is higher for the FDCA than for the IPHTA materials, as evidenced by their higher melting temperatures. Therefore, the crystallites formed during the strain crystallisation process on the FDCA TPUs are more stable than those of the IPHTA polymers

and are capable of acting as physical crosslinks hindering the recovery of the permanent structure, while those of IPHTA cannot.

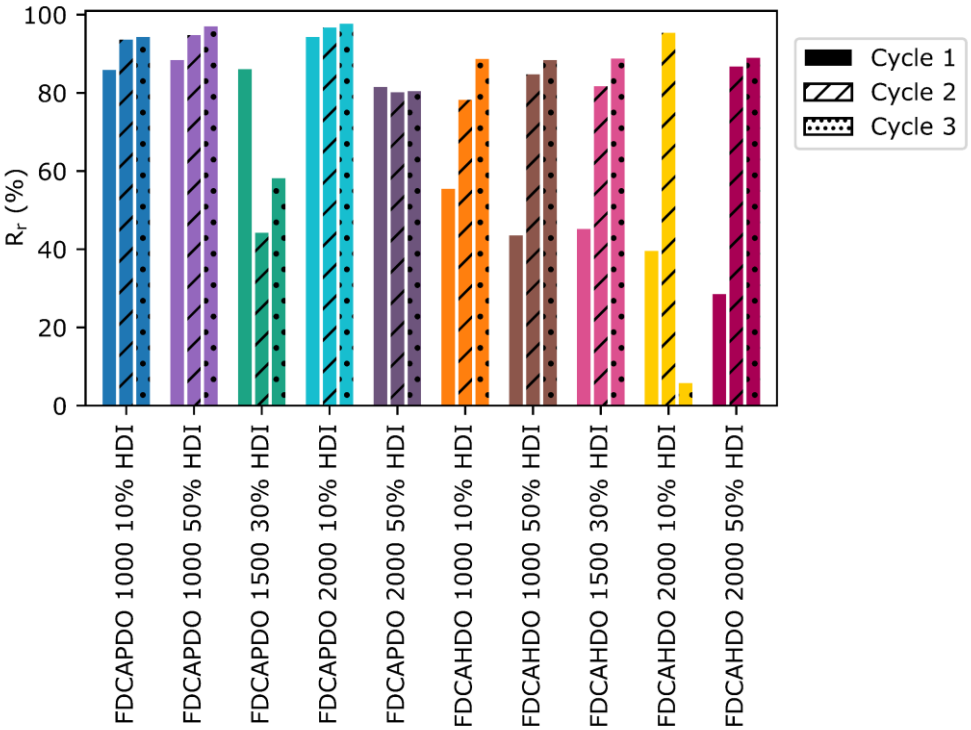

Figure 4.74: R_r of the FDCA HDI TPUs.

4.3.3.1.5 Overview

Considering all of the R_r and R_f data collected from the IPHTA and FDCA materials, some general remarks about the effect that the different phase morphologies have on the shape memory capabilities of the materials can be drawn. Overall, three factors affect R_r and R_f, the phase segregation of the materials the crystallisation capabilities of the SS domains, and the stability of the SS crystallites.

The phase segregation of the materials seems to affect for the most part their R_r. The presence of HS domains produce an increase in the shape recovery capabilities of the TPU materials, as they act as the physical crosslink that remembers the permanent shape. However, no direct correlation can be drawn between the values of phase segregation observed by SAXS and R_r beyond that the presence of HS domains increases the R_r of the materials.

The SS crystallinity of the materials seems to affect both the R_f and R_r of the materials. For both parameters, the presence of SS crystallites seems to be detrimental. In the case of R_f, the presence of crystallites appears to directly hinder the fixation of the temporary shape. Contrarily, R_r does not appear to be directly altered by the presence of SS crystallites. Rather, the strain induced crystallisation that the materials endure seems to be the root of this decline in R_r. The newly formed SS crystals generate a new, more stable structure than that of the permanent shape. Therefore, after the strain is released and the material is allowed to return to its most stable morphology, the material goes back to that newly generated, more stable structure, rather than to the initial permanent shape. However, for the crystallites generated through the strain crystallisation process to be able to hinder the shape recovery of the materials, the cohesion strength of the crystals needs to be quite high. Therefore, the negative effect that the strain crystallisation process has on the R_r of the materials can only be observed in the FDCA TPUs.

4.3.3.2 Actuation strength

One of the main drawbacks of SMPs is their low actuation strength, originated from their low tensile strength when they are above their switching temperature (T_s).[272,273] This means that most SMPs can only hold or move relatively low loads when performing the switch from the temporary to the permanent shape, inhibiting their use or requiring a high amount of material to perform their function.

To obtain high actuation strengths, two different characteristics need to be present in the polymers, a high crosslink density, and some sort of reversible interaction strong enough so that all the stress applied to the material can be stored into chemical energy. The higher the crosslink density, the maximum stress the material will be capable of experiencing, while the higher the number and strength of the reversible interactions, the more of that stress will be stored in the material. In the studied aromatic TPUs, the presence of a high number of relatively strong supramolecular interactions produced by the aromatic monomers on the SS (IPHTA and FDCA), could allow the generation of materials with excellent stress storage capabilities.

The actuation strength of a material is reflected in two different variables, its recovery stress (σ_r), and energy density (E_ρ). σ_r measures which is the maximum force that the polymer is capable of effectuating during the shape memory process, while E_ρ indicates which is the mechanical work that the material can produce during the recovery process.[272,274] σ_r is only dependent on the strain that the chains experience, while E_ρ depends on two factors, σ_r, and the recovery strain (ε_r) of the material since it is defined as the toughness or the material, which

corresponds to its area below the strain stress curve of the shape recovery process. Although there are different definitions employed for E_ρ, the most employed assumes that the unload of the stress is linear. Therefore, E_ρ is defined as the area below the triangle formed between ε_r and σ_r, and zero (**Equation 4.16**).[275] Note however, that this is an overestimation of E_ρ, as the unload profile of the strain during the shape memory process will not be a straight line, but rather a curve, the area of which will depend on many factors like the recovery rate or the load that is required to move during recovery.

$$E_\rho = \frac{\sigma_r \times \varepsilon_{max}}{2 \times 100}$$

Equation 4.16: Determination of E_ρ from σ_r and ε_{break}

Most reported polymeric materials exhibit σ_r and E_ρ in the range of 0.1-5 MPa and 0.01-0.88 MJ/m^3 respectively.[272,275] However, a couple of materials have been reported that far surpass said values, exhibiting excellent results regarding both σ_r and E_ρ. Two aromatic thermoset resins have been reported by Guoqiang Li *et al.*[276,277] one based on bisphenol A glyceroate dimethacrylate with a σ_r of 13.4 MPa and a E_ρ of 1.05 MJ/m^3 (**Figure 4.75**, **a**) and an epoxy resin, based on EPON826 and isophorone diamine with a σ_r of 17.0 MPa and an E_ρ of 3.82 MJ/m^3 (**Figure 4.75**, **b**). Moreover, both materials exhibit a good R_f and R_r of above 80%. However, although their σ_r is very elevated, their elongation at break, and therefore, their ε_r are quite low, of just 40-50%, which limits their E_ρ. In both cases, chemical crosslinks, acrylate or epoxy linkages, act as the architecture holding the permanent shape, while the extensive network of π-π stacking interactions and H-bonds are what enable the fixity of the permanent shape. More recently, a thermoplastic polypropylene glycol polyamide showing an extraordinary E_ρ of 19.6 MJ/m^3 has been reported by Zhenan Bao *et al*.[275] (**Figure 4.75**, **c**). Although this polymer also shows a large σ_r of 13.1 MPa, its main difference with the previous two thermoset polymers is its higher ε_r, being able to strain up to 300%. This high strain capability is obtained thanks to the flexible, polypropylene glycol units placed in the structure, while the high σ_r is obtained owing to the high M_n of the polymer. Rather than employing standard chemical or physical crosslinks based on chemical interactions as the structures driving the recovery of the permanent shape, the entanglement of the polymeric chains was employed. The polymer was designed so that its M_n was far above its critical molecular weight of entanglement (5-6 kDa), leading to a high entanglement density, which is responsible for the stress experienced by the polymeric chains. To store all that energy, the urea H-bonds were employed, generating highly ordered structures by strain induced crystallisation in the process.

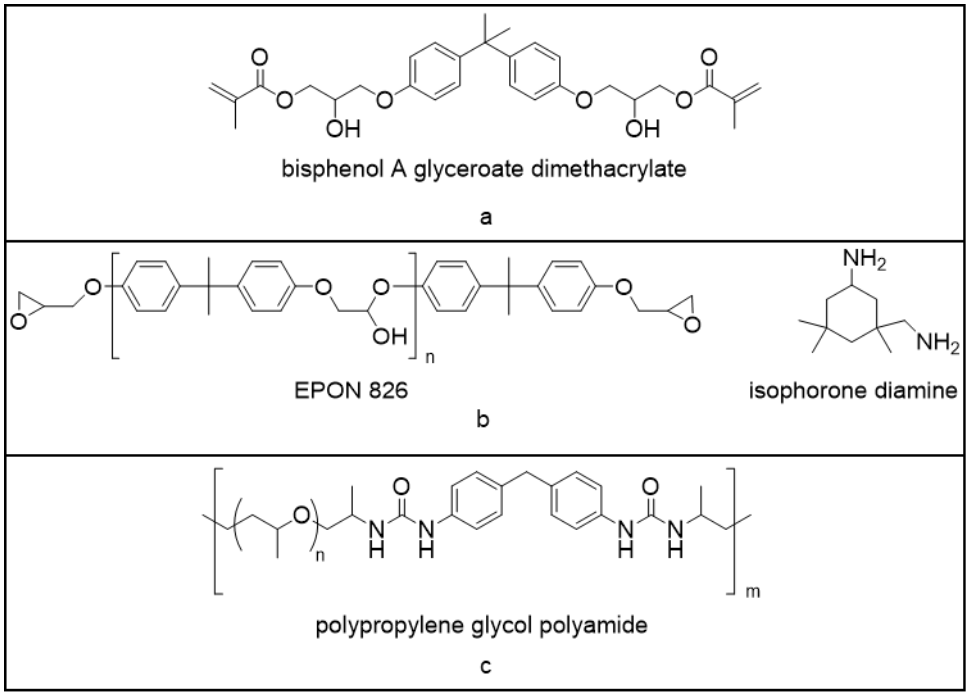

Figure 4.75: State-of-the-art of SMPs according to their E_ρ and σ_r.a: Guoqiang Li *et al*.[276] b: Guoqiang Li *et al*.[277] c: Zhenan Bao *et al*.[275]

To determine the σ_r and E_ρ of the TPUs prepared in this study and compare them to the state-of-the-art new tensile strength measurements need to be performed. However, a standard method to obtain both values has not been developed yet, with each author designing their own procedure depending on their available equipment and the specific characteristics of their materials.[272,274–277] In our case, a new method, employing a dynamometer coupled with a heating chamber has been employed, mirroring, when possible, the conditions used by Zhenan Bao *et al*.[275]. Firstly, the tensile strength (σ_{max}) of the materials at 20 °C above their T_g was assessed to determine their breaking point (**Annex A11**). Once this value was known, a new tensile strength test, this time elongating the materials to 90% of their σ_{max} at 20 °C above their T_g was carried out. Then, the materials were allowed to relax for 5 minutes to account for any hysteresis processes. The value of σ_r of the materials was taken as their stress right after the 5 minutes of relaxation, and the elongation of the polymers at the 90% σ_{max} as the ε_r to calculate E_ρ (**Experimental Section 6.1.10.2**).

4.3.3.2.1 IPHTA MDI TPUs

The first assessment of the σ_r and E_p of the materials has been carried out on the IPHTA MDI TPUs (**Annex A12**). The σ_r of the IPHTA MDI formulations are within the standard range of SMP materials, spanning from <0.1-2.5 MPa (**Figure 4.76**). However, on three of the materials, **IPHTAPDO 1000 10% MDI**, **IPHTAPDO 1000 50% MDI** and **IPHTAPDO 2000 10% MDI**, σ_r lower than 0.1 MPa were obtained and therefore they could not be quantified. The relatively low σ_r values can be understood by the lack of any HS domains in the polymers. As the HS domains are the structures responsible for blocking the chain slipping process and inducing strain into the structure, their absence inhibits the generation of any strong tensions within the polymeric chains. Interestingly, the σ_r of the IPHTAHDO MDI formulations seems to be overall higher than that of the IPHTAPDO ones, which is the inverse trend as what was observed on the ultimate tensile strength (σ_{max}) of the materials at room temperature. This modification of the trends is a result of the variation in chain mobility of the materials. At room temperature, all of the PDO materials were in their glassy state, and therefore, their σ_{max} was controlled by the chain mobility of the process. When they are assayed at 20 °C above their T_g however, the chain mobility of the materials is greatly improved, and therefore, the restriction to chain slipping disappears, being the presence of crosslinks what mainly affects the strength of the materials. Accordingly, it appears that the number of crosslinks in the IPHTAHDO polymers is higher than on the PDO analogous, although in both cases their presence is scarce, as no HS domains were observed in neither SAXS nor DSC on any IPHTA MDI polymer. In addition to the differences between the PDO and HDO polymers, further trends could be noted for the IPHTAHDO MDI formulations regarding their HS content and polyester M_n. Overall, it looks like, the higher those two parameters are, the higher σ_r is obtained.

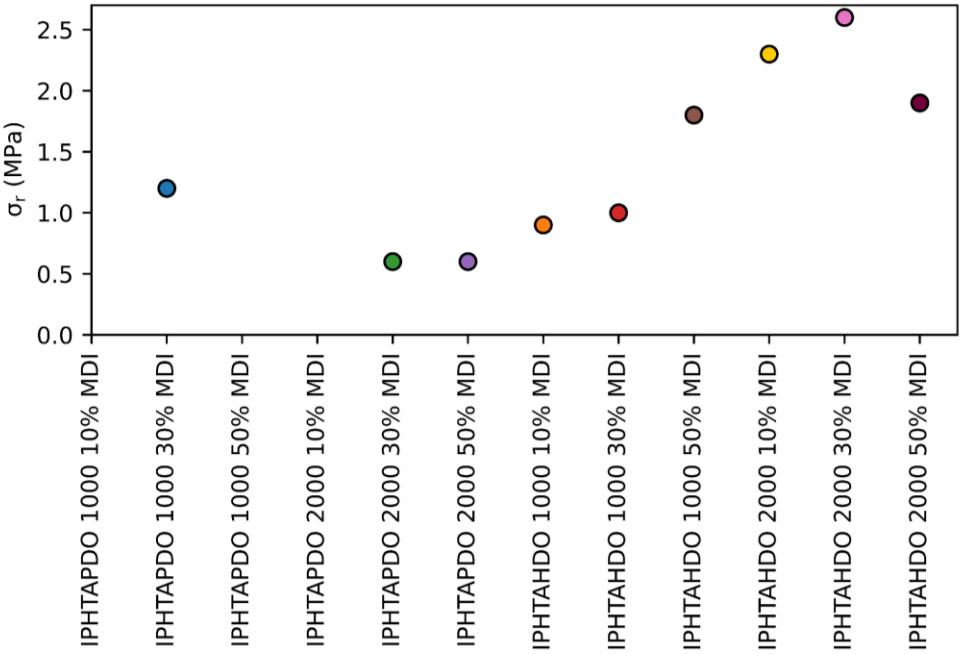

Figure 4.76: σ_r of the IPHTA MDI materials.

Better results have been obtained for the E_ρ of the IPHTA MDI materials. In some formulations, values comparable to the two thermosets reported by Guoqiang Li *et al*. (1.05 and 3.82 MJ/m^3)[276,277] could be obtained even despite their low σ_r (**Figure 4.77**). These high E_ρ arise from the high ε_{break} of the materials at 20 °C above their T_g, which in some cases surpassed 450% (**Annex A12**). Just as on σ_r, the highest E_ρ were obtained for the IPHTAHDO 2000 polymers, which is to be expected since E_ρ is proportional to σ_r. However, the trends that could be observed on the σ_r of IPHTAHDO MDI were not followed on their E_ρ, as no relationship with their HS content nor with their polyester M_n could be drawn.

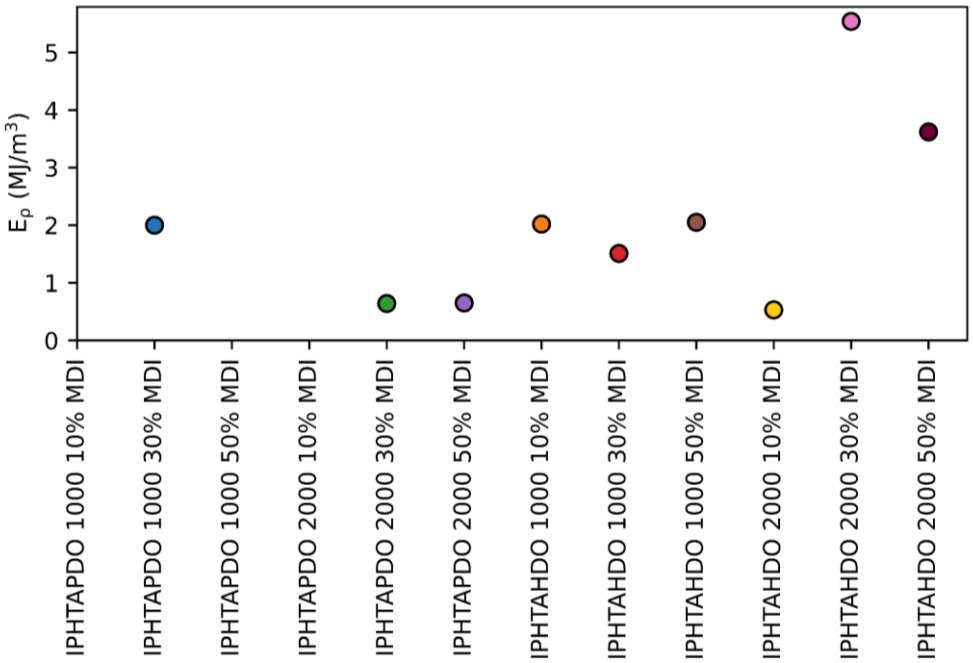

Figure 4.77 E_ρ of the IPHTA MDI materials.

4.3.3.2.2 IPHTA HDI TPUs

On the IPHTA HDI TPUs, a striking difference between the σ_r of the PDO and HDO formulations could be observed (**Figure 4.78**, **Annex A12**). The PDO formulations perform similarly to their MDI counterpart, while the HDO materials exhibit remarkably higher σ_r than their MDI analogous, with one of them, **IPHTAHDO 1000 30% HDI**, having a σ_r of 17.8 MPa, above the current state of the art, the thermoset epoxy resin reported by Guoqiang Li *et al*.[277] with a σ_r of 17.0 MPa. The clear distinction between PDO and HDO materials is derived from the different crosslink densities between both materials, with the PDO TPUs containing no HS domains nor SS crystallites, while the HDO formulations present both. However, on the HDO materials, the variation of σ_r with composition cannot be related to either the SS crystallinity, HS crystallinity or degree of phase segregation obtained by DSC, SAXS and WAXS. Therefore, it is not possible to establish if the improvement of σ_r is caused by the presence of HS domains, SS crystallites, or both. Moreover, the high shape fixity of above 98% of the IPHTAHDO HDI TPUs demonstrates that the high density and strength of the supramolecular interactions originated from the IPHTA moieties are capable of withstanding massive loads, of at least 17.8 MPa.

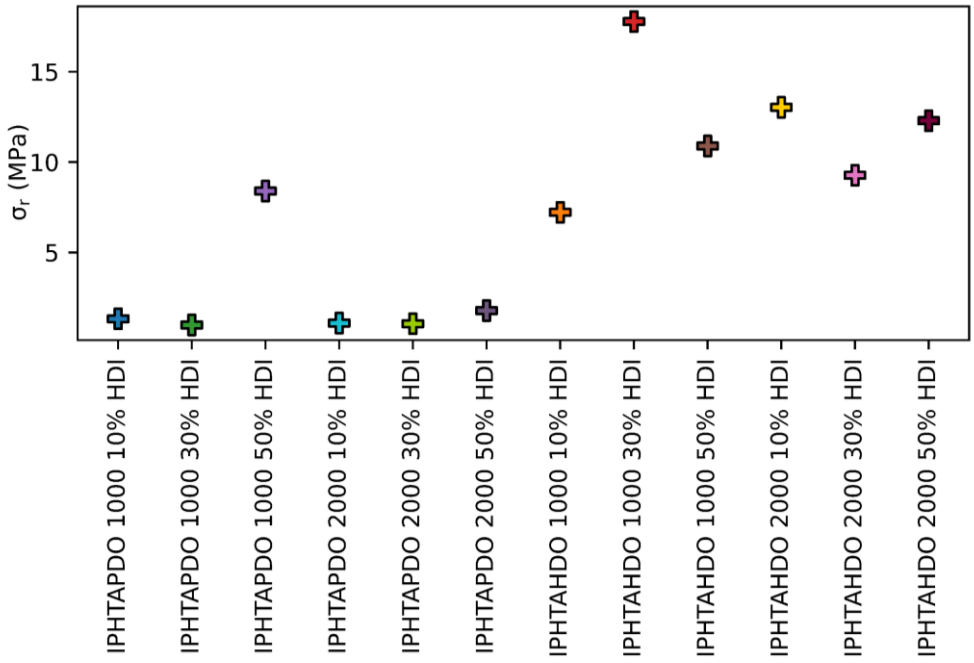

Figure 4.78: σ_r of the IPHTA HDI materials.

Similar results to those of σ_r were obtained for E_ρ, with the HDO formulations exhibiting a higher E_ρ than the PDO ones (**Figure 4.79**). Moreover, just as on σ_r, the **IPHTAHDO 1000 30% HDI** TPU exhibits a E_ρ of 24.5 MJ/m^3, higher than the current state of the art, the polyamide reported by Zhenan Bao *et al*.[275] with an E_ρ of 19.6 MJ/m^3. This is especially true if the temperatures at which the state-of-the-art E_ρ values are reported are taken into account. In their work, the E_ρ value is calculated at the same temperature as the T_g of the material not at 20 °C above the T_g, as is our case. However, as the σ_r at 20 °C above the T_g of their material is reported, an estimation of the E_ρ at that temperature can be calculated (**Figure 4.80**). The E_ρ of their material at 20 °C above the T_g, is of approximately 11.25 MJ/m^3, which indicates that one additional TPU, the **IPHTAHDO 2000 10% HDI** formulation, also presents a higher E_ρ than the state of the art, at 16.3 MJ/m^3. Note however, that the ε_r of their material at 20 °C above the T_g is not reported and therefore, the changes in ε_r when increasing the temperature have not been considered.

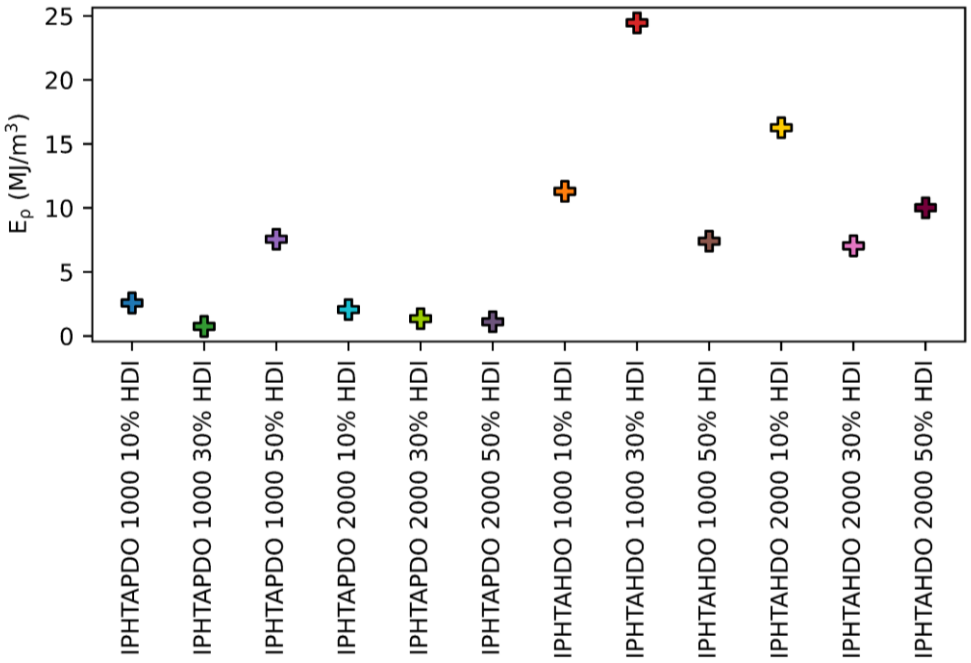

Figure 4.79 E_p of the IPHTA HDI materials.

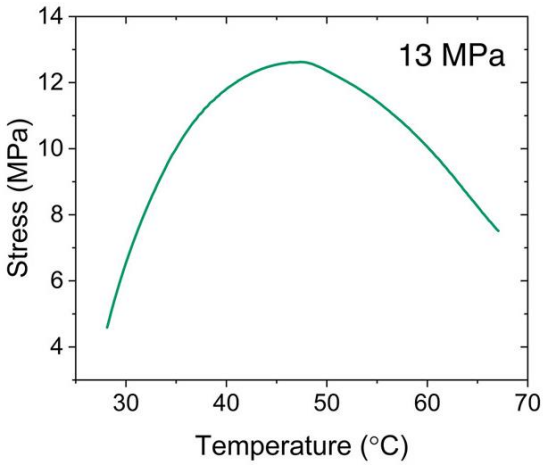

Figure 4.80: Reported σ_r *vs* temperature of the Zhenan Bao *et al*. polyamide.[275]

4.3.3.2.3 FDCA MDI TPUs

Most of the FDCA MDI TPUs exhibit low σ_r values close to those standard for SMP polymers, with two exceptions, the **FDCAHDO 2000 10% MDI** and **FDCAHDO 2000 50% MDI** formulations, on which σ_r of 8.8 and 6.5 MPa were obtained respectively (**Figure 4.81**, **Annex A12**). The higher σ_r in those specific two formulations allows the determination of one parameter than previously it was not possible to ascertain, the structure responsible for the high σ_r in the aromatic polyester TPUs. Two of the FDCA MDI formulations, **FDCAHDO 1000 10% MDI** and **FDCAHDO 2000 10% MDI** exhibit SS crystallinity by WAXS. Although **FDCAHDO 2000 10% MDI** presents both SS crystallites and a high σ_r, the σ_r of **FDCAHDO 1000 10% MDI** is quite low. Moreover, the degree of SS crystallinity of **FDCAHDO 1000 10% MDI** is higher than that of **FDCAHDO 2000 10% MDI** indicating that the SS crystallites are not the structure inducing the high σ_r of the materials. In contrast, only the material with the highest σ_r, **FDCAHDO 2000 10% MDI** exhibits HS domains by SAXS. This indicates that the HS domains, and not the SS crystallites, are the structures responsible for inducing the high stress of the materials.

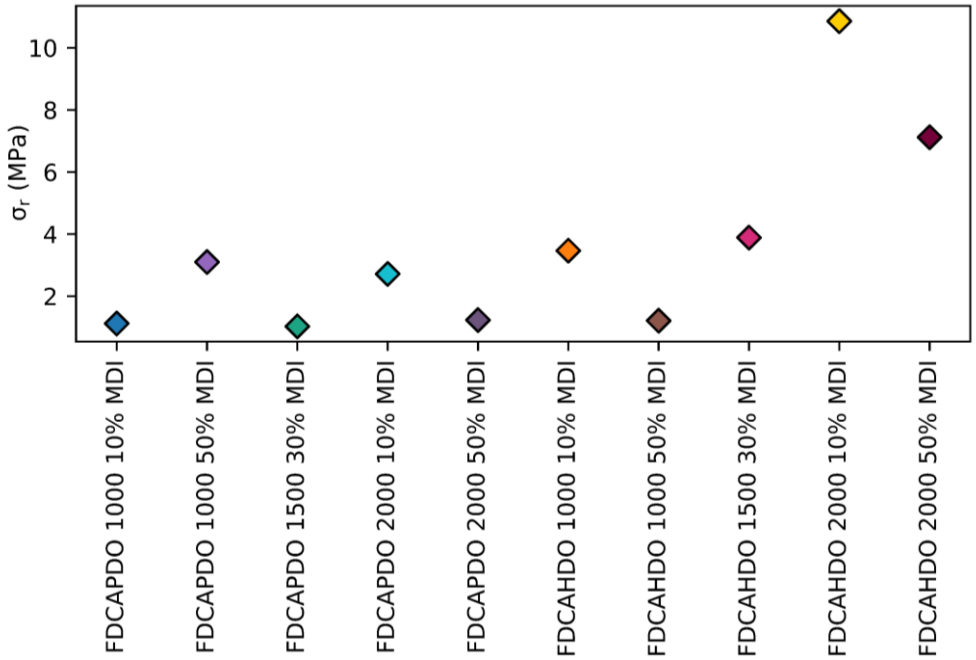

Figure 4.81: σ_r of the FDCA MDI materials.

The interpretation of the E_ρ for the FDCA MDI materials is slightly more complex than on the previous IPHTA materials, owing to one factor, the lower shape recovery index (R_r) of some of

the FDCAHDO MDI formulations. On the standard formula for the calculation of E_ρ, a complete recovery of the maximum stress is assumed. However, in these TPUs, R_r as low as 50% were obtained. Therefore, the direct application of the E_ρ formula would result in a great overestimation of E_ρ. To account for the low R_r of some of the formulations, in the materials with a R_r below 80%, R_r rather than the ε_r of the materials has been employed to calculate E_ρ. Unlike on σ_r, no FDCA MDI formulation exhibited far greater E_ρ than those standard for SMPs. Owing to their poor R_r, the overall mechanical work performed by the polymers that exhibited high σ_r, **FDCAHDO 2000 10% MDI** and **FDCAHDO 2000 50% MDI** was greatly diminished (**Figure** 4.82). Nonetheless, these two formulations still show above-average E_ρ at par with the thermoset resins reported by Guoqiang Li *et al*.[276,277]

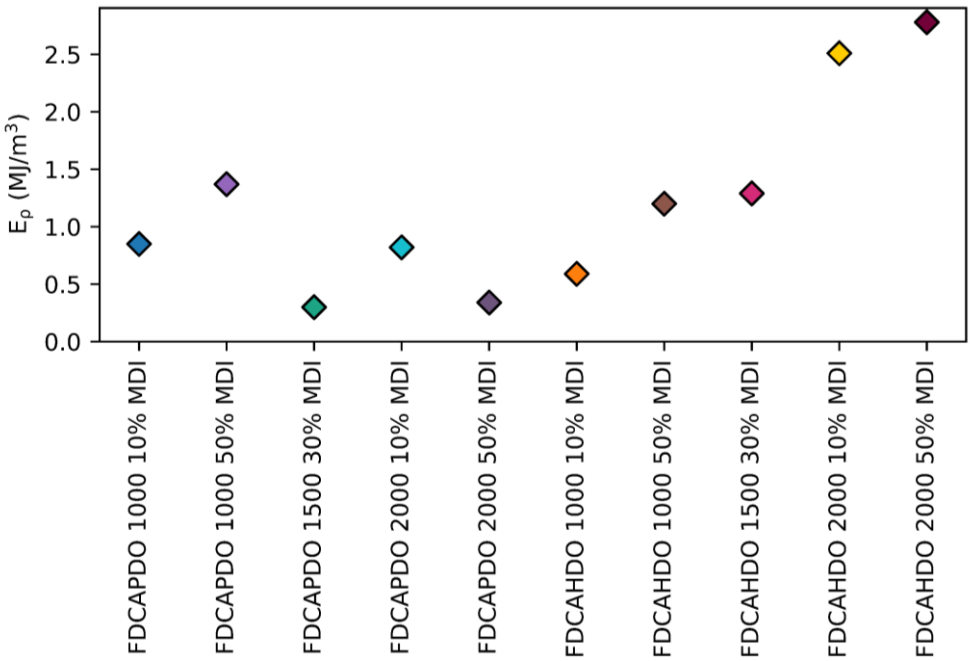

Figure 4.82 E_ρ of the FDCA MDI materials.

4.3.3.2.4 FDCA HDI TPUs.

Finally, the σ_r and E_ρ of the FDCA HDI formulations have been assessed (**Annex A12**). In these formulations, a high σ_r, exceeding that of their IPHTA analogous would be expected, as the phase segregation of the FDCA TPUs is higher than that of the IPHTA polymers, and therefore, their number of HS domains, which are responsible for generating high σ_r is greater. Indeed, the results show far greater σ_r for the FDCA HDI than for the IPHTA HDI TPUs, with most of the

FDCAHDO HDI formulations far exceeding the σ_r of the state-of-the-art epoxy resin, reaching values of up to 26.3 MPa (**Figure 4.83**).[277] A clear divide between the PDO and HDO materials can be observed, which can be understood by the higher phase segregation of the latter in comparison with the former, as observed by SAXS and DSC. Nonetheless, the PDO materials also exhibit greater σ_r than their IPHTA counterpart, demonstrating once again the greater phase segregation capabilities of the FDCA polymers in front of the IPHTA ones. Moreover, the high capability of the aromatic SS to store massive stress is proved once more, since even the materials that have σ_r above 20 MPa show good R_f of above 95%.

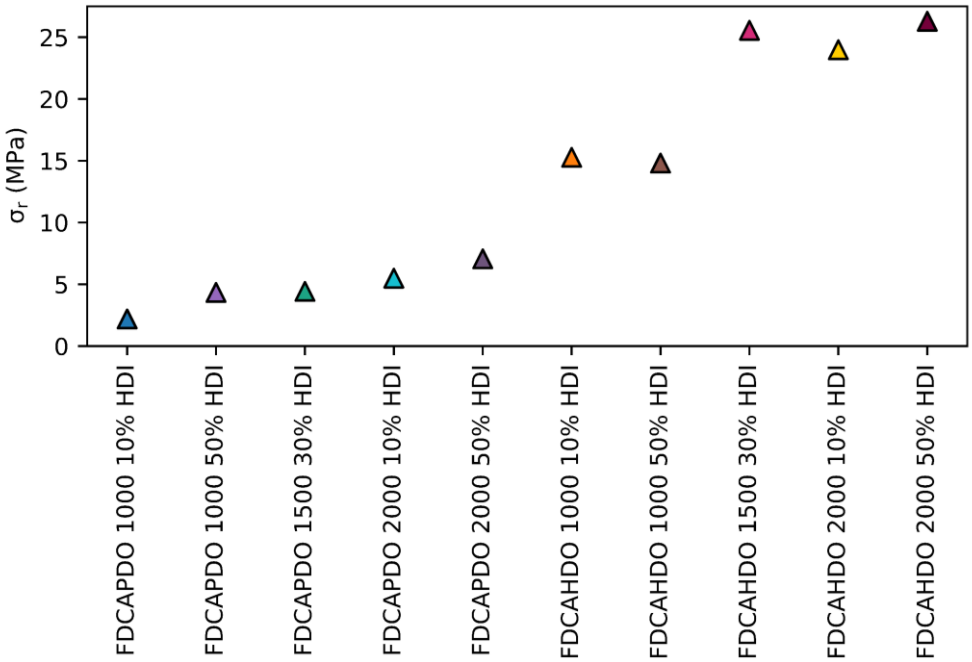

Figure 4.83: σ_r of the FDCA HDI materials.

Unfortunately, these good σ_r values are not directly translated into the E_ρ as, just on the FDCA MDI TPUs, the FDCAHDO HDI materials exhibit a poor R_r owing to the strain crystallisation process, limiting the maximum work that the polymers can effectuate (**Figure** 4.84). Although in a lot of cases, their E_ρ are above that of standard SMP, they are nowhere near close to the state of the art. Moreover, owing to the disparities in R_r between the PDO and HDO materials, with the former being above 85% while the latter are below 55%, the trends observed in the rest of the materials, with E_ρ being higher for the HDO formulations switch, and the PDO materials become the ones with the highest E_ρ.

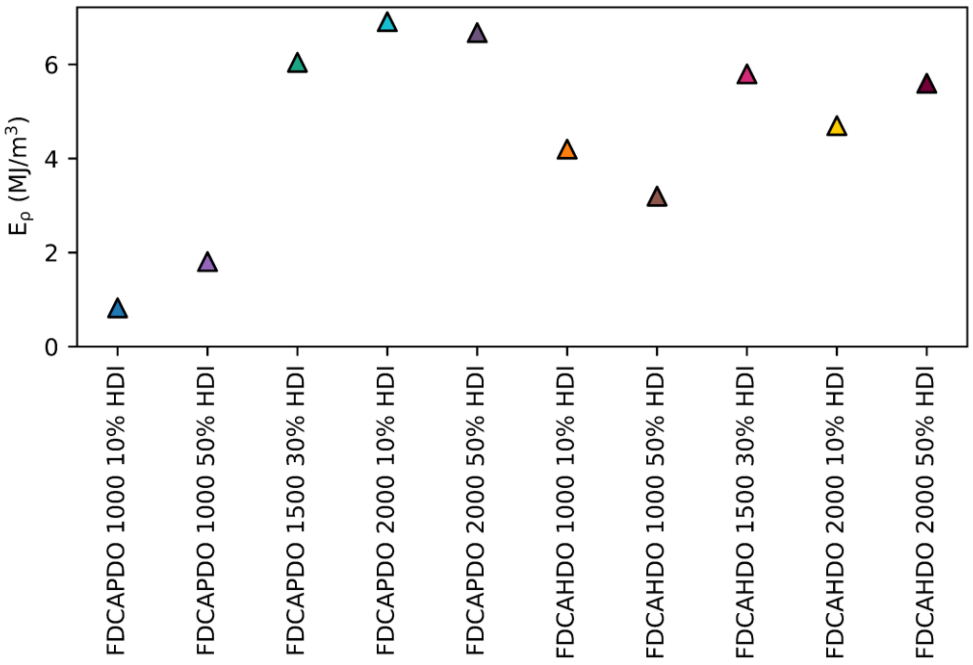

Figure 4.84 E_ρ of the FDCA HDI materials.

4.3.3.2.5 Overview

The IPHTA and FDCA materials show remarkable actuation strengths, with some formulations showing better properties than the current state-of-the-art. The capability of the materials to generate high σ_r and E_ρ is dependent on two factors, their phase segregation and the ability to store the mechanical work into chemical energy. The HS domains act as crosslink points for the SS matrix, inhibiting chain slipping during elongation and inducing tension to the polymeric chains. This σ_r can be stored by the TPUs into chemical energy owing to their high concentration of aromatic moieties in the SS, which enable the formation of π-π stacking interactions that are able to hold the induced stress. Ultimately, the high HS domain of some of the TPU formulations, coupled with the ability of the aromatic SS to store great amounts of stress, allows the generation of materials with high σ_r while maintaining good R_f. However, due to the low R_r of the materials with the highest σ_r caused by the strain crystallisation process, the potential outstanding E_ρ that said materials could achieve is limited, with only two formulations, **IPHTAHDO 1000 30% HDI** and **IPHTAHDO 2000 10% HDI** exhibiting E_ρ higher than the current state-of-the-art.

Overall, it looks like the materials with the highest phase segregation are the ones that present higher σ_r and E_ρ. Therefore, in an initial optimisation attempt, an annealing process has been carried out to increase the phase segregation of the TPUs and improve both σ_r and E_ρ.

4.3.4 Annealing tests

Since the degree of phase segregation of the TPUs plays an important role in producing materials with a high σ_r and E_ρ, annealing has been employed as an attempt to improve the actuation strength of the materials. This annealing process aims to increase the phase segregation of the polymers. If high annealing temperatures were employed, phase segregation would decrease, rather than increase, as the miscibility between the HS and SS domains increases. Therefore, to avoid the unravelling and mixing of the HS and SS domains, low annealing temperatures, of 20 °C above the T_g of each material, have been selected.

Rather than assessing the annealing of all the TPU formulations, only those that could potentially exhibit an increase in their phase segregation through thermal treatment have been evaluated. Accordingly, the IPHTA MDI TPUs were discarded as their high HS-SS compatibility would limit the effect of the thermal treatment. Furthermore, the annealing of the IPHTA HDI and FDCA HDI TPUs was not carried out as their T_g are already below their storage temperature and therefore, they are constantly under annealing conditions. Therefore the IPHTAPDO HDI, FDCAPDO MDI, FDCAHDO MDI and FDCAPDO HDI TPUs are the formulations upon which annealing was applied.

To check the effect that annealing has on the morphology of the TPUs, DSC, SAXS and WAXS were employed to compare their microstructure prior and after annealing. This morphological data was then employed to rationalise the variations in the shape memory properties of the annealed and unannealed materials.

4.3.4.1 DSC

The DSC of the annealed TPUs were performed following a similar procedure to that of their unannealed analogous. However, only the 1st heating cycle was carried out and analysed, as it is the process in which the morphological modifications derived from the annealing process can be found (**Experimental Section 6.1.9**). Accordingly, the comparison between the DSC of the annealed and unannealed materials was carried out on 1st heating cycle.

First of all, the time required to increase the phase segregation of the materials through annealing was determined by analysing, in a select number of formulations, the changes in the enthalpy of their melting transitions with time under the annealing conditions (**Figure 4.85**).

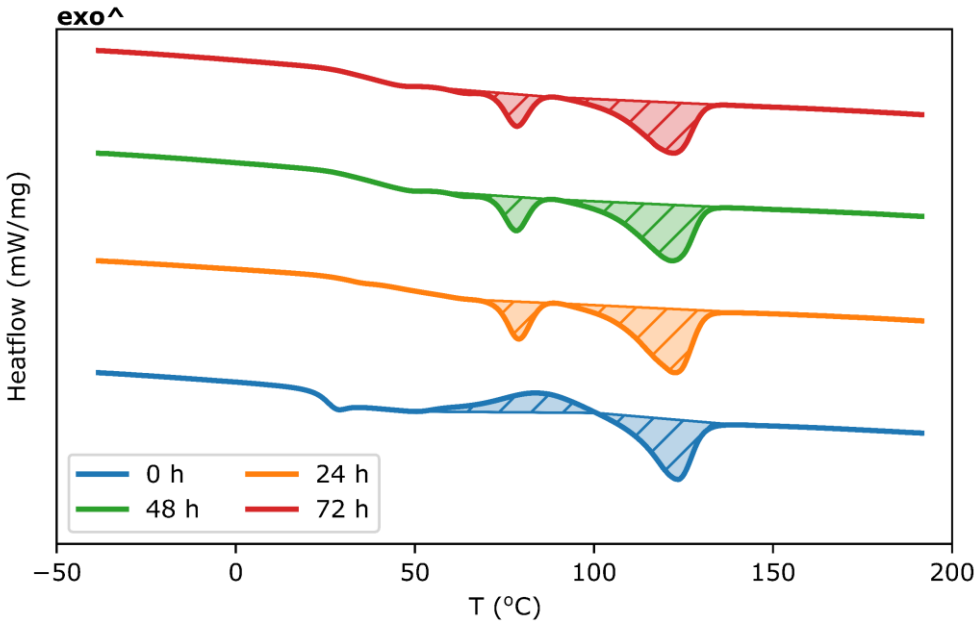

Figure 4.85: Example of the evolution of the morphology of TPUs with time at 20 °C above their T_g.

In all of the observed formulations, a rapid increase in phase segregation occurs once the materials are annealed, meaning that, when the materials reach a high enough chain mobility, the segregation process proceeds quite fast (**Figure 4.85**). Moreover, a slight decrease in the enthalpies of the melting transitions was observed the longer the annealing time is (**Table 4.22**). This indicates that high annealing times are counterproductive to achieving high phase segregations, as some of the HS and SS domains become mixed. Therefore, an annealing time of 24 h has been selected for the thermal treatment of all the formulations.

Table 4.22: Evolution of the melting enthalpies with time during annealing.

	T Peak 1 (°C)	ΔH_{melt} Peak 1 (mJ/g)	T Peak 2 (°C)	ΔH_{melt} Peak 2 (mJ/g)
0 h	-	-	123.18	-16.20
24 h	78.9	-6.2	122.4	-23.6
48 h	78.3	-6.2	121.7	-21.8
72 h	78.5	-6.0	122.4	-21.4

4.3.4.1.1 IPHTAPDO HDI TPUs

The annealing of the IPHTAPDO HDI TPUs results in an increase in the number of semicrystalline formulations, with the **IPHTAPDO 1000 30% HDI** and **IPHTAPDO 2000 30% HDI** polymers, which are amorphous before their annealing, exhibiting some melting transitions once thermally treated (**Figure 4.86**).

Two different melting transitions can be observed on the thermograms of the annealed samples, one located at 78-82 °C (peak 1) and another one at 99-126 °C (peak 2). Peak 1 can easily be assigned by comparing the thermograms of the annealed and unannealed **IPHTAPDO 1000 50% HDI** formulation. The low temperature peak that on the untreated sample is located at 57 °C increases to 79 °C after its annealing, which corresponds to approximately 30 °C above the annealing temperature of the sample. As aforementioned, it has been reported that the internal reorganisation of the HS domains is associated with a DSC melting transition whose position is dependent on the storage/annealing temperature of the materials and is usually found at 20-30 °C above it.[188] Therefore, peak 1 can be attributed to the internal reorganisation of the HS domains, as its position is modified by the storage and annealing temperature and is found consistently at 20-30 °C above it. The position of peak 2 matches the one previously found for the HDI HS domains, and therefore it can be assigned to the presence of HS crystallites.

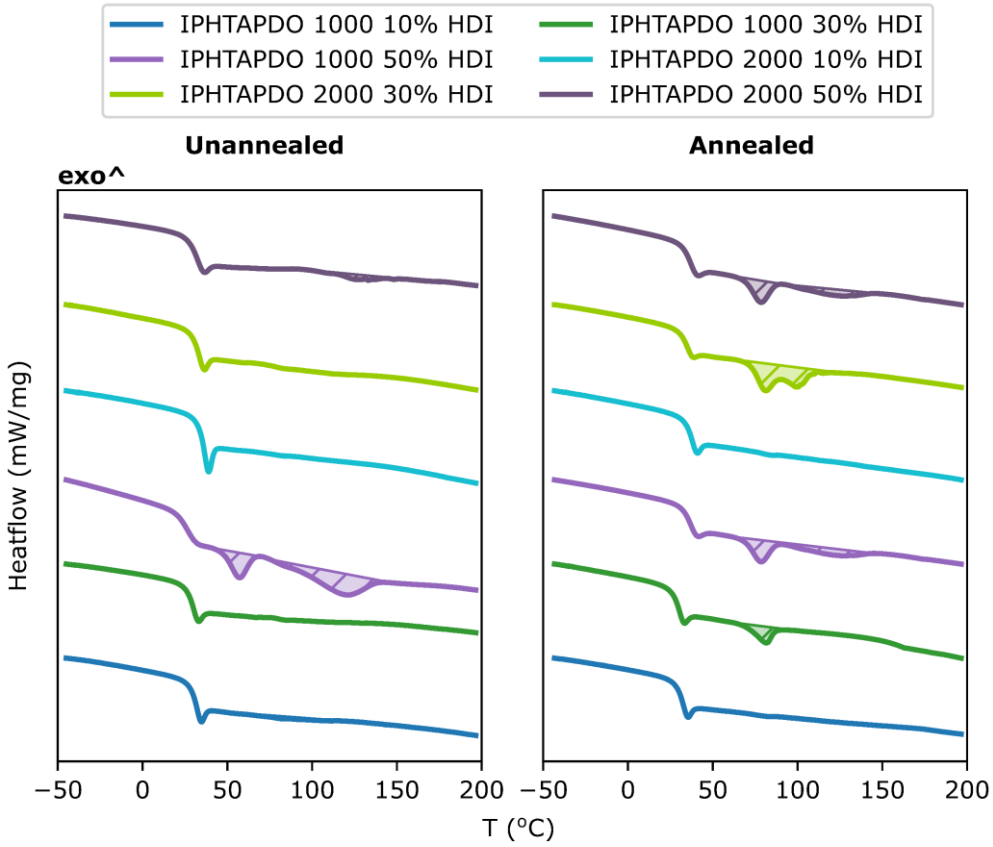

Figure 4.86: Comparison between the DSC thermograms of unannealed (left) and annealed (right) IPHTAPDO HDI TPUs.

In the two materials that presented some melting transition before their annealing, two different behaviours were observed. In **IPHTAPDO 2000 50% HDI**, the enthalpy associated with the two melting processes increases after annealing, as would be expected, while on **IPHTAPDO 1000 50% HDI,** although the enthalpy of peak 1 increases that of peak 2 and the overall crystallinity of the polymer decreases (**Table 4.23**). This might indicate that, on **IPHTAPDO 1000 50% HDI**, some of the HS domains become miscible with the SS after annealing, lowering the overall crystallinity of the polymer.

Table 4.23: Comparison between the T_m and enthalpies of annealed (AN) and unannealed (UnAN) IPHTAPDO HDI TPUs.

	T_m, Peak 1 (°C)		**ΔH_m, Peak 1 (J/g)**		**T_m, Peak 2 (°C)**		**ΔH_m, Peak 2 (J/g)**	
	UnAN	**AN**	**UnAN**	**AN**	**UnAN**	**AN**	**UnAN**	**AN**
IPHTAPDO 1000 10% HDI	–	–	–	–	–	–	–	–
IPHTAPDO 1000 30% HDI	–	81.4	–	2.70	–	–	–	–
IPHTAPDO 1000 50% HDI	57.1	78.6	3.7	6.5	119.4	126.2	9.9	5.2
IPHTAPDO 2000 10% HDI	–	–	–	–	–	–	–	–
IPHTAPDO 2000 30% HDI	–	81.2	–	4.7	–	99.0	–	4.3
IPHTAPDO 2000 50% HDI	72.2	78.2	1.5	3.5	117.1	122.37	1.7	2.7

The differences between the annealed and unannealed materials are not limited to their crystallinity. In all formulations, the T_g of the materials increases after their thermal treatment (**Table 4.24**). This contradicts the higher phase segregation of the annealed materials compared to that of the unannealed ones, by which the thermally treated TPUs should have a lower T_g. Although from just the DSC data it is difficult to verify the origin of this discrepancy, the higher T_g temperatures of the annealed materials suggest that, a reorganisation of the amorphous SS domain into a more stable, closely packed structure takes place.

Table 4.24: Comparison between the T_g of annealed (AN) and unannealed (UnAN) IPHTAPDO HDI TPUs.

	T_g (°C)			T_g (°C)	
	UnAN	**AN**		**UnAN**	**AN**
IPHTAPDO 1000 10% HDI	28.3	32.97	**IPHTAPDO 2000 10% HDI**	35.3	38.1
IPHTAPDO 1000 30% HDI	28.1	30.46	**IPHTAPDO 2000 30% HDI**	31.0	35.1
IPHTAPDO 1000 50% HDI	27.3	33.77	**IPHTAPDO 2000 50% HDI**	32.3	37.1

4.3.4.1.2 FDCAPDO MDI TPUs

In the FDCAPDO MDI TPUs, only one of the formulations, **FDCAPDO 1000 50% MDI** becomes semicrystalline after its thermal treatment, exhibiting two overlapping peaks at 87.5 and 106.5 °C with an enthalpy of 2.9 and 3.6 J/g respectively (**Figure 4.87**). These two overlapping peaks can be attributed to some sort of SS crystallite, as their temperature is too low to belong to the melting of the HS domains. The presence of only 1 semicrystalline FDCAPDO MDI formulation lies in contrast with the IPHTAPDO HDI formulations, in which 4 semicrystalline materials were found. The difference in crystallinity can be attributed to the higher HS-SS miscibility of the MDI TPUs than of the HDI polymers, which hinders their crystallisation and segregation.

The comparison between the T_g from the annealed and unannealed materials leads to similar results as those of the IPHTAPDO HDI formulations, with T_g being higher, in almost all formulations, for the thermally treated materials (**Table 4.25**). However, one notable exception can be identified, **FDCAPDO 1000 50% MDI**, in which T_g decreases after annealing. **FDCAPDO 1000 50% MDI** is the only formulation in which some crystalline structures can be identified after annealing and therefore, is the material with the highest phase segregation. Accordingly, the decrease in T_g might be associated with the increase in phase segregation originated from the annealing process.

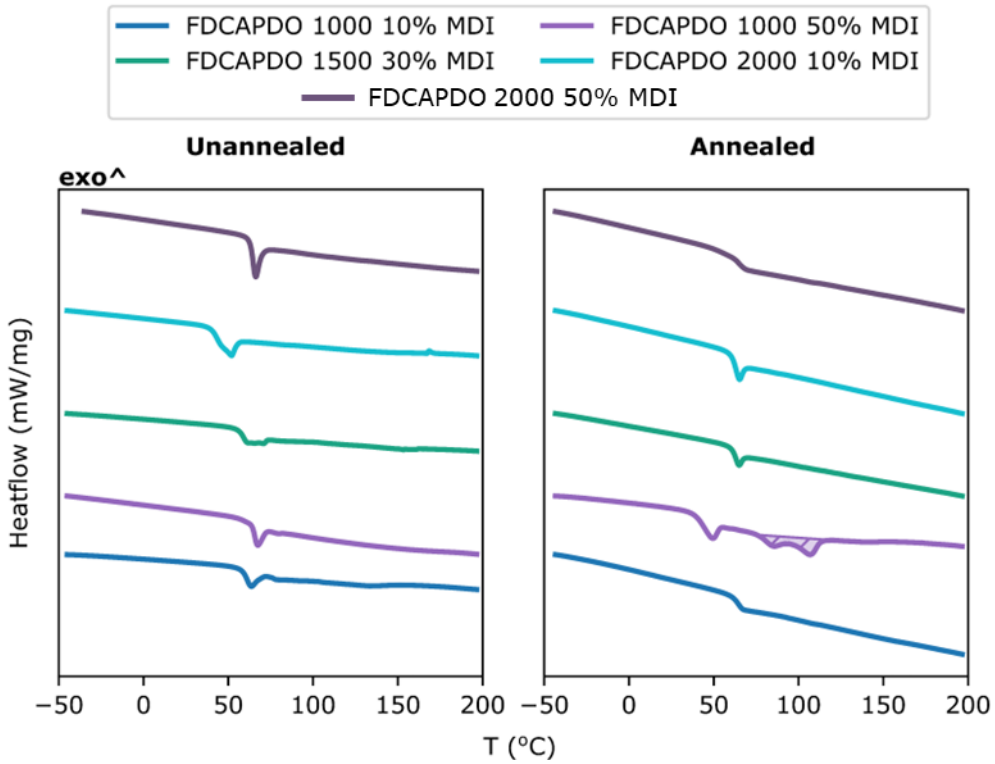

Figure 4.87: Comparison between the thermograms of unannealed (left) and annealed (right) FDCAPDO MDI TPUs.

Table 4.25: Comparison between the T_g of annealed (AN) and unannealed (UnAN) FDCAPDO MDI TPUs.

	T_g (°C)	
	UnAN	**AN**
FDCAPDO 1000 10% MDI	65.6	66.4
FDCAPDO 1000 50% MDI	61.4	46.6
FDCAPDO 1500 30% MDI	57.5	63.1
FDCAPDO 2000 10% MDI	43.5	63.2
FDCAPDO 2000 50% MDI	64.4	64.7

4.3.4.1.3 FDCAHDO MDI TPUs

On the FDCAHDO MDI TPUs, a striking increase in crystallinity is produced during the annealing process, with all the formulations exhibiting some melting transition (**Figure 4.88**). The higher crystallinity of the FDCAHDO MDI materials in comparison with the two previously discussed formulations can be explained by the higher segregation capabilities of the FDCA SS in comparison with the IPHTA ones and to the higher chain mobility of the HDO formulations that of the PDO materials.

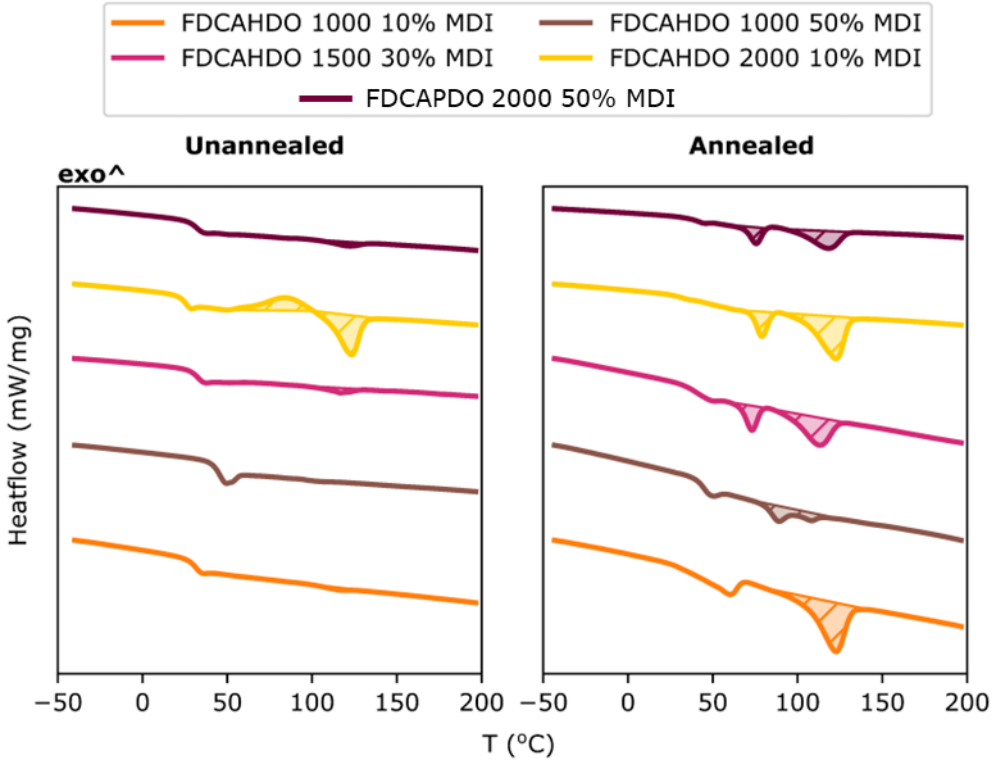

Figure 4.88: Comparison between the thermograms of unannealed (left) and annealed (right) FDCAHDO MDI TPUs.

In four of the formulations, **FDCAHDO 1000 10% MDI**, **FDCAHDO 1500 30% MDI**, **FDCAHDO 2000 10% MDI** and **FDCAHDO 2000 50% MDI** the two same peaks as on the previously discussed TPUs can be identified. The peak located at lower temperatures (peak 1) can be assigned to the internal reorganisation of the HS domains, as it is located at 20-30 °C above the annealing temperature, while the peak at higher temperatures (peak 2) is attributed to the presence of both HS and SS ordered domains. Although the integration of peak 1 on

FDCAHDO 1000 10% MDI could not be accomplished due to an overlap of the melting and glass transitions, overall, the crystallinity of the TPUs decreases with the increase of the HS content, as shown by the enthalpies of both peak 1 and peak 2 (**Table 4.26**). This seems to indicate that lower degrees of phase segregation are obtained as the HS increases, which is the same behaviour observed in the unannealed FDCAHDO HDI TPUs.

Table 4.26: Comparison between the T_m and enthalpies of annealed (AN) and unannealed (UnAN) FDCAHDO MDI TPUs.

	T_{melt}, Peak 1 (°C)		ΔH_{melt}, Peak 1 (J/g)		T_{melt}, Peak 2 (°C)		ΔH_{melt}, Peak 2 (J/g)	
	UnAN	**AN**	**UnAN**	**AN**	**UnAN**	**AN**	**UnAN**	**AN**
FDCAHDO 1000 10% MDI	–	60.8	–	–	115.0	122.2	2.2	28.9
FDCAHDO 1000 50% MDI	–	–	–	–	–	88.6	–	-9.4
FDCAHDO 1500 30% MDI	–	73.0	–	6.49	116.7	112.6	4.9	16.7
FDCAHDO 2000 10% MDI	–	78.9	–	6.2	122.7	122.37	18.9	23.6
FDCAHDO 2000 50% MDI	–	62.1	–	2.19	120.5	119.7	5.8	14.7

The same trends concerning T_g as in the previous formulations were found in the FDCAHDO MDI materials, with T_g being higher after annealing. This is an indication, once more, that there is some reorganisation of the amorphous SS domain during the annealing process which decreases the chain mobility of the materials.

Table 4.27: Comparison between the T_g of annealed (AN) and unannealed (UnAN) FDCAHDO MDI TPUs.

	T_g (°C)	
	UnAN	**AN**
FDCAHDO 1000 10% MDI	31.3	56.2
FDCAHDO 1000 50% MDI	45.5	46.7
FDCAHDO 1500 30% MDI	31.8	40.4
FDCAHDO 2000 10% MDI	28.3	30.1
FDCAHDO 2000 50% MDI	30.8	34.9

4.3.4.1.4 FDCAPDO HDI TPUs

The same effect on the morphology of the TPUs from annealing was observed in the FDCAPDO HDI formulations, with their degree of crystallisation increasing as a result of the thermal treatment (**Figure 4.89**). Although all of the samples show some melting transition, the one appearing on the **FDCAPDO 2000 10% HDI** formulation is extremely weak. The two most crystalline materials, **FDCAPDO 1000 10% HDI** and **FDCAPDO 2000 50% HDI** exhibit the two expected melting transitions, one at a low temperature, around 30 °C above their annealing temperature (peak 1), which corresponds to the reorganisation of the HS domains and another one at a higher temperature (peak 2), which can be attributed to the existence of both HS and SS domains, just as on the unannealed TPUs (**Table 4.28**).

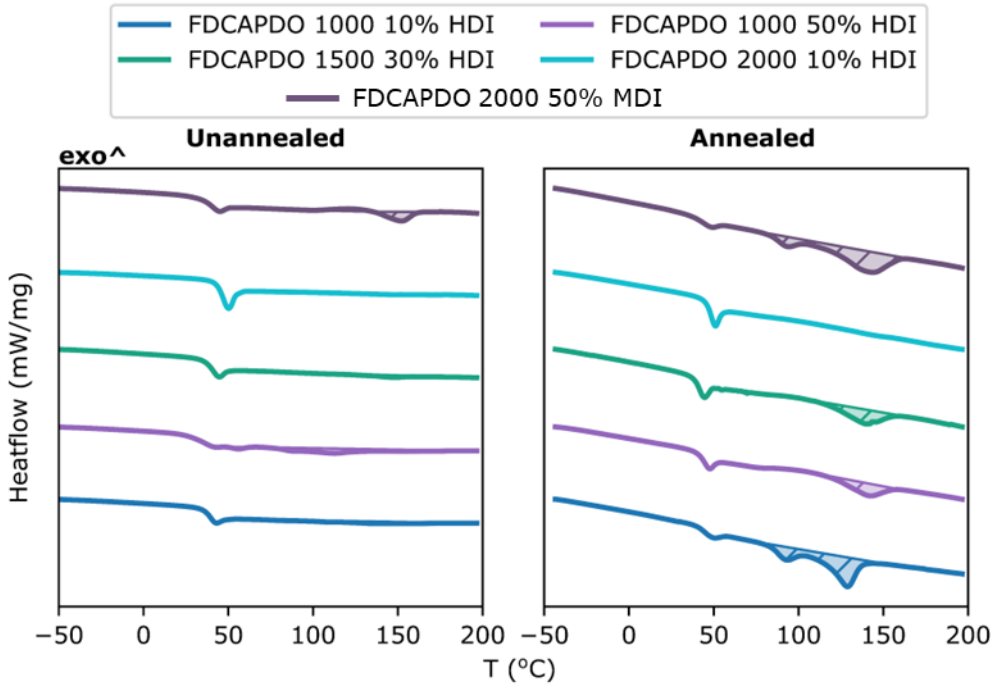

Figure 4.89: Comparison between the DSC thermograms of unannealed (left) and annealed (right) FDCAPDO HDI TPUs.

Table 4.28: Comparison between the T_m and enthalpies of annealed (AN) and unannealed (UnAN) FDCAPDO HDI TPUs.

	T_{melt}, Peak 1 (°C)		ΔH_{melt}, Peak 1 (J/g)		T_{melt}, Peak 2 (°C)		ΔH_{melt}, Peak 2 (J/g)	
	UnAN	**AN**	**UnAN**	**AN**	**UnAN**	**AN**	**UnAN**	**AN**
FDCAPDO 1000 10% HDI	–	93.0	–	7.6	133.5	128.7	4.5	21.5
FDCAPDO 1000 50% HDI	55.0	–	0.5	–	109.1	141.0	9.8	12.6
FDCAPDO 1500 30% HDI	–	–	–	–	143.6	138.9	3.5	14.1
FDCAPDO 2000 10% HDI	–	–	–	–	145.1	143.6	2.7	0.68
FDCAPDO 2000 50% HDI	–	93.5	–	5.8	150.9	141.8	4.7	25.8

Once again, the same behaviour regarding T_g as on most of the previously discussed annealed materials can be observed on the FDCAPDO HDI TPUs, with T_g being higher after annealing (**Table 4.29**).

Table 4.29: Comparison between the T_g of annealed (AN) and unannealed (UnAN) FDCAPDO HDI TPUs.

	T_g (°C)	
	UnAN	**AN**
FDCAPDO 1000 10% HDI	40.0	44.7
FDCAPDO 1000 50% HDI	36.3	44.6
FDCAPDO 1500 30% HDI	40.9	41.6
FDCAPDO 2000 10% HDI	46.8	48.5
FDCAPDO 2000 50% HDI	41.1	43.7

4.3.4.1.5 Overview

Overall, the phase segregation and crystallinity of the TPUs increase after annealing, which proves once more that one of the parameters that is restricting the crystallisation and segregation of the materials is their poor chain mobility. The time required to increase the phase segregation of the TPUs seems to be quite low, which indicates that once the materials achieve the necessary chain mobility to segregate, the process occurs quite rapidly. Moreover, higher annealing times result in lower crystallinities of the material, which indicates that over time, the HS and SS domains become miscible at temperatures above their T_g.

Surprisingly, an increase in the T_g of the materials can be observed as an effect of annealing. This is the opposite behaviour as what would be expected, as an increase in the phase segregation of the materials should result in an increase in their chain mobility. This effect of annealing seems to indicate that some sort of reorganisation of the SS amorphous domain of the materials takes place once the thermal treatment is applied, which reduces the chain mobility of the materials.

4.3.4.2 SAXS

The analysis of the SAXS data of the annealed materials was carried out just as for the unannealed TPUs. First, the presence or lack thereof of a peak in the Fourier region of the spectra was explored to determine which materials possess segregated HS domains. Then, the data from those materials in which the presence of HS domains was detected is fitted to the spherical form factor following a Flory-Schultz distribution and the Percus-Yevick and Zernike-Prins structure factors. This allows to gather the different morphological parameters that are associated with the presence of HS domains, namely, their domain size (R) and its standard deviation (σ_r), their volume fraction (Φ), their average interparticle distance (d) and their standard deviation (σ_d), and the width of the partially ordered shell surrounding the HS domains (h) (**Figure 4.90**, **Experimental Section 6.2.15**).

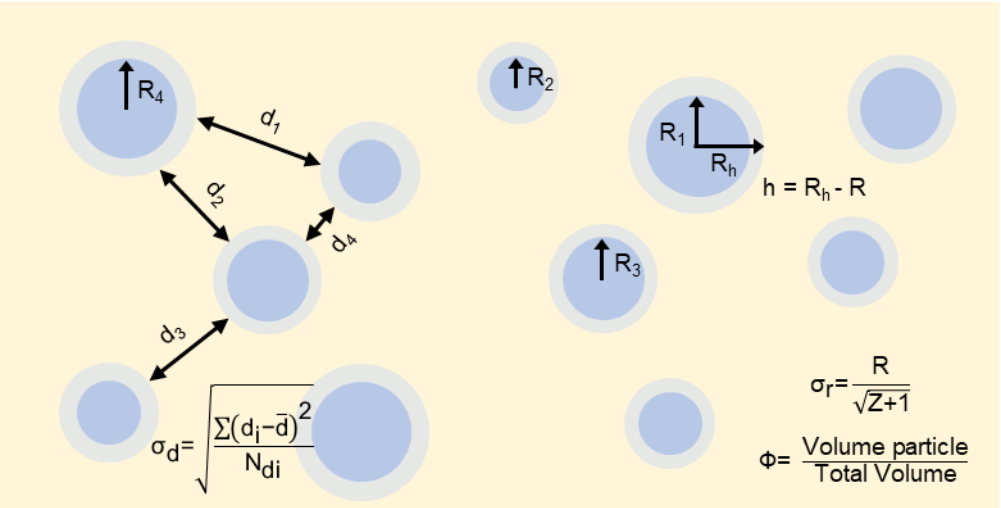

Figure 4.90: Graphical representation of the fitting parameters from the selected P(q) and S(q) models.

None of the FDCAPDO MDI TPUs exhibit a peak on SAXS, and only one of the IPHTAPDO HDI polymers does (**Annex A13**). This mirrors what was observed on their corresponding DSC since the FDCAPDO MDI materials show no melting transition associated with the HS domains and only the IPHTAPDO HDI formulation with the highest crystallinity by DSC, **IPHTAPDO 2000 30% HDI** exhibits a signal on SAXS. On the other two more crystalline TPU families, FDCAHDO MDI and FDCAPDO HDI, most of the materials display a peak on SAXS. Only one formulation of each TPU family, **FDCAHDO 1000 50% MDI** and **FDCAPDO 2000 10% HDI**, exhibit no signal in the Fourier region. These results match with the DSC data since those two formulations are the ones which have the lowest crystallinity by DSC. Most of the materials that

exhibit a peak on SAXS after annealing evolved from non-segregated materials. This corroborates that the annealing process favours the phase segregation of the TPUs, enabling the evolution of the polymers into their more stable, segregated structure by increasing their chain mobility. Only three of the TPU formulations exhibited segregated HS domains before their annealing, **FDCAHDO 2000 10% MDI**, **FDCAPDO 1000 50% HDI** and **FDCAPDO 2000 50% HDI**. Therefore, the direct comparison between annealed and unannealed samples of the same formulation can only be carried out on these three formulations (**Table 4.30**).

On the materials for which SAXS data could be gathered before and after annealing, two different behaviours were observed. In **FDCAHDO 2000 10% MDI**, an increase in the HS domains size (R), width of the shell surrounding the HS domains (h), volume fraction of the HS particles (Φ) and distance between the HS domains (d) was observed as a consequence of annealing (**Table 4.30**). This indicates that, in this formulation, the HS domains grow in size and reallocate to be further away from one another after annealing. The increase in Φ as a consequence of the thermal treatment of the material agrees with the results found in DSC, on which a higher melting transition enthalpy was observed after annealing. Contrarily, in the FDCAPDO HDI formulations, a reduction of the HS domain size (R), volume fraction (Φ) and particle distance (d) and an increase in the width of the shell surrounding the HS domains (h) were detected after annealing (**Table 4.30**). This indicates that the application of annealing on these formulations results in a decrease in their phase segregation. During the annealing process, the HS domains unravel, producing smaller particles with a wider surrounding shell, probably made out of part of the HS crystallite that has started to become miscible with the SS matrix. Therefore, to reach the highest phase segregation possible, a more in-depth optimisation of the annealing temperature and time would need to be carried out in further studies.

Table 4.30: Comparison of the morphological data obtained from the fitting of the Fourier region of SAXS between annealed (AN) and unannealed (UnAN) samples.

		$R \pm \sigma_R$ (Percus-Yevick) (nm)	$R \pm \sigma_R$ (Zernike-Prins) (nm)	R_h (nm)	h (nm)[a]	Φ	$d \pm \sigma_d$ (nm)
FDCAHDO 2000 10% MDI	**UnAN**	2.1 ± 1.2	2.3 ± 1.3	3.5	1.4	0.14	6.4 ± 3.0
	AN	2.9 ± 1.6	3.4 ± 1.9	4.9	2	0.16	9.1 ± 3.8
FDCAPDO 1000 50% HDI	**UnAN**	1.9 ± 1.2	2.0 ± 1.3	4.7	2.8	0.19	8.7 ± 3.5
	AN	1.5 ± 1.1	1.7 ± 1.1	4.6	3.1	0.14	8.0 ± 4.0
FDCAPDO 2000 50% HDI	**UnAN**	1.7 ± 1.1	1.9 ± 1.2	4.0	2.3	0.14	7.0 ± 3.5
	AN	1.5 ± 1.1	1.6 ± 1.2	4.2	2.7	0.11	6.8 ± 4.0

[a] $h = R_h - R$ (Percus-Yevick)

Regardless, the fitting of the SAXS data from all of the annealed TPUs yields overall similar morphologies to those of the unannealed formulations, albeit with some slight differences (**Table 4.31**). Although the HS domain radius (R) of the annealed and unannealed materials is in the same range (1.4-3.9 nm), two of the annealed formulations, **IPHTAPDO 2000 30% HDI** and **FDCAHDO 1500 30% MDI** present significantly higher R_h and d than the unannealed materials. Nonetheless, the same conclusions from the data can be drawn. The fact that the volume fraction of the HS domains (Φ) is very similar between the different samples of each TPU family, no matter their HS content, indicates that the concentration of HS domains is limited by some unknown factor and that once it reaches a certain threshold, it cannot grow beyond that. Moreover, Φ cannot be directly correlated to an increase in the R_h size nor to a decrease in d, which seems to indicate the formation of HS pockets between the SS crystallites, the concentration of which is what determines Φ.

Table 4.31: Morphological data obtained from the fitting of the SAXS data of the annealed polymers.

	$R \pm \sigma_R$ (Percus-Yevick) (nm)	$R \pm \sigma_R$ (Zernike-Prins) (nm)	R_h (nm)	h (nm)[a]	Φ	$d \pm \sigma_d$ (nm)
IPHTAPDO 2000 30% HDI	2.8 ± 1.8	3.2 ± 2.1	5.6	2.8	0.16	10.3 ± 4.4
FDCAHDO 1000 10% MDI	3.0 ± 1.6	3.4 ± 1.9	4.4	1.4	0.11	7.9 ± 4.0
FDCAHDO 1500 30% MDI	3.3 ± 1.8	3.9 ± 2.2	5.7	2.4	0.10	9.8 ± 5.0
FDCAHDO 2000 10% MDI	2.9 ± 1.6	3.4 ± 1.9	4.9	2	0.16	9.1 ± 3.8
FDCAHDO 2000 50% MDI	1.6 ± 1.0	1.8 ± 1.1	4.1	2.5	0.18	7.5 ± 3.1
FDCAPDO 1000 10% HDI	1.4 ± 0.9	1.8 ± 1.1	4.0	2.6	0.11	6.3 ± 3.5
FDCAPDO 1000 50% HDI	1.5 ± 1.1	1.7 ± 1.1	4.6	3.1	0.14	8.0 ± 4.0
FDCAPDO 1500 30% HDI	1.5 ± 0.9	1.7 ± 1.0	3.3	1.8	0.06	4.8 ± 3.3
FDCAPDO 2000 50% HDI	1.5 ± 1.0	1.6 ± 1.1	4.2	2.7	0.11	6.8 ± 4.0

[a] $h = R_h$ - R (Percus-Yevick)

4.3.4.2.1 Overview

Overall annealing has a positive effect on the phase segregation of the TPU materials, allowing the evolution of the materials towards their more stable, segregated state. The good fitting of the spherical form factor and the Percus-Yevick and Zernike-Prins models to the data from the annealed materials indicates that there is not a big change in the overall morphology of the HS domains after annealing. Nevertheless, a decrease in the phase segregation in materials that exhibited HS domains before their annealing can be noted, which indicates that the annealing temperatures and times selected are not the optimal ones to maximise phase segregation and that further optimisation of the annealing process should be carried out.

4.3.4.3 WAXS

The effect that the annealing process has on the crystalline structure and the degree of crystallinity of the SS was assessed by WAXS. As in the unannealed materials, deconvolution of the spectra was employed to determine the number, position and intensity of the bands corresponding to crystalline and amorphous structures.

The annealing of the FDCAHDO MDI TPUs results in the generation of both amorphous and semicrystalline materials, both of which present the same WAXS profile as their unannealed counterparts (**Figure 4.91**, **Annex A14**). The amorphous materials present the characteristic harmonic bands, while the semicrystalline materials exhibit the same two intense, narrow bands at *ca.* 11.4 and 16.5 nm^{-1} as their semicrystalline unannealed counterparts.

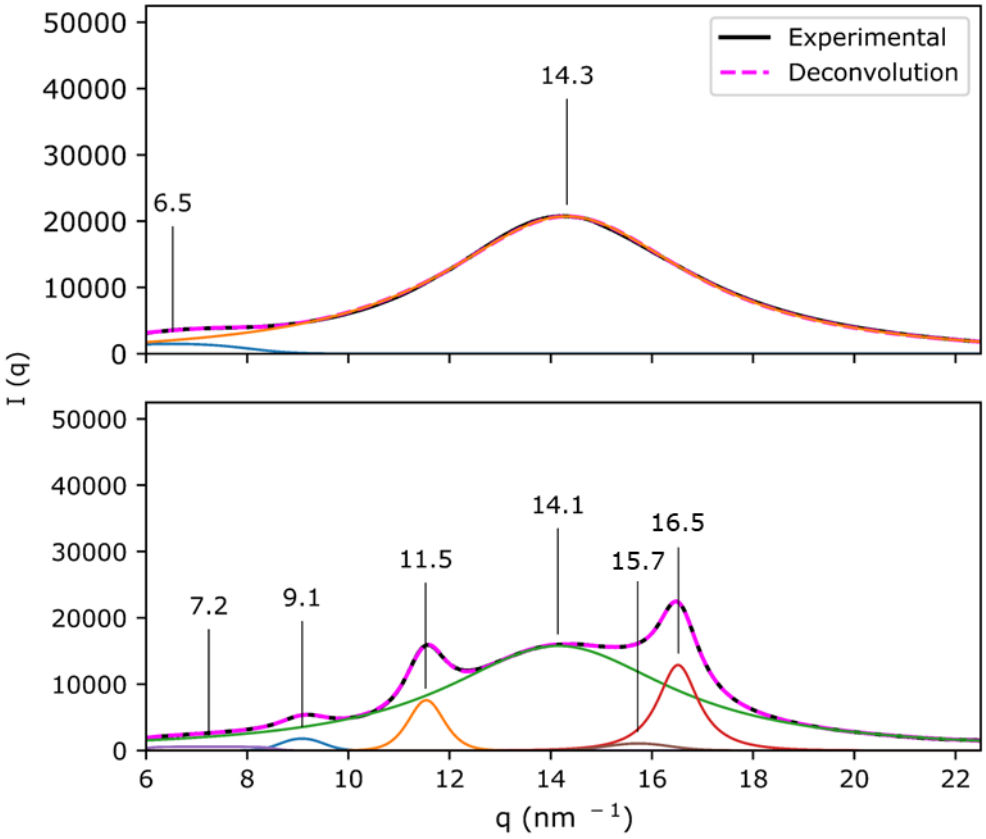

Figure 4.91: Example of the deconvolution of one amorphous (top) and semicrystalline (bottom) annealed FDCAHDO MDI TPUs.

The annealing of the TPUs increases the number of semicrystalline materials. Before their thermal treatment, only two of the FDCAHDO MDI TPUs exhibited any SS crystallisation, while after annealing, all the formulations except for **FDCAHDO 1000 50% MDI** are semicrystalline. Moreover, the degree of crystallisation Φ_C is higher for the annealed materials than for the unannealed samples (**Table 4.32**). This indicates that the annealing process enables the crystallisation of the SS domains by providing the polymers with enough chain mobility to enable the organisation of their SS chain fragments.

Table 4.32: Degree of crystallinity (Φ_C) of the annealed (AN) and unannealed (UnAN) FDCAHDO MDI TPUs

	Φ_C AN	**Φ_C UnAN**
FDCAHDO 1000 10% MDI	0.23	0.17
FDCAHDO 1000 50% MDI	0.00	0.00
FDCAHDO 1500 30% MDI	0.16	0
FDCAHDO 2000 10% MDI	0.18	0.08
FDCAHDO 2000 50% MDI	0.18	0

Similarly, the crystallinity of the PDO TPUs increases after annealing. Both amorphous and semicrystalline PDO materials are obtained after their thermal treatment, while before annealing, all of the PDO polymers were amorphous (**Annex A14**). The same formulations that exhibit a SS melting peak on DSC after annealing are the ones that show narrow peaks on WAXS, namely **IPHTAPDO 1000 50% HDI, IPHTAPDO 2000 30% HDI, IPHTAPDO 2000 50% HDI, FDCAPDO 1000 50% MDI**, and all of the FDCAPDO HDI TPUs. As expected, a higher number of semicrystalline formulations are obtained for the materials arising from HDI and FDCA than from MDI and IPHTA. This indicates that the behaviour regarding the crystallisation capabilities of the materials is maintained before and after annealing. The high chain mobility of the HDI materials and the high SS cohesion strength of the FDCA TPUs induces the highest phase segregation and SS crystallinity.

Although the amorphous PDO TPUs show the same wide bands as their HDO analogous, the WAXS profile of the semicrystalline PDO materials differs from that of the HDO formulations. Rather than the two high-intensity narrow peaks located at *ca.* 11.4 and 16.5 nm found in the semicrystalline HDO polymers, in the PDO materials, a higher number of less intense bands arise at *ca.* 3.9-8.8 and 17.1-17.4 nm^{-1} (**Figure 4.92**). This indicates that the PDO and HDO SS

generate a different crystalline structure, or that at least, the stacking distances between their different polymeric chains differ. If the same assignation as for the HDO materials is followed, the peaks located at higher q can be attributed to the π-π stacking distances and the peaks located at lower q correspond to the spacing between groups of stacked chain fragments. Therefore the π-π stacking distances of the PDO SS are in the order of 3.6-3.7 Å, roughly 0.2-0.3 Å smaller than the HDO ones, while the distance between the PDO stacked chain groups are in the range of 6.8-7.1 Å, 1.2-1.6 Å bigger than their HDO counterpart. The closer π-π stacking distances of the PDO materials than those of the HDO TPUs match with the observations from the odd-even effect, which indicates that the chain packing of the PDO chains is tighter than that of the HDO ones.

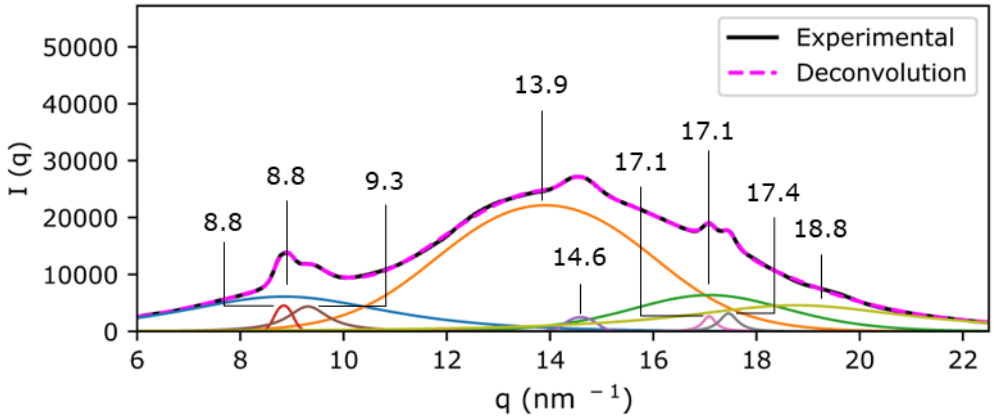

Figure 4.92: Example of the deconvolution of a semicrystalline annealed PDO TPU.

The results from the Φ_C of the PDO TPUs match all the previous observations. Overall, the crystallinity of the SS is bigger for the FDCA and HDI TPUs than for the IPHTA and MDI materials (**Table 4.33**, **Table 4.34**). Moreover, similar Φ_C could be found in both the HDO and PDO TPUs, which indicates that when the materials have enough chain mobility to segregate and order themselves, both formulations have similar reorganisation capabilities. Nonetheless, one notable exception to all these trends is **IPHTAPDO 2000 30% HDI**, which exhibits the biggest crystallinity of all the essayed TPUs.

Table 4.33: Degree of crystallinity (Φ_C) of the annealed IPHTAPDO HDI TPUs.

	Φ_C		Φ_C
IPHTAPDO 1000 10% HDI	0.00	**IPHTAPDO 2000 10% HDI**	0.00
IPHTAPDO 1000 30% HDI	0.00	**IPHTAPDO 2000 30% HDI**	0.33
IPHTAPDO 1000 50% HDI	0.01	**IPHTAPDO 2000 50% HDI**	0.01

Table 4.34: Degree of crystallinity (Φ_C) of the annealed FDCAPDO TPUs.

	Φ_C		Φ_C
FDCAPDO 1000 10% MDI	0.00	**FDCAPDO 1000 10% HDI**	0.17
FDCAPDO 1000 50% MDI	0.05	**FDCAPDO 1000 50% HDI**	0.04
FDCAPDO 1500 30% MDI	0.00	**FDCAPDO 1500 30% HDI**	0.08
FDCAPDO 2000 10% MDI	0.00	**FDCAPDO 2000 10% HDI**	0.02
FDCAPDO 2000 50% MDI	0.00	**FDCAPDO 2000 50% HDI**	0.10

4.3.4.3.1 Overview

The annealing process leads to an increase in the crystallinity of the SS domains, without producing a change in the crystalline structure of the SS crystallites, as reflected by the same peak distribution of the HDO TPUs before and after annealing. A different crystalline structure was identified for the PDO and HDO SS, evidencing the shorter interchain distances of the PDO than of the HDO SS domains. These results correlate with the density measurements, in which the odd-even effect pointed to a closer chain packing of the SS structure in the PDO than in the HDO TPUs.

4.3.4.4 Shape fixity and recovery index

Once the variations in morphology between the annealed and unannealed formulations were established, the shape memory properties of the annealed materials were assessed. The differences in morphology between the annealed and unannealed materials will be employed to rationalise the variations in shape fixity (R_f) and recovery (R_r) between the thermally treated and untreated samples. Both parameters have been measured following the same procedure

used for the unannealed materials, employing three deformation-recovery cycles (**Experimental Section 6.1.12, Annex A15**).

4.3.4.4.1 IPHTAPDO HDI TPUs.

No significant differences can be established between the R_f of the annealed and unannealed IPHTAPDO HDI formulations despite the fact that, in some of the polymers, the annealing process results in a modification of their morphology (**Figure 4.93**). As stated in previous sections, in **IPHTAPDO 2000 30% HDI**, **IPHTAPDO 1000 50% HDI** and **IPHTAPDO 2000 50%** the annealing process results in an increase in the concentration of SS crystallites. Moreover, in **IPHTAPDO 2000 30% HDI** the formation of HS domains through the annealing process was also appreciated. Despite their change in morphology, none of these formulations exhibits any significant change in R_f after annealing. This indicates that the presence of HS domains and SS crystallites has little to no effect on the R_f of the IPHTAPDO HDI materials.

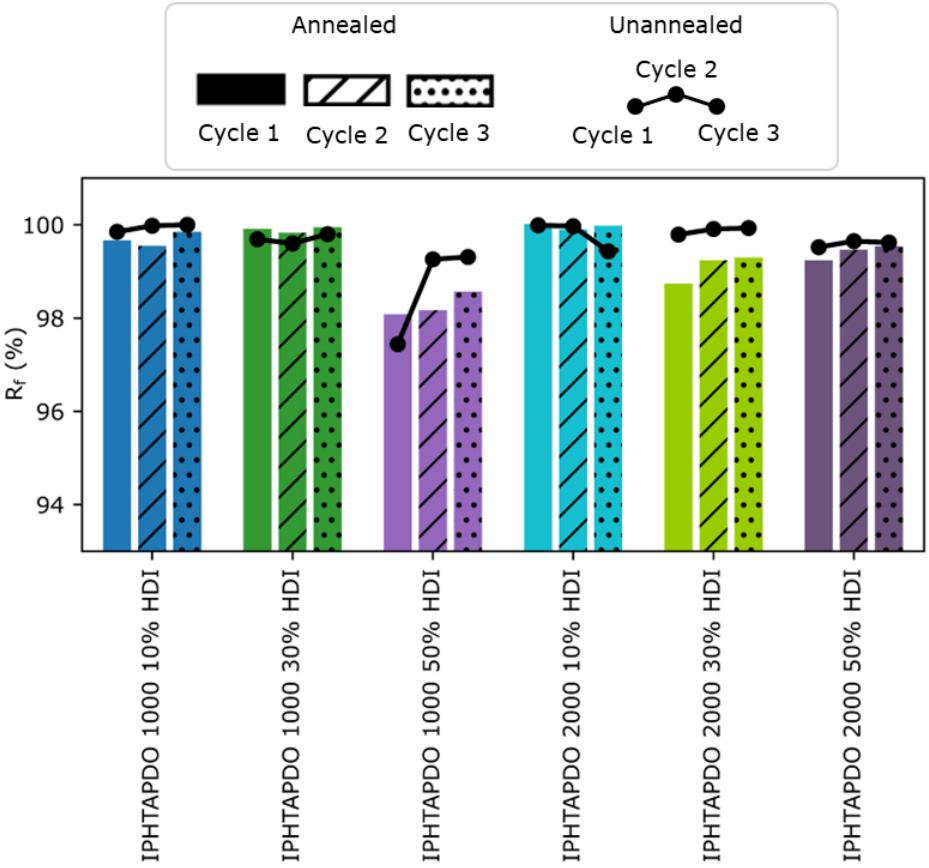

Figure 4.93: Comparison between the R_f of the annealed and unannealed IPHTAPDO HDI TPUs.

A greater variation between the R_r of the annealed and unannealed IPHTAPDO HDI TPUs was observed when compared with R_f (**Figure 4.94**). Three of the formulations, **IPHTAPDO 1000 10% HDI**, **IPHTAPDO 1000 30% HDI** and **IPHTAPDO 2000 10% HDI** suffer a significant decrease in R_r as a consequence of their annealing, while in the other three polymers, **IPHTAPDO 2000 30% HDI**, **IPHTAPDO 1000 50% HDI** and **IPHTAPDO 2000 50%** no significant variation in R_r can be appreciated. Surprisingly, the three formulations that exhibit a change in their R_r after annealing are the ones that do not suffer any modification to their phase segregation or SS crystallinity by the annealing process according to SAXS and WAXS. These results seem to contradict one another since, if the morphology of the materials is maintained through the annealing process, no modification of their properties should be observed. Although no variation in phase segregation or crystallinity could be noted, a change in their structure can be observed by DSC. The T_g of all the IPHTAPDO HDI formulations, including **IPHTAPDO 1000 10% HDI**, **IPHTAPDO 1000 30% HDI** and **IPHTAPDO 2000 10% HDI** increases after annealing. This change in T_g indicates a rearrangement of their amorphous domain, which might be linked to the decrease in R_r. Nonetheless, it is not clear why this change affects only the R_f of some of the formulations.

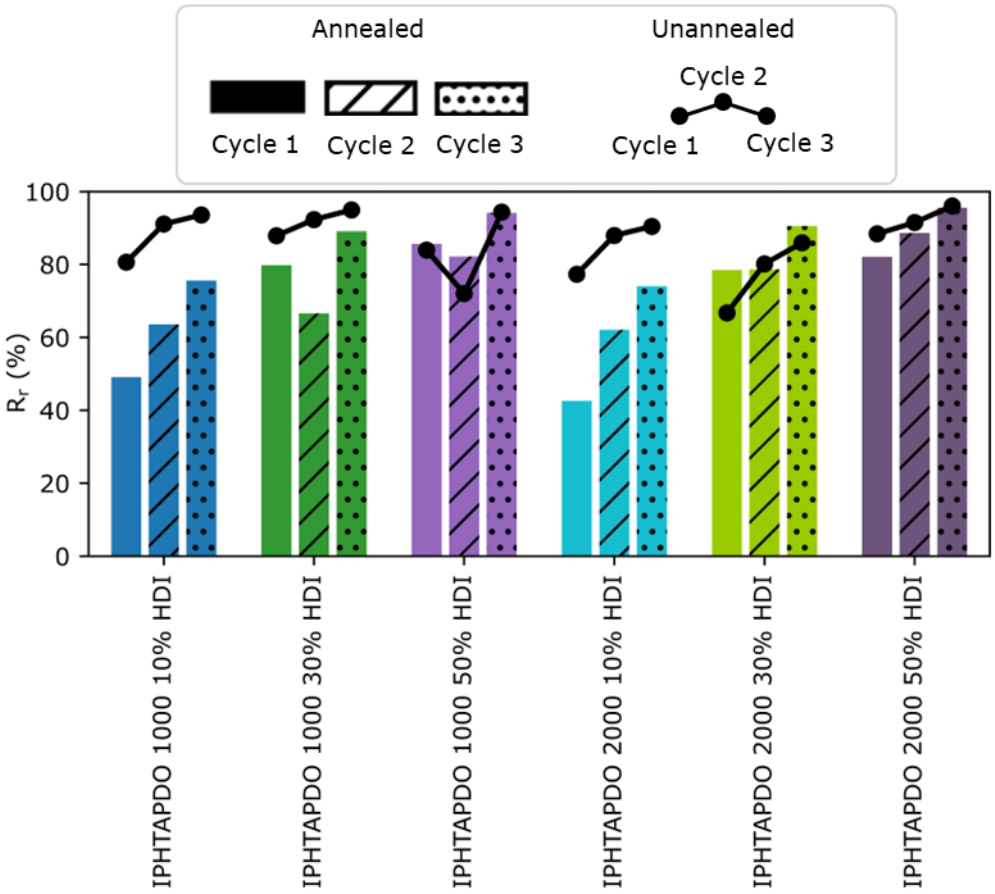

Figure 4.94: Comparison between the R_r of the annealed and unannealed IPHTAPDO HDI TPUs.

4.3.4.4.2 FDCAPDO MDI TPUs

Similarly to the IPHTAPDO HDI TPUs, the annealing of the FDCAPDO MDI formulations results in little variation in their R_f (**Figure 4.95**). This is to be expected since only one of the formulations, **FDCAPDO 1000 50% MDI**, exhibit a significant modification in morphology, generating SS crystallites as a result of the annealing process. Nonetheless, not even this sample shows any considerable modification of R_f.

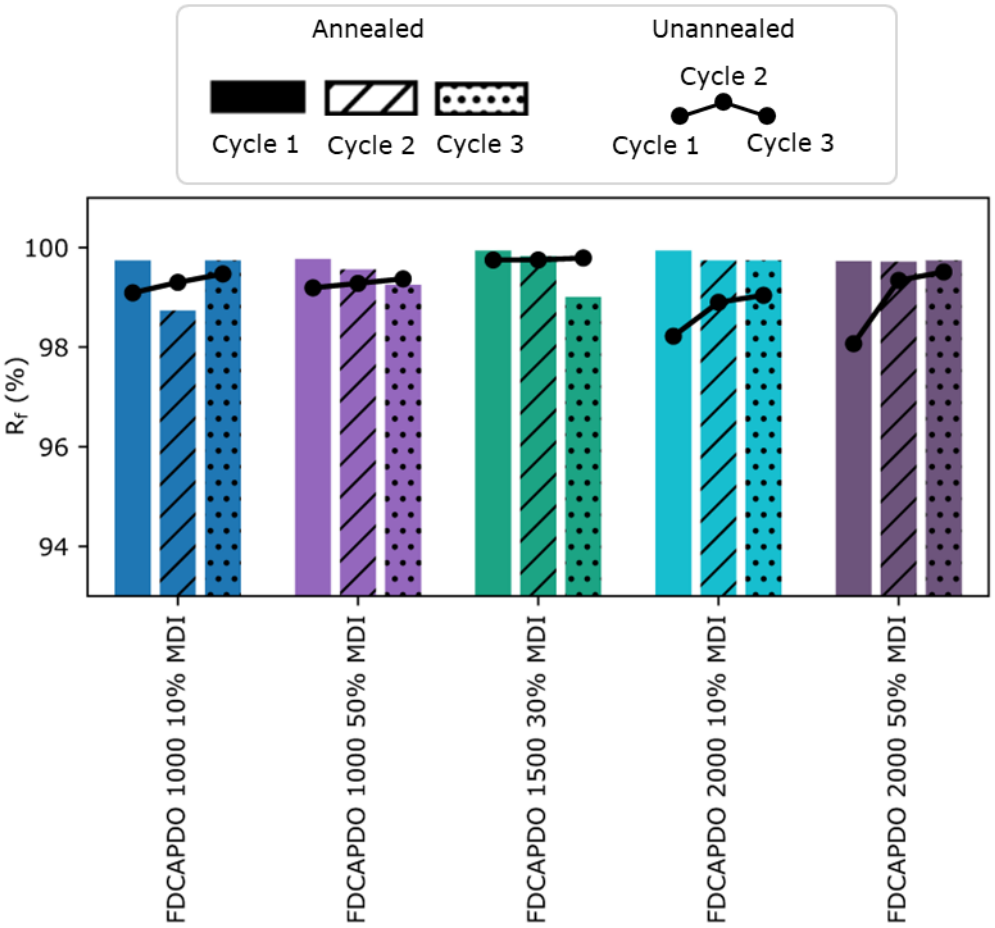

Figure 4.95: Comparison between the R_f of the annealed and unannealed FDCAPDO MDI TPUs.

Contrarily to the R_f results, **FDCAPDO 1000 50% MDI**, exhibits a significant variation in R_r during its first shape memory cycle, decreasing from a R_r of 87% before annealing to 60% after annealing (**Figure 4.96**). This material is the only FDCAPDO MDI formulation that exhibits a variation in its phase morphology during annealing. Therefore, the decrease in R_r seems to be linked to this modification in phase morphology These results are in contradiction to those found for the IPHTAPDO HDI TPUs, for which the formulations that generate SS crystallites through the annealing process are the ones that do not experience a modification of their R_r.

In two formulations, **FDCAPDO 1000 10% MDI** and **FDCAPDO 1500 30% MDI**, a significant decrease of R_r during the 2nd cycle was also observed on the annealed samples (**Figure 4.96**). However, during the 1st and 3rd cycles, quite similar R_r are obtained before and after annealing.

As the changes in morphology after each of the deformation cycles could not be obtained, no rationalisation of this behaviour can be extracted from the data.

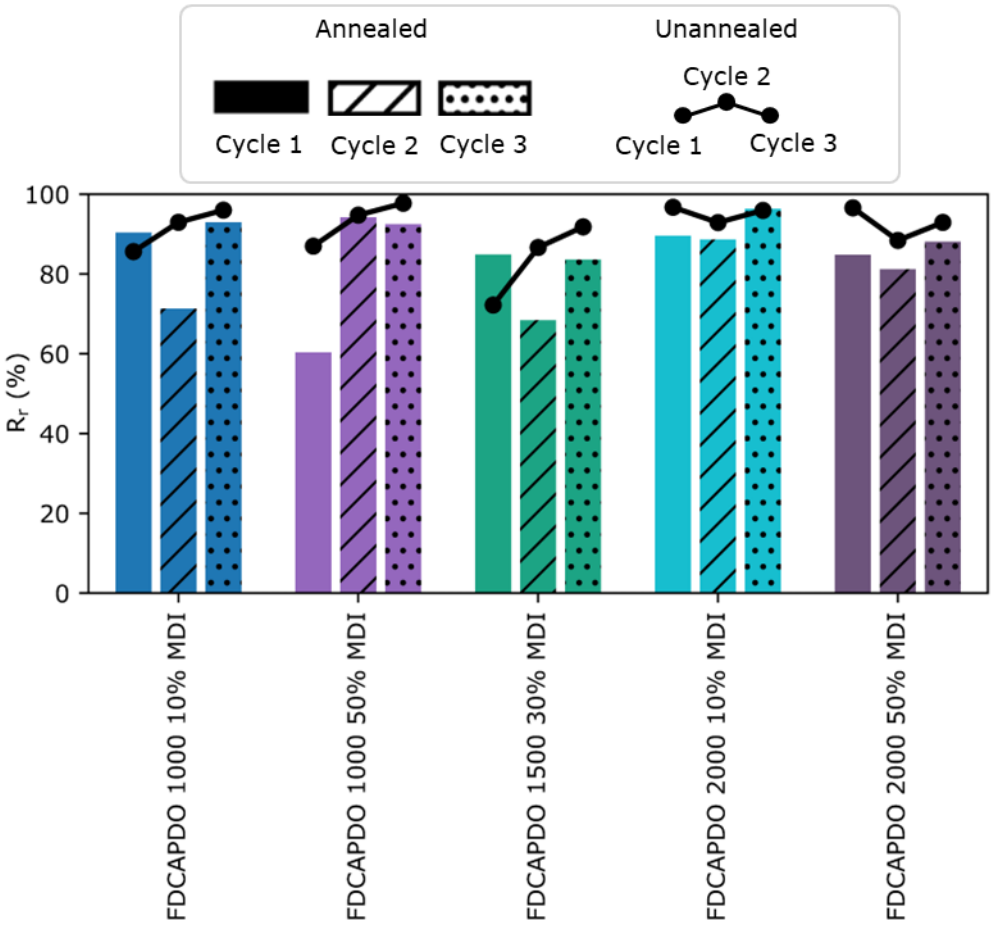

Figure 4.96: Comparison between the R_r of the annealed and unannealed FDCAPDO MDI TPUs.

4.3.4.4.3 FDCAHDO MDI TPUs

As in the two previously discussed TPU families, the annealing of the FDCAHDO MDI materials results in almost no modification to their R_f, even though the morphology of the polymers is modified during the annealing process (**Figure 4.97**).

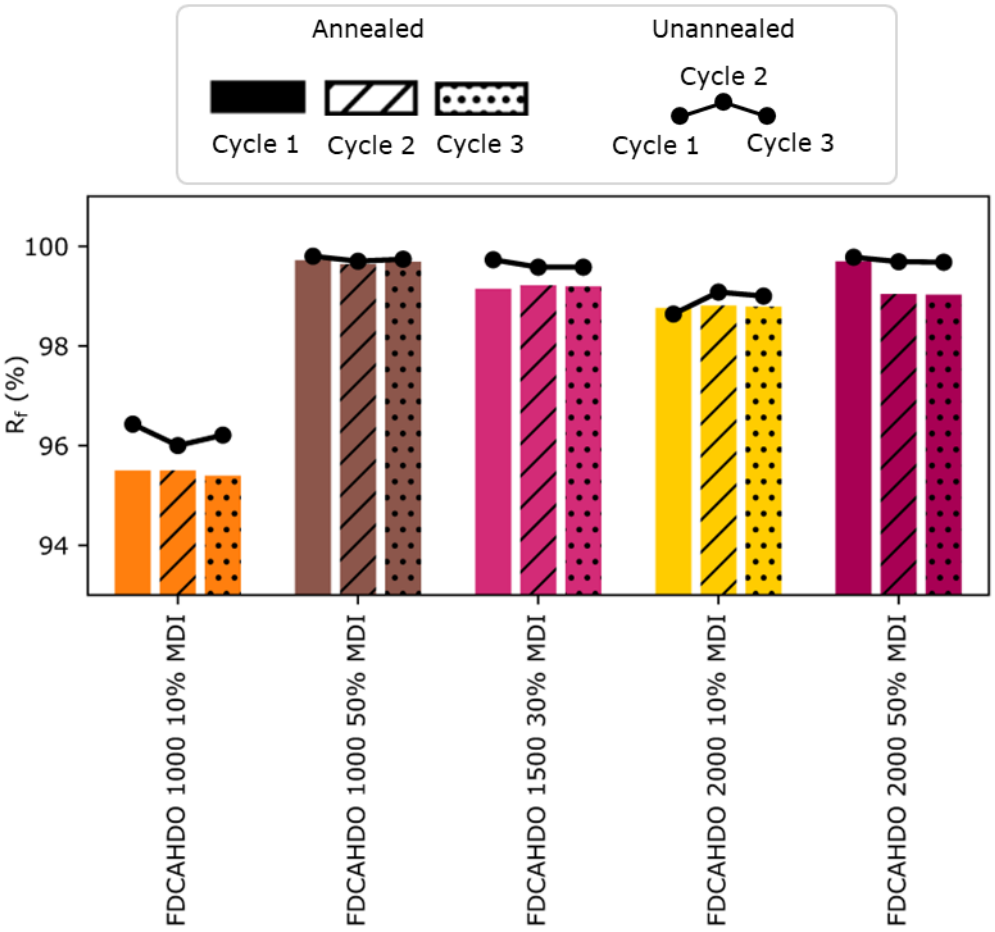

Figure 4.97: Comparison between the R_f of the annealed and unannealed FDCAHDO MDI TPUs.

Overall just a slight decrease in the R_r of the FDCAHDO MDI TPUs was observed after annealing. However, in the first deformation cycle of one of the formulations, **FDCAHDO 1500 30% MDI**, a significant decrease in R_r could be noted (**Figure 4.98**). The variation in morphology between the annealed and unannealed samples of this formulation is not noticeably different from that of the other FDCAHDO MDI TPUs, therefore, the origin behind this stark decrease in R_r cannot be pinpointed.

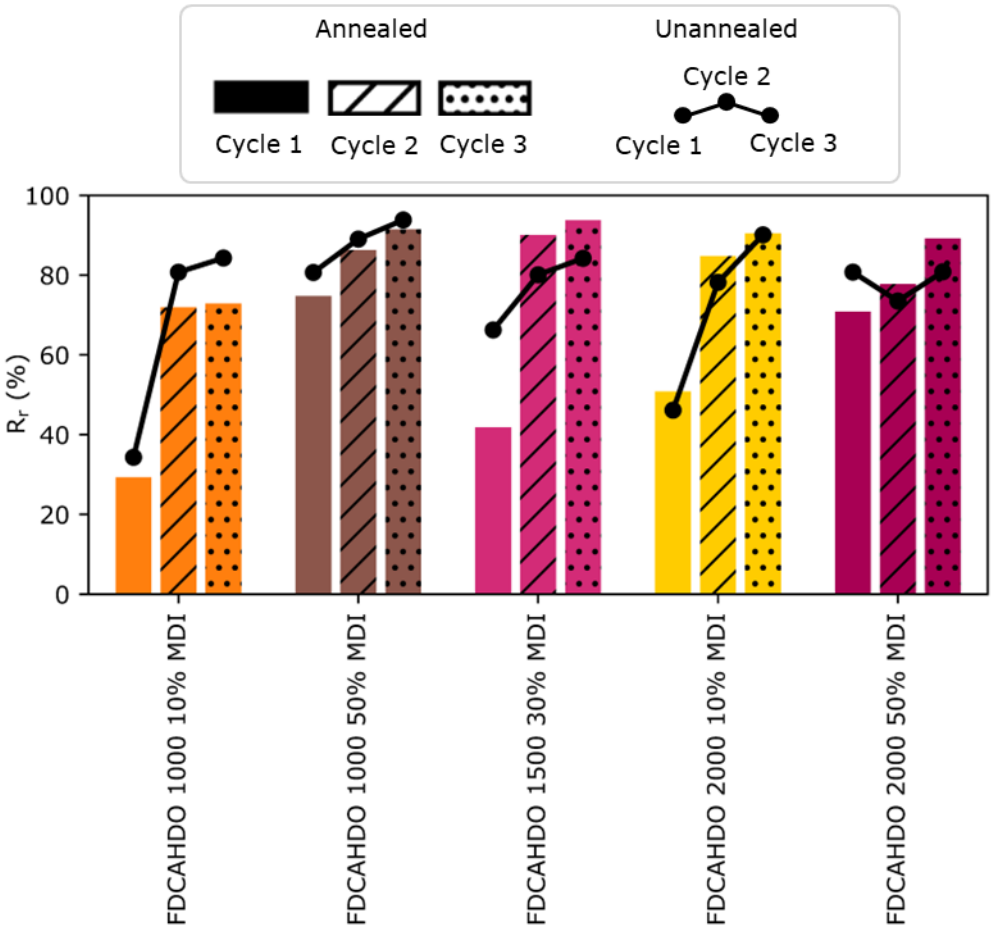

Figure 4.98: Comparison between the R_r of the annealed and unannealed FDCAHDO MDI TPUs.

4.3.4.4.4 FDCAPDO HDI TPUs

Like in all the previously discussed formulations, the annealing of the FDCAPDO HDI materials results in only a slight modification of their R_f, despite the modification of their structure through the annealing process (**Figure 4.99**). The highest change in R_f, amounting to 2%, corresponds to **FDCAPDO 1000 50% HDI**. Nonetheless, this decrease is not significant, so overall, no changes in R_f can be attributed to the annealing process.

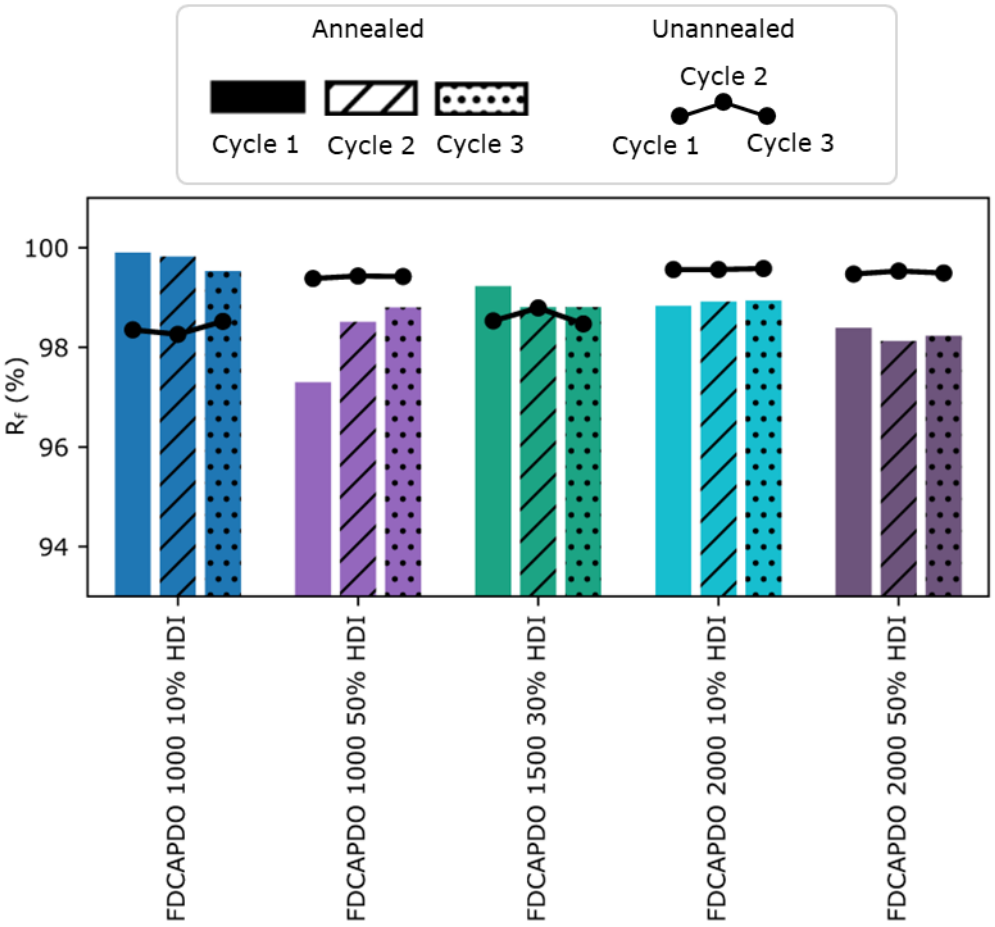

Figure 4.99: Comparison between the R_f of the annealed and unannealed FDCAPDO HDI TPUs.

Following the same trends observed in all of the other studied materials, on the 1st deformation cycle, an overall decrease in R_r results from the annealing process (**Figure 4.100**). However, no correlation between the degree of phase segregation (Φ), the degree of crystallinity (Φ_C) or the variation in T_g and the reduction in R_r could be established. Therefore, this decrease in R_f could not be directly correlated to either the changes in concentration of the HS domains or SS crystallites or to the decrease in the chain mobility of the materials after their annealing.

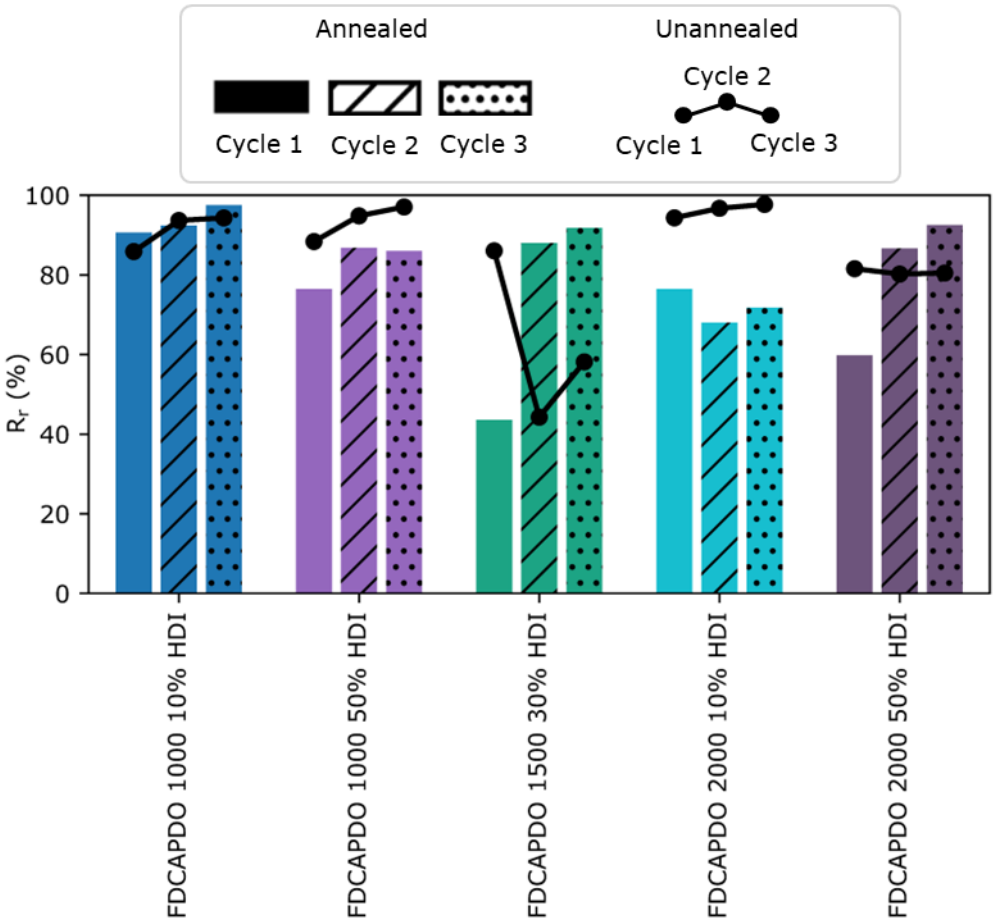

Figure 4.100: Comparison between the R_r of the annealed and unannealed FDCAPDO HDI TPUs.

4.3.4.4.5 Overview

The application of annealing on the materials caused little modification to their R_f, demonstrating that this parameter has little dependence on the phase morphology of the TPUs. Contrarily, an overall reduction of their R_r as a consequence of the annealing process was noted. However, this decrease in R_r could not be directly pinpointed to the modification of any of the morphological parameters during annealing. This might indicate that there are a lot of parameters that simultaneously modify the R_r of the TPUs. Therefore further studies are required to understand the effect that each of them has on R_r.

4.3.4.5 Actuation strength

Continuing with the study of the annealed materials, the impact that the annealing process has on the recovery stress (σ_r) and energy density (E_ρ) of the materials was assessed. Both parameters were measured following the same procedure as for the unannealed samples (**Experimental Section 6.1.10.2**). Moreover, for the materials with a R_r below 80%, R_r rather than their elongation at a 90% stress (ε_r) was employed to calculate E_ρ. The full strain/stress curves can be found in **Annex A16** and **A17**.

4.3.4.5.1 IPHTAPDO HDI TPUs

The annealing of the IPHTAPDO HDI TPUs results in little to no modification of their morphology. Accordingly, little variation could be observed between the σ_r of the annealed and unannealed samples (**Figure 4.101**). Only **IPHTAPDO 2000 30% HDI**, which transitions from an amorphous unsegregated material to a semicrystalline polymer after annealing, exhibiting HS domains and SS crystallites, shows any significant change to its σ_r after the annealing process. These results match with the previous hypothesis stating that the presence of HS domains increases the σ_r of the materials, as the number of physical crosslinks and therefore, the tension between the polymeric chains increases. Surprisingly, the polymer with the highest σ_r is not **IPHTAPDO 2000 30% HDI**, but rather **IPHTAPDO 1000 50% HDI**, which does not exhibit phase segregation nor SS crystallinity by SAXS or WAXS. However, by DSC, **IPHTAPDO 1000 50% HDI** does exhibit a HS melting transition, with an enthalpy higher than the one observed for the same melting transition of **IPHTAPDO 2000 30% HDI**. This seems to indicate that the **IPHTAPDO 1000 50% HDI** formulation contains a higher concentration of HS domains than the **IPHTAPDO 2000 30% HDI** polymer after annealing, but that their size is either too big or too small to be observed as a peak in the Fourier region by SAXS. This high number of HS domains is what produces the higher σ_r of the **IPHTAPDO 1000 50% HDI** polymer in comparison with the **IPHTAPDO 2000 30% HDI** polymer.

The higher σ_r of **IPHTAPDO 2000 30% HDI** after annealing is not translated into an increase of its E_ρ, as the annealing process reduces the R_r of the polymer, resulting in a material capable of exerting a lower mechanical work (**Figure 4.102**). Overall, a slight decrease of the E_ρ of the materials was observed as, in general, all of them experienced a decrease of their R_r to below 80%.

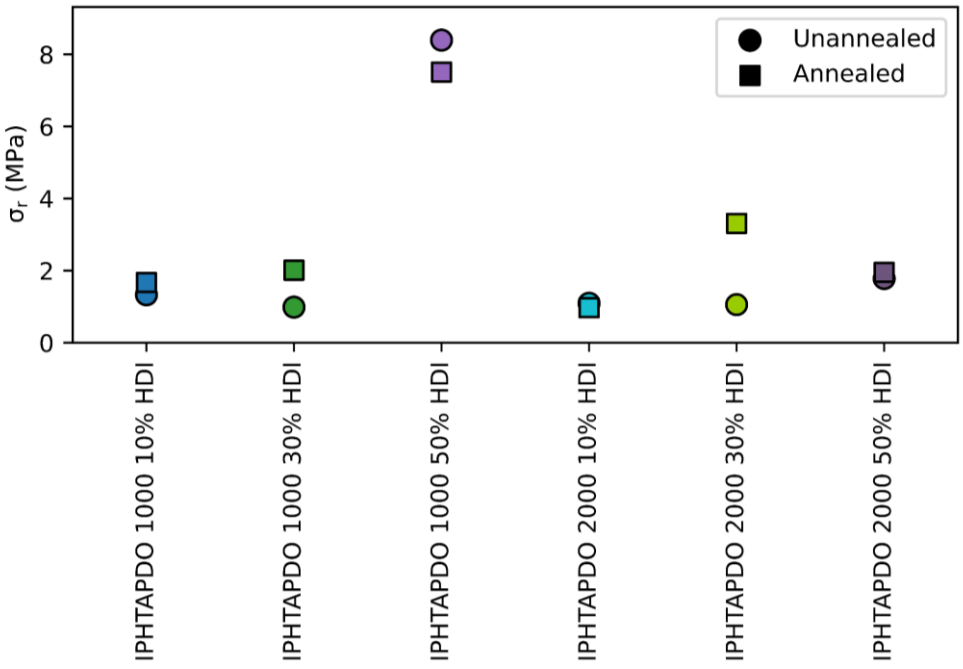

Figure 4.101: Comparison between the σ_r of the annealed and unannealed IPHTAPDO HDI TPUs.

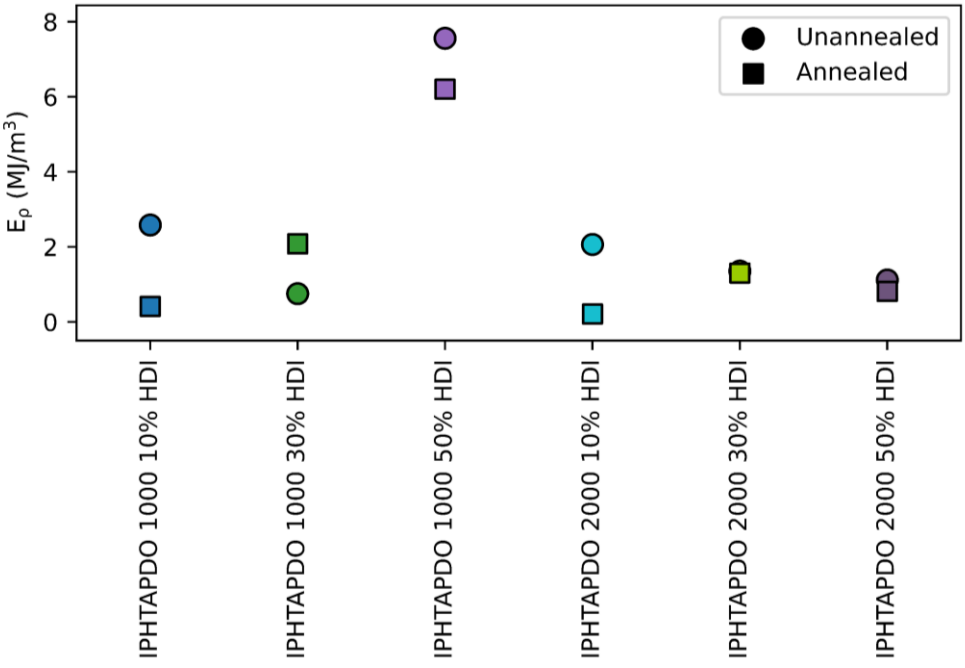

Figure 4.102: Comparison between the E_ρ of the annealed and unannealed IPHTAPDO HDI TPUs.

4.3.4.5.2 FDCAPDO MDI TPUs

The FDCAPDO MDI TPUs show a higher variation of σ_r between the annealed and unannealed polymers than their IPHTAPDO MDI counterpart, especially for the materials with a polyester M_n of 1000 g/mol (**Figure 4.103**). The higher σ_r of **FDCAPDO 1000 50% MDI** can be explained by its increase in crystallinity, as the material evolves from an amorphous polymer to a semicrystalline one through the annealing process. However, no modification of the structure of **FDCAPDO 1000 10% MDI** as a consequence of annealing was observed by either SAXS, WAXS or DSC, making it impossible to determine the origin of its increase in σ_r.

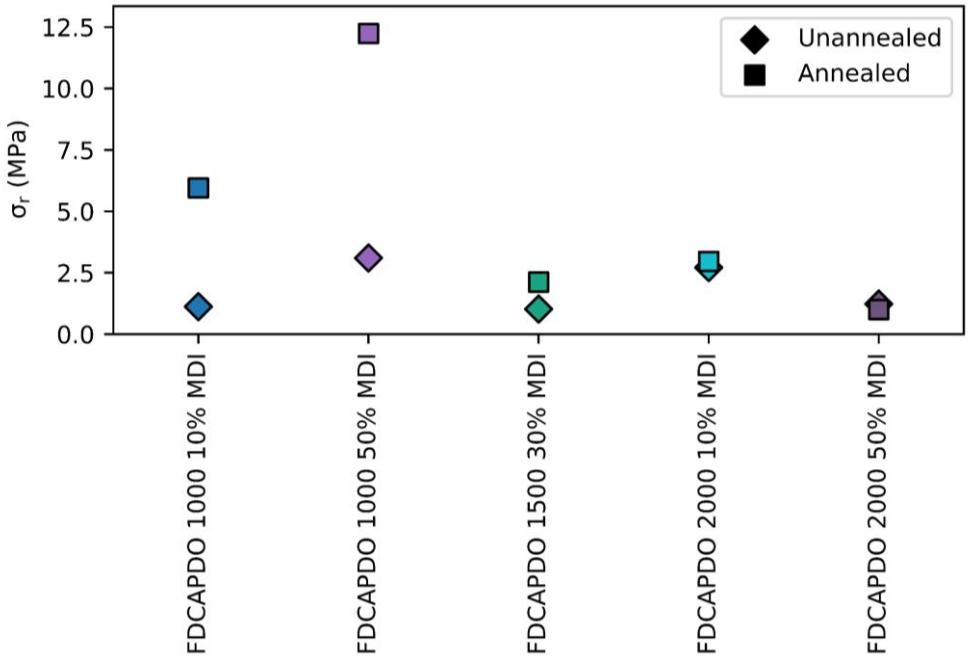

Figure 4.103: Comparison between the σ_r of the annealed and unannealed FDCAPDO MDI TPUs.

An increase in the E_ρ of the **FDCAPDO 1000 10% MDI** and **FDCAPDO 1000 50% MDI** formulations was also observed after annealing (**Figure 4.104**). However, in **FDCAPDO 1000 50% MDI**, this increase was lower than for σ_r since this formulation experiences a reduction of its shape recovery capabilities as a consequence of the annealing process.

Surprisingly, **FDCAPDO 1500 30% MDI** experienced a huge increase in E_ρ after annealing. This surge in E_ρ is derived from the higher ultimate elongation of the annealed material in comparison to the unannealed sample, which increases from 73 to 585 %.

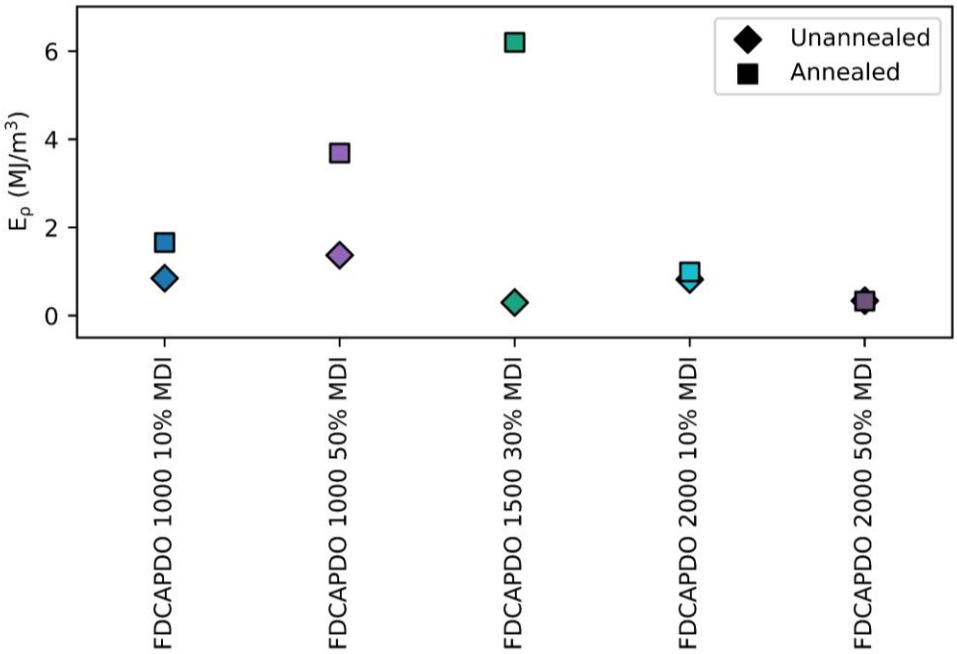

Figure 4.104: Comparison between the E_p of the annealed and unannealed FDCAPDO MDI TPUs.

4.3.4.5.3 FDCAHDO MDI TPUs

A high variation of σ_r before and after the annealing of the FDCAHDO MDI TPUs could be observed, with all of the annealed samples exhibiting higher σ_r values than their unannealed counterparts (**Figure 4.105**). This increase in σ_r is to be expected, as all of the materials gained HS domains and SS crystallites during their thermal treatment. Moreover, the formulation which exhibits the lowest increase in σ_r, **FDCAHDO 2000 10% MDI**, is the only material in which phase segregation was already observed before its annealing. Although its SS crystallinity increases by 10% during annealing, just a 2% gain in its HS domain concentration resulted as a consequence of the thermal treatment of the material. This timid increase in HS domain concentration agrees with the relatively small increase in σ_r that **FDCAHDO 2000 10% MDI** experiences after its annealing.

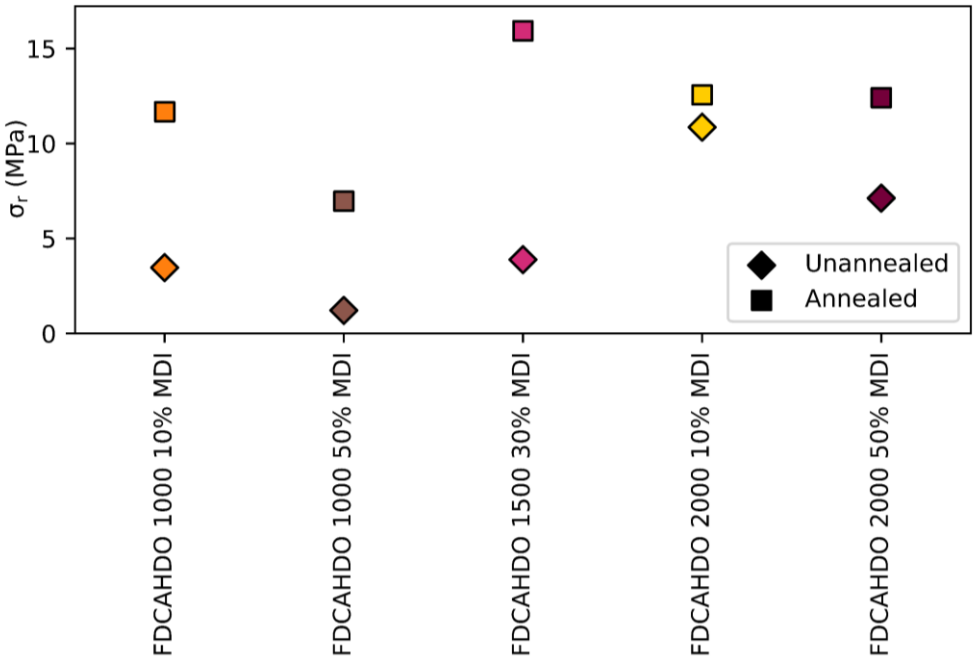

Figure 4.105: Comparison between the σ_r of the annealed and unannealed FDCAHDO MDI TPUs.

The increase in σ_r through annealing is mirrored in their E_ρ behaviour (**Figure 4.106**), with **FDCAHDO 2000 10% MDI** being the formulation that exhibits the smallest increase in E_ρ. Although some of the FDCAHDO MDI TPU materials exhibit a decrease in their R_r as a consequence of their thermal treatment, these polymers already presented low R_r to begin with, so the decrease in their mechanical work as a consequence of their lower shape recovery abilities is less marked that in the prior two TPU families.

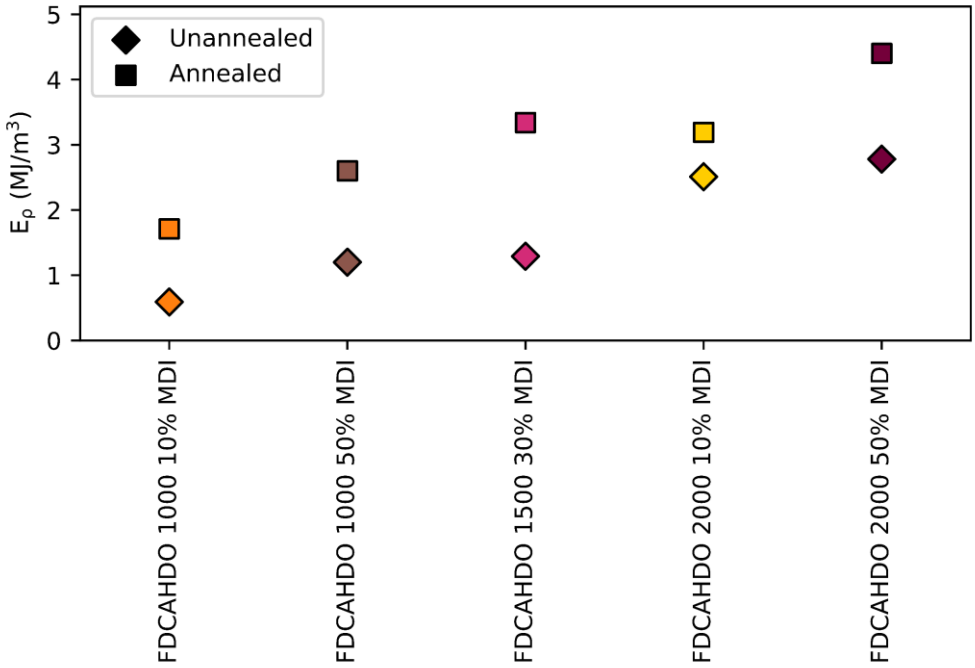

Figure 4.106: Comparison between the E_ρ of the annealed and unannealed FDCAHDO MDI TPUs.

4.3.4.5.4 FDCAPDO HDI TPUs

In the FDCAPDO HDI TPUs, annealing has a similar effect as in the FDCAHDO MDI polymers, with most of the formulations exhibiting an increase of their σ_r after their thermal treatment (**Figure 4.107**). This rise in σ_r is associated, as in the previously discussed materials, with an increase in the phase segregation of the formulations. This can be clearly demonstrated from the behaviour of **FDCAPDO 2000 10% HDI** which is the only FDCAPDO HDI polymer that exhibits a decrease of its HS domain concentration by DSC. In this formulation, the annealing process produces a decrease in σ_r. This clearly shows that the HS domain concentration is the crucial parameter to obtaining high σ_r.

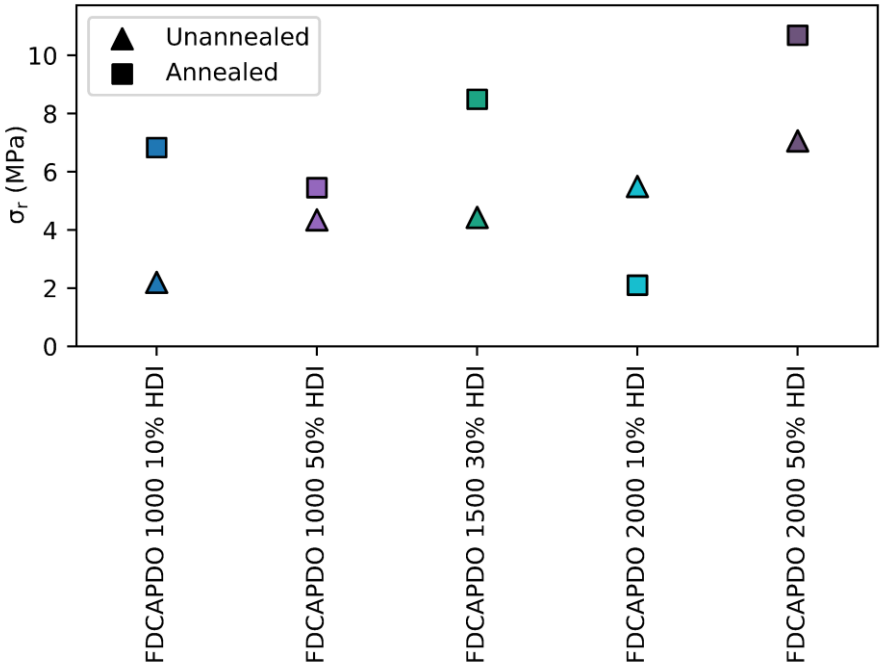

Figure 4.107: Comparison between the σ_r of the annealed and unannealed FDCAPDO HDI TPUs.

The E_ρ behaviour of the FDCAPDO HDI formulations follows the same trends as those of all the other annealed TPUs. Those materials which experience a drop in their R_r after their thermal treatment suffer a reduction of their E_ρ while the other formulations show an increase in their E_ρ as a result of annealing (**Figure 4.108**).

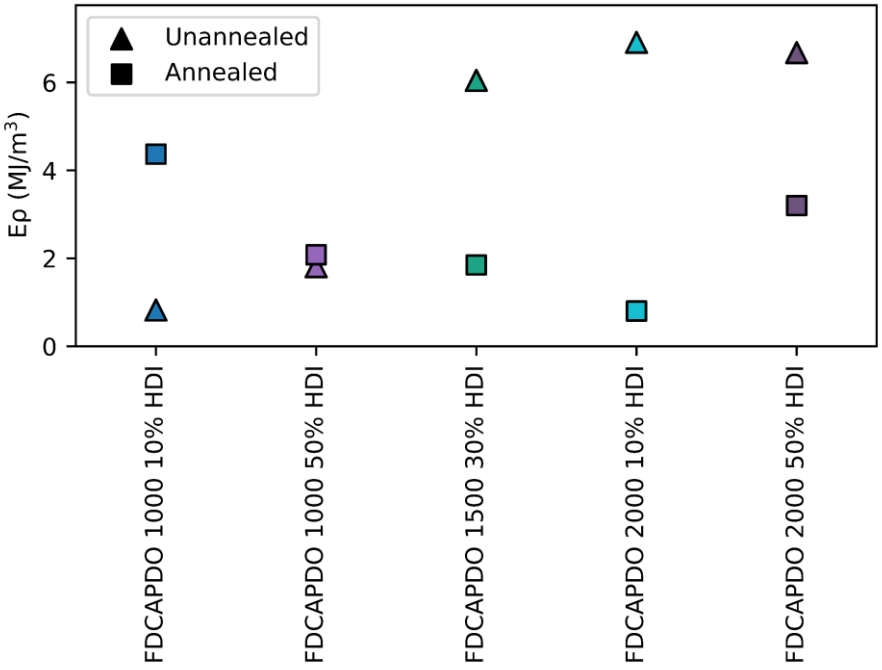

Figure 4.108: Comparison between the E_ρ of the annealed and unannealed FDCAPDO HDI TPUs.

4.3.4.5.5 Overview

The differences in σ_r and E_ρ between the annealed and unannealed materials follow two different behaviours. In materials in which the annealing process results in an increase in their phase segregation a rise in σ_r can be observed as a consequence of the annealing process, while those materials that do not exhibit any change in morphology show no significant σ_r variation. On the other hand, overall the increase in E_ρ of the formulations which experience a change in their morphology through annealing is less marked than that of σ_r. The annealing process reduces the shape recovery capabilities of the TPUs. Therefore, the work that the materials are capable of performing decreases.

Chapter 5: Final Remarks and General Conclusions

This chapter encompasses the different accomplishments of this PhD dissertation and details the general conclusions that can be gathered from them.

In this work, an extensive number of thermoplastic polyurethanes (TPUs) formulations containing biobased 2,5-furandicarboxylate polyesters (FDCA TPUs) and petrochemical isophthalate polyesters (IPHTA TPUs) were successfully synthesised. Polyesters of 1,3-propanediol (PDO) and 1,6-hexanediol (HDO) were prepared with both diacids with a M_n range of 1000-2000 g/mol and introduced into TPUs. These TPUs were synthesised with two different diisocyanates, methylene diphenyl diisocyanate (MDI) and hexamethylene diisocyanate (HDI), allowing the study of the materials under a wide array of compositions. The mechanical properties of these materials are quite exceptional, allowing, amongst others, the obtention of TPUs with high hardness but low diisocyanate content and of shape memory polymers (SMP) with outstanding actuation strength, overcoming those of the current state-of-the-art. In the case of the FDCA TPUs, this opens the door toward the generation of a novel family of functional products with a reduced carbon footprint, owing to the renewable origin of 2,5-furandicarboxylic acid.

Although the specific conclusions of each of the explored properties of the materials can be found in each of their corresponding sections, some general conclusions that encompass all the studies carried out in this dissertation can be drawn.

Overall, the properties of the studied TPUs depend on just one factor, which are the supramolecular interactions present in the materials. These supramolecular interactions govern all of the characteristics of the materials, from their microphase morphology and chain mobility to their mechanical and shape memory properties. These supramolecular interactions can be

divided into two groups, the cohesion forces within each of the domains, hard segment (HS) and soft segment (SS), and the interactions between them. As a general trend, strong cohesion forces result in polymers with a high segregation and crystallisation capability, while strong interactions between the phases inhibit the segregation process, limiting the crystallinity of the materials. The degree of phase segregation of the materials is responsible for many of their mechanical properties and therefore, the factors that reduce this phase segregation produce materials with worst mechanical properties. Accordingly, the low interaction of the aliphatic HDI moieties from the HS with the highly aromatic SS domains results in materials with a high phase segregation and therefore, excellent mechanical properties, namely, tensile strength, and actuation strength. Likewise, the high cohesion forces of the SS containing FDCA moieties induce the segregation of the polymers, resulting in polymers with outstanding mechanical properties.

All of these findings have been achieved thanks to the DOE approach employed for the selection of the formulations that were to be studied during this work, demonstrating the utility of employing systematic approaches to evaluate the factors that affect the properties of polymers. Moreover, a deep understanding of the effect that each of the monomers has on the morphology and properties of the materials has been reached thanks to the complementary use of computational tools and experimental data. The use of both simple linear regressions and more complex density functional theory (DFT) or spectral modelling (small-angle X-ray scattering) has opened the door to a more in-depth exploration of the materials, demonstrating the usefulness of the hybrid computational-experimental approach in the study of polymers.

Chapter 6: Experimental Section

The specific methods, equipment, and experimental procedures employed during this study are summarised in this chapter.

6.1 Instrumentation and operation proceeding

6.1.1 Nuclear magnetic resonance (NMR)

All NMR spectra have been recorded at *Servei de Resonància Magnètica Nuclear* at UAB on 4 different spectrometers: Bruker Ascend 300 MHz, Bruker Avance DPX 360 MHz, Bruker Avance III 400 MHz and Bruker Ascend 400 MHz.

^{1}H NMR spectra were referenced by employing the chemical shifts of the residual non-deuterated solvent signal.[278] ^{13}C{^{1}H} NMR spectra were referenced employing the chemical shifts of the solvent.[278]

All ^{1}H NMR spectra were recorded with a delay time between pulses of 10 seconds to ensure the proper quantification of the nuclei required for the accurate determination of the polymer's M_n.

NMR spectra were performed at 298 K for the case of all polymers except for the FDCAPDO polyesters, which were recorded at 393 K to increase their solubility.

The samples were prepared by dissolving 10-50 mg of each product in the corresponding deuterated solvent (either $CDCl_3$ or DMSO-d_6). In the case of the TPUs, the solvent-polymer mixtures were subjected to 3-10 h of ultrasounds to achieve a homogeneous solution.

6.1.2 Gel permeation chromatography (GPC)

GPC were performed on a Waters chromatograph fitted with a Waters 1515 Isocratic HPLC pump, a Waters 2414 Refractive Index Detector, a Waters 2707 Autosampler, a Waters GPC/SEC 50 x 7.5 mm Guard Column and two Phenomenex Phenogel™ 5 µm 10E4 Å 300 x 7.8 mm columns employing THF as eluent.

The equipment was calibrated employing Agilent EasyVial GPC polystyrene 12-point calibration standards with M_n in the ranges of 1140 - 348500 g/mol.

All samples were prepared by mixing 0.1000 g of polymer in 5 mL of *N,N*-dimethylacetamide, heating the mixtures to 50 ^oC until all the TPU was dissolved (2-4 h), adding 5 mL of THF, and filtering 1 mL of the resulting solution through a Scharlau PFTE 30 mm, 0.45 µm syringe filter.

6.1.3 Infrared spectrometry (IR)

IR spectra were recorded at *Servei d'Anàlisis Quimica* at UAB in a Bruker IT Tensor 27 spectrometer fitted with an ATR Specac Golden Gate single reflection diamond ATR system with a resolution of 4 cm^{-1} in the range of 4000-600 cm^{-1} accumulating 16 scans by sample.

6.1.4 Rotatory viscometry

The viscosity of the polyesters was analysed on a Brookfield RST Rheometer. To perform the measurements, the samples were heated to 140 °C and placed in the equipment's heating plate until the temperature was stabilised, upon which the measurement was started.

6.1.5 Polymer shredding

The shredding of the TPU materials was performed on a Mateu y Solè mecanofil shredder fitted with a 1 cm mesh filter.

6.1.6 Polymer injection

The polymers were formed into 8 x 9 x 0.25 cm plates on an Engel victory 50 injector. To obtain the plates, the shredded polymer was fed into the equipment, which melted them at a specific temperature for each polymer before the injection (**Annex A18**). The polymers were fed into the equipment with a 40% dosage speed, a counterpressure of 5 bar, an injection speed of 40 mm/s, a post pressure of 35 bar, a post pressure time of 40 seconds and a cooling time of 20 s.

After their injection, all the materials were stored for at least 1 week under 21 °C before any of their analysis.

6.1.7 Hardness testing

Shore D hardness of the materials was measured on a ZwickRoell Postfach 4350 D-7900 Ulm connected to a ZwickRoell H04.3150 apparatus. The durometer was calibrated using 40 Shore D metal discs.

The hardness of the different materials was measured using different areas of three different injected plates for each polymer and with a total number of ten measurements by polymer at a controlled temperature of 21 °C.

6.1.8 Density measurement

The density of the samples was measured with a Mettler Toledo XSR105 balance equipped with a Mettler Toledo XPR-S density kit using distilled water as liquid phase.

For each TPU, five injected plate pieces of around 0.1-0.2 g were cut and measured to obtain the density of the materials.

6.1.9 Differential scanning calorimetry (DSC)

DSC were measured on a Mettler Toledo DSC 3+ calorimeter coupled to a cooling system under a N_2 inert atmosphere. The samples were prepared by weighing 3-10 mg of polymer in aluminium crucibles. Two different cooling systems were employed, one that allowed a minimum temperature of -50 °C and another one that could cool down to -75 °C. Therefore, two different minimum temperatures were employed depending on the equipment.

The following temperature program was employed for the sample's measurement:

- 1st Cooling: 25 °C → -75 or -50 °C at a rate of - 10 °C/min.
- 1st Heating: -75 °C → 200 °C at a rate of 10 °C/min.
- 2nd Cooling: 200 °C → -75 or -50 °C at a rate of - 10 °C/min.
- 2nd Heating: -75 or -50 °C → 200 °C at a rate of 10 °C/min.
- 3rd Cooling: 200 °C → 25 °C at a rate of - 10 °C/min.

For the annealing test, the same conditions but applying only the 1st Cooling, 1st Heating and 3rd Cooling cycles were employed.

6.1.10 Dynamometer

Tensile tests were recorded in two different pieces of equipment, a Zwick/Roell Z010 dynamometer and another Zwick/Roell Z010 dynamometer fitted with both a Zwick/Roell lightXtens and a Zwick/Roell BTE-TC02.00 temperature chamber. The samples were prepared by cutting dumbbell shapes from the injected plates with a press following ISO37. For each TPU, at least 2 dumbbells from 2 different plates were employed for the analysis. Depending on the test, tensile strength or actuation strength, different methods were employed.

6.1.10.1 Tensile testing

For the tensile strength, methods employing two different elongation speeds, 5 and 200 mm/min were used. In both methods, the clamp distance was 4 cm, and the initial measurement distance was 2 cm. The analyses were carried out at a temperature of 21°C. Recovery stress and Energy density.

6.1.10.2 Actuation strength

To obtain the recovery stress (σ_r) and energy density (E_ρ), first, the ultimate tensile strength of the materials at 20 °C above their T_g has been determined. To that avail, first, the materials were introduced into the heating chamber of the dynamometer at 20 °C above their T_g and equilibrated for 10 minutes. Afterwards, the materials were elongated using a strain rate of 50 %/min, employing a clamp distance of 4 cm and an initial measurement distance of 2 cm.

Once the ultimate tensile strength was determined, the σ_r and E_ρ of the materials were measured. First, the materials were introduced into the heating chamber of the dynamometer at 20 °C above their T_g and equilibrated for 10 minutes. Then, the polymers were elongated at a rate of 50 %/min until they reached 90% of their ultimate tensile strength. Once this value was reached, the elongation was stopped, and the materials were allowed to relax under fixed elongation (ε_r) for 5 minutes. The strain of the material after these 5 minutes was considered as their σ_r, while the E_ρ was calculated from the area below the interpolated triangle made from the ε_r and σ_r of the materials, and zero.

6.1.11 X-ray scattering

Both small-angle X-ray scattering (SAXS) and wide-angle X-ray scattering (WAXS) have been recorded simultaneously at the NCD-SWEET beamline BL11 at the ALBA Synchrotron facility. The data was collected using an X-ray energy of 12.40 keV (λ=0.9999 Å) and two different detectors, one for SAXS and another one for WAXS. For SAXS, a Pilatus 1M detector from

Dectris (981 x 1043 pixels, 172 x 172 μm^2 each) mounted orthogonal to the beam path at a distance of 6.677 m from the sample was employed. For WAXS, a LX255-HS detector from Rayonix (960 x 2880 pixels, 88 x 88 μm^2 each) mounted orthogonal to the beam path at a distance of 112.0 mm from the sample was used. The SAXS signal was calibrated employing silver behenate, while chromium(III) oxide was used for the WAXS signal calibration.

6.1.12 Dynamic mechanical analyser (DMA)

Shape memory assays were performed in a TA DMA Q800 coupled to a TA ACS-3 cooling system. The measurements were done on a film clamp with injected plate samples cut to 8 x 0.1 x 0.1 mm size samples.

The shape memory assays were performed with the following method:

- Step 1: Heat the sample to T = T_g + 20 °C.
- Step 2: Stabilise temperature for 30 min.
- Step 3: Elongate the sample to 100%.
- Step 4: Isothermal for 5 min.
- Step 5: Cool down the sample to T = T_g - 20 °C at a rate of 10 °C/min.
- Step 6: Isothermal for 5 min.
- Step 7: Decrease force to 0.001 N.
- Step 8: Isothermal for 5 min.
- Step 9: Increase temperature to T = T_g + 20 °C at a rate of 10 °C/min.
- Step 10: Isothermal 30 min.
- Step 11: Repeat from step 3 two times.

6.1.13 Gas chromatography-mass spectrometry (GC-MS)

GC-MS were measured at *Servei d'Anàlisis Química* at UAB on an Agilent Technologies 6890 chromatograph with a Hewlett-Packard 5973 detector and a Phenomen 7HG-G002-11 capillary column. An injection volume of 0.50 μL with a 1:1 split ratio and an injection temperature of 280 °C were selected for the analysis. Moreover, an oven initial temperature of 35 °C and a heating ramp of 10 °C/min with a maximum temperature of 280 °C were employed.

6.2 Experimental procedures

6.2.1 Acidity index

The determination of the acidity index (IA) was carried out with three samples and two blanks. For the samples, in three 250 mL Erlenmeyers, 100 mL of either DCM (IPHTAPDO, IPHTAHDO, IPHTABDO, and FDCAHDO) or DMSO (FDCAPDO) and 0.5-1.5 g of polymer were added and dissolved. In the case of FDCAPDO, the mixture was heated to 100 °C to obtain a homogeneous solution. For the blanks, in two additional Erlenmeyers, the same procedure but without the addition of the samples was carried out.

Once all the samples and blanks had been prepared, a titration employing phenolphthalein as indicator was performed with a standardised 0.05 M KOH_{MeOH} solution onto the samples and blanks.

The final IA value, given as mg KOH/g polymer was calculated by subtracting the titration volumes of the blank from those of the sample (**Equation 6.1**).

$$IA = \frac{(\text{titration volume sample} - \text{titration volume blank}) \times M\ KOH \times M_w KOH}{\text{g polymer}}$$

Equation 6.1: IA calculation from titration with a KOH solution.

6.2.2 Hydroxyl index

Three ground-glass neck 250 mL Erlenmeyer, containing 0.5-1.5 g of polymer and 100 mL of DCM and an additional two Erlemneyers with only the solvent were prepared. Then, 2.00 mL of 1-methylimidazole and 10.0 mL of an acetylating solution (40 mL of acetic anhydride in 0.5 L of THF) were added to both the samples and blanks. The Erlenmeyer were fitted to Dimroth condensers and heated to reflux temperature for 15 minutes. After this time, 10 mL of distilled water were added, and the reaction was continued for another 10 minutes. Then, the heating was stopped and a titration with a standardised 0.5 M KOH_{MeOH} solution was performed. The value of IOH was obtained by subtracting the volumes from the titration of the blank from those of the samples (**Equation 6.2**).

$$IOH = \frac{(\text{titration volume blank} - \text{titration volume sample}) \times M\ KOH \times M_w KOH}{\text{g polymer}}$$

Equation 6.2: IOH calculation from indirect titration with a KOH solution.

6.2.3 Methyl ester index

To obtain the methyl ester index (IOMe), first, the mols of methyl ester end-groups were measured from the ^{1}H NMR spectra by calculating the percentage of all the terminations that correspond to methyl esters (**Figure 6.1**, **Equation 6.3**).

$$\frac{\text{mol methyl ester}}{\text{mol polymer}} = \text{proportion of methyl ester termination} \times \text{total number of terminations} =$$

$$\frac{\text{integral terminal diol}/2}{\text{integral methyl ester}/3 + \text{integral terminal diol}/2} \times \left(\frac{\text{integral diol ester}/2}{\text{integral methyl ester}/3 + \text{integral terminal diol}/2} + 1 \right)$$

Equation 6.3: Obtention of the number of methyl esters present in the sample by ^{1}H NMR.

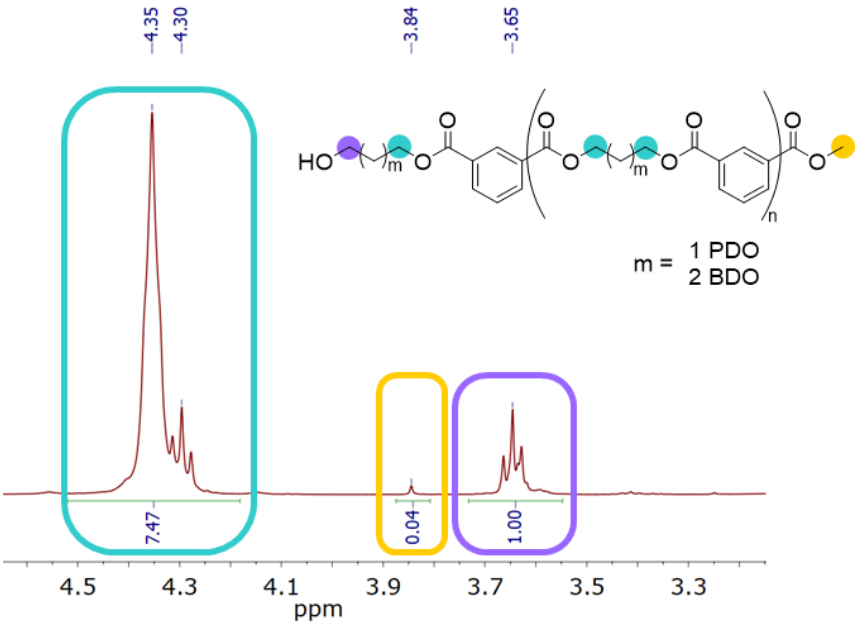

Figure 6.1: ^{1}H NMR signals employed for the determination of IOMe.

With this value in hand, **Equation 6.4** can be employed to calculate the value of IOMe, which is equivalent to the theoretical titration with KOH of the methyl ester end-groups.

$$\text{IOMe} = \frac{\text{mol methyl ester}}{\text{mol polymer}} \times \frac{1000 \times M_w\text{KOH}}{M_n \text{ polyester}}$$

Equation 6.4: Value of the hypothetical titration of methyl esters by KOH.

6.2.4 M_n determination by IOH

The molecular weight of the polymer can be obtained by the IA and IOH values from the following expression (**Equation 6.5**).

$$M_n = \frac{2 \times M_w KOH \times 1000}{IOH + IA}$$

Equation 6.5: Obtention of M_n from IA and IOH or IOMe.

6.2.5 M_n determination by ^{1}H NMR spectroscopy

The determination of the M_n by ^{1}H NMR spectroscopy was achieved by determining the ratio between the number of IPHTA or FDCA moieties and the number of terminal diols (n). This value is determined by the ratio of the integrals corresponding to the CH_2OCO protons of the alcohol and the terminal α-alcohol protons of the polymers (**Figure 6.2**, **Equation 6.6**). To ensure that the integration is representative of the quantity of each specie, the delay time for the acquisition of the spectrum is set to 10 seconds.

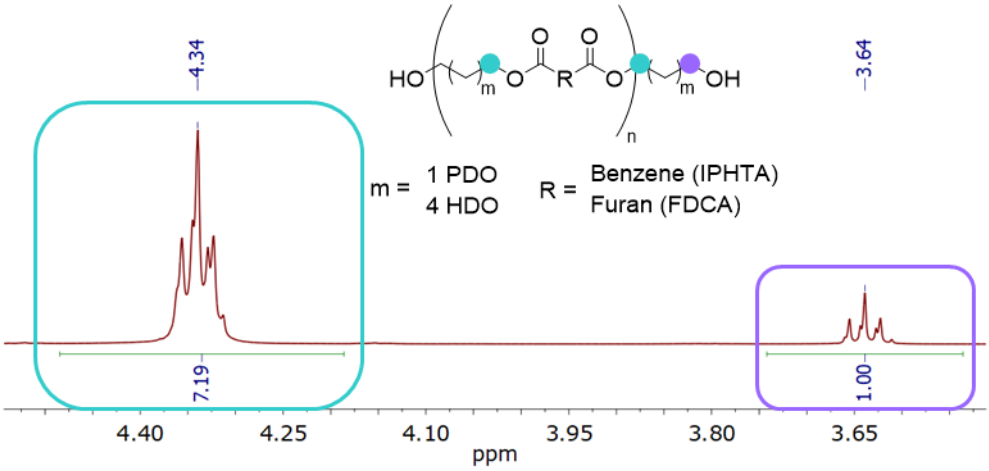

Figure 6.2: ^{1}H NMR signals for the determination of the M_n.

$$n = \frac{\text{integral alcohol } CH_2COO \text{ protons}}{\text{integral terminal alpha alcohol protons}}$$

Equation 6.6: Determination of the number of diacids by polymer chain by ^{1}H NMR spectroscopy.

This n value is employed to obtain the M_n of a difunctional polymer in which all the terminations are alcohols (**Equation 6.7**).

$$M_n = M_w \text{ diacid} \times n + M_w \text{ diol} \times (n + 1) - 2 \times M_w H_2O \times n$$

Equation 6.7: Determination of the M_n by ^{1}H NMR spectroscopy.

However, this value omits that not all the terminations are alcohols, but rather that a small amount of them could be carboxylic acids. Hence, to account for this fact, the M_n obtained solely by ^{1}H NMR spectroscopy is transformed into an IOH value through **Equation 6.8** and applied in **Equation 6.5** to determine the true M_n of the polyester.

$$IOH = \frac{1000 \times 2 \times M_w KOH}{M_n}$$

Equation 6.8: Determination of IOH from ^{1}H NMR M_n spectroscopy.

6.2.6 Polyester synthesis

The basic synthetic process followed for the synthesis of all the polyesters will be disclosed henceforth, with the specific proportions and changes to the procedure specified in each section.

In either a 1, 2 or 10 Kg reactor fitted with a nitrogen and vacuum connection, mechanical stirring, an internal temperature sensor, and a fractional distillation system (**Figure 6.3**), the corresponding reagents for each synthesis were added and deoxygenated by 10 pump-fill cycles with N_2. Afterwards, under a N_2 flow, the system was heated to 180 °C and let react while distilling the water generated during the reaction. Once an IA or IOMe value was lower than 30 mg KOH/g polymer was achieved, the catalyst, $SnCl_2$, was added (20 ppm), and vacuum was applied to the system. The reaction was constantly monitored by either ^{1}H NMR spectroscopy in $CDCl_3$ (IPHTAME) or IA (IPHTA and FDCA). Once the desired IA or IOMe values were reached, the M_n of the polymer was assessed by either IOH (**Experimental Procedures 6.2.4**) or ^{1}H NMR spectroscopy (**Experimental Procedures 6.2.5**). If the M_n of the mixture was higher than that of the target, it was corrected by the addition of further diol, while if it was lower, vacuum was applied to the system. Once the target IA and M_n were obtained, the polymer was transferred to a silicone vessel for cooling.

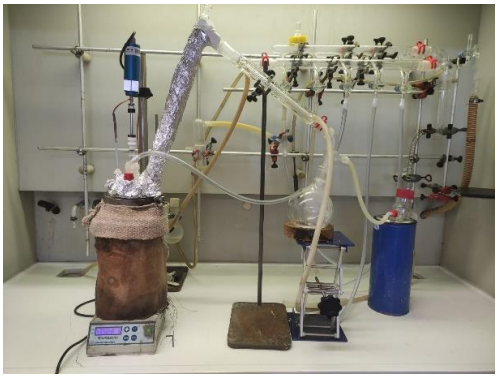

Figure 6.3: 1 Kg reactor assembly for polyester synthesis.

13.6.1. IPHTAPDO 1000 g/mol synthesis from IPHTME and PDO

Scale 1000 g. Experimental conditions: 5.48 mol PDO (416.97 g), 4.48 mol IPHTME (869.92 g). 20 ppm $SnCl_2$ catalyst added after 24 h of reaction. Temperature = 180 °C.

Time (h)	Vacuum	M_n (g/mol)	IOMe (mg KOH/g polymer)	Extra PDO (g)
24	Off	550	30.15	-
48	Off	612	27.67	-
55	On	891	17.68	-
72	On	1026	15.06	-
120	On	1968	7.53	35
144	On	1197	7.51	-

13.6.2. IPHTABDO 1000 g/mol synthesis from IPHTME and BDO

Scale: 1000 g. Experimental conditions: 5.12 mol BDO (461.42 g), 4.13 mol IPHTAME (801.96 g). 20 ppm $SnCl_2$ catalyst added after 91 h of reaction. Temperature = 180 °C.

Time (h)	Vacuum	M_n (g/mol)	IOMe (mg KOH/g polymer)	Extra BDO (g)
24	Off	675	104.31	-
48	Off	1081	64.42	-
72	Off	2170	44.04	-
91	Off	1579	35.23	30
139	On	2206	13.45	-
144	On	1157	13.49	80
163	On	926	10.84	50
190	On	1390	2.36	-
216	On	2408	1.52	150
240	On	816	0.93	-

13.6.3. IPHTAPDO 1000 g/mol synthesis from IPHTA and PDO

Scale 1000 g. Experimental conditions: 5.48 mol PDO (416.58 g), 4.48 mol IPHTA (744.30 g). 20 ppm $SnCl_2$ catalyst added after 18 h of reaction. Temperature 180 °C.

Time (h)	Vacuum	IA (mg KOH/g polymer)	Addition PDO (mL)
18	Off	36.73	-
34.5	On	7.06	-
55.5	On	3.02	-
61.5	On	1.87	20
85.5	On	0.50	-
98	On	0.43	35

Final M_n by ^1H NMR end-group analysis: 1260 g/mol. Final M_n by IOH: 1220 g/mol.

13.6.4. IPHTAPDO 2000 g/mol synthesis from IPHTA and PDO. Test without catalyst

Scale 1000 g. Experimental conditions: 5.66 mol PDO (430.67 g), 4.66 mol IPHTA (774.21 g). Temperature 180 °C.

Time (h)	Vacuum	IA (mg KOH/g polymer)	Addition PDO (mL)
22.5	Off	25.68	-
30.5	On	13.70	-
47	On	6.32	20
71	On	3.83	10
95	On	2.08	8
105	On	1.81	4
143	On	0.46	-

Final M_n by ^1H NMR end-group analysis: 2390 g/mol. Final M_n by IOH: 2260 g/mol.

13.6.5. IPHTABDO 1000 g/mol synthesis from IPHTA and BDO. Test with excess BDO

Scale 1000 g. Experimental conditions: 8.26 mol BDO (744.39 g), 4.13 mol IPHTA (686.16 g). 20 ppm $SnCl_2$ catalyst added after 23 h of reaction. Temperature = 180 °C.

Time (h)	Vacuum	IA (mg KOH/g polymer)	Addition BDO (mL)
23	Off	11.54	-
47	On	6.75	-
71.5	On	4.27	30
95	On	2.83	22
144	On	2.01	15
168	On	2.32	18
192	On	2.25	15
216	On	1.96	14
230	On	2.78	-

13.6.6. IPHTABDO 2000 g/mol synthesis from IPHTA and BDO. Test increasing temperature

Scale 1000 g. Experimental conditions: 5.29 mol BDO (476.74 g), 4.45 mol IPHTA (739.32 g). 20 ppm $SnCl_2$ catalyst added after 24 h of reaction. Temperature = 230 °C.

Time (h)	Vacuum	IA (mg KOH/g polymer)	Addition BDO (mL)
46	Off	16.18	150
70	On	11.31	90
94	On	9.04	71
142	On	4.98	45
166	On	4.21	33
180	On	2.36	15

13.6.7. IPHTABDO 1000 g/mol synthesis from IPHTA and BDO. Test decreasing temperature

Scale 1000 g. Experimental conditions: 8.25 mol BDO (743.50 g), 4.12 mol IPHTA (684.49 g). 20 ppm. $SnCl_2$ catalyst added after 24h of reaction. Additional 20 ppm $SnCl_2$ catalyst added after 72 h of reaction.

Time (h)	Vacuum	Temperature (°C)	IA (mg KOH/g polymer)	Addition BDO (mL)
24	Off	160	19.53	150
48	On	160	8.45	60
72	On	160	5.73	45
98	On	150	3.57	25

13.6.8. IPHTAHDO 1000 g/mol synthesis from IPHTA and HDO

Scale 1000 g. Experimental conditions: 4.36 mol HDO (515.22 g), 3.36 mol, IPHTA (558.23 g). 20 ppm $SnCl_2$ catalyst added after 16 h of reaction. Temperature = 180 °C.

Time (h)	Vacuum	IA (mg KOH/g polymer)	Addition HDO (g)
16	Off	15.56	-
40	On	<0.01	9.87
64	Off	<0.01	-

Final M_n by ^{1}H NMR end-group analysis: 1280 g/mol. Final M_n by IOH: 1165 g/mol.

13.6.9. IPHTAPDO 1000 g/mol production

Experimental conditions: Temperature=180 °C. 20 ppm $SnCl_2$.

Batch	Scale (kg)	IPHTA (g)	PDO (g)	Reaction time (h)	M_n by ^{1}H NMR (g/mol)
1	1	744	417	144	942
2	1	744	417	109	1072
3	2.5	1786.2	1029	93	977
4	10	7443	4170	88	1113

13.6.10. IPHTAPDO 2000 g/mol production

Experimental conditions: Temperature = 180 °C. 20 ppm $SnCl_2$.

Batch	Scale (kg)	IPHTA (g)	PDO (g)	Reaction time (h)	M_n by ^{1}H NMR (g/mol)
1	1	774	392	120	2080
2	2.5	1860	943	92	1907
3	10	7750	3926	87	1980

13.6.11. IPHTAHDO 1000 g/mol production

Experimental conditions: Temperature = 180 °C. 20 ppm $SnCl_2$.

Batch	Scale (kg)	IPHTA (g)	HDO (g)	Reaction time (h)	M_n by ^1H NMR (g/mol)
1	1	558	515	64	1163
2	2	1200	1100	92	1061
3	2.5	1291	1420	60	977
4	10	5898	5377	42	1049

13.6.12. IPHTAHDO 2000 g/mol production

Experimental conditions: Temperature = 180 °C. 20 ppm $SnCl_2$.

Batch	Scale (kg)	IPHTA (g)	HDO (g)	Reaction time (h)	M_n by ^1H NMR (g/mol)
1	1	630	507	72	1839
2	2.5	1511	1217	45	2211
3	10	5069	6297	44	1849

13.6.13. FDCAPDO 1000 g/mol synthesis

Scale 1000 g. Experimental conditions: 5.70 mol PDO (433.71 g), 4.70 mol FDCA (733.62 g). Temperature = 180 °C. 20 ppm $SnCl_2$ catalyst added after 43 h.

Time (h)	Vacuum	IA (mg KOH/g pol)
43	Off	10.35
66	On	2.56
86	On	0.50

Final M_n by ^1H NMR end-group analysis = 1235 g/mol

13.6.14. FDCAPDO 1500 g/mol synthesis

Scale 2000 g. Experimental conditions: 10.81 mol PDO (822.53 g), 9.81 mol FDCA (1531.24 g). Temperature = 180 °C. 20 ppm $SnCl_2$ catalyst added after 39 h.

Time (h)	Vacuum	IA (mg KOH/g pol)
21	Off	38.0
39	On	18.5
62	On	8.9
86	On	0.4

Final M_n by ^{1}H NMR end-group analysis = 1569 g/mol

13.6.15. FDCAPDO 1000 g/mol production

Experimental conditions: Temperature = 180 °C. 20 ppm $SnCl_2$.

Batch	Scale (kg)	IPHTA (g)	PDO (g)	Reaction time (h)	M_n by ^{1}H NMR (g/mol)
1	2.5	1740	869	96	1270
2	2.5	1470	869	74	1205

13.6.16. FDCAPDO 1500 g/mol production

Experimental conditions: Temperature = 180 °C. 20 ppm $SnCl_2$.

Batch	Scale (kg)	IPHTA (g)	PDO (g)	Reaction time (h)	M_n by ^{1}H NMR (g/mol)
1	2	1531	822	89	1614

13.6.17. FDCAPDO 2000 g/mol production

Experimental conditions: Temperature = 180 °C. 20 ppm $SnCl_2$.

Batch	Scale (kg)	IPHTA (g)	PDO (g)	Reaction time (h)	M_n by ^1H NMR (g/mol)
1	2.5	1531	822	89	2213
2	2.5	1530	822	64	1943

13.6.18. FDCAHDO 1000 g/mol production

Experimental conditions: Temperature = 180 °C. 20 ppm $SnCl_2$.

Batch	Scale (kg)	IPHTA (g)	HDO (g)	Reaction time (h)	M_n by ^1H NMR (g/mol)
1	4	2311	2222	53	1230
2	4	2311	2222	67	1183

13.6.19. FDCAHDO 1500 g/mol production

Experimental conditions: Temperature = 180 °C. 20 ppm $SnCl_2$.

Batch	Scale (kg)	IPHTA (g)	HDO (g)	Reaction time (h)	M_n by ^1H NMR (g/mol)
1	2	1207	1071	47	1603
2	2	1207	1071	53	1734

13.6.20. FDCAHDO 2000 g/mol production

Experimental conditions: Temperature = 180 °C. 20 ppm $SnCl_2$.

Batch	Scale (kg)	IPHTA (g)	HDO (g)	Reaction time (h)	M_n by ^1H NMR (g/mol)
1	4	2466	2103	49	2321
2	4	2466	2103	52	2223

6.2.7 FDCAHDO and IPHTAHDO reactivity comparison test

Both reactions were carried out in parallel in a Starfish™ workstation. On two 50 mL two-necked round bottom flasks, 0.11 mmols of the diacid (IPHTA 18.27 g, FDCA 17.17 g) and 0.14 mmol of HDO (16.54 g) were added. The flasks were fitted with a magnetic stirrer, a distillation apparatus fitted with a gas/vacuum entrance and deoxygenated by standard Schlenk techniques. Then, the system was heated to 180 °C under a N_2 atmosphere and monitored by IA analysis. After 74 h, 0.03 mmol of $SnCl_2$ were added to each reaction mixture and vacuum was applied to the systems.

Time (h)	IPHTA IA mg KOH/g pol	FDCA IA mg KOH/g pol
6	659	569
24	215	193
42	160	115
50	113	98
67	64	69
74	35	24
90	< 0.01	< 0.01

6.2.8 Derivatisation of carboxylic acids to their methyl esters with BF_3·MeOH

In a 20 mL two-necked round bottom flask equipped with a Dimroth condenser, 0.1 g of FDCA, 4 mL of MeOH, and 4 mL of the BF_3·MeOH solution were added and heated to reflux temperature. After 1h, the heating was removed, and once cooled, the solution was transferred to a centrifuge tube with an additional 2 mL of MeOH. To the tube, 8 mL of a 200 g/L $NaCl_{(aq)}$ solution, as well as 4 mL of DCM, were added. The mixture was stirred to ensure a correct phase transfer and centrifugated at 3000 rpm for 3 minutes. Then, carefully with a syringe, the organic phase was collected, and stored for GC-MS analysis, while the aqueous phase was discarded.

6.2.9 Impurity extraction tests from FDCA and colour test

On ten 20 mL glass vials, 1 g of FDCA was added followed by 5 mL of one of the following solvents: acetonitrile, ethyl acetate, tetrahydrofuran, hexane, cyclohexane, diethyl ether, dichloromethane, methanol, petroleum ether or toluene. The mixtures were stirred for 1 h and filtered with a Büchner funnel. The process was repeated three times.

To another ten 20 mL glass vials, the cleaned FDCA and 2 mL of PDO were added. Each vial was equipped with a magnetic stirring bar and the system was heated to 160 °C for 2 h. After this time, the reactions were stopped, and the colour of each mixture was evaluated.

6.2.10 DFT dimerisation studies

The geometry optimisation and interaction energy calculations were performed employing a density functional theory (DFT) with dispersion function method. The calculations were carried out with the WB97XD functional[279] and 6-311G(2d,2p) basis set on the Gaussian 09 software.[280] Initially, the geometry of the monomers was optimised and then, the initial dimer conformation was created by placing two of the optimised monomers close to one another with either the carbonyl groups facing the same or opposite directions. Afterwards, the optimisation of the dimeric structure and the calculation of its energy was performed by employing the counterpoise correction method to compensate for the basis set superposition error.[281]

6.2.11 TPU reactivity test

A 1 wt% polyester-catalyst mixture was prepared by adding 0.25 g of catalyst to 25 g of melted polyester. On an aluminium container fitted with a mechanical stirrer and a thermometer, 150 g of polyester were heated to 90 °C and once the temperature was reached, 0.23 g of the polymer-catalyst mixture were added followed by the addition of a stoichiometric amount of MDI.

Just after the addition of the diisocyanate, the temperature of the mixture was monitored. At the moment when the temperature stops dropping due to the addition of the room temperature diisocyanate (5-10s), the mechanical stirrer and thermometer were removed, and the aluminium vessel was transferred to a rotational viscometer fitted with a temperature probe. Then the change in viscosity and temperature were recorded for 2-6 minutes depending on the sample.

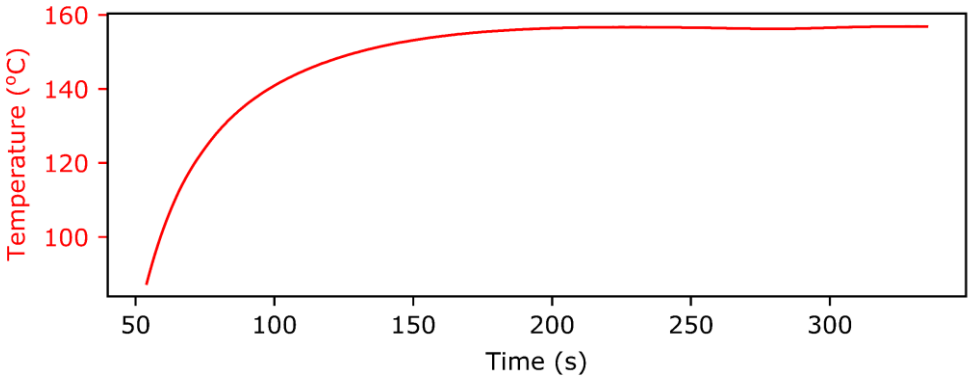

Figure 6.4: Reactivity test of an IPHTAHDO 2000 polyester and MDI.

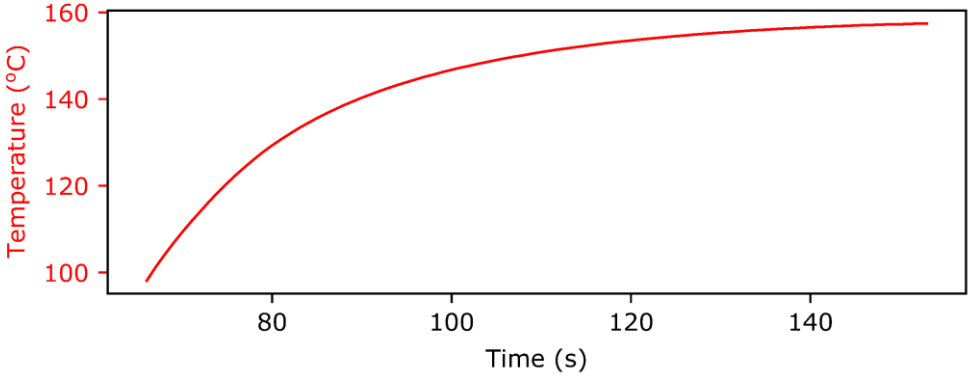

Figure 6.5: Reactivity test of an IPHTAPDO 1000 polyester and MDI.

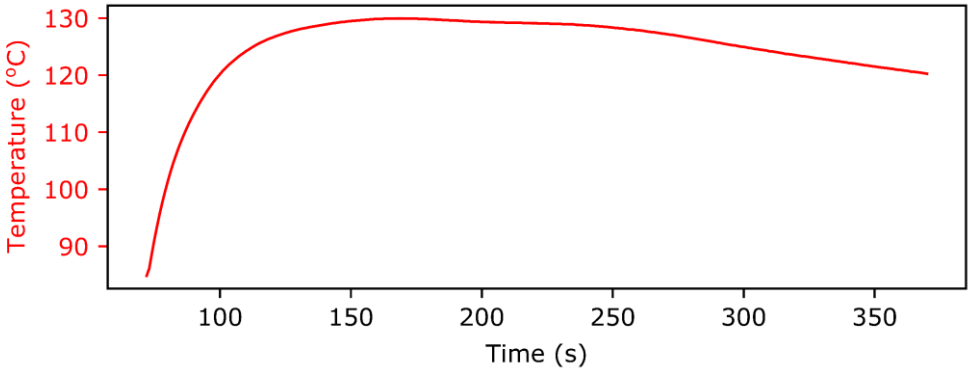

Figure 6.6: Reactivity test of an IPHTAPDO 2000 polyester and MDI.

6.2.12 TPU synthesis procedure

Prior to the reaction, in a 2 L teflonated vessel, the polyester was weighed, melted, and a small sample was taken for the determination of the exact M_n of that polymer batch fraction by ^1H NMR spectroscopy. That M_n was then employed to adjust the proportion of the reagents in each TPU formulation.

Afterwards, the vessel was fitted with a teflonated mechanical stirrer and a thermometer and heated to 160 °C for the case of IPHTA polyesters and 180 °C for the FDCA polyols. Once the target temperature was reached, the additives were added to the reaction crude and a strip of aluminium foil, in which the catalyst had been weighted, was dipped for a few seconds until the catalyst had transferred. Subsequently, BDO, which had been previously been dried with CaH_2 and distillation was weighed in a syringe and added to the reaction mixture, followed by the addition of the corresponding diisocyanate. Afterwards, the crude was monitored until the temperature stopped increasing (1-2 min). Finally, the reaction crude was transferred to a teflonated mould and cured.

6.2.12.1 IPHTAPDO MDI TPU formulations

Code	IPHTAPDO 1000 10% MDI	IPHTAPDO 1000 30% MDI	IPHTAPDO 1000 50% MDI	IPHTAPDO 2000 10% MDI	IPHTAPDO 2000 30% MDI	IPHTAPDO 2000 50% MDI
HS (mol%)	10	30	50	10	30	50
Polyester M_n (g/mol)	988	988	1113	1949	1949	2301
Polyester (g)	851.68	785.19	644.80	827.67	747.98	982.72
BDO (g)	827.67	747.98	52.9	4.25	14.82	38.48
MDI (g)	239.69	284.11	293.79	118.08	137.20	213.73
Cat (g)	0.02	0.02	0.02	0.01	0.01	0.02
Add 1 (g)	1.65	1.65	1.50	1.43	1.35	1.85
Add 2 (g)	2.20	2.20	2.00	1.90	1.80	2.47
Scale (g)	1100	1100	1000	950	900	1235

6.2.12.2 IPHTAHDO MDI TPU formulations

Code	IPHTAHDO 1000 10% MDI	IPHTAHDO 1000 30% MDI	IPHTAHDO 1000 50% MDI	IPHTAHDO 2000 10% MDI	IPHTAHDO 2000 30% MDI	IPHTAHDO 2000 50% MDI
HS (mol%)	10	30	50	10	30	50
Polyester M_n (g/mol)	1027	1027	1027	2023	2023	2023
Polyester (g)	859.04	793.82	634.88	831.58	752.63	696.62
BDO (g)	8.38	29.85	55.71	4.12	14.37	31.03
MDI (g)	232.58	276.33	309.40	114.30	133.00	172.35
Cat (g)	0.02	0.02	0.02	0.01	0.01	0.01
Add 1 (g)	1.65	1.65	1.50	1.43	1.35	1.35
Add 2 (g)	2.20	2.20	2.00	1.90	1.80	1.80
Scale (g)	1100	1100	1000	950	900	900

Code	IPHTAHDO 2000 10% MDI S_2	IPHTAHDO 2000 30% MDI S_2
HS (mol%)	10	30
Polyester M_n (g/mol)	1906	1933
Polyester (g)	786.59	751.18
BDO (g)	4.13	15.01
MDI (g)	114.74	138.93
Cat (g)	0.01	0.01
Add 1 (g)	1.36	1.36
Add 2 (g)	1.81	1.81
Scale (g)	905	905

6.2.12.3 IPHTAPDO HDI TPU formulations

Code	IPHTAPDO 1000 10% HDI	IPHTAPDO 1000 30% HDI	IPHTAPDO 1000 50% HDI	IPHTAPDO 2000 10% HDI	IPHTAPDO 2000 30% HDI	IPHTAPDO 2000 50% HDI
HS (mol%)	10	30	50	10	30	50
Polyester M_n (g/mol)	1111	1128	1101	2378	2477	2524
Polyester (g)	850.08	797.73	740.01	910.37	899.63	824.22
BDO (g)	7.66	27.31	60.57	3.83	14.03	29.43
HDI (g)	143.00	169.93	226.10	71.55	87.27	109.85
Cat (g)	0.02	0.02	0.02	0.02	0.02	0.02
Add 1 (g)	2.00	1.99	2.05	1.97	2.00	1.93
Add 2 (g)	1.50	1.49	1.54	1.48	1.50	1.45
Scale (g)	1001	995	1027	986	1001	964

Code	IPHTAPDO 1000 50% HDI S_2
HS (mol%)	50
Polyester M_n (g/mol)	1106
Polyester (g)	630.90
BDO (g)	51.41
HDI (g)	191.89
Cat (g)	0.02
Add 1 (g)	1.75
Add 2 (g)	1.31
Scale (g)	874

6.2.12.4 IPHTAHDO HDI TPU formulations

Code	IPHTAHDO 1000 10% HDI	IPHTAHDO 1000 30% HDI	IPHTAHDO 1000 50% HDI	IPHTAHDO 2000 10% HDI	IPHTAHDO 2000 30% HDI	IPHTAHDO 2000 50% HDI
HS (mol%)	10	30	50	10	30	50
Polyester M_n (g/mol)	1181	1181	1181	1896	1683	1916
Polyester (g)	857.12	783.94	734.70	910.37	872.00	824.22
BDO (g)	7.27	25.64	56.06	4.81	20.01	38.77
HDI (g)	135.64	159.50	209.27	89.73	124.50	144.72
Cat (g)	0.02	0.02	0.02	0.02	0.02	0.02
Add 1 (g)	2.00	1.94	2.00	2.01	2.03	2.02
Add 2 (g)	1.50	1.45	1.50	1.51	1.52	1.51
Scale (g)	1000	969	1000	1005	1017	1008

6.2.12.5 FDCAPDO MDI TPU formulations

Code	FDCAPDO 1000 10% MDI	FDCAPDO 1000 50% MDI	FDCAPDO 1500 30% MDI	FDCAPDO 2000 10% MDI	FDCAPDO 2000 50% MDI
HS (mol%)	10	50	30	10	50
Polyester M_n (g/mol)	1126	1056	1663	1822	2213
Polyester (g)	853.99	686.32	881.65	868.30	849.22
BDO (g)	7.6	58.57	20.47	4.78	34.59
MDI (g)	210.95	325.27	189.51	132.53	192.11
Cat (g)	0.02	0.02	0.02	0.01	0.02
Add 1 (g)	1.61	1.61	1.64	1.51	1.61
Add 2 (g)	2.14	2.14	2.18	2.01	2.15
Scale (g)	1072	1070	1091	1006	1076

6.2.12.6 FDCAHDO MDI TPU formulations

Code	FDCAHDO 1000 10% MDI	FDCAHDO 1000 50% MDI	FDCAHDO 1500 30% MDI	FDCAHDO 2000 10% MDI	FDCAHDO 2000 50% MDI
HS (mol%)	10	50	30	10	50
Polyester M_n (g/mol)	1120	1220	1617	2114	2128
Polyester (g)	853.99	691.55	870.20	961.51	849.22
BDO (g)	7.15	51.11	20.79	4.56	35.97
MDI (g)	198.57	283.84	192.39	126.48	199.75
Cat (g)	0.02	0.02	0.02	0.02	0.02
Add 1 (g)	1.59	1.54	1.62	1.64	1.63
Add 2 (g)	2.12	2.05	2.17	2.19	2.17
Scale (g)	1060	1027	1083	1093	1085

6.2.12.7 FDCAPDO HDI TPU formulations

Code	FDCAPDO 1000 10% HDI	FDCAPDO 1000 50% HDI	FDCAPDO 1500 30% HDI	FDCAPDO 2000 10% HDI	FDCAPDO 2000 50% HDI
HS (mol%)	10	50	30	10	50
Polyester M_n (g/mol)	1175	1053	1655	1822	1954
Polyester (g)	919.04	771.04	936.71	849.75	906.65
BDO (g)	7.83	65.99	21.86	4.67	41.83
HDI (g)	146.21	246.31	135.97	87.16	156.13
Cat (g)	0.02	0.02	0.02	0.01	0.02
Add 1 (g)	1.61	1.62	1.64	1.41	1.66
Add 2 (g)	2.15	2.17	1.64	1.88	2.21
Scale (g)	1073	1083	1094	942	1104

6.2.12.8 FDCAHDO HDI TPU formulations

Code	FDCAHDO 1000 10% HDI	FDCAHDO 1000 50% HDI	FDCAHDO 1500 30% HDI	FDCAHDO 2000 10% HDI	FDCAHDO 2000 50% HDI
HS (mol%)	10	50	30	10	50
Polyester M_n (g/mol)	1045	1040	1562	2005	1986
Polyester (g)	668.39	560.80	680.61	728.30	659.38
BDO (g)	6.69	50.54	16.53	3.65	29.71
HDI (g)	124.92	188.65	102.86	68.06	110.91
Cat (g)	0.01	0.01	0.01	0.01	0.01
Add 1 (g)	1.61	1.62	1.64	1.41	1.66
Add 2 (g)	2.15	2.17	1.64	1.88	2.21
Scale (g)	800.00	800.00	800.00	800.00	800.00

6.2.13 T_g linear regression analysis

The linear regression analysis of the T_g of the different TPUs was performed employing the linear regression tool of the data analysis toolbox from the Excel software. The fitting was carried out by employing three T_g replicates as input.

Different fitting variables were selected for the different regression tests. The fitting variables selected were:

-Polyester M_n: M_n calculated by ^{1}H NMR and displayed in the TPU synthesis procedure section (**6.2.12**).

-HS (mol%): 10, 30 or 50% depending on the formulation.

-IPHTA molality: Calculated from the polyester M_n, weight of polyester, and weight of synthesised TPU from each formulation.

-Chain packing parameter (CP): Given a value of 1 for PDO and 2 for HDO TPUs.

-Diacid type (DA): Given a value of 1 for IPHTA and 2 for FDCA.

6.2.14 Synthesis of the pure soft segment polymers

On a teflonated vessel, the corresponding polyester was weighted and melted (**Table 6.1**). Approximately 10-15 mg were taken from the melted polymers and employed for their M_n determination by ^{1}H NMR end-group analysis. Afterwards, the polymers were heated to either 160 °C (IPHTA) or 180 °C (FDCA) and once they reached the desired temperature, the corresponding diisocyanate was added so that the mols of polyester were always n+1 those of the diisocyanate (**Table 6.1**). Then, the reaction crude was mixed employing a teflonated bar and, once a highly viscous material was obtained, placed into an oven to cure.

Table 6.1: Weights for the pure SS synthesis

Polyester	Polyester M_n (g/mol)	Polyester weight (g)	Diisocyanate	Diisocyanate weight (g)
FDCAPDO	1265	10.34	MDI	1.37
FDCAPDO	1708	12.87	MDI	1.27
FDCAPDO	2344	10.55	MDI	0.76
FDCAHDO	1190	10.04	MDI	1.42
FDCAHDO	1586	10.26	MDI	1.09
FDCAHDO	2010	9.58	MDI	0.80
FDCAPDO	1214	10.59	HDI	1.47
FDCAPDO	1412	10.85	HDI	1.29
FDCAPDO	2834	9.53	HDI	0.57
FDCAHDO	1226	11.47	HDI	1.57
FDCAHDO	1602	9.97	HDI	1.05
FDCAHDO	1991	10.32	HDI	0.87

6.2.15 Small-angle X-ray scattering data fitting

The fitting of the I(q) experimental data to the different models has been performed employing the solver tool in Excel. First, the background was subtracted from the experimental signal by normalizing both, background, and sample data to their corresponding radiation intensities. Then the local minimum which marks the separation between the Guinier and Fourier regions was manually selected, with the data corresponding to the former being discarded, as only the Fourier and Porod regions are fitted. Once the data range to be fitted was selected, first, Excel's evolutionary minimisation algorithm was employed to approximate the simulated and the experimental data, by minimisation of the sum of the residuals squared. Then, the GRG Nonlinear minimisation algorithm was employed to ensure that the true minimum had been reached during the fitting. Both minimisations were carried out with a convergence of 0.0001, by modifying the different fitting parameters for each model.

The validity of the fitting was checked by starting the minimisation algorithm from three different random starting points.

6.2.16 Wide-angle X-ray scattering deconvolution

The deconvolution of the WAXS spectra has been performed on Origin, employing its peak fit function in a range of q of 6-88 nm^{-1}. First, a linear background belonging to the incoherent scattering was calculated and subtracted from the X-ray profiles according to the analytical equations of Chapman *et al.*[282] Then, several Gaussian-Cauchy (called Gaussian-LorenCross in the software) curves were added to the spectra and minimised employing a Levenberg-Marquardt optimisation algorithm with a tolerance of 10^{-15}. The number of Gaussian-Cauchy peaks was increased until a good fitting of the spectra was obtained.

6.3 Small-angle x-ray scattering models

6.3.1 Spheric form factor with Flory-Schultz distribution

According to the decoupling approximation:

$$\bar{P}(q)=\int_0^{\infty} P(q,R)\times f(R)\,dR, \text{ with: } \frac{P(q)=\text{Scale}\times\left|\frac{\sin(qR)-qR\cos(qR)}{qR^3}\right|^2}{f(R)=(Z+1)^{Z+1}\times x^Z\frac{e^{[-(Z+1)x]}}{\bar{R}\Gamma(Z+1)} \quad \text{and} \quad Z=\frac{1}{p^2}-1}$$

Analytical solution:

$$\bar{P}(q)=8\pi^2\Delta\rho^2\bar{R}^6(z+1)^{-6}\alpha^{z+7}G_1(x), \text{ with:}$$

$$\alpha=\frac{Z+1}{q\bar{R}}$$

$$G_1(x)=\alpha^{-(Z+1)} - \left(4+\alpha^2\right)^{\frac{-(Z+1)}{2}} \times \cos\left[(Z+1)\arctan\left(\frac{2}{\alpha}\right)\right] + (Z+2)(Z+1) \times \left\{\alpha^{-(Z+3)}+\left(4+\alpha^2\right)^{\frac{-(Z+3)}{2}} \cos\left[(Z+3)\arctan\left(\frac{2}{\alpha}\right)\right]\right\} -2(Z+1) \times \left(4+\alpha^2\right)^{\frac{-(Z+2)}{2}} \sin\left[(Z+2)\arctan\left(\frac{2}{\alpha}\right)\right]$$

6.3.2 Percus-Yevick hard sphere structure factor

$$S(q)=\left[1+\frac{24\Phi}{x}G(x)\right]^{-1}, \text{ with:}$$

$$x=2qR_h$$

$$G(x)=\frac{\alpha}{x^2}(\sin x-x\cos x) + \frac{\beta}{x^3}\left[\left(2x\sin x+(2-x^2)\cos x-2\right]\right. + \frac{\gamma}{x^5}\left[24-x^4\cos x + \left(12x^2-24\right)\cos x + \left(4x^3-24x\right)\sin x\right]$$

with:

$$\alpha=\frac{(1+2\Phi)^2}{(1-\Phi)^4} \qquad \beta=\frac{-6\Phi(1+0.5\Phi)^2}{(1-\Phi)^4} \qquad \gamma=\frac{\Phi}{2}\alpha$$

6.3.3 Zernike-Prins structure factor

$$S(q)=\frac{1-A^2}{1-2A\cos(qd)+A^2}, \text{ with:} \qquad A=e^{-q^2\sigma^2/2}$$

Chapter 7: Bibliography

The references employed in the discussion of this work can be found hereinafter.

(1) Garcia-Martos, D.; Riba, M. J.; Kocić, N.; Bayón, J. C. Thermoplastic Polyurethane Compositions with Shape Memory Properties. EP 22382851.8, 2022.

(2) NOAA National Centers for Environmental information. State of the Climate: Global Climate Report for Annual 2020 https://www.ncdc.noaa.gov/sotc/global/202013 (accessed Apr 16, 2021).

(3) Berkeley Earth. Global Temperature Report for 2020 http://berkeleyearth.org/global-temperature-report-for-2020/ (accessed Apr 16, 2021).

(4) NASA Goddard Institute for Space Studies; GISTEMP Team. 2021: GISS Surface Temperature Analysis (GISTEMP) https://data.giss.nasa.gov/gistemp/ (accessed Apr 16, 2021).

(5) *Paris Agreement*; 2015.

(6) United Nations Framework Convention on Climate Change. *Information on Global Warming Potentials*; 2004.

(7) Alcaraz, O.; Buenestado, P.; Escribano, B.; Sureda, B.; Turon, A.; Xercavins, J. The Global Carbon Budget and the Paris Agreement. *Int. J. Clim. Chang. Strateg. Manag.* **2019**, *11* (3), 310–325. https://doi.org/10.1108/IJCCSM-06-2017-0127.

(8) Friedlingstein, P.; Jones, M. W.; O'Sullivan, M.; Andrew, R. M.; Hauck, J.; Peters, G. P.; Peters, W.; Pongratz, J.; Sitch, S.; Le Quéré, C.; DBakker, O. C. E.; Canadell1, J. G.; Ciais1, P.; Jackson, R. B.; Anthoni1, P.; Barbero, L.; Bastos, A.; Bastrikov, V.; Becker, M.; Bopp, L.; Buitenhuis, E.; Chandra, N.; Chevallier, F.; Chini, L. P.; Currie, K. I.; Feely, R. A.; Gehlen, M.; Gilfillan, D.; Gkritzalis, T.; Goll, D. S.; Gruber, N.; Gutekunst, S.; Harris, I.; Haverd, V.; Houghton, R. A.; Hurtt, G.; Ilyina, T.; Jain, A. K.; Joetzjer, E.; Kaplan, J. O.; Kato, E.; Goldewijk, K. K.; Korsbakken, J. I.; Landschützer, P.; Lauvset, S. K.; Lefèvre, N.; Lenton, A.; Lienert, S.; Lombardozzi, D.; Marland, G.; McGuire, P. C.; Melton, J. R.; Metzl, N.; Munro, D. R.; Nabel, J. E. M. S.; Nakaoka, S. I.; Neill, C.; Omar, A. M.; Ono, T.; Peregon, A.; Pierrot, D.; Poulter, B.; Rehder, G.; Resplandy, L.; Robertson, E.; Rödenbeck, C.; Séférian, R.; Schwinger, J.; Smith, N.; Tans, P. P.; Tian, H.; Tilbrook, B.; Tubiello, F. N.; Van Der Werf, G. R.; Wiltshire, A. J.; Zaehle, S. Global Carbon Budget 2019. *Earth Syst. Sci. Data* **2019**, *11* (4), 1783–1838.

(9) Zheng, J.; Suh, S. Strategies to Reduce the Global Carbon Footprint of Plastics. *Nat. Clim. Chang.* **2019**, *9*, 374–378. https://doi.org/10.1038/s41558-019-0459-z.

(10) Hamilton, L. A.; Feit, S.; Muffett, C.; Kelso, M.; Rubright, S. M.; Bernhard, C.; Schaeffer, E.; Moon, D.; Morris, J.; Labbé-Bellas, R. *Plastic & Climate: The Hidden Costs of a Plastic Planet*; 2019.

(11) Ellen Macarthur Foundation; World Economic Forum; McKinsey & Company. *The New Plastics Economy. Rethinking the Future of Plastics*; 2006. https://doi.org/10.4324/9780203965450.

(12) Ellen MacArthur Foundation. *The New Plastics Economy: Rethinking the Future of Plastics*; 2016.

(13) Pilz, H.; Schweighofer, J.; Kletzer, E. *The Contribution of Plastic Products to Resource Efficiency*; 2005.

(14) *The Compelling Facts About Plastics 2009*; 2009.

(15) Nessi, S.; Sinkko, T.; Bulgheroni, C.; Garcia-Guiterrez, P.; Giuntoli, J.; Konti, A.; Sanye-Mengual, E.; Tonini, D.; Pant, R.; Marelli, L. *Comparative Life Cycle Assessment (LCA) of Alternative Feedstock for Plastics Production*; 2020.

(16) *Plastics and Climate in Perspective*; 2020.

(17) Geyer, R.; Jambeck, J. R.; Law, K. L. Production, Use, and Fate of All Plastics Ever Made. *Sci. Adv.* **2017**, *3* (7), 25–29. https://doi.org/10.1126/sciadv.1700782.

(18) Edwards, C.; Meyhoff Fry, J. *Life Cycle Assessment of Supermarket Carrier Bags: A Review of the Bags Available in 2006*; 2006.

(19) Bisinella, V.; Albizzati, P. F.; Astrup, T. F.; Damgaard, A. *Life Cycle Assessment of Grocery Carrier Bags*; 2018.

(20) Michaud, J.-C.; Farrant, L.; Jan, O.; Kjær, B.; Bakas, I. *Environmental Benefits of Recycling - 2010 Update*; 2010.

(21) Lazarevic, D.; Aoustin, E.; Buclet, N.; Brandt, N. Plastic Waste Management in the Context of a European Recycling Society: Comparing Results and Uncertainties in a Life Cycle Perspective. *Resour. Conserv. Recycl.* **2010**, *55* (2), 246–259. https://doi.org/10.1016/j.resconrec.2010.09.014.

(22) Plastics Europe. *Plastics - the Facts 2019*; 2019.

(23) Ignatyev, I. A.; Thielemans, W.; Vander Beke, B. Recycling of Polymers: A Review. *ChemSusChem* **2014**, *7* (6), 1579–1593. https://doi.org/10.1002/cssc.201300898.

(24) Pivnenko, K.; Jakobsen, L. G.; Eriksen, M. K.; Damgaard, A.; Astrup, T. F. Challenges in Plastics Recycling. In *Fifteenth International Waste Management and Landfill Symposium feedstock*; 2015.

(25) EuRIC. *Plastic Recycling Factsheet*; 2020.

(26) Schyns, Z. O. G.; Shaver, M. P. Mechanical Recycling of Packaging Plastics: A Review. *Macromol. Rapid Commun.* **2021**, *42* (3), 1–27. https://doi.org/10.1002/marc.202000415.

(27) Recycling, M.; Upgrading, R. M.; Plastics, B.; Gas, W. *Industrial Applications of Renewable Plastics*; 2017. https://doi.org/10.1016/c2015-0-06835-6.

(28) Helmer Pedersen, T.; Conti, F. Improving the Circular Economy via Hydrothermal Processing of High-Density Waste Plastics. *Waste Manag.* **2017**, *68*, 24–31. https://doi.org/10.1016/j.wasman.2017.06.002.

(29) Kaminsky, W.; Predel, M.; Sadiki, A. Feedstock Recycling of Polymers by Pyrolysis in a Fluidised Bed. *Polym. Degrad. Stab.* **2004**, *85* (3 SPEC. ISS.), 1045–1050. https://doi.org/10.1016/j.polymdegradstab.2003.05.002.

(30) Punkkinen, H.; Oasmaa, A.; Laatikainen-, J. *Thermal Conversion of Plastic- Containing Waste : A Review*; 2017.

(31) Belboom, S.; Léonard, A. Does Biobased Polymer Achieve Better Environmental Impacts than Fossil Polymer? Comparison of Fossil HDPE and Biobased HDPE Produced from Sugar Beet and Wheat. *Biomass and Bioenergy* **2016**, *85*, 159–167. https://doi.org/10.1016/j.biombioe.2015.12.014.

(32) Eerhart, A. J. J. E.; Faaij, A. P. C.; Patel, M. K. Replacing Fossil Based PET with Biobased PEF; Process Analysis, Energy and GHG Balance. *Energy Environ. Sci.* **2012**, *5* (4), 6407–6422. https://doi.org/10.1039/c2ee02480b.

(33) Thathiana Benavides, P.; Lee, U.; Zarè-Mehrjerdi, O. Life Cycle Greenhouse Gas Emissions and Energy Use of Polylactic Acid, Bio-Derived Polyethylene, and Fossil-Derived Polyethylene. *J. Clean. Prod.* **2020**, *277*. https://doi.org/10.1016/j.jclepro.2020.124010.

(34) Chen, G. Q.; Patel, M. K. Plastics Derived from Biological Sources: Present and Future: A Technical and Environmental Review. *Chem. Rev.* **2012**, *112* (4), 2082–2099. https://doi.org/10.1021/cr200162d.

(35) Nova Institute. *Market Study on Bio-Based Polymers in the World*; 2013.

(36) Hottle, T. A.; Bilec, M. M.; Landis, A. E. Sustainability Assessments of Bio-Based Polymers. *Polym. Degrad. Stab.* **2013**, *98* (9), 1898–1907. https://doi.org/10.1016/j.polymdegradstab.2013.06.016.

(37) Niaounakis, M. *BIOPOLYMERS : REUSE , RECYCLING , AND DISPOSAL*; Elsevier B.V., 2013. https://doi.org/10.1016/B978-1-4557-3145-9.00001-4.

(38) Nakajima, H.; Dijkstra, P.; Loos, K. The Recent Developments in Biobased Polymers toward General and Engineering Applications: Polymers That Are Upgraded from Biodegradable Polymers, Analogous to Petroleum-Derived Polymers, and Newly Developed. *Polymers (Basel).* **2017**, *9* (10), 1–26. https://doi.org/10.3390/polym9100523.

(39) Gooch, J. W. *Natural Polymers Industry Techniques and Applications*; Springer US, 2016. https://doi.org/10.1007/978-3-319-26414-1.

(40) Masutani, K.; Kimura, Y. Biobased Polymers. In *Encyclopedia of Polymeric Nanomaterials*; Kobayashi, S., Müllen, K., Eds.; Springer Berlin Heidelberg: Berlin, Heidelberg, 2021; pp 1–7. https://doi.org/10.1007/978-3-642-36199-9_390-1.

(41) Brizga, J.; Hubacek, K.; Feng, K. The Unintended Side Effects of Bioplastics: Carbon, Land, and Water Footprints. *One Earth* **2020**, *3* (1), 45–53. https://doi.org/10.1016/j.oneear.2020.06.016.

(42) F.H., N. THE FORMATION OF FURAN COMPOUNDS FROM HEXOSES. *Adv. Carbohydr. Chem.* **1951**, *6*, 83–106. https://doi.org/https://doi.org/10.1016/S0096-5332(08)60064-8.

(43) H.B., H.; H.E., S. Dehydroschleimsäure Aus δ-Methylbrenzschleimsäure. *Eur. J. Inorg. Chem.* **1894**, *27* (2). https://doi.org/https://doi.org/10.1002/cber.18940270281.

(44) Avantium. Avantium FDCA press release https://www.avantium.com/press-releases/alpla-joins-coca-cola-company-danone-avantiums-pef-bottle-development/ (accessed Jun 8, 2021).

(45) Tao, L.; Yan, T. H.; Li, W.; Zhao, Y.; Zhang, Q.; Liu, Y. M.; Wright, M. M.; Li, Z. H.; He, H. Y.; Cao, Y. Toward an Integrated Conversion of 5-Hydroxymethylfurfural and Ethylene for the Production of Renewable p-Xylene. *Chem* **2018**, *4* (9), 2212–2227. https://doi.org/10.1016/j.chempr.2018.07.007.

(46) Fadzil, N. A. M.; Rahim, M. H. A.; Maniam, G. P. A Brief Review of Para-Xylene Oxidation to Terephthalic Acid as a Model of Primary C-H Bond Activation. *Chinese J. Catal.* **2014**, *35* (10), 1641–1652. https://doi.org/10.1016/S1872-2067(14)60193-5.

(47) Peters, M. W.; Taylor, J. D.; Jenni, M.; Manzer, L. E.; Henton, D. E. Integrated Process To Selectively Convert Renewable Isobutanol to P-Xylene. US 2011/0087000 A1, 2010.

(48) Makarouni, D.; Lycourghiotis, S.; Kordouli, E.; Bourikas, K.; Kordulis, C.; Dourtoglou, V. Transformation of Limonene into P-Cymene over Acid Activated Natural Mordenite Utilizing Atmospheric Oxygen as a Green Oxidant: A Novel Mechanism. *Appl. Catal. B Environ.* **2018**, *224* (October 2017), 740–750. https://doi.org/10.1016/j.apcatb.2017.11.006.

(49) Neaţu, F.; Culică, G.; Florea, M.; Parvulescu, V. I.; Cavani, F. Synthesis of Terephthalic Acid by P-Cymene Oxidation Using Oxygen: Toward a More Sustainable Production of Bio-Polyethylene Terephthalate. *ChemSusChem* **2016**, *9* (21), 3102–3112. https://doi.org/10.1002/cssc.201600718.

(50) Herbst, A.; Janiak, C. Selective Glucose Conversion to 5-Hydroxymethylfurfural (5-HMF) Instead of Levulinic Acid with MIL-101Cr MOF-Derivatives. *New J. Chem.* **2016**, *40* (9), 7958–7967. https://doi.org/10.1039/c6nj01399f.

(51) Weingarten, R.; Rodriguez-Beuerman, A.; Cao, F.; Luterbacher, J. S.; Alonso, D. M.; Dumesic, J. A.; Huber, G. W. Selective Conversion of Cellulose to Hydroxymethylfurfural in Polar Aprotic Solvents. *ChemCatChem* **2014**, *6* (8), 2229–2234. https://doi.org/10.1002/cctc.201402299.

(52) Davidson, M. G.; Elgie, S.; Parsons, S.; Young, T. J. Production of HMF, FDCA and Their Derived Products: A Review of Life Cycle Assessment (LCA) and Techno-Economic Analysis (TEA) Studies. *Green Chem.* **2021**, *23* (9), 3154–3171. https://doi.org/10.1039/d1gc00721a.

(53) Wang, H.; Zhu, C.; Li, D.; Liu, Q.; Tan, J.; Wang, C.; Cai, C.; Ma, L. Recent Advances in Catalytic Conversion of Biomass to 5-Hydroxymethylfurfural and 2, 5-Dimethylfuran. *Renew. Sustain. Energy Rev.* **2019**, *103*, 227–247. https://doi.org/10.1016/j.rser.2018.12.010.

(54) Zhou, H.; Xu, H.; Wang, X.; Liu, Y. Convergent Production of 2,5-Furandicarboxylic Acid from Biomass and CO 2. *Green Chem.* **2019**, *21* (11), 2923–2927.

https://doi.org/10.1039/C9GC00869A.

(55) Khatoon, H.; Iqbal, S.; Irfan, M.; Darda, A.; Rawat, N. K. A Review on the Production, Properties and Applications of Non-Isocyanate Polyurethane: A Greener Perspective. *Prog. Org. Coatings* **2021**, *154* (September 2020), 106124. https://doi.org/10.1016/j.porgcoat.2020.106124.

(56) Szycher, M. *Szycher's Handbook of Polyurethanes*; 2013. https://doi.org/10.1021/ja004704k.

(57) Datta, J.; Kasprzyk, P. Thermoplastic Polyurethanes Derived from Petrochemical or Renewable Resources: A Comprehensive Review. *Polym. Eng. Sci.* **2018**, *58*. https://doi.org/10.1002/pen.24633.

(58) George Drobny, J. Thermoplastic Polyurethane Elastomers. In *Handbook of thermoplastic elastomers*; Elsevier, 2014; pp 233–253. https://doi.org/10.1016/C2013-0-00140-5.

(59) Bonart, R.; Muller, E. H. Phase Separation in Urethane Elastomers as Judged by Low-Angle X-Ray Scattering. I. Fundamentals. *J. Macromol. Sci. Part B Phys.* **1974**, *10* (1), 177–189. https://doi.org/10.1080/00222347408219403.

(60) Velankar, S.; Cooper, S. L. Microphase Separation and Rheological Properties of Polyurethane Melts. 3. Effect of Block Incompatibility on the Viscoelastic Properties. *Macromolecules* **2000**, *33* (2), 395–403. https://doi.org/10.1021/ma9908189.

(61) Yoon, P. J.; Han, C. D. Effect of Thermal History on the Rheological Behavior of Thermoplastic Polyurethanes. *Macromolecules* **2000**, *33* (6), 2171–2183. https://doi.org/10.1021/ma991741r.

(62) Velankar, S.; Cooper, S. L. Microphase Separation and Rheological Properties of Polyurethane Melts. 2. Effect of Block Incompatibility on the Microstructure. *Macromolecules* **2000**, *33*, 395–403. https://doi.org/10.1021/ma990817g.

(63) Velankar, S.; Cooper, S. L. Microphase Separation and Rheological Properties of Polyurethane Melts. 1. Effect of Block Length. *Macromolecules* **1998**, *31* (26), 9181–9192. https://doi.org/10.1021/ma9811472.

(64) Brown, R. A.; Masters, A. J.; Price, C.; Yuan, X. F. Chain Segregation in Block Copolymers. In *Comprehensive Polymer Science and Supplements*; Pergamon, 1989; pp 155–198. https://doi.org/10.1016/b978-0-08-096701-1.00043-4.

(65) Leibler, L. Theory of Microphase Separation in Block Copolymers. *Macromolecules* **1980**, *13* (6), 1602–1617. https://doi.org/10.1021/ma60078a047.

(66) Zdrahala, R. J.; Gerkin, R. M.; Hager, S. L.; Critchfield, F. E. Polyether-Based Thermoplastic Polyurethanes. I. Effect of the Hard-Segment Content. *J. Appl. Polym. Sci.* **1979**, *24* (9), 2041–2050. https://doi.org/10.1002/app.1979.070240912.

(67) Klinedinst, D. B.; Yilgör, I.; Yilgör, E.; Zhang, M.; Wilkes, G. L. The Effect of Varying Soft and Hard Segment Length on the Structure–Property Relationships of Segmented Polyurethanes Based on a Linear Symmetric Diisocyanate, 1,4-Butanediol and PTMO Soft Segments. *Polymer (Guildf).* **2012**, *53* (23), 5358–5366. https://doi.org/10.1016/j.polymer.2012.08.005.

(68) Bennett, T. M.; Pei, K.; Cheng, H.-H.; Thurecht, K. J.; Jack, K. S.; Blakey, I. Can Ionic Liquid Additives Be Used to Extend the Scope of Poly(Styrene)-Block-Poly(Methyl Methacrylate) for Directed Self-Assembly? *J. Micro/Nanolithography, MEMS, MOEMS* **2014**, *13* (3), 031304. https://doi.org/10.1117/1.JMM.13.3.031304.

(69) Barbeau, P.; Gerard, J. F.; Magny, B.; Pascault, J. P. Effect of the Diisocyanate on the Structure and Properties of Polyurethane Acrylate Prepolymers. *J. Polym. Sci. Part B Polym. Phys.* **2000**, *38* (21), 2750–2768. https://doi.org/10.1002/1099-0488(20001101)38:21<2750::AID-POLB50>3.0.CO;2-B.

(70) Javni, I.; Zhang, W.; Petrović, Z. S. Effect of Different Isocyanates on the Properties of Soy-Based Polyurethanes. *J. Appl. Polym. Sci.* **2003**, *88* (13), 2912–2916. https://doi.org/10.1002/app.11966.

(71) Corcuera, M. A.; Rueda, L.; Saralegui, A.; Martin, M. D.; Fernandez-d'Arlas, B.; Mondragon, I.; Ecezia, A. Effect of Diisocyanate Structure on the Properties and Microstructure of Polyurethanes Based on Polyols Derived from Renewable Resources Ma. *J. Appl. Polym. Sci.* **2011**, *122* (5), 2658–2667. https://doi.org/10.1002/app.34781.

(72) Pandya, M. V.; Deshpande, D. D.; Hundiwale, D. G. Effect of Diisocyanate Structure on Viscoelastic, Thermal, Mechanical and Electrical Properties of Cast Polyurethanes. *J. Appl. Polym. Sci.* **1986**, *32* (5), 4959–4969. https://doi.org/10.1002/app.1986.070320518.

(73) Desai, S.; Thakore, I. M.; Sarawade, B. D.; Devi, S. Effect of Polyols and Diisocyanates on Thermo-Mechanical and Morphological Properties of Polyurethanes. *Eur. Polym. J.* **2000**, *36* (4), 711–725. https://doi.org/10.1016/S0014-3057(99)00114-7.

(74) Sheth, J. P.; Klinedinst, D. B.; Wilkes, G. L.; Yilgor, I.; Yilgor, E. Role of Chain Symmetry and Hydrogen Bonding in Segmented Copolymers with Monodisperse Hard Segments. *Polymer (Guildf).* **2005**, *46* (18), 7317–7322. https://doi.org/10.1016/j.polymer.2005.04.041.

(75) He, Y.; Xie, D.; Zhang, X. The Structure, Microphase-Separated Morphology, and Property of Polyurethanes and Polyureas. *J. Mater. Sci.* **2014**, *49* (21), 7339–7352. https://doi.org/10.1007/s10853-014-8458-y.

(76) Huang, S.-L.; Lai, J.-Y. Structure-Tensile Properties of Polyurethanes. *Eur. Polym. J.* **1997**, *33* (10–12), 1563–1567. https://doi.org/10.1016/S0014-3057(97)00058-X.

(77) Panwiriyarat, W.; Tanrattanakul, V.; Pilard, J. F.; Pasetto, P.; Khaokong, C. Effect of the Diisocyanate Structure and the Molecular Weight of Diols on Bio-Based Polyurethanes. *J. Appl. Polym. Sci.* **2013**, *130* (1), 453–462. https://doi.org/10.1002/app.39170.

(78) Hepburn, C. *Polyurethane Elastomers*; Elsevier, 1982. https://doi.org/10.1007/978-94-011-2924-4.

(79) Priscariu, C. *Polyurethane Elastomers From Morphology to Mechanical Aspects*; Springer-Verlag/Wien, 2011. https://doi.org/10.1007/978-3-7091-0514-6.

(80) M. Chapman, T. Models for Polyurethane Hydrolysis under Moderately Acidic Conditions : A Comparative Study of Hydrolysis Rates. *J. Polym. Sci. Part A Polym. Chem.* **1989**, *27* (1989), 1993–2005. https://doi.org/https://doi.org/10.1002/pola.1989.080270620.

(81) Xie, F.; Zhang, T.; Bryant, P.; Kurusingal, V.; Colwell, J. M.; Laycock, B. Degradation and Stabilization of Polyurethane Elastomers. *Prog. Polym. Sci.* **2019**, *90*, 211–268. https://doi.org/10.1016/j.progpolymsci.2018.12.003.

(82) Rosu, D.; Rosu, L.; Cascaval, C. N. IR-Change and Yellowing of Polyurethane as a Result of UV Irradiation. *Polym. Degrad. Stab.* **2009**, *94* (4), 591–596. https://doi.org/10.1016/j.polymdegradstab.2009.01.013.

(83) Rahman, M. M.; Kim, H. Do; Lee, W. K. Properties of Waterborne Polyurethane Adhesives: Effect of Chain Extender and Polyol Content. *J. Adhes. Sci. Technol.* **2009**, *23* (1), 177–193. https://doi.org/10.1163/156856108X344667.

(84) Moghaddam, M. P.; Abdi, H.; Javidi, M. H. Effect of Chain Extender Length on Gas Permeation Properties of Polyurethane Membranes. *Iran. Polym. J.* **2008**, *17* (6), 431–440.

(85) Tatai, L.; Moore, T. G.; Adhikari, R.; Malherbe, F.; Jayasekara, R.; Griffiths, I.; Gunatillake, P. A. Thermoplastic Biodegradable Polyurethanes: The Effect of Chain Extender Structure on Properties and in-Vitro Degradation. *Biomaterials* **2007**, *28* (36), 5407–5417. https://doi.org/10.1016/j.biomaterials.2007.08.035.

(86) Lee, C.-F.; Chen, C.-W.; Rwei, S.-P.; Chuang, F.-S. Thermal Behavior and Morphology of Thermoplastic Polyurethane Derived from Different Chain Extenders of 1,3-and 1,4-Butanediol. *Appl. Sci.* **2021**, *11* (2), 1–18. https://doi.org/10.3390/app11020698.

(87) Blackwell, J.; Nagarajan, M. R.; Hoitink, T. B. Structure of Polyurethane Elastomers: Effect of Chain Extender Length on the Structure of MDI/Diol Hard Segments. *Polymer (Guildf).* **1982**, *23*

(7), 950–956. https://doi.org/10.1016/0032-3861(82)90392-5.

(88) Born, L.; Hespe, H.; Crone, J.; Wolf, K. H. The Physical Crosslinking of Polyurethane Elastomers Studied by X-Ray Investigation of Model Urethanes. *Colloid Polym. Sci.* **1982**, *260* (9), 819–828. https://doi.org/10.1007/BF01419091.

(89) Hojabri, L.; Kong, X.; Narine, S. S. Functional Thermoplastics from Linear Diols and Diisocyanates Produced Entirely from Renewable Lipid Sources. *Biomacromolecules* **2010**, *11* (4), 911–918. https://doi.org/10.1021/bm901308c.

(90) Prisacariu, C.; Scortanu, E. Influence of the Type of Chain Extender and Urethane Group Content on the Mechanical Properties of Polyurethane Elastomers with Flexible Hard Segments. *High Perform. Polym.* **2011**, *23* (4), 308–313. https://doi.org/10.1177/0954008311405696.

(91) Touchet, T. J.; Cosgriff-Hernandez, E. M. Hierarchal Structure–Property Relationships of Segmented Polyurethanes. In *Advances in Polyurethane Biomaterials*; Chung, S., Webster, T. J., Eds.; 2016; pp 3–22. https://doi.org/10.1016/C2014-0-04143-3.

(92) Chang, C. C.; Chen, K. S.; Yu, T. L.; Chen, Y. S.; Tsai, C. L.; Tseng, Y. H. Phase Segregation of Polyester Based-Polyurethanes. *Polym. J.* **1999**, *31* (12), 1205–1210. https://doi.org/10.1295/polymj.31.1205.

(93) Shibaev, L. A.; Stepanov, N. G.; Zuev, V. V.; Solovskaya, N. A.; Sazanov, Y. N. Odd-Even Effect and Thermal Stability in the Series of Vinyl Polymers. Part 1. Poly-4-n-Alkylstyrenes. *Thermochim. Acta* **1991**, *186* (1), 19–34. https://doi.org/10.1016/0040-6031(91)87019-S.

(94) Zhou, C.; Wei, Z.; Yu, Y.; Shao, S.; Leng, X.; Wang, Y.; Li, Y. Biobased Long-Chain Aliphatic Polyesters of 1,12-Dodecanedioic Acid with a Variety of Diols: Odd-Even Effect and Mechanical Properties. *Mater. Today Commun.* **2019**, *19* (May), 450–458. https://doi.org/10.1016/j.mtcomm.2019.05.005.

(95) Klinedinst, D. B.; Yilgör, I.; Yilgör, E.; Zhang, M.; Wilkes, G. L. The Effect of Varying Soft and Hard Segment Length on the Structure e Property Relationships of Segmented Polyurethanes Based on a Linear Symmetric Diisocyanate , 1,4-Butanediol and PTMO Soft Segments. *Polymer (Guildf).* **2012**, *53* (23), 5358–5366. https://doi.org/10.1016/j.polymer.2012.08.005.

(96) Chang, C.-C.; Chen, K.-S.; Yu, T. L.; Chen, Y.-S.; Tsai, C.-L.; Tseng, Y.-H. Phase Segregation of Polyester Based-Polyurethanes. *Polym. J.* **1999**, *31* (12), 1205–1210. https://doi.org/10.1295/polymj.31.1205.

(97) Camberlin, Y.; Pascault, J. P. Phase Segregation Kinetics in Segmented Linear Polyurethanes: Relations Between Equilibrium Time and Chain Mobility and Between Equilibrium Degree of Segregation and Interaction Parameter. *J. Polym. Sci. Part A-2, Polym. Phys.* **1984**, *22* (10), 1835–1844. https://doi.org/10.1002/pol.1984.180221011.

(98) Chen, K. S.; Yu, T. L.; Chen, Y. S.; Lin, T. L.; Liu, W. J. Soft- and Hard-Segment Phase Segregation of Polyester-Based Polyurethane. *Journal of Polymer Research*. 2001, pp 99–109. https://doi.org/10.1007/s10965-006-0139-3.

(99) Chang, S. L.; Yu, T. L.; Huang, C. C.; Chen, W. C.; Linliu, K.; Lin, T. L. Effect of Polyester Side-Chains on the Phase Segregation of Polyurethanes Using Small-Angle X-Ray Scattering. *Polymer (Guildf).* **1998**, *39* (15), 3479–3489. https://doi.org/10.1016/S0032-3861(97)10070-2.

(100) Brocas, A. L.; Mantzaridis, C.; Tunc, D.; Carlotti, S. Polyether Synthesis: From Activated or Metal-Free Anionic Ring-Opening Polymerization of Epoxides to Functionalization. *Prog. Polym. Sci.* **2013**, *38* (6), 845–873. https://doi.org/10.1016/j.progpolymsci.2012.09.007.

(101) Schneider, N. S.; Sung, C. S. P. Transition Behavior and Phase Segregation in TDI Polyurethanes. *Polym. Eng. Sci.* **1977**, *17* (2), 73–80. https://doi.org/10.1002/pen.760170203.

(102) B. Wang, C.; L. Cooper, W. Morphology and Properties of Segmented Copolymers. *Macromolecules* **1983**, *16*, 775–786. https://doi.org/https://doi.org/10.1021/ma00239a014.

(103) Ragaert, K.; Delva, L.; Van Damme, N.; Kuzmanovic, M.; Hubo, S.; Cardon, L. Microstructural

Foundations of the Strength and Resilience of LLDPE Artificial Turf Yarn. *J. Appl. Polym. Sci.* **2016**, *133* (43), 1–12. https://doi.org/10.1002/app.44080.

(104) Kolgjini, B.; Schoukens, G.; Kiekens, P. Influence of Stretching on the Resilience of LLDPE Monofilaments for Application in Artificial Turf. *J. Appl. Polym. Sci.* **2012**, *124* (5), 4081–4089. https://doi.org/10.1002/app.35014.

(105) Voda, A.; Beck, K.; Schauber, T.; Adler, M.; Dabisch, T.; Bescher, M.; Viol, M.; Demco, D. E.; Blümich, B. Investigation of Soft Segments of Thermoplastic Polyurethane by NMR, Differential Scanning Calorimetry and Rebound Resilience. *Polym. Test.* **2006**, *25* (2), 203–213. https://doi.org/10.1016/j.polymertesting.2005.10.007.

(106) Monteiro, E. E. C.; Fonseca, J. L. C. Phase Segregation and Viscoelastic Behavior of Poly(Ether Urethane Urea)S. *J. Appl. Polym. Sci.* **1997**, *65* (11), 2227–2236. https://doi.org/10.1002/(SICI)1097-4628(19970912)65:11<2227::AID-APP20>3.0.CO;2-Z.

(107) Sacchetti, G.; Mussini, S.; Maccari, B. New CFC Free Polyether Microcellular Polyurethane for Footwear. *J. Cell. Plast.* **1993**, *29* (January), 13–28. https://doi.org/https://doi.org/10.1177/0021955X9302900101.

(108) Saldivar-Guerra, E.; Vivaldo-Lima, E. *Handbook of Polymer Synthesis, Characterization and Processing*; Wiley, 2013. https://doi.org/10.1002/9781118480793.

(109) R. Kricheldorf, H.; Nuyken, O.; Swift, G. *Plastics Engineering*; Marcel Dekker, 2005. https://doi.org/10.1007/978-1-4684-4919-8_37.

(110) Howard, G. T. Biodegradation of Polyurethane: A Review. *Int. Biodeterior. Biodegrad.* **2002**, *49* (4), 245–252. https://doi.org/10.1016/S0964-8305(02)00051-3.

(111) Schollenberger, C. S.; Stewart, F. D. Thermoplastic Polyurethane Hydrolysis Stability. *J. Elastoplast.* **1971**, *3* (1), 28–56. https://doi.org/10.1177/009524437100300103.

(112) Vilas D., A.; Mona A., K. Effect of Dicarboxylic Acids on the Performance Properties of Polyurethane Dispersions. *J. Appl. Polym. Sci.* **2010**, *117* (1), 572–580. https://doi.org/https://doi.org/10.1002/app.31267.

(113) Bostick E., E.; King A. Jr., J. *Handbook of Polycarbonate Science and Technology*; Legrand G., D., Bendler T., J., Eds.; CRC Press, 1999. https://doi.org/10.1201/9781482273694.

(114) Fukuoka, S.; Kawamura, M.; Komiya, K.; Tojo, M.; Hachiya, H.; Hasegawa, K.; Aminaka, M.; Okamoto, H.; Fukawa, I.; Konno, S. A Novel Non-Phosgene Polycarbonate Production Process Using by-Product CO2 as Starting Material. *Green Chem.* **2003**, *5* (5), 497–507. https://doi.org/10.1039/B304963A.

(115) Komiya, K.; Tojo, M.; Fukuoka, S. Process for the Producing of Aromatic Carbonate. US5872275, 1996.

(116) Lee, D.-K.; Tsai, H.-B.; Tsai, R.-S.; Chen, P. H. Preparation and Properties of Transparent Thermoplastic Segmented Polyurethanes Derived from Different Polyols. *Polym. Eng. Sci.* **2007**, *47* (5), 695–701. https://doi.org/10.1002/pen.20742.

(117) Kang, S. Y.; Ji, Z.; Tseng, L. F.; Turner, S. A.; Villanueva, D. A.; Johnson, R.; Albano, A.; Langer, R. Design and Synthesis of Waterborne Polyurethanes. *Adv. Mater.* **2018**, *30* (18), 1–7. https://doi.org/10.1002/adma.201706237.

(118) Kwiatkowski, K.; Nachman, M. The Abrasive Wear Resistance of the Segmented Linear Polyurethane Elastomers Based on a Variety of Polyols as Soft Segments. *Polymers (Basel).* **2017**, *9* (12), 705. https://doi.org/10.3390/polym9120705.

(119) Zhu, R.; Wang, Y.; Zhang, Z.; Ma, D.; Wang, X. Synthesis of Polycarbonate Urethane Elastomers and Effects of the Chemical Structures on Their Thermal, Mechanical and Biocompatibility Properties. *Heliyon* **2016**, *2* (6). https://doi.org/10.1016/j.heliyon.2016.e00125.

(120) Harris, R. F.; Joseph, M. D.; Davidson, C.; Deporter, C. D.; Dais, V. A. Polyurethane Elastomers

Based on Molecular Weight Advanced Poly(Ethylene Ether Carbonate) Diols. I. Comparison to Commercial Diols. *J. Appl. Polym. Sci.* **1990**, *41* (3–4), 487–507. https://doi.org/10.1002/app.1990.070410304.

(121) Sánchez-Adsuar, M. S.; Papon, E.; Villenave, J.-J. Influence of the Synthesis Conditions on the Properties of Thermoplastic Polyurethane Elastomers. *J. Appl. Polym. Sci.* **2000**, *76* (10), 1590–1595. https://doi.org/10.1002/(SICI)1097-4628(20000606)76:10<1590::AID-APP14>3.0.CO;2-2.

(122) Miller, J. A.; Lin, S. B.; Hwang, K. K. S.; Wu, K. S.; Gibson, P. E.; Cooper, S. L. Properties of Polyether-Polyurethane Block Copolymers: Effects of Hard Segment Length Distribution. *Macromolecules* **1985**, *18* (1), 32–44. https://doi.org/10.1021/ma00143a005.

(123) International, A. ASTM D2572-19, Standard Test Method for Isocyanate Groups in Urethane Materials or Prepolymers 1 https://www.astm.org/Standards/D2572.htm. https://doi.org/10.1520/D2572-19.

(124) De, D.; Gaymans, R. J. Polyurethanes with Narrow- and Polydisperse Hard Segment Distributions. *Macromol. Marerials Eng.* **2008**, *293*, 887–894. https://doi.org/10.1002/mame.200800147.

(125) Pattamaprom, C.; Wu, C. H.; Chen, P. H.; Huang, Y. L.; Ranganathan, P.; Rwei, S. P.; Chuan, F. S. Solvent-Free One-Shot Synthesis of Thermoplastic Polyurethane Based on Bio-Poly(1,3-Propylene Succinate) Glycol with Temperature-Sensitive Shape Memory Behavior. *ACS Omega* **2020**, *5* (8), 4058–4066. https://doi.org/10.1021/acsomega.9b03663.

(126) Xu, M.; J. MacKnight, W.; Y. Chen, C. H.; L. Thomas, E. Structure and Morphology of Segmented Polyurethanes : 1 . Influence of Incompatability on Hard-Segment Sequence Length. *Polymer (Guildf).* **1983**, *24* (10), 1327–1332. https://doi.org/10.1016/0032-3861(83)90068-X.

(127) Y. Chen, C. H.; M. Briner, R.; L. Thomas, E.; Xu, M.; J. MacKnight, W. Structure and Morphology of Segmented Polyurethanes : 2 . Influence of Reactant Incompatibility. *Polymer (Guildf).* **1983**, *24* (10), 1333–1340. https://doi.org/https://doi.org/10.1016/0032-3861(83)90069-1.

(128) Vlachopoulos, J.; Strutt, D. Polymer Processing. *Mater. Sci. Technol.* **2003**, *19* (9), 1161–1169. https://doi.org/10.1179/026708303225004738.

(129) Xu, W.; Jambhulkar, S.; Zhu, Y.; Ravichandran, D.; Kakarla, M.; Vernon, B.; Lott, D. G.; Cornella, J. L.; Shefi, O.; Miquelard-Garnier, G.; Yang, Y.; Song, K. 3D Printing for Polymer/Particle-Based Processing: A Review. *Compos. Part B Eng.* **2021**, *223* (June), 109102. https://doi.org/10.1016/j.compositesb.2021.109102.

(130) Zhou, L.; Fu, J.; He, Y. A Review of 3D Printing Technologies for Soft Polymer Materials. *Adv. Funct. Mater.* **2020**, *30* (28), 2000187. https://doi.org/10.1002/adfm.202000187.

(131) Dadbakhsh, S.; Verbelen, L.; Vandeputte, T.; Strobbe, D.; Van Puyvelde, P.; Kruth, J. P. Effect of Powder Size and Shape on the SLS Processability and Mechanical Properties of a TPU Elastomer. *Phys. Procedia* **2016**, *83*, 971–980. https://doi.org/10.1016/j.phpro.2016.08.102.

(132) Lu, G.; Kalyon, D. M.; Yilgör, I.; Yilgör, E. Rheology and Extrusion of Medical-Grade Thermoplastic Polyurethane. *Polym. Eng. Sci.* **2003**, *43* (12), 1863–1877. https://doi.org/10.1002/pen.10158.

(133) Xiao, J.; Gao, Y. The Manufacture of 3D Printing of Medical Grade TPU. *Prog. Addit. Manuf.* **2017**, *2* (3), 117–123. https://doi.org/10.1007/s40964-017-0023-1.

(134) Leung, L. M.; Koberstein, J. T. DSC Annealing Study of Microphase Separation and Multiple Endothermic Behavior in Polyether-Based Polyurethane Block Copolymers. *Macromolecules* **1986**, *19* (3), 706–713. https://doi.org/10.1021/ma00157a038.

(135) Lee, H. S.; Hsu, S. L. An Analysis of Phase Separation Kinetics of Model Polyurethanes. *Macromolecules* **1989**, *22* (3), 1100–1105. https://doi.org/10.1021/ma00193a017.

(136) Yanagihara, Y.; Osaka, N.; Murayama, S.; Saito, H. Thermal Annealing Behavior and Structure Development of Crystalline Hard Segment Domain in a Melt-Quenched Thermoplastic

Polyurethane. *Polymer (Guildf).* **2013**, *54* (8), 2183–2189. https://doi.org/10.1016/j.polymer.2013.02.005.

(137) Hu, W.; Koberstein, J. T. The Effect of Thermal Annealing on the Thermal Properties and Molecular Weight of a Segmented Polyurethane Copolymer. *J. Polym. Sci. Part B Polym. Phys.* **1994**, *32* (3), 437–446. https://doi.org/10.1002/polb.1994.090320304.

(138) Yingjie, L.; Gao, T.; Liu, J.; Linliu, K.; Deeper, C. R.; Chu, B. Multiphase Structure of a Segmented Polyurethane: Effects of Temperature and Annealing. *Macromolecules* **1992**, *25* (26), 7365–7372. https://doi.org/10.1021/ma00052a045.

(139) Koenig, J. L. *Infrared and Raman Spectroscopy of Polymers*; iSmithers Rapra Publishing, 2001.

(140) Schrader, B. *Infrared and Raman Spectroscopy, Method and Applications*; VCH, 1995. https://doi.org/10.1002/9783527615438.

(141) Gurunathan, T.; Mohanty, S.; Nayak, S. K. Isocyanate Terminated Castor Oil-Based Polyurethane Prepolymer: Synthesis and Characterization. *Prog. Org. Coatings* **2015**, *80*, 39–48. https://doi.org/10.1016/j.porgcoat.2014.11.017.

(142) Liu, W.-K.; Zhao, Y.; Wang, R.; Luo, F.; Li, J.-S.; Li, J.-H.; Tan, H. Effect of Chain Extender on Hydrogen Bond and Microphase Structure of Biodegradable Thermoplastic Polyurethanes. *Chinese J. Polym. Sci.* **2018**, *36* (4), 514–520. https://doi.org/10.1007/s10118-018-2020-3.

(143) Król, B.; Król, P.; Byczyński, Ł.; Szałański, P. Methods of Increasing Hydrophobicity of Polyurethane Materials: Important Applications of Coatings with Low Surface Free Energy. *Colloid Polym. Sci.* **2017**, *295* (12), 2309–2321. https://doi.org/10.1007/s00396-017-4202-x.

(144) Rogulska, M.; Maciejewska, M.; Olszewska, E. New Thermoplastic Poly(Carbonate-Urethane)s Based on Diphenylethane Derivative Chain Extender. *J. Therm. Anal. Calorim.* **2020**, *139* (2), 1049–1068. https://doi.org/10.1007/s10973-019-08433-z.

(145) Hu, J.; Tao, C.; Yuan, A.; Bao, J.; Cheng, Q.; Xu, G.; Huang, Y. Effects of Isosorbide on the Microphase Separation and Properties of Waterborne Polyurethane Coatings. *Polym. Korea* **2019**, *43* (2), 169–180. https://doi.org/10.7317/pk.2019.43.2.169.

(146) Zhao, X.; Qi, Y. H.; Li, K. J.; Zhang, Z. P. Hydrogen Bonds and FTIR Peaks of Polyether Polyurethane-Urea. *Key Eng. Mater.* **2019**, *815*, 151–156. https://doi.org/10.4028/www.scientific.net/KEM.815.151.

(147) Niemczyk, A.; Piegat, A.; Sonseca Olalla, Á.; El Fray, M. New Approach to Evaluate Microphase Separation in Segmented Polyurethanes Containing Carbonate Macrodiol. *Eur. Polym. J.* **2017**, *93* (May), 182–191. https://doi.org/10.1016/j.eurpolymj.2017.05.046.

(148) M. Striegel, A.; W. Yau, W.; J. Kirkland, J.; D. Bly, D. *Modern Size-Exclusion Liquid Chromatography: Practice of Gel Permeation and Gel Filtration Chromatography*; Wiley, 2009. https://doi.org/10.1016/S0021-9673(00)96826-2.

(149) *ISO 13885-1 Gel Permeation Chormatography (GPC)-Part 1: Tetrahydrofuran (THF) as Eluent*; 2020.

(150) Laíz Treceño, M.; Joan Carles, B. R. Synthesis and Characterization of Fluorinated Polymers, Universitat Autònoma de Barcelona, 2022.

(151) *ISO 2114: Plastics (Polyester Resins) and Paints and Varnishes (Binders) — Determination of Partial Acid Value and Total Acid Value*; 2000.

(152) *ISO 2554: Plastics - Unsaturated Polyester Resins - Determination of Hydroxyl Value*; 2000.

(153) Molland, A. F. *The Maritime Engineering Reference Book*; Elsevier, 2008. https://doi.org/10.1016/B978-0-7506-8987-8.X0001-7.

(154) Lohbauer, U.; Zinelis, S.; Rahiotis, C.; Petschelt, A.; Eliades, G. The Effect of Resin Composite Pre-Heating on Monomer Conversion and Polymerization Shrinkage. *Dent. Mater.* **2009**, *25* (4),

514–519. https://doi.org/10.1016/j.dental.2008.10.006.

(155) *ISO1183-1 Plastics – Methods for Determining the Density of Non-Cellular Plastics. Part 1: Immersion Method, Liquid Pyknometer and Titration Method*; 2019.

(156) Höhne, G. W. H.; Hemminger, W. F.; Flammersheim, H.-J. *Differential Scanning Calorimetry*; Springer. https://doi.org/10.3139/9781569906446.007.

(157) Frick, A.; Rochman, A. Characterization of TPU-Elastomers by Thermal Analysis (DSC). *Polym. Test.* **2004**, *23* (4), 413–417. https://doi.org/10.1016/j.polymertesting.2003.09.013.

(158) Kong, Y.; Hay, J. N. The Measurement of the Crystallinity of Polymers by DSC. **2002**, *43*, 3873–3878. https://doi.org/10.1016/S0032-3861(02)00235-5.

(159) Davis, J. R. *Tensile Testing*; ASM International, 2004.

(160) *ISO 37: Rubber, Vulcanized or Thermoplastic - Determination of Tensile Stress-Strain Properties*; 2017.

(161) *ISO48 Rubber, Vulcanized or Thermoplastic - Determination of Hardness (Hardness between 10 IRHD and 100 IRHD)*; 2018.

(162) Suryanarayana, C.; Grant Norton, M. *X-Ray Diffraction. A Practical Approach*; Springer, 1998. https://doi.org/10.1007/978-1-4899-0148-4.

(163) Glatter, O.; Kratky, O. *Small-Angle x-Ray Scattering*; Academic Press, 1982. https://doi.org/10.1002/actp.1985.010360520.

(164) Guinier, A.; Fournet, G. *Small-Angle Scattering of X-Rays*; Chapman & Hall, 1955. https://doi.org/10.1002/pol.1956.120199326.

(165) H. Choi, K.; Morais, M. Use of Small-Angle X-Ray Scattering to Investigate the Structure and Function of Dengue Virus NS3 and NS5; Humana Press; pp 241–252. https://doi.org/10.1007/978-1-4939-0348-1_15.

(166) Craievich, A. F. Small-Angle X-Ray Scattering by Nanostructured Materials. In *Handbook of Sol-Gel Science and Technology*; Springer International Publishing, 2016. https://doi.org/10.1007/978-3-319-19454-7_37-1.

(167) Lipfert, J.; Columbus, L.; Chu, V. B.; Lesley, S. A.; Doniach, S. Size and Shape of Detergent Micelles Determined by Small-Angle X-Ray Scattering. *J. Phys. Chem. B* **2007**, *111* (43), 12427–12438. https://doi.org/10.1021/jp073016l.

(168) Mohammed, A. S. A.; Carino, A.; Testino, A.; Andalibi, M. R.; Cervellino, A. A Dilute Gold Nanoparticle Suspension as Small-Angle X-Ray Scattering Standard for an Absolute Scale Using an Extended Guinier Approximation. *J. Appl. Crystallogr.* **2019**, *52* (2), 344–350. https://doi.org/10.1107/S1600576719001109.

(169) Chu, B.; Hsiao, B. S. Small-Angle X-Ray Scattering of Polymers. *Chem. Rev.* **2001**, *101* (6), 1727–1762. https://doi.org/10.1021/cr9900376.

(170) Kojio, K.; Matsuo, K.; Motokucho, S.; Yoshinaga, K.; Shimodaira, Y.; Kimura, K. Simultaneous Small-Angle X-Ray Scattering/Wide-Angle X-Ray Diffraction Study of the Microdomain Structure of Polyurethane Elastomers during Mechanical Deformation. *Polym. J.* **2011**, *43* (8), 692–699. https://doi.org/10.1038/pj.2011.48.

(171) Asensio, M.; Costa, V.; Nohales, A.; Bianchi, O.; Gómez, C. M. Tunable Structure and Properties of Segmented Thermoplastic Polyurethanes as a Function of Flexible Segment. *Polymers (Basel).* **2019**, *11* (12), 1910. https://doi.org/10.3390/polym11121910.

(172) Laity, P. R.; Taylor, J. E.; Wong, S. S.; Khunkamchoo, P.; Norris, K.; Cable, M.; Andrews, G. T.; Johnson, A. F.; Cameron, R. E. A 2-Dimensional Small-Angle X-Ray Scattering Study of the Microphase-Separated Morphology Exhibited by Thermoplastic Polyurethanes and Its Response to Deformation. *Polymer (Guildf).* **2004**, *45* (15), 5215–5232.

https://doi.org/10.1016/j.polymer.2004.05.032.

(173) Koberstein, J. T.; Stein, R. S. Small-Angle X-Ray Scattering Studies of Microdomain Structure in Segmented Polyurethane Elastomers. *J. Polym. Sci. Polym. Phys. Ed.* **1983**, *21* (8), 1439–1472. https://doi.org/10.1002/pol.1983.180210814.

(174) Hamley, I.; Castelletto, V. Small-Angle Scattering of Block Copolymers. In *Soft Matter Characterization*; Springer Netherlands: Dordrecht, 2008; pp 1021–1081. https://doi.org/10.1007/978-1-4020-4465-6_20.

(175) Ślusarczyk, C.; Sieradzka, M.; Fabia, J.; Fryczkowski, R. Supermolecular Structure of Poly(Butylene Terephthalate) Fibers Formed with the Addition of Reduced Graphene Oxide. *Polymers (Basel).* **2020**, *12* (7), 1456. https://doi.org/10.3390/polym12071456.

(176) Cerrada, M. L.; Benavente, R.; Zamfirova, G.; Pérez, E. Influence of the Type of Fiber on the Structure and Viscoelastic Relaxations in Composites Based on a Metallocenic Ethylene-1-Octene Copolymer. *Polym. J.* **2002**, *34* (3), 175–183. https://doi.org/10.1295/polymj.34.175.

(177) Parodi, E.; Peters, G.; Govaert, L. Structure–Properties Relations for Polyamide 6, Part 1: Influence of the Thermal History during Compression Moulding on Deformation and Failure Kinetics. *Polymers (Basel).* **2018**, *10* (7), 710. https://doi.org/10.3390/polym10070710.

(178) Mohamed, H. F. M.; Abdel-Hady, E. E.; Abdel-Hamed, M. O. Proton Conductivity and Free Volume Properties in Per-Fluorinated Sulfonic Acid/PTFE Copolymer for Fuel Cell. *Acta Phys. Pol. A* **2017**, *132* (5), 1509–1514. https://doi.org/10.12693/APhysPolA.132.1509.

(179) Hedesiu, C.; Demco, D. E.; Kleppinger, R.; Poel, G. Vanden; Remerie, K.; Litvinov, V. M.; Blümich, B.; Steenbakkers, R. Aging Effects on the Phase Composition and Chain Mobility of Isotactic Poly(Propylene). *Macromol. Mater. Eng.* **2008**, *293* (10), 847–857. https://doi.org/10.1002/mame.200800140.

(180) Mo, Z.; Zhang, H. The Degree of Crystallinity in Polymers by Wide-Angle X-Ray Diffraction (Waxd). *J. Macromol. Sci. Part C Polym. Rev.* **1995**, *35* (4), 555–580. https://doi.org/10.1080/15321799508021751.

(181) Devroede, J.; België, J. Study of the THF Formation during the TPA-Based Synthesis of Study of the THF Formation during the TPA-Based Synthesis of PBT Jan Devroede, Eindhoven University of Technology, 2022. https://doi.org/10.6100/IR630627.

(182) Devroede, J.; Duchateau, R.; Koning, C. E.; Meuldijk, J. The Synthesis of Poly(Butylene Terephthalate) from Terephthalic Acid, Part I: The Influence of Terephthalic Acid on the Tetrahydrofuran Formation. *J. Appl. Polym. Sci.* **2009**, *114* (4), 2435–2444. https://doi.org/10.1002/app.30782.

(183) Weinberger, S.; Pellis, A.; Comerford, J.; Farmer, T.; Guebitz, G. Efficient Physisorption of Candida Antarctica Lipase B on Polypropylene Beads and Application for Polyester Synthesis. *Catalysts* **2018**, *8* (9), 369. https://doi.org/10.3390/catal8090369.

(184) Polymer Database. Polyester database https://polymerdatabase.com/polymer index/polyesters.html (accessed Apr 5, 2022).

(185) Antony, J. *Design of Experiments for Engineers and Scientists*; Elsevier, 2014. https://doi.org/10.1016/C2012-0-03558-2.

(186) Shirai, K. A Thermodynamic Description of the Hysteresis in Specific-Heat Curves in Glass Transitions. *J. Phys. Commun.* **2021**, *5* (1), 015004. https://doi.org/10.1088/2399-6528/abd808.

(187) Kalogeras, I. M. Glass-Transition Phenomena in Polymer Blends. In *Encyclopedia of Polymer Blends*; Wiley-VCH Verlag GmbH & Co. KGaA: Weinheim, Germany, 2016; Vol. 3, pp 1–134. https://doi.org/10.1002/9783527653966.ch1.

(188) Seymour, R. W.; Cooper, S. L. Thermal Analysis of Polyurethane Block Polymers. *Macromolecules* **1973**, *6* (1), 48–53. https://doi.org/10.1021/ma60031a008.

(189) Koyvanich, K.; Sirisathitkul, C.; Rugmai, S. Effect of Cobalt Fillers on Polyurethane Segmentations Investigated by Synchrotron Small Angle X-Ray Scattering. *Adv. Mater. Sci. Eng.* **2013**, *2013* (1), 1–8. https://doi.org/10.1155/2013/493867.

(190) Chen-Tsai, C. H. Y.; Thomas, E. L.; MacKnight, W. J.; Schneider, N. S. Structure and Morphology of Segmented Polyurethanes: 3. Electron Microscopy and Small Angle X-Ray Scattering Studies of Amorphous Random Segmented Polyurethanes. *Polymer (Guildf).* **1986**, *27* (5), 659–666. https://doi.org/10.1016/0032-3861(86)90121-7.

(191) Madkour, T. M.; Mohamed, S. K. Heterocyclic and Aromatic Based Polyurethane Scaffolds: Morphology and Crystallinity Studied by X-Ray Diffraction, Small-Angle X-Ray Scattering and Differential Scanning Calorimetry. *J. Appl. Crystallogr.* **2013**, *46* (4), 980–992. https://doi.org/10.1107/S0021889813013733.

(192) Sokolova, M.; Bugrov, A.; Smirnov, M.; Smirnov, A.; Lahderanta, E.; Svetlichnyi, V.; Toikka, A. Effect of Domain Structure of Segmented Poly(Urethane-Imide) Membranes with Polycaprolactone Soft Blocks on Dehydration of n-Propanol via Pervaporation. *Polymers (Basel).* **2018**, *10* (11), 1222. https://doi.org/10.3390/polym10111222.

(193) Laity, P. R.; Taylor, J. E.; Wong, S. S.; Khunkamchoo, P.; Cable, M.; Andrews, G. T.; Johnson, A. F.; Cameron, R. E. Morphological Behaviour of Thermoplastic Polyurethanes During Repeated Deformation. *Macromol. Mater. Eng.* **2006**, *291* (4), 301–324. https://doi.org/10.1002/mame.200500339.

(194) Lee, D.; Register, R. A.; Yang, C.; Cooper, S. L. MDI-Based Polyurethane Ionomers. 1. New Small-Angle x-Ray Scattering Model. *Macromolecules* **1988**, *21* (4), 998–1004. https://doi.org/10.1021/ma00182a026.

(195) Pontoni, D.; Finet, S.; Narayanan, T.; Rennie, A. R. Interactions and Kinetic Arrest in an Adhesive Hard-Sphere Colloidal System. *J. Chem. Phys.* **2003**, *119* (12), 6157–6165. https://doi.org/10.1063/1.1601605.

(196) Botet, R.; Kwok, S.; Cabane, B. Percus–Yevick Structure Factors Made Simple. *J. Appl. Crystallogr.* **2020**, *53* (6), 1570–1582. https://doi.org/10.1107/S1600576720014041.

(197) Zernike, F.; Prins, J. A. Die Beugung von Röntgenstrahlen in Flüssigkeiten Als Effekt Der Molekülanordnung. *Zeitschrift für Phys. A Hadron. Nucl.* **1927**, *41* (2–3), 184–194. https://doi.org/10.1007/BF01391926.

(198) Tencé-Girault, S.; Lebreton, S.; Bunau, O.; Dang, P.; Bargain, F. Simultaneous SAXS-WAXS Experiments on Semi-Crystalline Polymers: Example of PA11 and Its Brill Transition. *Crystals* **2019**, *9* (5), 271. https://doi.org/10.3390/cryst9050271.

(199) Rabiej, S.; Wlochowicz, A. SAXS and WAXS Investigations of the Crystallinity in Polymers. *Angew. Chemie* **1990**, *175* (1), 81–97. https://doi.org/https://doi.org/10.1002/apmc.1990.051750107.

(200) Hermans, P. H.; Weidinger, A. Quantitative X-Ray Investigations on the Crystallinity of Cellulose Fibers. A Background Analysis. *J. Appl. Phys.* **1948**, *19* (5), 491–506. https://doi.org/10.1063/1.1698162.

(201) Mita, K.; Okumura, H.; Kimura, K.; Isaki, T.; Takenaka, M.; Kanaya, T. Simultaneous Small- and Wide-Angle X-Ray Scattering Studies on the Crystallization Dynamics of Poly(4-Methylpentene-1) from Melt. *Polym. J.* **2013**, *45* (1), 79–86. https://doi.org/10.1038/pj.2012.204.

(202) Baptista, C.; Azagury, A.; Shin, H.; Baker, C. M.; Ly, E.; Lee, R.; Mathiowitz, E. The Effect of Temperature and Pressure on Polycaprolactone Morphology. *Polymer (Guildf).* **2020**, *191*, 122227. https://doi.org/10.1016/j.polymer.2020.122227.

(203) Sajkiewicz, P.; Hashimoto, T.; Saijo, K.; Gradys, A. 'Intermediate Phase' in Poly(Ethylene) as Elucidated by the WAXS. Analysis of Crystallization Kinetics. *Polymer (Guildf).* **2005**, *46* (2), 513–521. https://doi.org/10.1016/j.polymer.2004.11.018.

(204) Wang, Z.-G.; Hsiao, B. S.; Sirota, E. B.; Srinivas, S. A Simultaneous Small- and Wide-Angle X-Ray Scattering Study of the Early Stages of Melt Crystallization in Polyethylene. *Polymer (Guildf).* **2000**, *41* (25), 8825–8832. https://doi.org/10.1016/S0032-3861(00)00225-1.

(205) Viljanen, M.; Suomela, J. A.; Svedström, K. Wide-Angle X-Ray Scattering Studies on Contemporary and Ancient Bast Fibres Used in Textiles – Ultrastructural Studies on Stinging Nettle. *Cellulose* **2022**, *29* (4), 2645–2661. https://doi.org/10.1007/s10570-021-04400-w.

(206) Farge, L.; Boisse, J.; Dillet, J.; André, S.; Albouy, P.-A.; Meneau, F. Wide-Angle X-Ray Scattering Study of the Lamellar/Fibrillar Transition for a Semi-Crystalline Polymer Deformed in Tension in Relation with the Evolution of Volume Strain. *J. Polym. Sci. Part B Polym. Phys.* **2015**, *53* (20), 1470–1480. https://doi.org/10.1002/polb.23790.

(207) Kojio, K.; Matsuo, K.; Motokucho, S.; Yoshinaga, K.; Shimodaira, Y.; Kimura, K. Simultaneous Small-Angle X-Ray Scattering/Wide-Angle X-Ray Diffraction Study of the Microdomain Structure of Polyurethane Elastomers during Mechanical Deformation. *Polym. J.* **2011**, *43* (8), 692–699. https://doi.org/10.1038/pj.2011.48.

(208) Korley, L. T. J.; Pate, B. D.; Thomas, E. L.; Hammond, P. T. Effect of the Degree of Soft and Hard Segment Ordering on the Morphology and Mechanical Behavior of Semicrystalline Segmented Polyurethanes. *Polymer (Guildf).* **2006**, *47* (9), 3073–3082. https://doi.org/10.1016/j.polymer.2006.02.093.

(209) Roberts, D. R. T.; Holder, S. J. Mechanochromic Systems for the Detection of Stress, Strain and Deformation in Polymeric Materials. *J. Mater. Chem.* **2011**, *21* (23), 8256. https://doi.org/10.1039/c0jm04237d.

(210) Rao, N.; O'Brien, K. *Mechanical Properties of Solid Polymers*; Wiley: München, 1998. https://doi.org/10.3139/9783446402447.001.

(211) François, D.; Pineau, A.; Zaoui, A. *Mechanical Behaviour of Materials: Volume II: Fracture Mechanics and Damage*; 2012. https://doi.org/10.1007/978-94-007-4930-6.

(212) Gibbs, J. H.; DiMarzio, E. A. Nature of the Glass Transition and the Glassy State. *J. Chem. Phys.* **1958**, *28* (3), 373–383. https://doi.org/10.1063/1.1744141.

(213) Robertson, R. E. Theory for the Plasticity of Glassy Polymers. *J. Chem. Phys.* **1966**, *44* (10), 3950–3956. https://doi.org/10.1063/1.1726558.

(214) Gibbs, J. H.; DiMarzio, E. A. Glass Temperature of Copolymers. *J. Polym. Sci.* **1959**, *40* (136), 121–131. https://doi.org/10.1002/pol.1959.1204013609.

(215) Boyer, R. F. Dependence of Mechanical Properties on Molecular Motion in Polymers. *Polym. Eng. Sci.* **1968**, *8* (3), 161–185. https://doi.org/10.1002/pen.760080302.

(216) Sogolova, T. I.; Demina, M. I. Temperature Dependence of the Mechanical Properties of Polymers of Different Chemical Structure in the Temperature Range from 4.2 to 300 °K. *Polym. Mech.* **1978**, *13* (3), 333–337. https://doi.org/10.1007/BF00859411.

(217) Wu, J.; Chen, L.; Li, H. H.; Su, B. L.; Wang, Y. S. Effect of Temperature on Tensile Fatigue Life of Natural Rubber. *IOP Conf. Ser. Mater. Sci. Eng.* **2018**, *389* (1), 012024. https://doi.org/10.1088/1757-899X/389/1/012024.

(218) Stachurski, Z. Deformation Mechanisms and Yield Strength in Amorphous Polymers. *Prog. Polym. Sci.* **1997**, *22* (3), 407–474. https://doi.org/10.1016/S0079-6700(96)00024-X.

(219) Matyjaszewski, K.; Môller, M. *Polymer Science : A Comprehensive Reference*; Elsevier; Vol. 1.

(220) Tolinski, M. *Additives for Polyolefins. Getting the Most out of Polypropylene, Polyethylene and TPO*; Elsevier, 2015. https://doi.org/10.1016/B978-0-323-35884-2.00019-3.

(221) Likhtman, A. E.; McLeish, T. C. B. Quantitative Theory for Linear Dynamics of Linear Entangled Polymers. *Macromolecules* **2002**, *35* (16), 6332–6343. https://doi.org/10.1021/ma0200219.

(222) Bowden, P. B.; Young, R. J. Deformation Mechanisms in Crystalline Polymers. *J. Mater. Sci.* **1974**, *9* (12), 2034–2051. https://doi.org/10.1007/BF00540553.

(223) Uneyama, T.; Masubuchi, Y. Multi-Chain Slip-Spring Model for Entangled Polymer Dynamics. *J. Chem. Phys.* **2012**, *137* (15), 154902. https://doi.org/10.1063/1.4758320.

(224) Berdichevsky, V. L.; Herman, J. N. On Rheology of Cross-Linked Polymers: 1. Slippage of Polymer Chains and Its Macroscopic Modeling. *Int. J. Eng. Sci.* **2016**, *100*, 183–198. https://doi.org/10.1016/j.ijengsci.2015.01.003.

(225) Jabbari-Farouji, S.; Rottler, J.; Lame, O.; Makke, A.; Perez, M.; Barrat, J.-L. Plastic Deformation Mechanisms of Semicrystalline and Amorphous Polymers. *ACS Macro Lett.* **2015**, *4* (2), 147–150. https://doi.org/10.1021/mz500754b.

(226) Oprea, S. Effect of Composition and Hard-Segment Content on Thermo-Mechanical Properties of Cross-Linked Polyurethane Copolymers. *High Perform. Polym.* **2009**, *21* (3), 353–370. https://doi.org/10.1177/0954008308092071.

(227) Zdrahala, R. J.; Gerkin, R. M.; Hager, S. L.; Critchfield, F. E. Polyether-based Thermoplastic Polyurethanes. I. Effect of the Hard-segment Content. *J. Appl. Polym. Sci.* **1979**, *24* (9), 2041–2050. https://doi.org/10.1002/app.1979.070240912.

(228) Zhao, J.; Yu, P.; Dong, S. The Influence of Crosslink Density on the Failure Behavior in Amorphous Polymers by Molecular Dynamics Simulations. *Materials (Basel).* **2016**, *9* (4), 234. https://doi.org/10.3390/ma9040234.

(229) Seefried, C. G.; Koleske, J. V.; Critchfield, F. E. Thermoplastic Urethane Elastomers. II. Effects of Variations in Hard-Segment Concentration. *J. Appl. Polym. Sci.* **1975**, *19* (9), 2503–2513. https://doi.org/10.1002/app.1975.070190913.

(230) Harris, R. F.; Joseph, M. D.; Davidson, C.; Deporter, C. D.; Dais, V. A. Polyurethane Elastomers Based on Molecular Weight Advanced Poly(Ethylene Ether Carbonate) Diols. II. Effects of Variations in Hard Segment Concentration. *J. Appl. Polym. Sci.* **1990**, *41* (34), 509–525. https://doi.org/10.1002/app.1990.070410305.

(231) Petrović, Z. S.; Ilavský, M.; Du??ek, K.; Vidaković, M.; Javni, I.; Banjanin, B. The Effect of Crosslinking on Properties of Polyurethane Elastomers. *J. Appl. Polym. Sci.* **1991**, *42* (2), 391–398. https://doi.org/10.1002/app.1991.070420211.

(232) Keith, H. D.; Passaglia, E. Dislocations in Polymer Crystals. *J. Res. Natl. Bur. Stand. Sect. A Phys. Chem.* **1964**, *68A* (5), 513. https://doi.org/10.6028/jres.068A.048.

(233) Behl, M.; Lendlein, A. Shape-Memory Polymers. *Mater. Today* **2007**, *10* (4), 20–28. https://doi.org/10.1016/S1369-7021(07)70047-0.

(234) Lendlein, A.; Kelch, S. Shape-Memory Polymers. *Angew. Chemie Int. Ed.* **2002**, *41* (12), 2034. https://doi.org/10.1002/1521-3773(20020617)41:12<2034::AID-ANIE2034>3.0.CO;2-M.

(235) Han, X.; Dong, Z.; Fan, M.; Liu, Y.; Li, J.-H.; Wang, Y.; Yuan, Q.; Li, B.; Zhang, S. PH-Induced Shape-Memory Polymers. *Macromol. Rapid Commun.* **2012**, *33* (12), 1055–1060. https://doi.org/10.1002/marc.201200153.

(236) Leng, J.; Lan, X.; Liu, Y.; Du, S. Shape-Memory Polymers and Their Composites: Stimulus Methods and Applications. *Prog. Mater. Sci.* **2011**, *56* (7), 1077–1135. https://doi.org/10.1016/j.pmatsci.2011.03.001.

(237) Lendlein, A.; Jiang, H.; Jünger, O.; Langer, R. Light-Induced Shape-Memory Polymers. *Nature* **2005**, *434* (7035), 879–882. https://doi.org/10.1038/nature03496.

(238) Basak, S.; Bandyopadhyay, A. Solvent Responsive Shape Memory Polymers- Evolution, Current Status, and Future Outlook. *Macromol. Chem. Phys.* **2021**, *222* (19), 2100195. https://doi.org/10.1002/macp.202100195.

(239) Ze, Q.; Kuang, X.; Wu, S.; Wong, J.; Montgomery, S. M.; Zhang, R.; Kovitz, J. M.; Yang, F.; Qi,

H. J.; Zhao, R. Magnetic Shape Memory Polymers with Integrated Multifunctional Shape Manipulation. *Adv. Mater.* **2020**, *32* (4), 1906657. https://doi.org/10.1002/adma.201906657.

(240) Zare, M.; Prabhakaran, M. P.; Parvin, N.; Ramakrishna, S. Thermally-Induced Two-Way Shape Memory Polymers: Mechanisms, Structures, and Applications. *Chem. Eng. J.* **2019**, *374*, 706–720. https://doi.org/10.1016/j.cej.2019.05.167.

(241) Xu, J.; Song, J. Thermal Responsive Shape Memory Polymers for Biomedical Applications. In *Biomedical Engineering - Frontiers and Challenges*; InTech, 2011. https://doi.org/10.5772/19256.

(242) Zhou, J.; Li, H.; Tian, R.; Dugnani, R.; Lu, H.; Chen, Y.; Guo, Y.; Duan, H.; Liu, H. Fabricating Fast Triggered Electro-Active Shape Memory Graphite/Silver Nanowires/Epoxy Resin Composite from Polymer Template. *Sci. Rep.* **2017**, *7* (1), 5535. https://doi.org/10.1038/s41598-017-05968-9.

(243) Mishra, S. R.; Tracy, J. B. Sequential Actuation of Shape-Memory Polymers through Wavelength-Selective Photothermal Heating of Gold Nanospheres and Nanorods. *ACS Appl. Nano Mater.* **2018**, *1* (7), 3063–3067. https://doi.org/10.1021/acsanm.8b00394.

(244) Amornkitbamrung, L.; Srisaard, S.; Jubsilp, C.; Bielawski, C. W.; Um, S. H.; Rimdusit, S. Near-Infrared Light Responsive Shape Memory Polymers from Bio-Based Benzoxazine/Epoxy Copolymers Produced without Using Photothermal Filler. *Polymer (Guildf).* **2020**, *209* (June), 122986. https://doi.org/10.1016/j.polymer.2020.122986.

(245) van Vilsteren, S. J. M.; Yarmand, H.; Ghodrat, S. Review of Magnetic Shape Memory Polymers and Magnetic Soft Materials. *Magnetochemistry* **2021**, *7* (9), 123. https://doi.org/10.3390/magnetochemistry7090123.

(246) Liu, Y.; Lv, H.; Lan, X.; Leng, J.; Du, S. Review of Electro-Active Shape-Memory Polymer Composite. *Compos. Sci. Technol.* **2009**, *69* (13), 2064–2068. https://doi.org/10.1016/j.compscitech.2008.08.016.

(247) Du, F.-P.; Ye, E.-Z.; Yang, W.; Shen, T.-H.; Tang, C.-Y.; Xie, X.-L.; Zhou, X.-P.; Law, W.-C. Electroactive Shape Memory Polymer Based on Optimized Multi-Walled Carbon Nanotubes/Polyvinyl Alcohol Nanocomposites. *Compos. Part B Eng.* **2015**, *68*, 170–175. https://doi.org/10.1016/j.compositesb.2014.08.043.

(248) Yakacki, C. M.; Shandas, R.; Lanning, C.; Rech, B.; Eckstein, A.; Gall, K. Unconstrained Recovery Characterization of Shape-Memory Polymer Networks for Cardiovascular Applications. *Biomaterials* **2007**, *28* (14), 2255–2263. https://doi.org/10.1016/j.biomaterials.2007.01.030.

(249) Bovesecchi, G.; Corasaniti, S.; Costanza, G.; Tata, M. E. A Novel Self-Deployable Solar Sail System Activated by Shape Memory Alloys. *Aerospace* **2019**, *6* (7), 78. https://doi.org/10.3390/aerospace6070078.

(250) Cooper, C. B.; Nikzad, S.; Yan, H.; Ochiai, Y.; Lai, J. C.; Yu, Z.; Chen, G.; Kang, J.; Bao, Z. High Energy Density Shape Memory Polymers Using Strain-Induced Supramolecular Nanostructures. *ACS Cent. Sci.* **2021**, *7* (10), 1657–1667. https://doi.org/10.1021/acscentsci.1c00829.

(251) Liu, C.; Qin, H.; Mather, P. T. Review of Progress in Shape-Memory Polymers. *J. Mater. Chem.* **2007**, *17* (16), 1543. https://doi.org/10.1039/b615954k.

(252) Zheng, Y.; Dong, R.; Shen, J.; Guo, S. Tunable Shape Memory Performances via Multilayer Assembly of Thermoplastic Polyurethane and Polycaprolactone. *ACS Appl. Mater. Interfaces* **2016**, *8* (2), 1371–1380. https://doi.org/10.1021/acsami.5b10246.

(253) Saralegi, A.; Johan Foster, E.; Weder, C.; Eceiza, A.; Corcuera, M. A. Thermoplastic Shape-Memory Polyurethanes Based on Natural Oils. *Smart Mater. Struct.* **2014**, *23* (2), 025033. https://doi.org/10.1088/0964-1726/23/2/025033.

(254) Wang, H.; Yuen, U. Synthesis of Thermoplastic Polyurethane and Its Physical and Shape Memory Properties. *J. Appl. Polym. Sci.* **2006**, *102* (1), 607–615.

https://doi.org/10.1002/app.24335.

(255) Mohammadzadeh, F.; Haddadi-Asl, V.; Balzade, Z.; Sahebi Jouibari, I. Switch Segment and Halloysite Nanotube Role in the Phase Separation Behavior of Shape-memory Thermoplastic Polyurethane. *Polym. Compos.* **2020**, *41* (7), 2625–2633. https://doi.org/10.1002/pc.25561.

(256) Saralegi, A.; Fernandes, S. C. M.; Alonso-Varona, A.; Palomares, T.; Foster, E. J.; Weder, C.; Eceiza, A.; Corcuera, M. A. Shape-Memory Bionanocomposites Based on Chitin Nanocrystals and Thermoplastic Polyurethane with a Highly Crystalline Soft Segment. *Biomacromolecules* **2013**, *14* (12), 4475–4482. https://doi.org/10.1021/bm401385c.

(257) Jing, X.; Mi, H.; Huang, H.; Turng, L. Shape Memory Thermoplastic Polyurethane (TPU)/Poly(ε-Caprolactone) (PCL) Blends as Self-Knotting Sutures. *J. Mech. Behav. Biomed. Mater.* **2016**, *64*, 94–103. https://doi.org/10.1016/j.jmbbm.2016.07.023.

(258) Lai, S.-M.; Lan, Y.-C. Shape Memory Properties of Melt-Blended Polylactic Acid (PLA)/Thermoplastic Polyurethane (TPU) Bio-Based Blends. *J. Polym. Res.* **2013**, *20* (5), 140. https://doi.org/10.1007/s10965-013-0140-6.

(259) Gorbunova, M. A.; Anokhin, D. V; Badamshina, E. R. Recent Advances in the Synthesis and Application of Thermoplastic Semicrystalline Shape Memory Polyurethanes. *Polym. Sci. Ser. B* **2020**, *62* (5), 427–450. https://doi.org/10.1134/S1560090420050073.

(260) Park, J.; Dao, T.; Lee, H.; Jeong, H.; Kim, B. Properties of Graphene/Shape Memory Thermoplastic Polyurethane Composites Actuating by Various Methods. *Materials (Basel).* **2014**, *7* (3), 1520–1538. https://doi.org/10.3390/ma7031520.

(261) Chan, B. Q. Y.; Liow, S. S.; Loh, X. J. Organic–Inorganic Shape Memory Thermoplastic Polyurethane Based on Polycaprolactone and Polydimethylsiloxane. *RSC Adv.* **2016**, *6* (41), 34946–34954. https://doi.org/10.1039/C6RA04041A.

(262) Zhou, X.; Hu, B.; Xiao, W. Q.; Yan, L.; Wang, Z. J.; Zhang, J. J.; Lin, H. L.; Bian, J.; Lu, Y. Morphology and Properties of Shape Memory Thermoplastic Polyurethane Composites Incorporating Graphene-Montmorillonite Hybrids. *J. Appl. Polym. Sci.* **2018**, *135* (15), 46149. https://doi.org/10.1002/app.46149.

(263) Jeong, H. M.; Song, J. H.; Lee, S. Y.; Kim, B. K. Miscibility and Shape Memory Property of Poly (Vinyl Chloride)/Thermoplastic Polyurethane Blends. *J. Mater. Sci.* **2001**, *36*, 5457–5463. https://doi.org/https://doi.org/10.1023/A:1012481631570.

(264) Jeong, H. M.; Ahn, B. K.; Kim, B. K. Miscibility and Shape Memory Effect of Thermoplastic Polyurethane Blends with Phenoxy Resin. *Eur. Polym. J.* **2001**, *37* (11), 2245–2252. https://doi.org/10.1016/S0014-3057(01)00123-9.

(265) Petrović, Z. S.; Milić, J.; Zhang, F.; Ilavsky, J. Fast-Responding Bio-Based Shape Memory Thermoplastic Polyurethanes. *Polymer (Guildf).* **2017**, *121*, 26–37. https://doi.org/10.1016/j.polymer.2017.05.072.

(266) Liu, T.; Huang, R.; Qi, X.; Dong, P.; Fu, Q. Facile Preparation of Rapidly Electro-Active Shape Memory Thermoplastic Polyurethane/Polylactide Blends via Phase Morphology Control and Incorporation of Conductive Fillers. *Polymer (Guildf).* **2017**, *114*, 28–35. https://doi.org/10.1016/j.polymer.2017.02.077.

(267) Wang, W.; Liao, X.; Guo, F.; Wang, G.; Yan, Z.; Liu, F.; Li, G. Facile Fabrication of Lightweight Shape Memory Thermoplastic Polyurethane/Polylactide Foams by Supercritical Carbon Dioxide Foaming. *Ind. Eng. Chem. Res.* **2020**, *59* (16), 7611–7623. https://doi.org/10.1021/acs.iecr.0c00404.

(268) Chen, T.; Fang, L.; Lu, C.; Xu, Z. Effects of Blended Reversible Epoxy Domains on Structures and Properties of Self-Healing/Shape-Memory Thermoplastic Polyurethane. *Macromol. Mater. Eng.* **2020**, *305* (1), 1900578. https://doi.org/10.1002/mame.201900578.

(269) Chen, J.; Zhang, Z.; Huang, W.; Li, J.; Yang, J.; Wang, Y.; Zhou, Z.; Zhang, J. Carbon Nanotube

Network Structure Induced Strain Sensitivity and Shape Memory Behavior Changes of Thermoplastic Polyurethane. *Mater. Des.* **2015**, *69*, 105–113. https://doi.org/10.1016/j.matdes.2014.12.054.

(270) Ahmed, N.; Kausar, A.; Muhammad, B. Advances in Shape Memory Polyurethanes and Composites: A Review. *Polym. Plast. Technol. Eng.* **2015**, *54* (13), 1410–1423. https://doi.org/10.1080/03602559.2015.1021490.

(271) Rousseau, I. A. Challenges of Shape Memory Polymers: A Review of the Progress toward Overcoming SMP's Limitations. *Polym. Eng. Sci.* **2008**, *48* (11), 2075–2089. https://doi.org/10.1002/pen.21213.

(272) Anthamatten, M.; Roddecha, S.; Li, J. Energy Storage Capacity of Shape-Memory Polymers. *Macromolecules* **2013**, *46* (10), 4230–4234. https://doi.org/10.1021/ma400742g.

(273) Sultan, M. T. H.; Mat Yazik, M. H. Shape Memory Polymer and Its Composites as Morphing Materials. In *Failure Analysis in Biocomposites, Fibre-Reinforced Composites and Hybrid Composites*; Woodhead Publishing, 2019; pp 181–198. https://doi.org/10.1016/C2016-0-04423-6.

(274) Rapp, S.; Baier, H. Determination of Recovery Energy Densities of Shape Memory Polymers via Closed-Loop, Force-Controlled Recovery Cycling. *Smart Mater. Struct.* **2010**, *19* (4). https://doi.org/10.1088/0964-1726/19/4/045018.

(275) Cooper, C. B.; Nikzad, S.; Yan, H.; Ochiai, Y.; Lai, J.-C.; Yu, Z.; Chen, G.; Kang, J.; Bao, Z. High Energy Density Shape Memory Polymers Using Strain-Induced Supramolecular Nanostructures. *ACS Cent. Sci.* **2021**, *7* (10), 1657–1667. https://doi.org/10.1021/acscentsci.1c00829.

(276) Li, A.; Fan, J.; Li, G. Recyclable Thermoset Shape Memory Polymers with High Stress and Energy Output: Via Facile UV-Curing. *J. Mater. Chem. A* **2018**, *6* (24), 11479–11487. https://doi.org/10.1039/c8ta02644k.

(277) Fan, J.; Li, G. High Enthalpy Storage Thermoset Network with Giant Stress and Energy Output in Rubbery State. *Nat. Commun.* **2018**, *9* (1), 642. https://doi.org/10.1038/s41467-018-03094-2.

(278) Fulmer, G. R.; Miller, A. J. M.; Sherden, N. H.; Gottlieb, H. E.; Nudelman, A.; Stoltz, B. M.; Bercaw, J. E.; Goldberg, K. I. NMR Chemical Shifts of Trace Impurities: Common Laboratory Solvents, Organics, and Gases in Deuterated Solvents Relevant to the Organometallic Chemist. *Organometallics* **2010**, *29* (9), 2176–2179. https://doi.org/10.1021/om100106e.

(279) Chai, J.-D.; Head-Gordon, M. Long-Range Corrected Hybrid Density Functionals with Damped Atom–Atom Dispersion Corrections. *Phys. Chem. Chem. Phys.* **2008**, *10* (44), 6615. https://doi.org/10.1039/b810189b.

(280) Frisch, M. J.; Trucks, G. W.; Schlegel, H. B.; Scuseria, G. E.; Robb, M. a.; Cheeseman, J. R.; Scalmani, G.; Barone, V.; Petersson, G. a.; Nakatsuji, H.; Li, X.; Caricato, M.; Marenich, a. V.; Bloino, J.; Janesko, B. G.; Gomperts, R.; Mennucci, B.; Hratchian, H. P.; Ortiz, J. V.; Izmaylov, a. F.; Sonnenberg, J. L.; Williams; Ding, F.; Lipparini, F.; Egidi, F.; Goings, J.; Peng, B.; Petrone, A.; Henderson, T.; Ranasinghe, D.; Zakrzewski, V. G.; Gao, J.; Rega, N.; Zheng, G.; Liang, W.; Hada, M.; Ehara, M.; Toyota, K.; Fukuda, R.; Hasegawa, J.; Ishida, M.; Nakajima, T.; Honda, Y.; Kitao, O.; Nakai, H.; Vreven, T.; Throssell, K.; Montgomery Jr., J. a.; Peralta, J. E.; Ogliaro, F.; Bearpark, M. J.; Heyd, J. J.; Brothers, E. N.; Kudin, K. N.; Staroverov, V. N.; Keith, T. a.; Kobayashi, R.; Normand, J.; Raghavachari, K.; Rendell, a. P.; Burant, J. C.; Iyengar, S. S.; Tomasi, J.; Cossi, M.; Millam, J. M.; Klene, M.; Adamo, C.; Cammi, R.; Ochterski, J. W.; Martin, R. L.; Morokuma, K.; Farkas, O.; Foresman, J. B.; Fox, D. J. Gaussian 09.

(281) Boys, S. F.; Bernardi, F. The Calculation of Small Molecular Interactions by the Differences of Separate Total Energies. Some Procedures with Reduced Errors. *Mol. Phys.* **1970**, *19* (4), 553–566. https://doi.org/10.1080/00268977000101561.

(282) Smith, V. H.; Thakkar, A. J.; Chapman, D. C. A New Analytic Approximation to Atomic Incoherent X-Ray Scattering Intensities. *Acta Crystallogr. Sect. A* **1975**, *31* (3), 391–392. https://doi.org/10.1107/S056773947500085X.

Annex

Table of Contents

A1 Infrared spectroscopy

The IR spectra of the polyesters, TPUs and pure SS samples can be found in this section.

A1.1. Polyesters

The most important IR features from the polyesters are shared among all of the different polymers. Therefore, the assignation of these bands will only be shown in the first polyester shown hereinafter.

A1.1.1. IPHTAPDO 1000

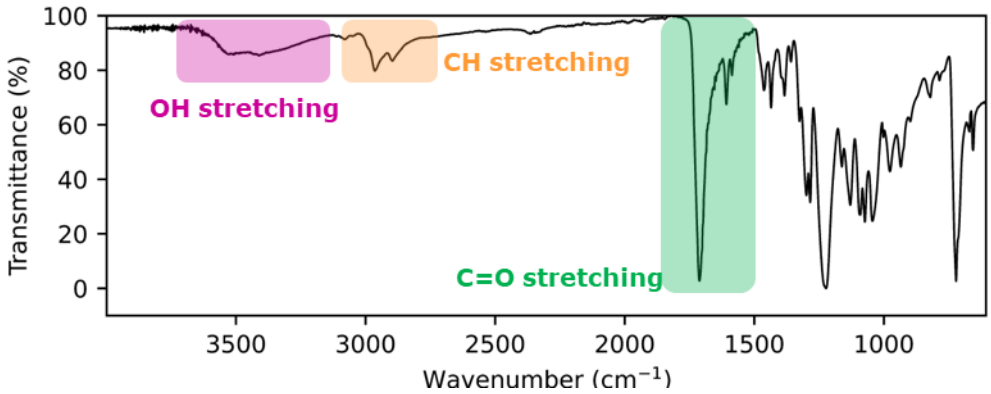

A1.1.2. IPHTAPDO 2000

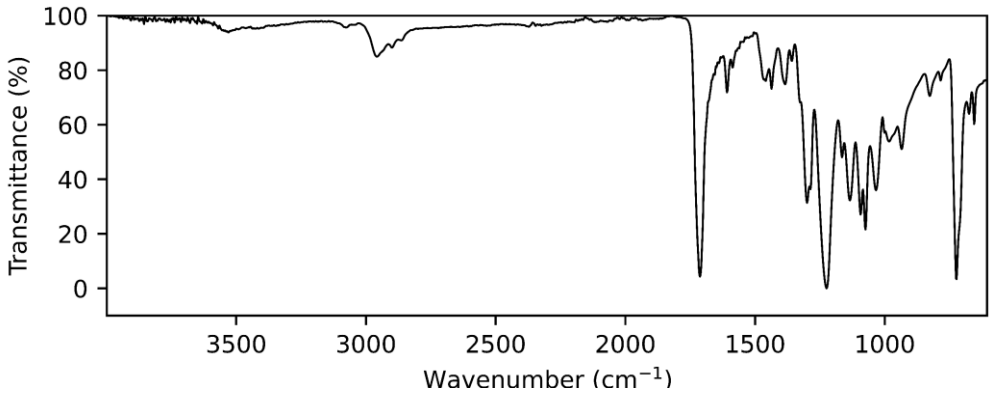

A1.1.3. IPHTAHDO 1000

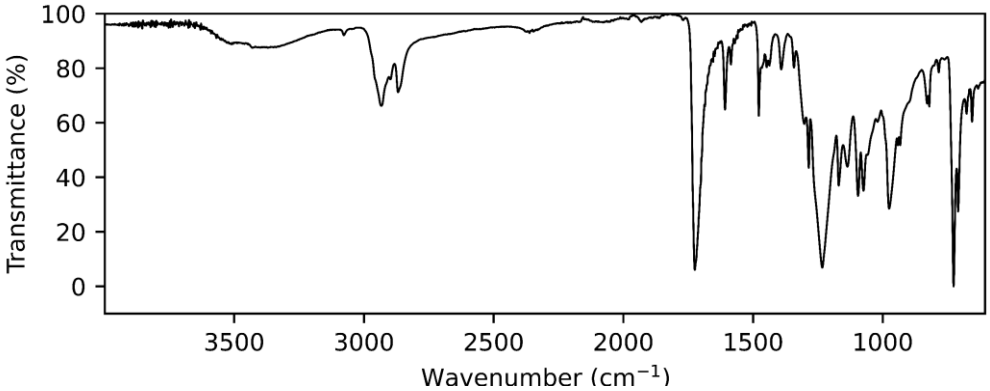

A1.1.4. IPHTAHDO 2000

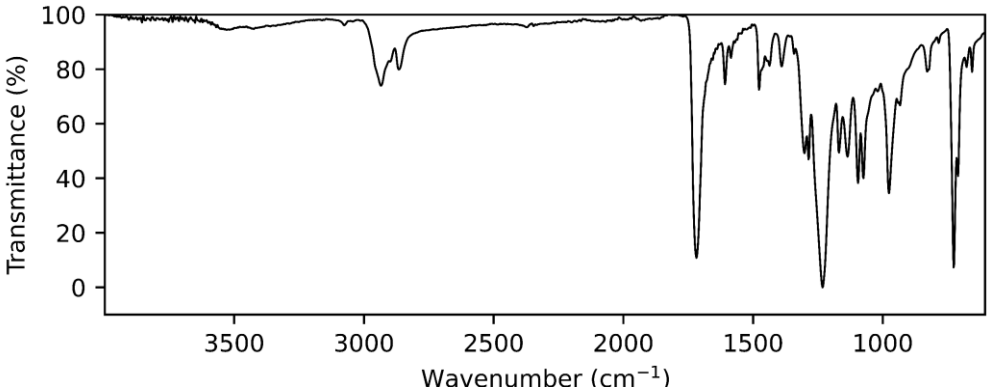

A1.1.5. FDCAPDO 1000

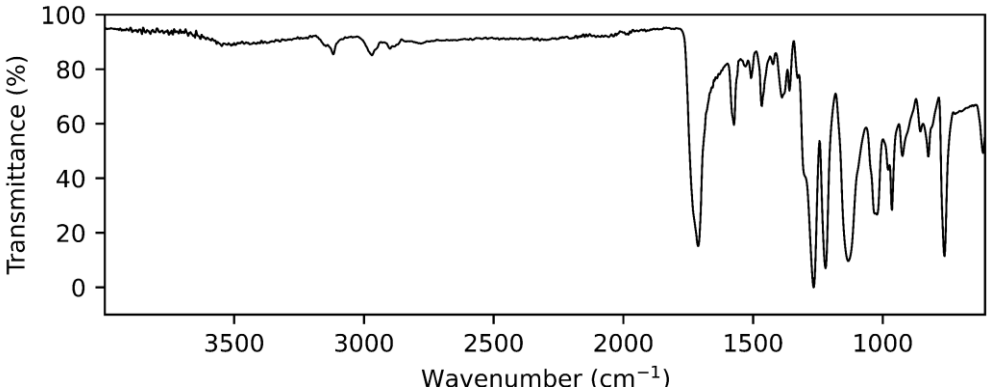

A1.1.6. FDCAPDO 1500

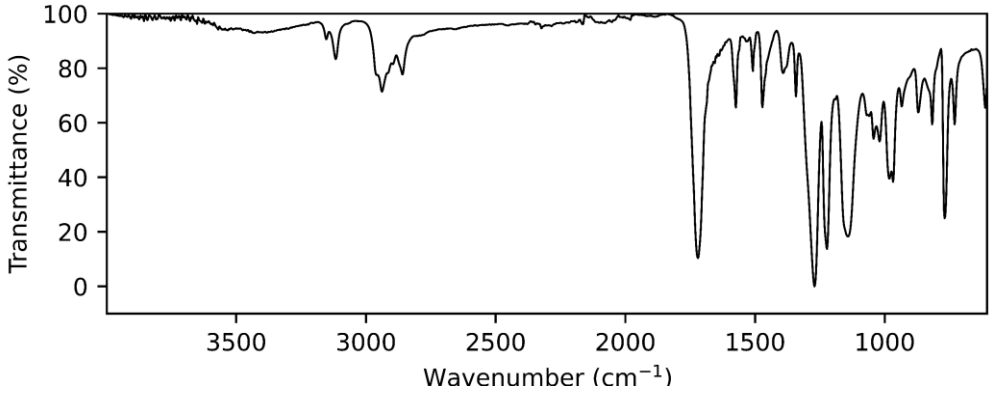

A1.1.7. FDCAPDO 2000

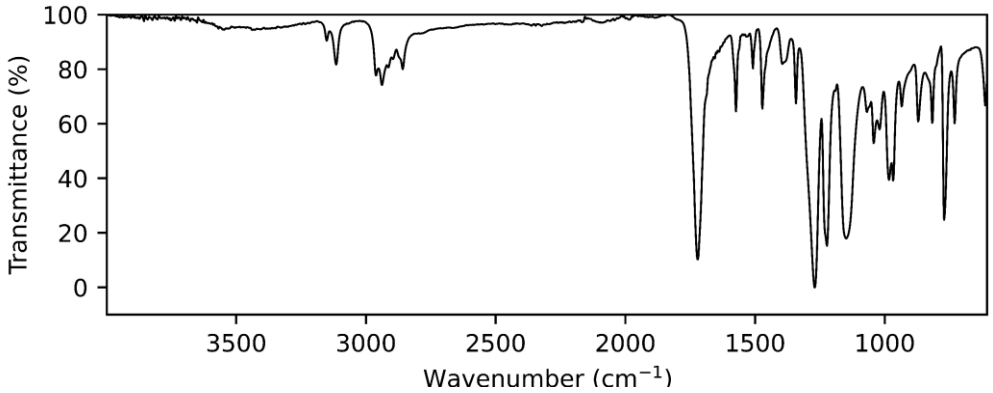

A1.1.8. FDCAHDO 1000

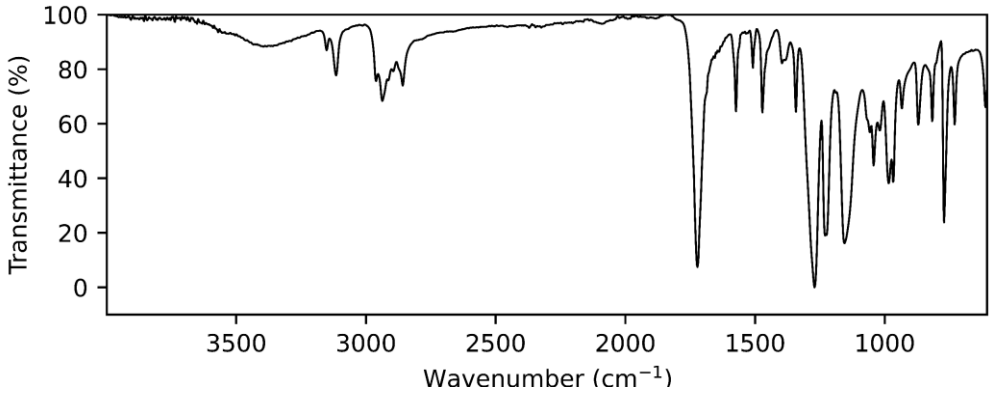

A1.1.9. FDCAHDO 1500

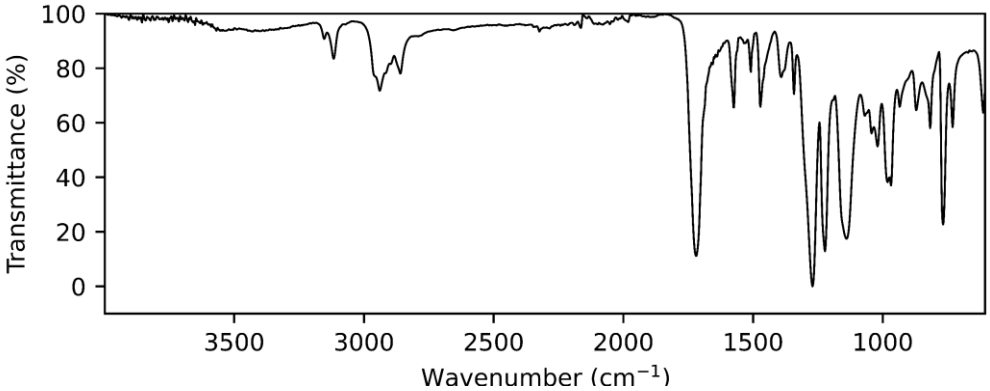

A1.1.10. FDCAHDO 2000

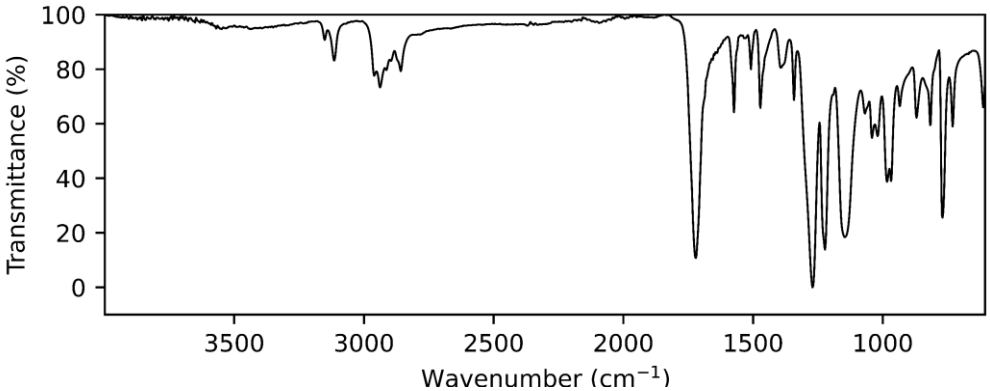

A1.2. TPUs

The most important IR features from the TPUs are shared among all of the different formulations. Therefore, the assignation of these bands will only be shown in the first TPU shown hereinafter.

A1.2.1. IPHTAPDO 1000 10% MDI

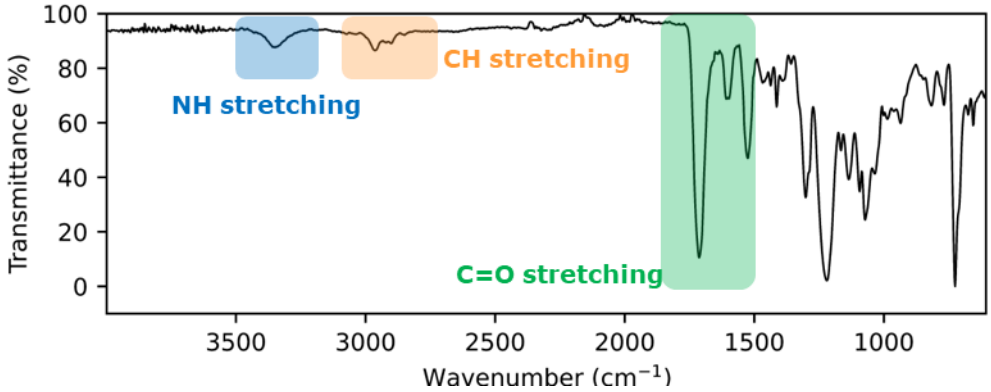

A1.2.2. IPHTAPDO 1000 30% MDI

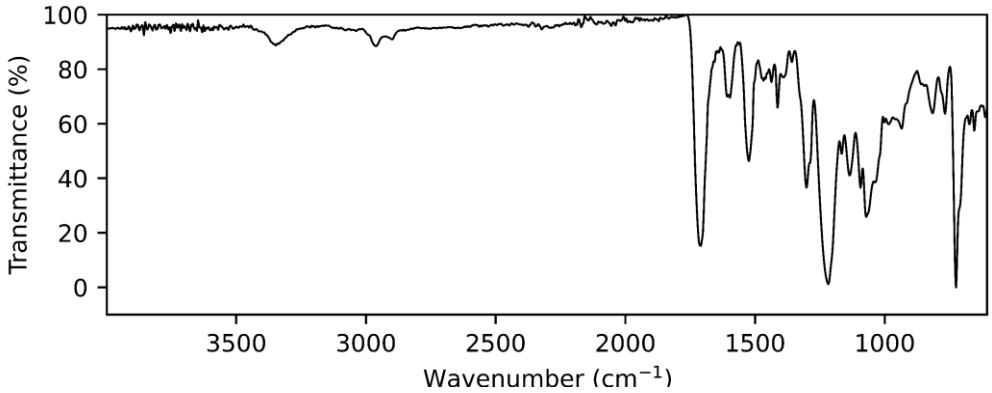

A1.2.3. IPHTAPDO 1000 50% MDI

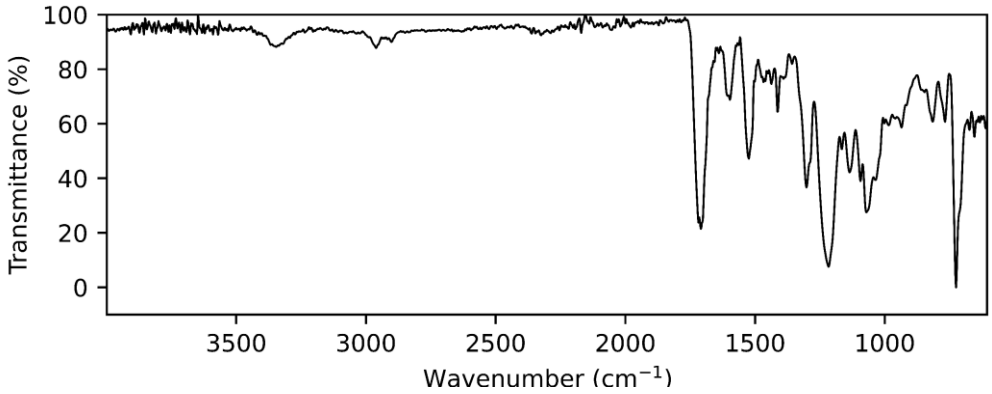

A1.2.4. IPHTAPDO 2000 10% MDI

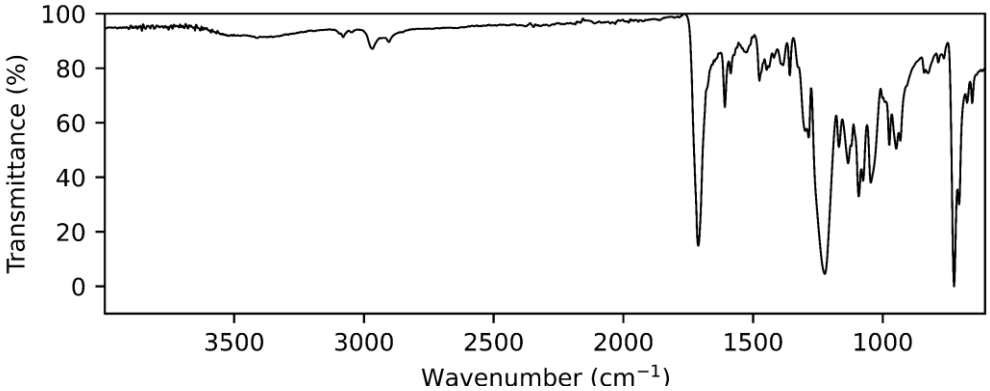

A1.2.5. IPHTAPDO 2000 30% MDI

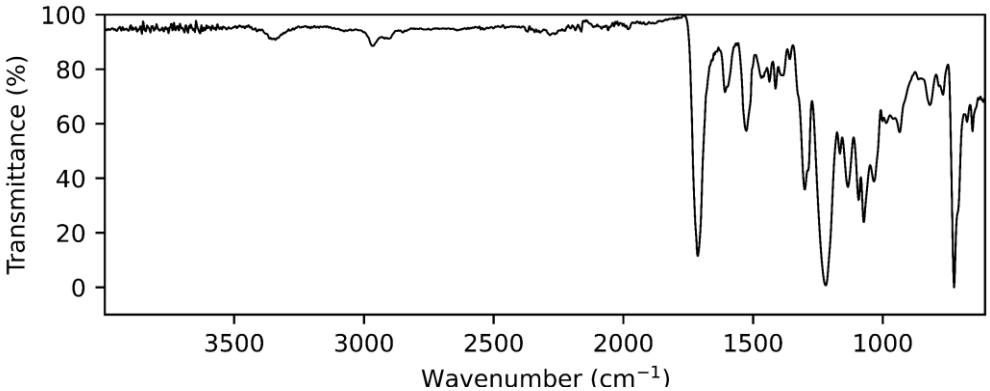

A1.2.6. IPHTAPDO 2000 50% MDI

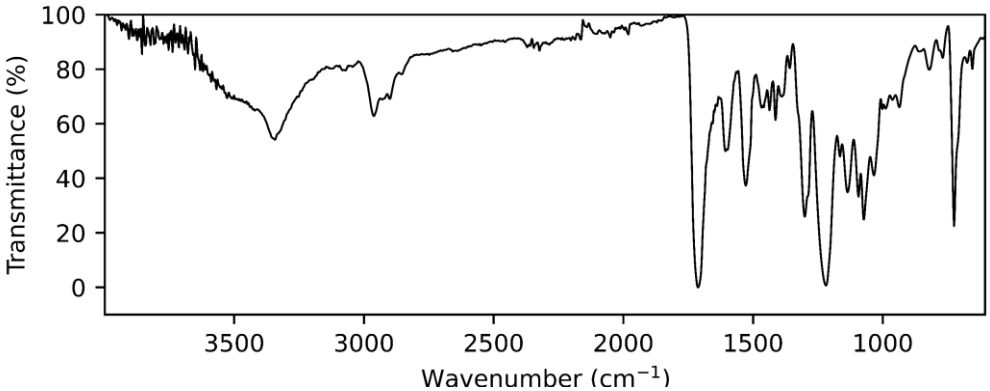

A1.2.7. IPHTAHDO 1000 10% MDI

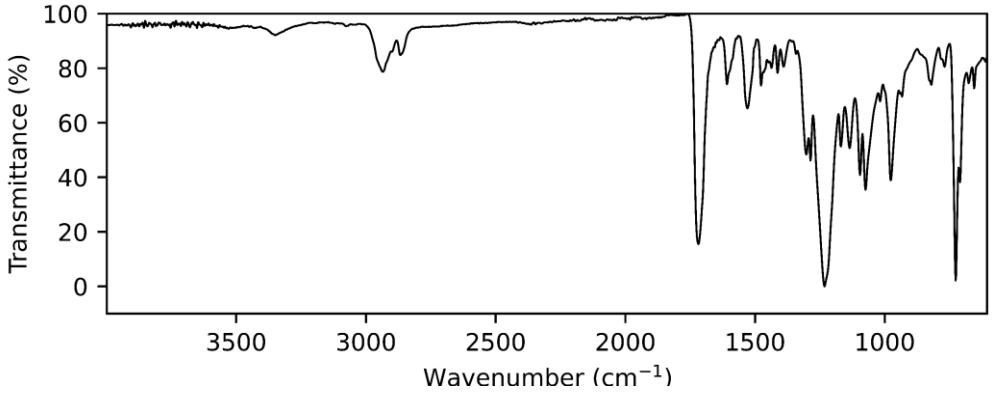

A1.2.8. IPHTAHDO 1000 30% MDI

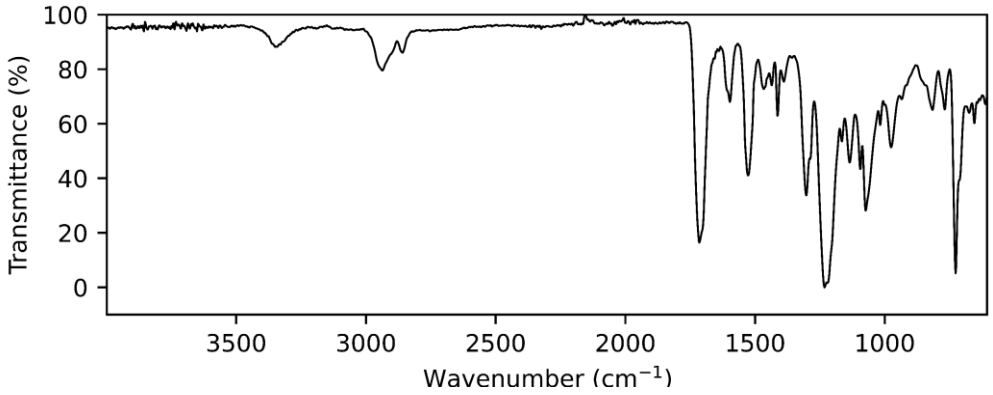

A1.2.9. IPHTAHDO 1000 50% MDI

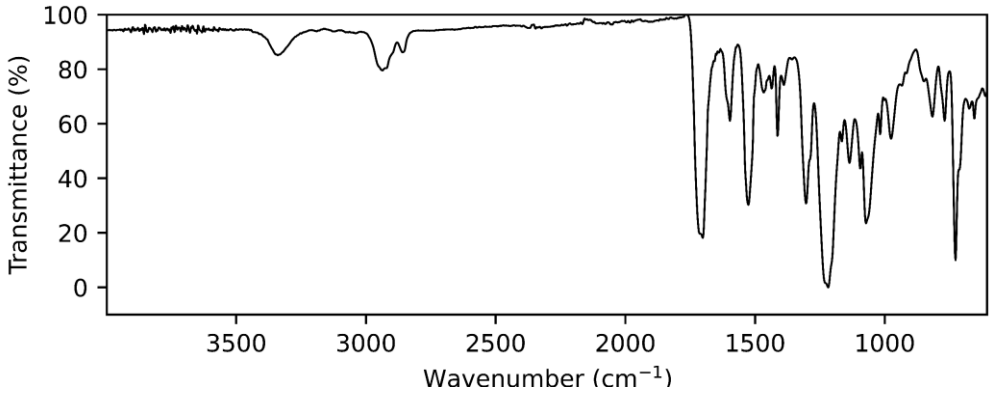

A1.2.10. IPHTAHDO 2000 10% MDI

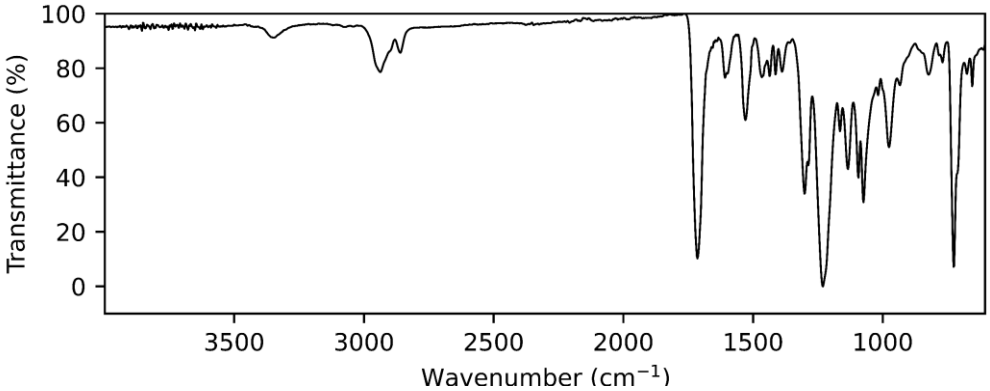

A1.2.11. IPHTAHDO 2000 30% MDI

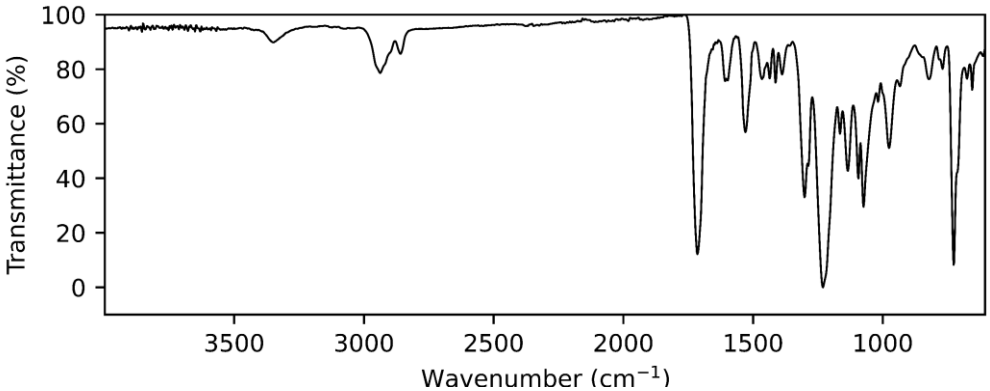

A1.2.12. IPHTAHDO 2000 50% MDI

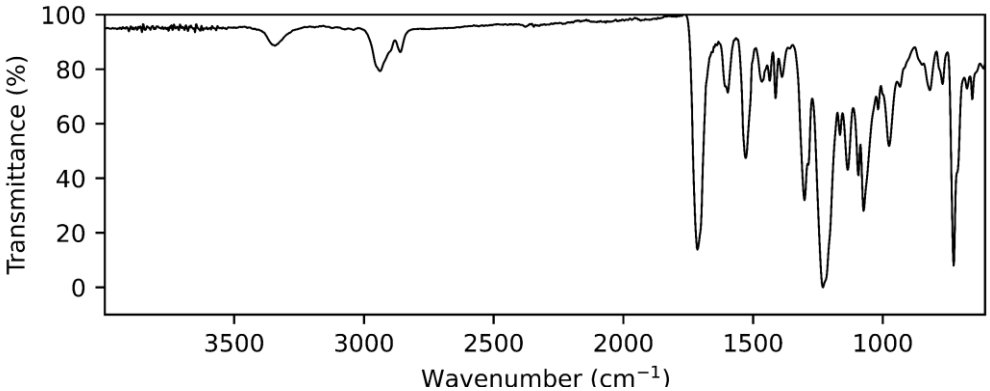

A1.2.13. IPHTAPDO 1000 10% HDI

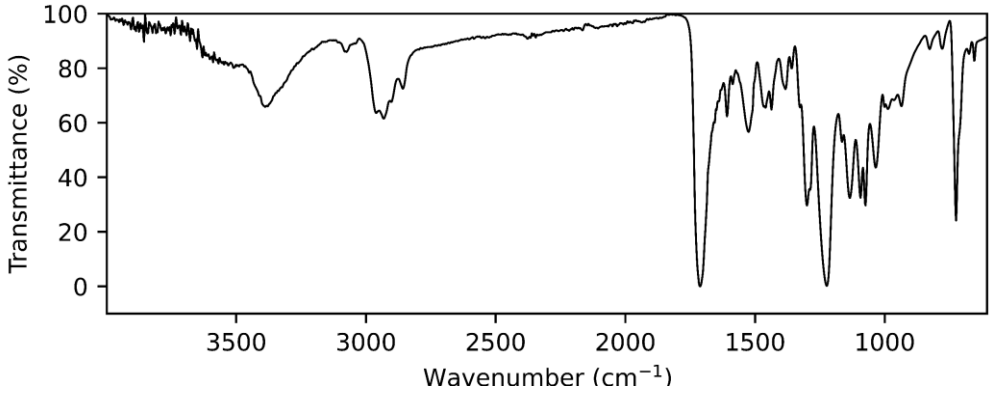

A1.2.14. IPHTAPDO 1000 30% HDI

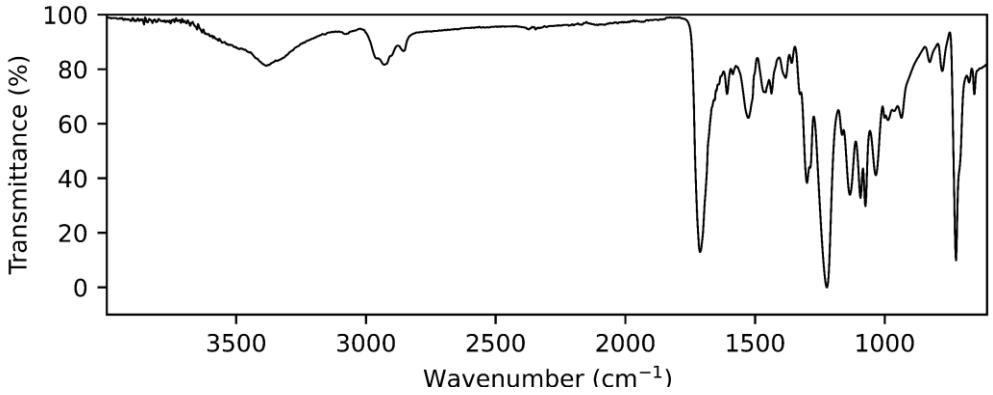

A1.2.15. IPHTAPDO 1000 50% HDI

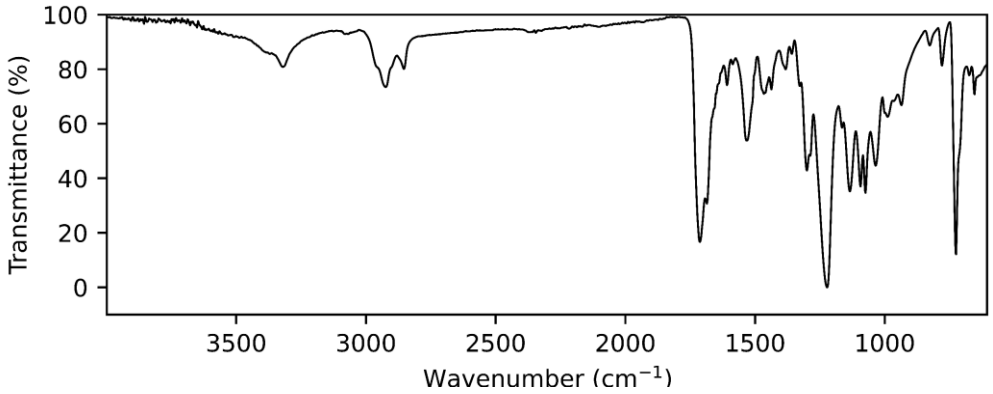

A1.2.16. IPHTAPDO 2000 10% HDI

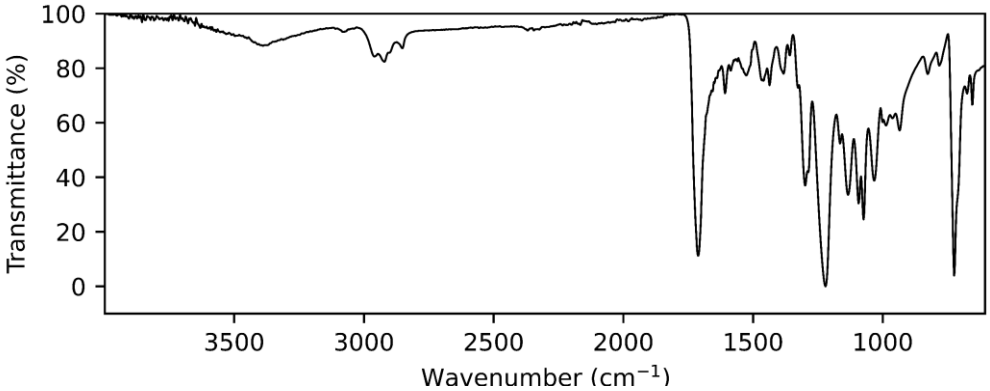

A1.2.17. IPHTAPDO 2000 30% HDI

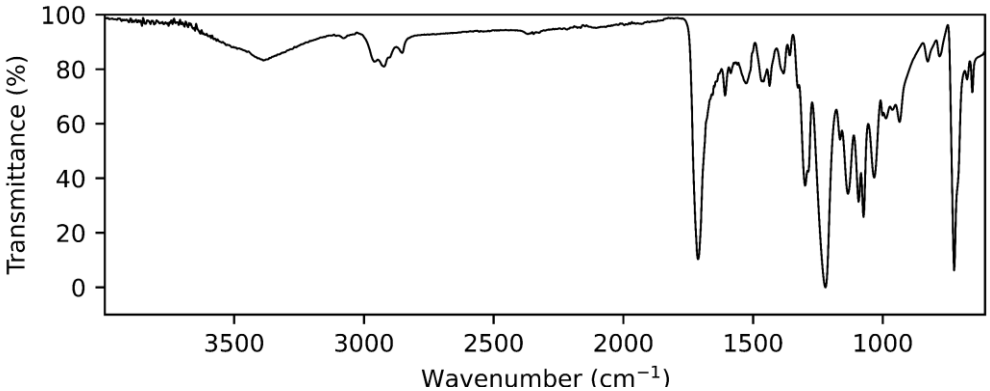

A1.2.18. IPHTAPDO 2000 50% HDI

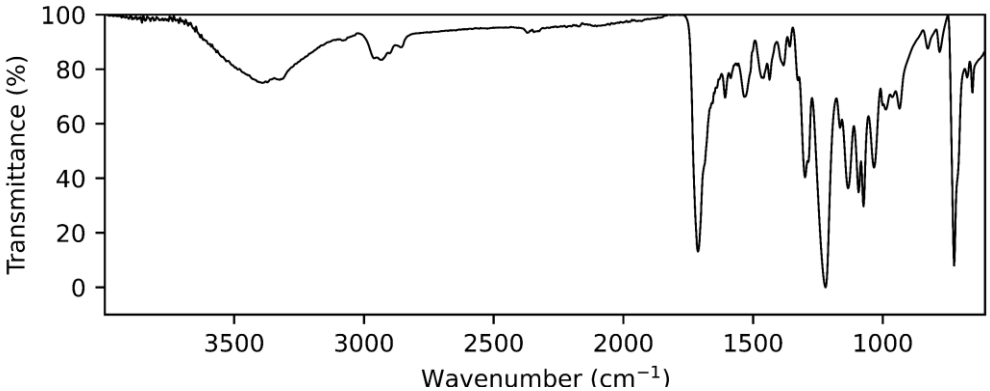

A1.2.19. IPHTAHDO 1000 10% HDI

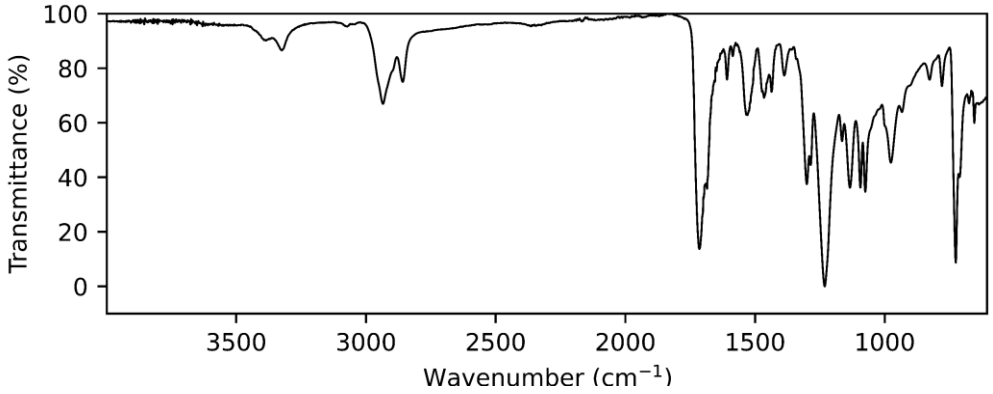

A1.2.20. IPHTAHDO 1000 30% HDI

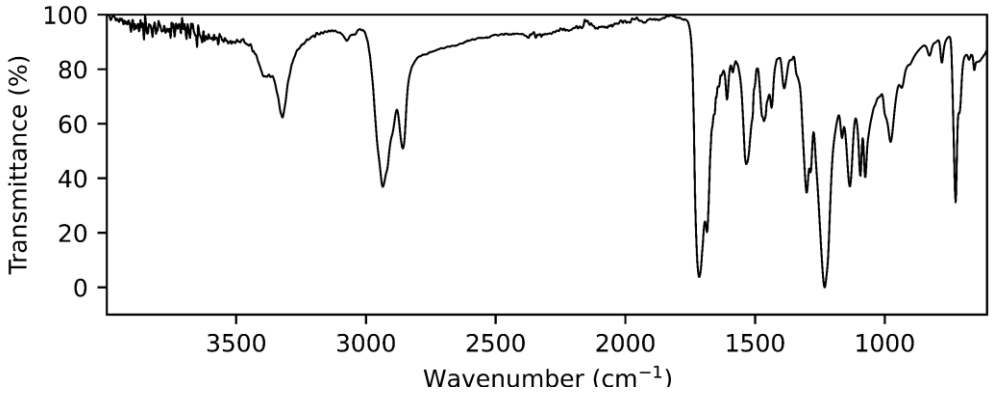

A1.2.21. IPHTAHDO 1000 50% HDI

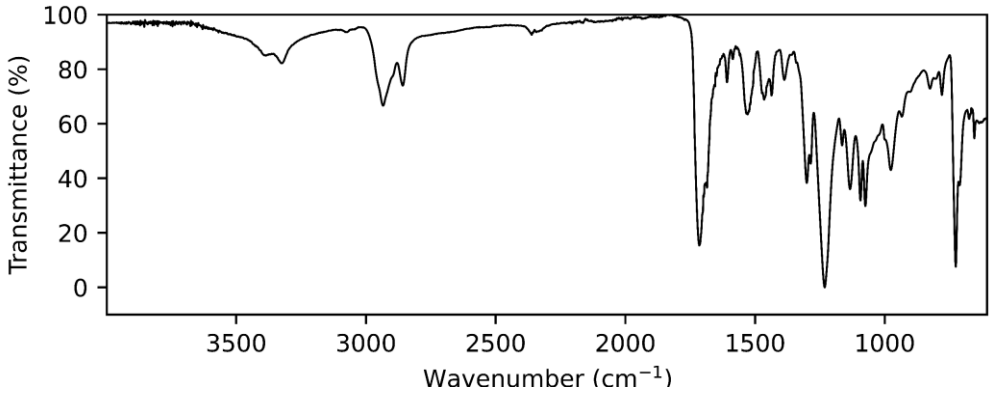

A1.2.22. IPHTAHDO 2000 10% HDI

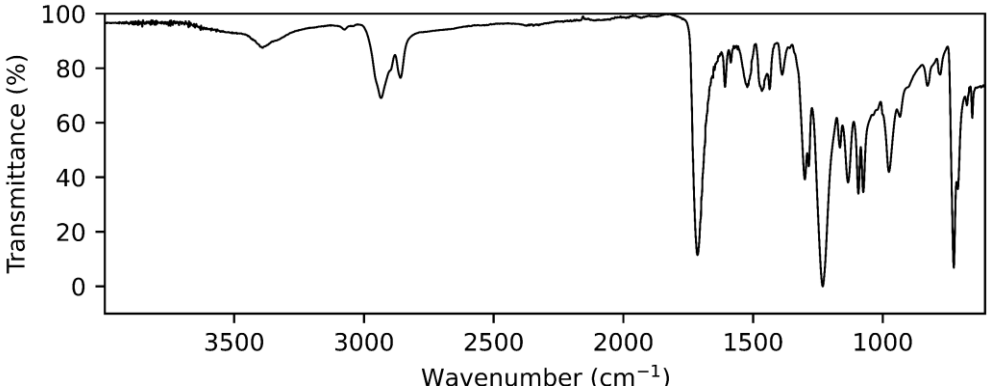

A1.2.23. IPHTAHDO 2000 30% HDI

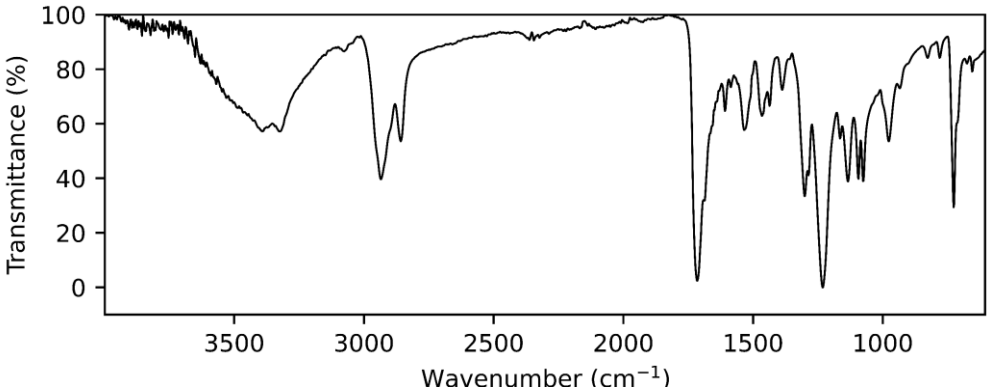

A1.2.24. IPHTAHDO 2000 50% HDI

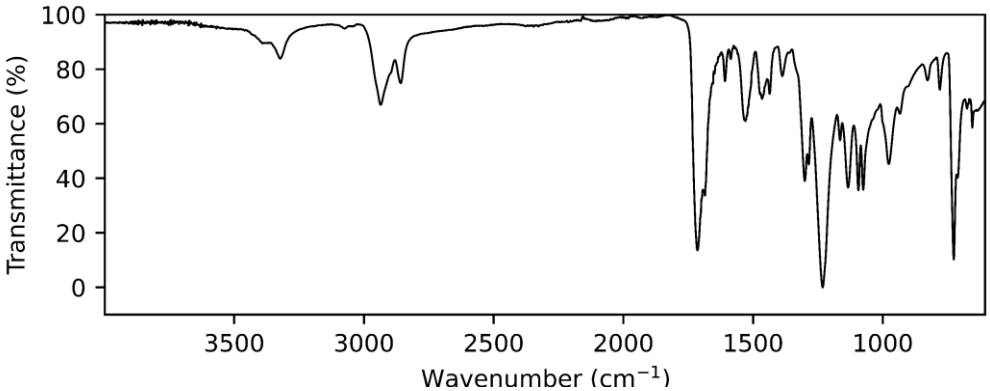

A1.2.25. FDCAPDO 1000 10% MDI

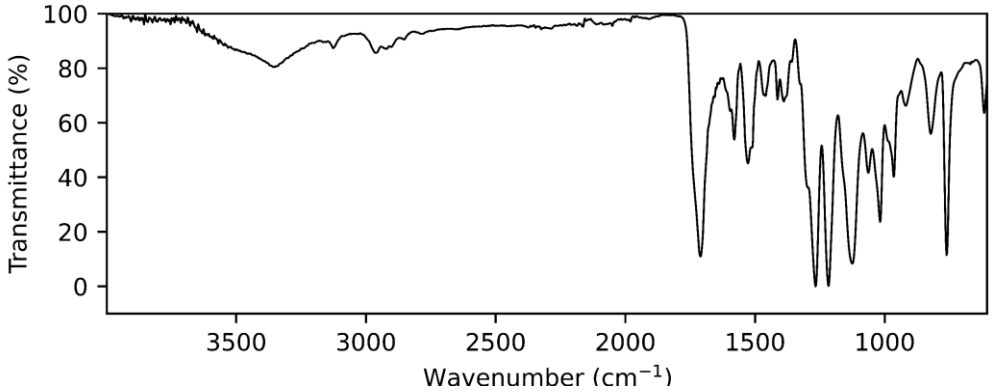

A1.2.26. FDCAPDO 1000 50% MDI

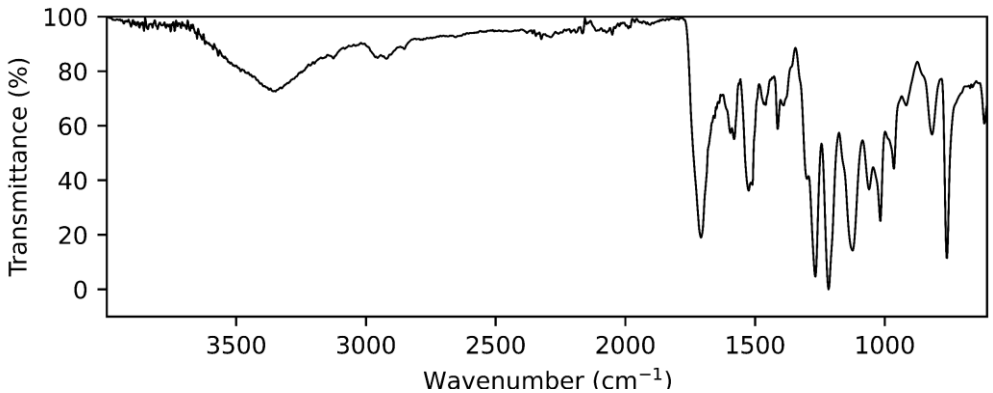

A1.2.27. FDCAPDO 1500 30% MDI

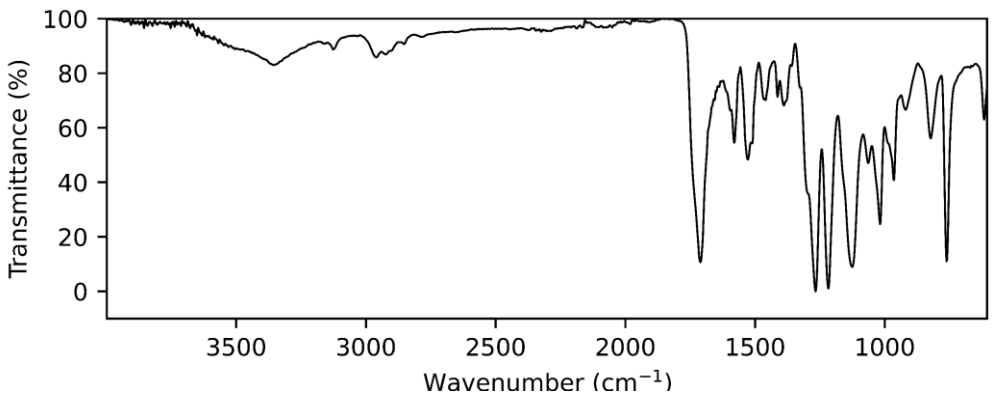

A1.2.28. FDCAPDO 2000 10% MDI

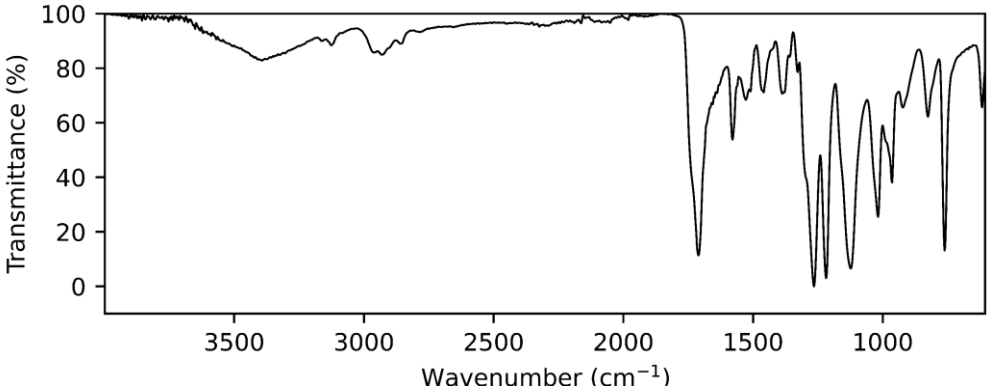

A1.2.29. FDCAPDO 2000 50% MDI

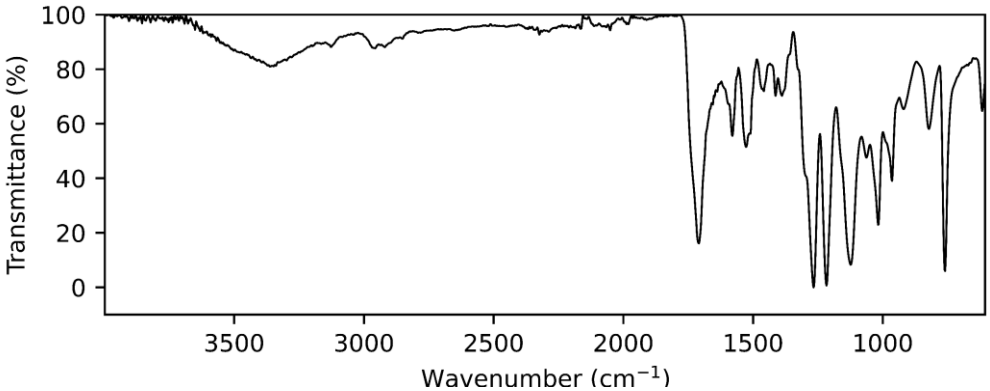

A1.2.30. FDCAHDO 1000 10% MDI

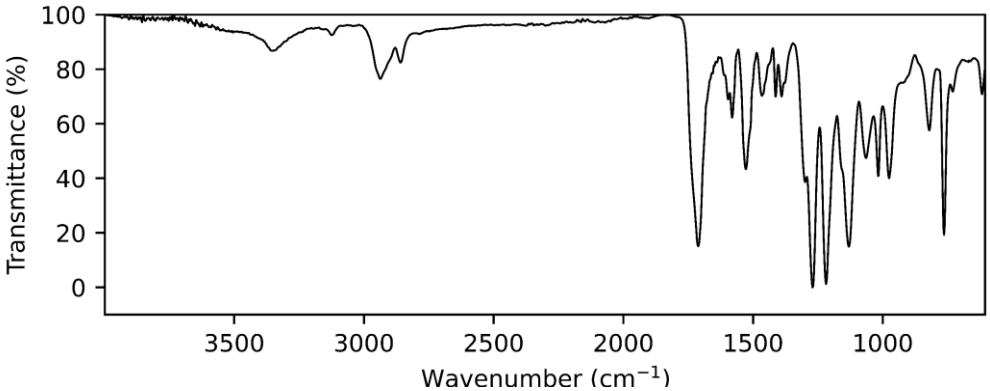

A1.2.31. FDCAHDO 1000 50% MDI

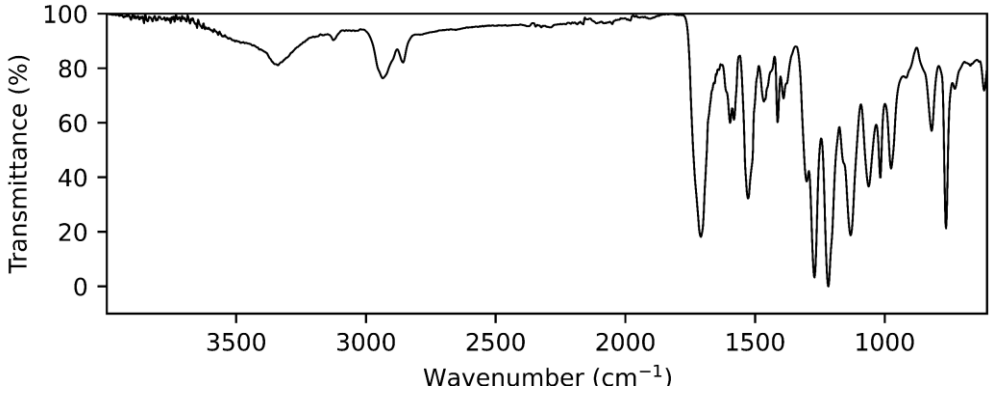

A1.2.32. FDCAHDO 1500 30% MDI

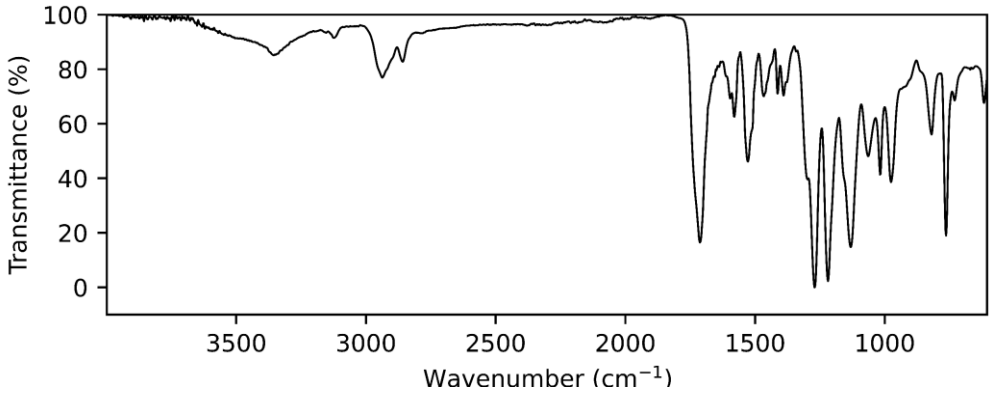

A1.2.33. FDCAHDO 2000 10% MDI

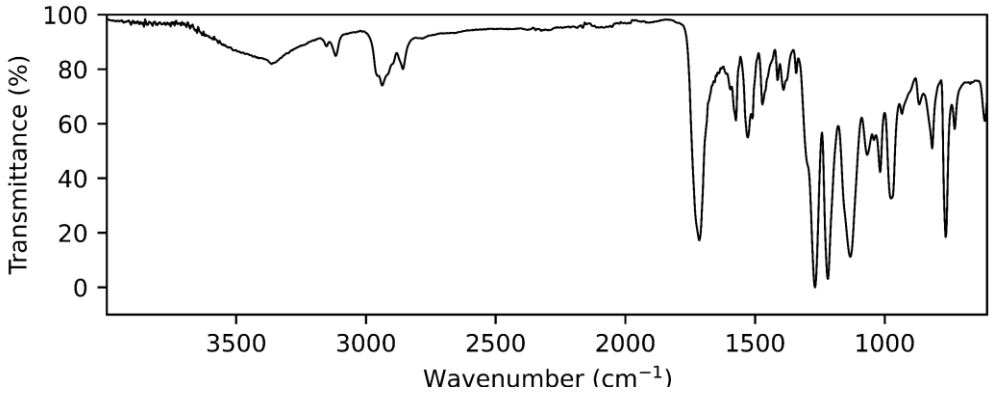

A1.2.34. FDCAHDO 2000 50% MDI

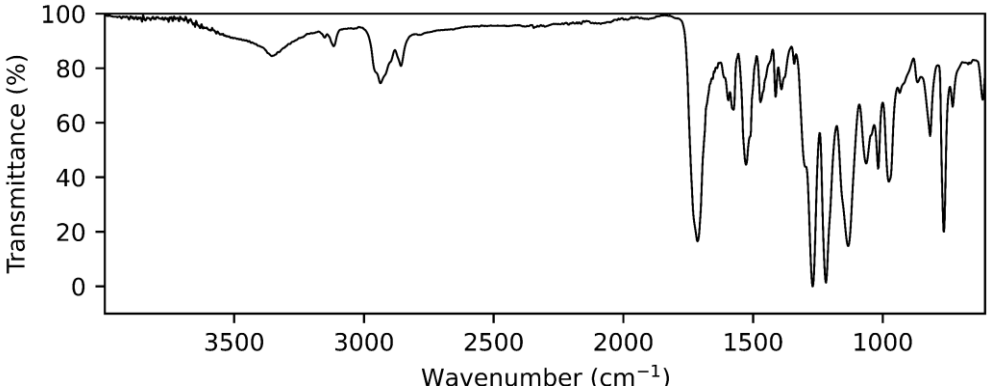

A1.2.35. FDCAPDO 1000 10% MDI

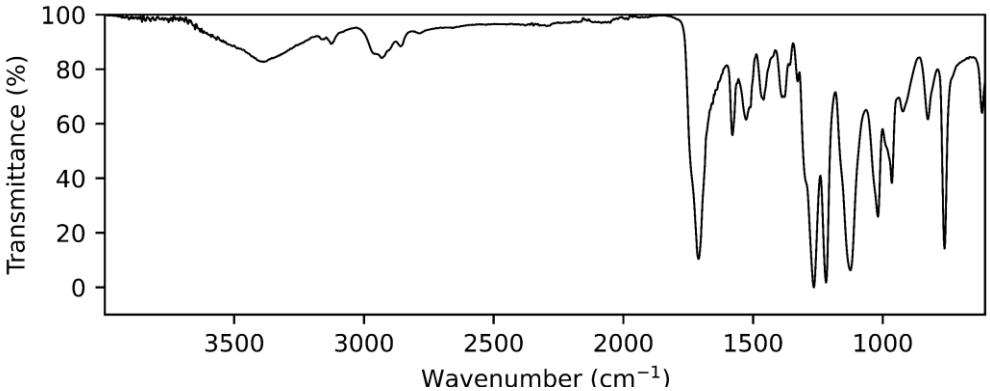

A1.2.36. FDCAPDO 1000 50% HDI

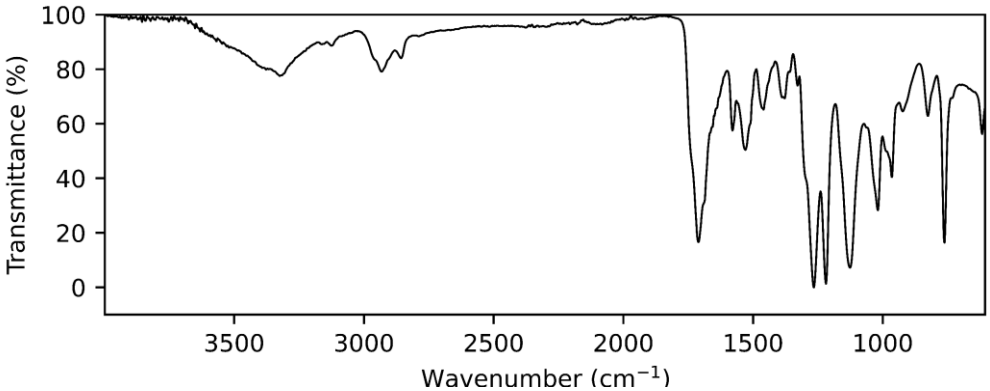

A1.2.37. FDCAPDO 1500 30% HDI

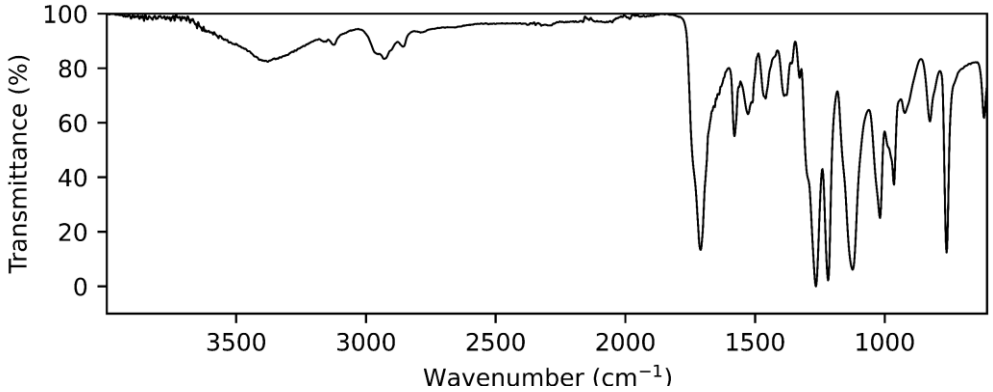

A1.2.38. FDCAPDO 2000 10% HDI

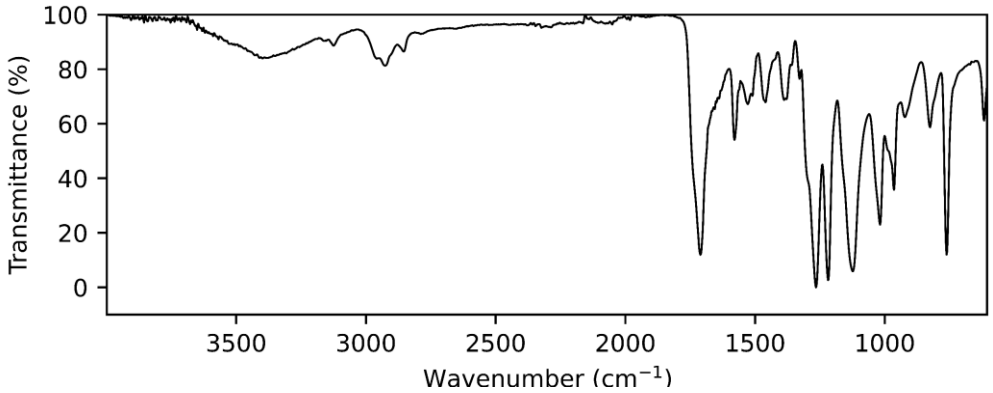

A1.2.39. FDCAPDO 2000 50% HDI

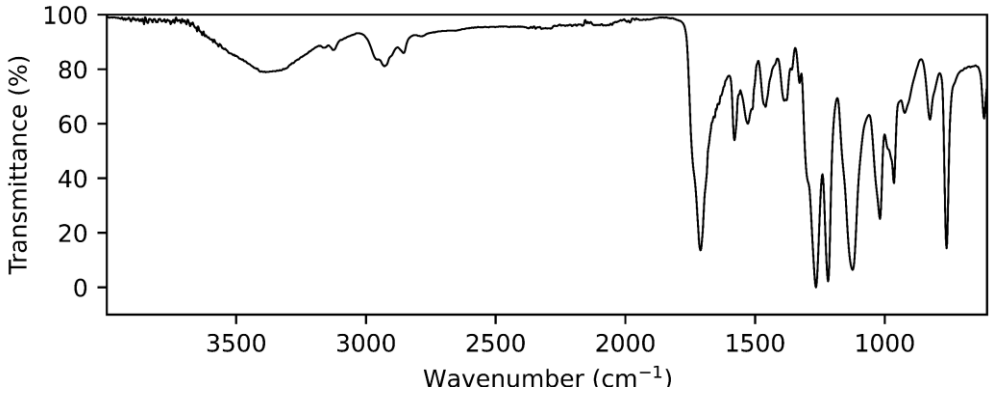

A1.2.40. FDCAHDO 1000 10% HDI

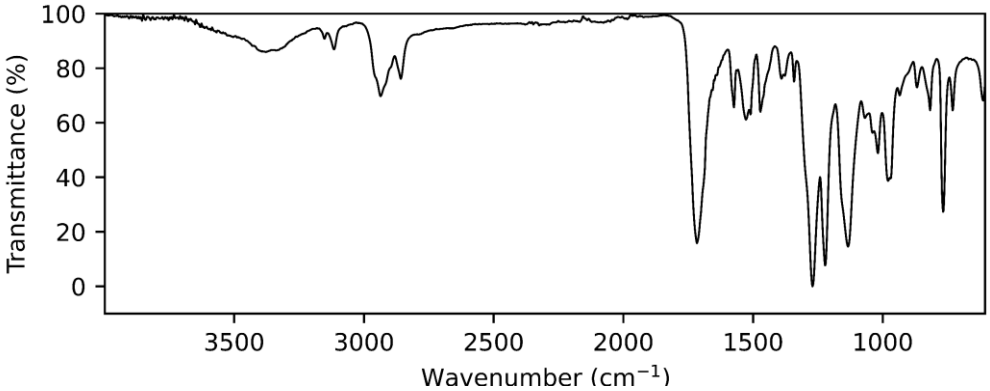

A1.2.41. FDCAHDO 1000 50% HDI

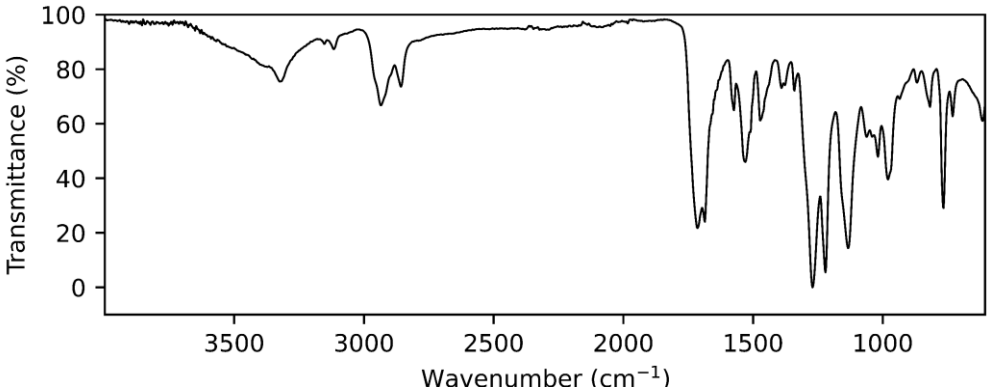

A1.2.42. FDCAHDO 1500 30% HDI

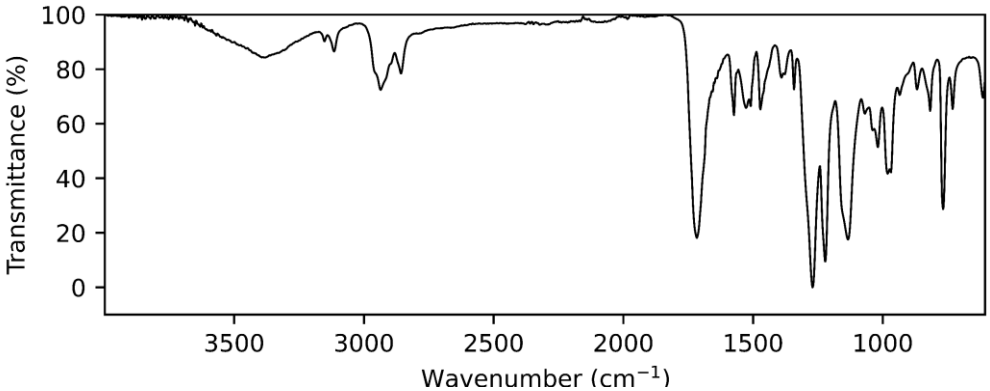

A1.2.43. FDCAHDO 2000 10% HDI

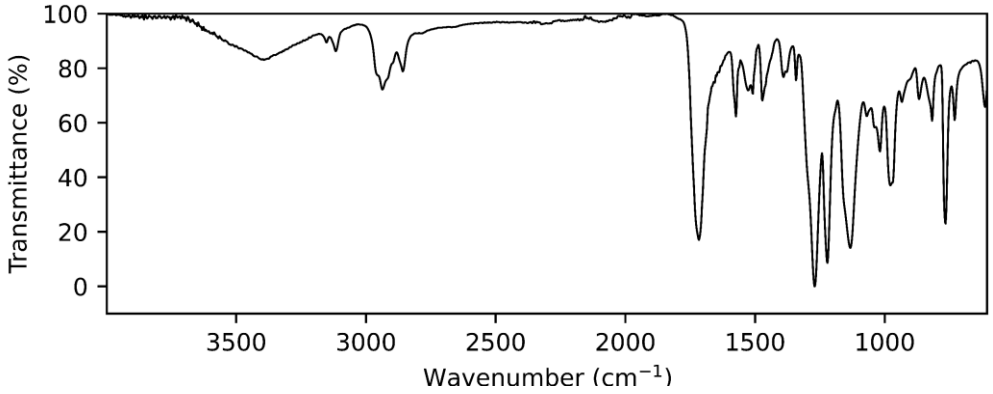

A1.2.44. FDCAHDO 2000 50% HDI

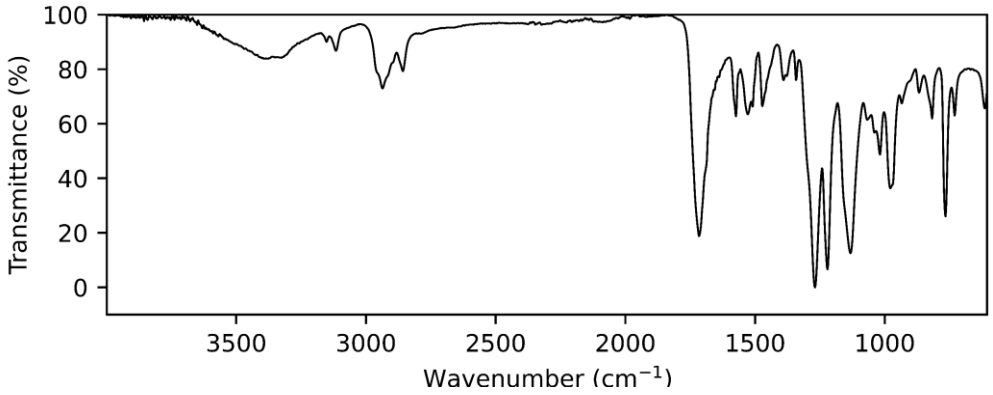

A1.3. Pure soft segment

The most important IR features from the pure SS samples are shared among all of the different polymers. Therefore, the assignation of these bands will only be shown in the first pure SS sample shown hereinafter.

A1.3.1. FDCAPDO 1000 MDI SS

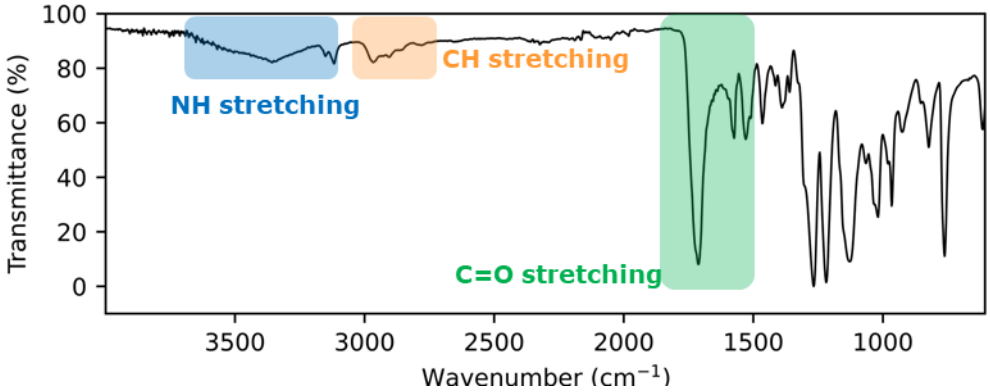

A1.3.2. FDCAPDO 1500 MDI SS

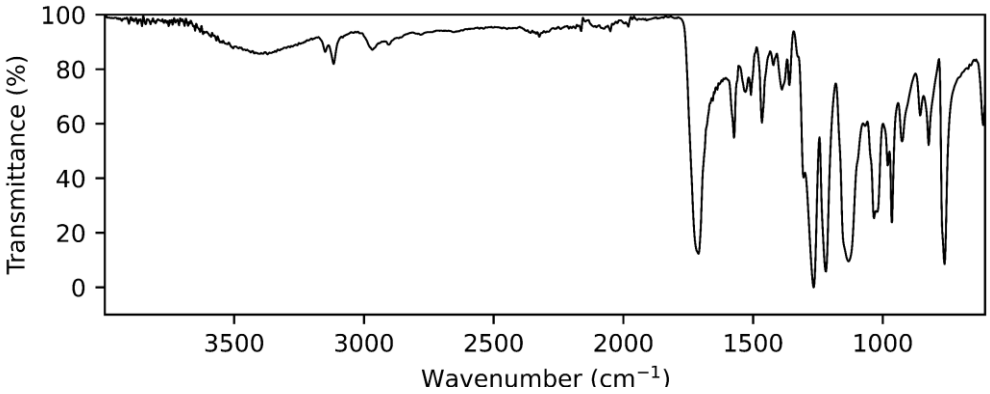

A1.3.3. FDCAPDO 2000 MDI SS

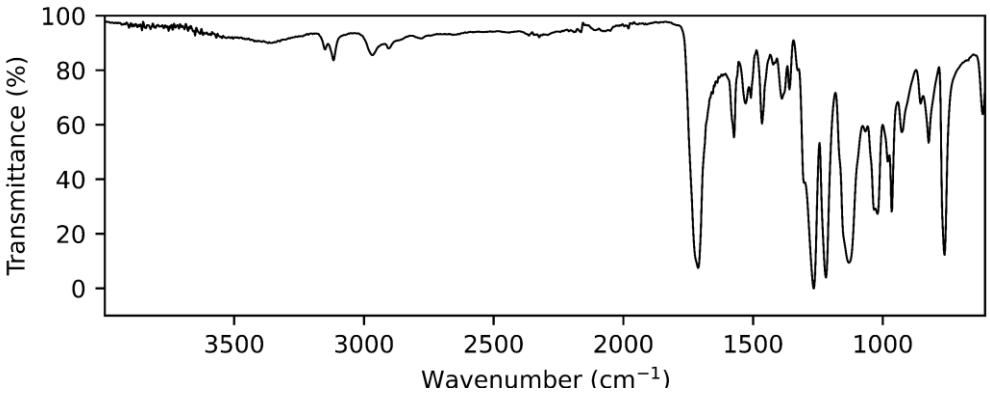

A1.3.4. FDCAHDO 1000 MDI SS

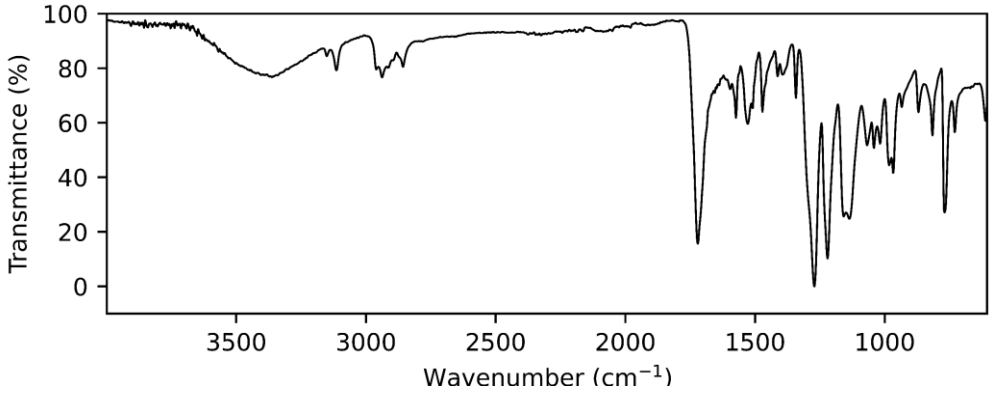

A1.3.5. FDCAHDO 1500 MDI SS

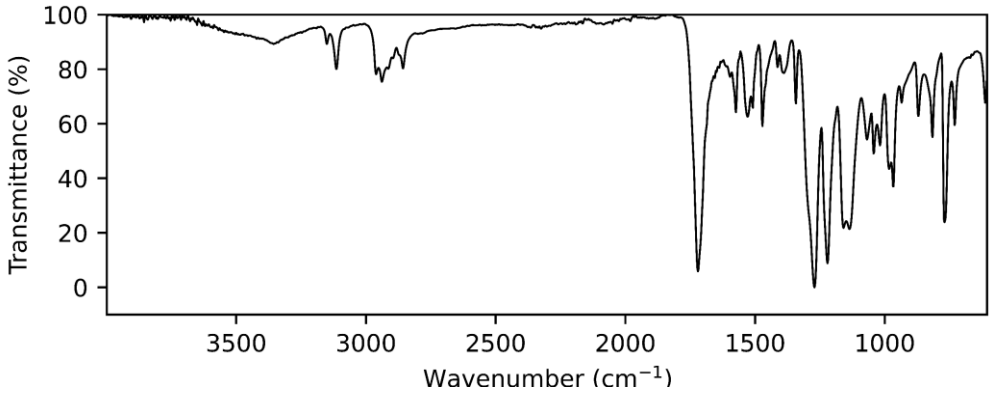

A1.3.6. FDCAHDO 2000 MDI SS

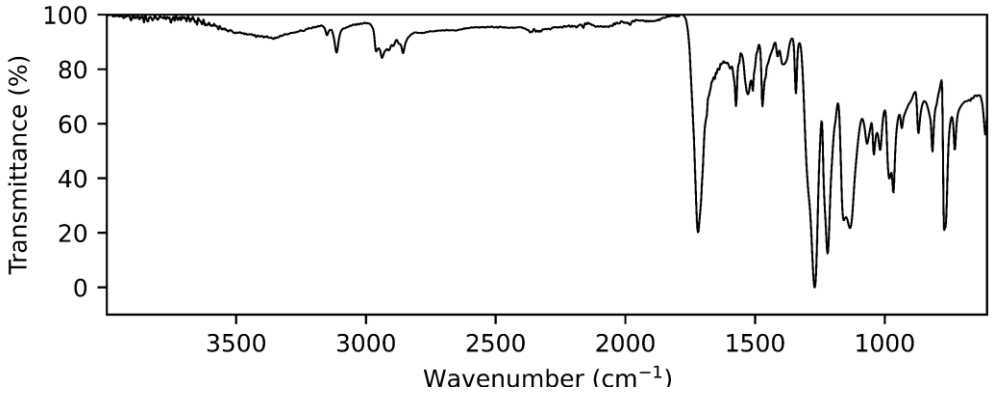

A1.3.7. FDCAPDO 1000 HDI SS

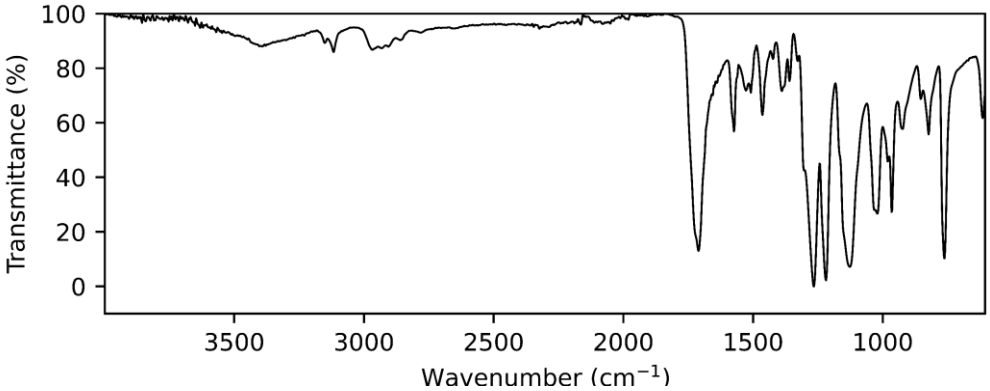

A1.3.8. FDCAPDO 1500 HDI SS

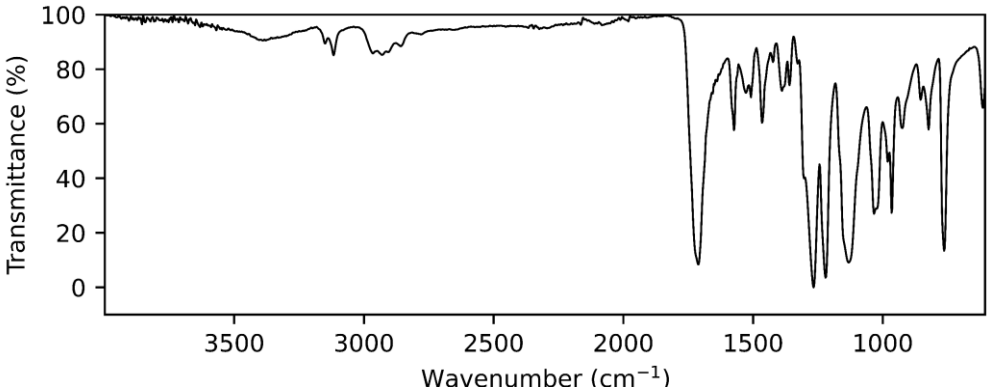

A1.3.9. FDCAPDO 2000 HDI SS

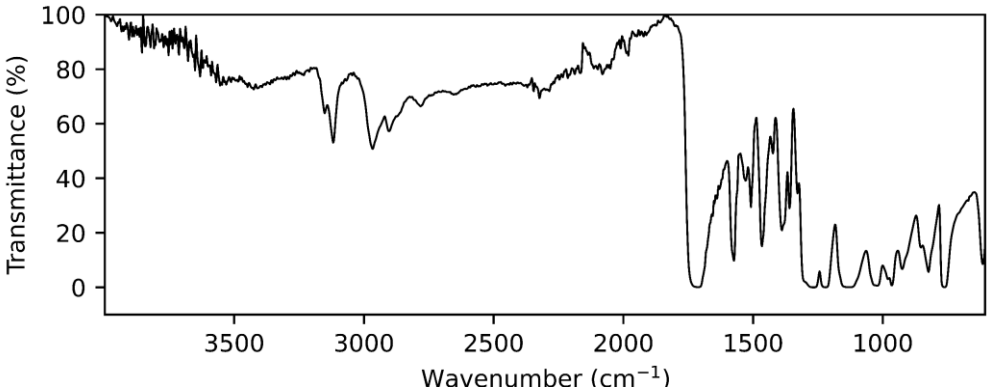

A1.3.10. FDCAHDO 1000 HDI SS

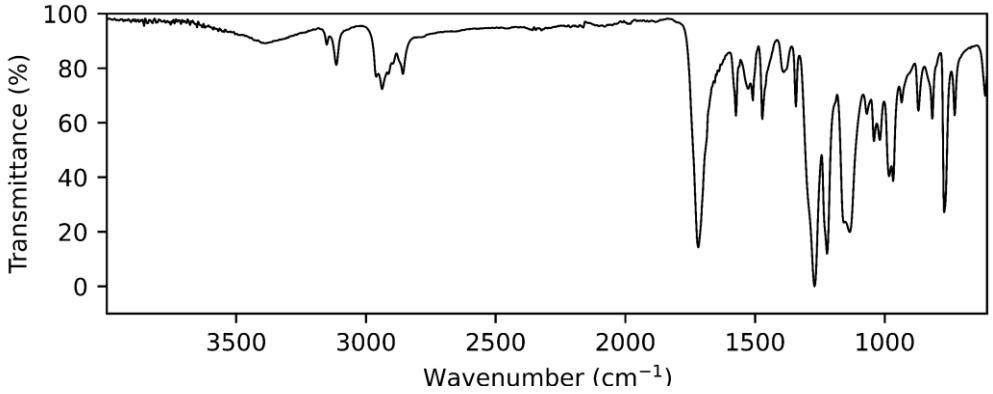

A1.3.11. FDCAHDO 1500 HDI SS

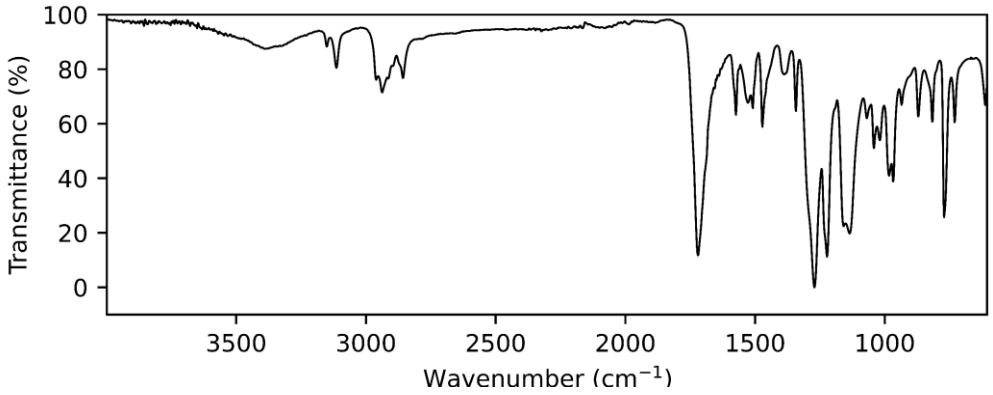

A1.3.12. FDCAHDO 2000 HDI SS

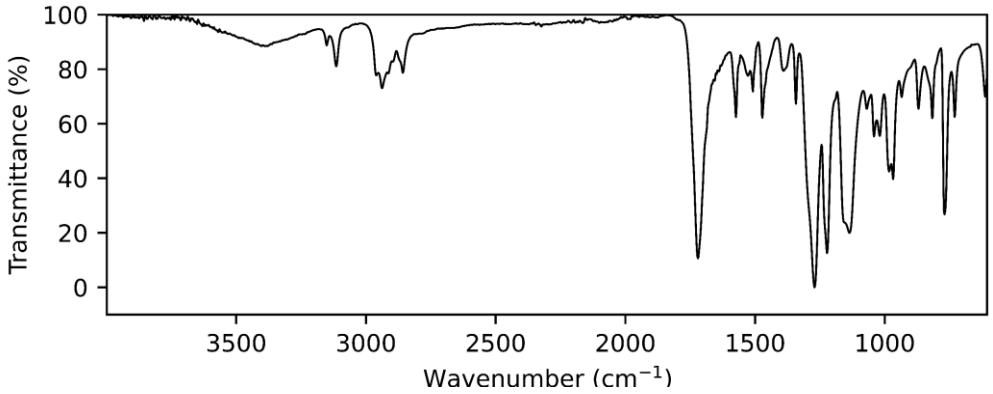

A2 NMR spectroscopy

The ^{1}H NMR and $^{13}C\{^{1}H\}$ NMR spectra of the polyesters and soluble TPUs are shown in this section.

A2.1. Polyesters

The position of the ^{1}H NMR and $^{13}C\{^{1}H\}$ NMR spectra peaks are shared for each of the types of polyester. Therefore, their assignation will only be shown in the first of each of the polyester types displayed below.

A2.1.1. IPHTAPDO 1000

- ^{1}H NMR

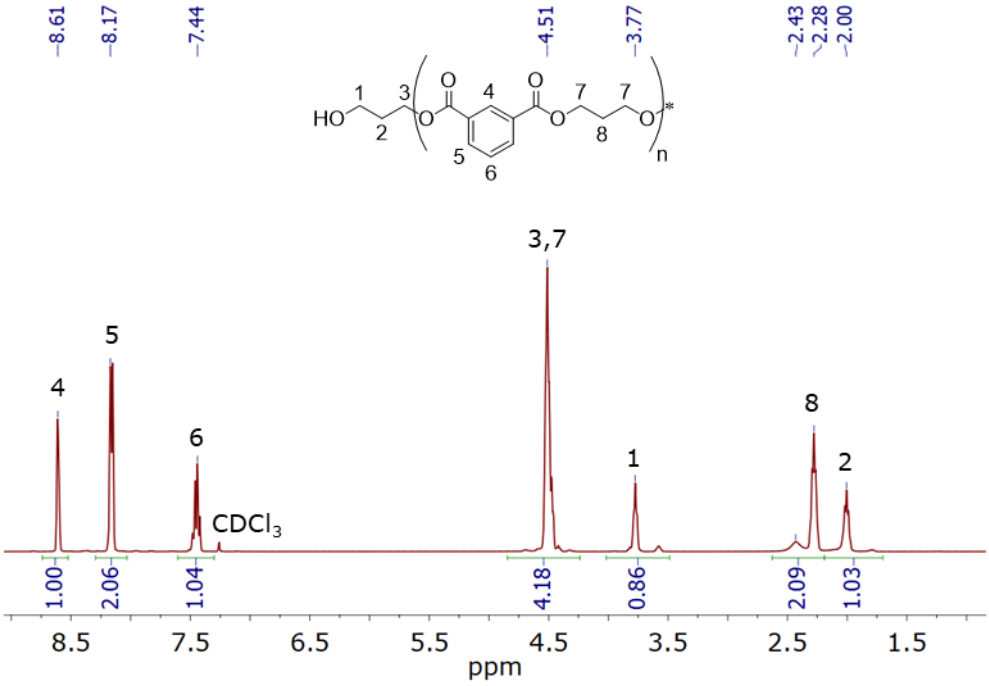

- $^{13}C\{^{1}H\}$ NMR

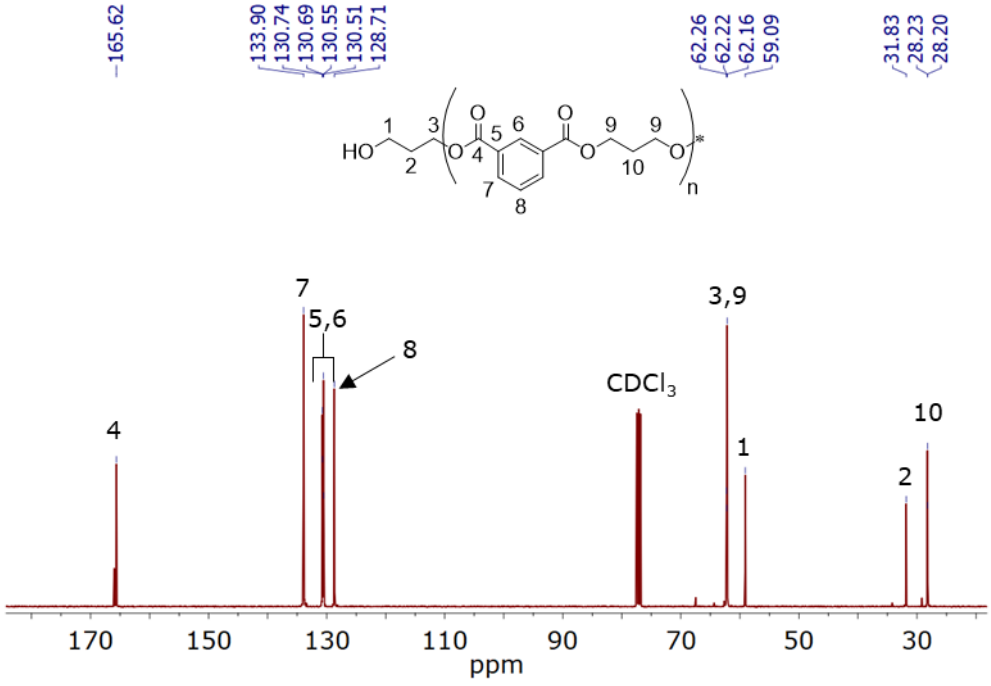
165.62
133.90
130.74
130.69
130.55
130.51
128.71
62.26
62.22
62.16
59.09
31.83
28.23
28.20
HO
1
2
3
O
4
5
6
7
8
O
9
9
10
O
n
*
4
7
5,6
8
CDCl3
3,9
1
2
10
170
150
130
110
90
70
50
30
ppm

A2.1.2. IPHTAPDO 2000

- ^{1}H NMR

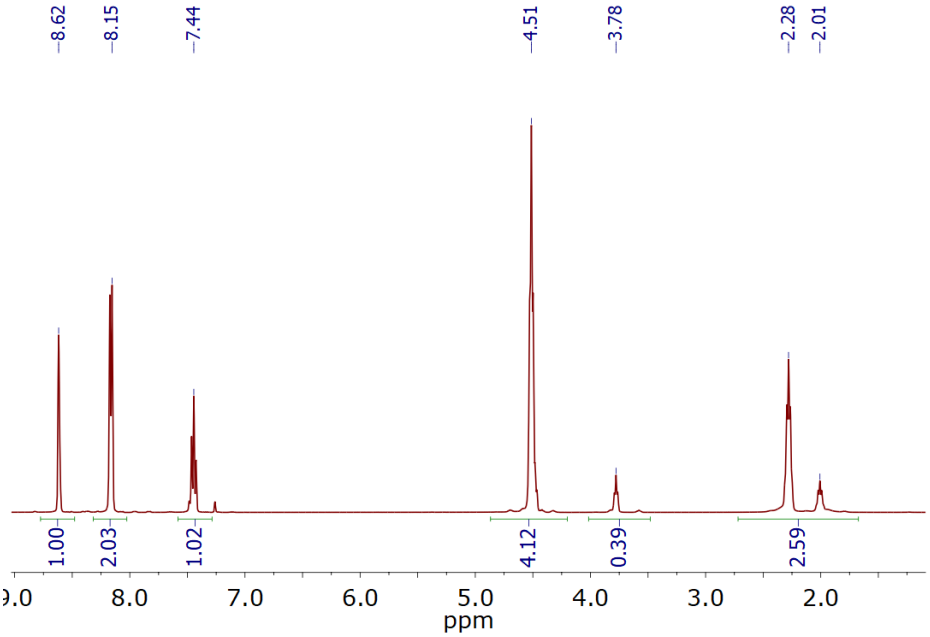

- $^{13}C\{^{1}H\}$ NMR

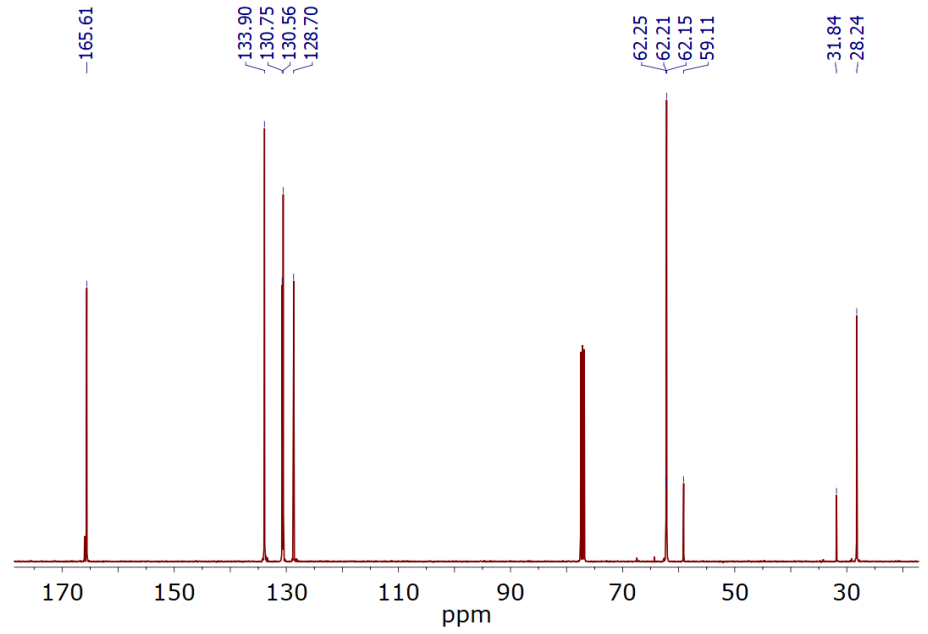

A2.1.3. IPHTAHDO 1000

- ^{1}H NMR

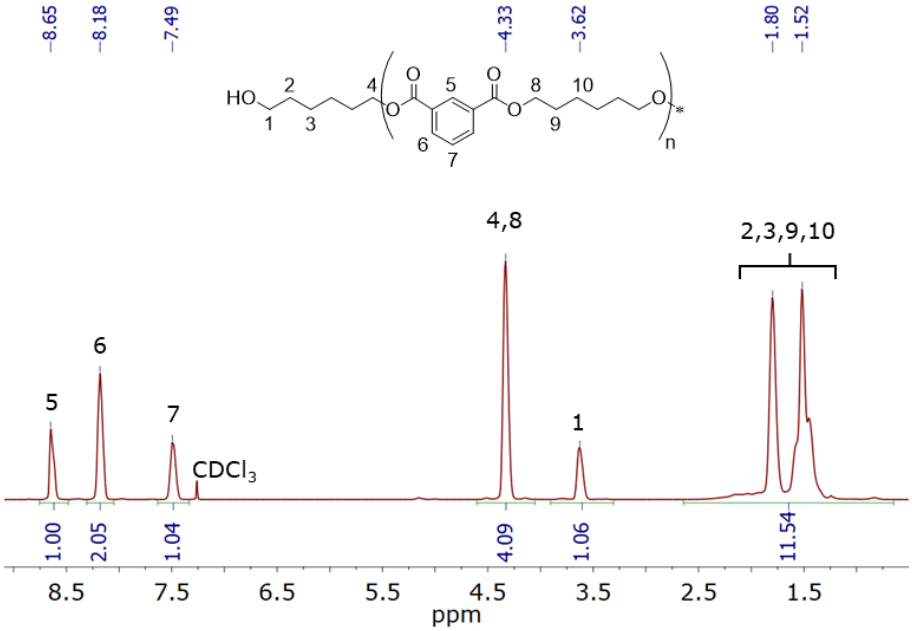

- $^{13}C\{^{1}H\}$ NMR

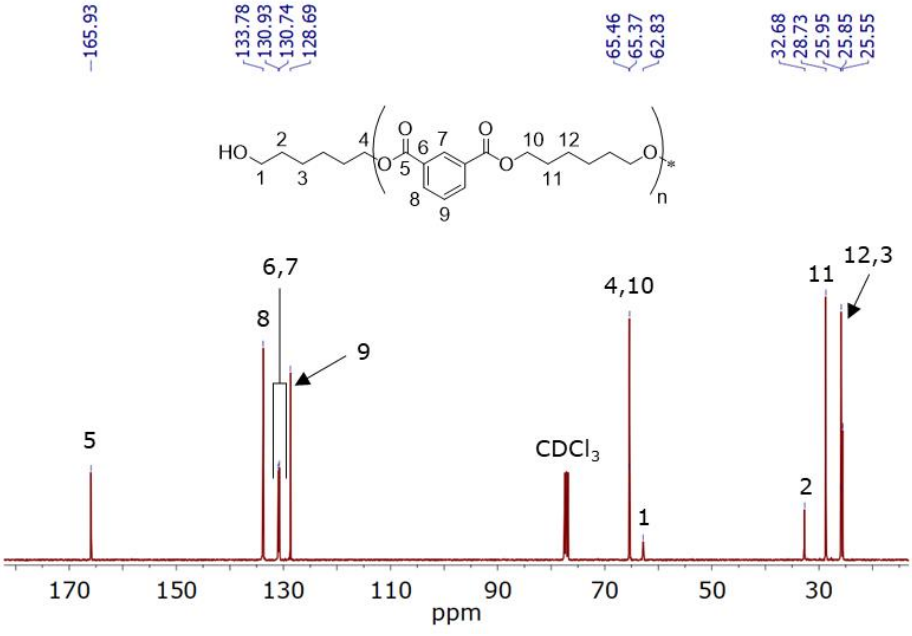

A2.1.4. IPHTAHDO 2000

- ^{1}H NMR

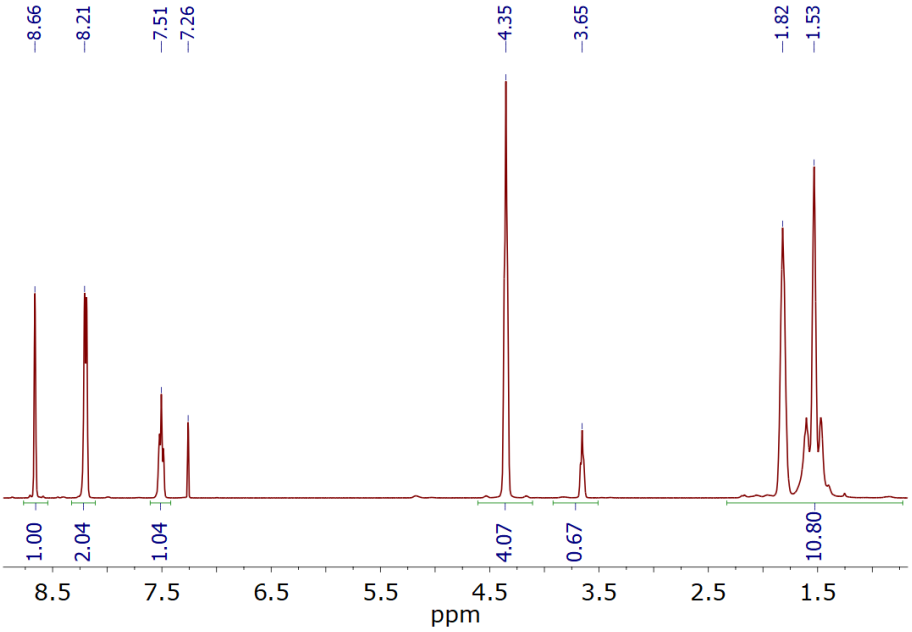

- ^{13}C{1H} NMR

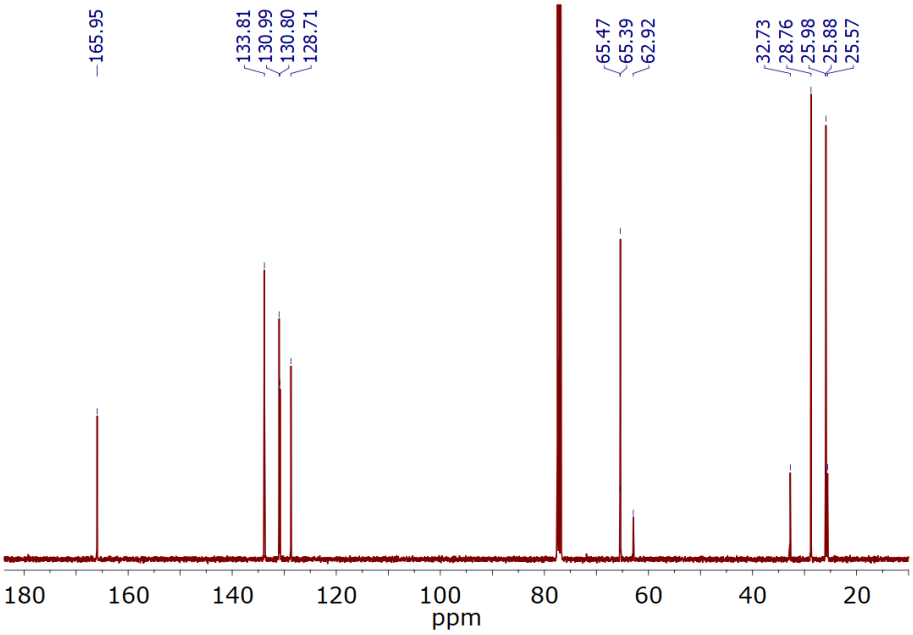

A2.1.5. FDCAPDO 1000

- ^{1}H NMR

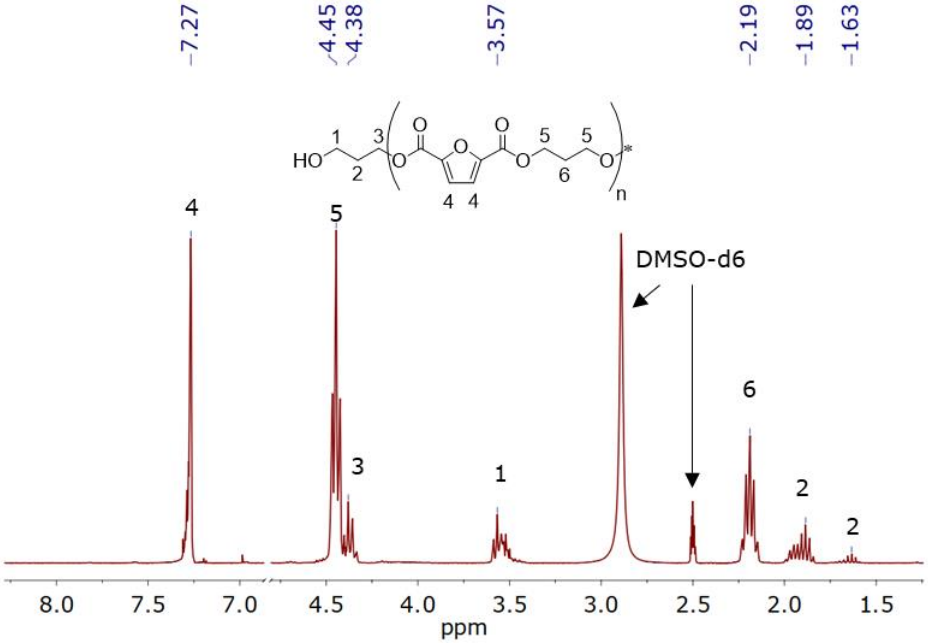

- ^{13}C{^{1}H} NMR

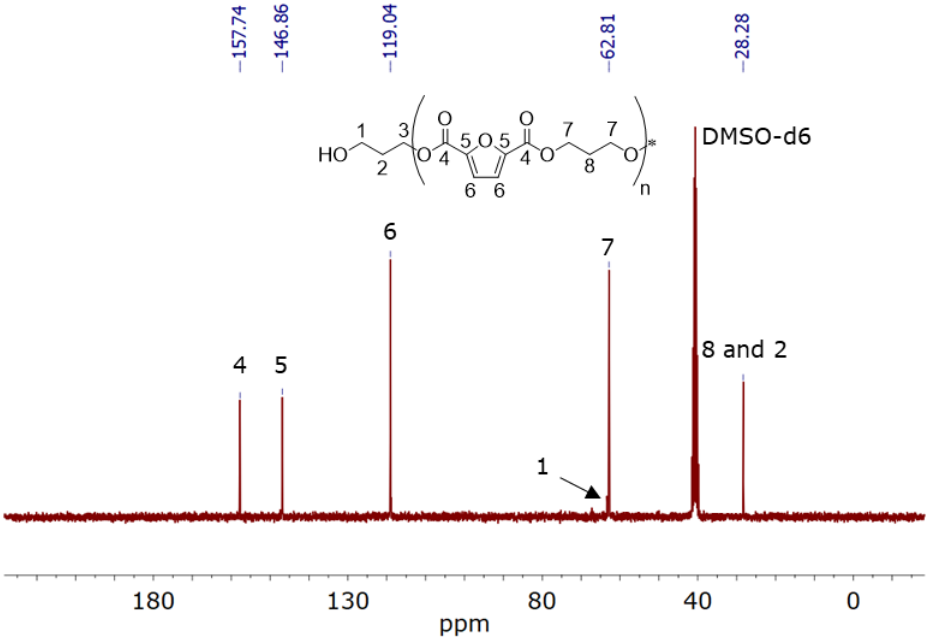

A2.1.6. FDCAPDO 1500

- ^{1}H NMR

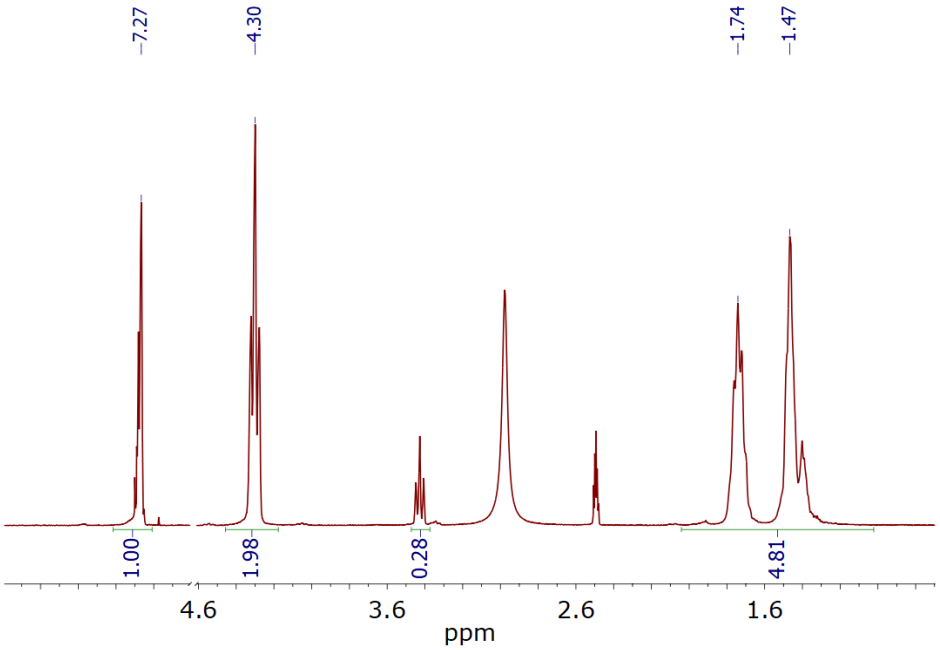

- $^{13}C\{^{1}H\}$ NMR

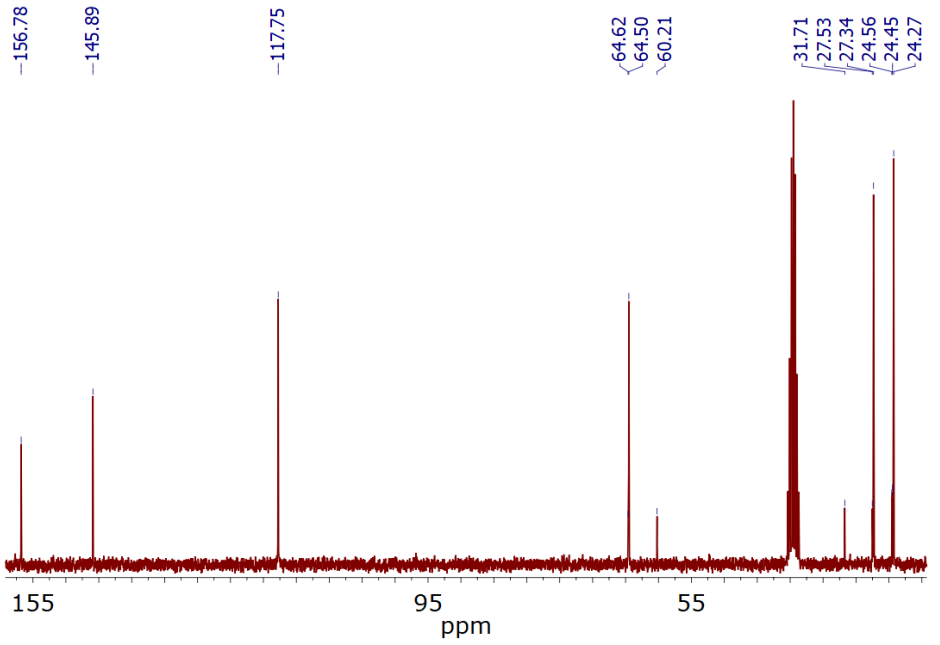

A2.1.7. FDCAPDO 2000

- ^{1}H NMR

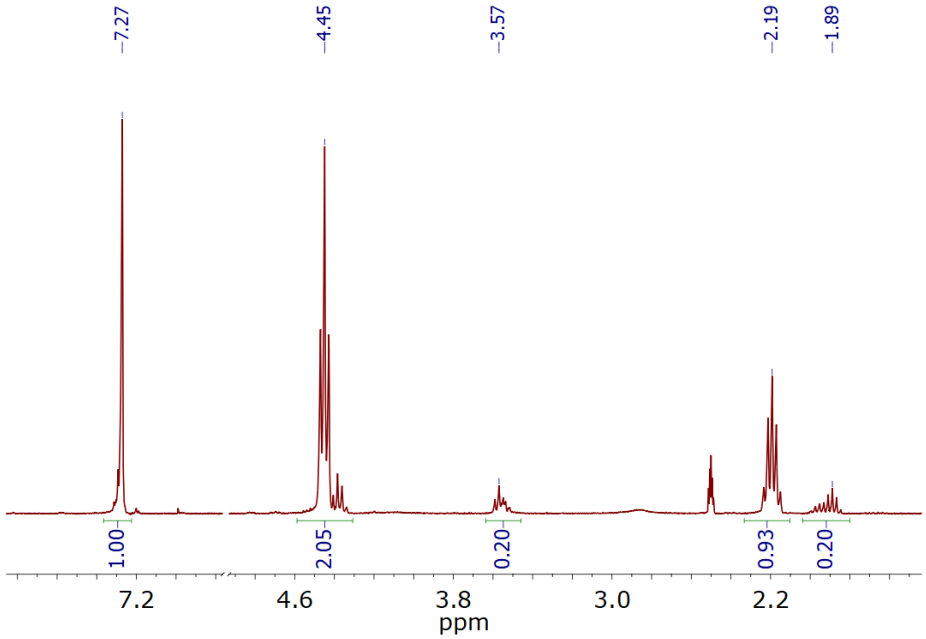

- $^{13}C\{^{1}H\}$ NMR

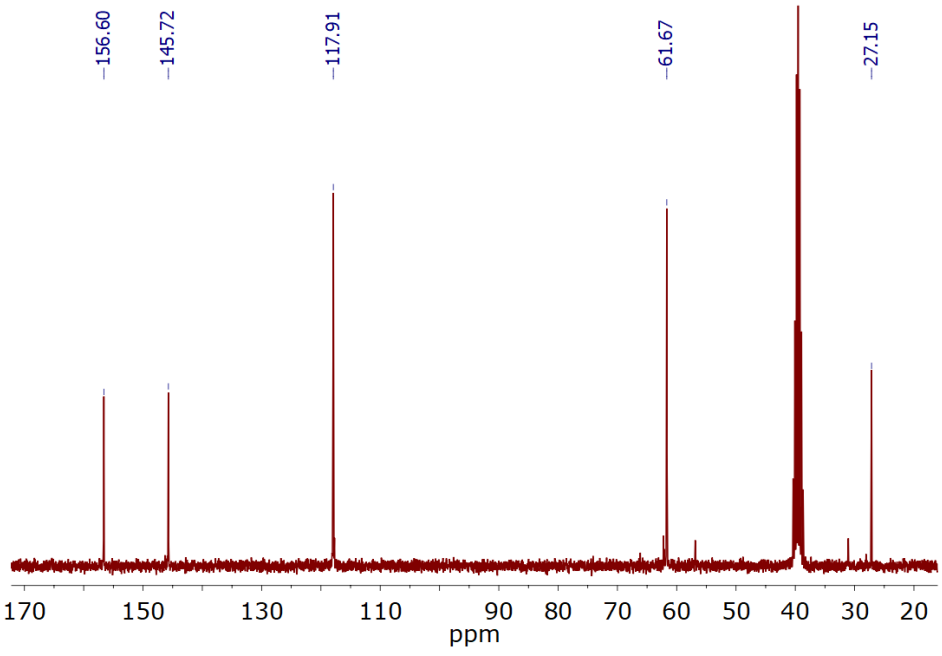

A2.1.8. FDCAHDO 1000

- ^{1}H NMR

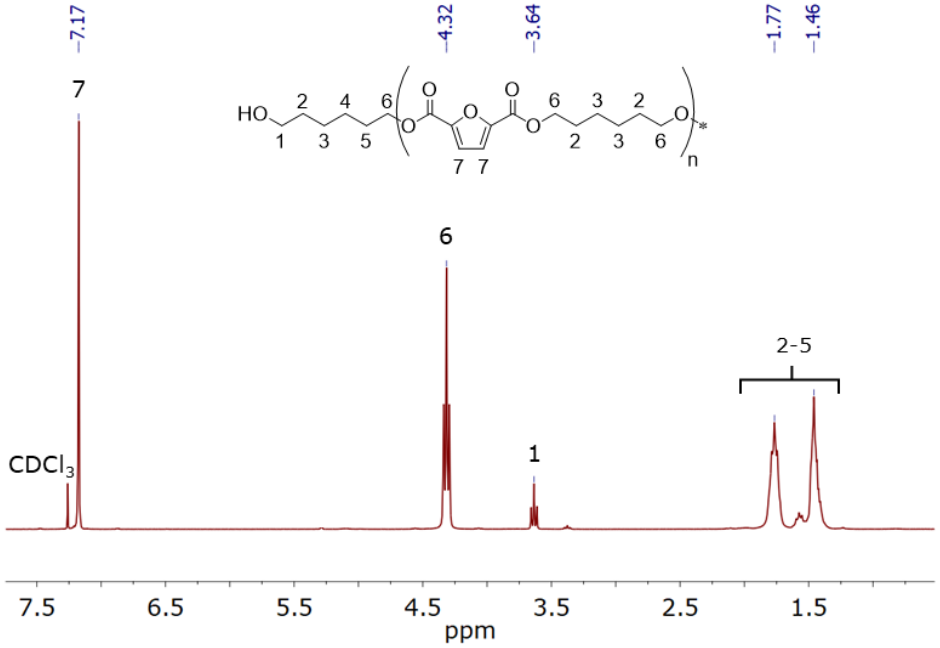

- $^{13}C\{^{1}H\}$ NMR

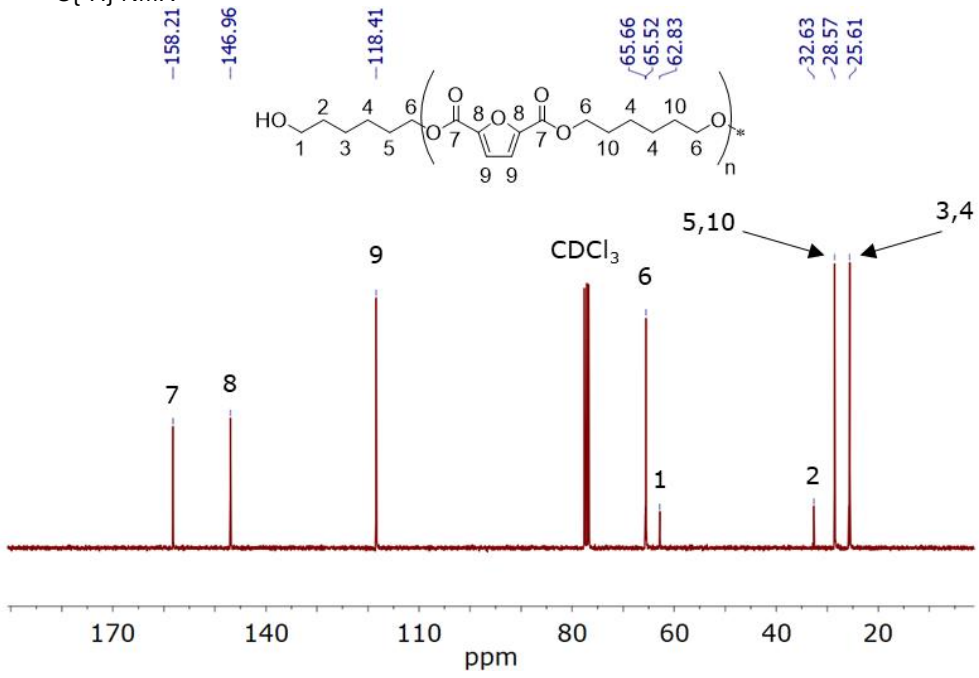

A2.1.9. FDCAHDO 1500

- ^{1}H NMR

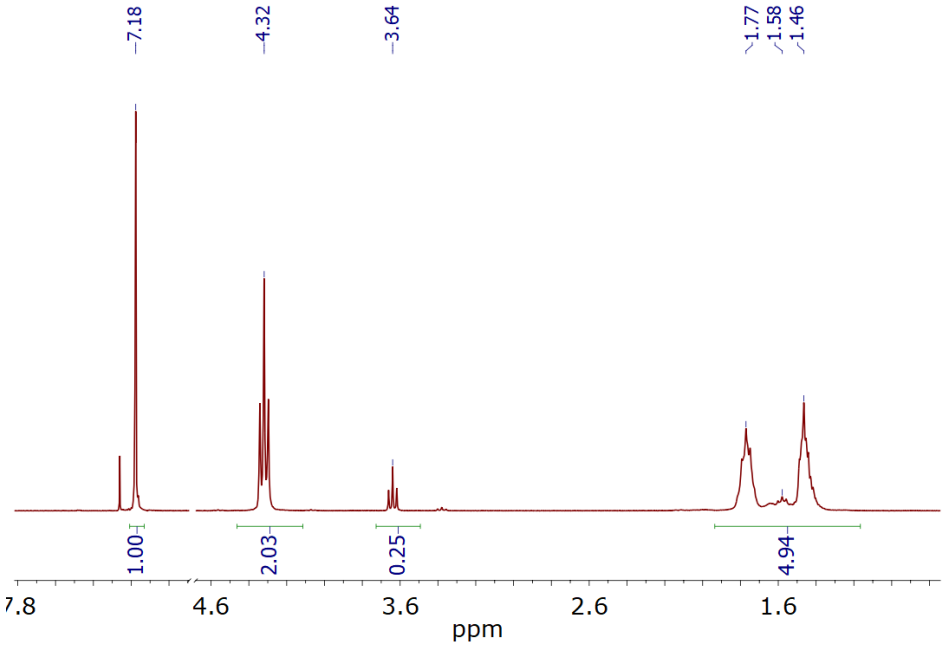

- $^{13}C\{^{1}H\}$ NMR

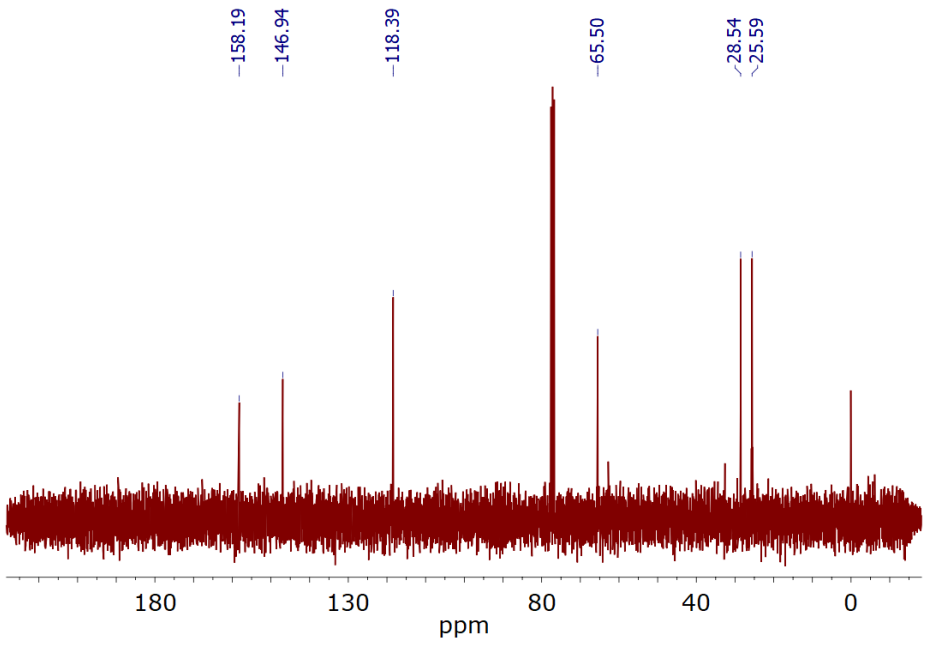

A2.1.10. FDCAHDO 2000

- ^{1}H NMR

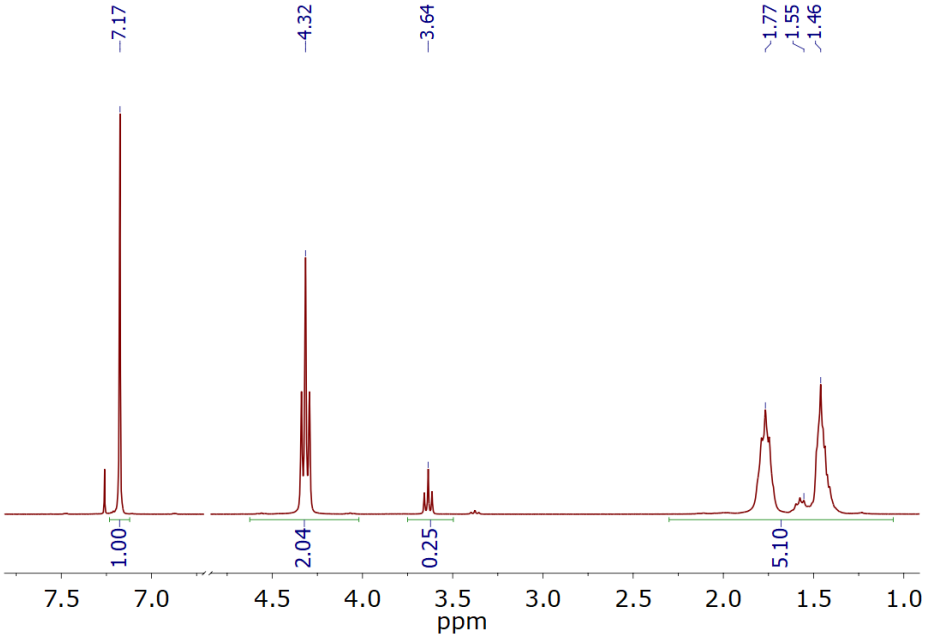

- $^{13}C\{^{1}H\}$ NMR

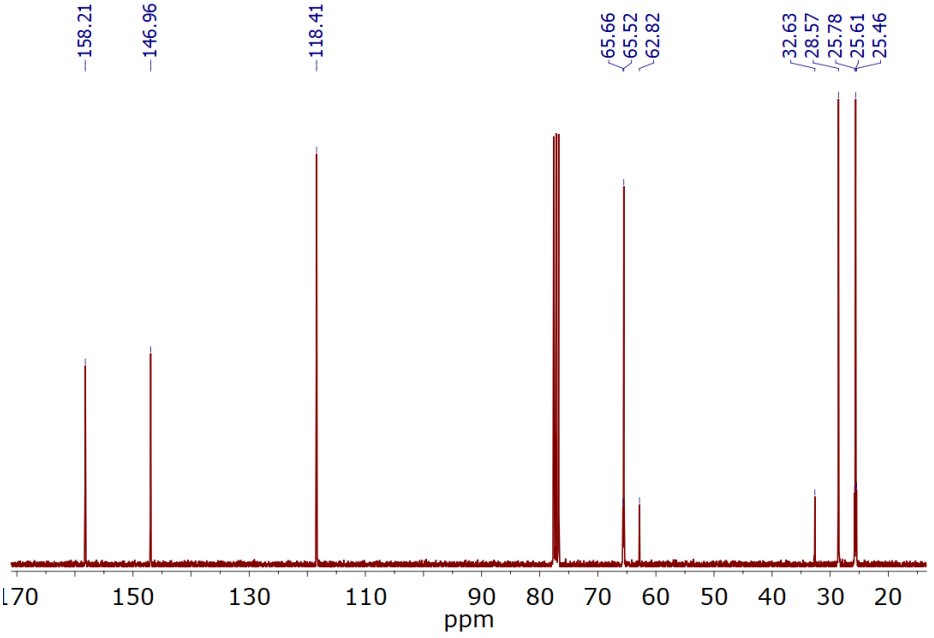

A2.2. TPUs

The position of the ^{1}H NMR and $^{13}C\{^{1}H\}$ NMR spectral peaks are shared for each of the types of TPUs. Therefore, their assignation will only be shown in the first of each of the TPUs types displayed below.

A2.2.1. IPHTAPDO 1000 10 MDI

- ^{1}H NMR

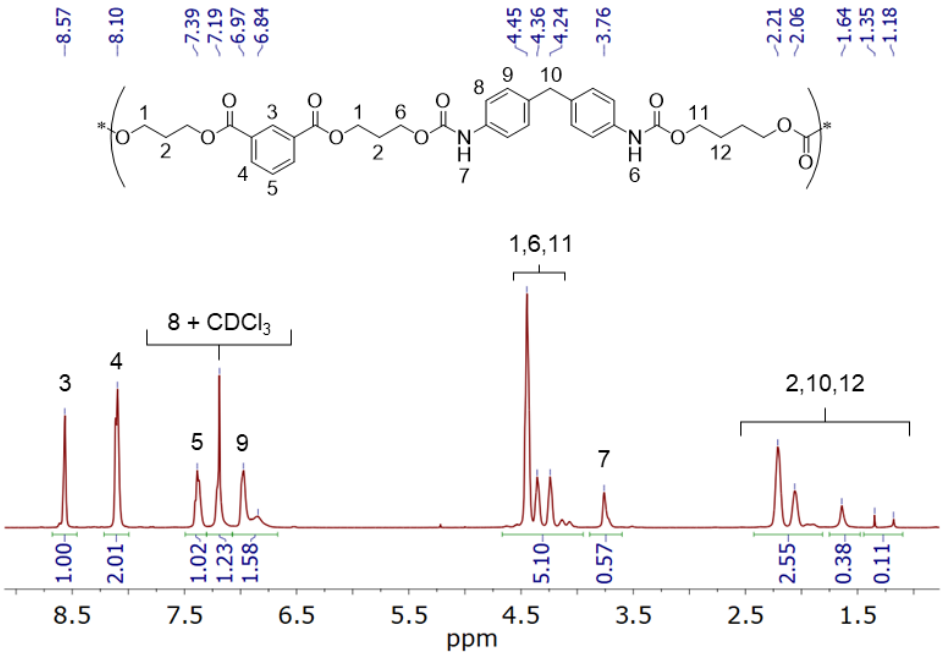

- $^{13}C\{^{1}H\}$ NMR

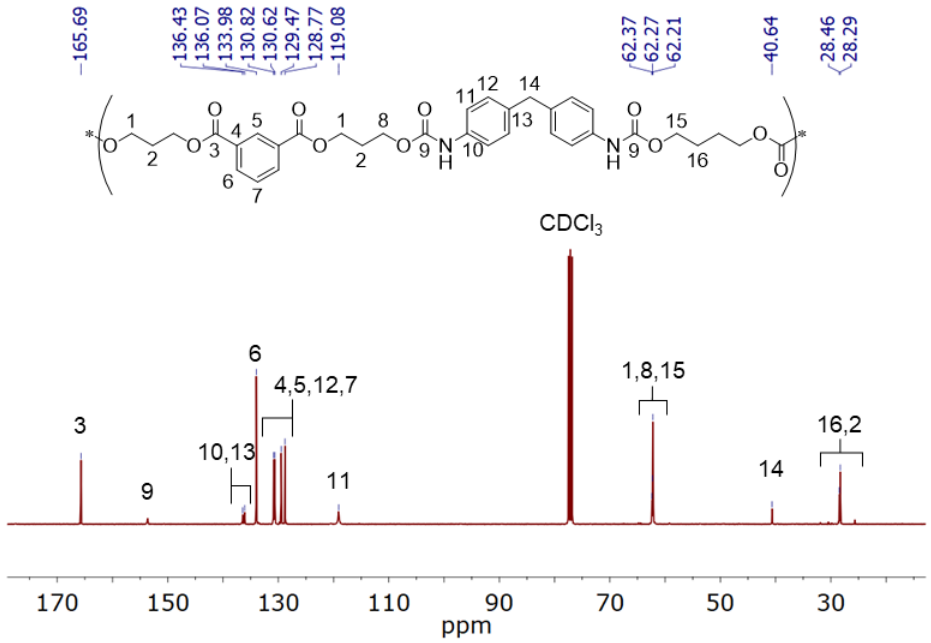
165.69
136.43
136.07
133.98
130.82
130.62
129.47
128.77
119.08
62.37
62.27
62.21
40.64
28.46
28.29
CDCl3
6
4,5,12,7
1,8,15
3
10,13
16,2
9
11
14
170
150
130
110
90
70
50
30
ppm

A2.2.2. IPHTAPDO 1000 30 MDI

- ^{1}H NMR

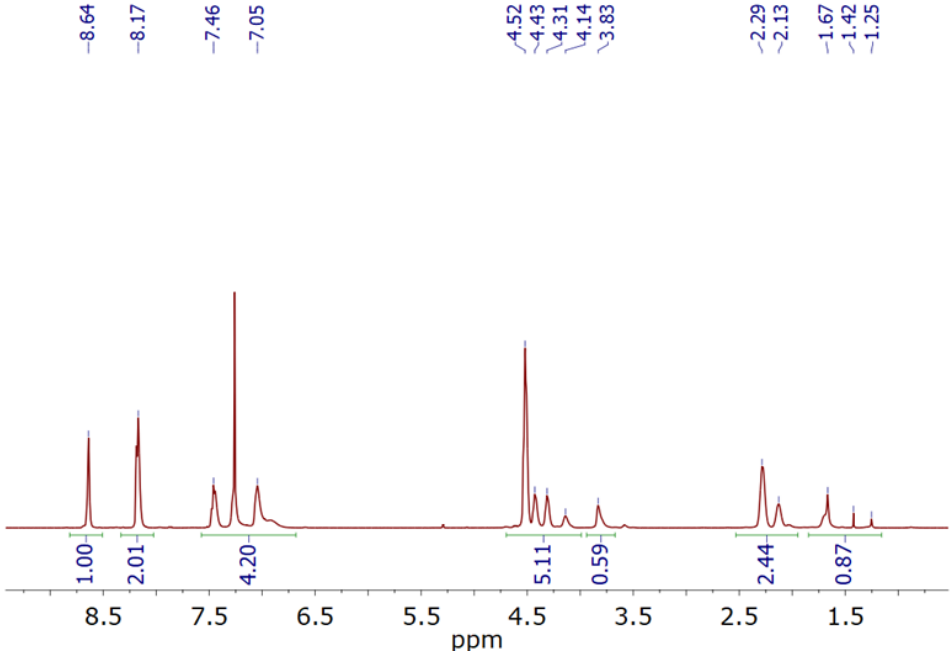

- $^{13}C\{^{1}H\}$ NMR

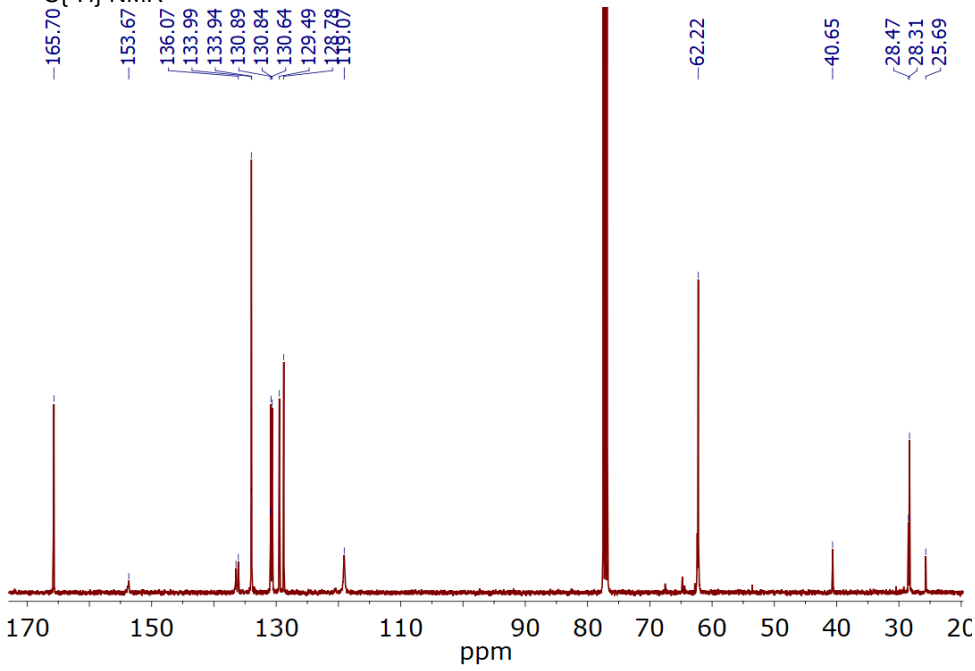

A2.2.3. IPHTAPDO 1000 50 MDI

- ^{1}H NMR

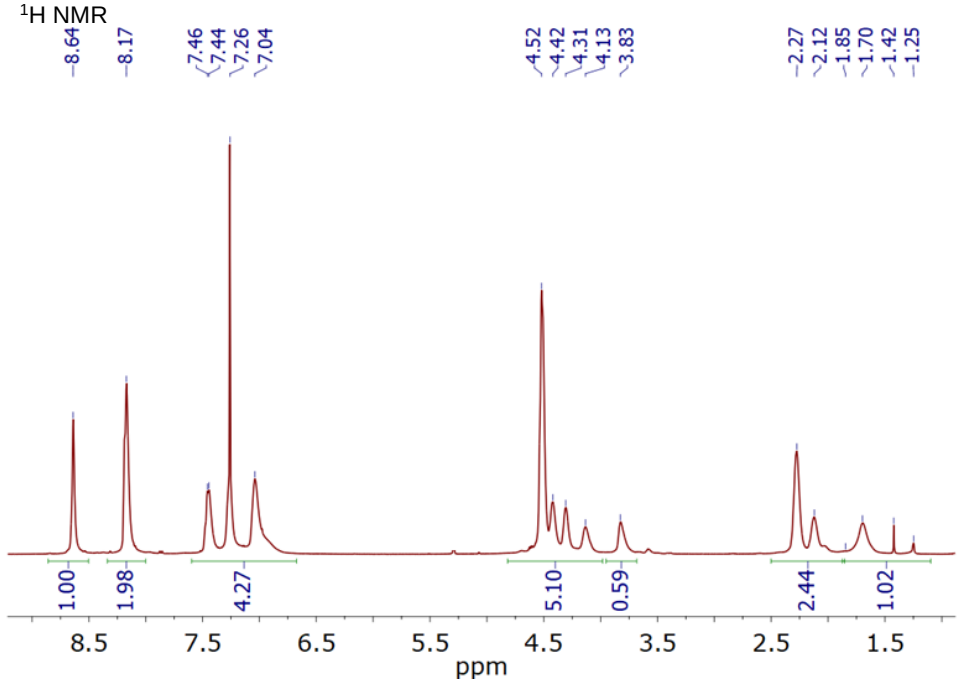

- $^{13}C\{^{1}H\}$ NMR

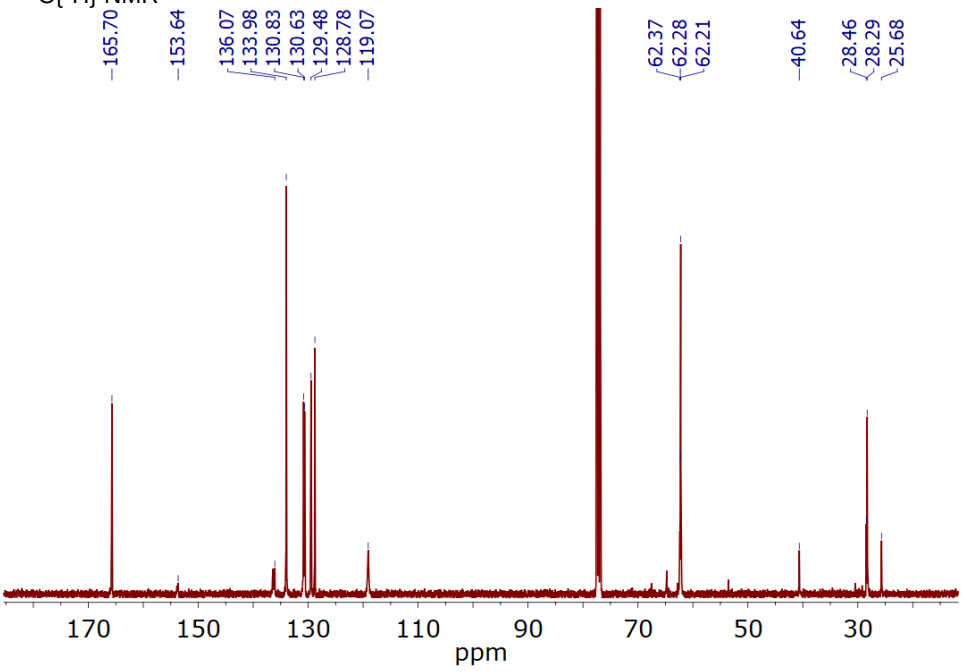

A2.2.4. IPHTAPDO 2000 10 MDI

- ^{1}H NMR

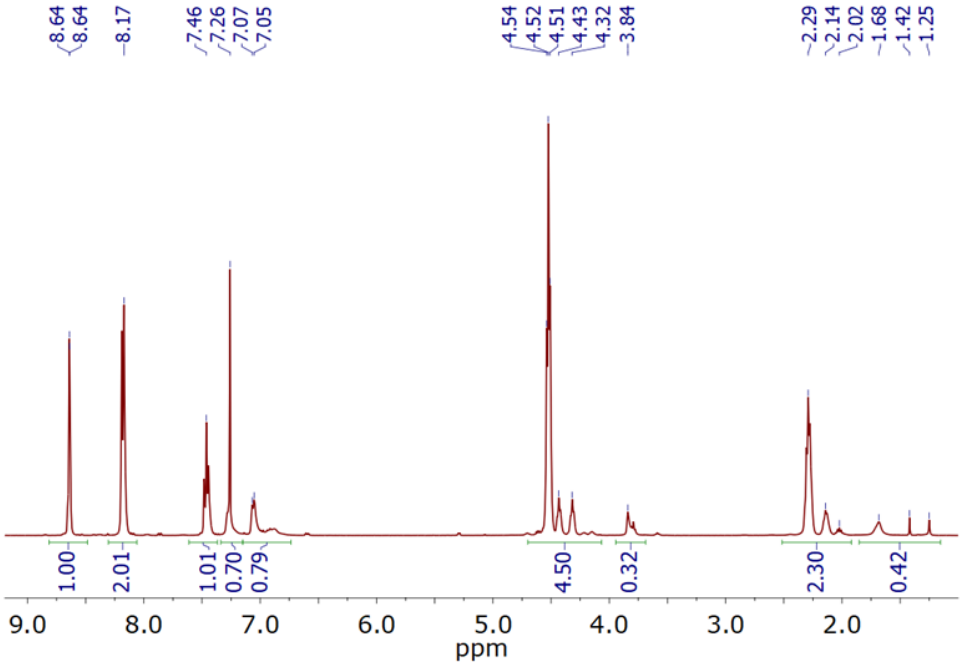

- ^{13}C{^{1}H} NMR

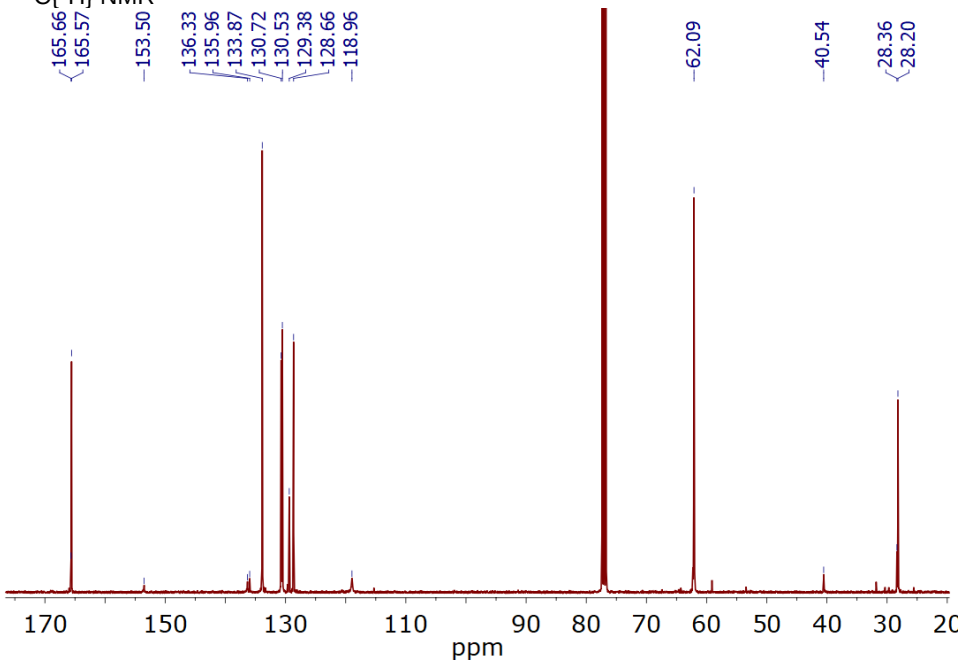

A2.2.5. IPHTAPDO 2000 30 MDI

- ^{1}H NMR

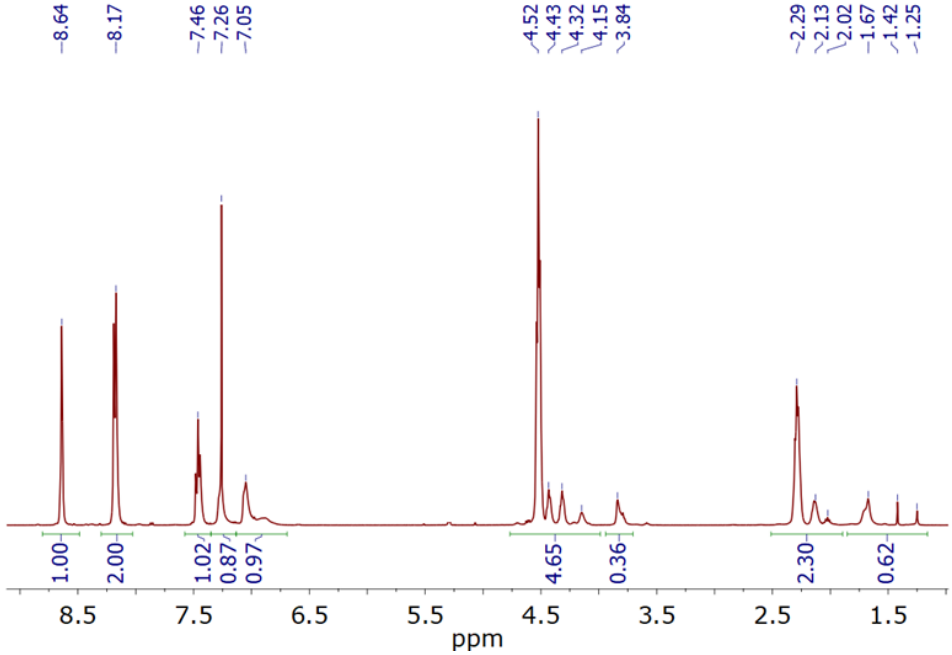

- $^{13}C\{^{1}H\}$ NMR

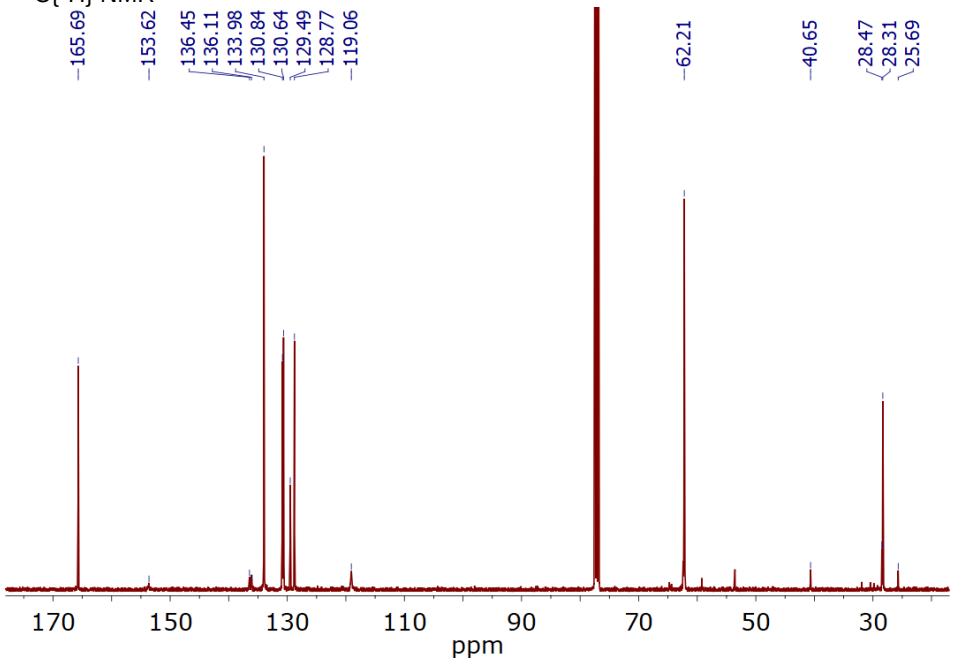

A2.2.6. IPHTAPDO 2000 50 MDI

- ^{1}H NMR

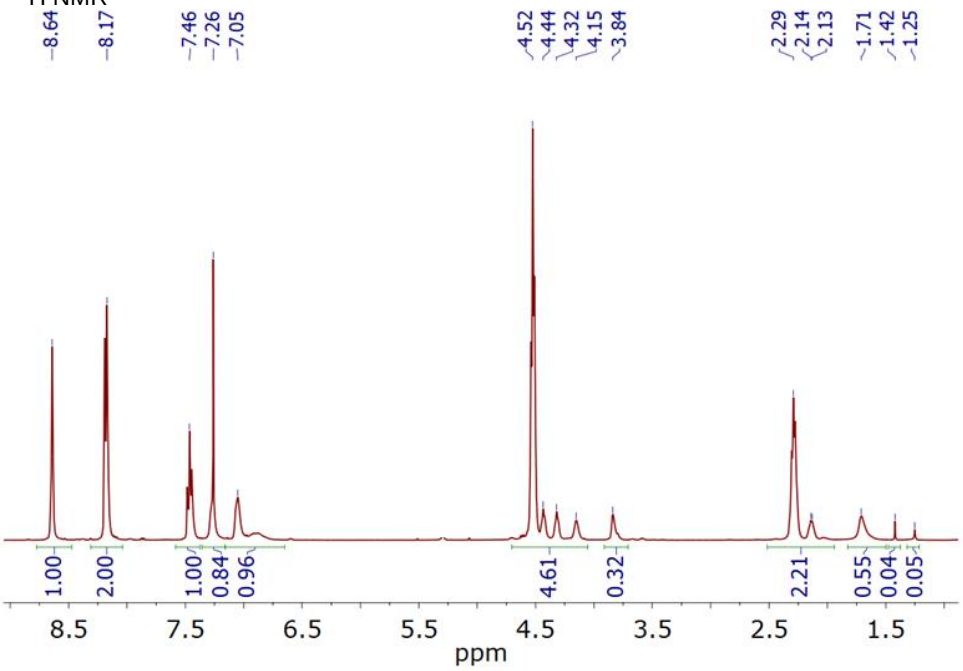

- $^{13}C\{^{1}H\}$ NMR

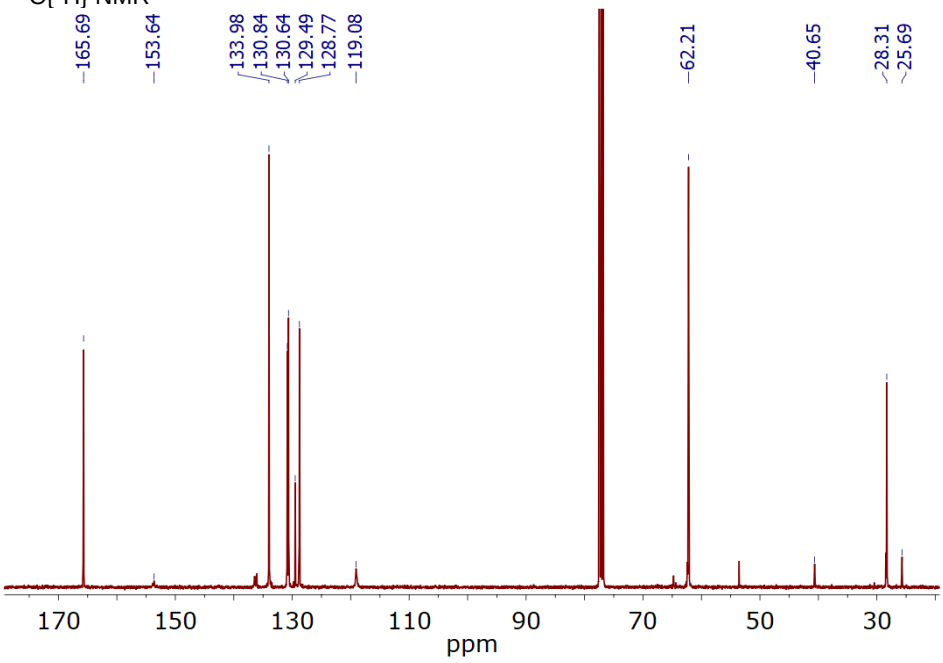

A2.2.7. IPHTAHDO 1000 10 MDI

- ^{1}H NMR

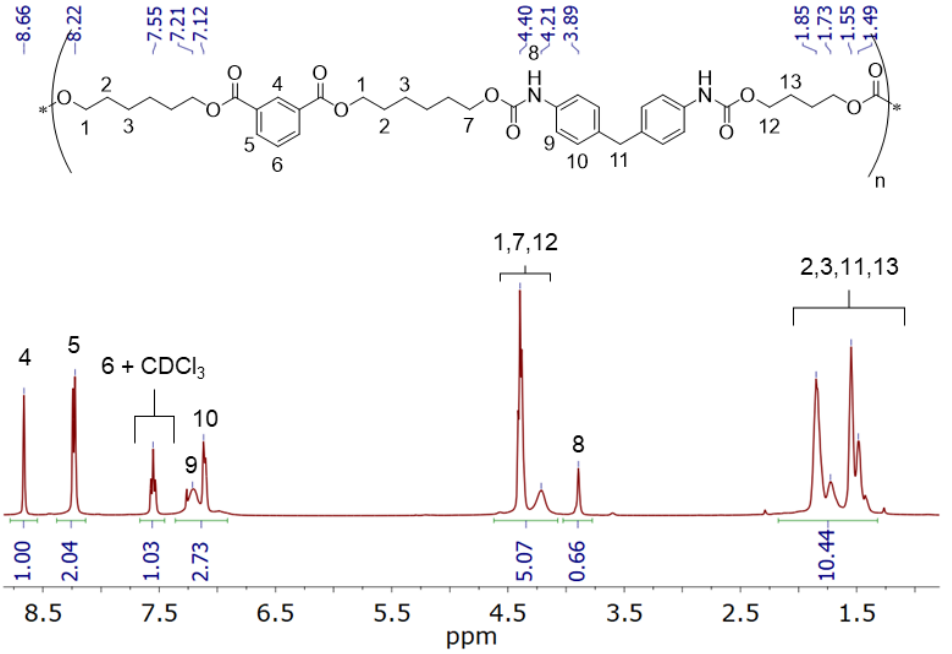

- $^{13}C\{^{1}H\}$ NMR

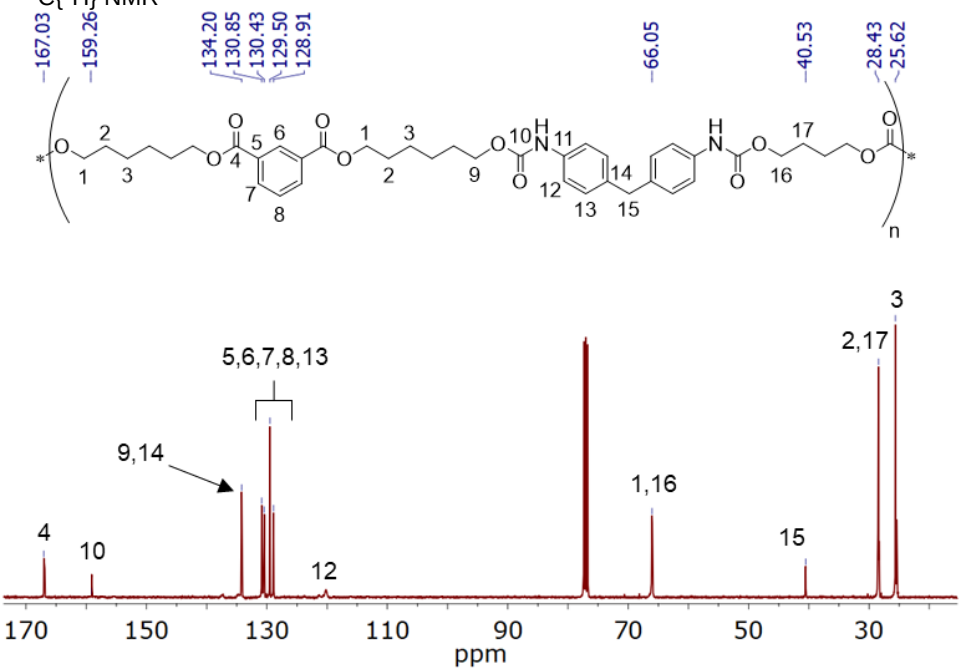

A2.2.8. IPHTAHDO 1000 30 MDI

- ^{1}H NMR

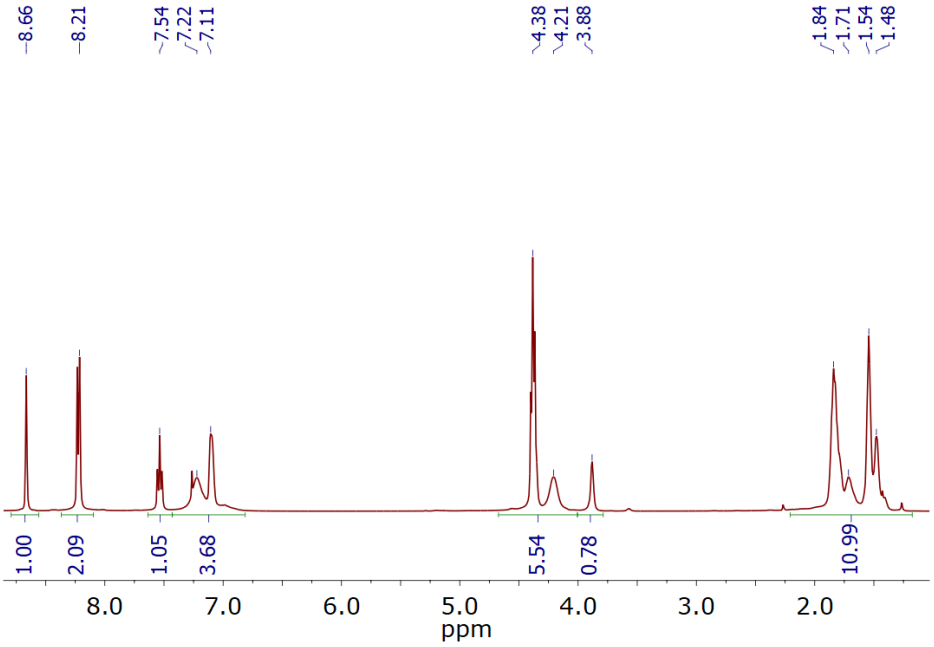

- $^{13}C\{^{1}H\}$ NMR

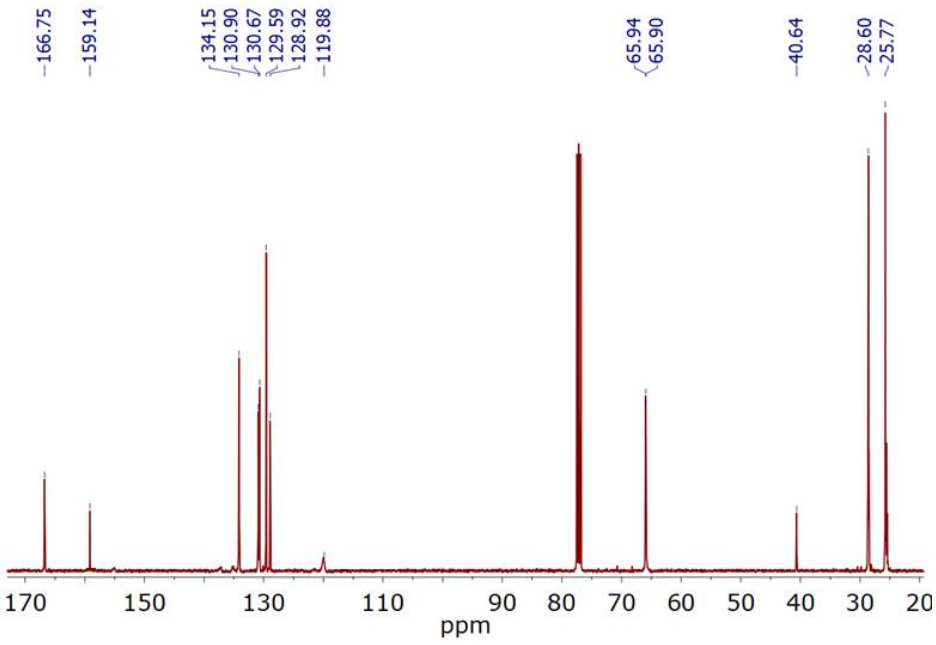

A2.2.9. IPHTAHDO 1000 50 MDI

- ^{1}H NMR

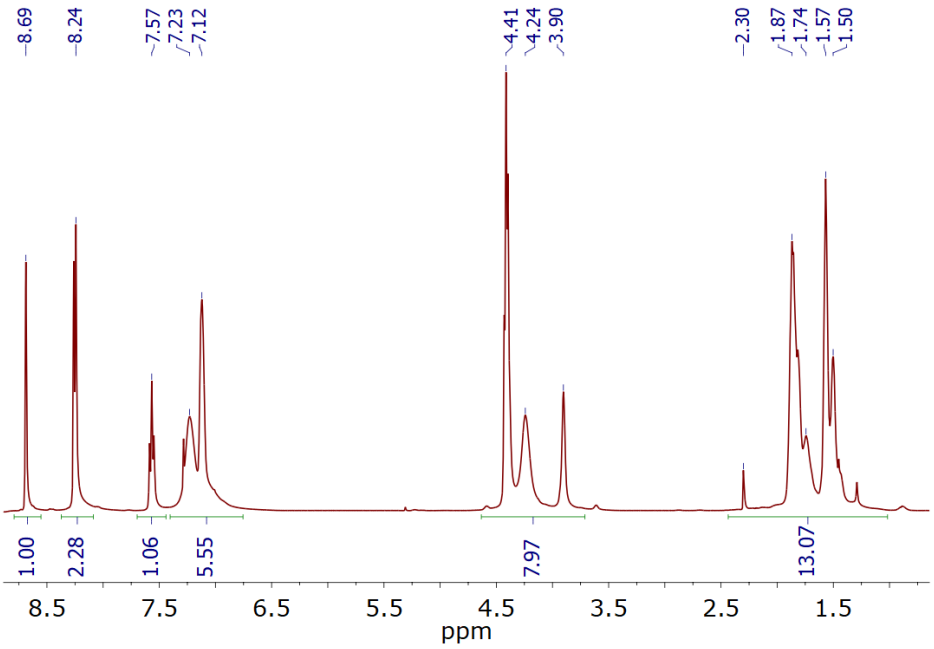

- $^{13}C\{^{1}H\}$ NMR

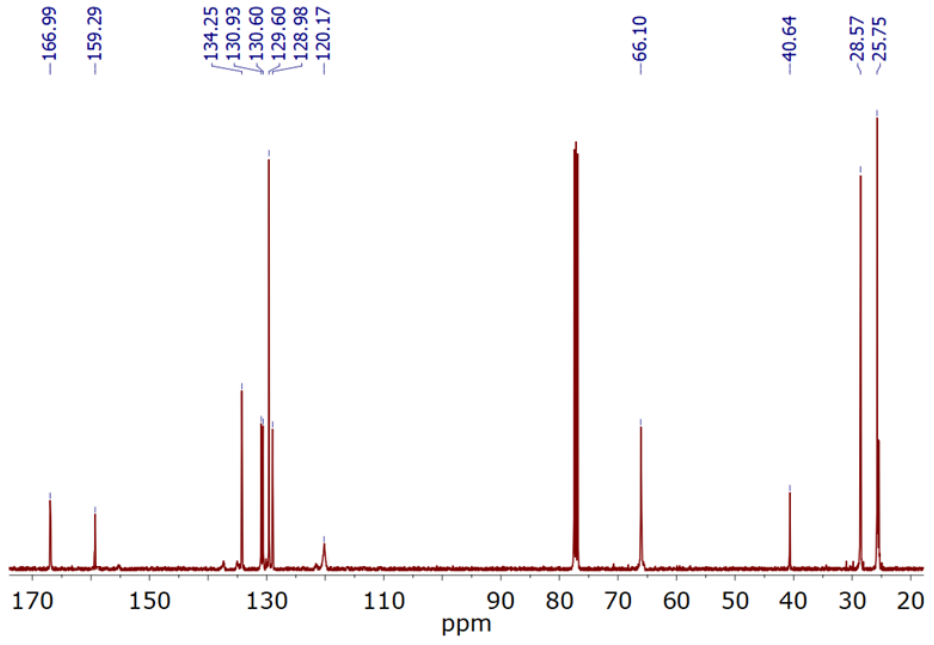

A2.2.10. IPHTAHDO 2000 10 MDI

- ^{1}H NMR

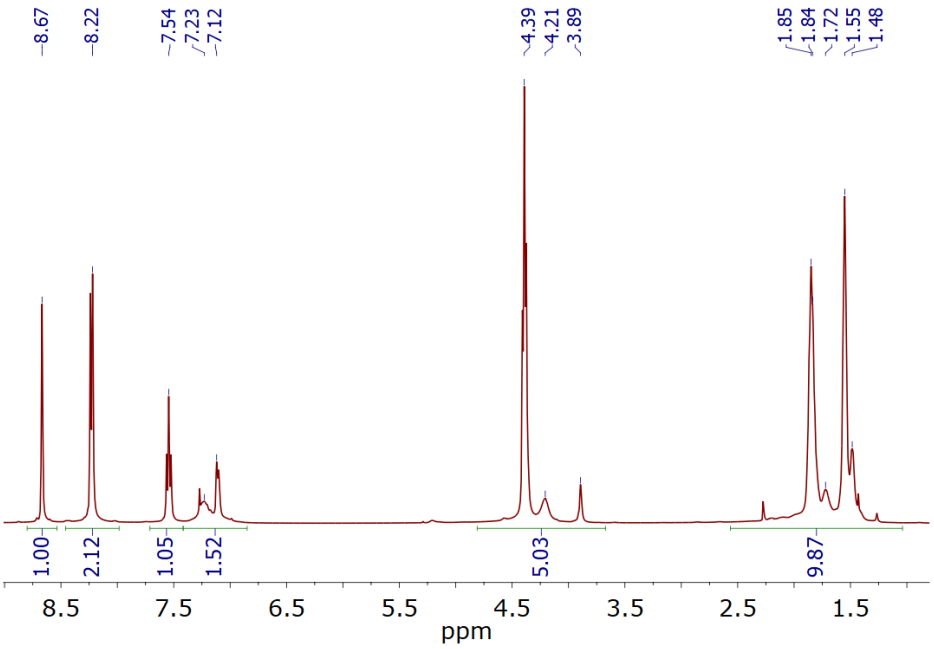

- $^{13}C\{^{1}H\}$ NMR

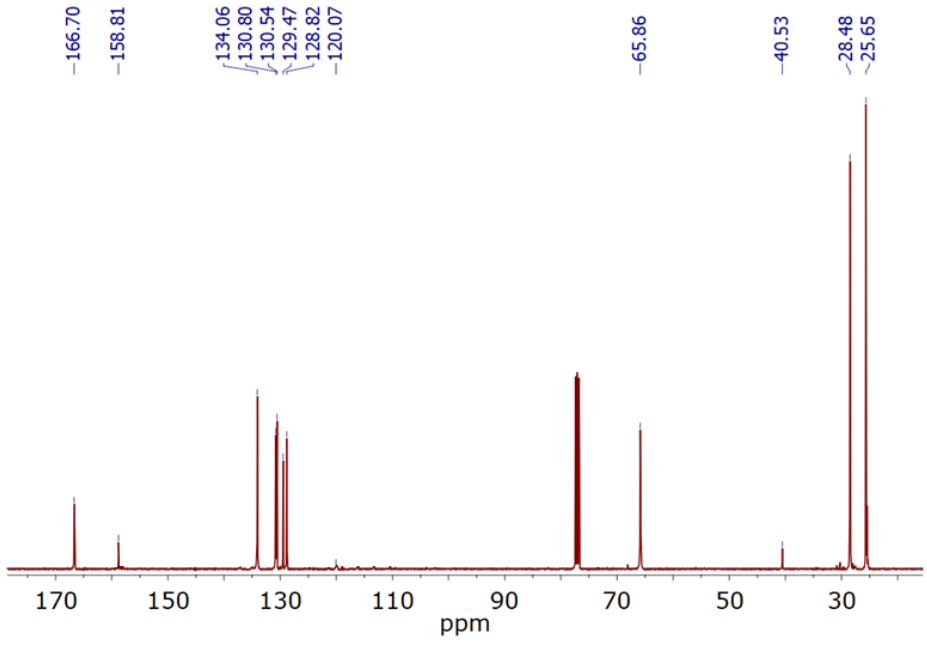

A2.2.11. IPHTAHDO 2000 30 MDI

- ^{1}H NMR

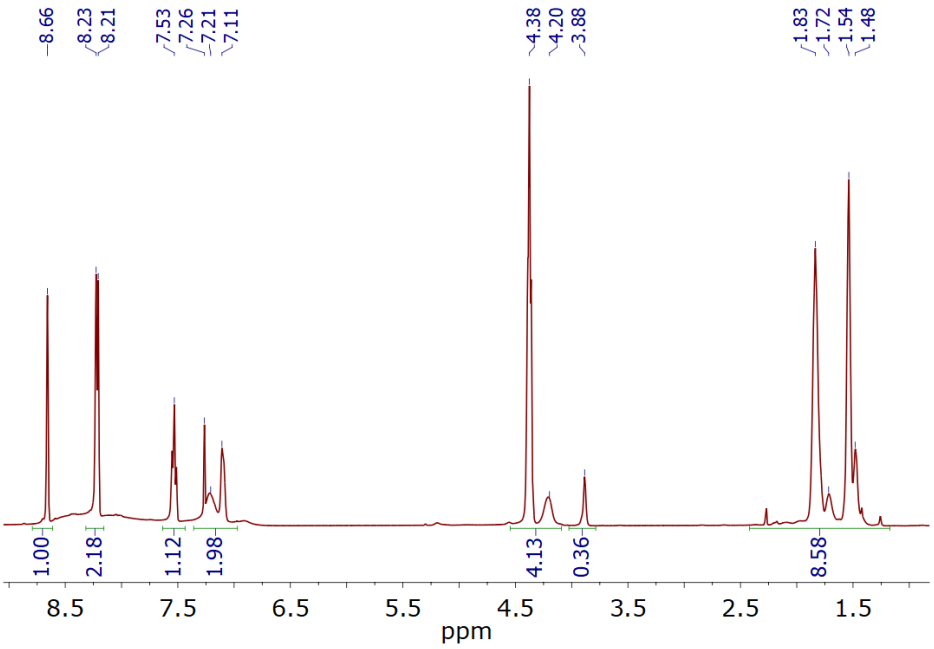

- $^{13}C\{^{1}H\}$ NMR

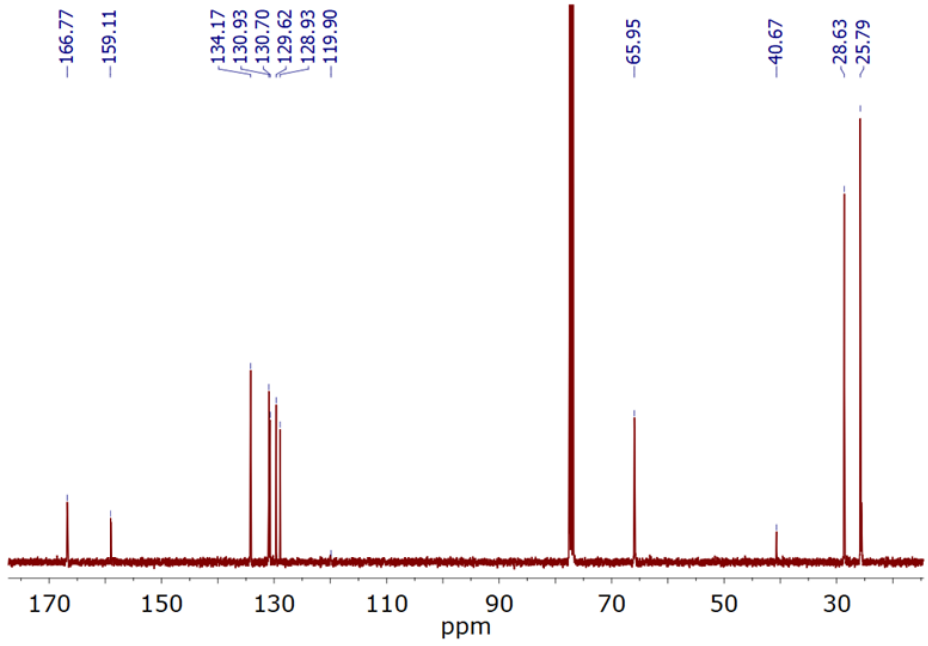

A2.2.12. IPHTAHDO 2000 50 MDI

- ^{1}H NMR

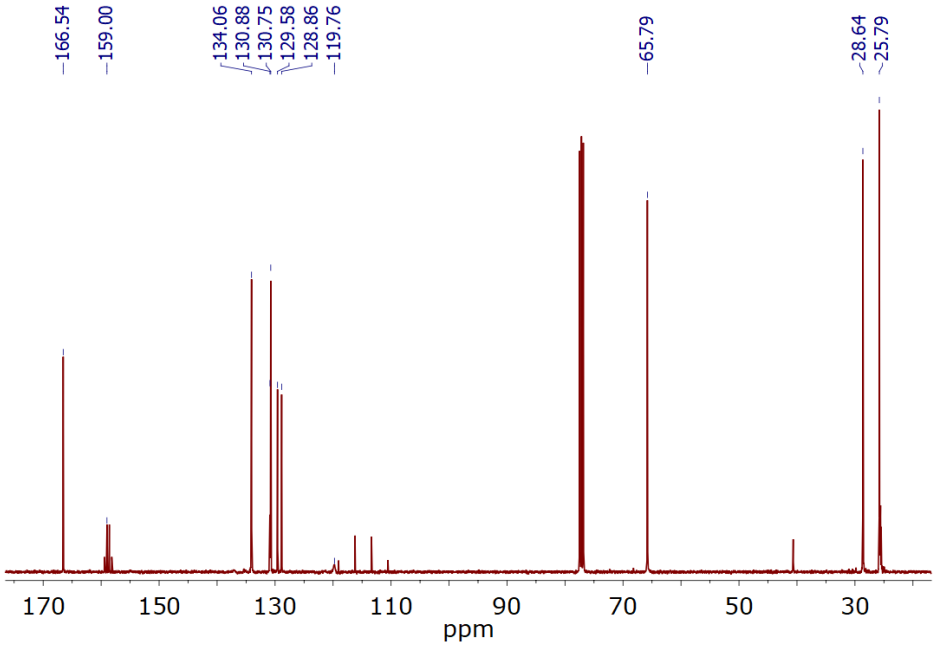

- $^{13}C\{^{1}H\}$ NMR

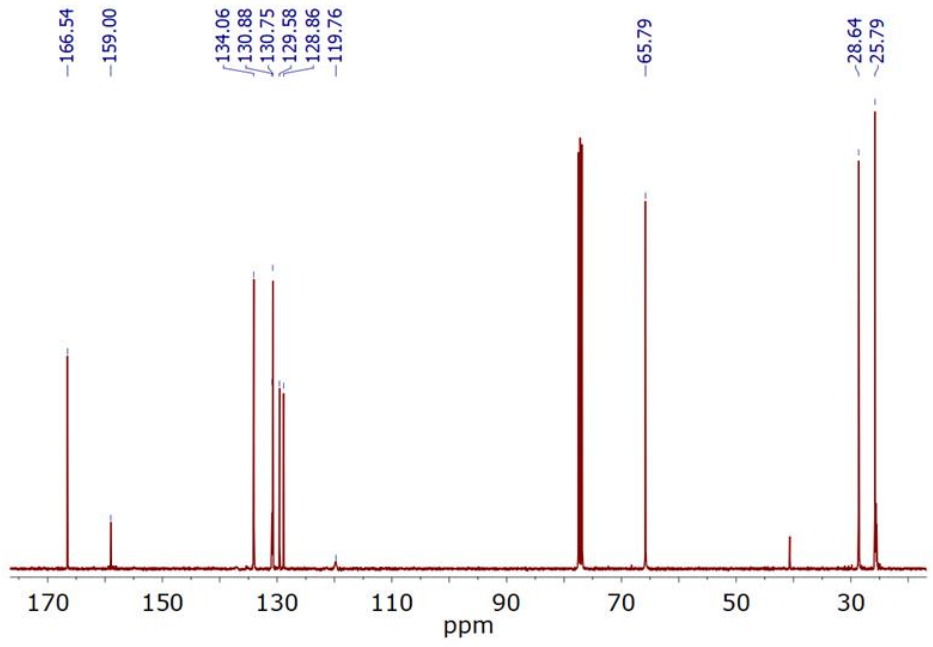

A2.2.13. IPHTAPDO 1000 10 HDI

- ^{1}H NMR

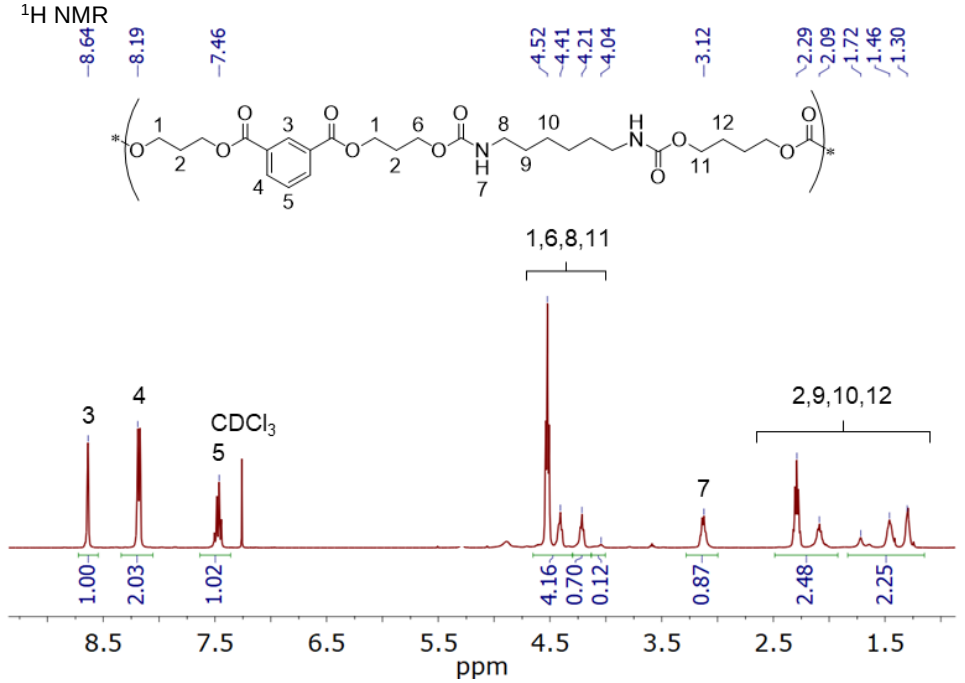

- ^{13}C{^{1}H} NMR

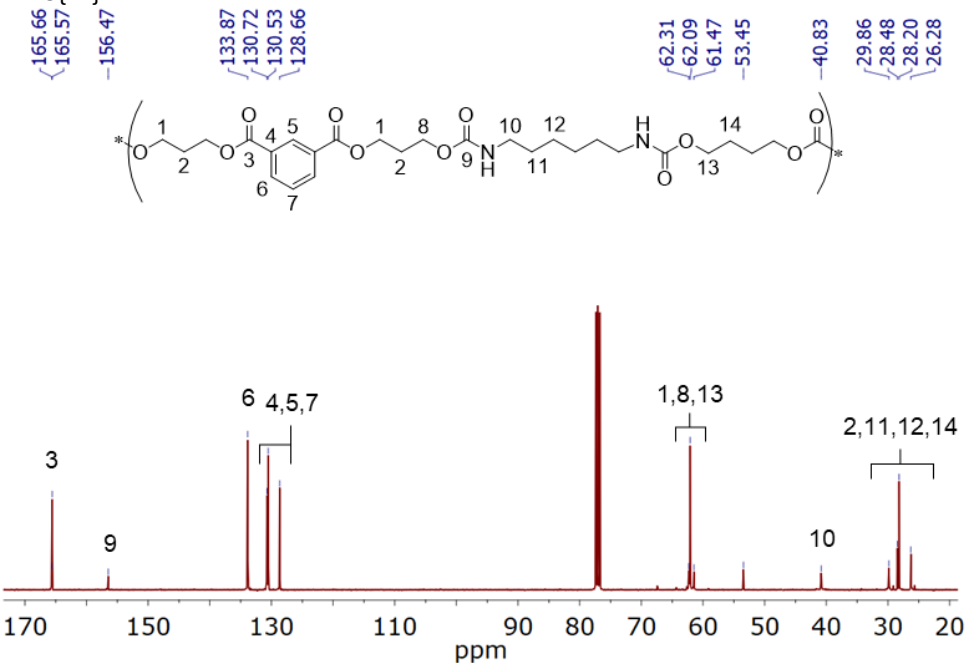

A2.2.14. IPHTAPDO 1000 30 HDI

- ^{1}H NMR

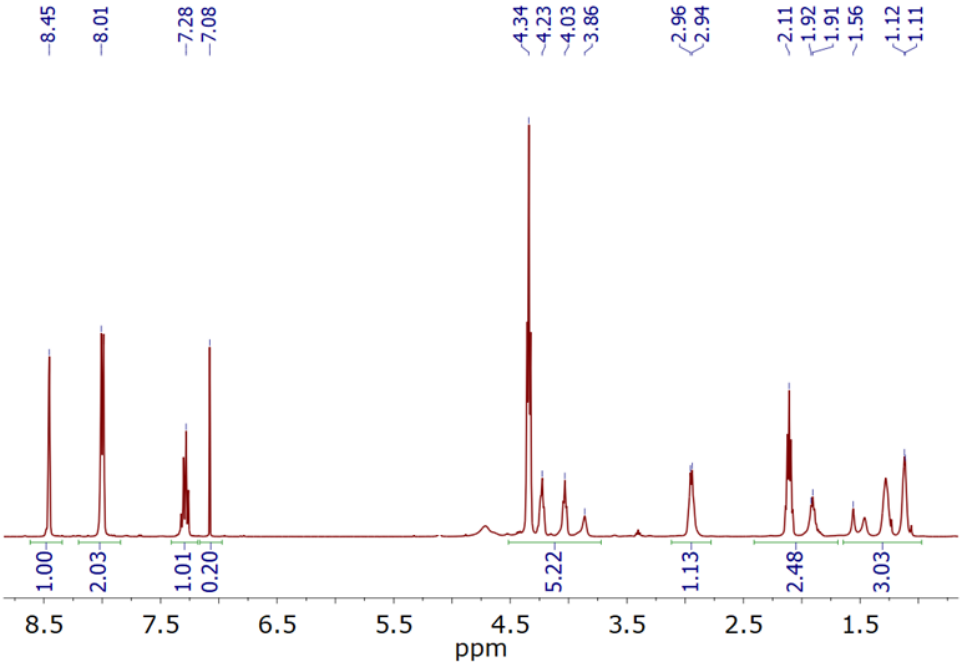

- $^{13}C\{^{1}H\}$ NMR

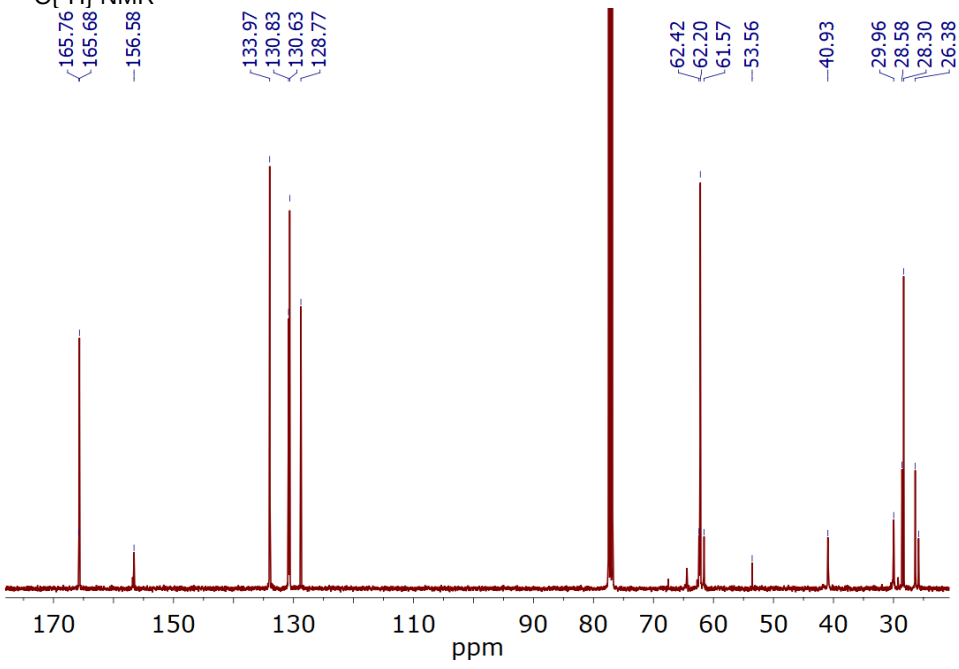

A2.2.15. IPHTAPDO 2000 10 HDI

- ^{1}H NMR

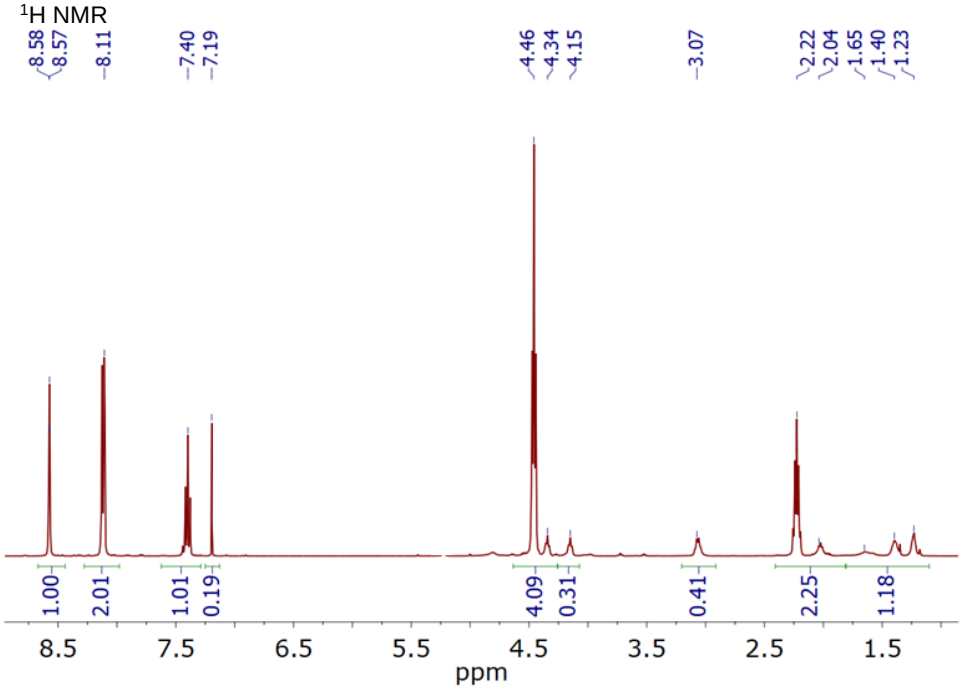

- ^{13}C{^{1}H} NMR

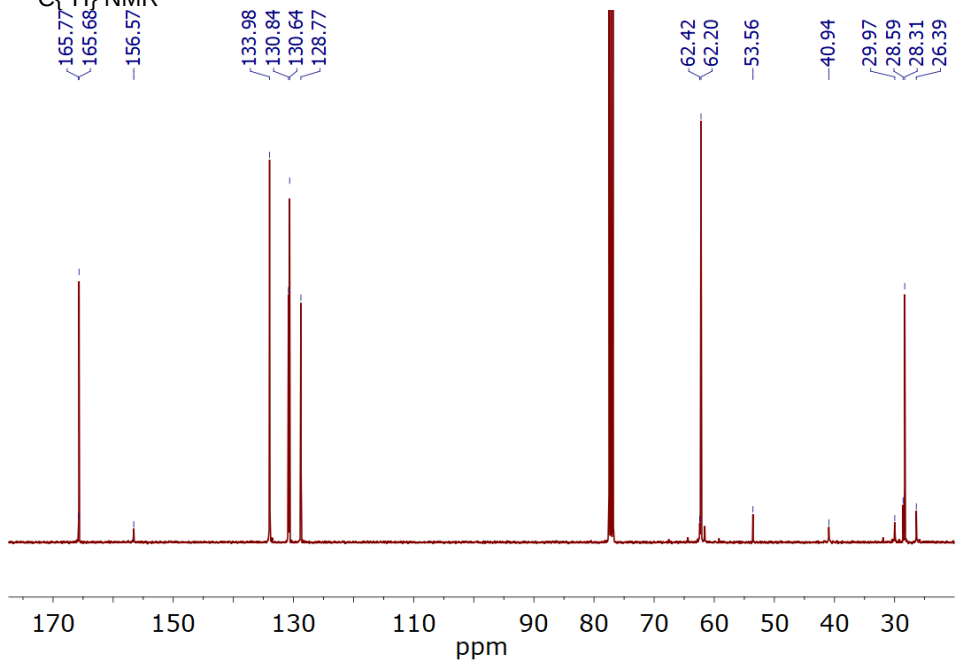

A2.2.16. IPHTAPDO 2000 30 HDI

- ^{1}H NMR

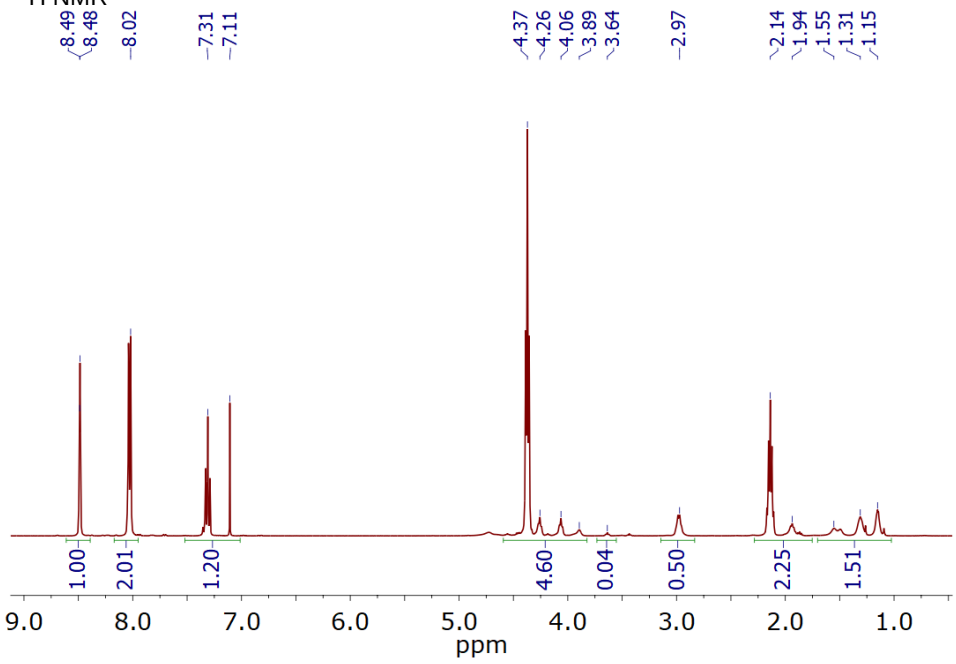

- $^{13}C\{^{1}H\}$ NMR

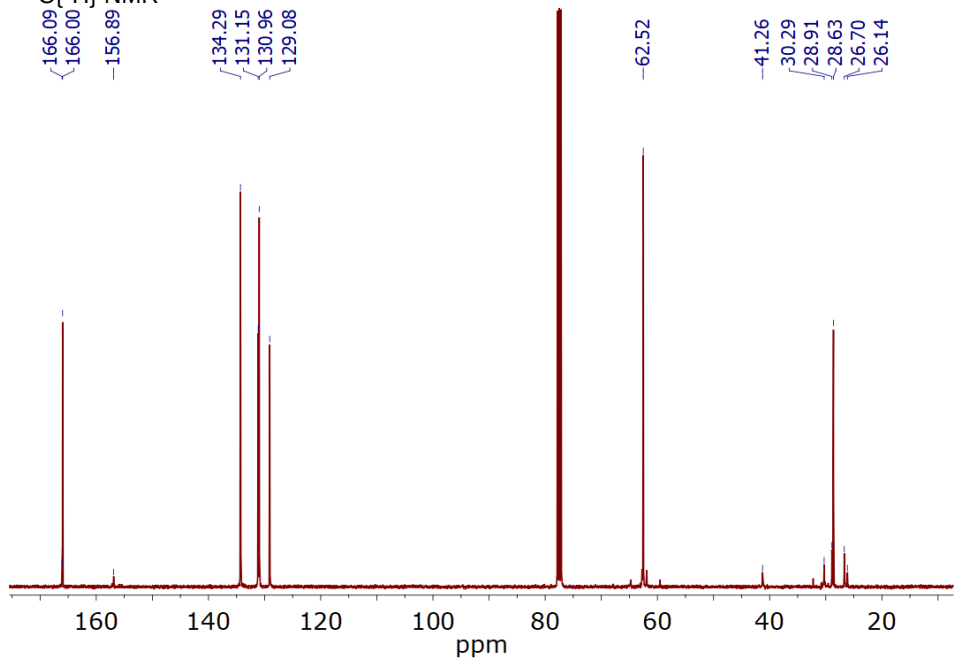

A2.2.17. IPHTAPDO 2000 50 HDI

- ^{1}H NMR

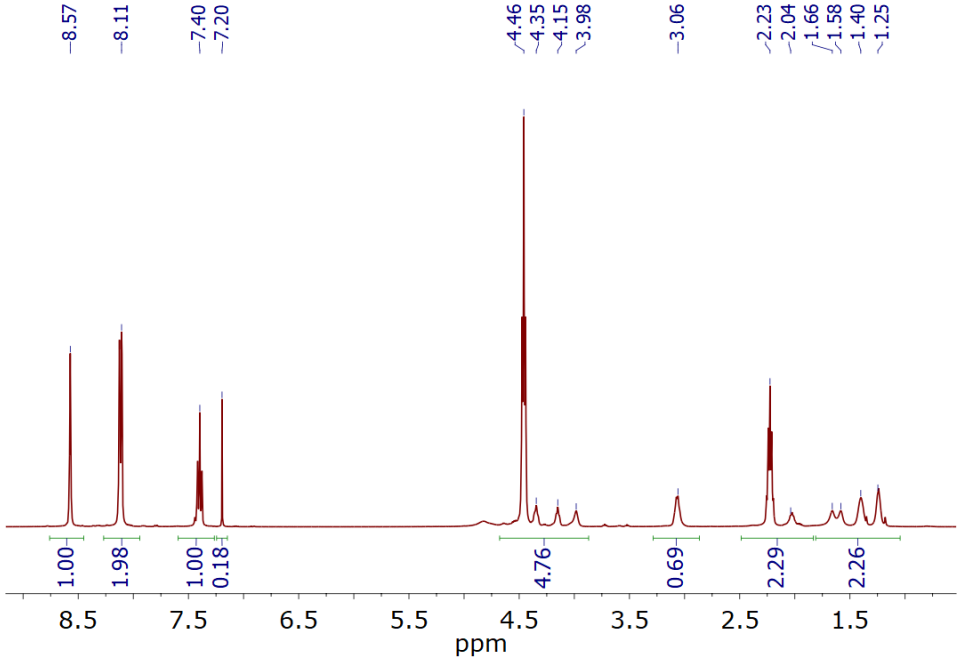

- ^{13}C{^{1}H} NMR

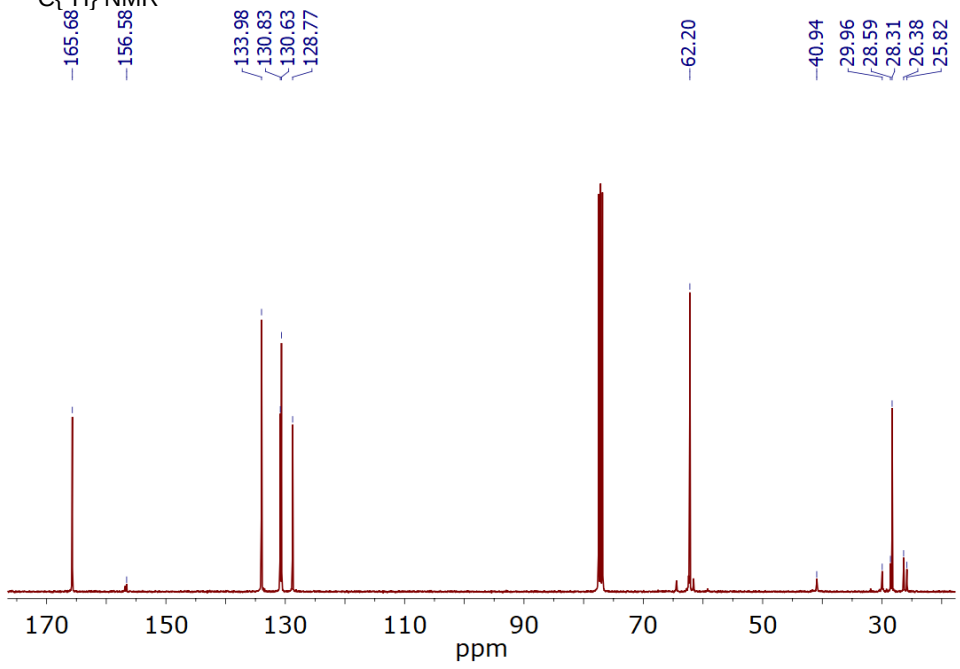

A2.2.18. IPHTAHDO 1000 10 HDI

- ^{1}H NMR

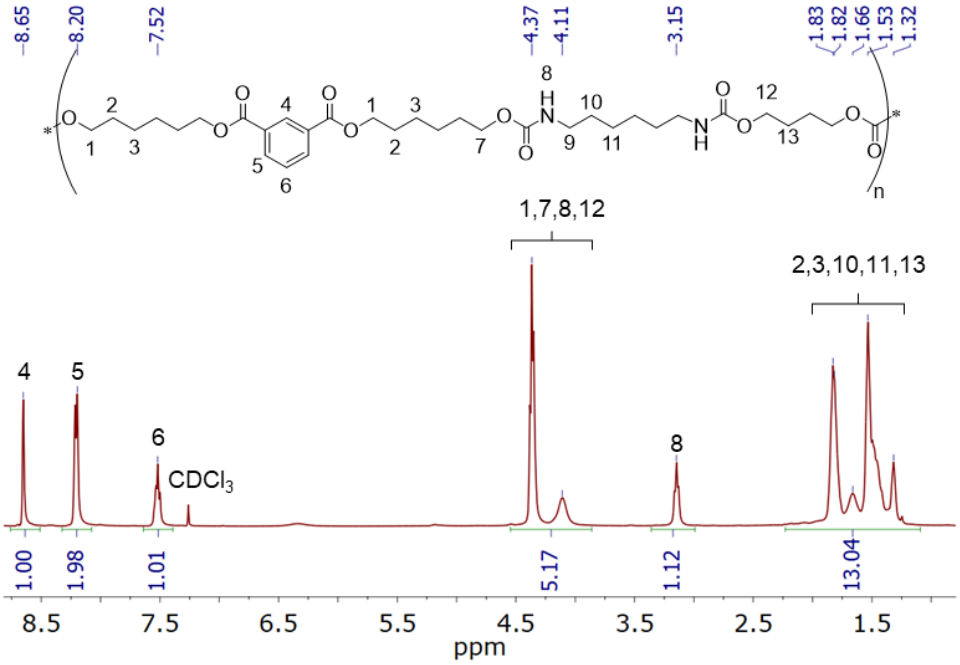

- ^{13}C{^{1}H} NMR

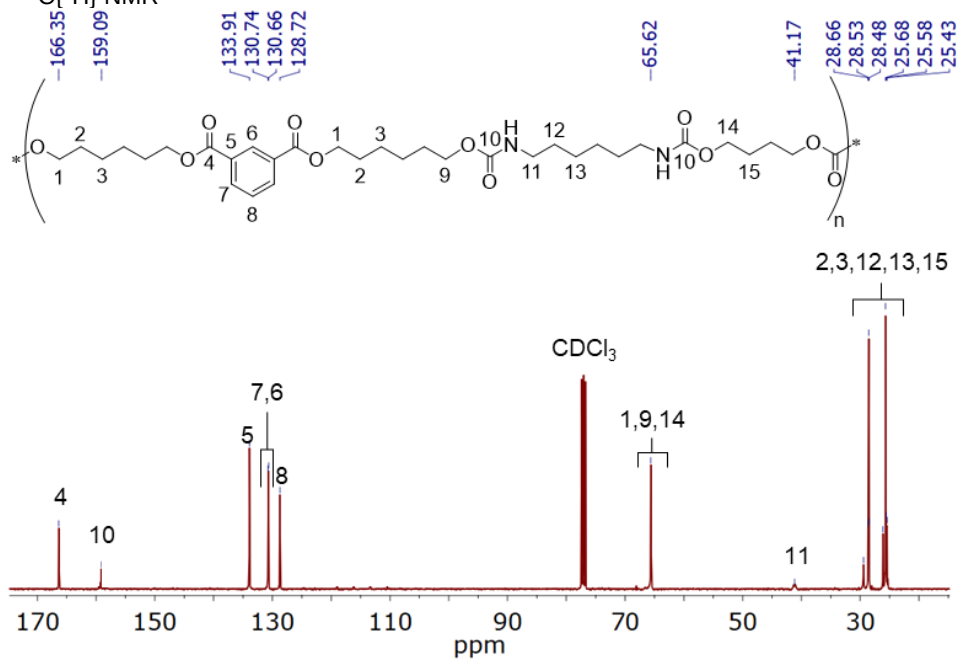

A2.2.19. IPHTAHDO 1000 30 HDI

- ^{1}H NMR

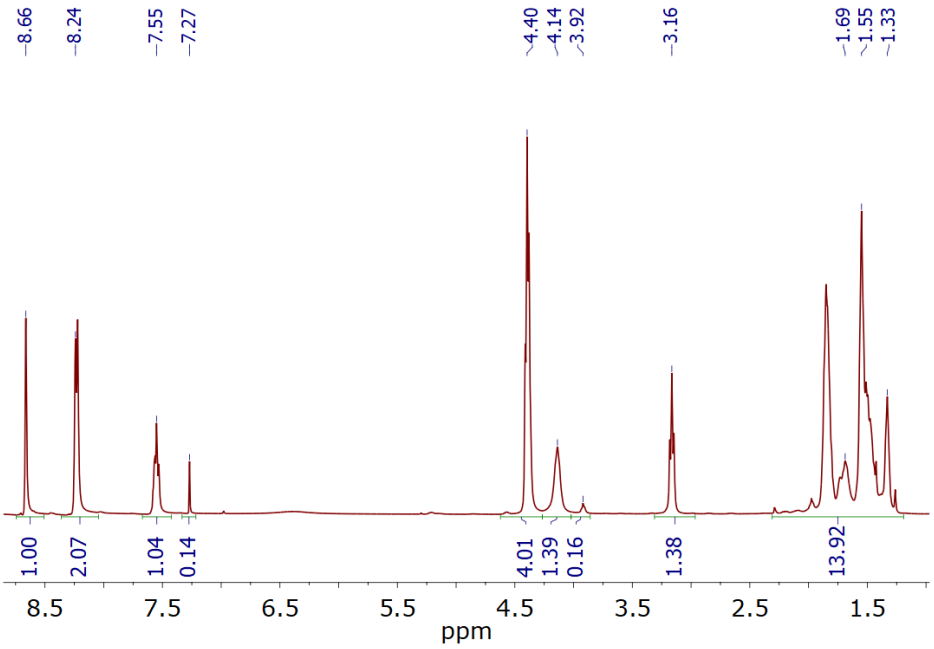

- $^{13}C\{^{1}H\}$ NMR

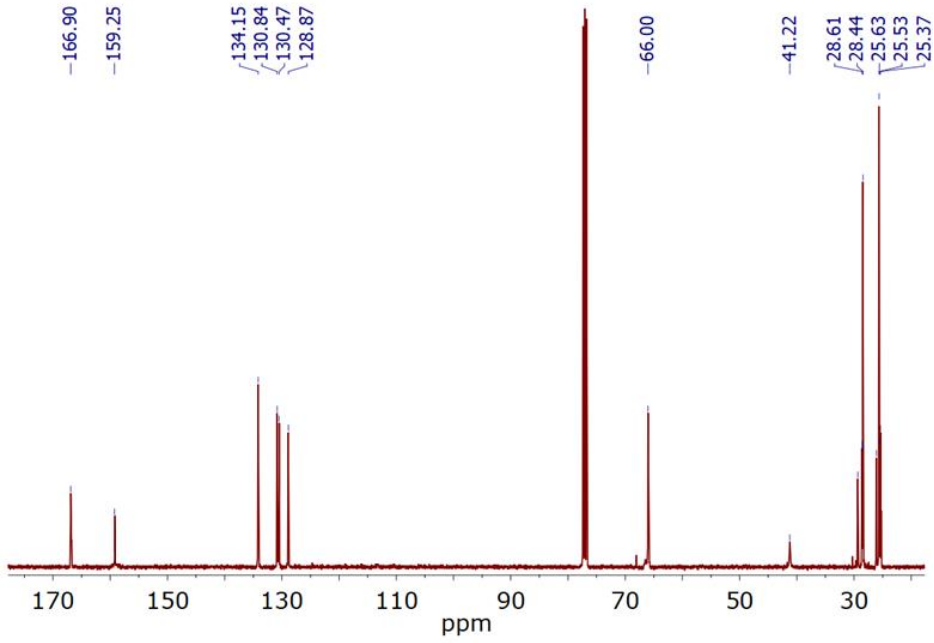

A2.2.20. IPHTAHDO 1000 50 HDI

- ^{1}H NMR

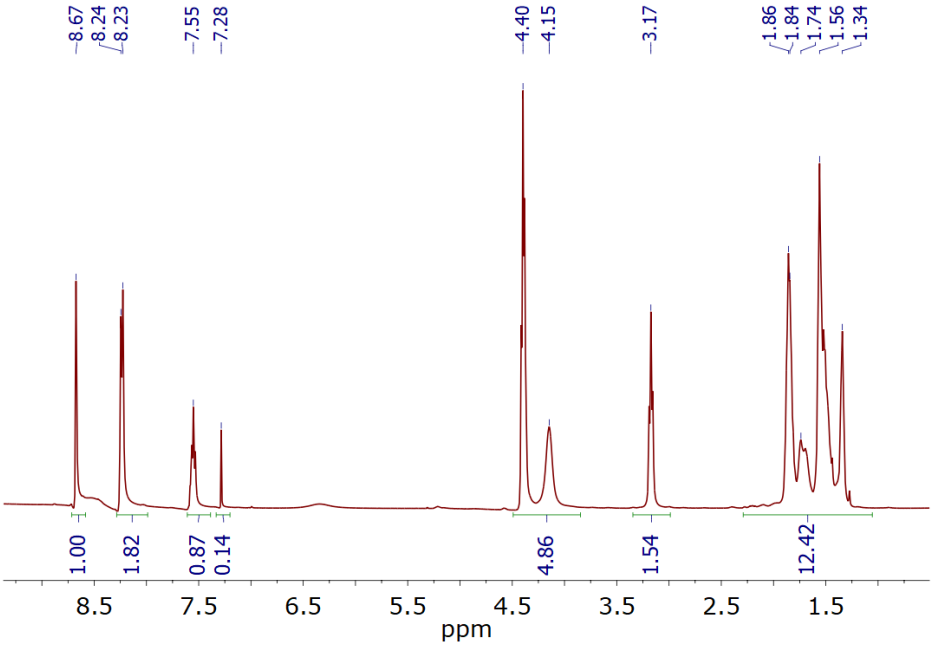

- $^{13}C\{^{1}H\}$ NMR

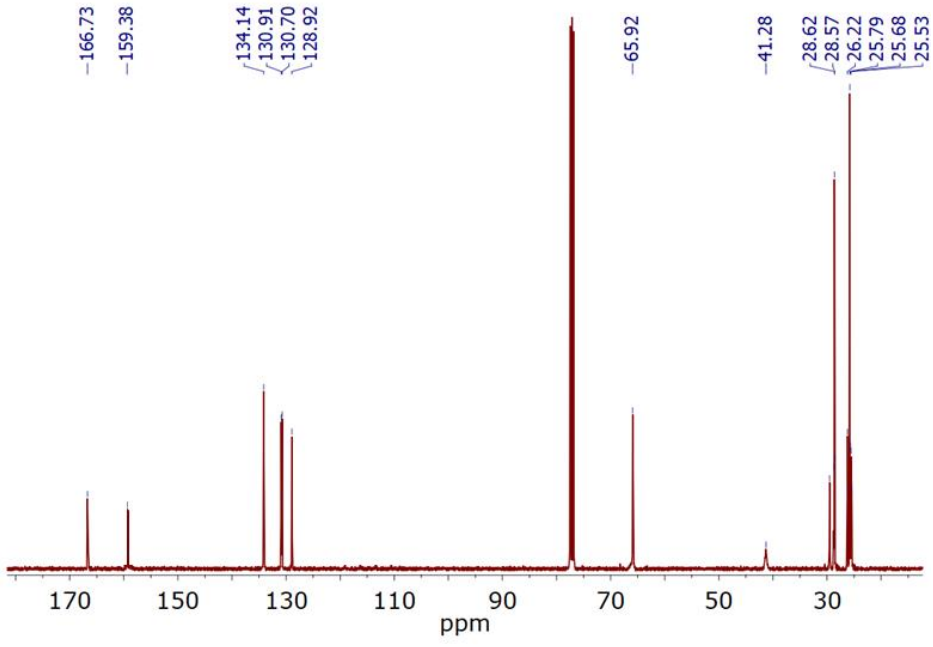

A2.2.21. IPHTAHDO 2000 10 HDI

- ^{1}H NMR

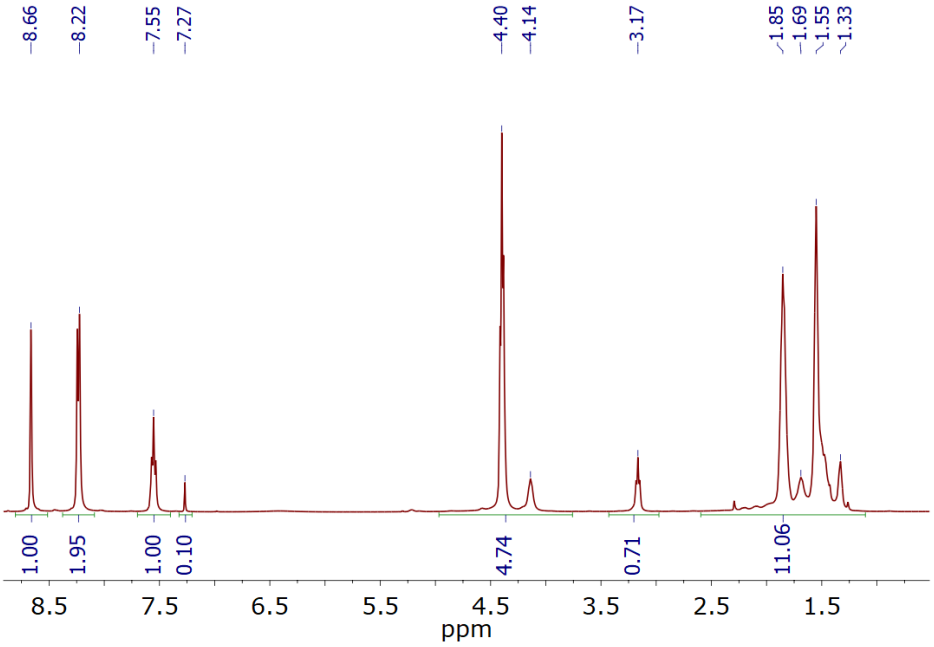

- $^{13}C\{^{1}H\}$ NMR

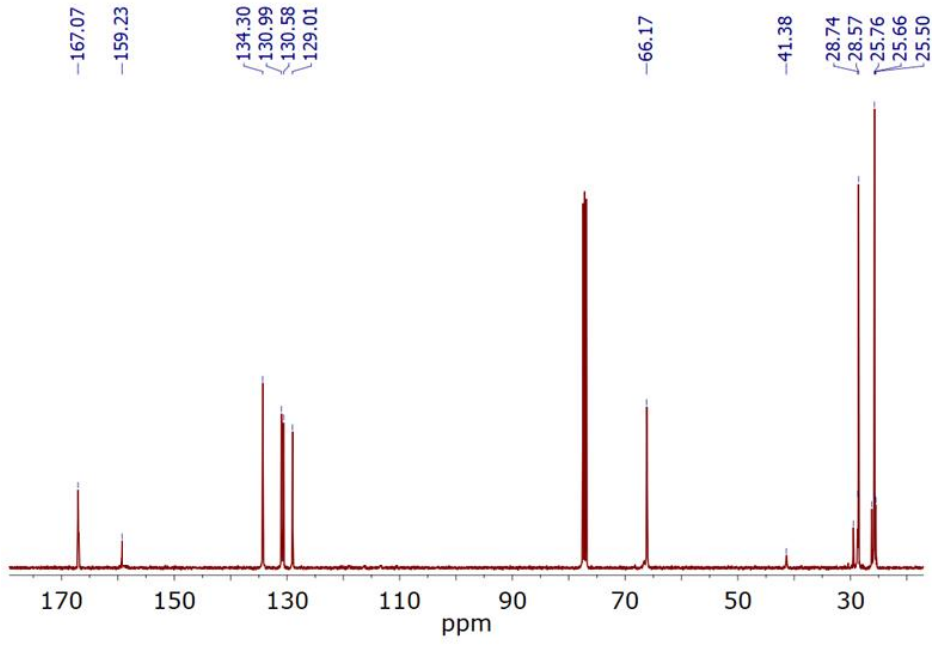

A2.2.22. IPHTAHDO 2000 30 HDI

- ^{1}H NMR

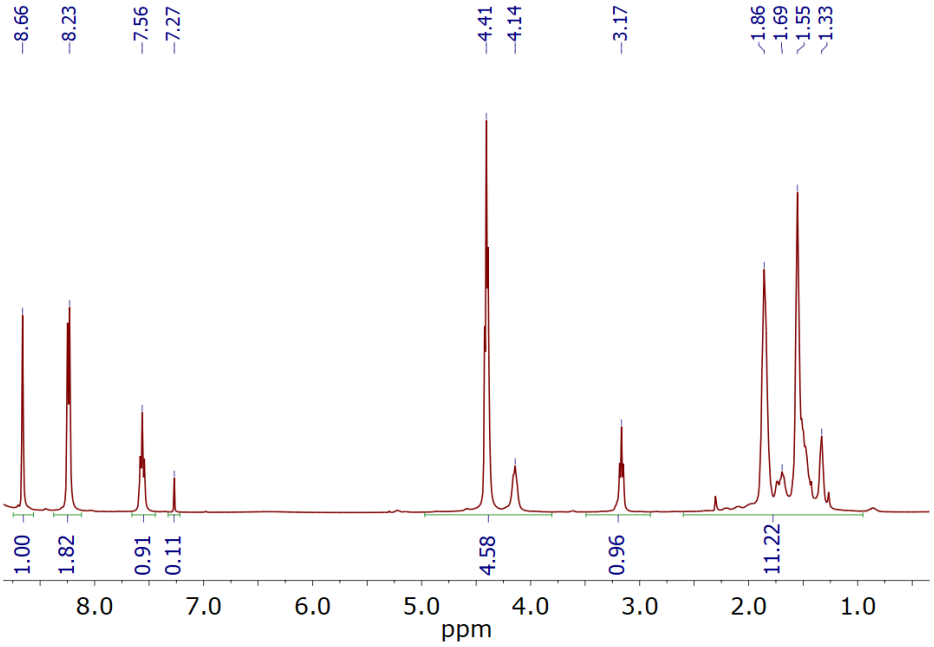

- $^{13}C\{^{1}H\}$ NMR

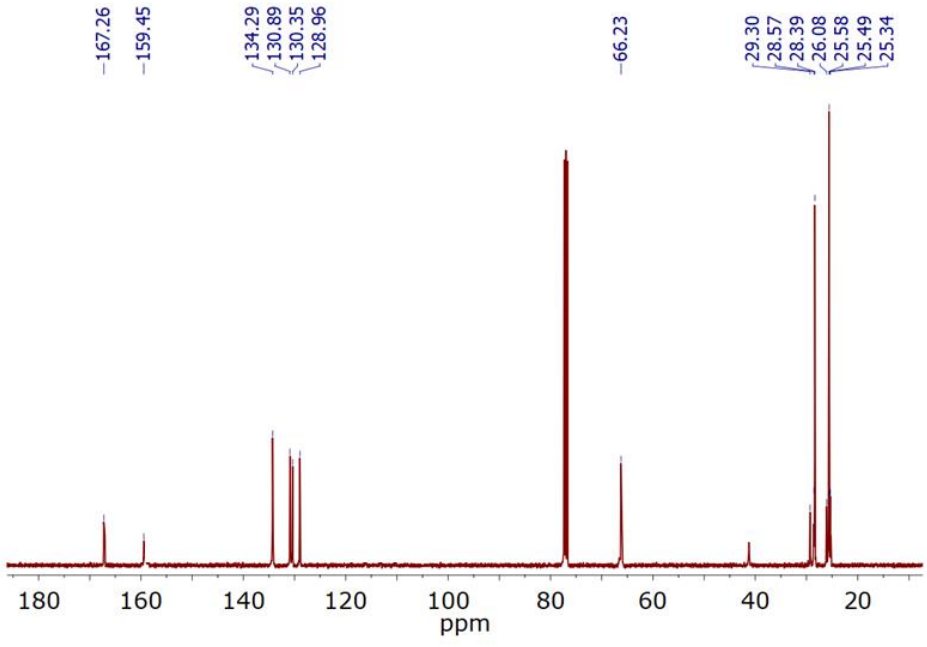

A2.2.23. IPHTAHDO 2000 50 HDI

- ^{1}H NMR

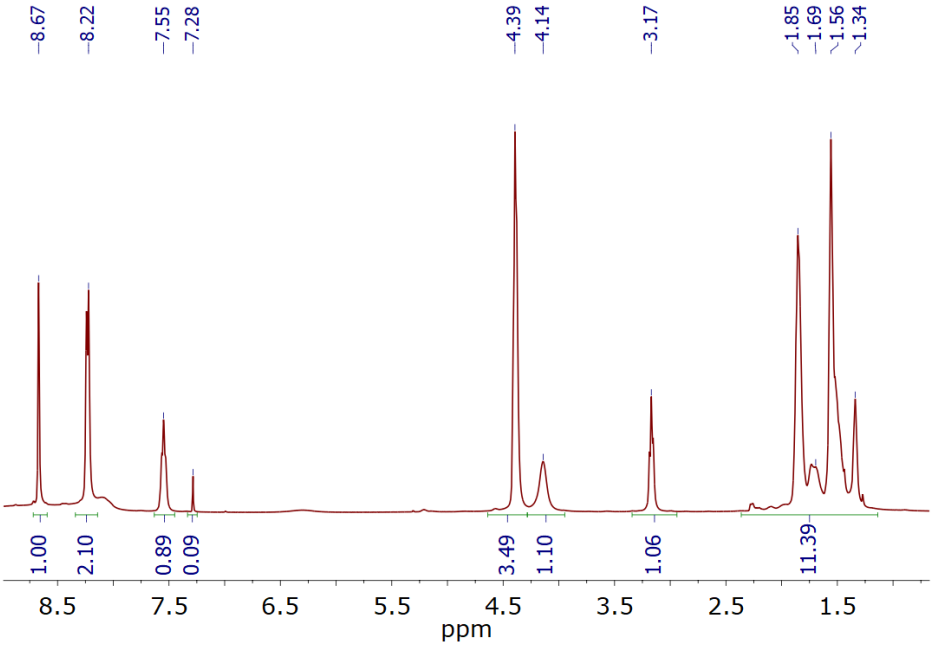

- $^{13}C\{^{1}H\}$ NMR

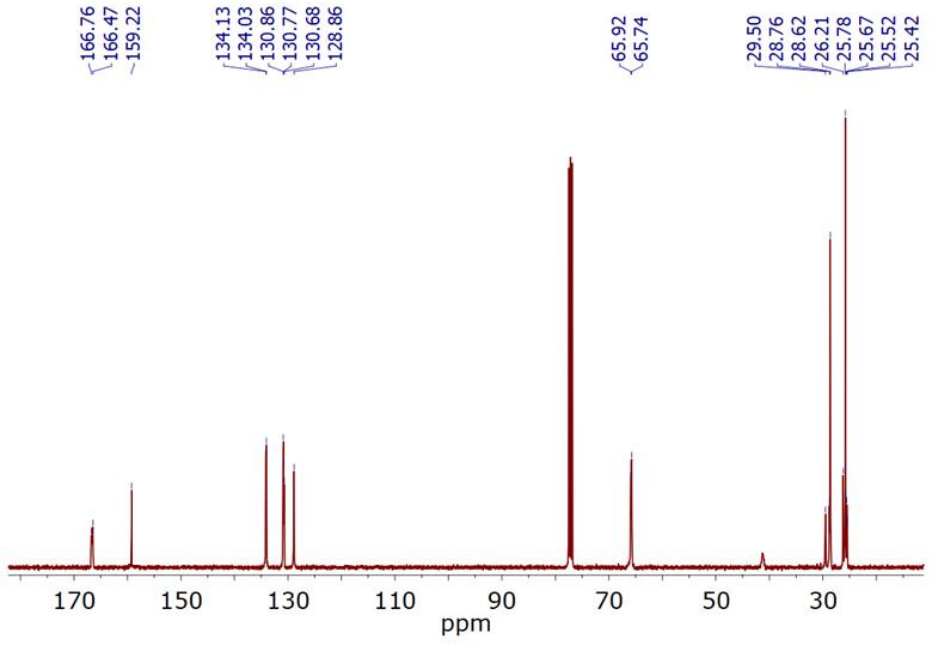

A2.2.24. FDCAHDO 1000 10 MDI

- ^{1}H NMR

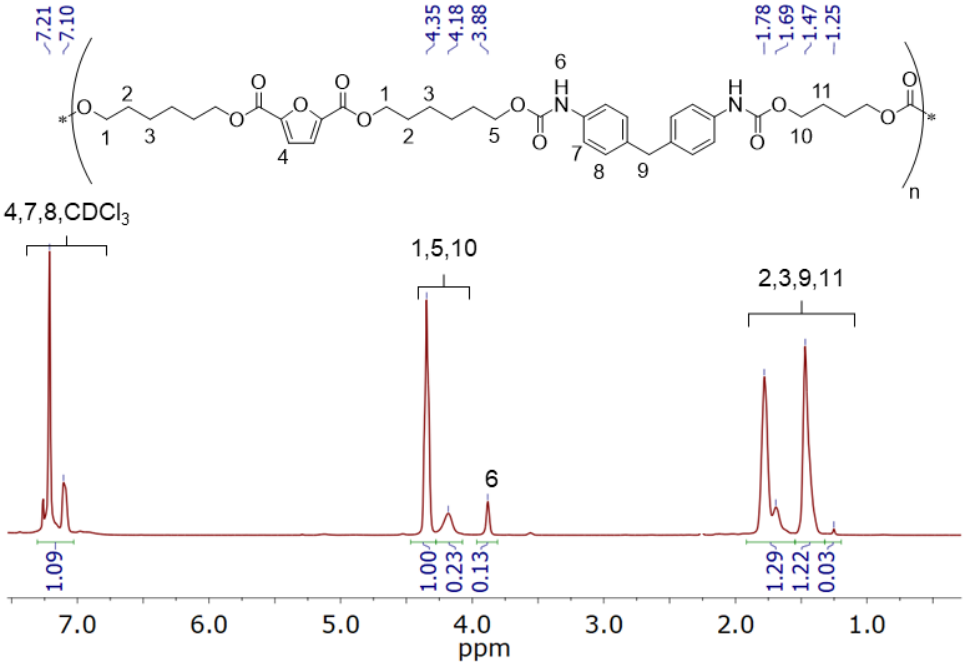

- $^{13}C\{^{1}H\}$ NMR

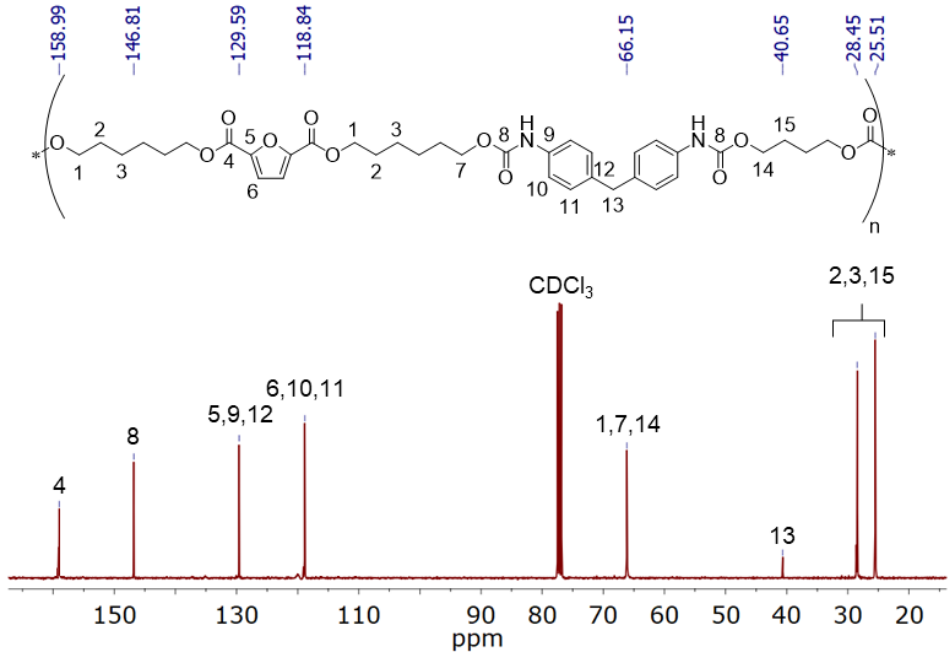

A2.2.25. FDCAHDO 1000 50 MDI

- ^{1}H NMR

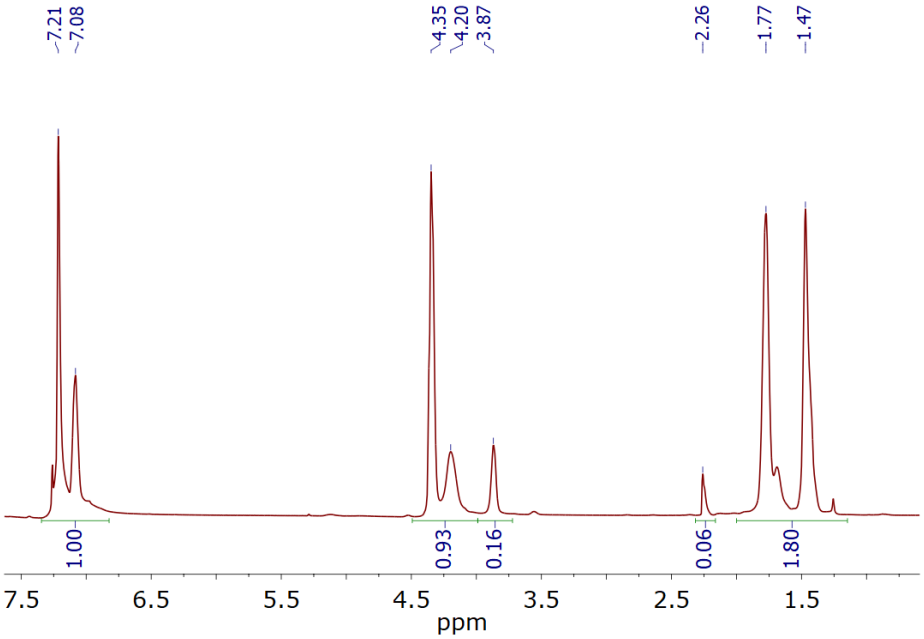

- ^{13}C{^{1}H} NMR

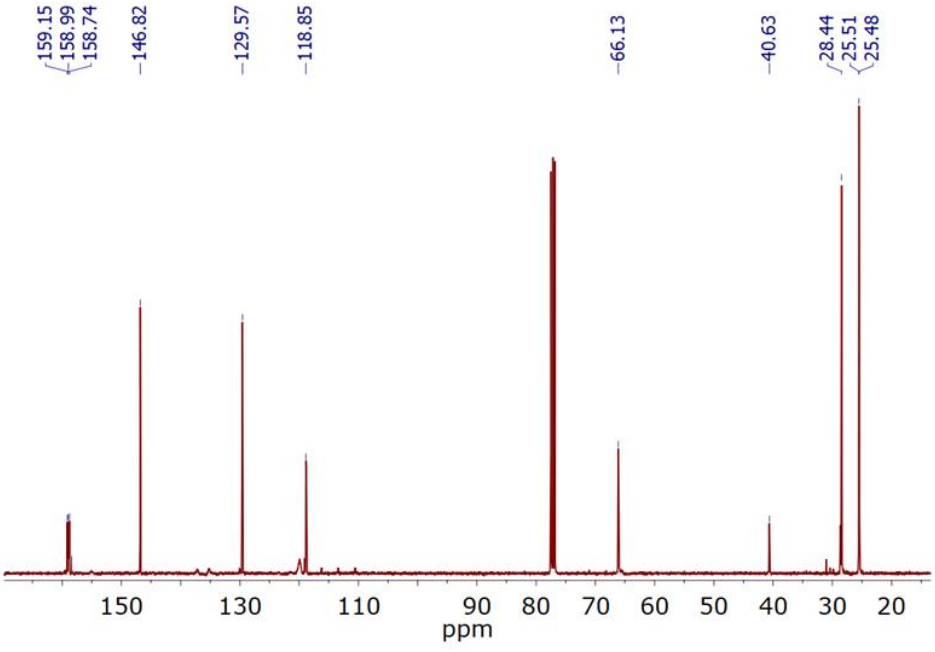

A2.2.26. FDCAHDO 1000 10 HDI

- ^{1}H NMR

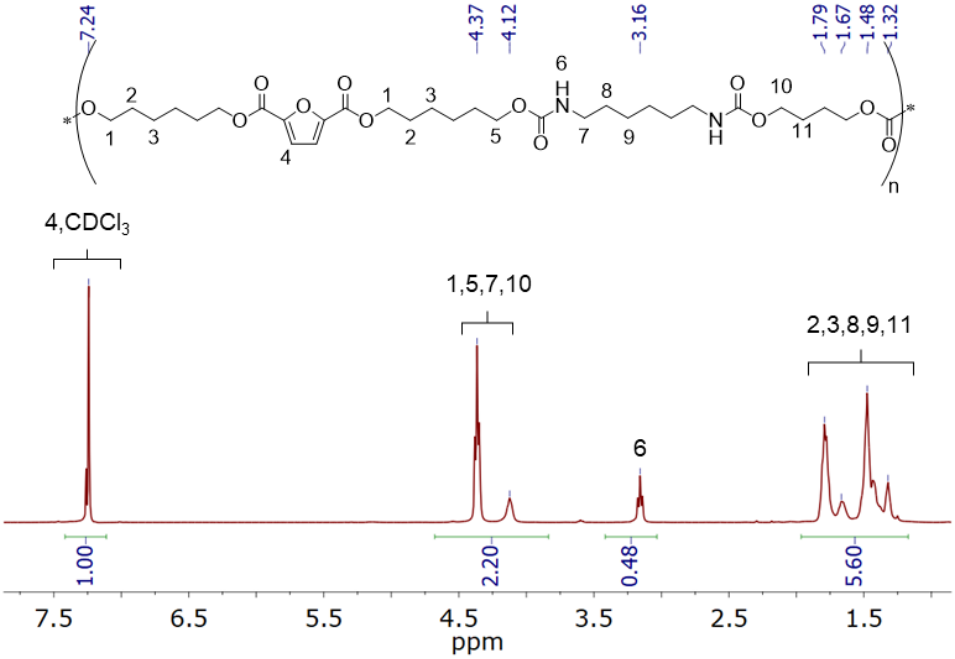

- ^{13}C{^{1}H} NMR

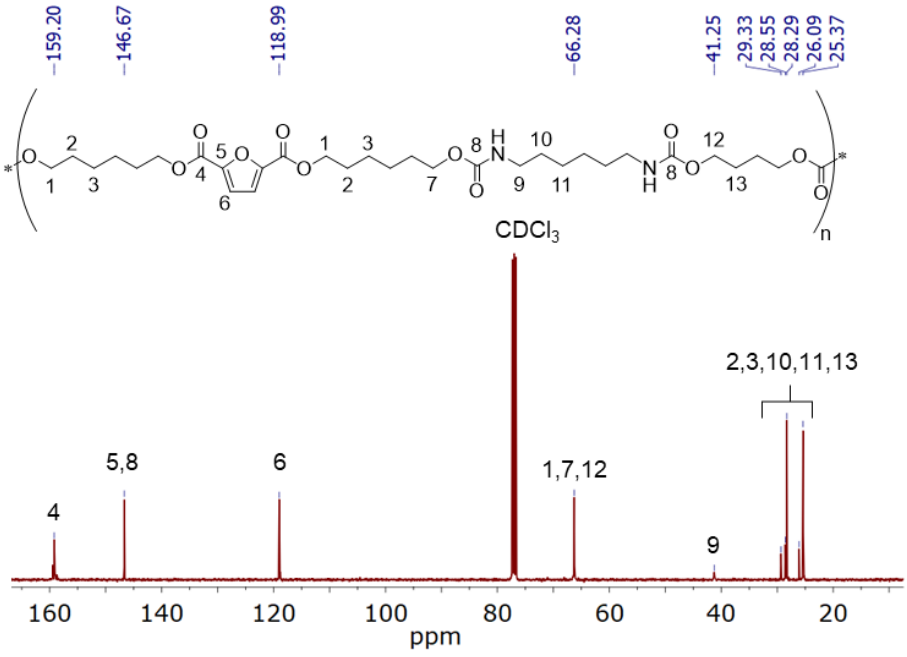

A2.2.27. FDCAHDO 1000 50 HDI

- ^{1}H NMR

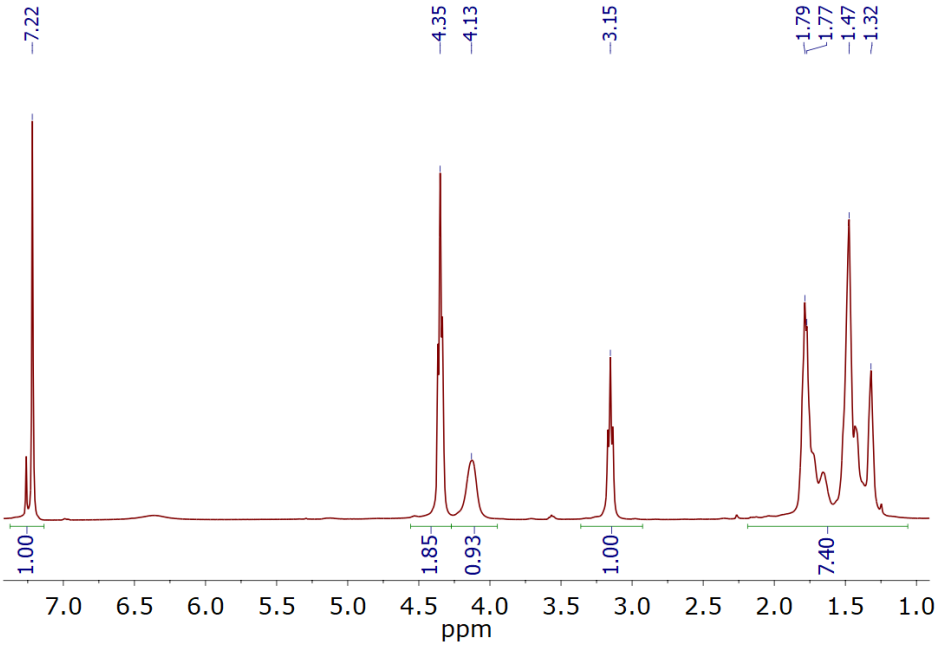

- $^{13}C\{^{1}H\}$ NMR

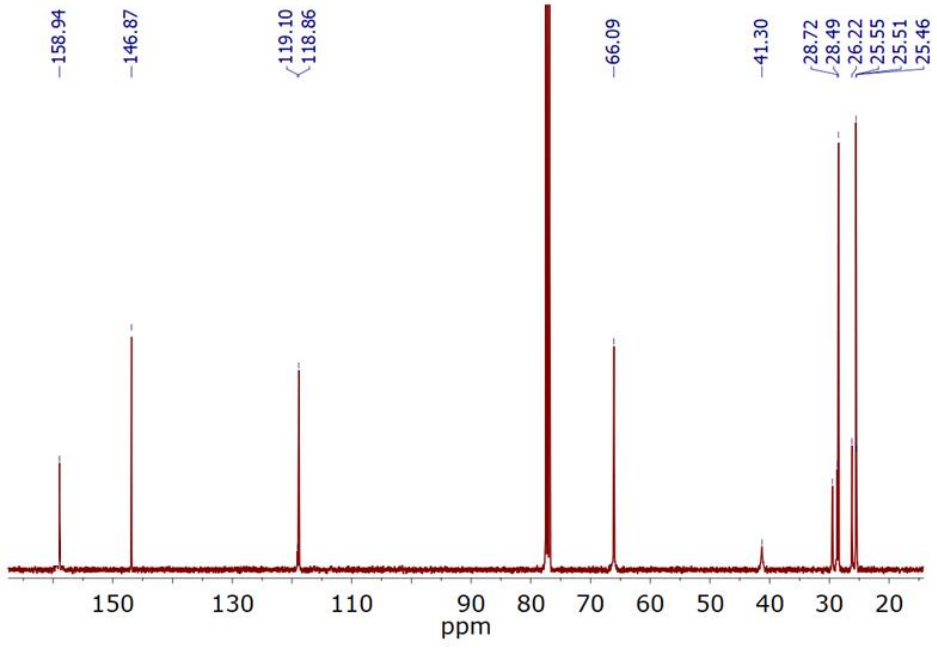

A2.2.28. FDCAHDO 1500 30 HDI

- ^{1}H NMR

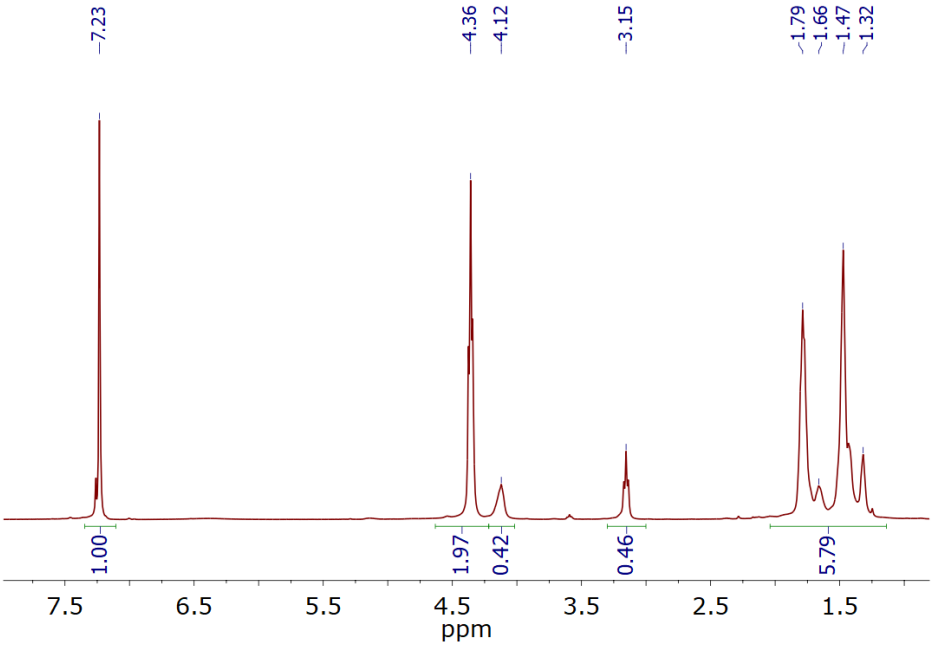

- $^{13}C\{^{1}H\}$ NMR

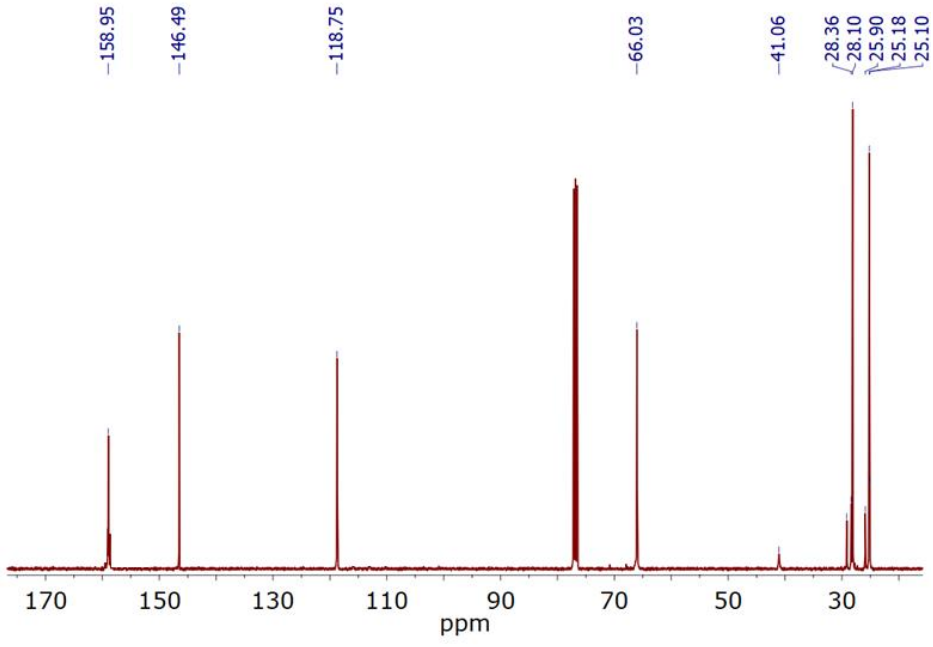

A2.2.29. FDCAHDO 2000 10 HDI

- ^{1}H NMR

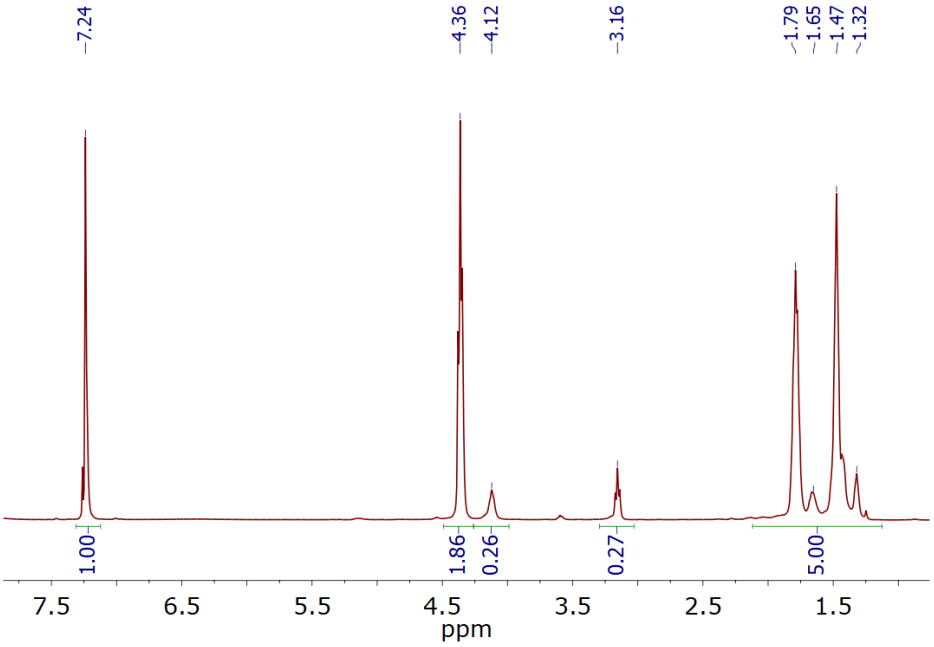

- $^{13}C\{^{1}H\}$ NMR

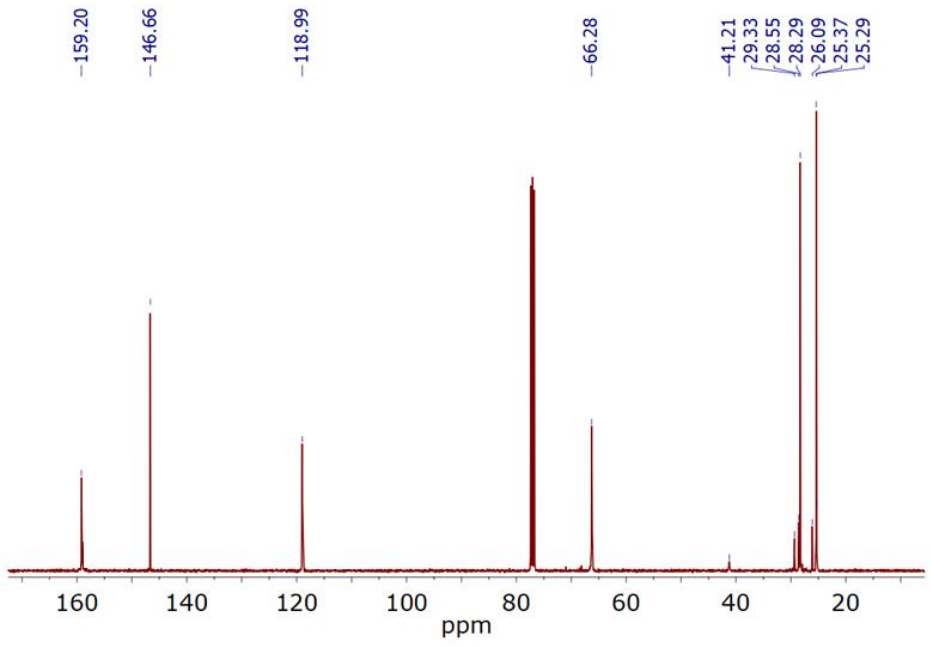

A2.2.30. FDCAHDO 2000 50 HDI

- ^{1}H NMR

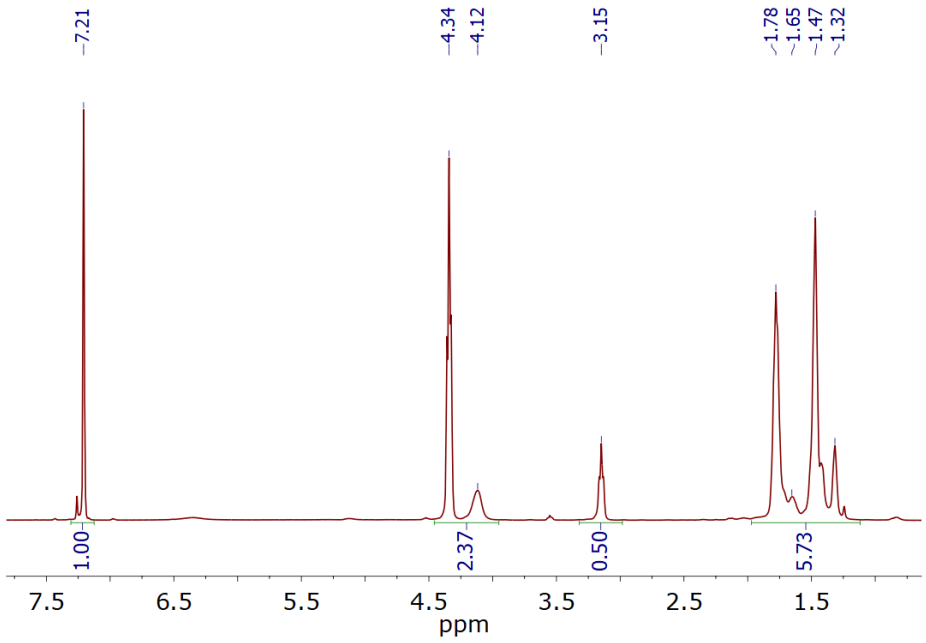

- $^{13}C\{^{1}H\}$ NMR

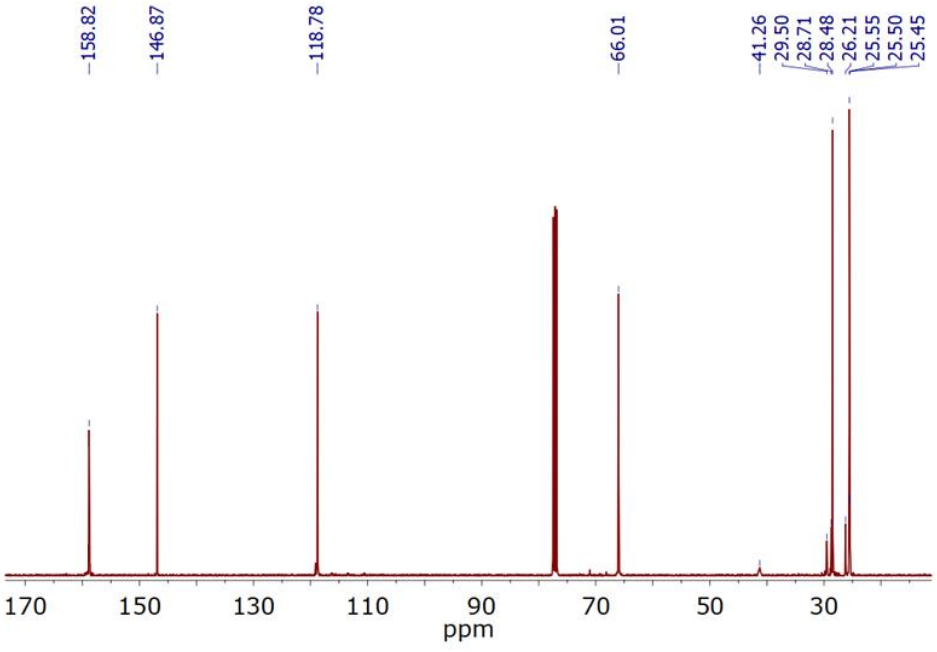

A3 Impurities detection

A3.1. GC-MS

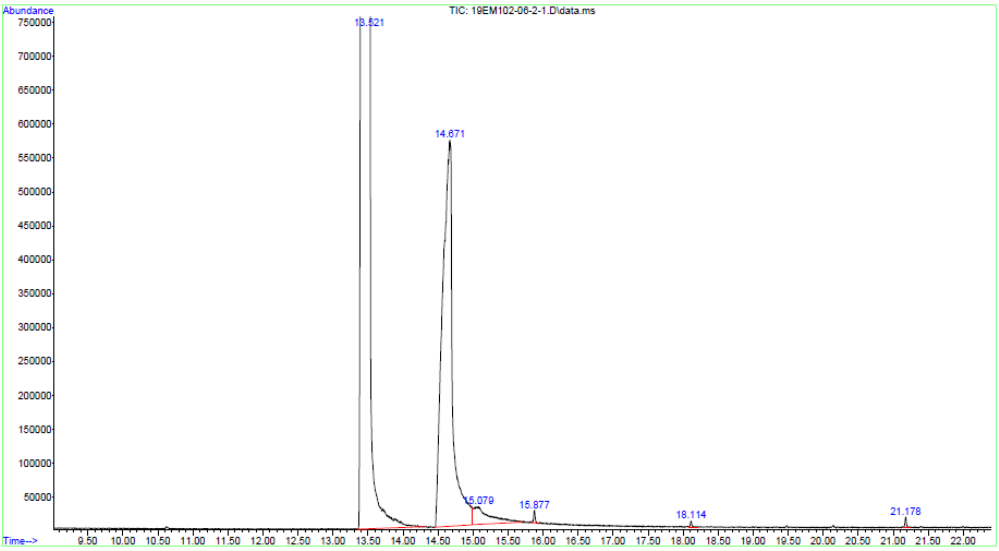

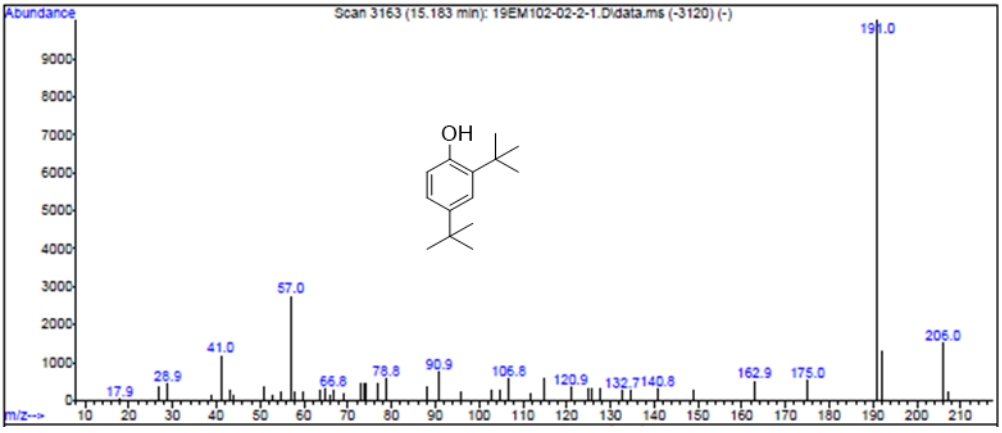

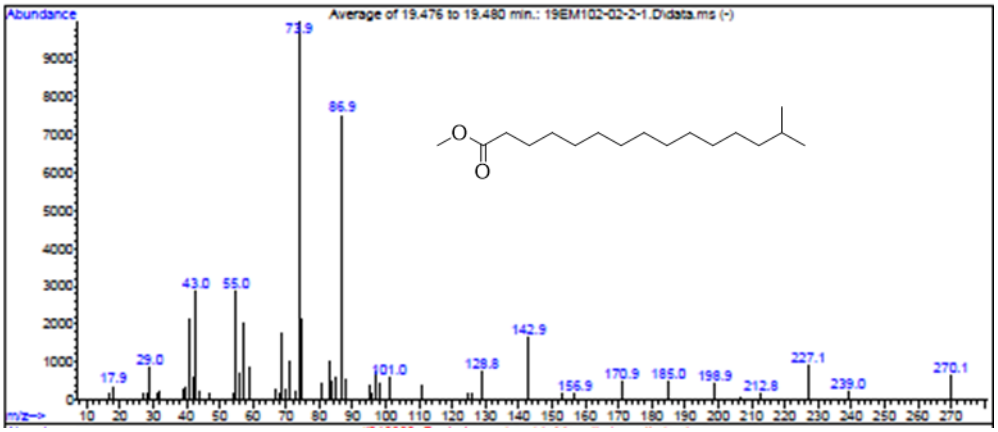
Abundance
Average of 19.476 to 19.480 min.: 19EM102-02-2-1.Didata.ms (-)
73.9
86.9
43.0
55.0
142.9
29.0
17.9
101.0
128.8
156.9
170.9
185.0
198.9
212.8
227.1
239.0
270.1
m/z-->

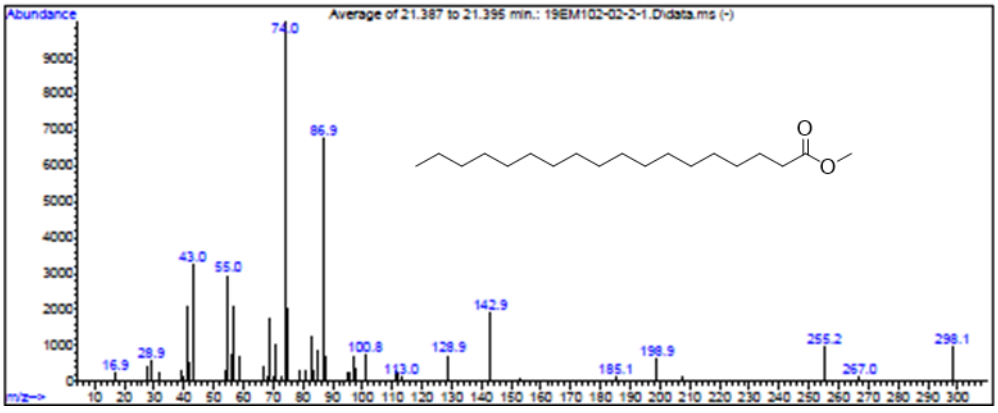
Abundance
Average of 21.387 to 21.395 min.: 19EM102-02-2-1.Didata.ms (-)
74.0
86.9
43.0
55.0
142.9
16.9
28.9
100.8
113.0
128.9
185.1
198.9
255.2
267.0
298.1
m/z-->

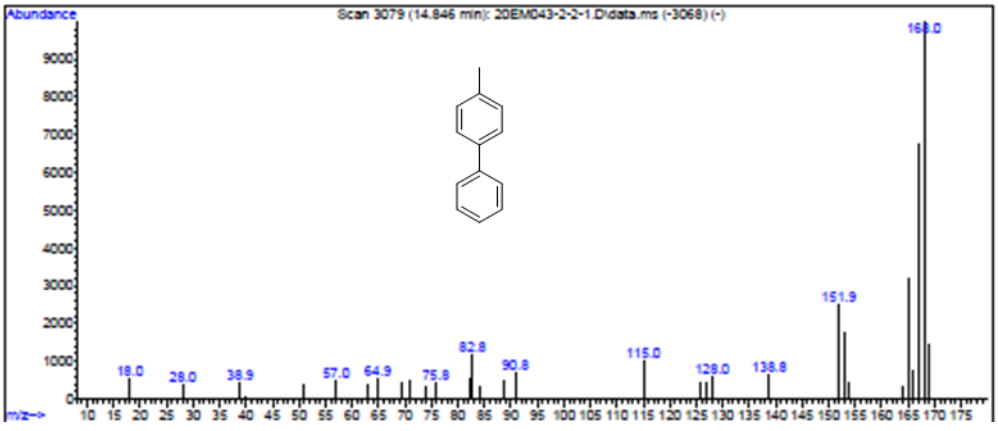
Abundance
Scan 3079 (14.846 min): 20EM043-2-2-1.Didata.ms (-3068) (-)
168.0
151.9
82.8
90.8
115.0
18.0
28.0
38.9
57.0
64.9
75.8
128.0
138.8
m/z-->

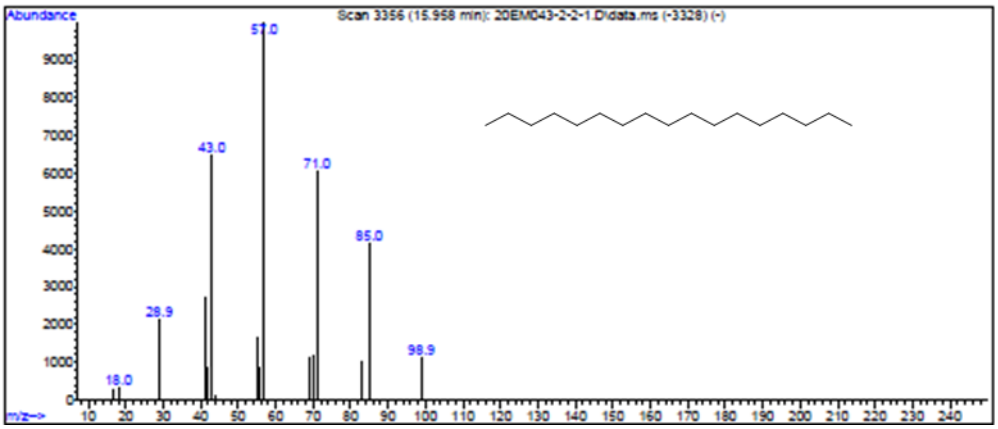
Abundance
Scan 3356 (15.958 min): 20EM043-2-2-1.D\data.ms (-3328) (-)
57.0
43.0
71.0
85.0
28.9
98.9
18.0
m/z-->

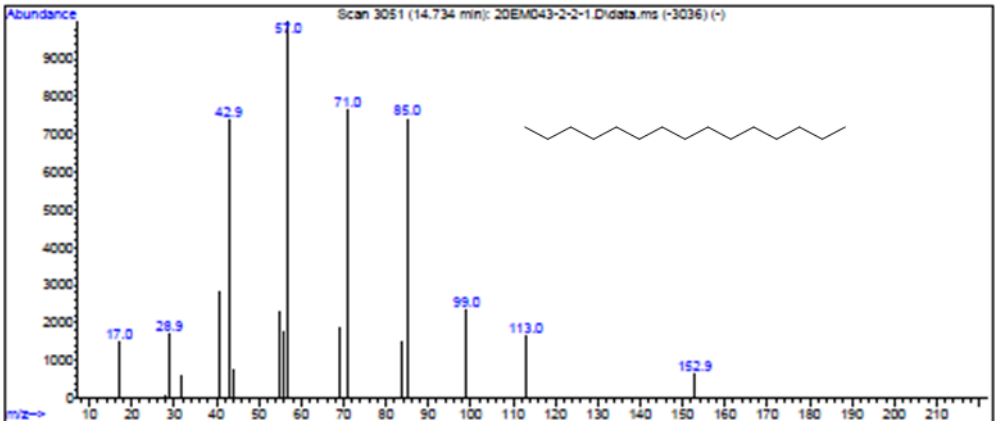
Abundance
Scan 3051 (14.734 min): 20EM043-2-2-1.D\data.ms (-3036) (-)
57.0
42.9
71.0
85.0
99.0
113.0
28.9
17.0
152.9
m/z-->

A3.2. NMR spectroscopy

- ^{1}H NMR

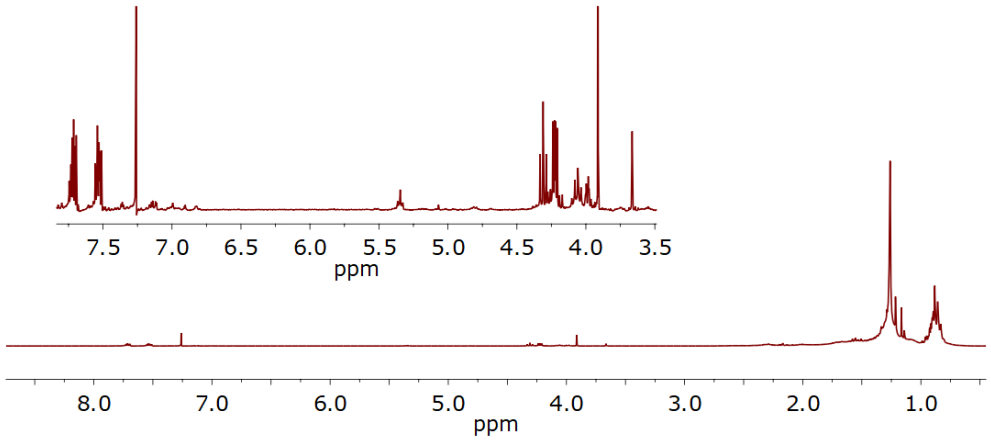

- ^{13}C{^{1}H} NMR

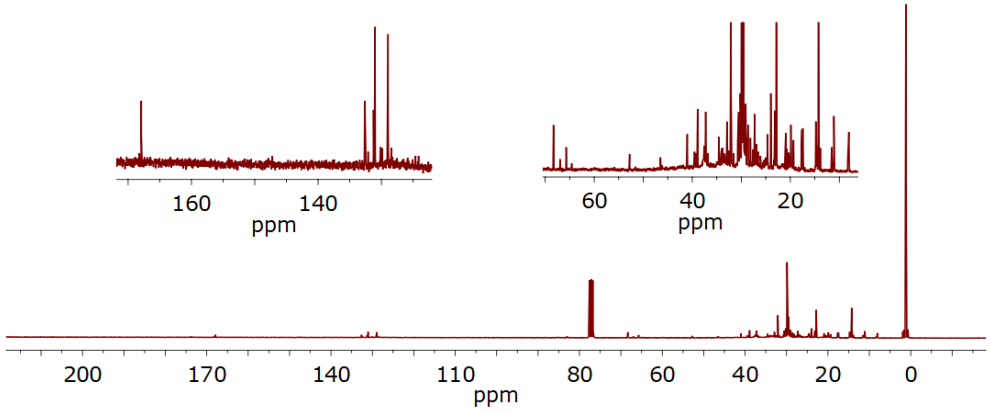

- COSY

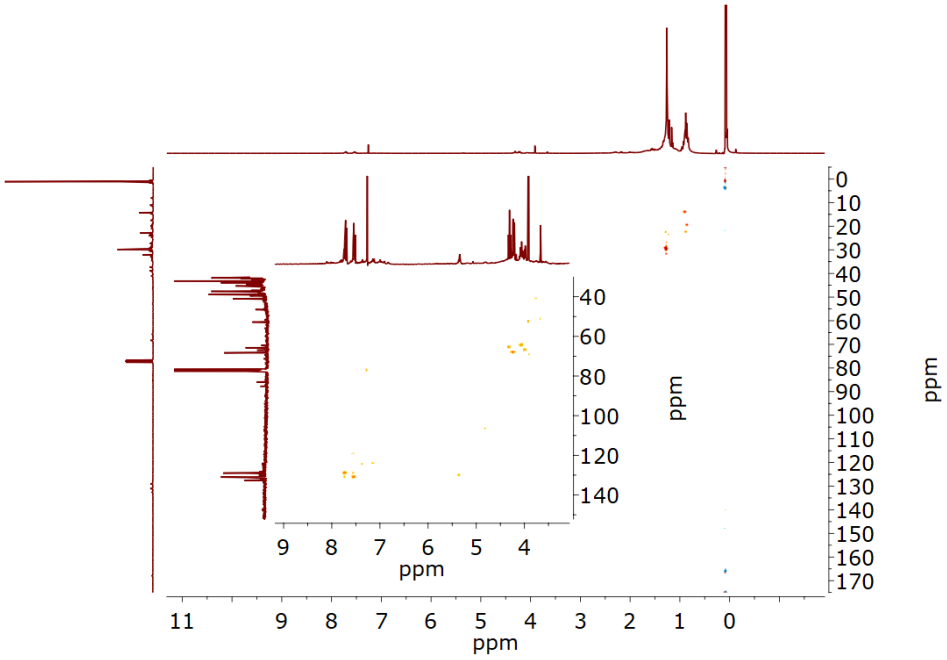
0
10
20
30
40
50
60
70
80
90
100
110
120
130
140
150
160
170
ppm
40
60
80
100
120
140
ppm
9 8 7 6 5 4
ppm
11 9 8 7 6 5 4 3 2 1 0
ppm

- HSQC

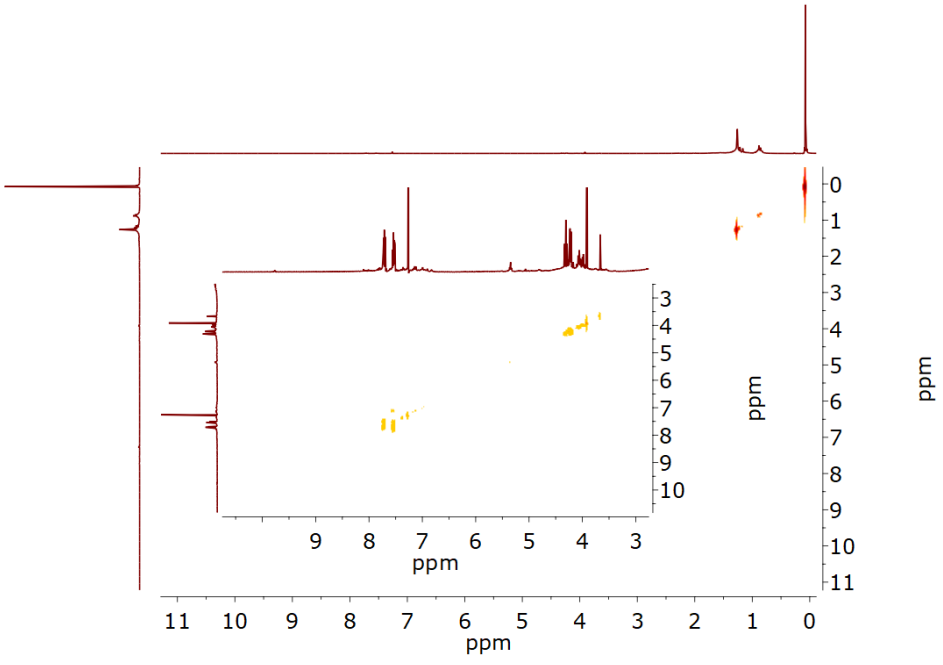
0
1
2
3
4
5
6
7
8
9
10
11
ppm
3
4
5
6
7
8
9
10
ppm
9 8 7 6 5 4 3
ppm
11 10 9 8 7 6 5 4 3 2 1 0
ppm

A4 Gel permeation chromatography

A4.1. IPHTAPDO 1000 10 MDI

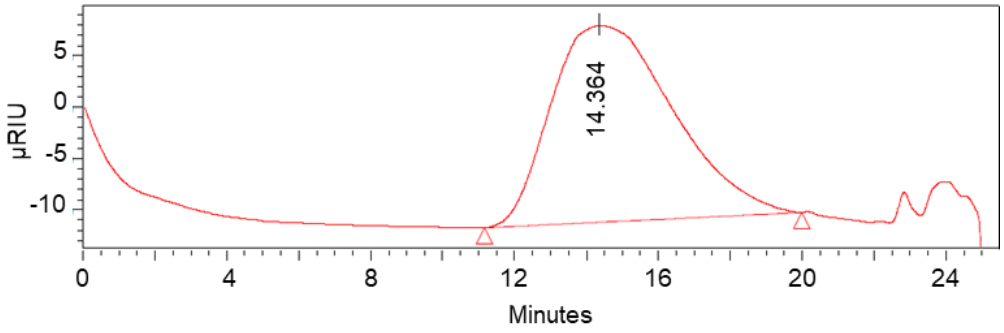

Retention time (min)	Area (µVxsec)	M_n	M_w	M_z	Polydispersity
14.364	4518320	30878	60809	97105	1.97

A4.2. IPHTAPDO 1000 30 MDI

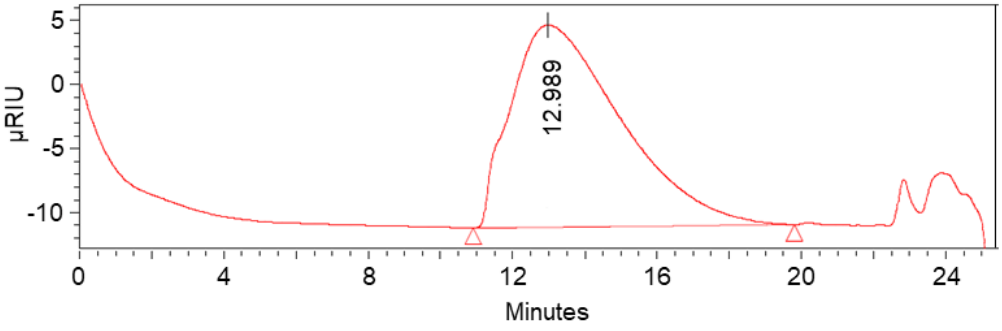

Retention time (min)	Area (µVxsec)	M_n	M_w	M_z	Polydispersity
12.989	3353546	55650	114266	178322	2.05

A4.3. IPHTAPDO 1000 50 MDI

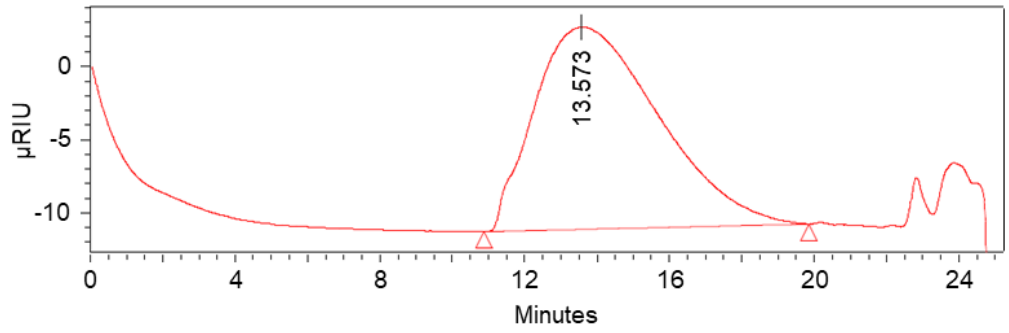

Retention time (min)	Area (µVxsec)	M_n	M_w	M_z	Polydispersity
13.573	3300644	42871	91908	153680	2.14

A4.4. IPHTAPDO 2000 10 MDI

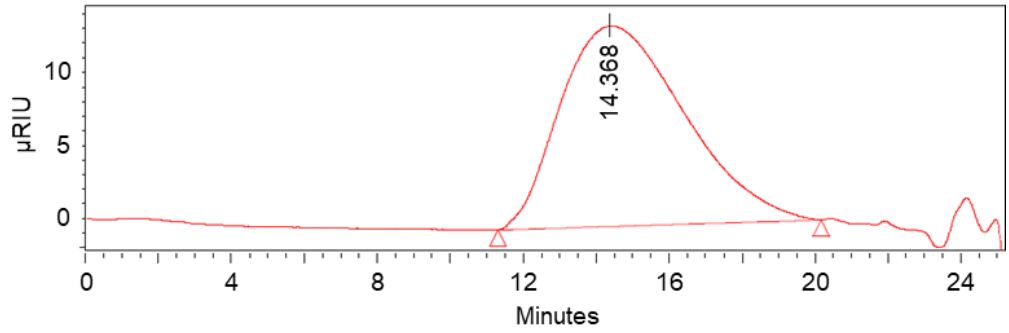

Retention time (min)	Area (µVxsec)	M_n	M_w	M_z	Polydispersity
14.368	3258205	29707	61182	99832	2.06

A4.5. IPHTAPDO 2000 30 MDI

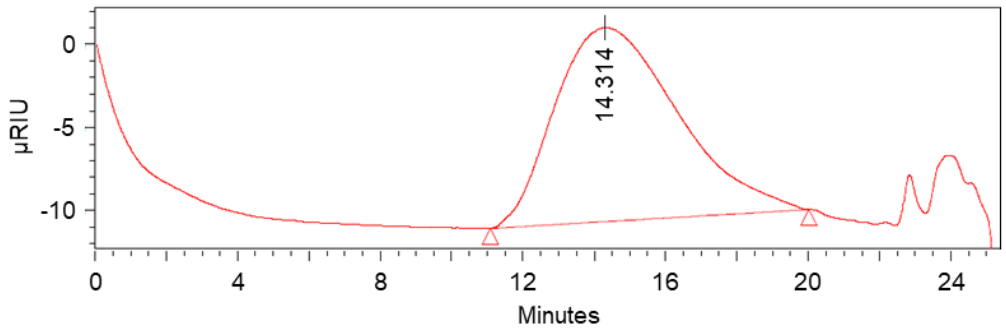

Retention time (min)	Area (µVxsec)	M_n	M_w	M_z	Polydispersity
14.314	2798153	30333	65632	110204	2.16

A4.6. IPHTAPDO 2000 50 MDI

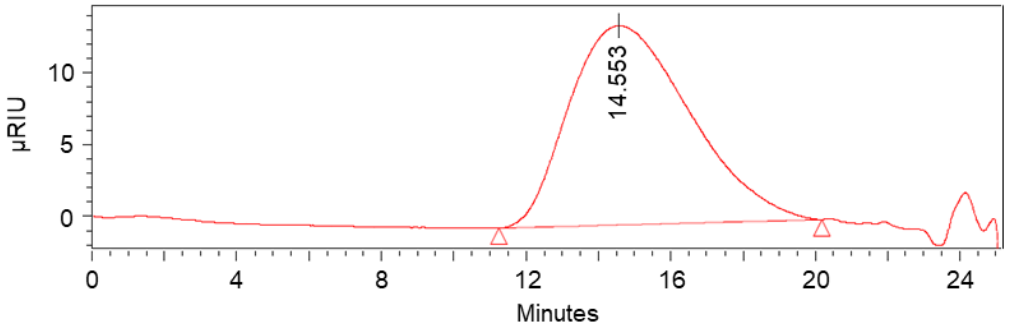

Retention time (min)	Area (µVxsec)	M_n	M_w	M_z	Polydispersity
14.553	3226244	28301	56183	90172	1.99

A4.7. IPHTAHDO 1000 10 MDI

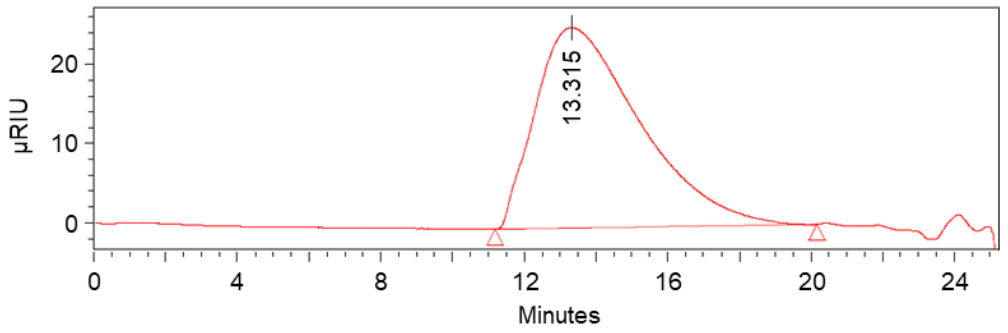

Retention time (min)	Area (µVxsec)	M_n	M_w	M_z	Polydispersity
13.315	5125648	48712	93714	140335	1.92

A4.8. IPHTAHDO 1000 30 MDI

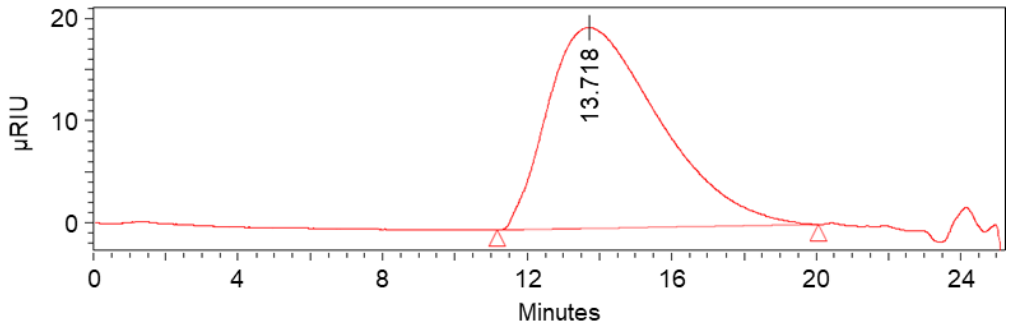

Retention time (min)	Area (µVxsec)	M_n	M_w	M_z	Polydispersity
13.718	4237943	40401	79325	121711	1.96

A4.9. IPHTAHDO 1000 50 MDI

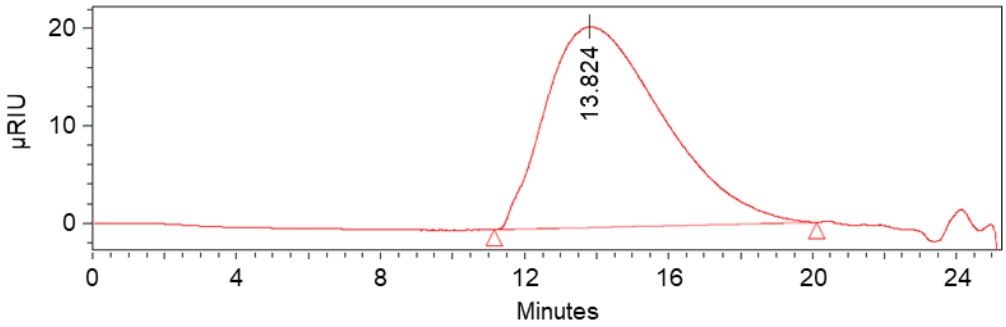

Retention time (min)	Area (µVxsec)	M_n	M_w	M_z	Polydispersity
13.824	4699286	37680	77291	123100	2.05

A4.10. IPHTAHDO 2000 10 MDI

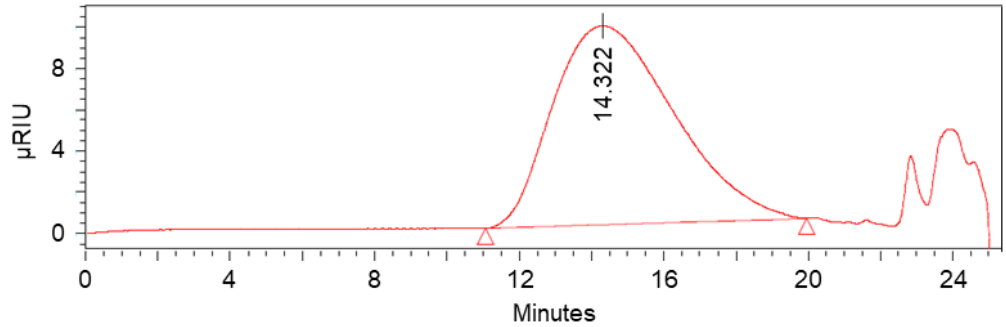

Retention time (min)	Area (µVxsec)	M_n	M_w	M_z	Polydispersity
14.322	2247498	32304	64755	105239	2.00

A4.11. IPHTAHDO 2000 30 MDI

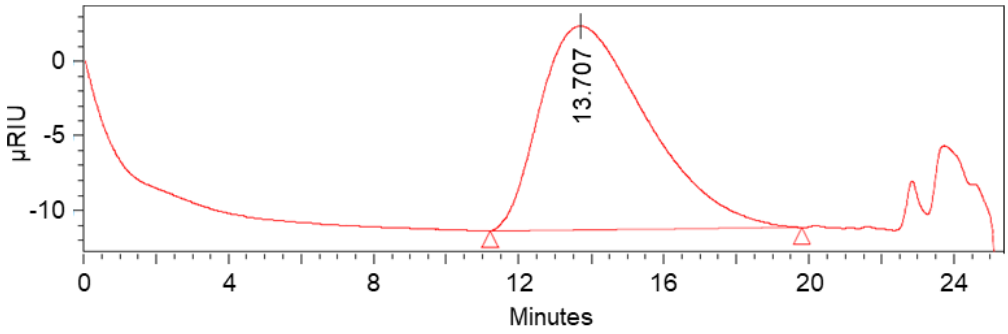

Retention time (min)	Area (µVxsec)	M_n	M_w	M_z	Polydispersity
13.707	2812388	43252	80158	120240	1.85

A4.12. IPHTAHDO 2000 50 MDI

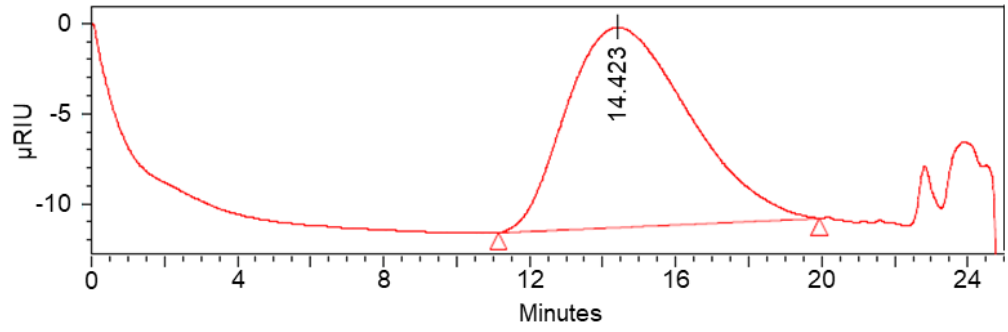

Retention time (min)	Area (µVxsec)	M_n	M_w	M_z	Polydispersity
14.423	2593367	31056	62843	99583	2.02

A4.13. IPHTAPDO 1000 10 HDI

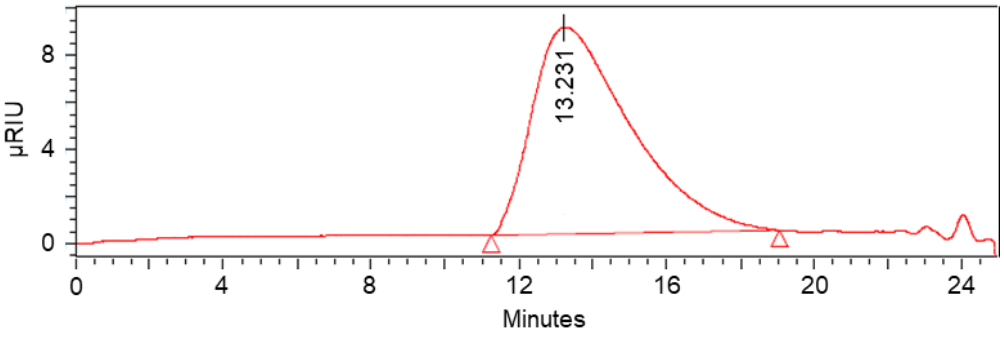

Retention time (min)	Area (µVxsec)	M_n	M_w	M_z	Polydispersity
13.231	1624741	54687	94858	135654	1.73

A4.14. IPHTAPDO 1000 30 HDI

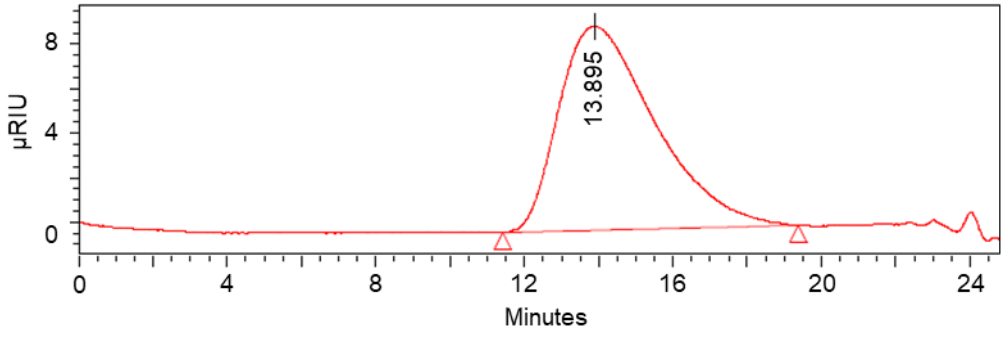

Retention time (min)	Area (µVxsec)	M_n	M_w	M_z	Polydispersity
13.895	1650463	43533	70560	97466	1.62

A4.15. IPHTAHDO 1000 10 HDI

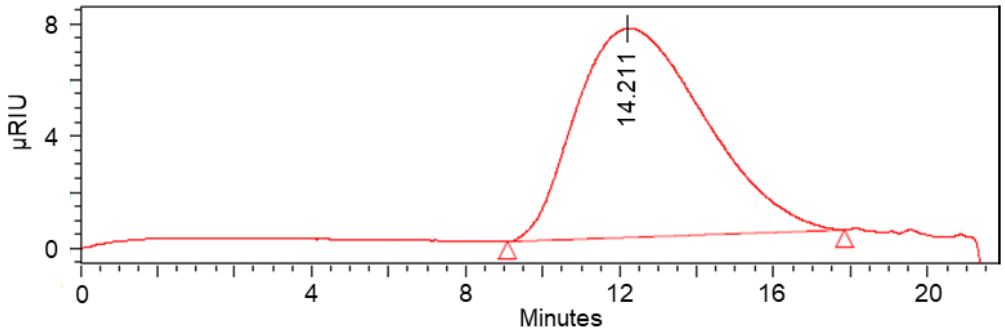

Retention time (min)	Area (μVxsec)	M_n	M_w	M_z	Polydispersity
14.211	1732378	34147	67022	108411	1.96

A4.16. IPHTAHDO 1000 30 HDI

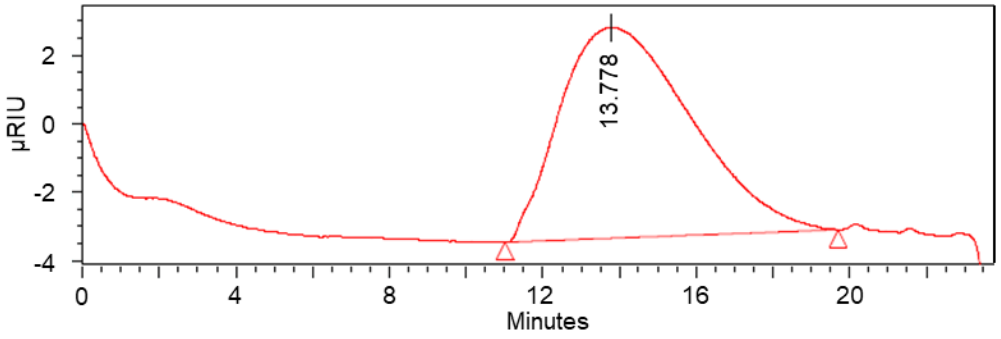

Retention time (min)	Area (μVxsec)	M_n	M_w	M_z	Polydispersity
13.778	1460036	40527	83186	137056	2.05

A4.17. IPHTAHDO 1000 50 HDI

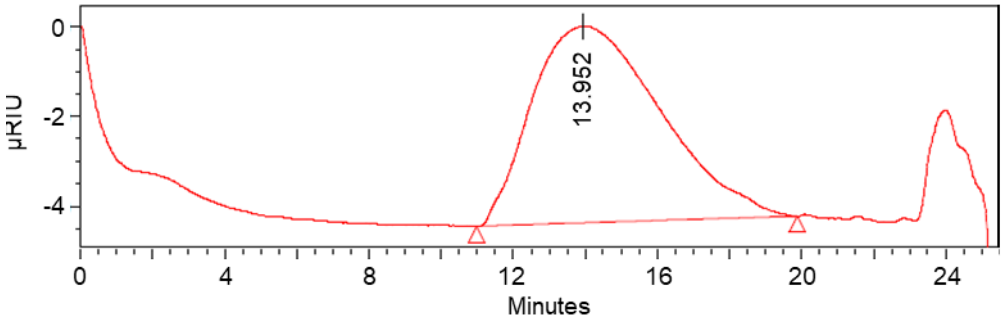

Retention time (min)	Area (µVxsec)	M_n	M_w	M_z	Polydispersity
13.952	1087580	36043	78387	187337	2.17

A4.18. IPHTAHDO 2000 10 HDI

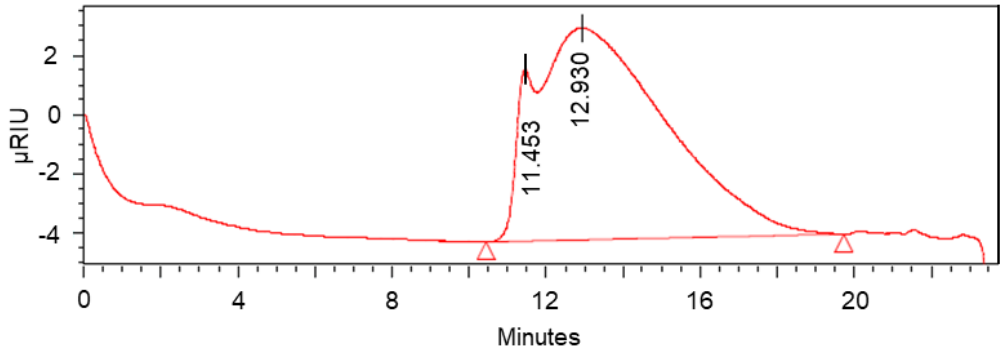

Retention time (min)	Area (µVxsec)	M_n	M_w	M_z	Polydispersity
12.930	1734695	56170	130572	220596	2.32

A4.19. IPHTAHDO 2000 30 HDI

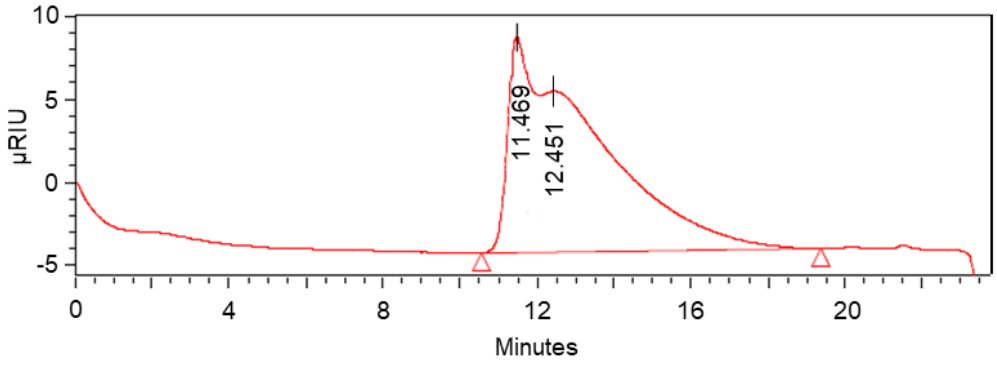

Retention time (min)	Area (µVxsec)	M_n	M_w	M_z	Polydispersity
12.451	2081148	80545	173467	259090	2.15

A4.20. IPHTAHDO 2000 50 HDI

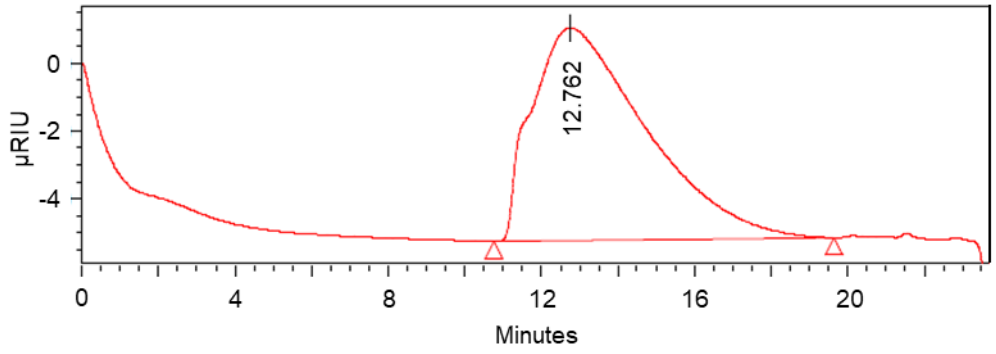

Retention time (min)	Area (µVxsec)	M_n	M_w	M_z	Polydispersity
12.762	1299262	61849	128448	198720	2.08

A4.21. FDCAPDO 1000 10 MDI

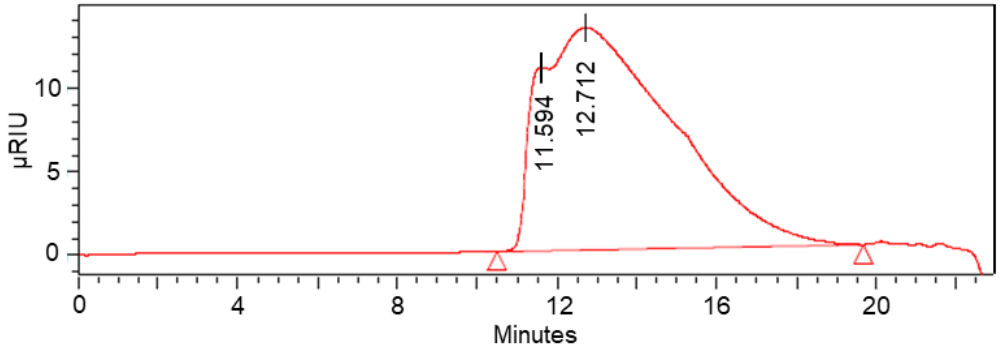

Retention time (min)	Area (µVxsec)	M_n	M_w	M_z	Polydispersity
12.712	3106007	60625	135965	220739	2.24

A4.22. FDCAPDO 1500 30 MDI

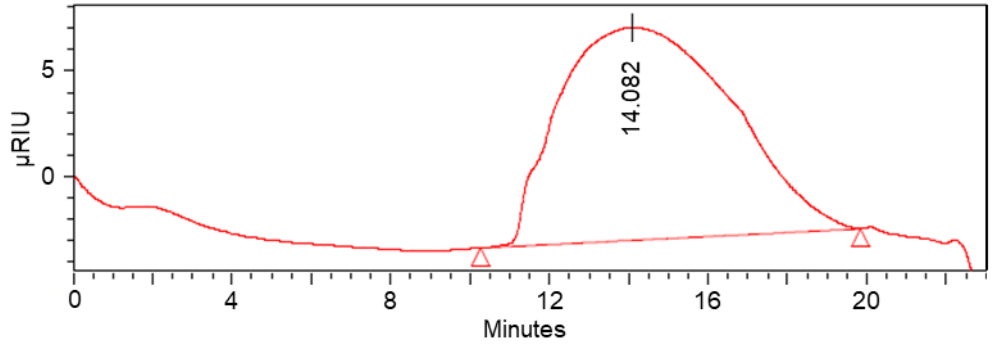

Retention time (min)	Area (µVxsec)	M_n	M_w	M_z	Polydispersity
14.082	3035398	32851	83950	162083	2.56

A4.23. FDCAPDO 2000 50 MDI

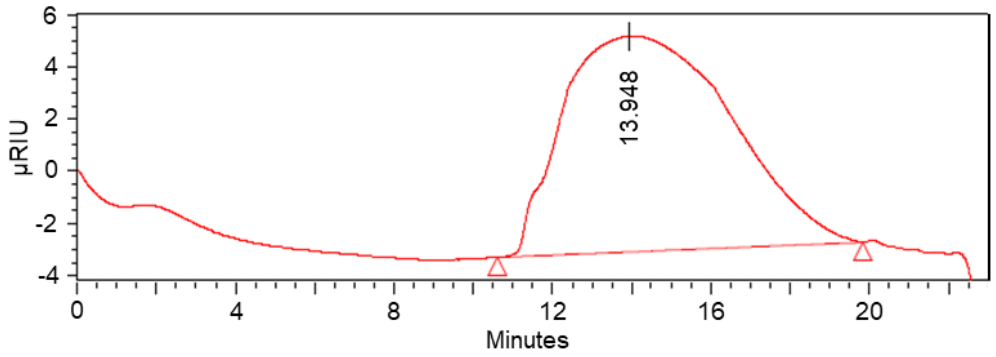

Retention time (min)	Area (µVxsec)	M_n	M_w	M_z	Polydispersity
13.948	2434182	33553	82579	154183	2.46

A4.24. FDCAHDO 1000 10 MDI

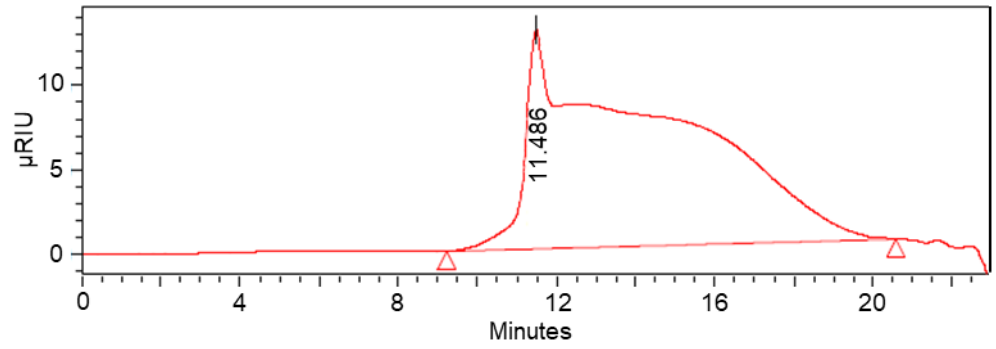

Retention time (min)	Area (µVxsec)	M_n	M_w	M_z	Polydispersity
11.486	3162560	32398	131667	317284	4.06

A4.25. FDCAHDO 1000 50 MDI

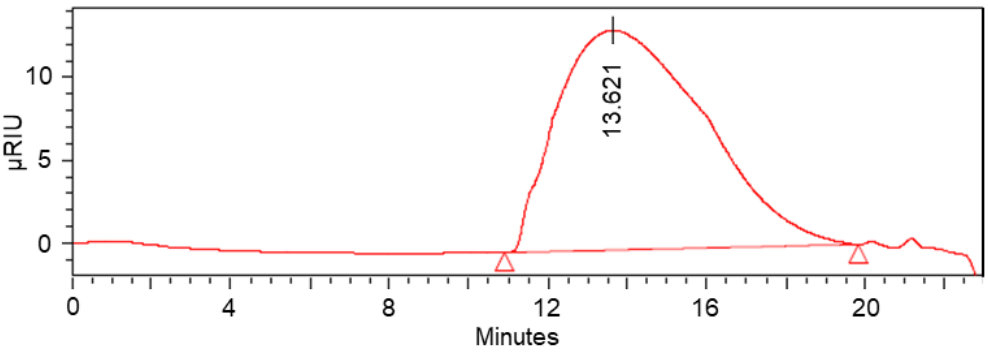

Retention time (min)	Area (µVxsec)	M_n	M_w	M_z	Polydispersity
13.621	3427176	40281	89028	151958	2.21

A4.26. FDCAHDO 2000 10 MDI

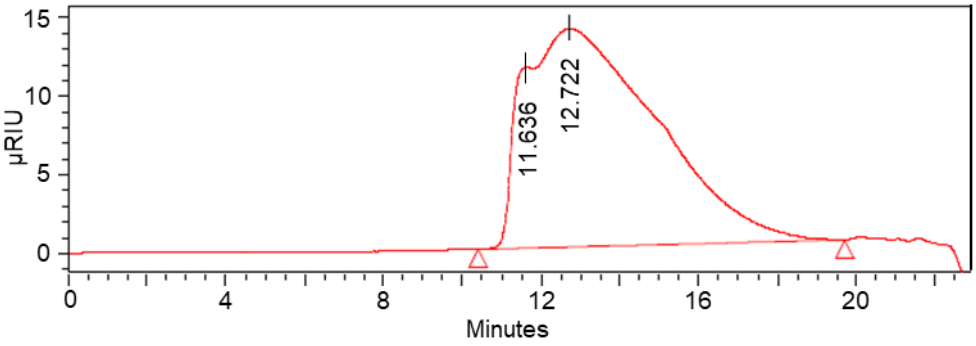

Retention time (min)	Area (µVxsec)	M_n	M_w	M_z	Polydispersity
12.722	3266105	60984	135501	219980	2.22

A4.27. FDCAHDO 2000 50 MDI

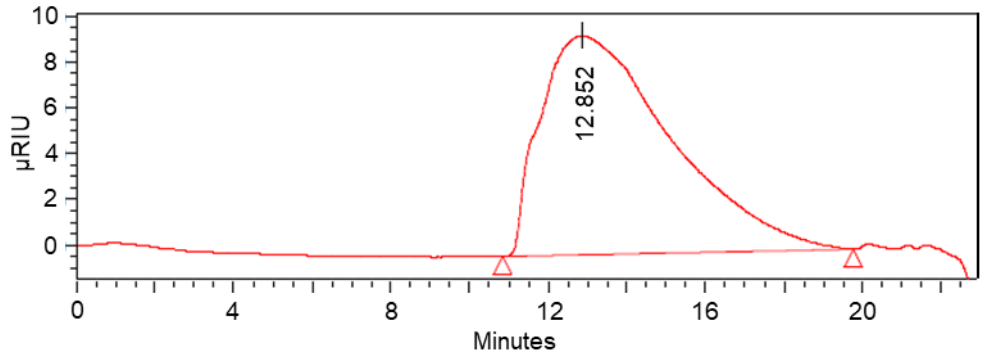

Retention time (min)	Area (µVxsec)	M_n	M_w	M_z	Polydispersity
12.852	2203368	50212	115543	186099	2.30

A4.28. FDCAHDO 1000 10 HDI

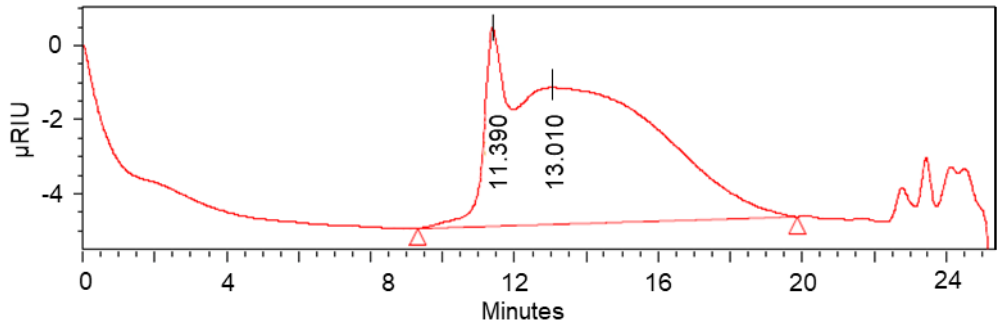

Retention time (min)	Area (µVxsec)	M_n	M_w	M_z	Polydispersity
11.390	1262380	41081	137709	315310	3.35

A4.29. FDCAHDO 1500 30 HDI

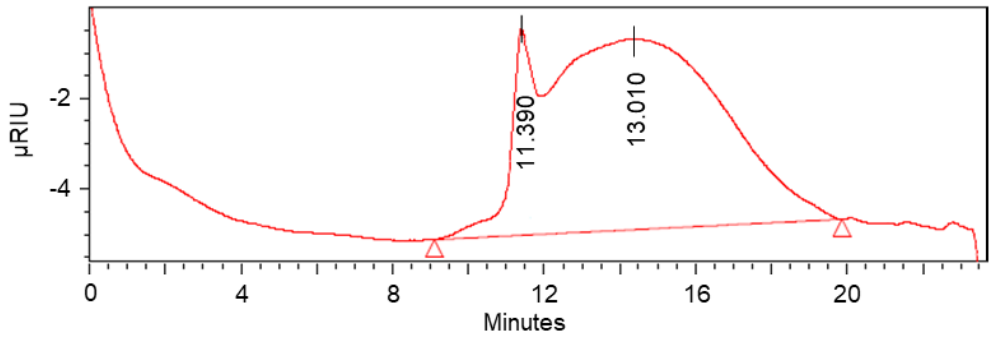

Retention time (min)	Area (µVxsec)	M_n	M_w	M_z	Polydispersity
11.406	1479181	34305	123720	360261	3.61

A4.30. FDCAHDO 2000 10 HDI

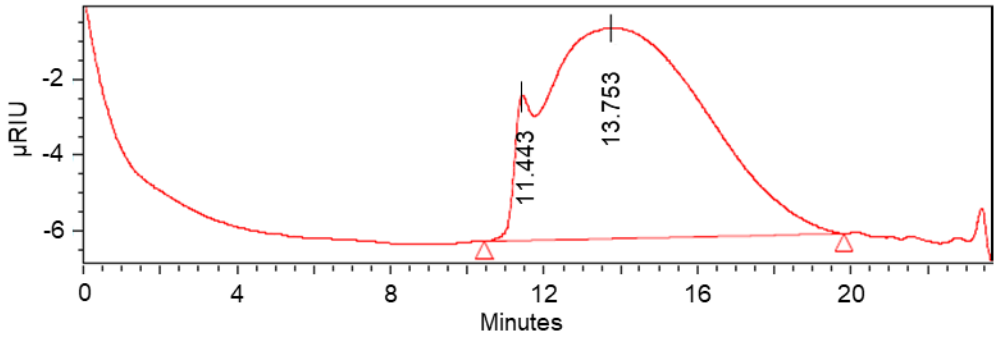

Retention time (min)	Area (µVxsec)	M_n	M_w	M_z	Polydispersity
13.735	1654880	38638	102530	198313	2.65

A4.31. FDCAHDO 2000 50 HDI

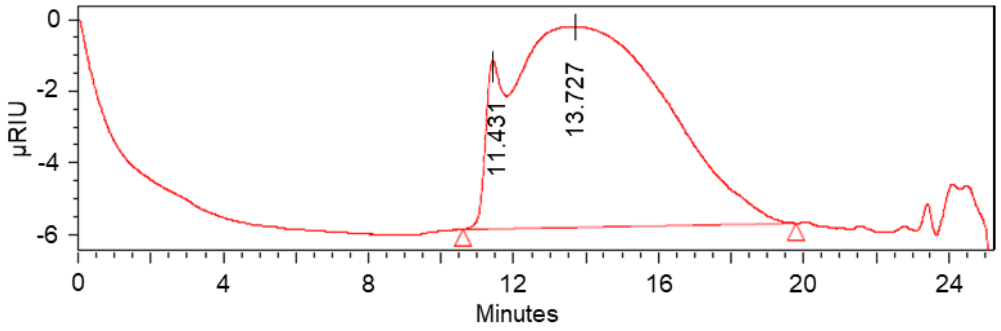

Retention time (min)	Area (µVxsec)	M_n	M_w	M_z	Polydispersity
13.727	1730689	39499	106481	205842	2.70

A5 Density

A5.1. IPHTA MDI TPUs

	Density (g/mL)	St. dev.
IPHTAPDO 1000 10% MDI	1.274	0.005
IPHTAPDO 1000 30% MDI	1.274	0.003
IPHTAPDO 1000 50% MDI	1.275	0.002
IPHTAPDO 2000 10% MDI	1.280	0.006
IPHTAPDO 2000 30% MDI	1.277	0.004
IPHTAPDO 2000 50% MDI	1.276	0.005
IPHTAHDO 1000 10% MDI	1.202	0.002
IPHTAHDO 1000 30% MDI	1.214	0.008
IPHTAHDO 1000 50% MDI	1.218	0.004
IPHTAHDO 2000 10% MDI	1.181	0.003
IPHTAHDO 2000 30% MDI	1.197	0.004
IPHTAHDO 2000 50% MDI	1.220	0.006

A5.2. IPHTA HDI TPUs

	Density (g/mL)	St. dev.
IPHTAPDO 1000 10% HDI	1.271	0.007
IPHTAPDO 1000 30% HDI	1.264	0.003
IPHTAPDO 1000 50% HDI	1.244	0.009
IPHTAPDO 2000 10% HDI	1.285	0.012
IPHTAPDO 2000 30% HDI	1.277	0.009
IPHTAPDO 2000 50% HDI	1.269	0.010
IPHTAHDO 1000 10% HDI	1.173	0.012
IPHTAHDO 1000 30% HDI	1.175	0.007
IPHTAHDO 1000 50% HDI	1.179	0.007
IPHTAHDO 2000 10% HDI	1.177	0.005
IPHTAHDO 2000 30% HDI	1.186	0.002
IPHTAHDO 2000 50% HDI	1.191	0.004

A5.3. FDCA MDI TPUs

	Density (g/mL)	St. dev.
FDCAPDO 1000 10% MDI	1.361	0.020
FDCAPDO 1000 50% MDI	1.330	0.009
FDCAPDO 1500 30% MDI	1.341	0.006
FDCAPDO 2000 10% MDI	1.364	0.012
FDCAPDO 2000 50% MDI	1.339	0.009
FDCAHDO 1000 10% MDI	1.229	0.008
FDCAHDO 1000 50% MDI	1.255	0.009
FDCAHDO 1500 30% MDI	1.254	0.010
FDCAHDO 2000 10% MDI	1.241	0.008
FDCAHDO 2000 50% MDI	1.256	0.010

A5.4. FDCA HDI TPUs

	Density (g/mL)	St. dev.
FDCAPDO 1000 10% HDI	1.354	0.017
FDCAPDO 1000 50% HDI	1.311	0.008
FDCAPDO 1500 30% HDI	1.327	0.013
FDCAPDO 2000 10% HDI	1.355	0.005
FDCAPDO 2000 50% HDI	1.342	0.007
FDCAHDO 1000 10% HDI	1.223	0.002
FDCAHDO 1000 50% HDI	1.220	0.004
FDCAHDO 1500 30% HDI	1.233	0.002
FDCAHDO 2000 10% HDI	1.235	0.005
FDCAHDO 2000 50% HDI	1.234	0.007

A6 SAXS of the unannealed TPUs

The SAXS data of the unannealed TPUs, and when a peak is present in the Fourier region, its fitting can be found hereinafter.

A6.1. IPHTAPDO 1000 10 MDI

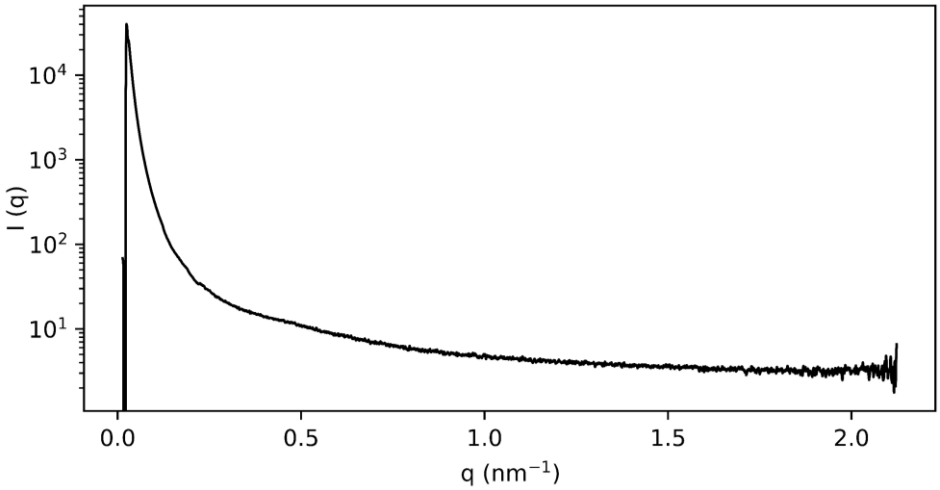

A6.2. IPHTAPDO 1000 30 MDI

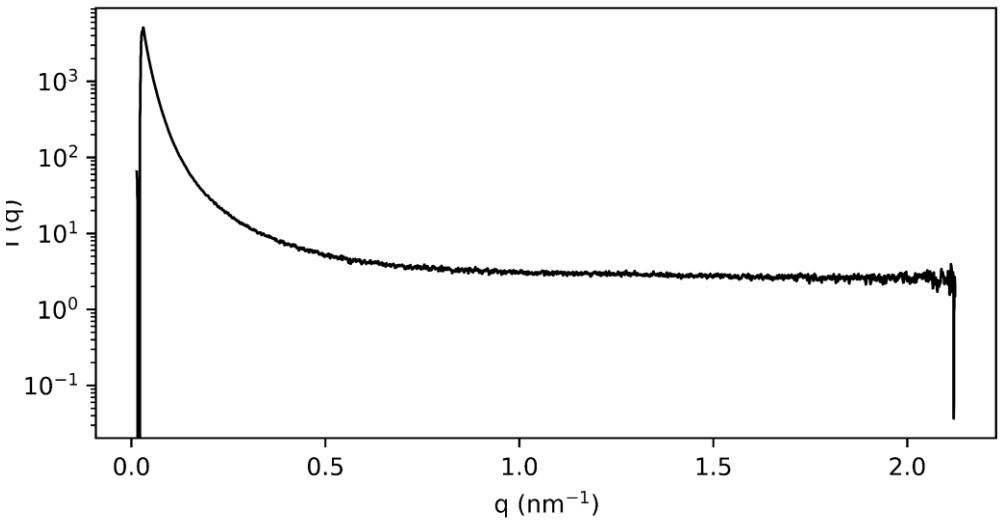

A6.3. IPHTAPDO 1000 50 MDI

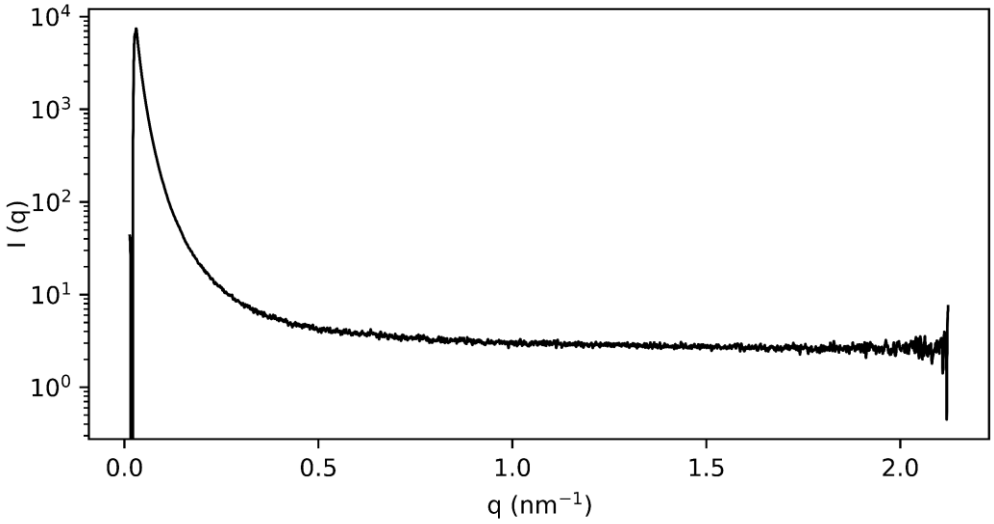

A6.4. IPHTAPDO 2000 10 MDI

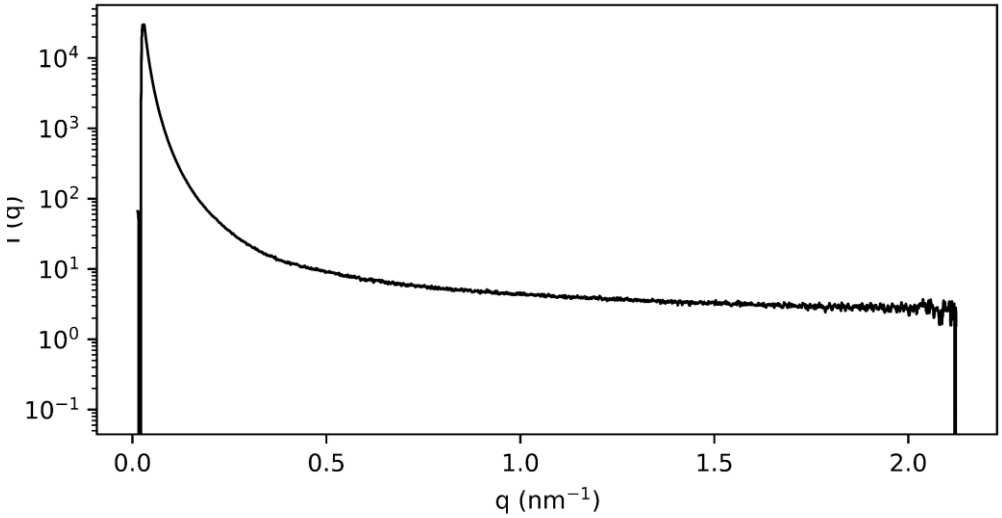

A6.5. IPHTAPDO 2000 30 MDI

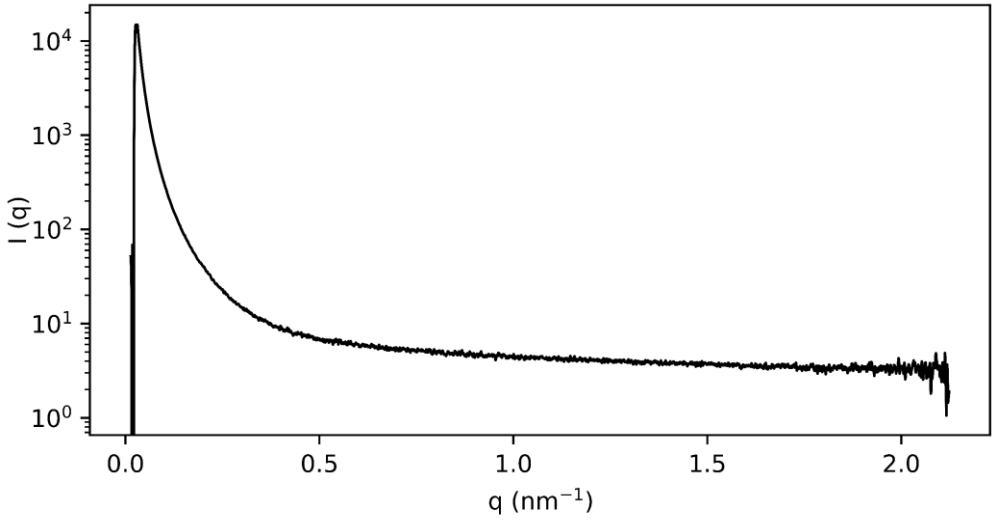

A6.6. IPHTAPDO 2000 50 MDI

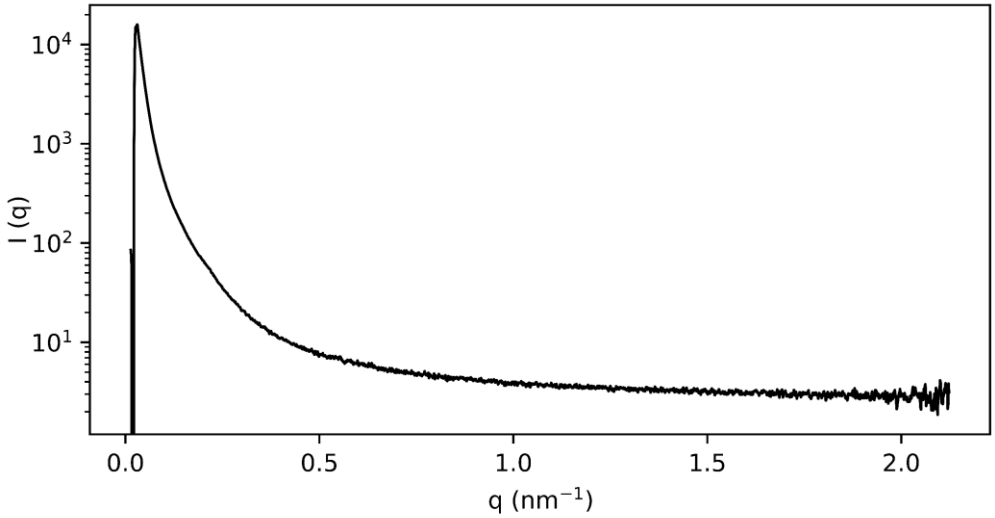

A6.7. IPHTAHDO 1000 10 MDI

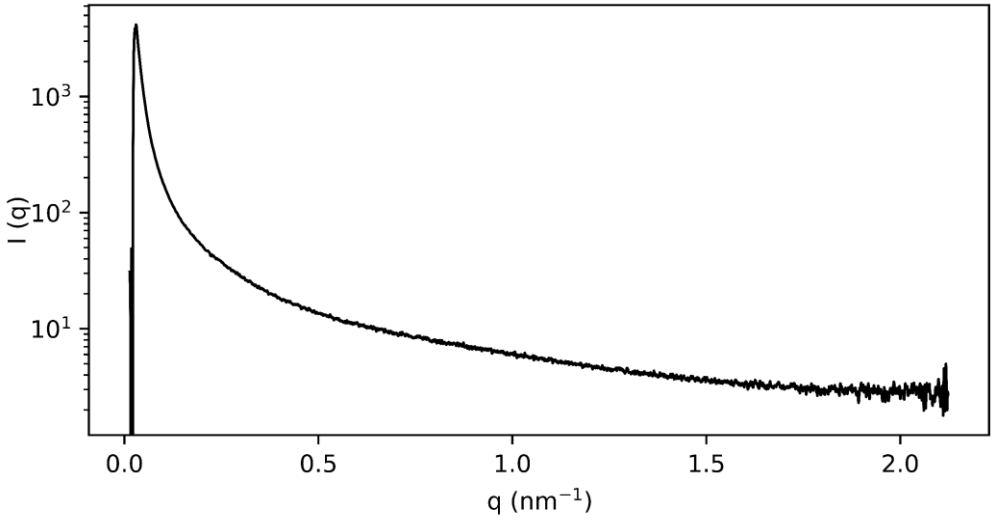

A6.8. IPHTAHDO 1000 30 MDI

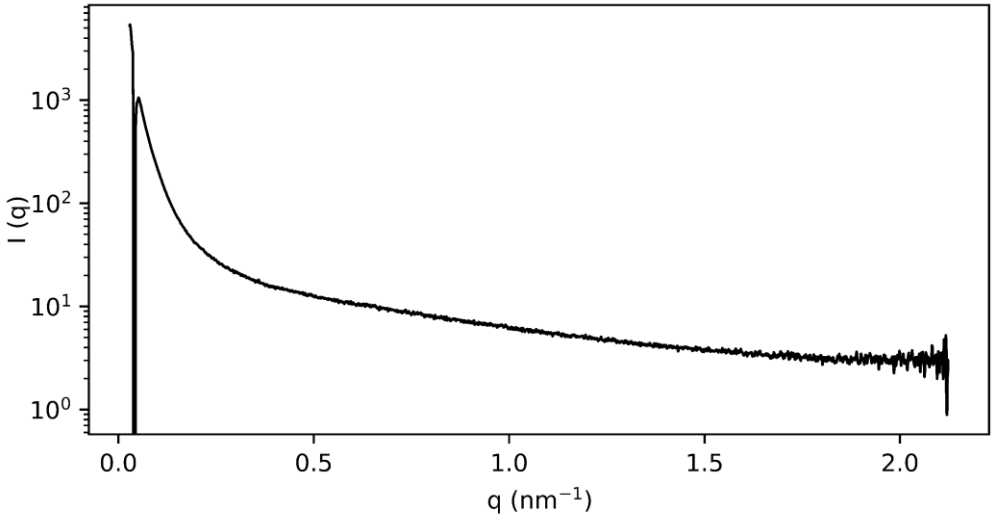

A6.9. IPHTAHDO 1000 50 MDI

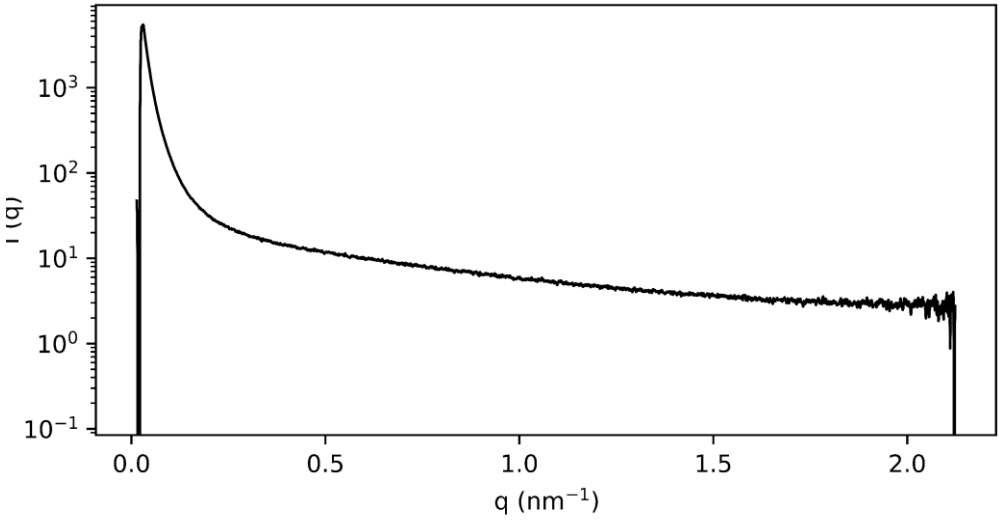

A6.10. IPHTAHDO 2000 10 MDI

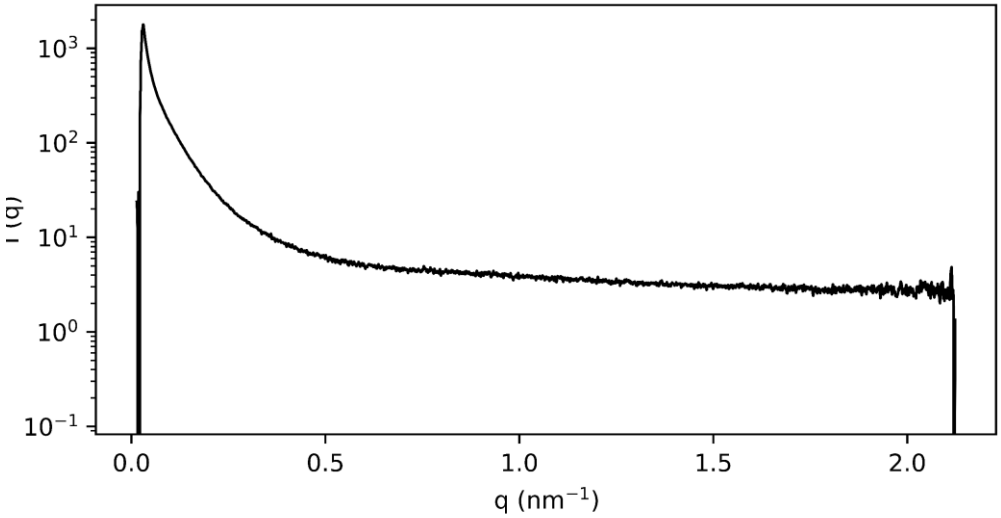

A6.11. IPHTAHDO 2000 30 MDI

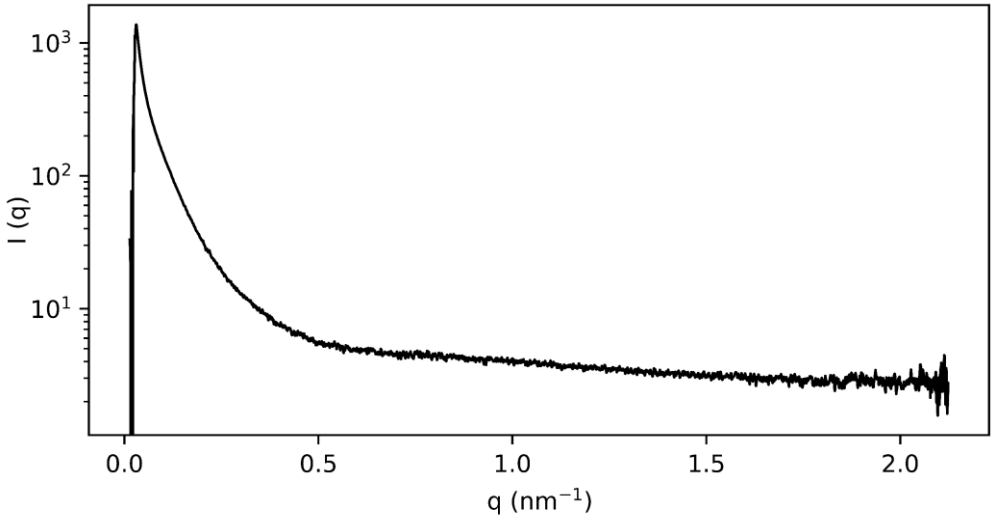

A6.12. IPHTAHDO 2000 50 MDI

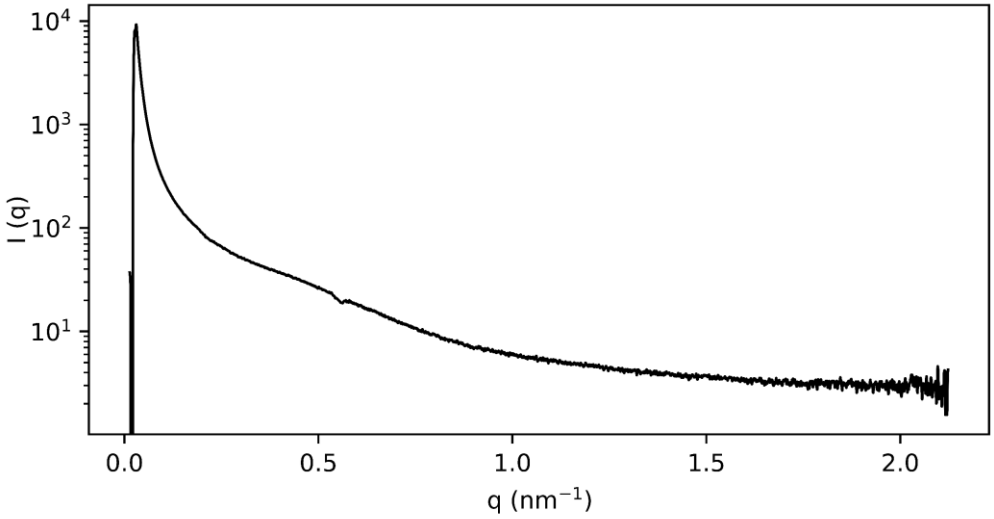

A6.13. IPHTAPDO 1000 10 HDI

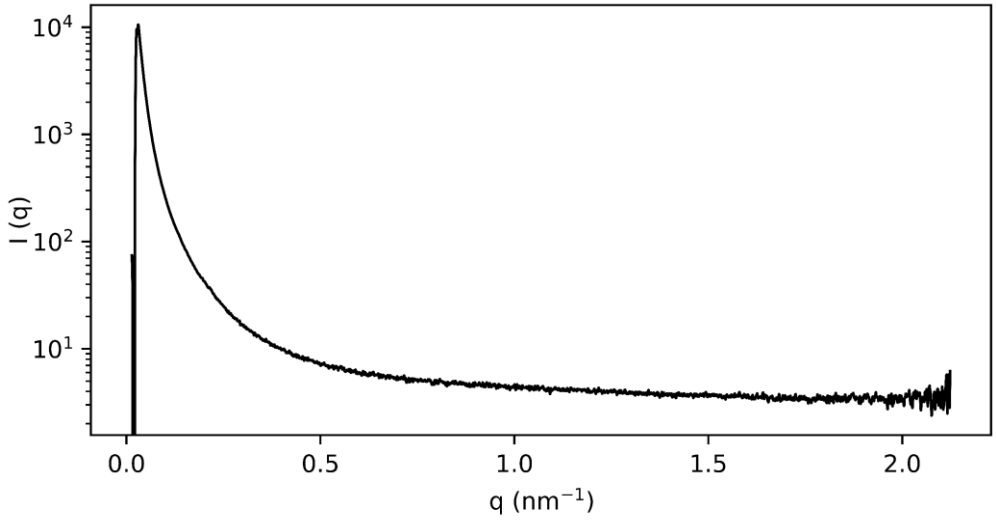

A6.14. IPHTAPDO 1000 30 HDI

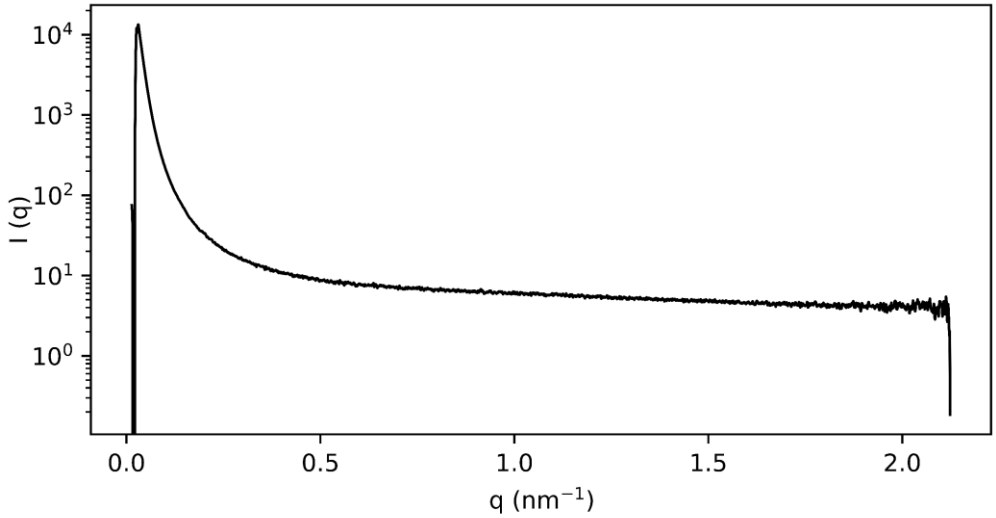

A6.15. IPHTAPDO 1000 50 HDI

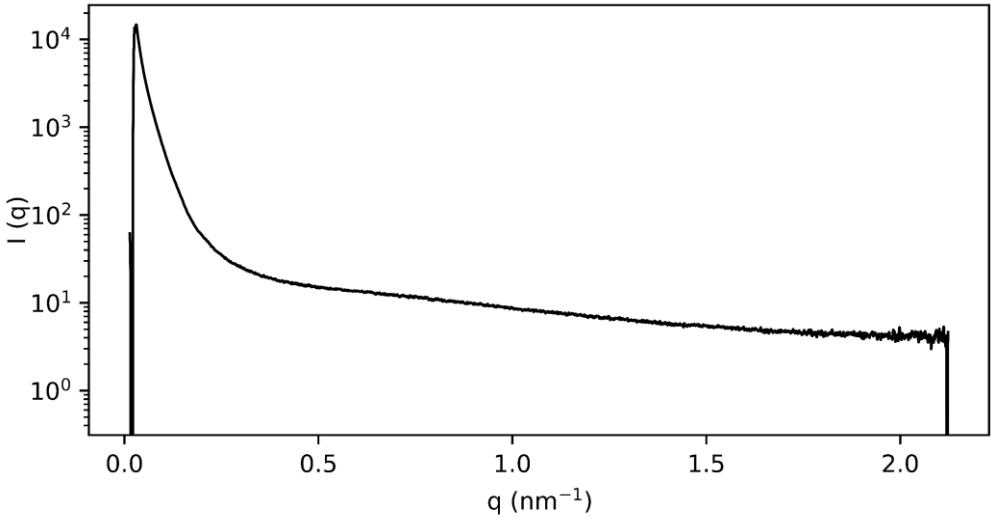

A6.16. IPHTAPDO 2000 10 HDI

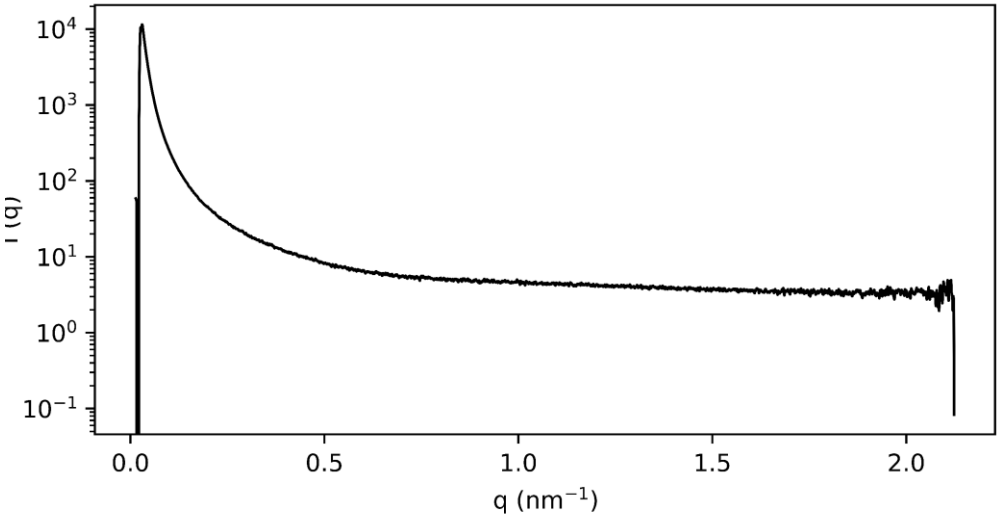

A6.17. IPHTAPDO 2000 30 HDI

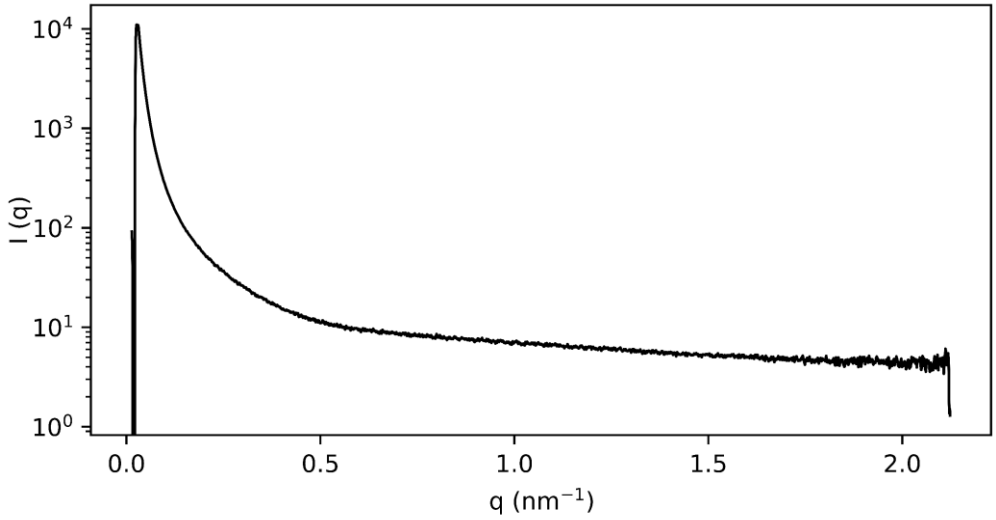

A6.18. IPHTAPDO 2000 50 HDI

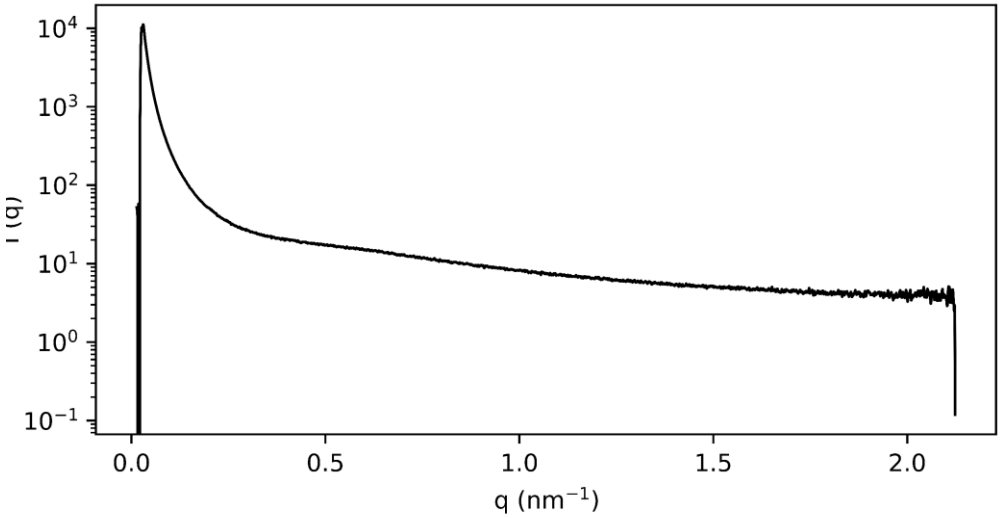

A6.19. IPHTAHDO 1000 10 HDI

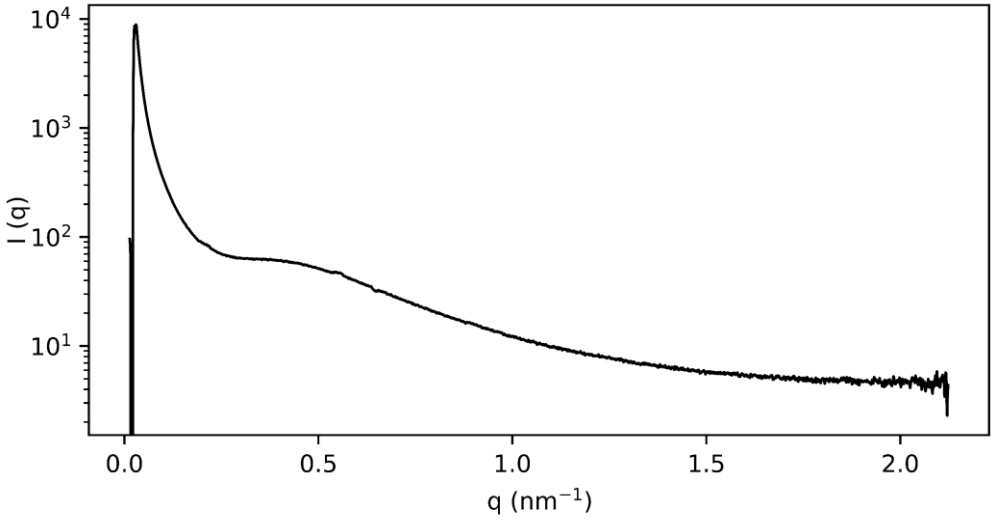

- Fitting

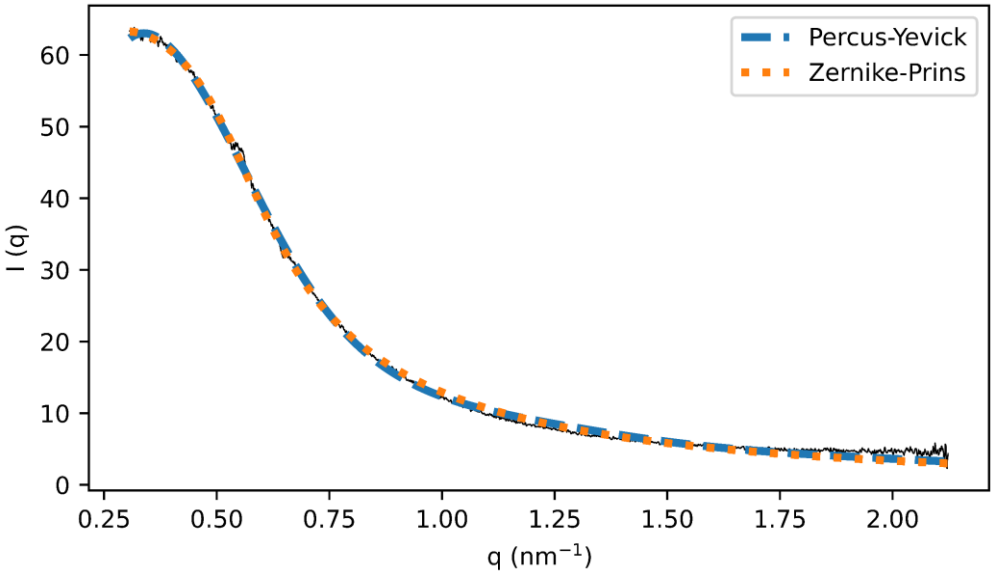

A6.20. IPHTAHDO 1000 30 HDI

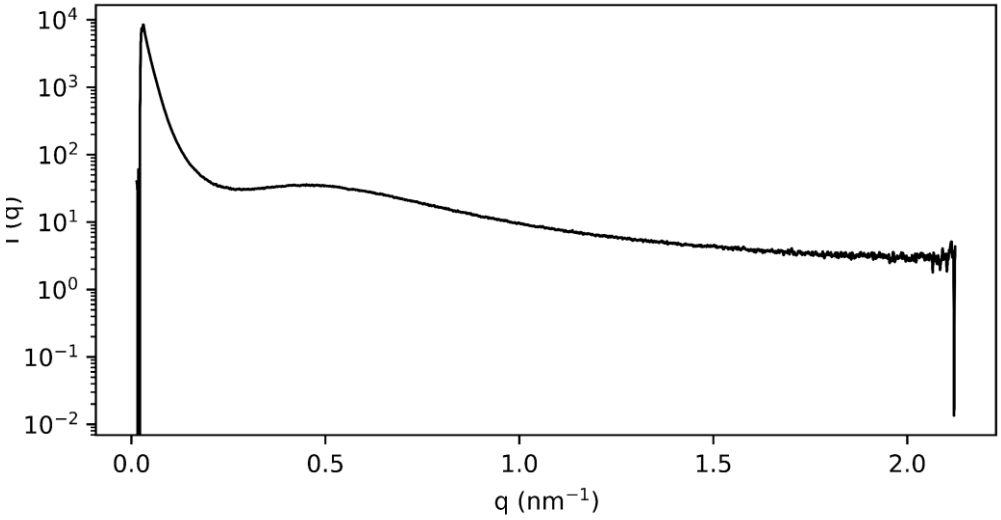

- Fitting

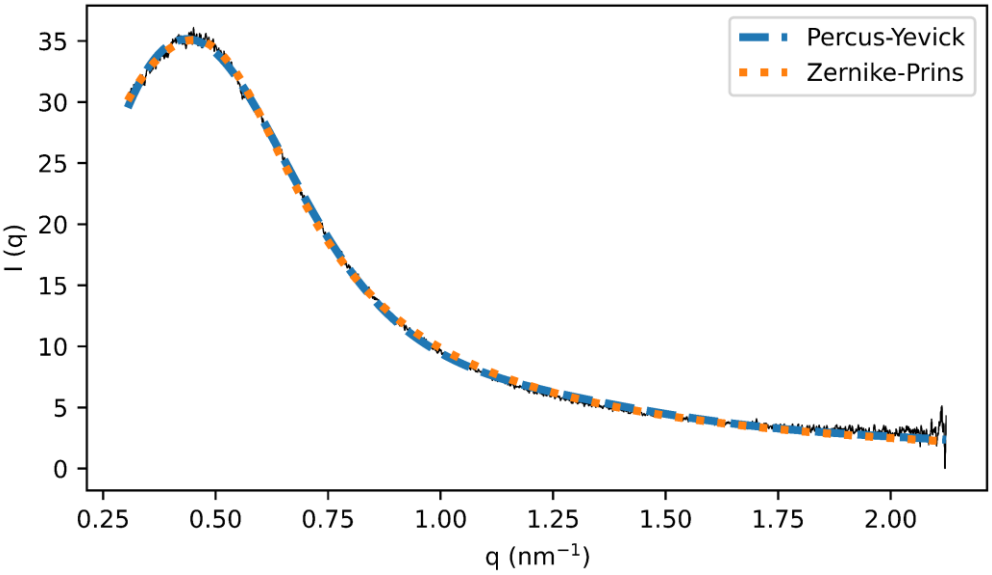

A6.21. IPHTAHDO 1000 50 HDI

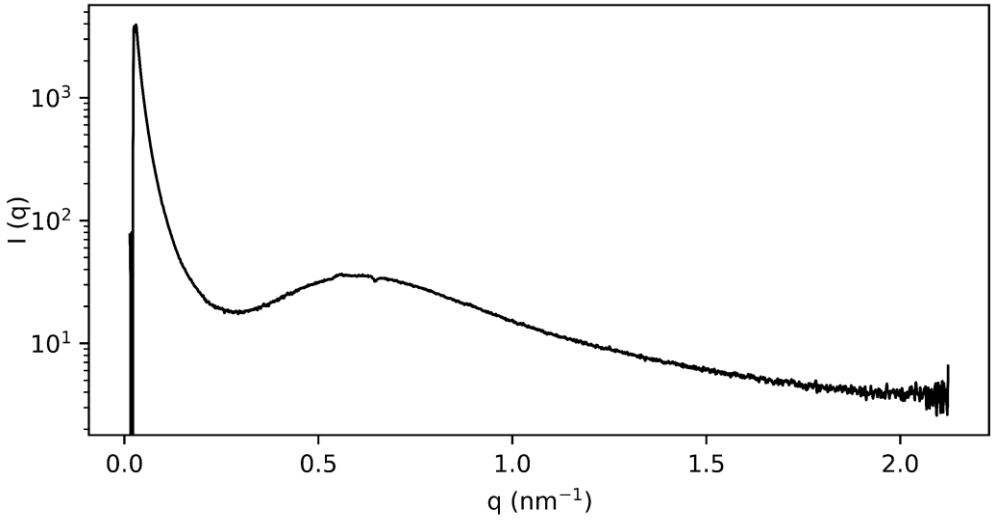

- Fitting

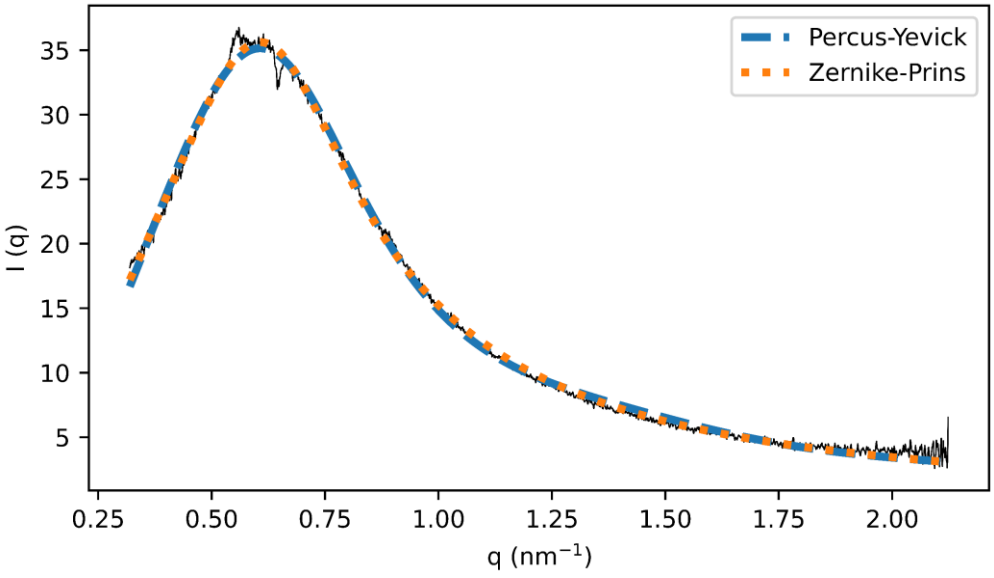

A6.22. IPHTAHDO 2000 10 HDI

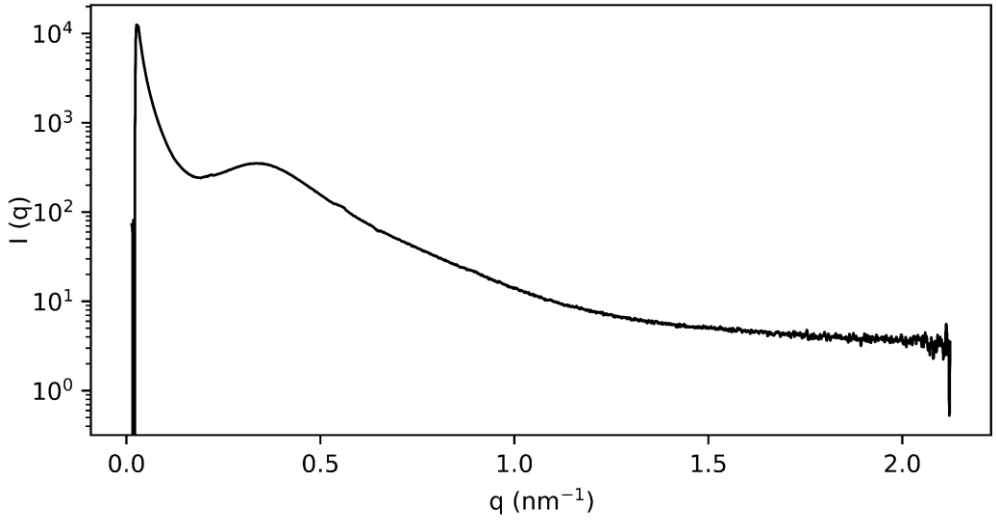

- Fitting

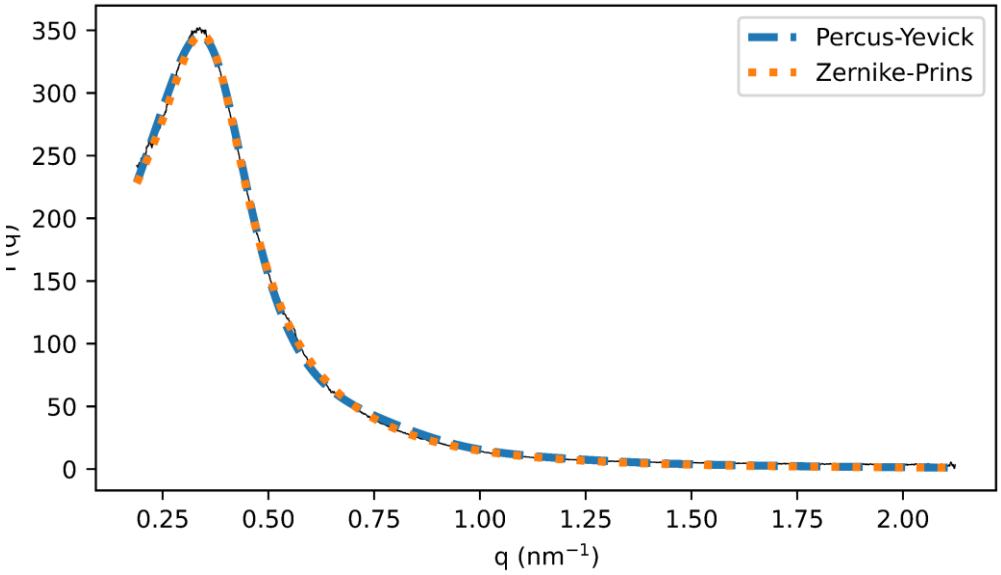

A6.23. IPHTAHDO 2000 30 HDI

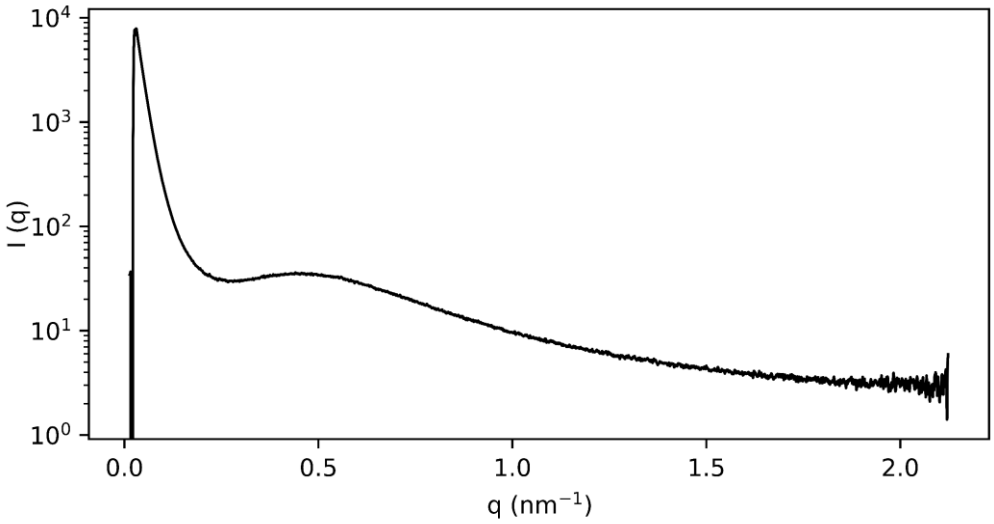

- Fitting

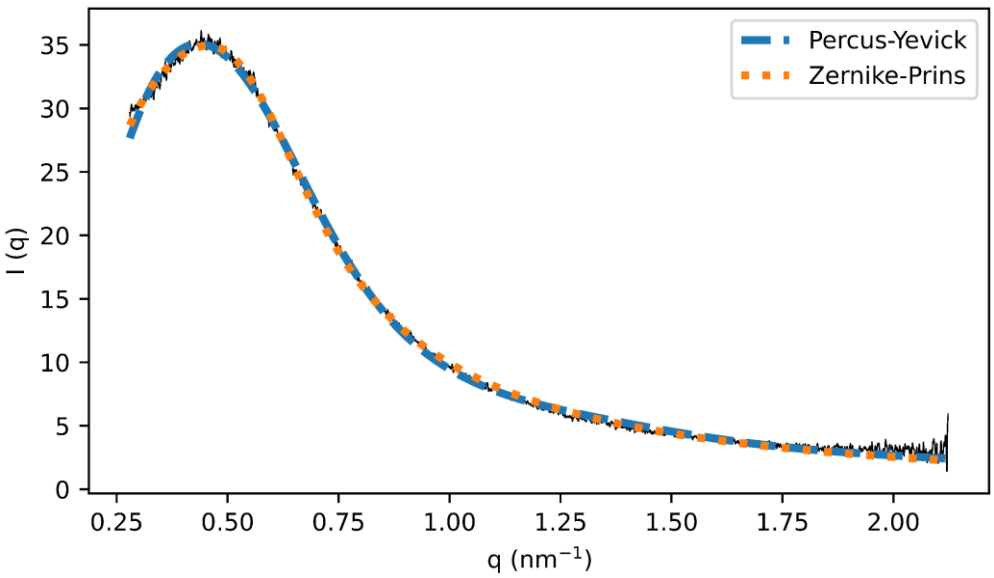

A6.24. IPHTAHDO 2000 50 HDI

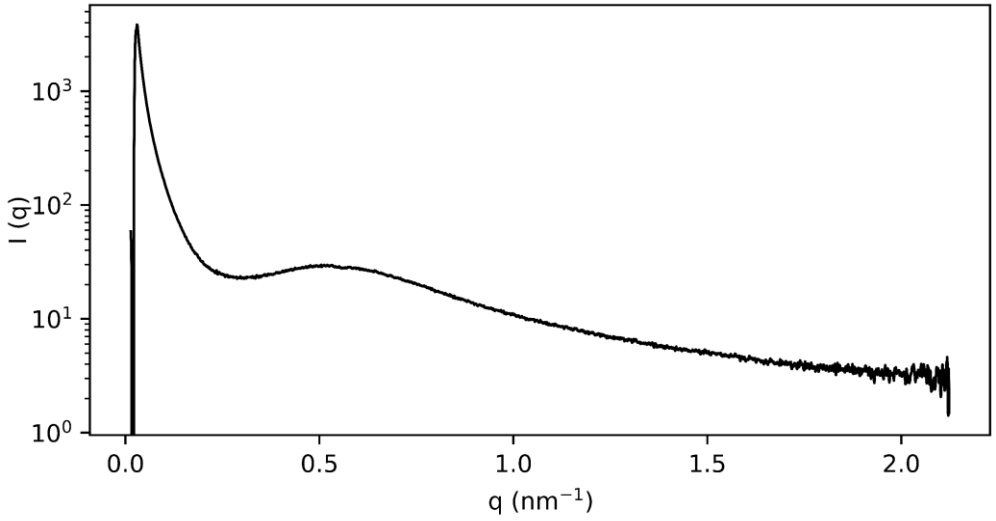

- Fitting

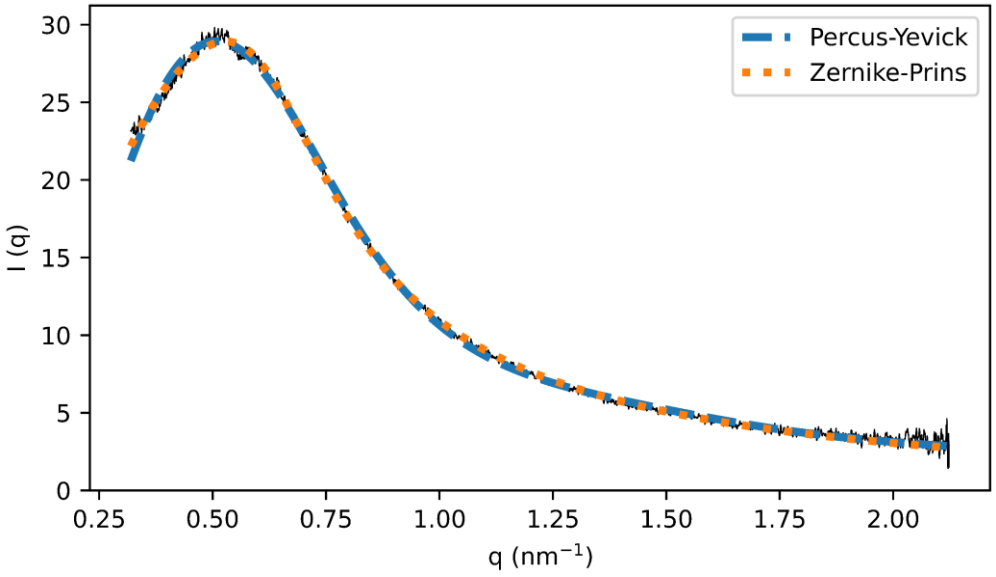

A6.25. FDCAPDO 1000 10 MDI

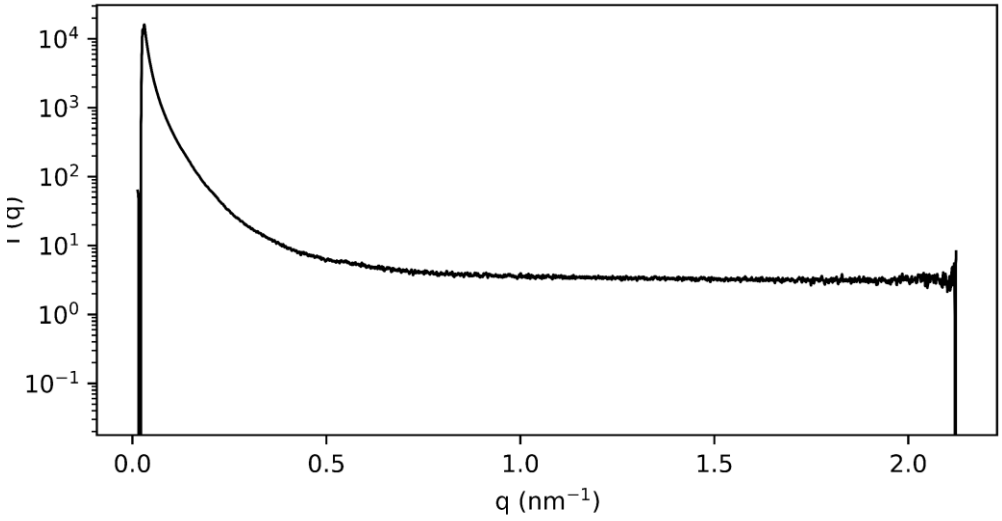

A6.26. FDCAPDO 1000 50 MDI

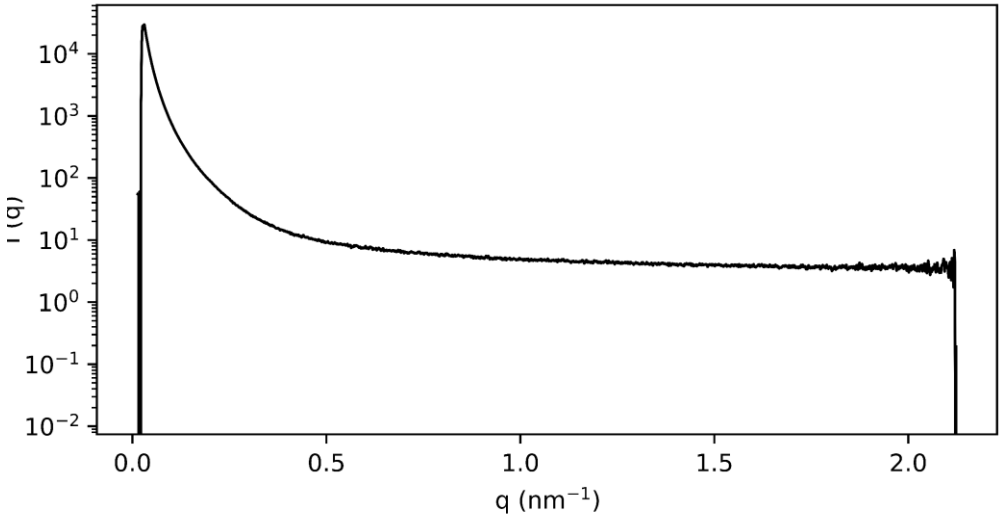

A6.27. FDCAPDO 1500 30 MDI

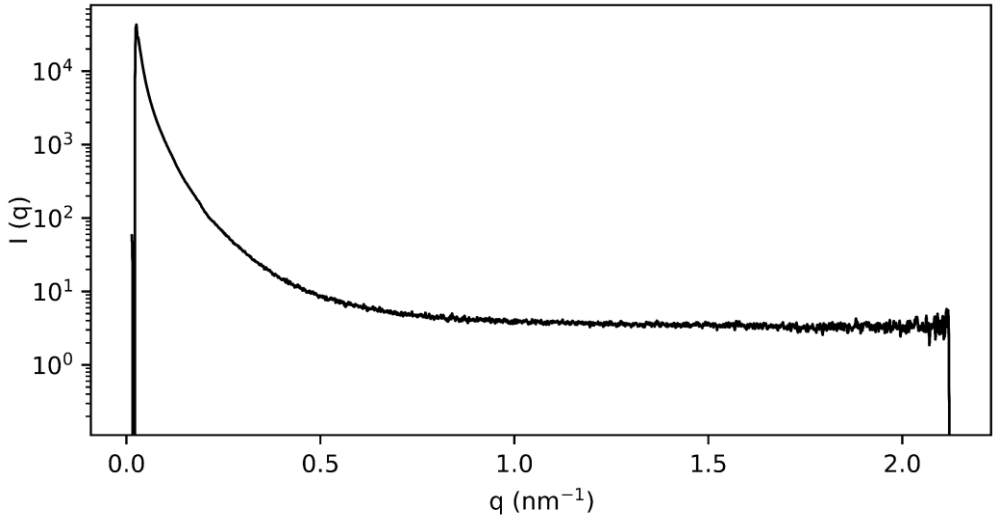

A6.28. FDCAPDO 2000 10 MDI

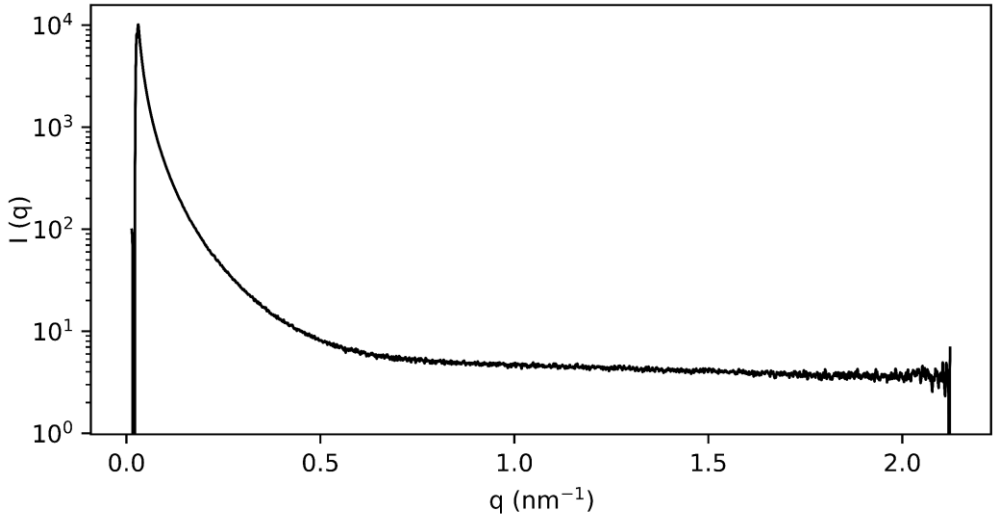

A6.29. FDCAPDO 2000 50 MDI

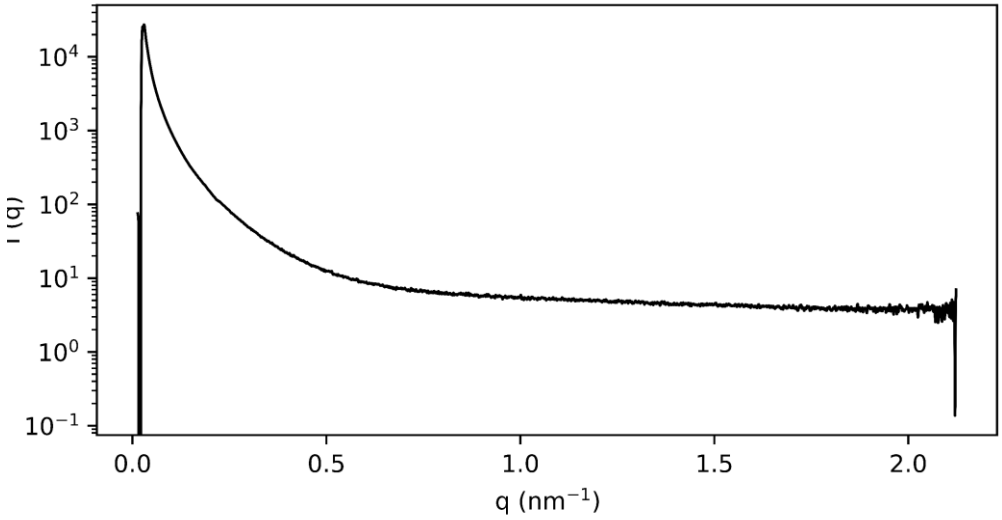

A6.30. FDCAHDO 1000 10 MDI

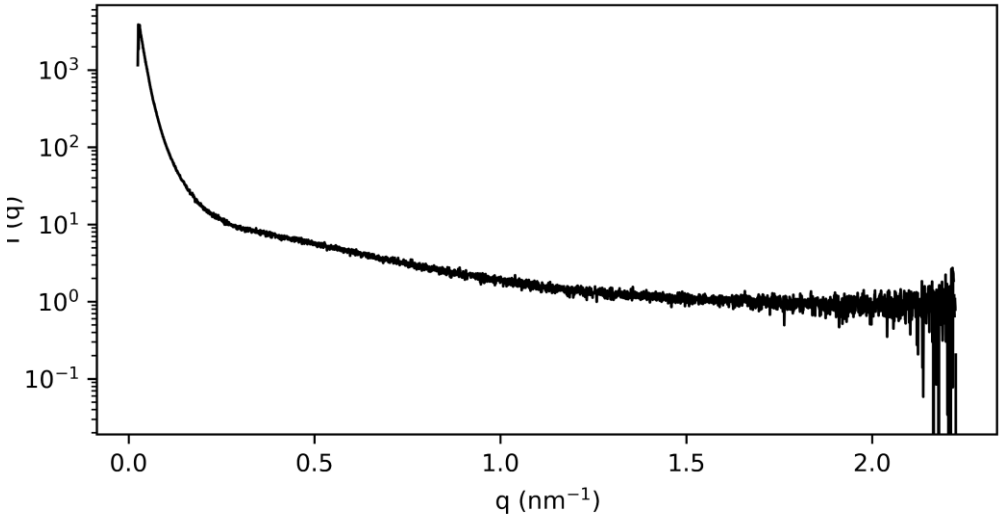

A6.31. FDCAHDO 1000 50 MDI

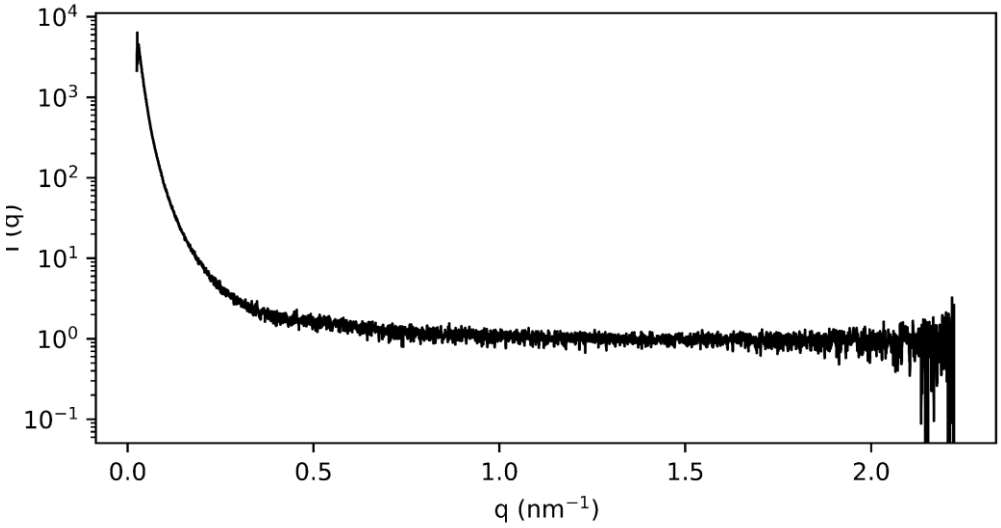

A6.32. FDCAHDO 1500 30 MDI

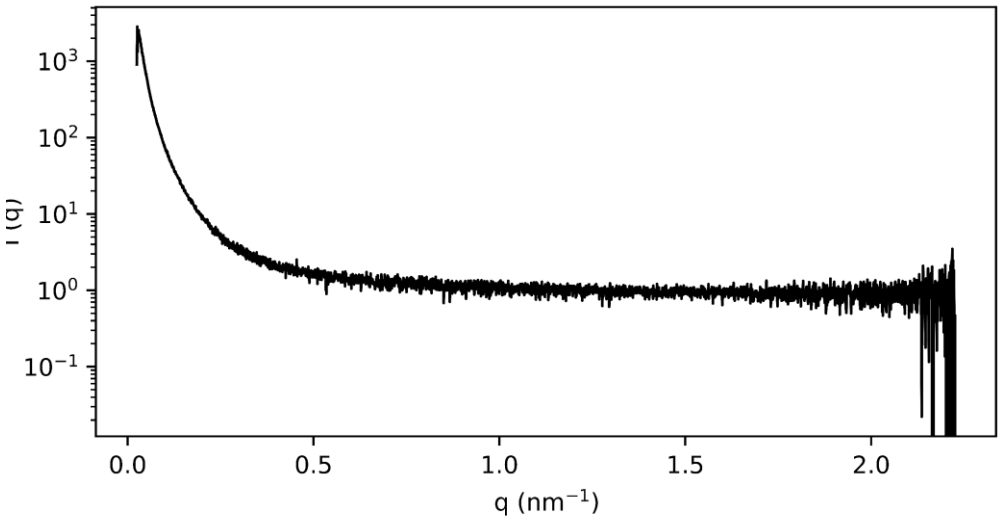

A6.33. FDCAHDO 2000 10 MDI

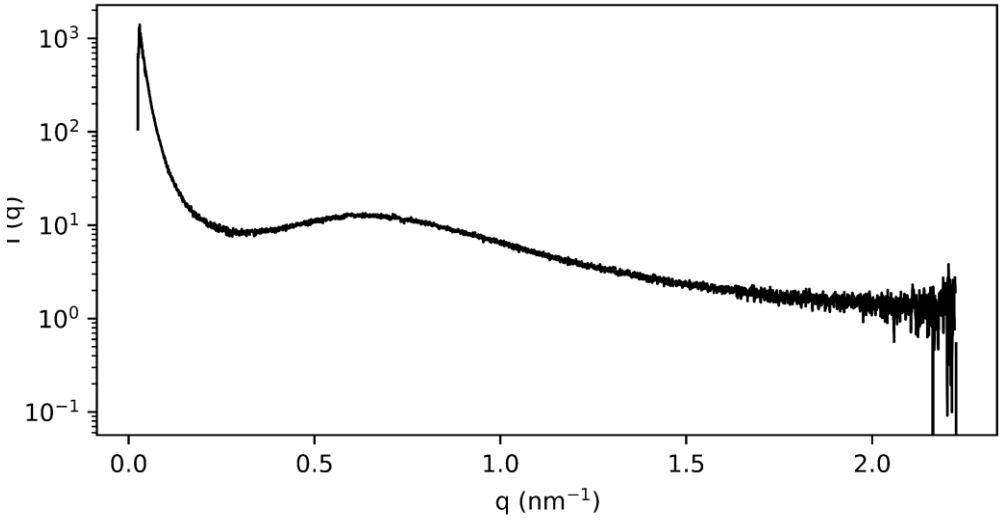

- Fitting

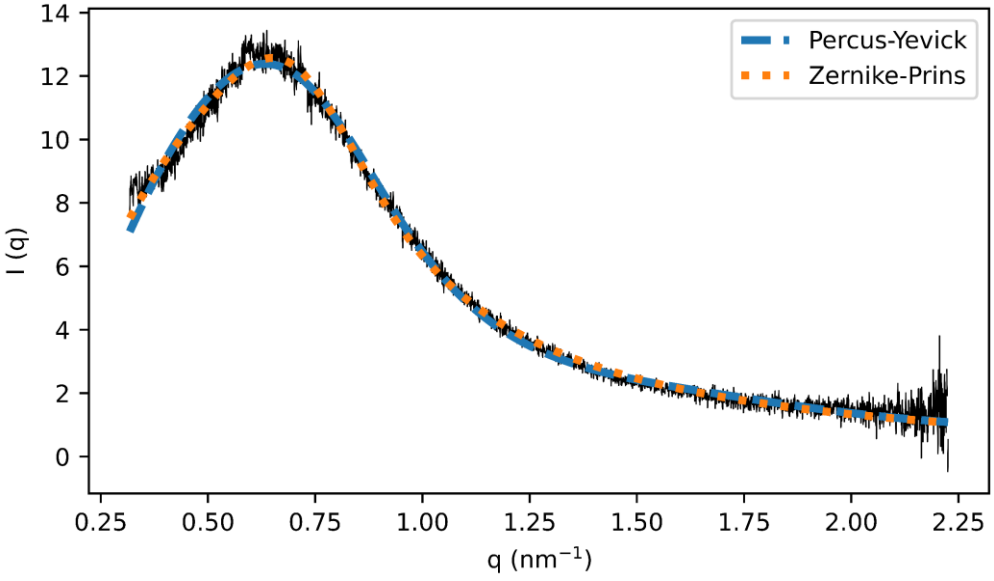

A6.34. FDCAHDO 2000 50 MDI

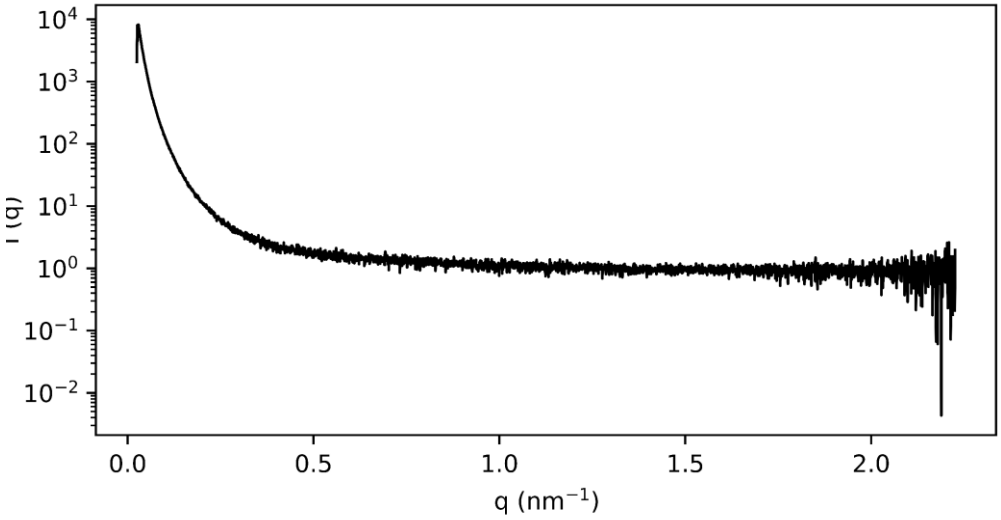

A6.35. FDCAPDO 1000 10 HDI

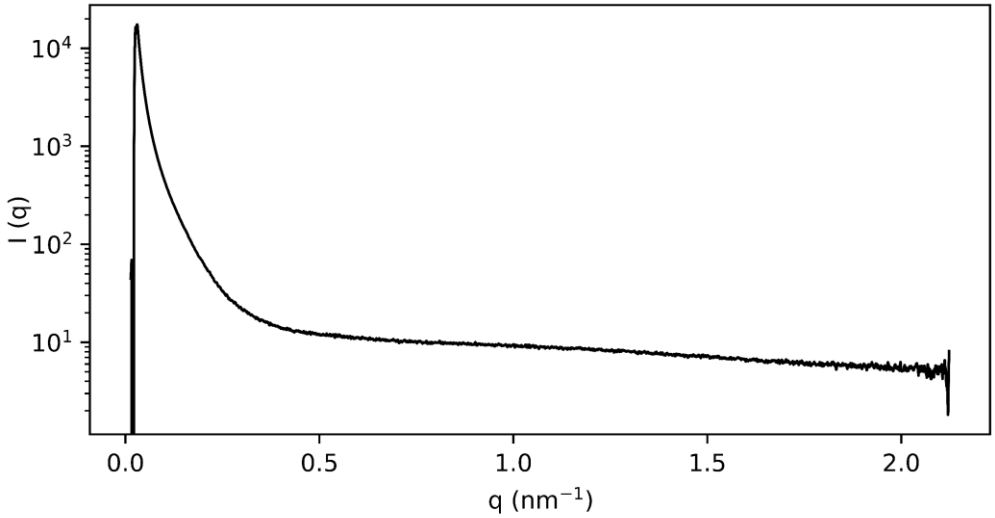

A6.36. FDCAPDO 1000 50 HDI

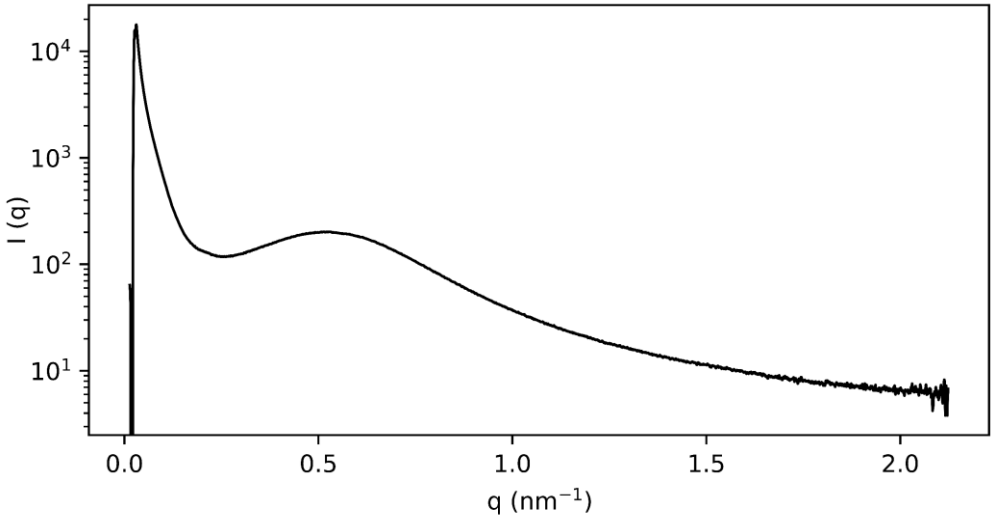

- Fitting

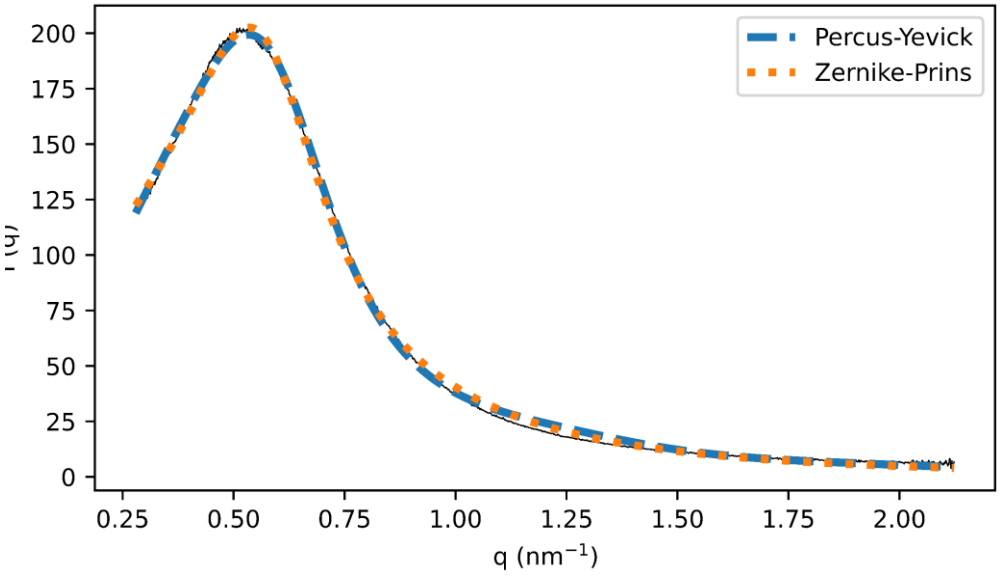

A6.37. FDCAPDO 1500 30 HDI

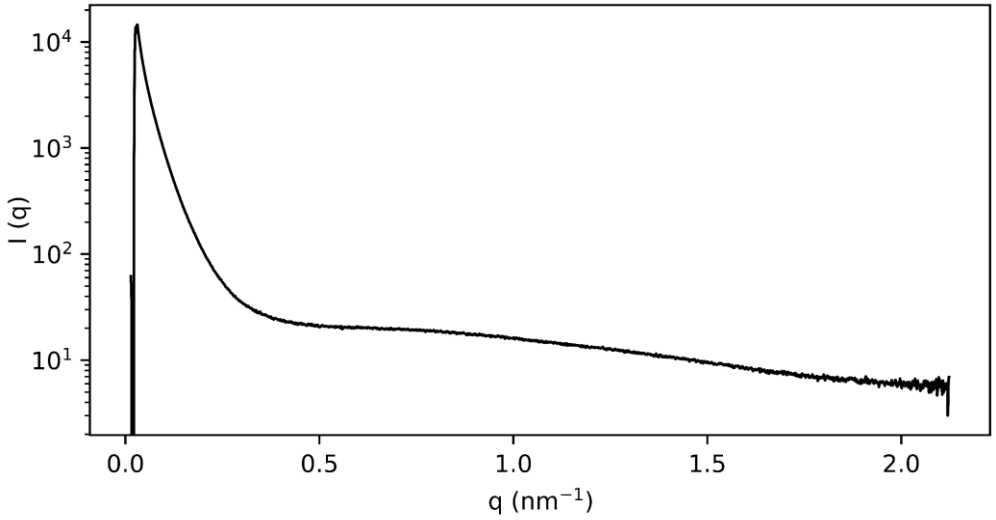

A6.38. FDCAPDO 2000 10 HDI

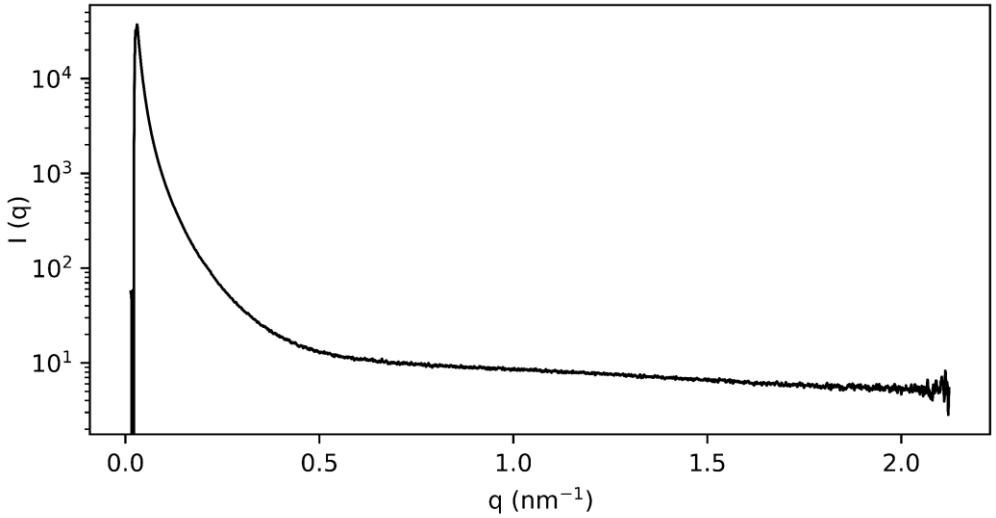

A6.39. FDCAPDO 2000 50 HDI

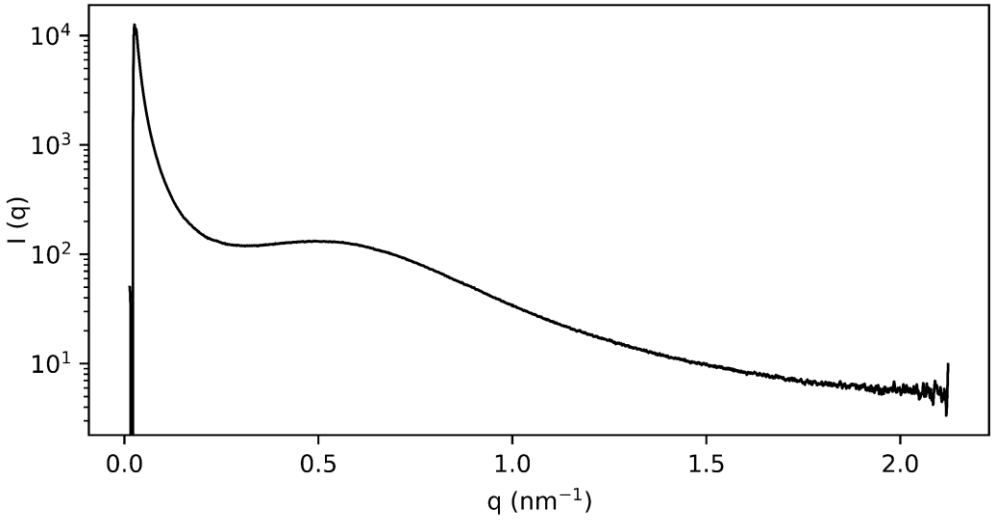

- Fitting

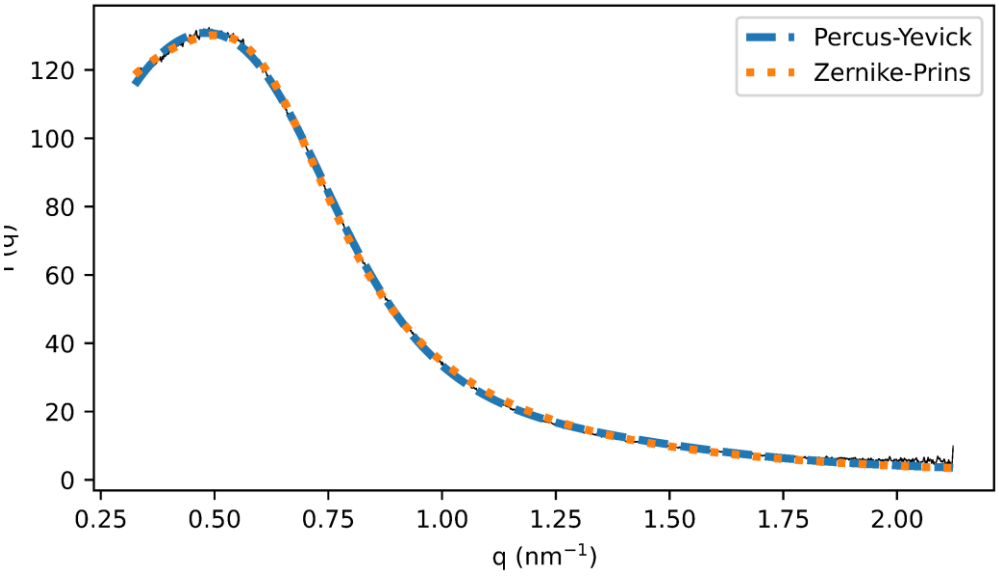

A6.40. FDCAHDO 1000 10 HDI

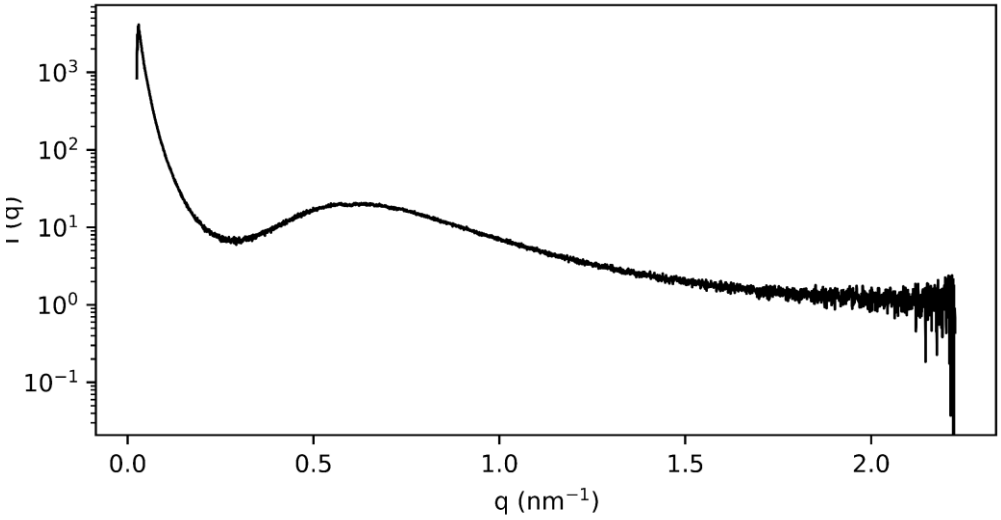

- Fitting

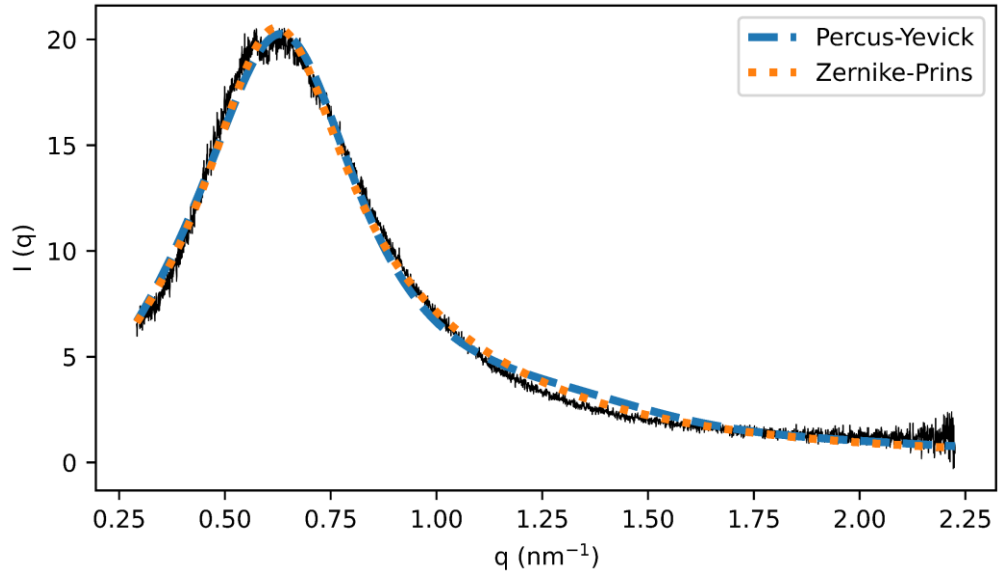

A6.41. FDCAHDO 1000 50 HDI

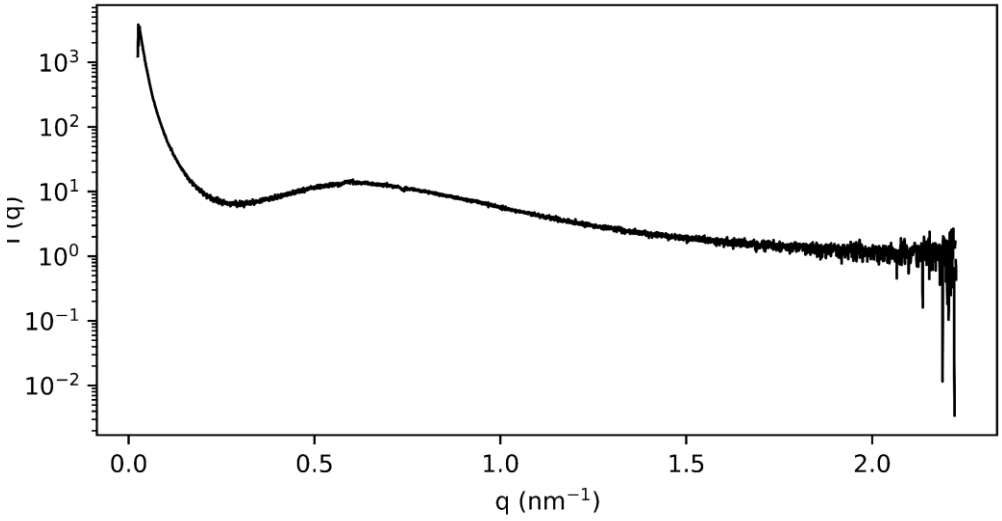

- Fitting

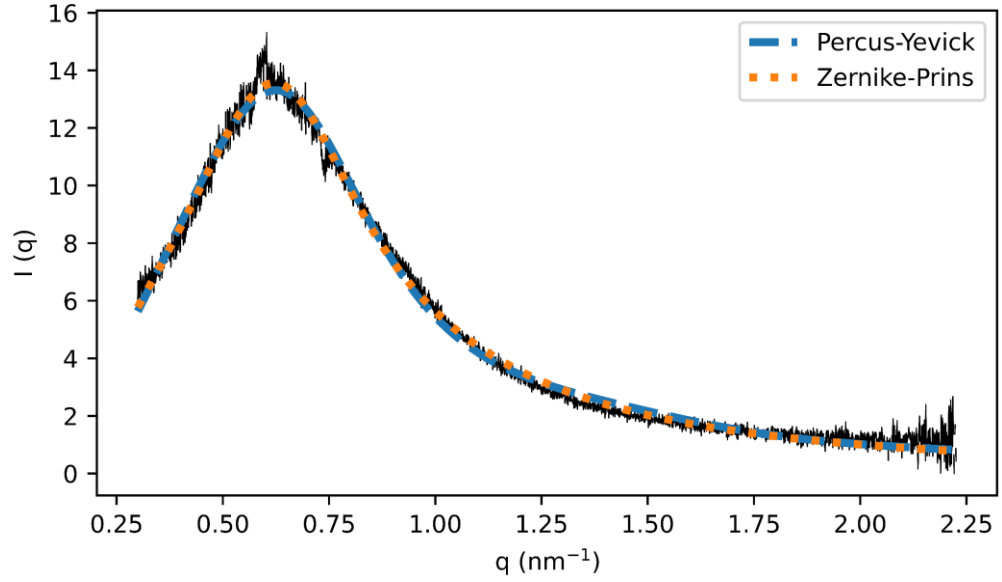

A6.42. FDCAHDO 1500 30 HDI

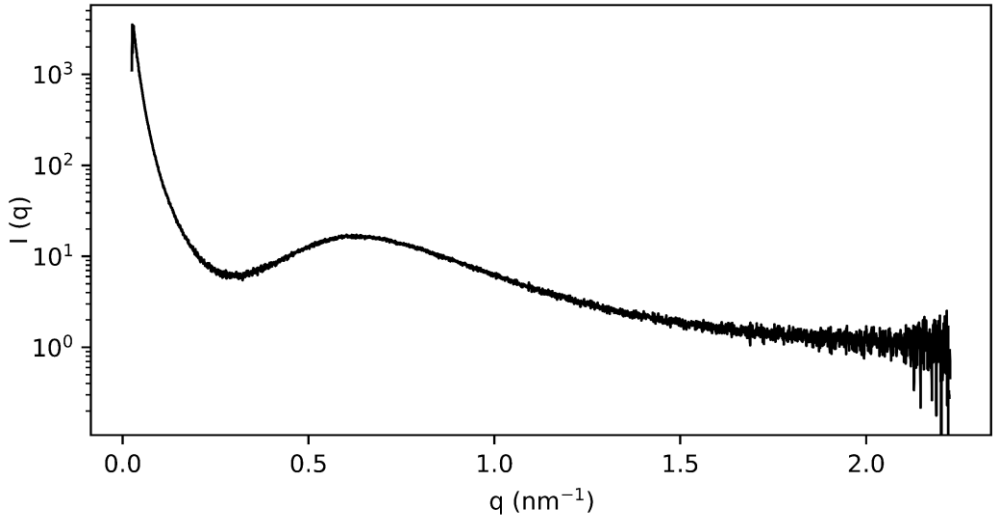

- Fitting

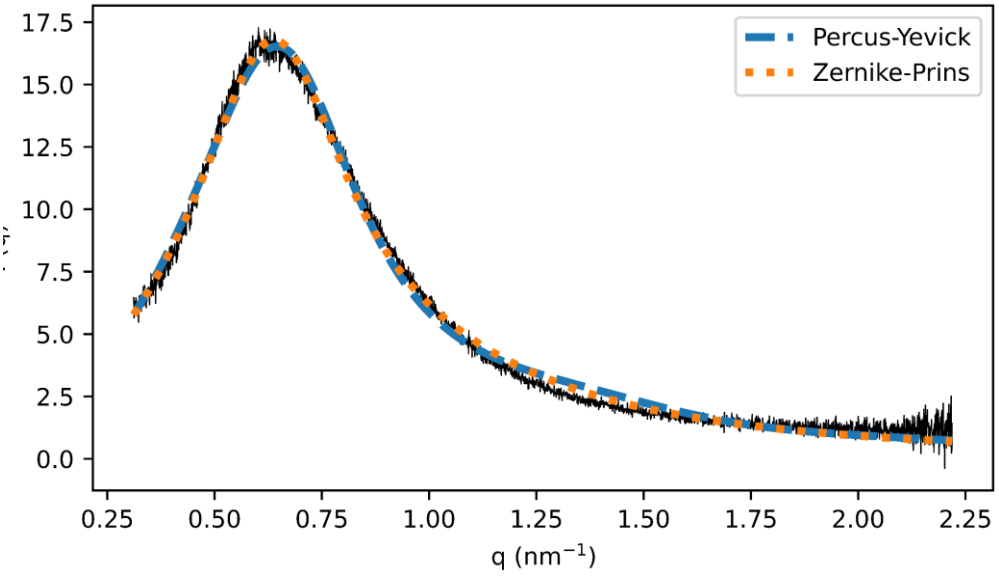

A6.43. FDCAHDO 2000 10 HDI

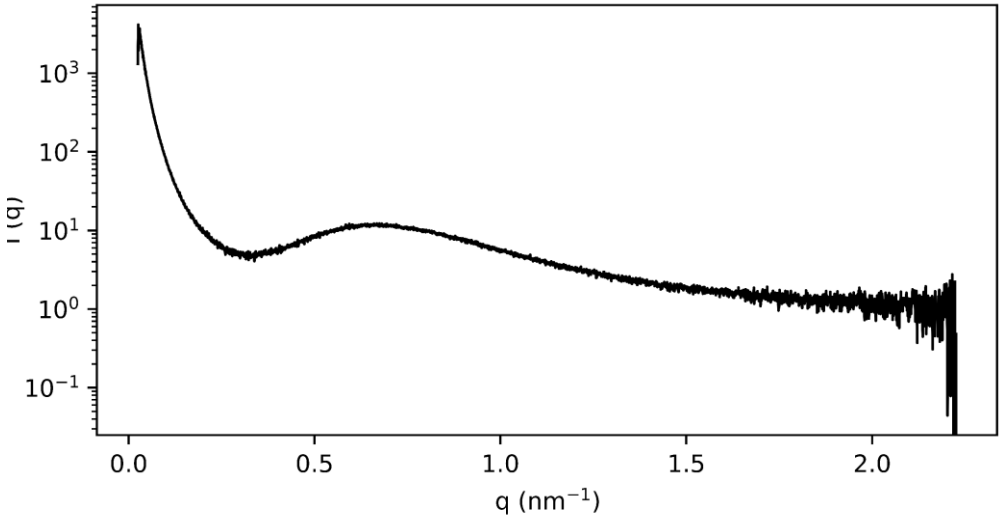

- Fitting

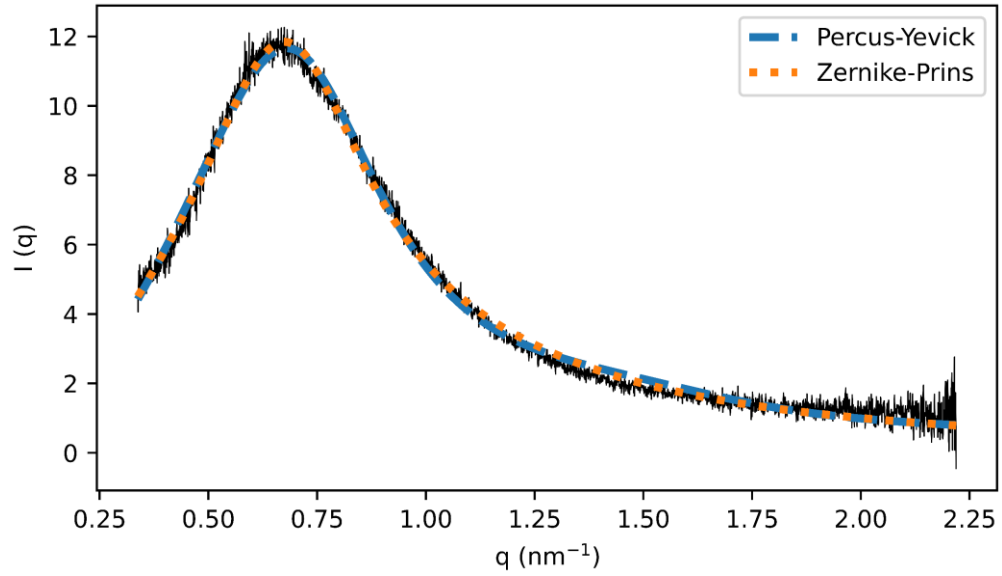

A6.44. FDCAHDO 2000 50 HDI

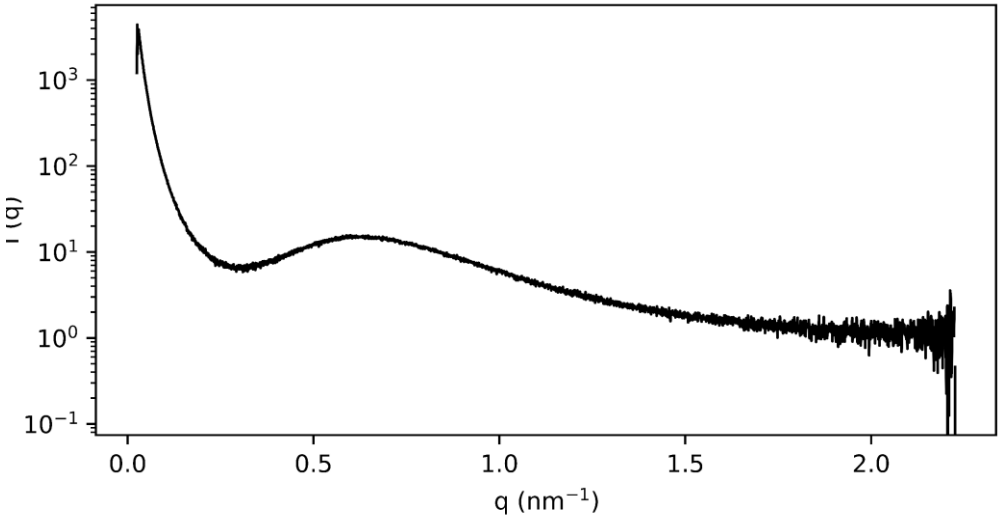

- Fitting

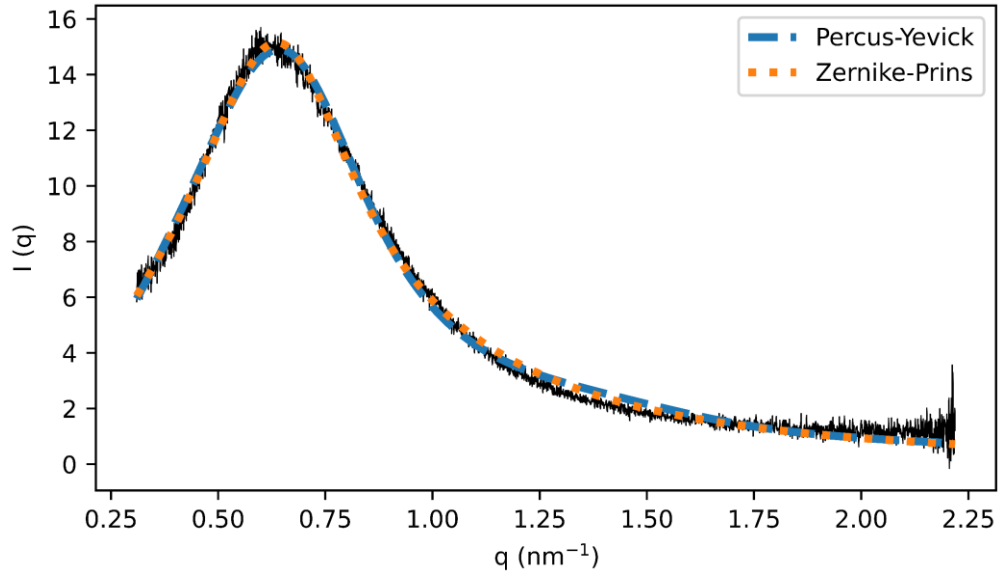

A7 WAXS of the unannealed TPUs

A7.1. IPHTAPDO 1000 10 MDI

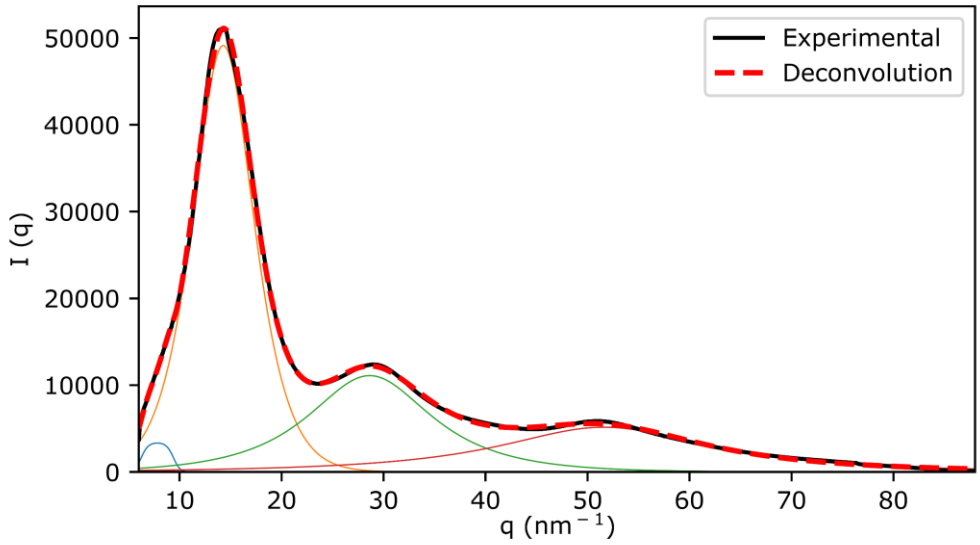

A7.2. IPHTAPDO 1000 30 MDI

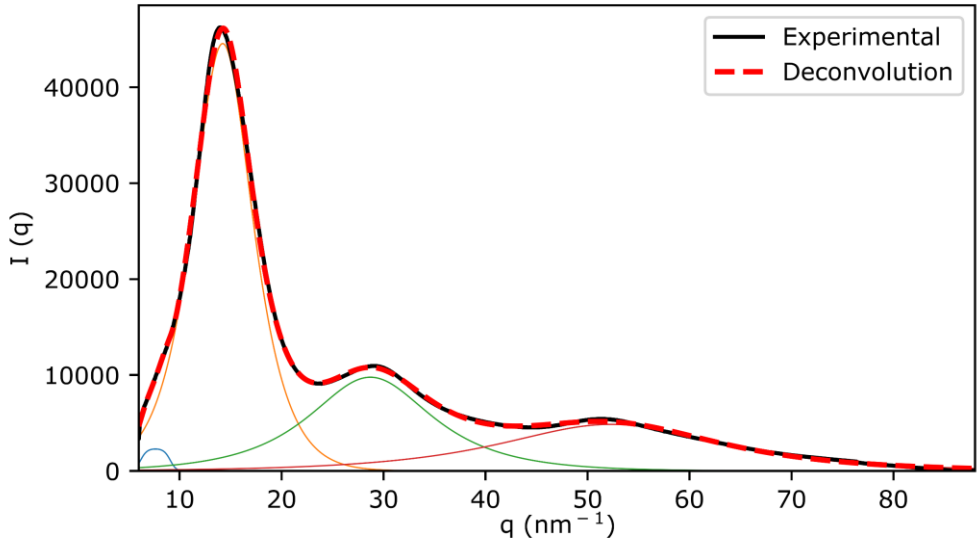

A7.3. IPHTAPDO 1000 50 MDI

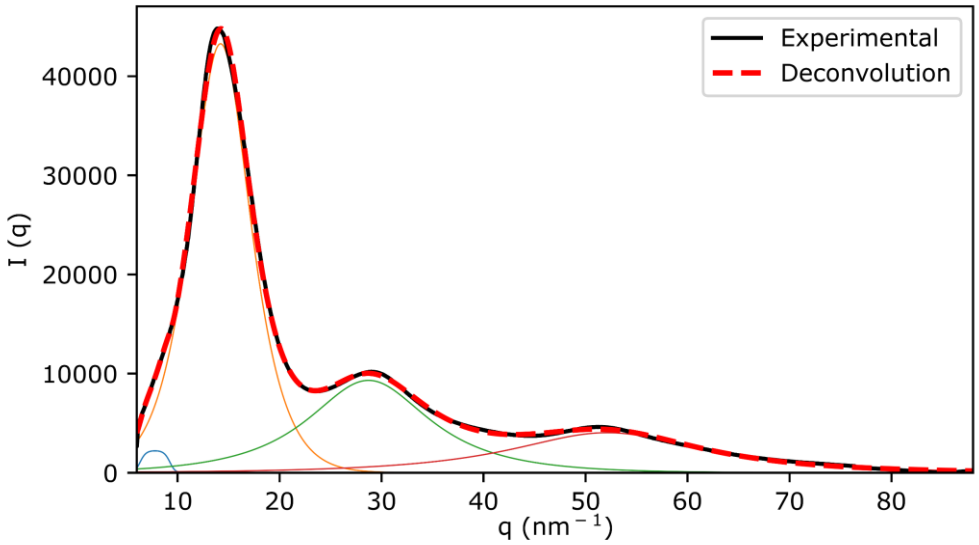

A7.4. IPHTAPDO 2000 10 MDI

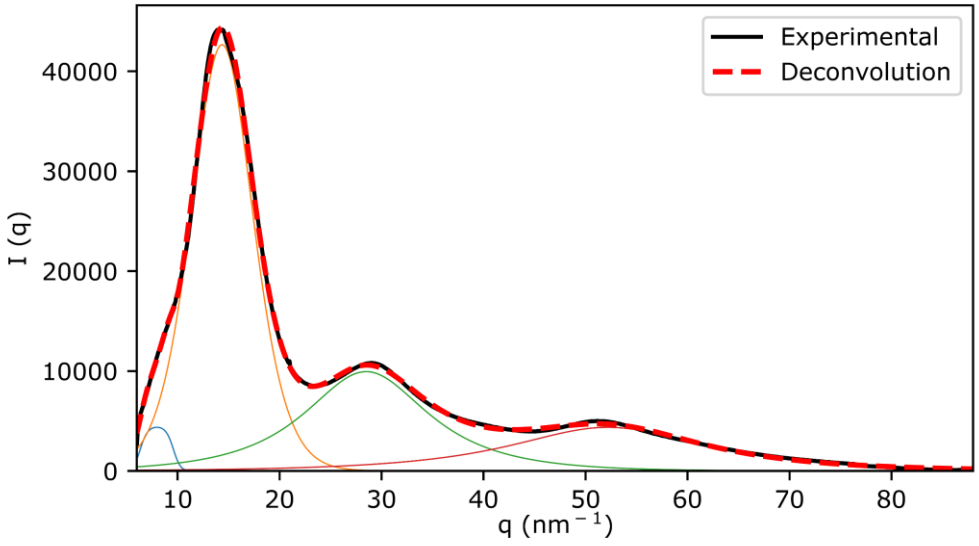

A7.5. IPHTAPDO 2000 30 MDI

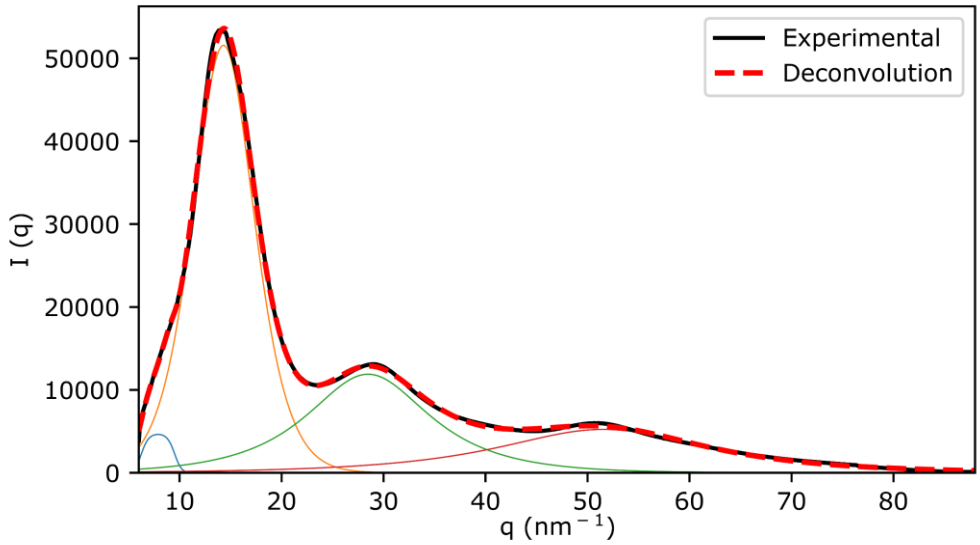

A7.6. IPHTAPDO 2000 50 MDI

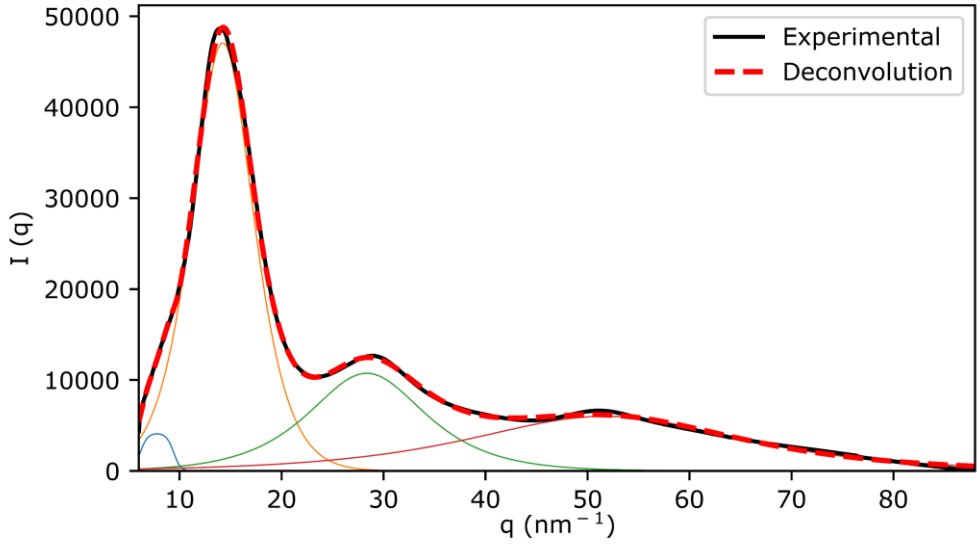

A7.7. IPHTAHDO 1000 10 MDI

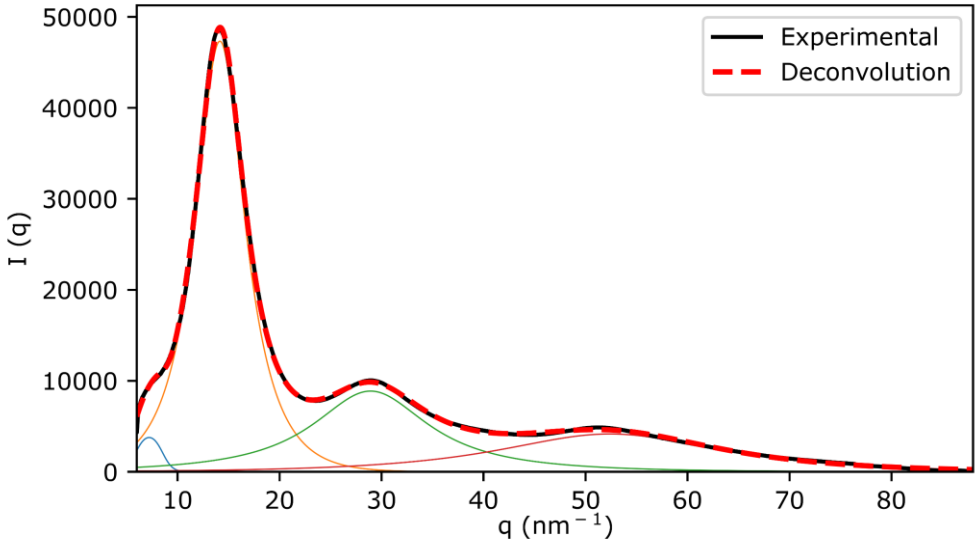

A7.8. IPHTAHDO 1000 30 MDI

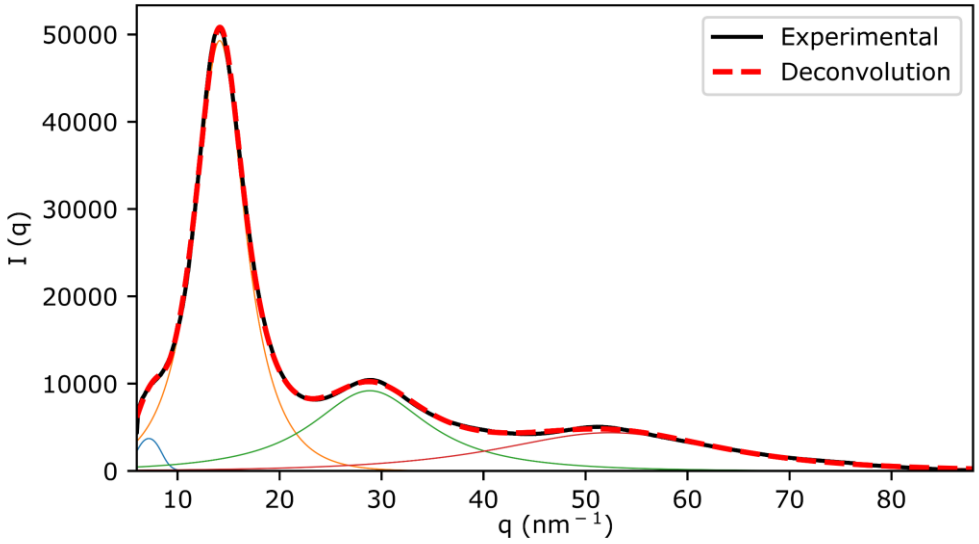

A7.9. IPHTAHDO 1000 50 MDI

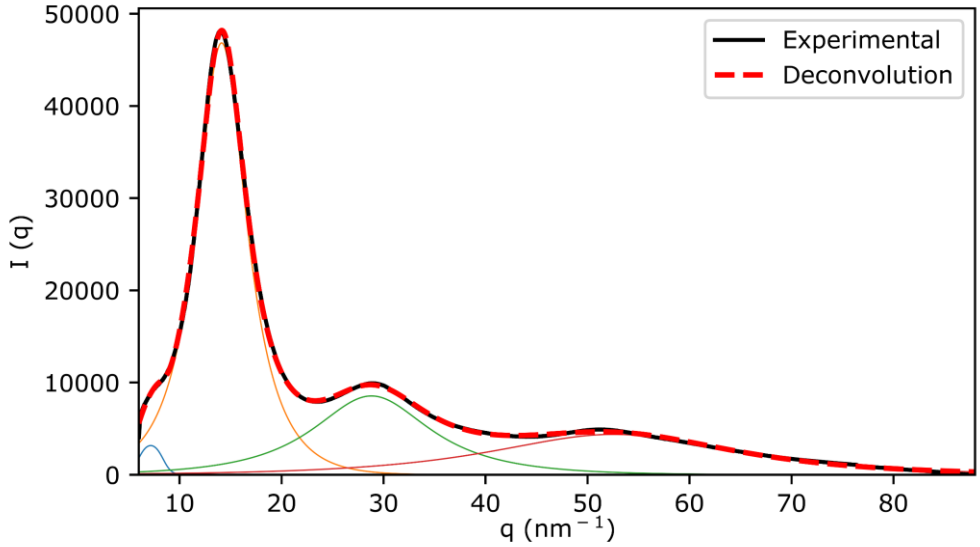

A7.10. IPHTAHDO 2000 10 MDI

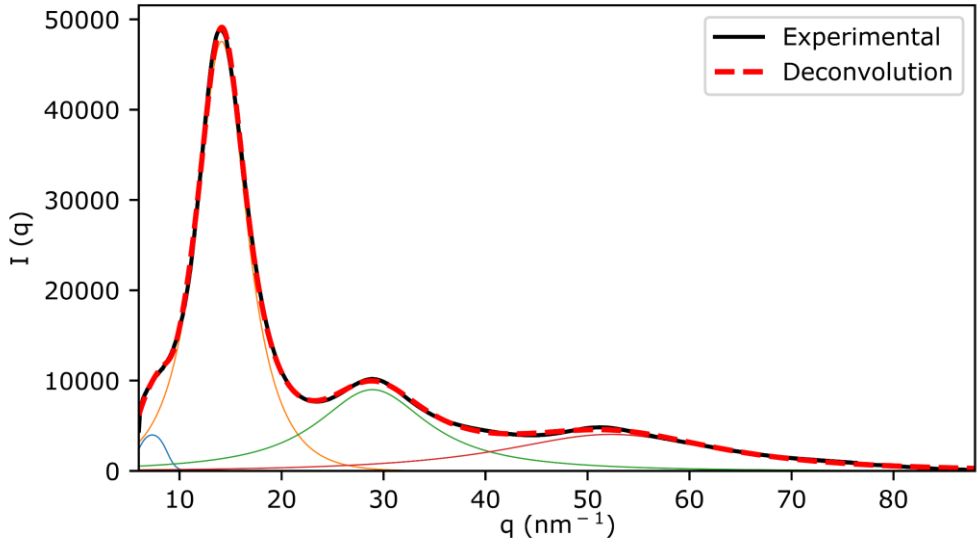

A7.11. IPHTAHDO 2000 30 MDI

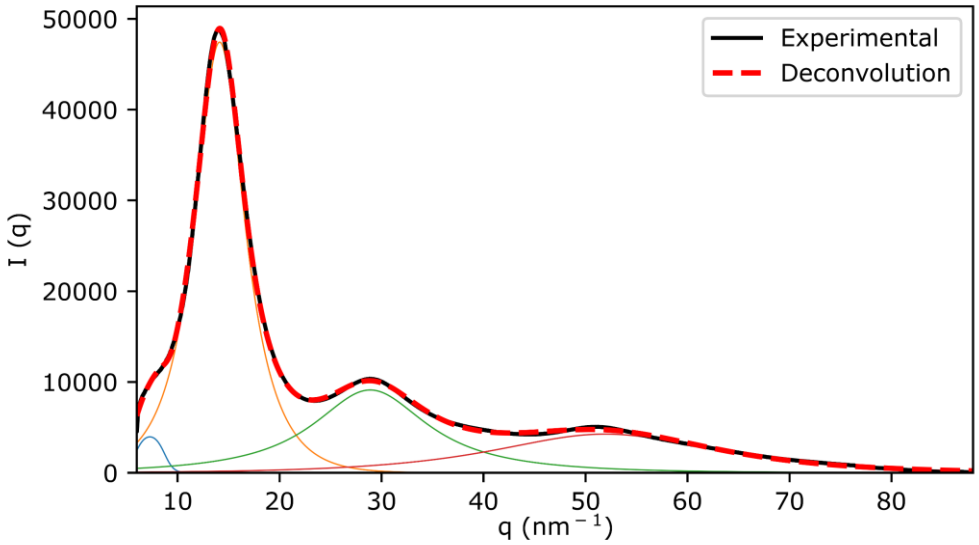

A7.12. IPHTAHDO 2000 50 MDI

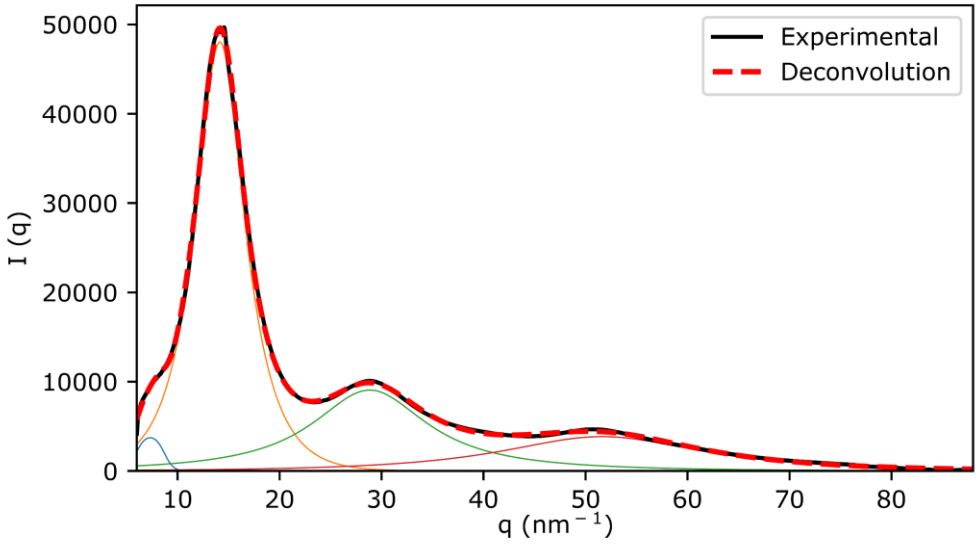

A7.13. IPHTAPDO 1000 10 HDI

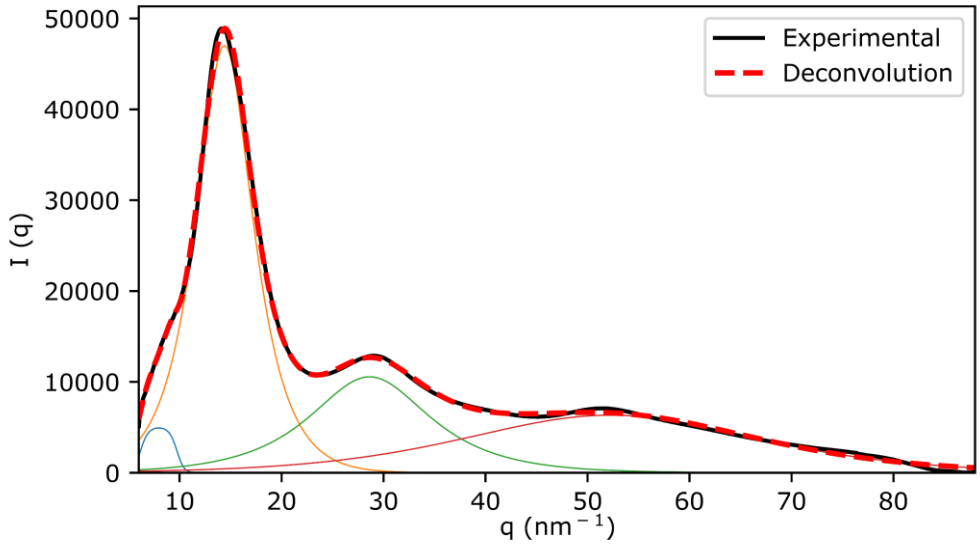

A7.14. IPHTAPDO 1000 30 HDI

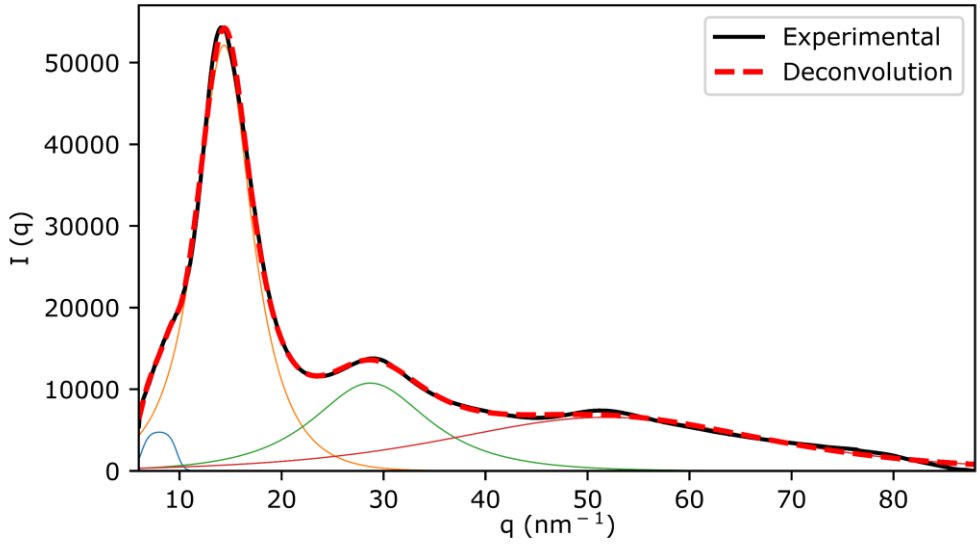

A7.15. IPHTAPDO 1000 50 HDI

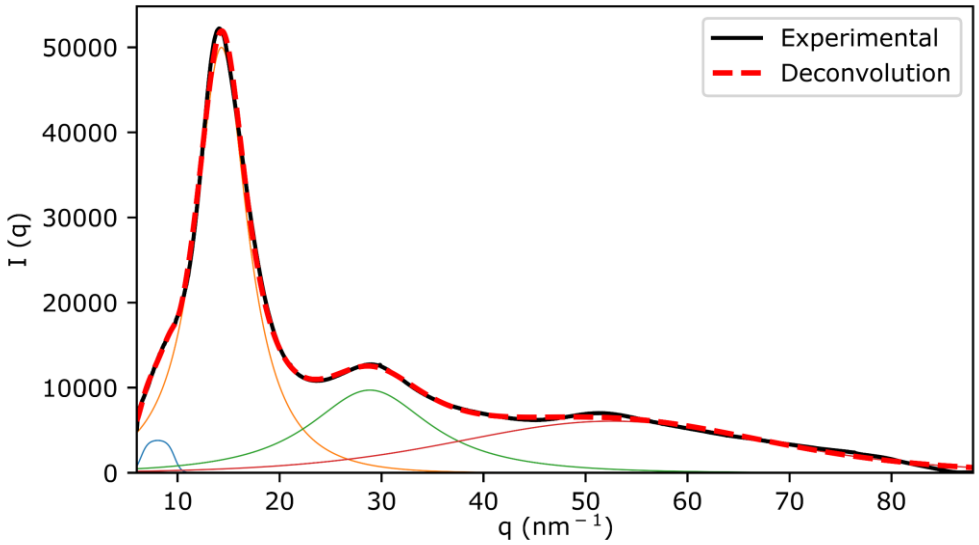

A7.16. IPHTAPDO 2000 10 HDI

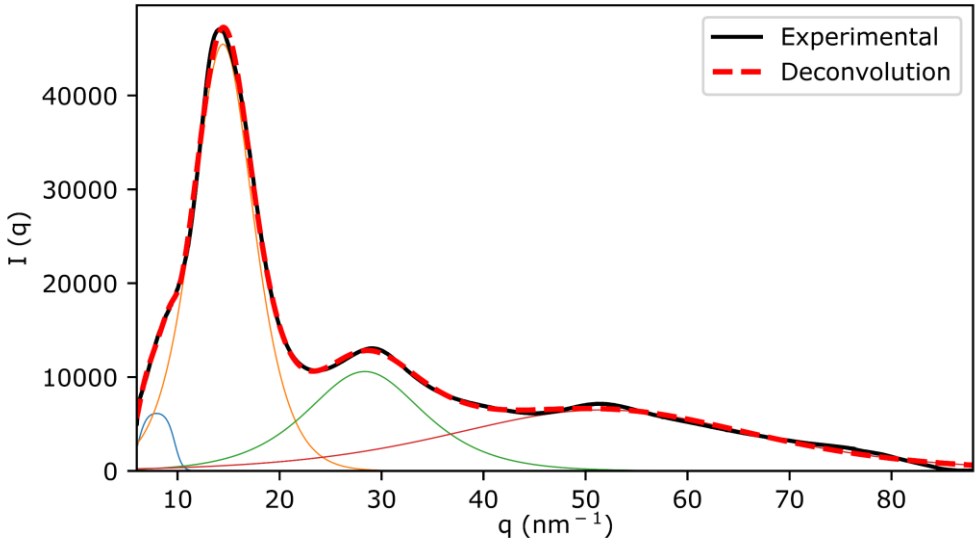

A7.17. IPHTAPDO 2000 30 HDI

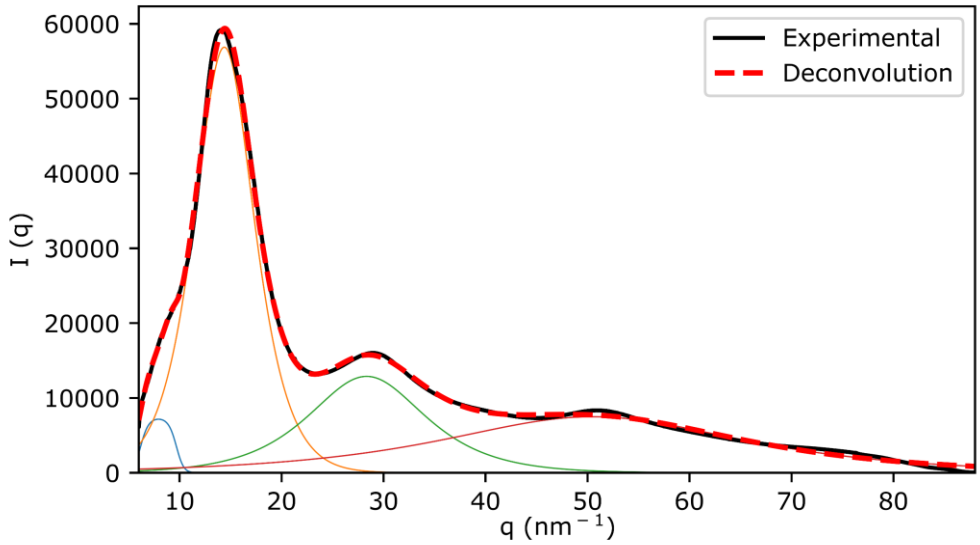

A7.18. IPHTAPDO 2000 50 HDI

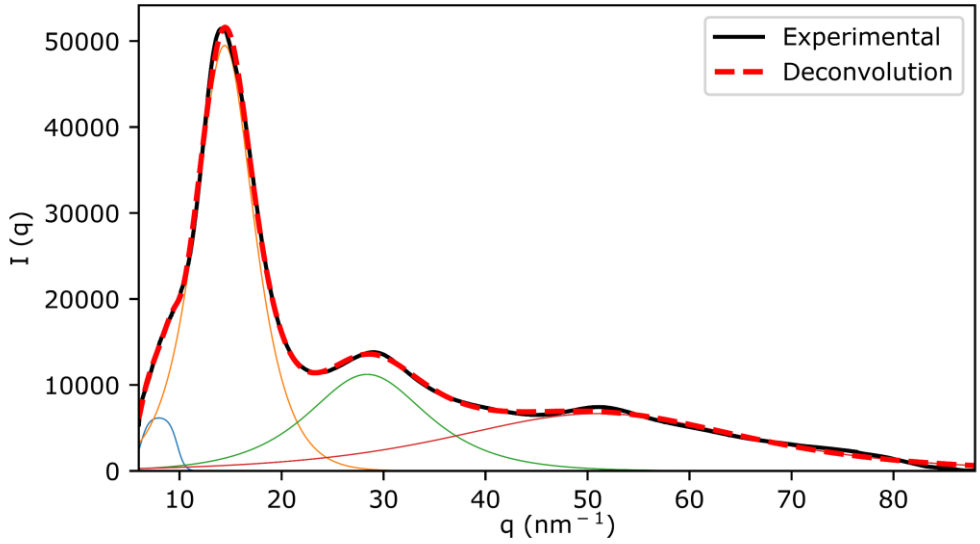

A7.19. IPHTAHDO 1000 10 HDI

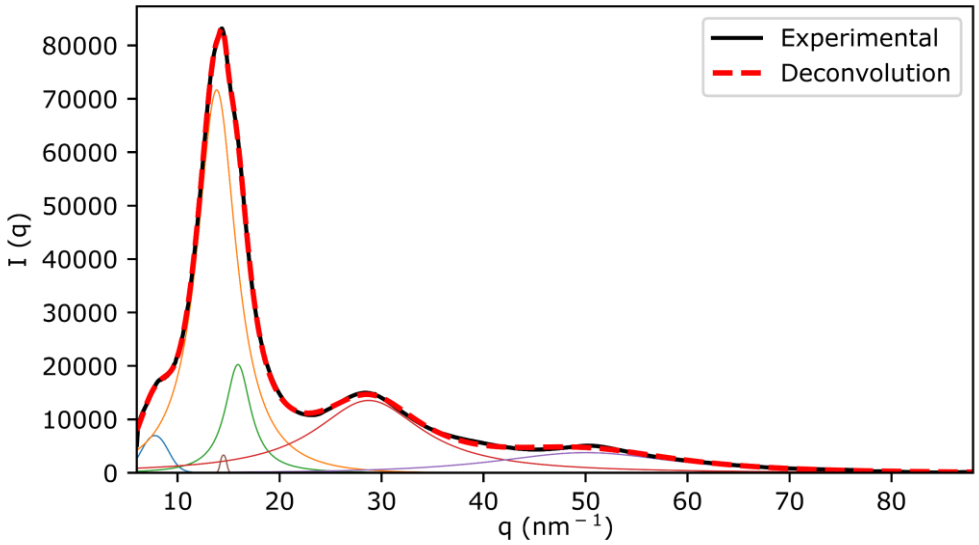

A7.20. IPHTAHDO 1000 30 HDI

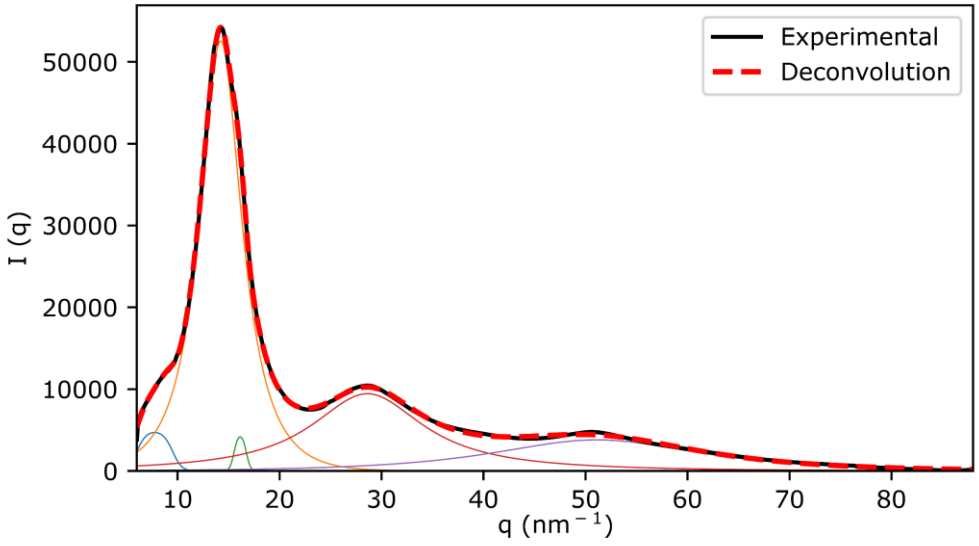

A7.21. IPHTAHDO 1000 50 HDI

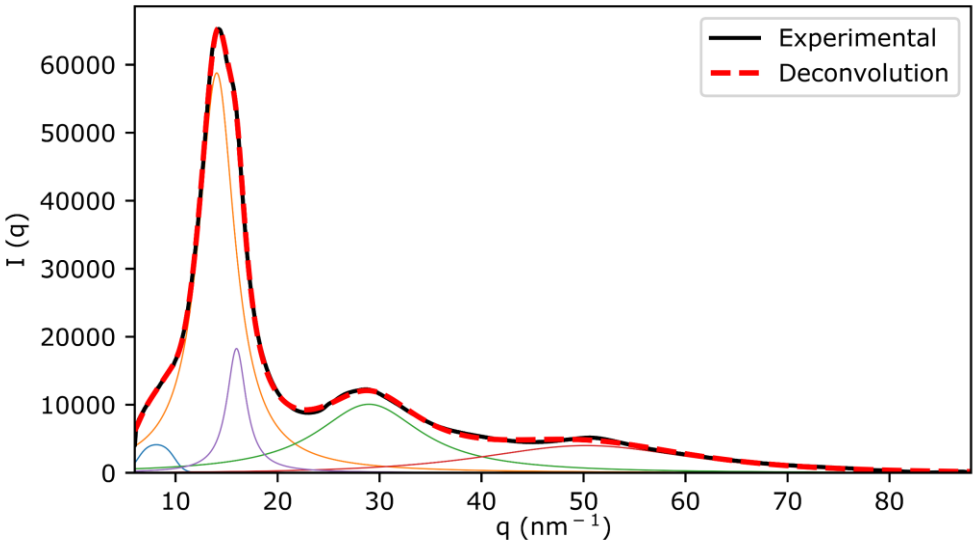

A7.22. IPHTAHDO 2000 10 HDI

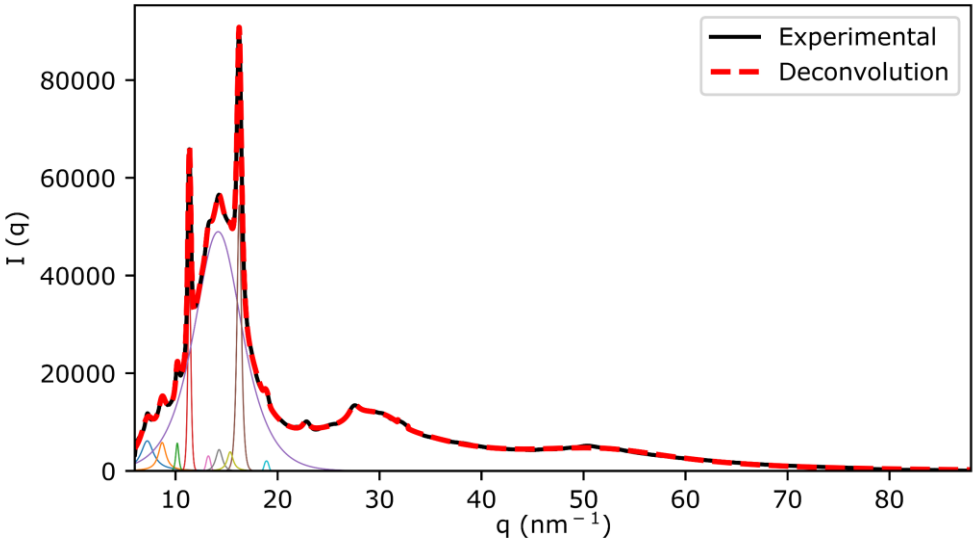

A7.23. IPHTAHDO 2000 30 HDI

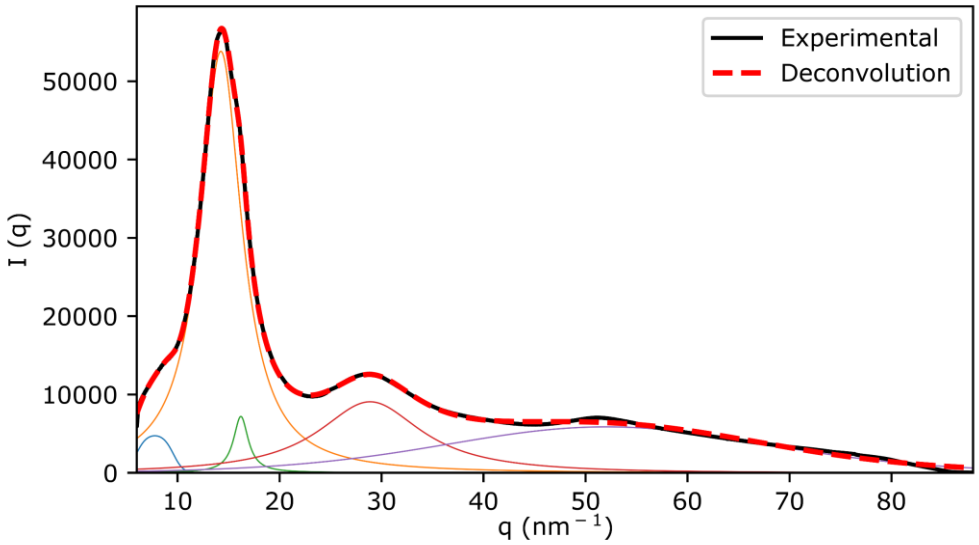

A7.24. IPHTAHDO 2000 50 HDI

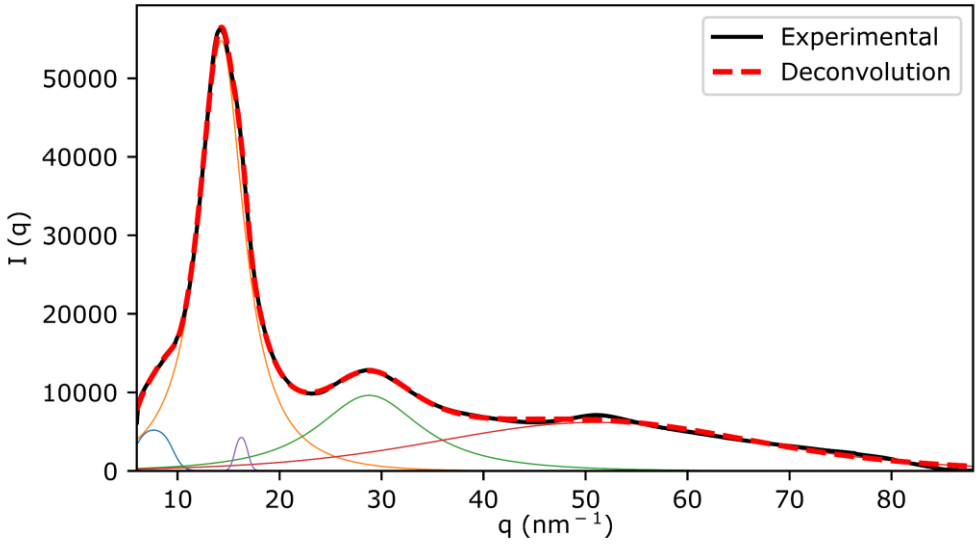

A7.25. FDCAPDO 1000 10 MDI

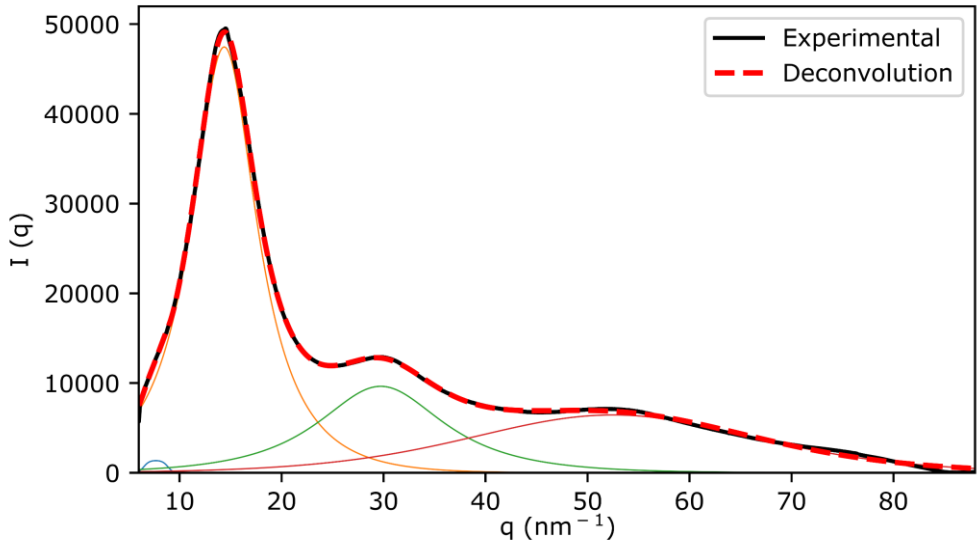

A7.26. FDCAPDO 1000 50 MDI

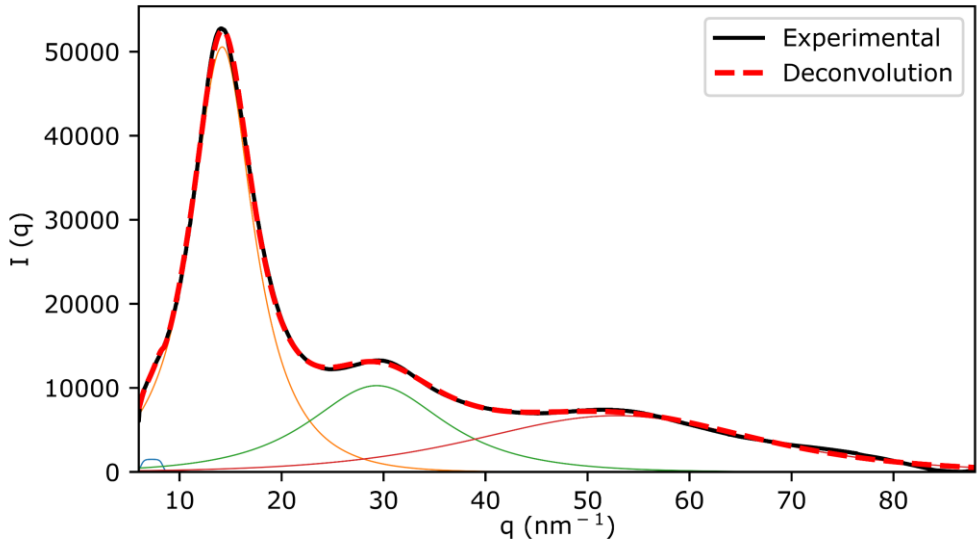

A7.27. FDCAPDO 1500 30 MDI

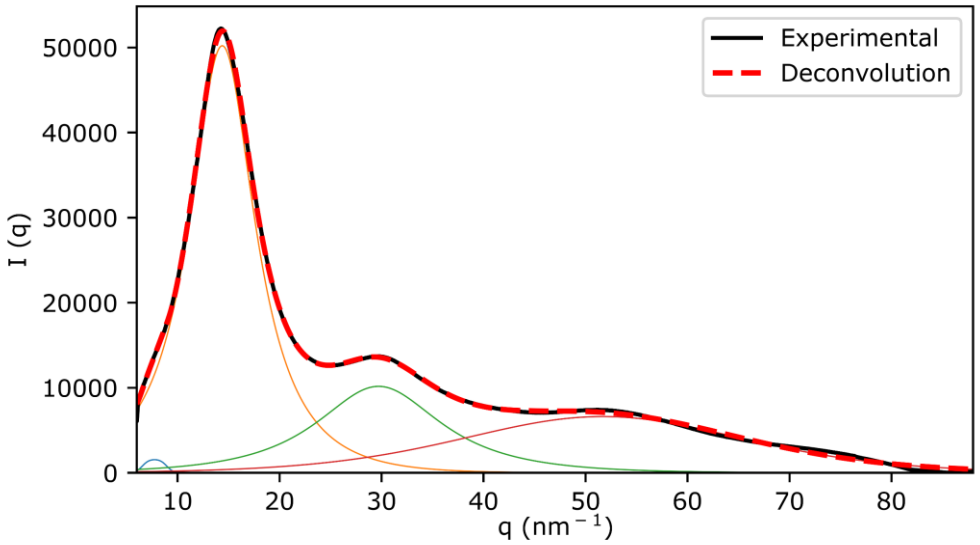

A7.28. FDCAPDO 2000 10 MDI

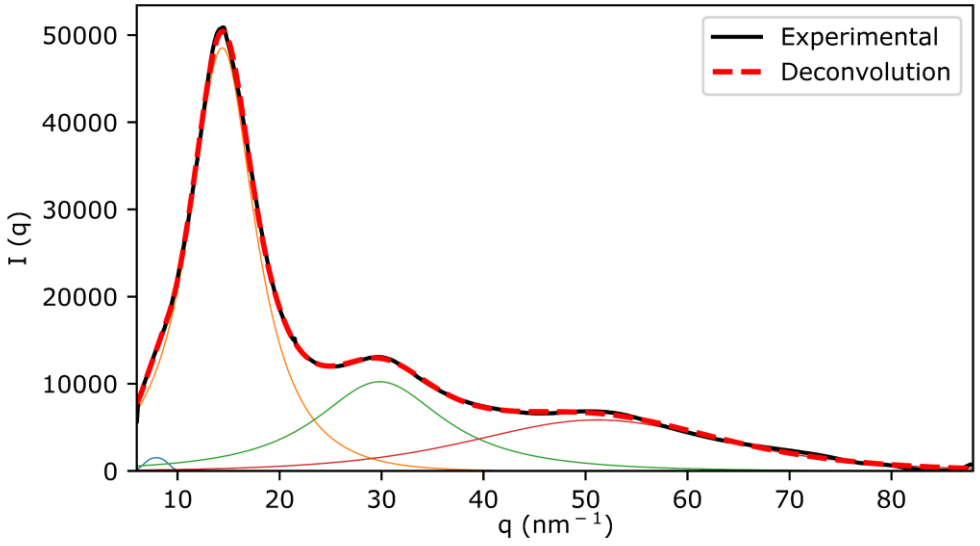

A7.29. FDCAPDO 2000 50 MDI

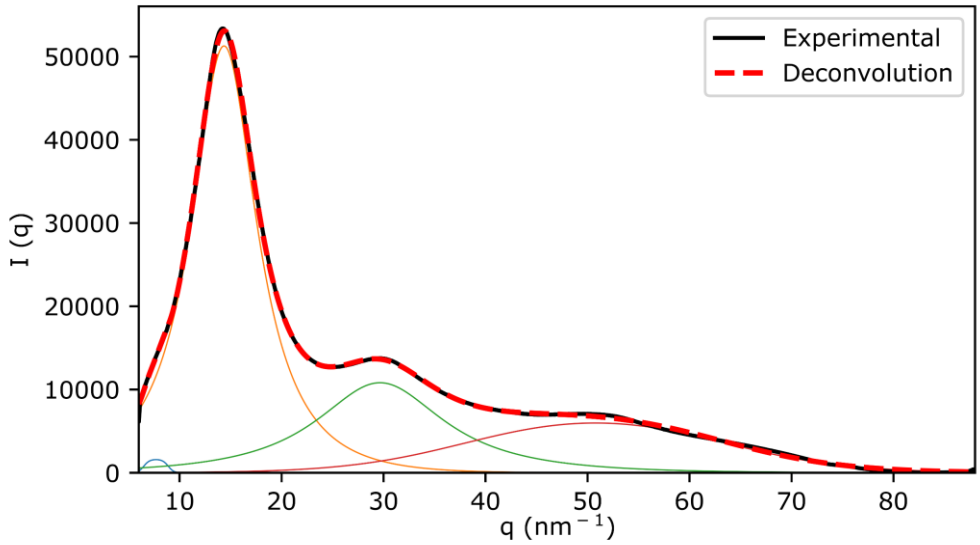

A7.30. FDCAHDO 1000 10 MDI

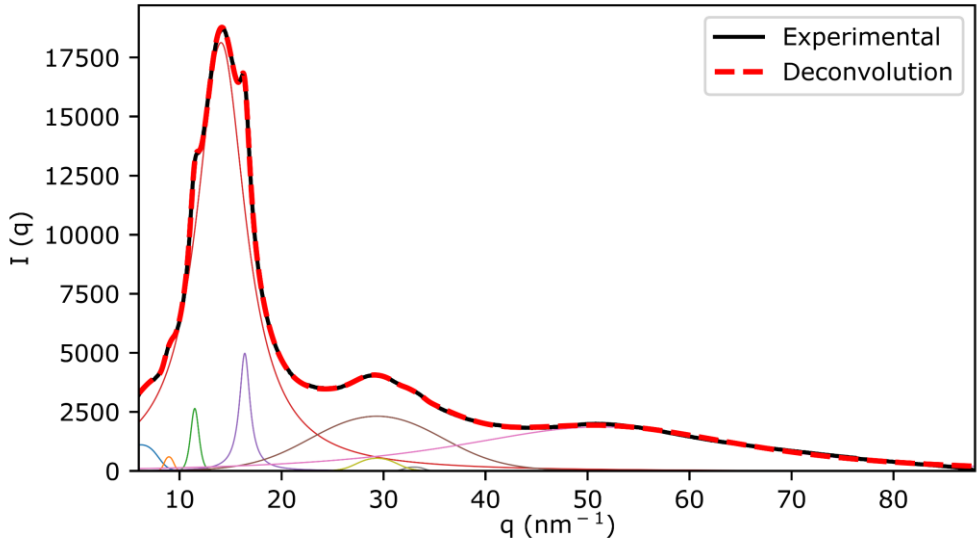

A7.31. FDCAHDO 1000 50 MDI

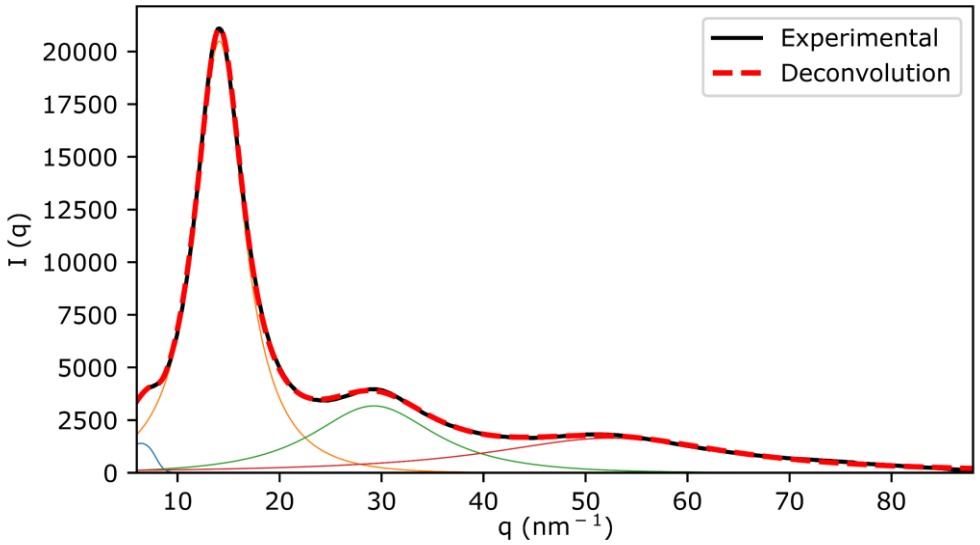

A7.32. FDCAHDO 1500 30 MDI

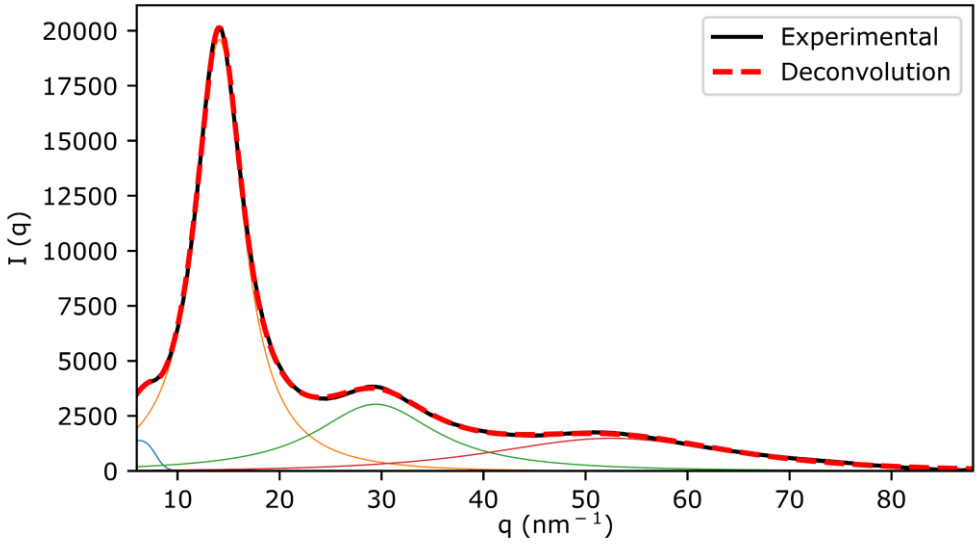

A7.33. FDCAHDO 2000 10 MDI

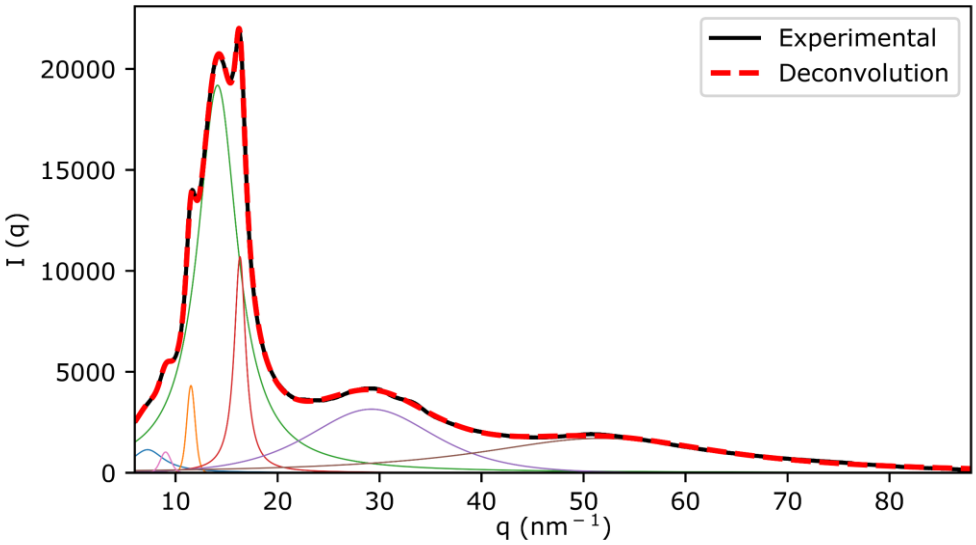

A7.34. FDCAHDO 2000 50 MDI

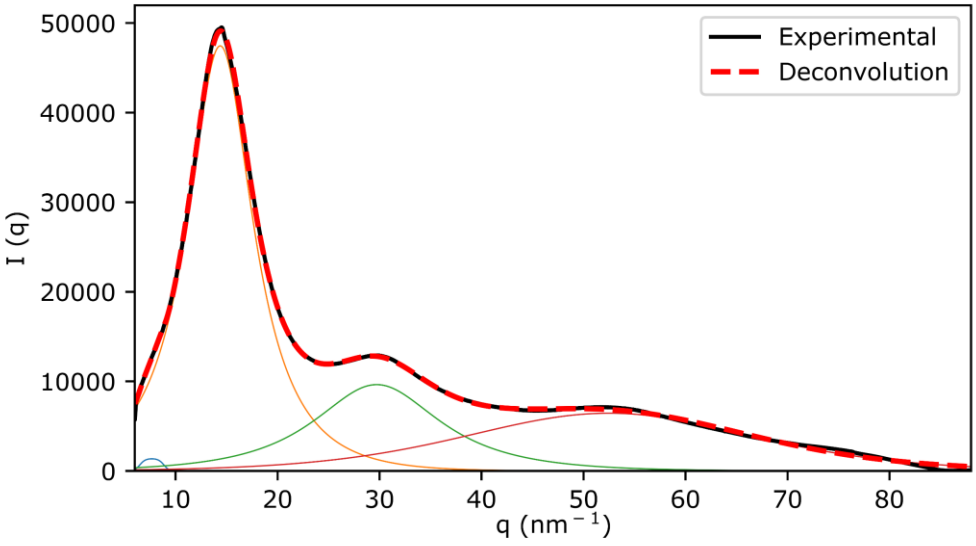

A7.35. FDCAPDO 1000 10 HDI

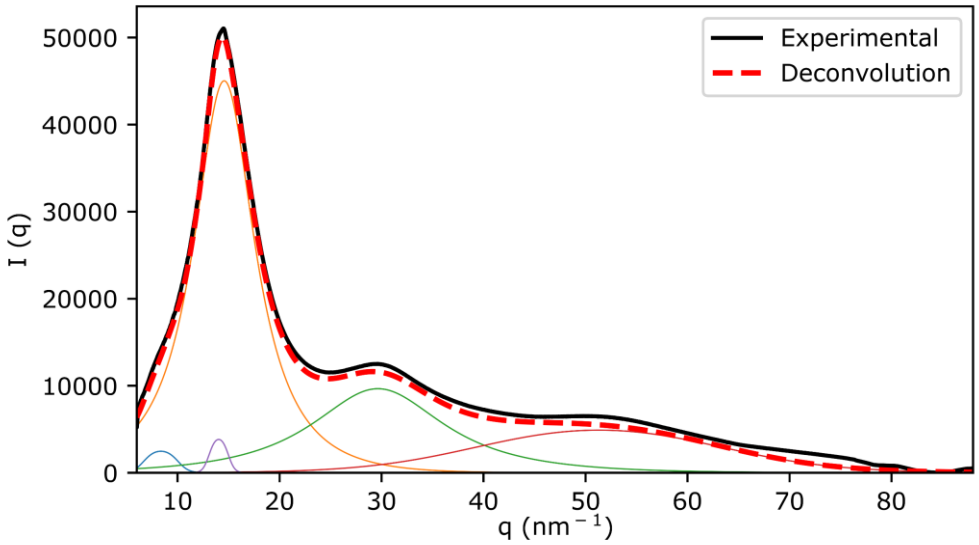

A7.36. FDCAPDO 1000 50 HDI

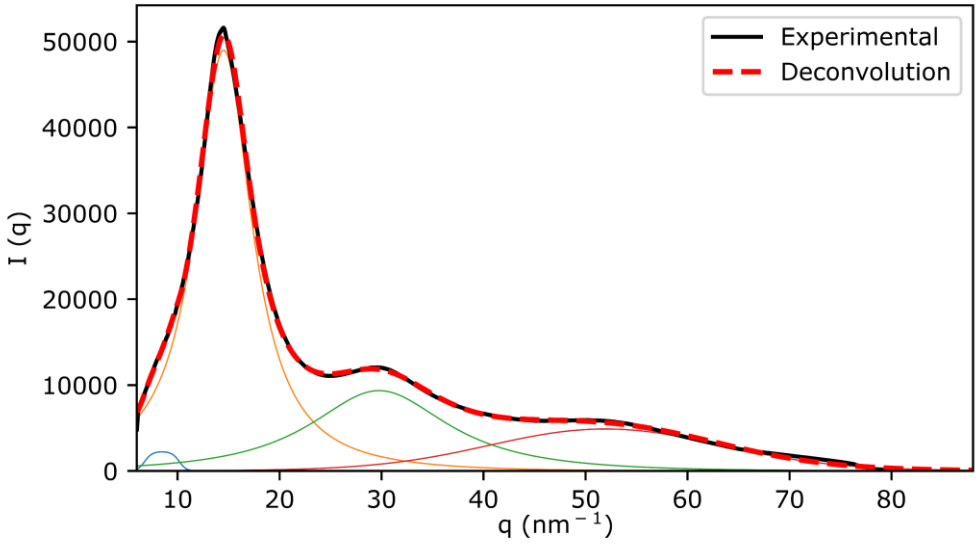

A7.37. FDCAPDO 1500 30 HDI

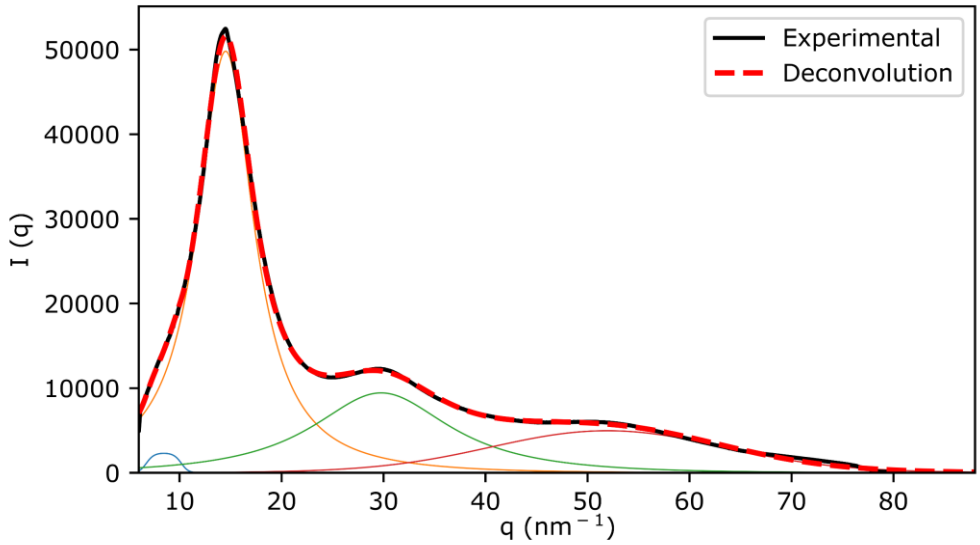

A7.38. FDCAPDO 2000 10 HDI

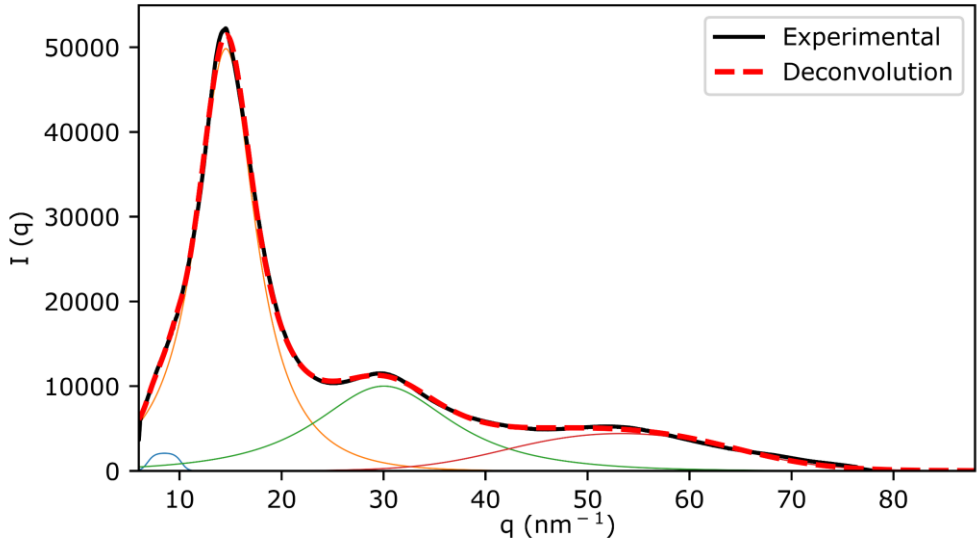

A7.39. FDCAPDO 2000 50 HDI

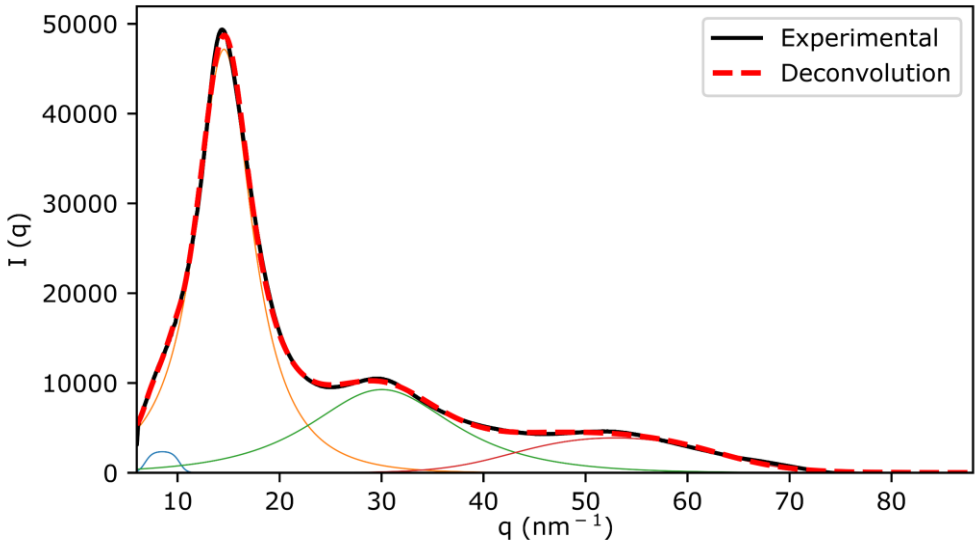

A7.40. FDCAHDO 1000 10 HDI

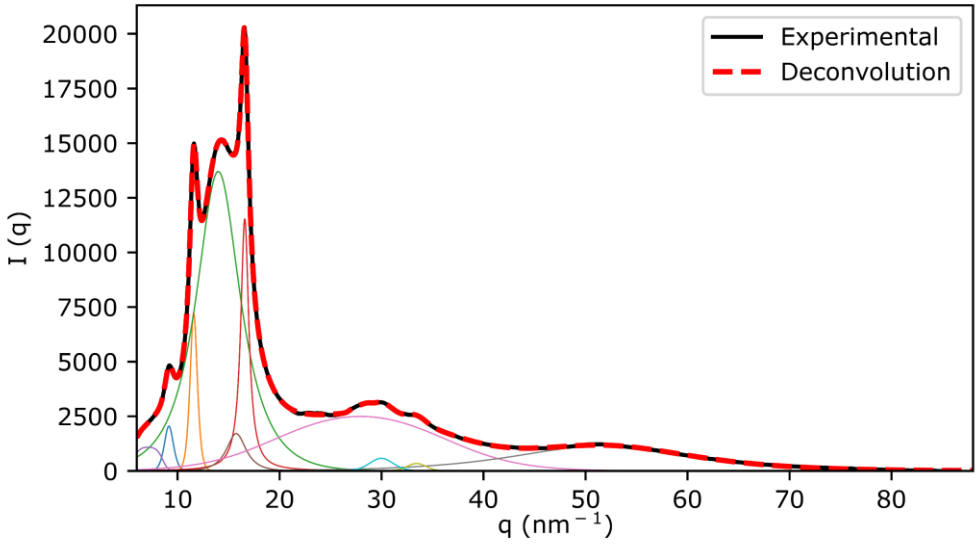

A7.41. FDCAHDO 1000 50 HDI

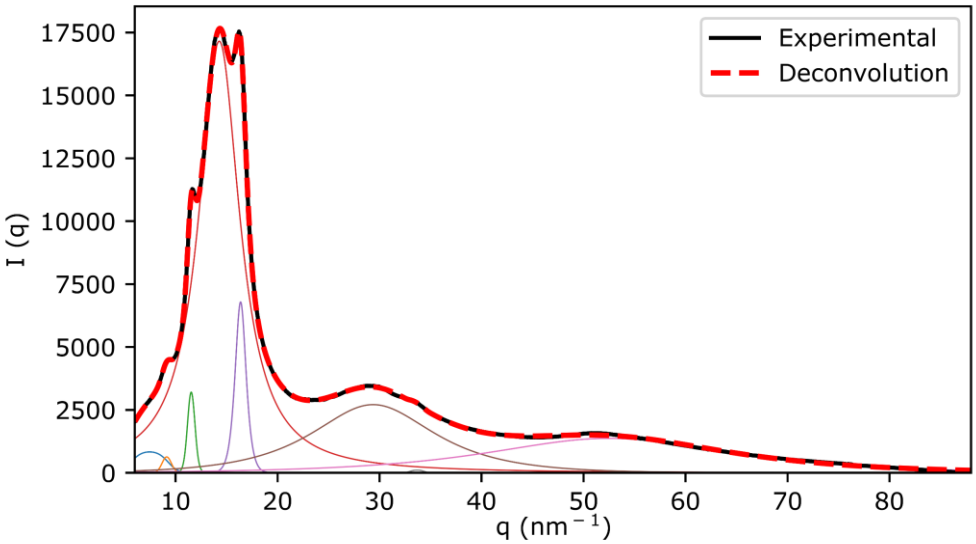

A7.42. FDCAHDO 1500 30 HDI

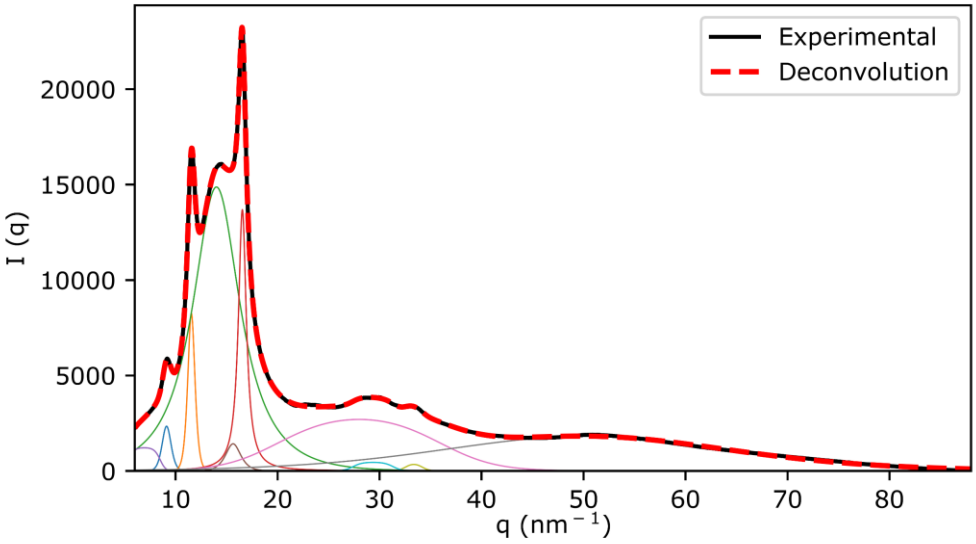

A7.43. FDCAHDO 2000 10 HDI

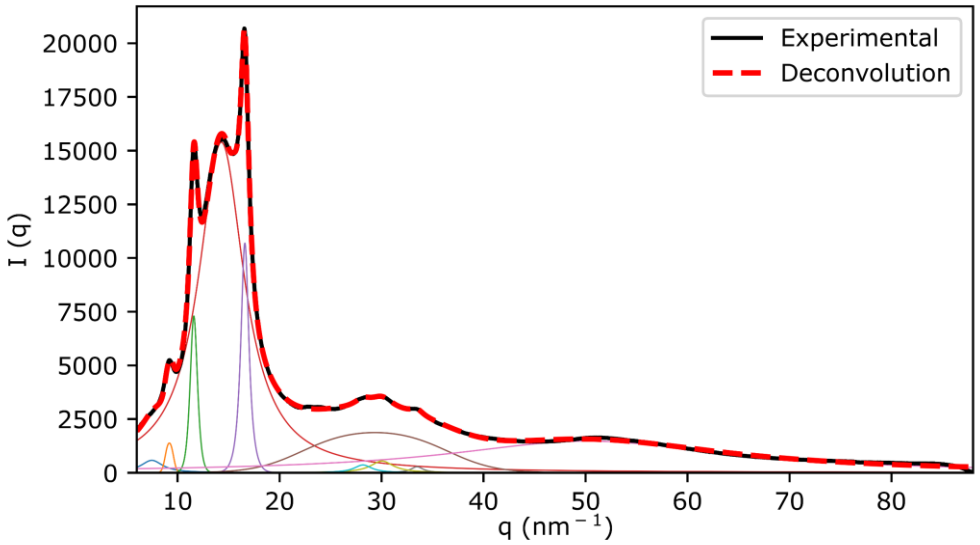

A7.44. FDCAHDO 2000 50 HDI

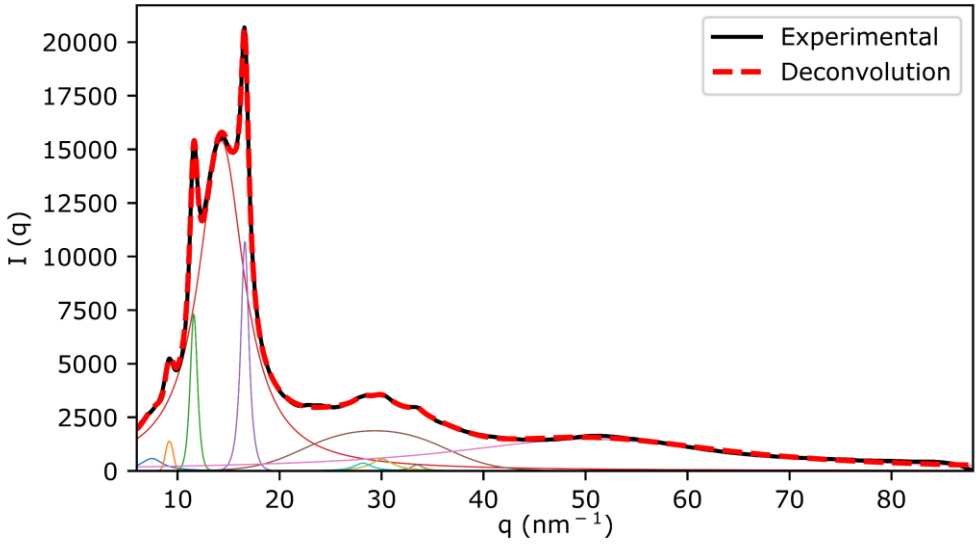

A8 Hardness

A8.1. IPHTA MDI TPUs

	Shore D hardness	St. dev.
IPHTAPDO 1000 10% MDI	80.7	0.8
IPHTAPDO 1000 30% MDI	80.8	0.8
IPHTAPDO 1000 50% MDI	77.1	2.5
IPHTAPDO 2000 10% MDI	80.7	0.5
IPHTAPDO 2000 30% MDI	85.5	4.3
IPHTAPDO 2000 50% MDI	79.7	2.3
IPHTAHDO 1000 10% MDI	70.2	1.1
IPHTAHDO 1000 30% MDI	73.8	1.5
IPHTAHDO 1000 50% MDI	75.0	4.2
IPHTAHDO 2000 10% MDI	32.5	2.3
IPHTAHDO 2000 30% MDI	38.8	3.0
IPHTAHDO 2000 50% MDI	64.5	2.2

A8.2. IPHTA HDI TPUs

	Shore D hardness	St. dev.
IPHTAPDO 1000 10% HDI	80.7	0.8
IPHTAPDO 1000 30% HDI	80.9	0.8
IPHTAPDO 1000 50% HDI	72.0	0.1
IPHTAPDO 2000 10% HDI	75.4	1.0
IPHTAPDO 2000 30% HDI	73.7	2.6
IPHTAPDO 2000 50% HDI	71.8	1.1
IPHTAHDO 1000 10% HDI	31.9	1.5
IPHTAHDO 1000 30% HDI	36.1	1.0
IPHTAHDO 1000 50% HDI	44.7	0.4
IPHTAHDO 2000 10% HDI	32.5	2.3
IPHTAHDO 2000 30% HDI	38.8	3.0
IPHTAHDO 2000 50% HDI	39.4	1.3

A8.3. FDCA MDI TPUs

	Shore D hardness	St. dev.
FDCAPDO 1000 10% MDI	89.9	3.9
FDCAPDO 1000 50% MDI	91.4	4.7
FDCAPDO 1500 30% MDI	95.9	0.7
FDCAPDO 2000 10% MDI	95.1	1.5
FDCAPDO 2000 50% MDI	96.0	1.8
FDCAHDO 1000 10% MDI	95.6	0.7
FDCAHDO 1000 50% MDI	93.3	1.6
FDCAHDO 1500 30% MDI	96.1	1.0
FDCAHDO 2000 10% MDI	94.6	1.6
FDCAHDO 2000 50% MDI	96.0	0.6

A8.4. FDCA HDI TPUs

	Density (g/mL)	St. dev.
FDCAPDO 1000 10% HDI	92.7	3.9
FDCAPDO 1000 50% HDI	93.3	5.7
FDCAPDO 1500 30% HDI	94.4	1.9
FDCAPDO 2000 10% HDI	95.1	0.8
FDCAPDO 2000 50% HDI	93.3	3.4
FDCAHDO 1000 10% HDI	61.0	0.9
FDCAHDO 1000 50% HDI	62.0	1.1
FDCAHDO 1500 30% HDI	65.0	0.8
FDCAHDO 2000 10% HDI	66.0	0.9
FDCAHDO 2000 50% HDI	62.7	1.8

A9 Tensile testing

A9.1. IPHTAPDO 1000 10 MDI

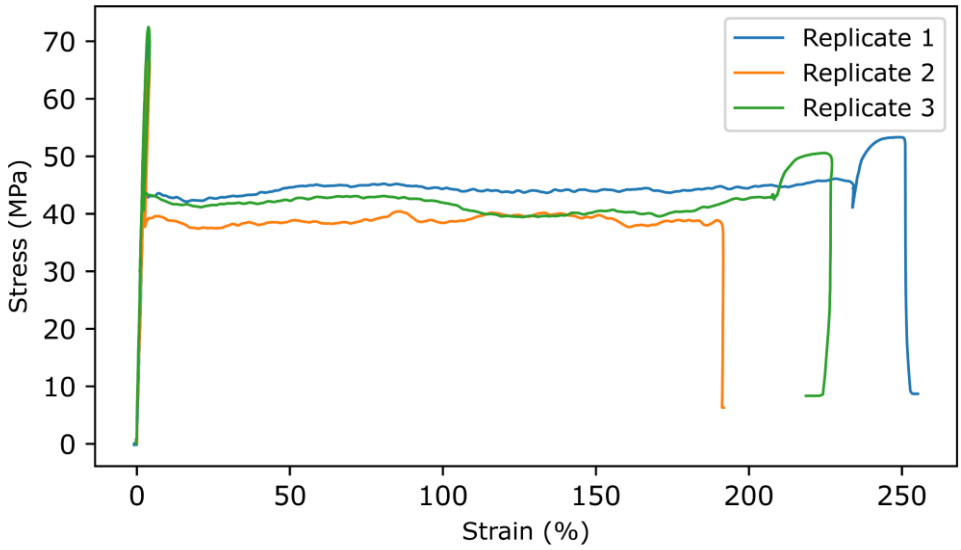

A9.2. IPHTAPDO 1000 30 MDI

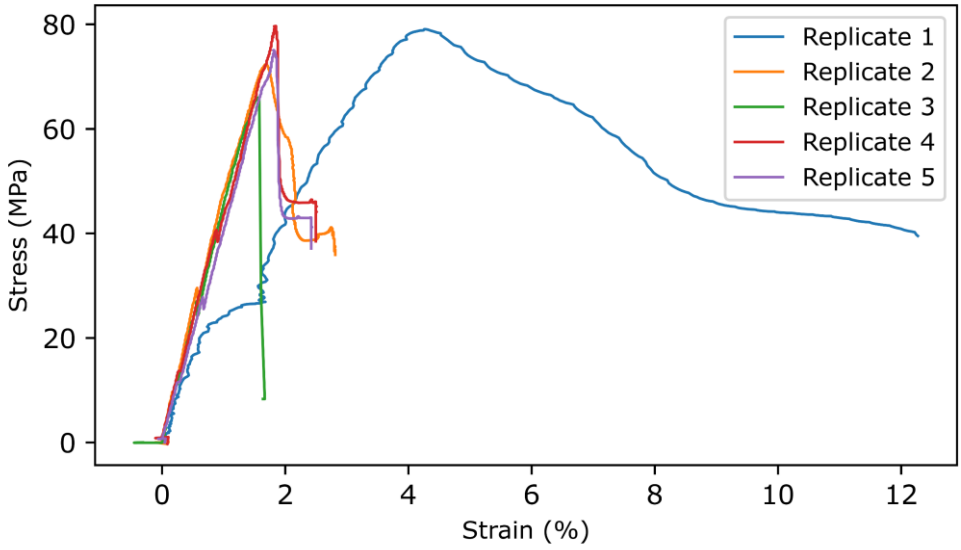

A9.3. IPHTAPDO 1000 50 MDI

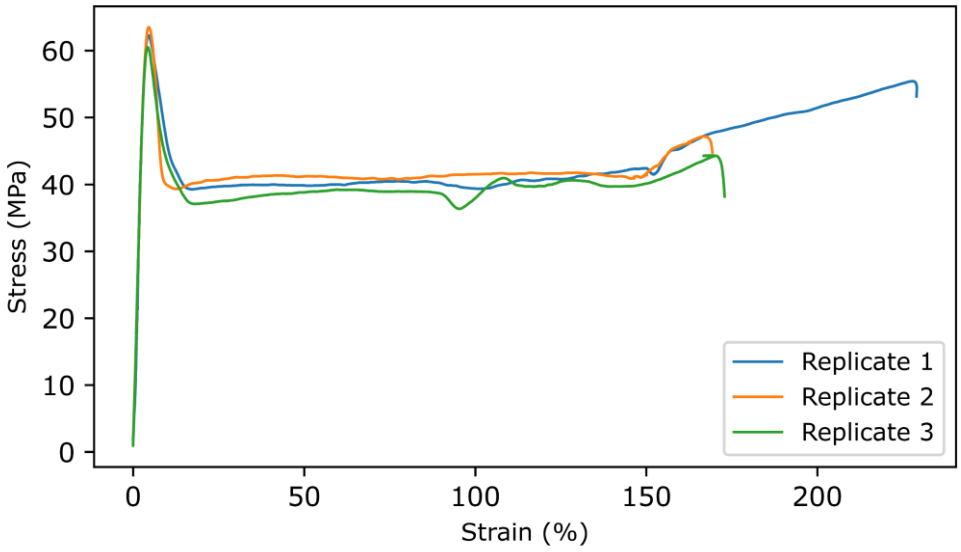

A9.4. IPHTAPDO 2000 10 MDI

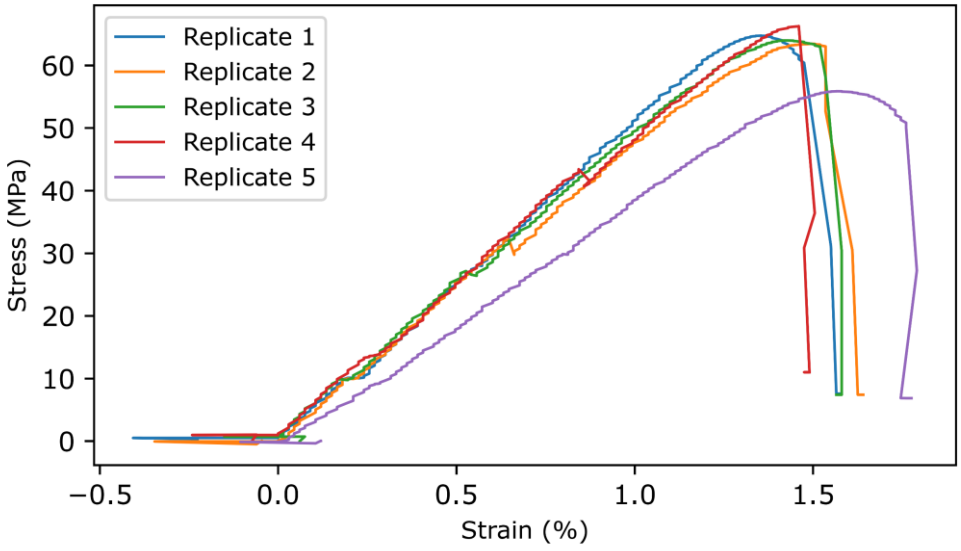

A9.5. IPHTAPDO 2000 30 MDI

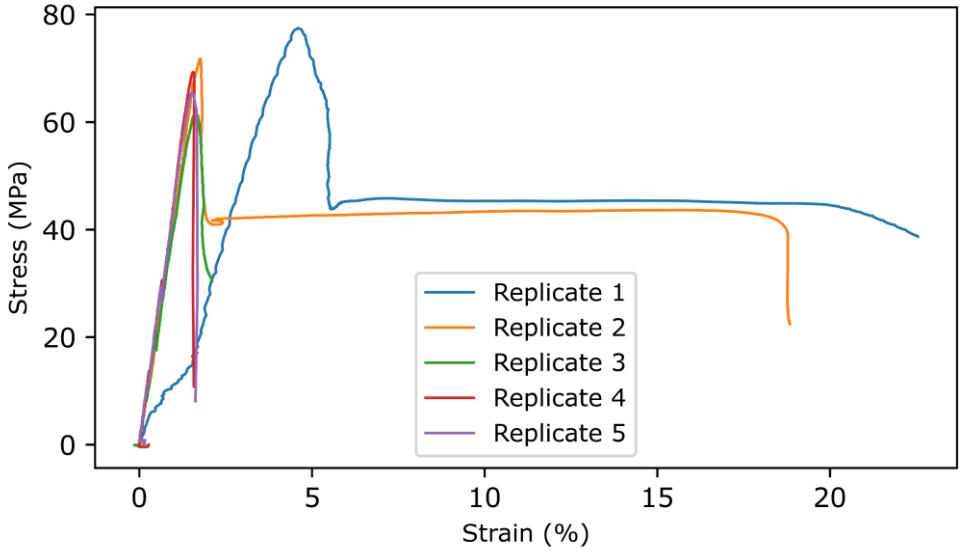

A9.6. IPHTAPDO 2000 50 MDI

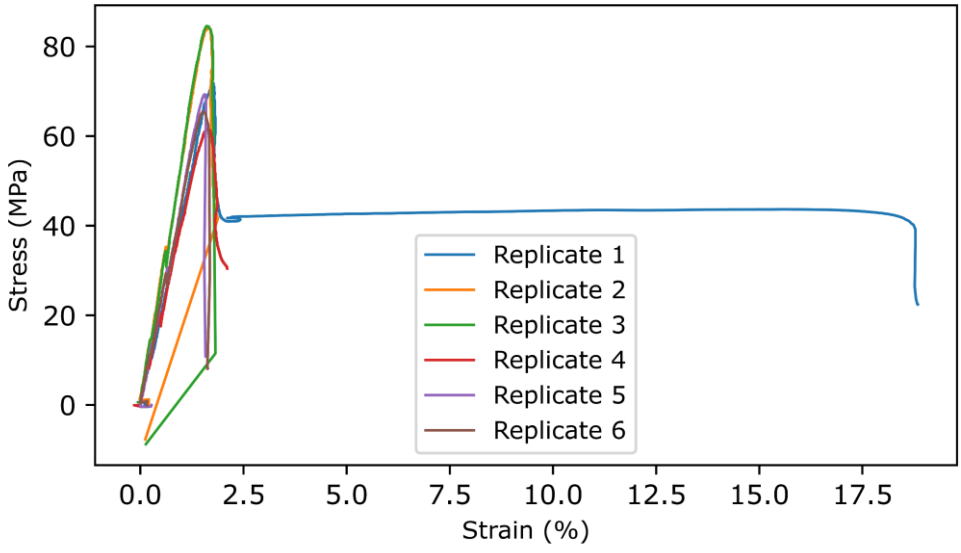

A9.7. IPHTAHDO 1000 10 MDI

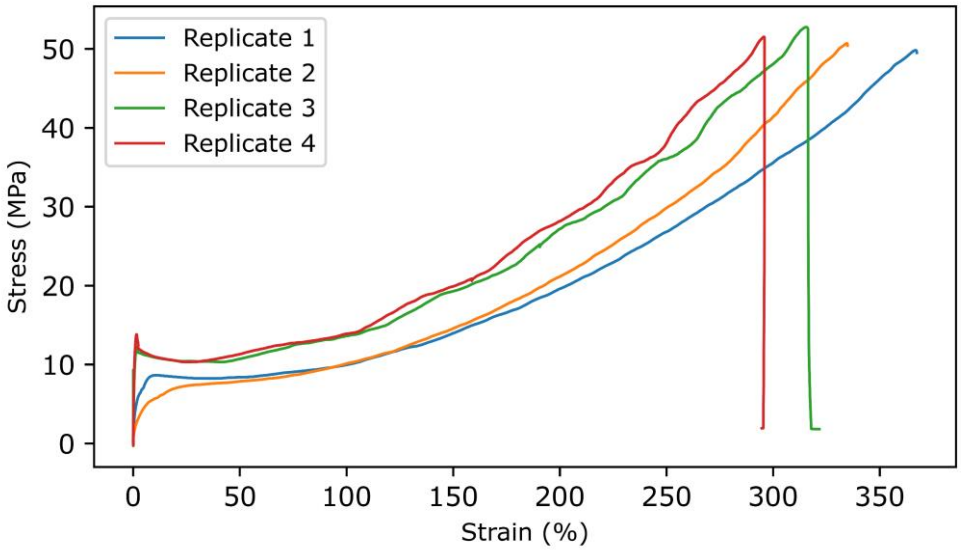

A9.8. IPHTAHDO 1000 30 MDI

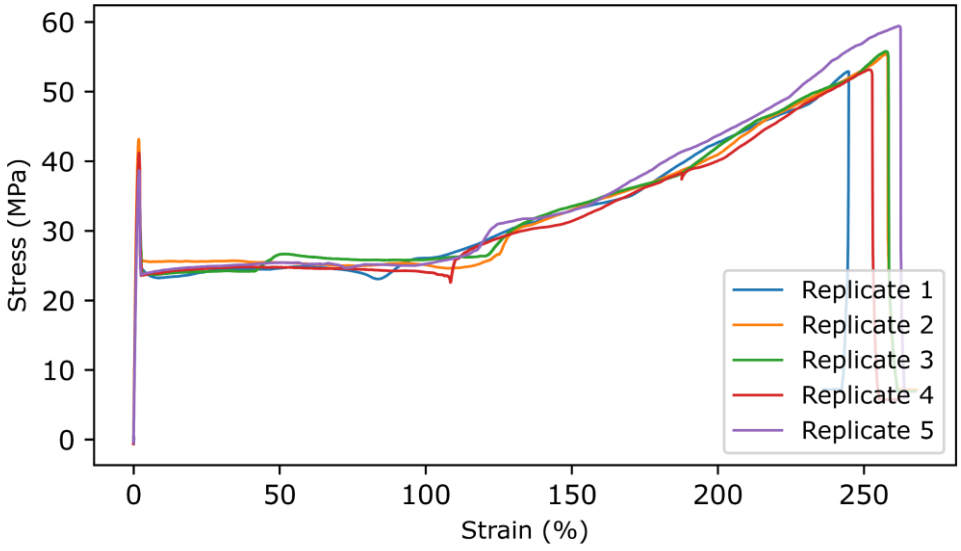

A9.9. IPHTAHDO 1000 50 MDI

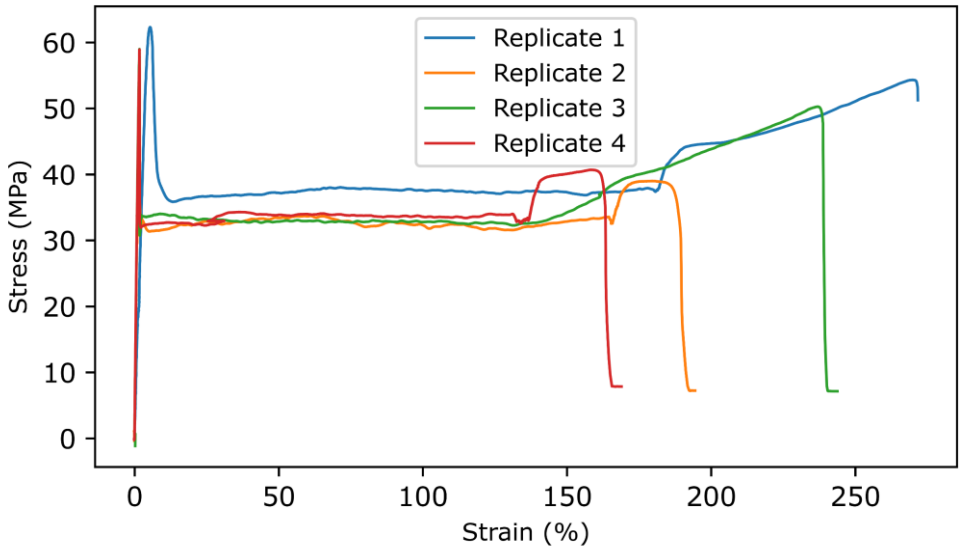

A9.10. IPHTAHDO 2000 10 MDI

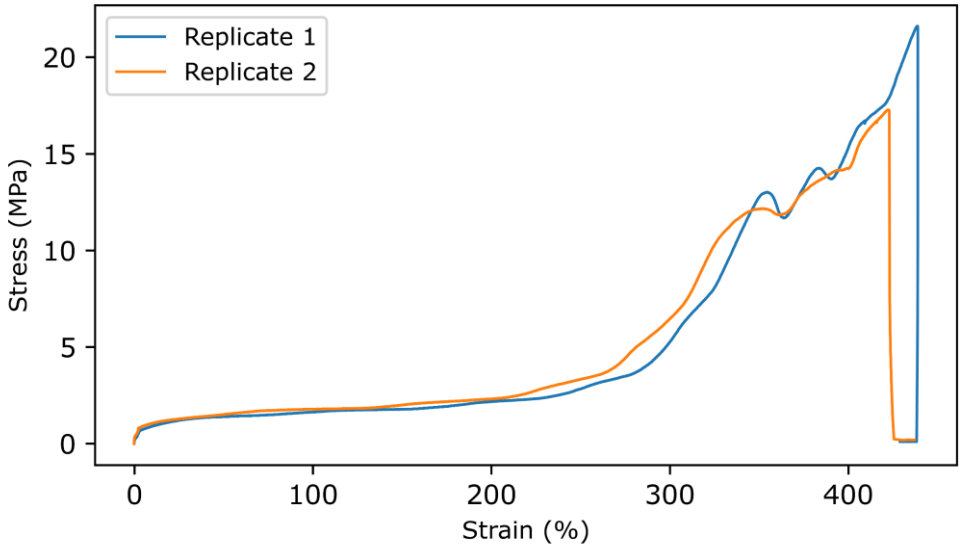

A9.11. IPHTAHDO 2000 30 MDI

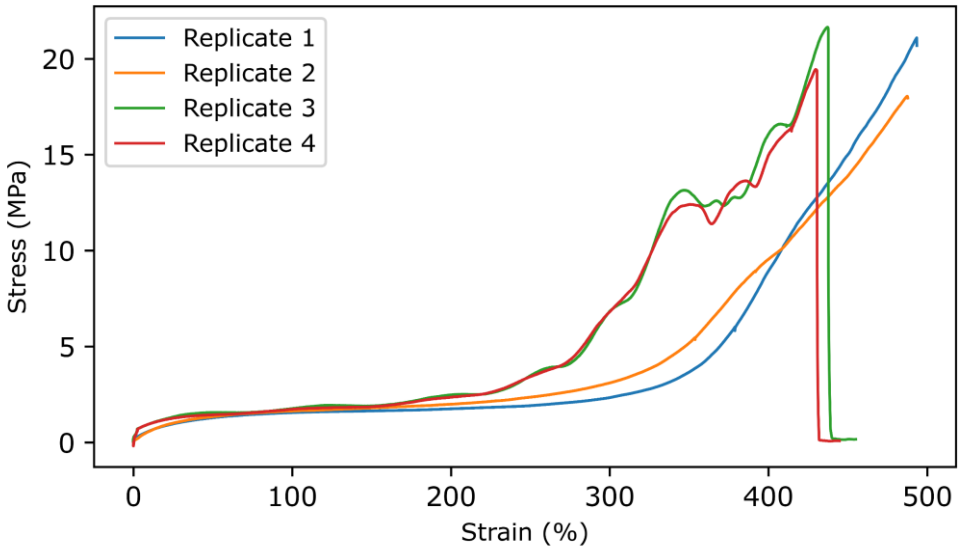

A9.12. IPHTAHDO 2000 50 MDI

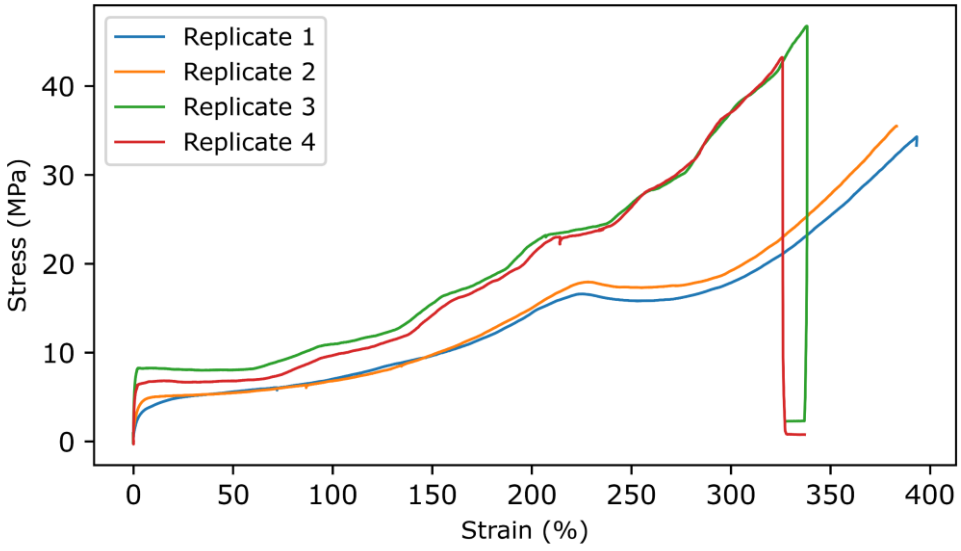

A9.13. IPHTAPDO 1000 10 HDI

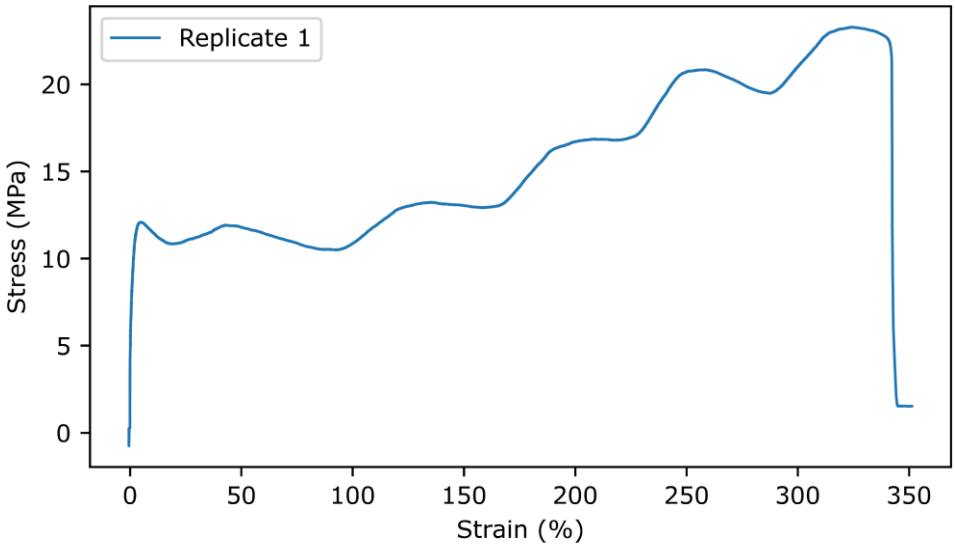

A9.14. IPHTAPDO 1000 30 HDI

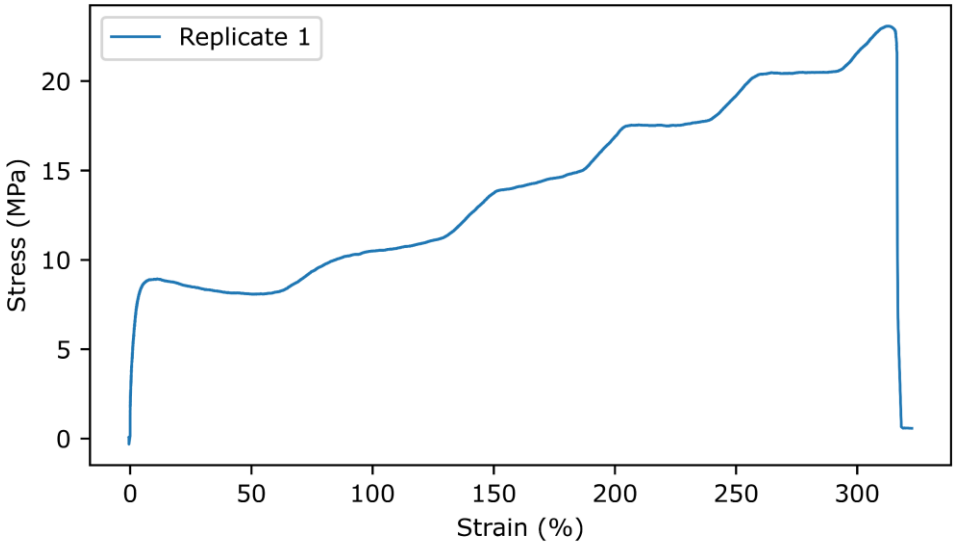

A9.15. IPHTAPDO 1000 50 HDI

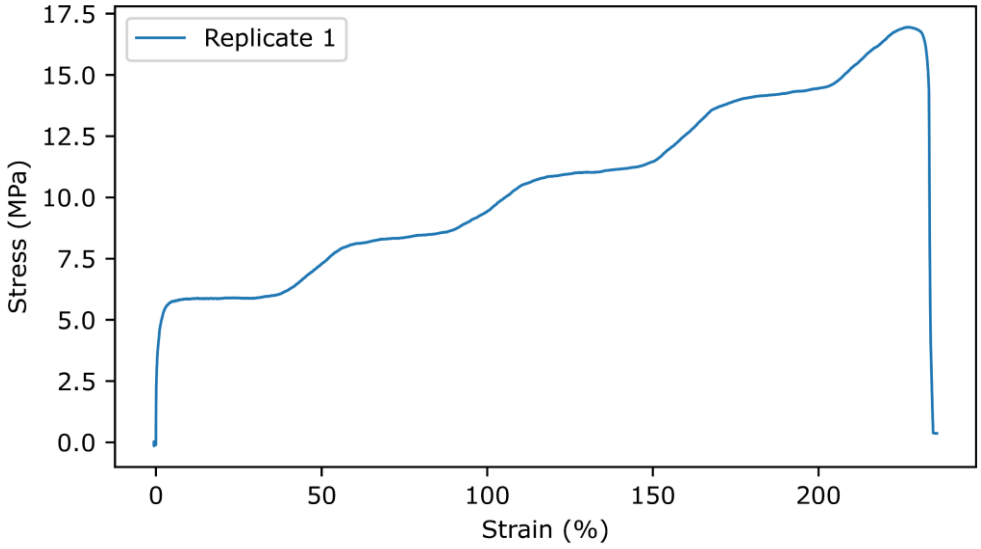

A9.16. IPHTAHDO 1000 10 HDI

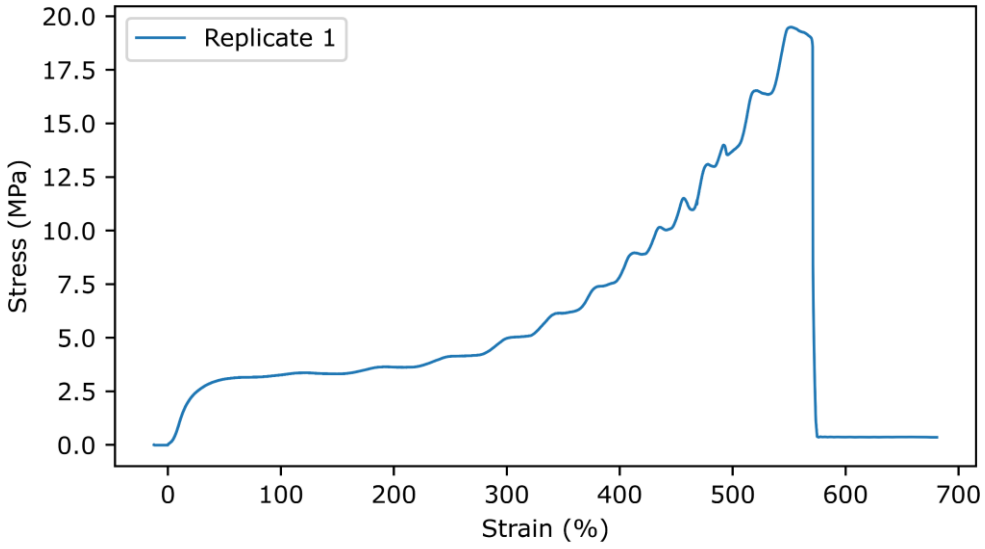

A9.17. IPHTAHDO 1000 30 HDI

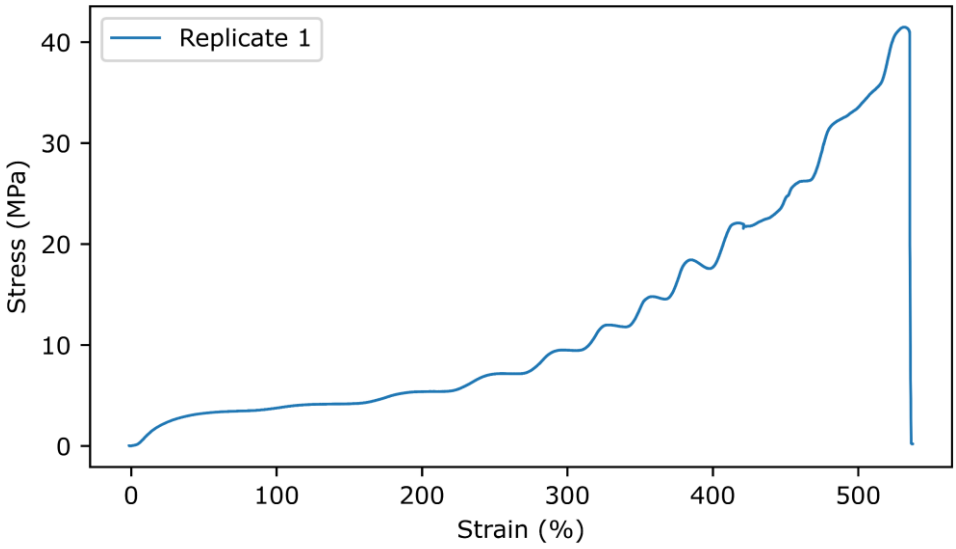

A9.18. IPHTAHDO 1000 50 HDI

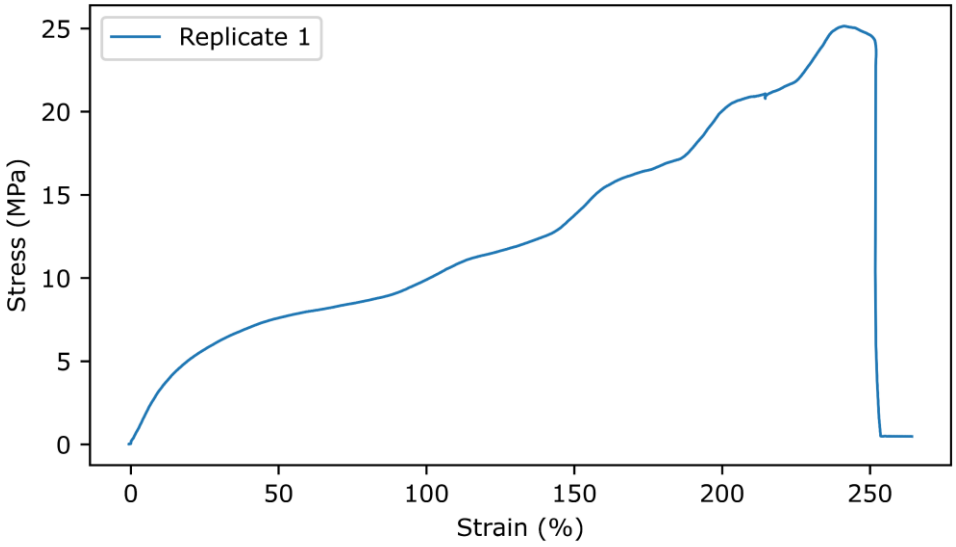

A9.19. IPHTAHDO 2000 10 HDI

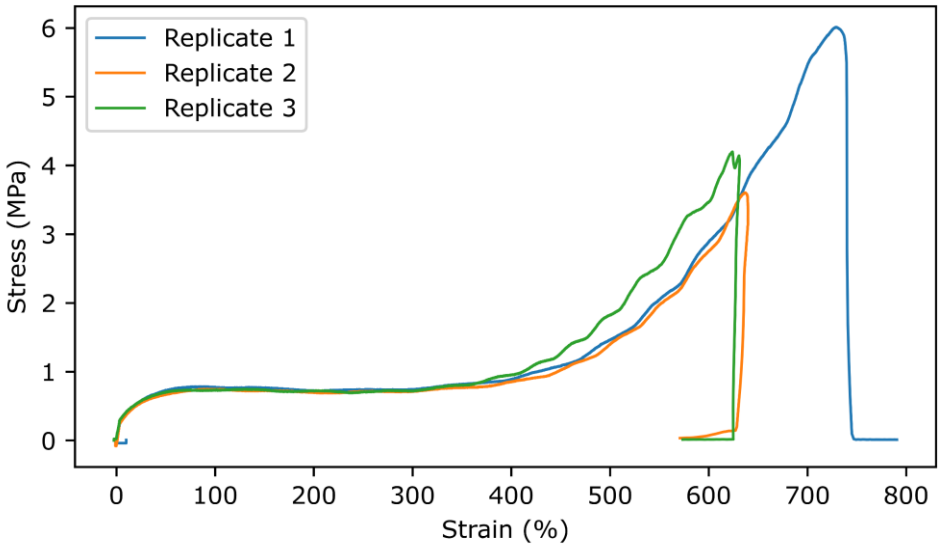

A9.20. IPHTAHDO 2000 30 HDI

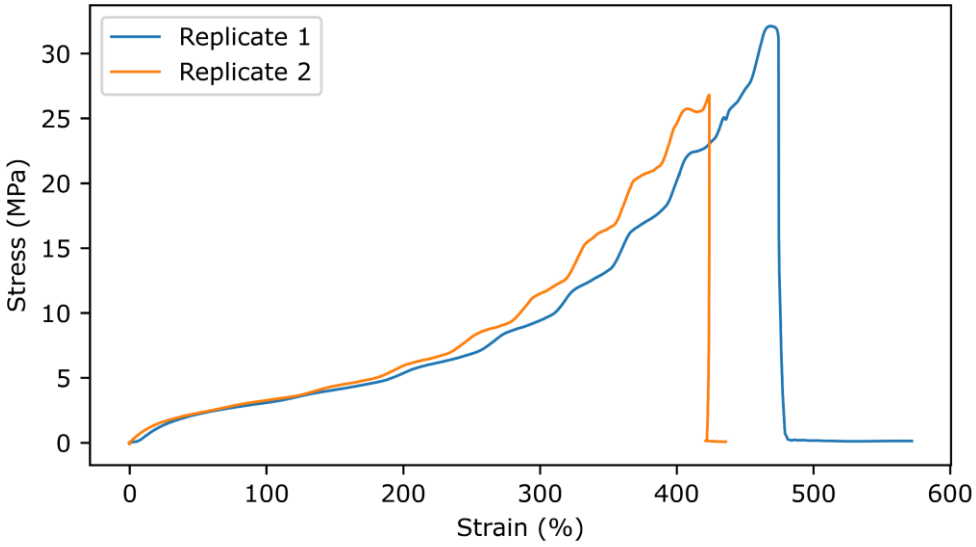

A9.21. IPHTAHDO 2000 50 HDI

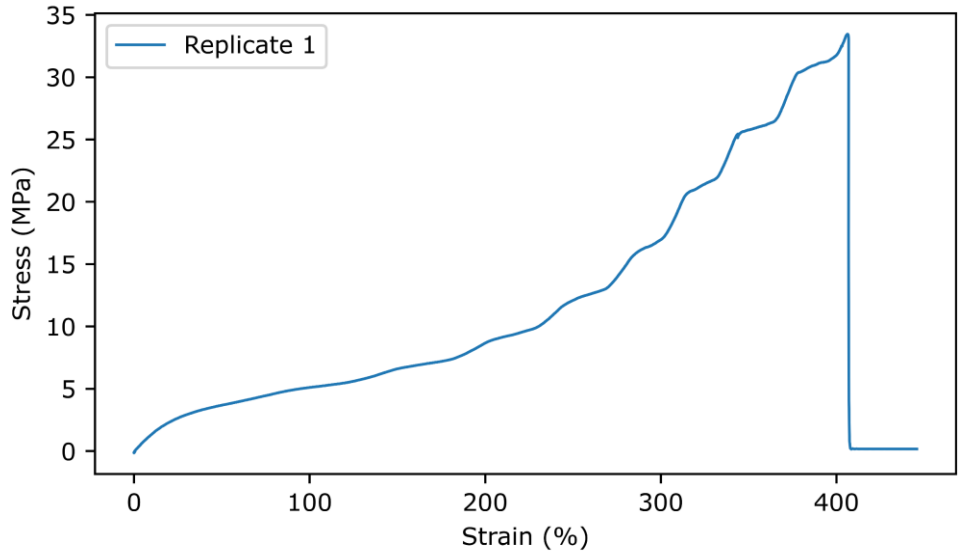

A9.22. FDCAPDO 1000 10 MDI

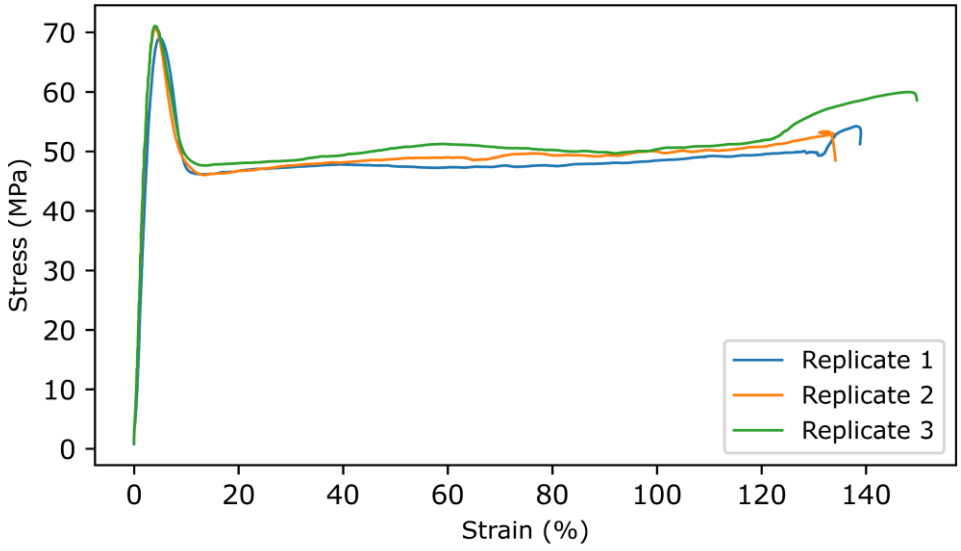

A9.23. FDCAPDO 1000 50 MDI

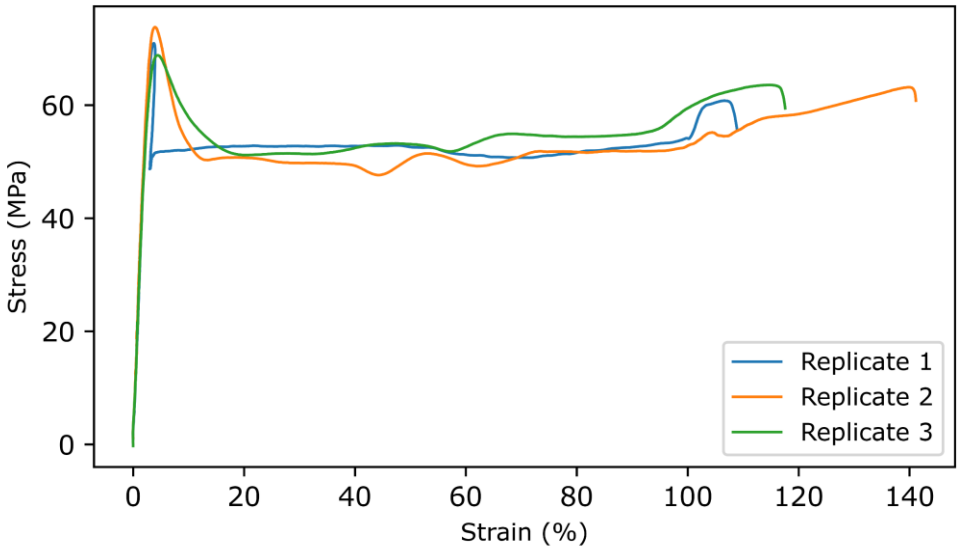

A9.24. FDCAPDO 1500 30 MDI

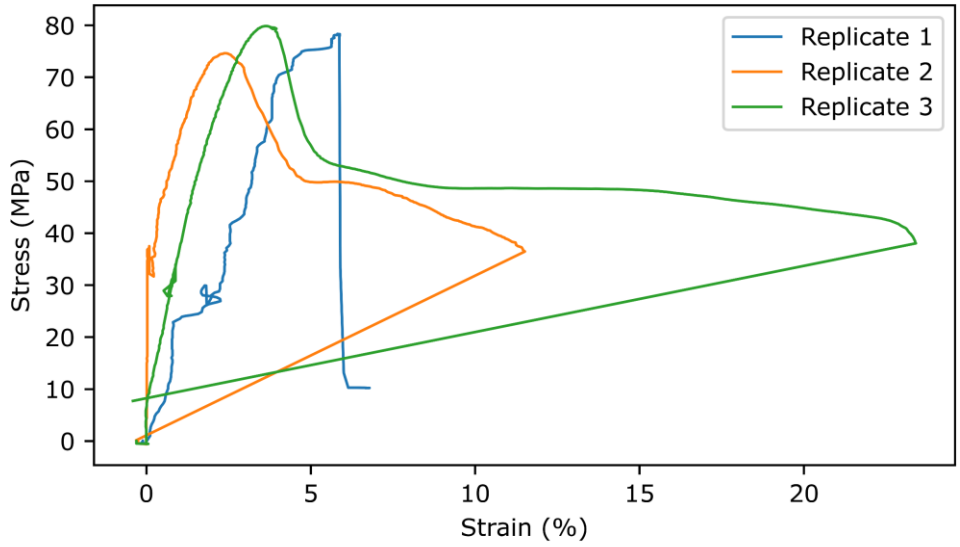

A9.25. FDCAPDO 2000 10 MDI

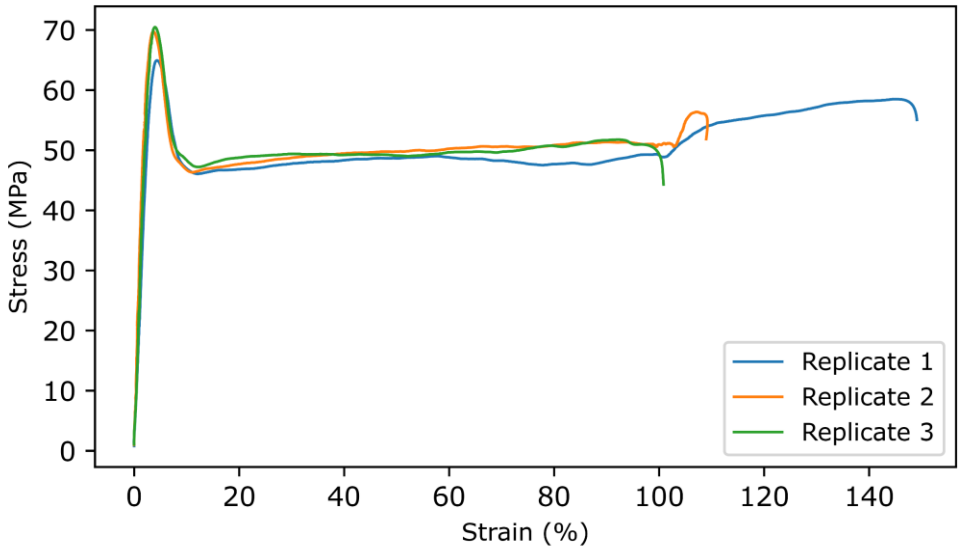

A9.26. FDCAPDO 2000 50 MDI

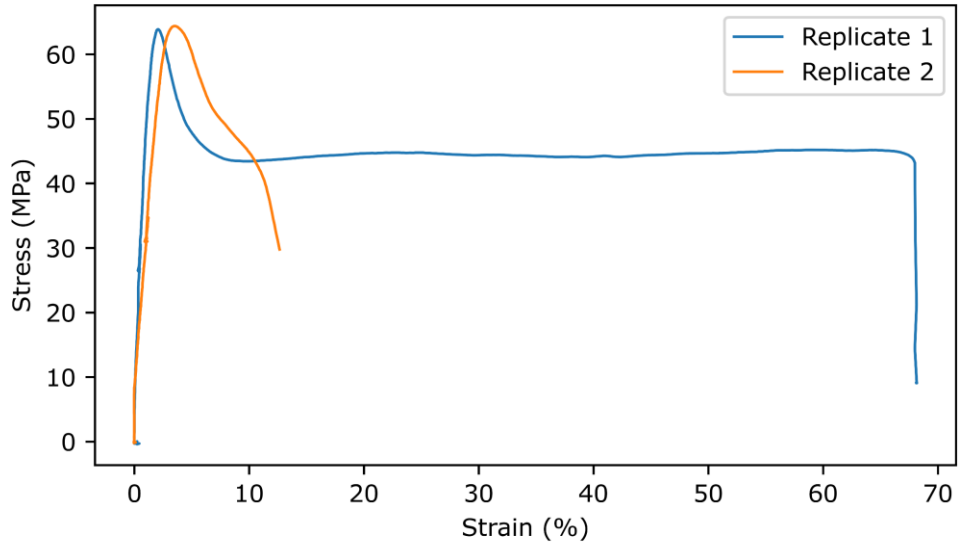

A9.27. FDCAHDO 1000 10 MDI

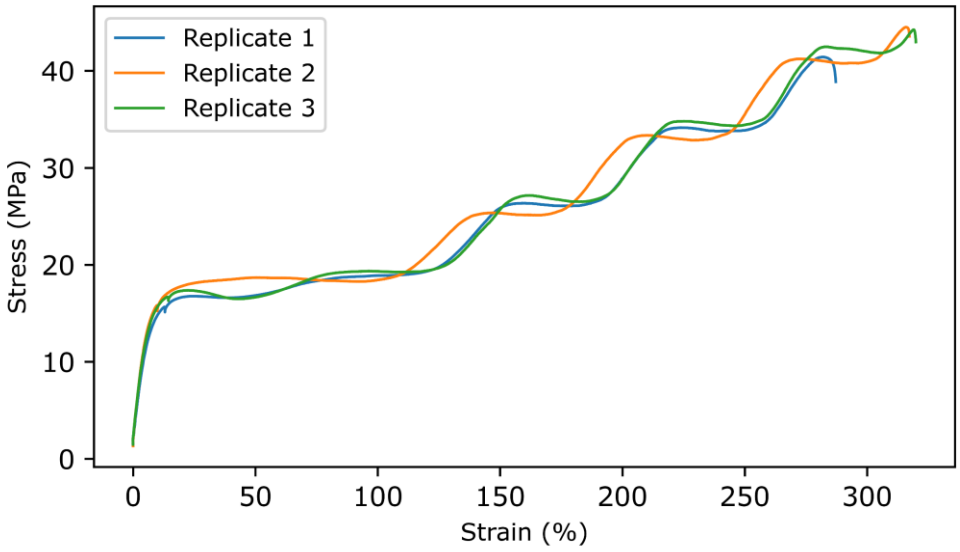

A9.28. FDCAHDO 1000 50 MDI

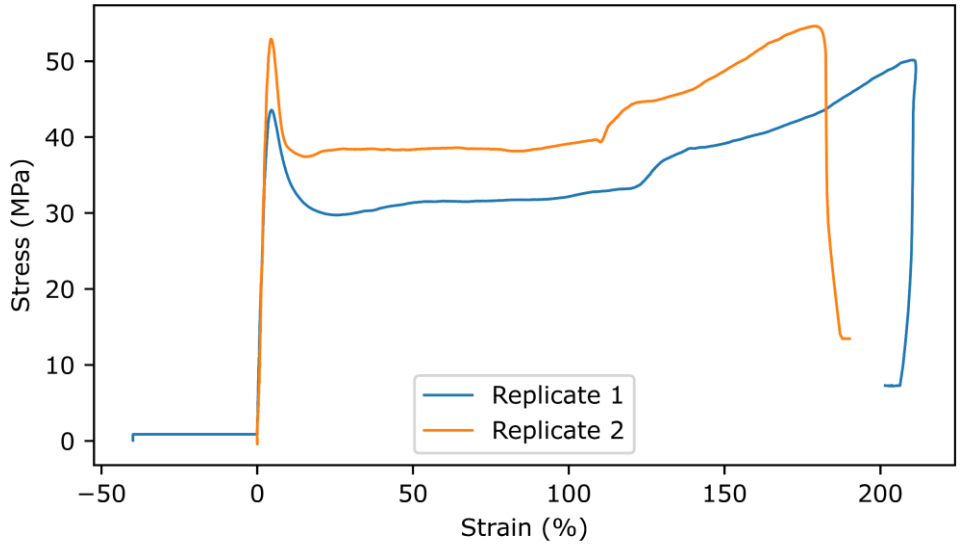

A9.29. FDCAHDO 1500 30 MDI

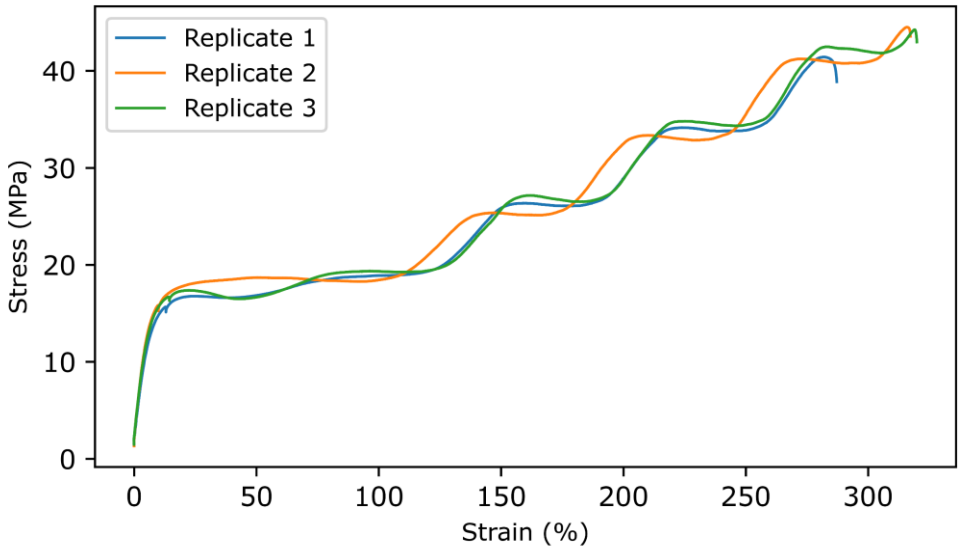

A9.30. FDCAHDO 2000 10 MDI

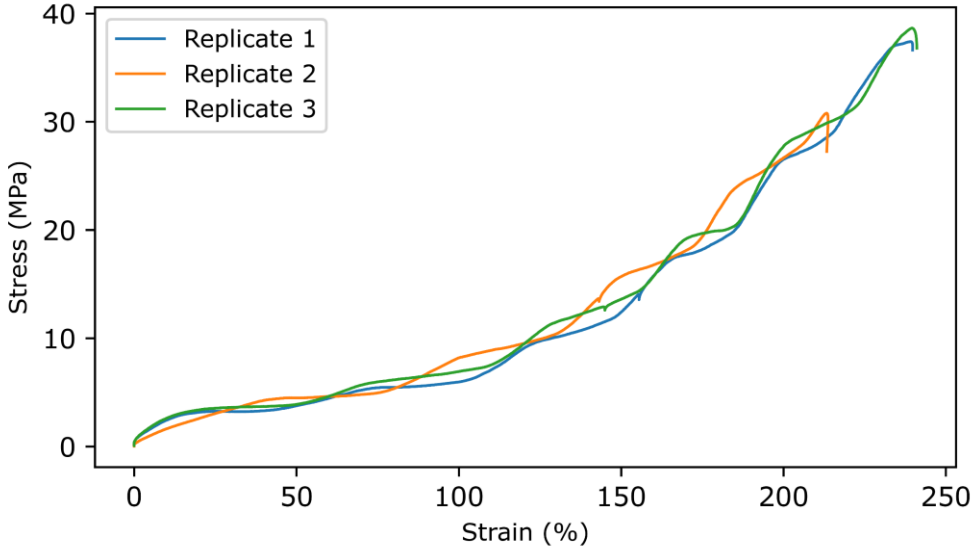

A9.31. FDCAHDO 2000 50 MDI

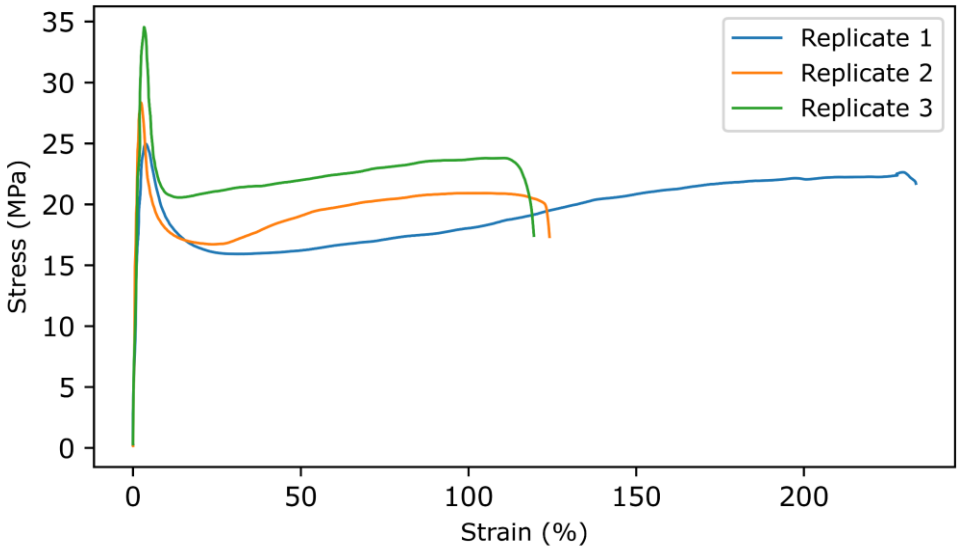

A9.32. FDCAPDO 1000 10 HDI

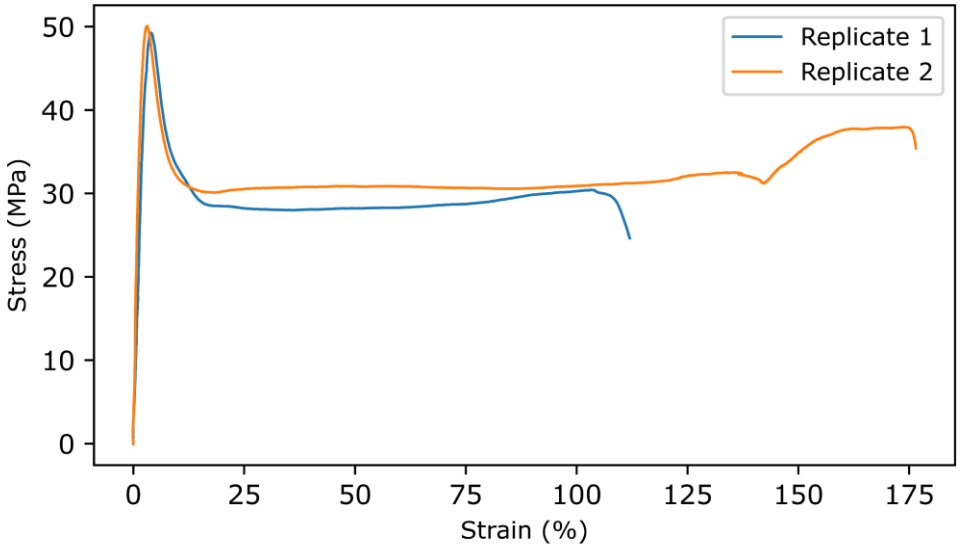

A9.33. FDCAPDO 1000 50 HDI

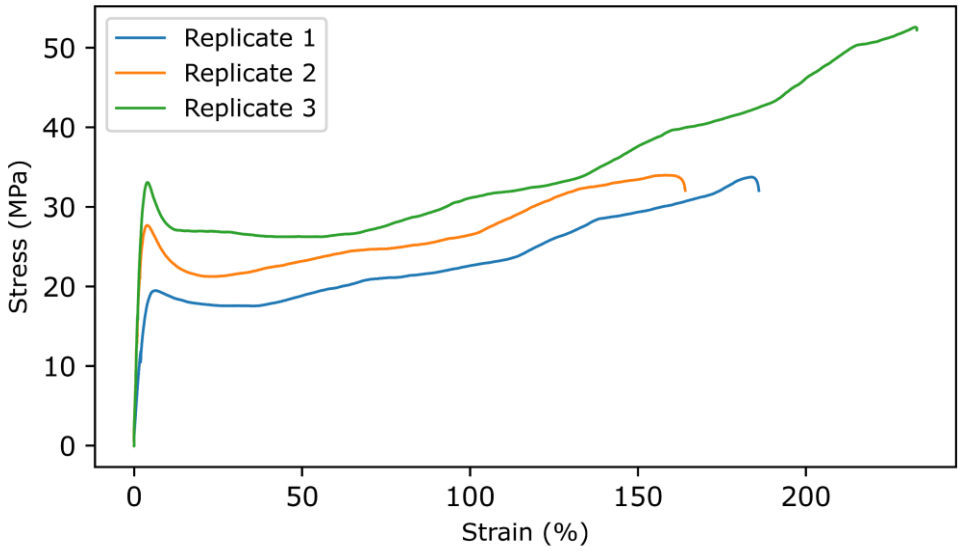

A9.34. FDCAPDO 1500 30 HDI

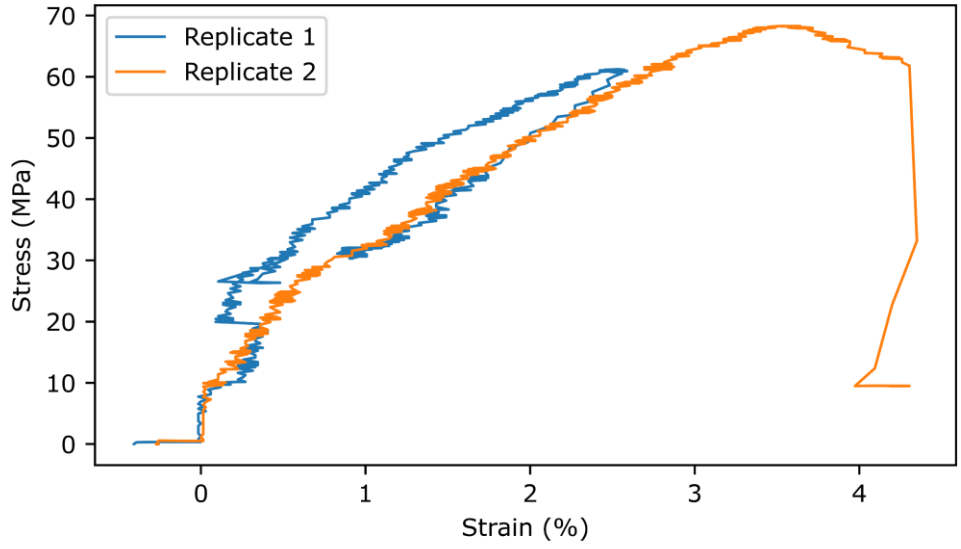

A9.35. FDCAPDO 2000 10 HDI

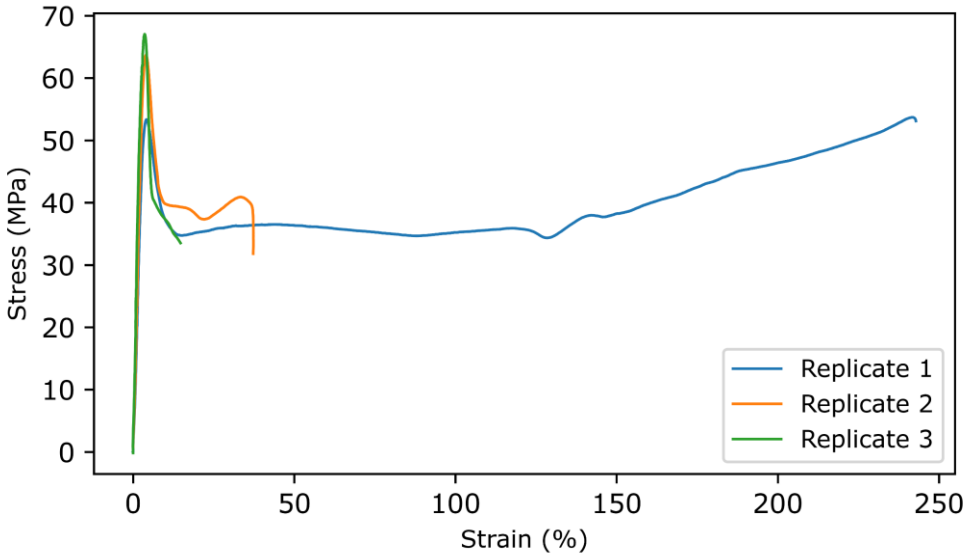

A9.36. FDCAPDO 2000 50 HDI

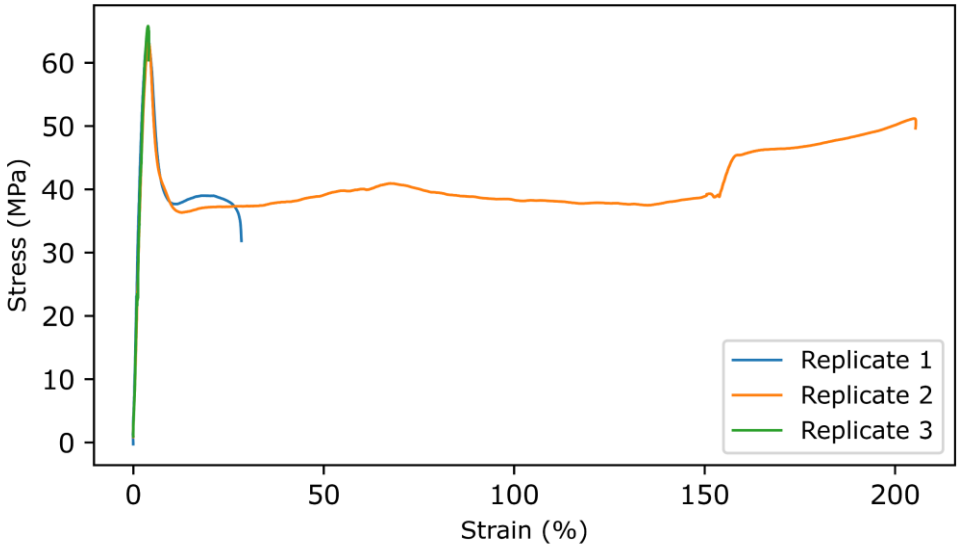

A9.37. FDCAHDO 1000 10 HDI

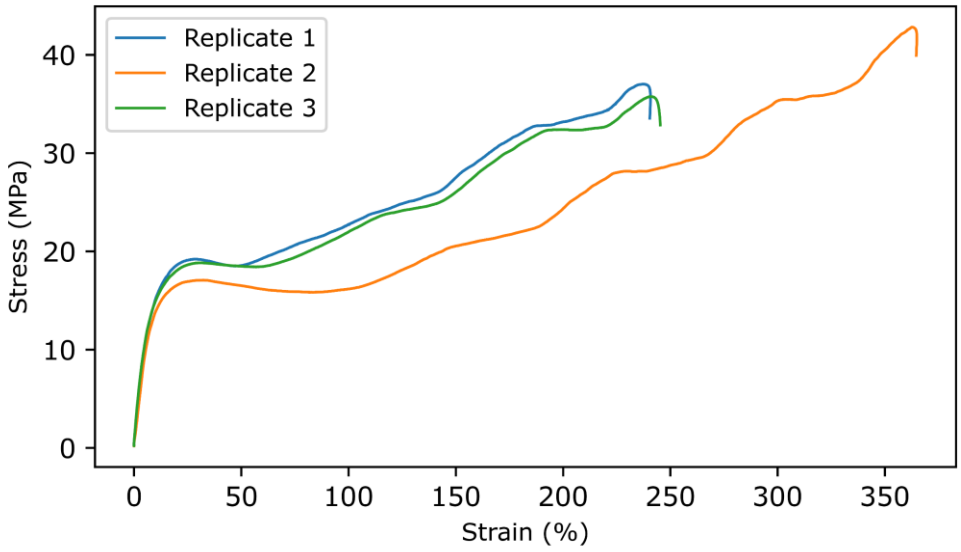

A9.38. FDCAHDO 1000 50 HDI

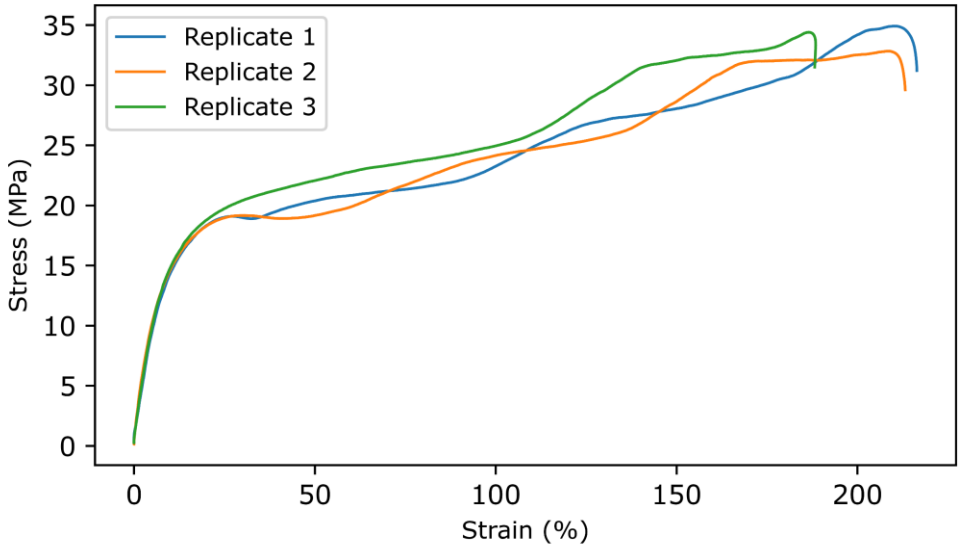

A9.39. FDCAHDO 1500 30 HDI

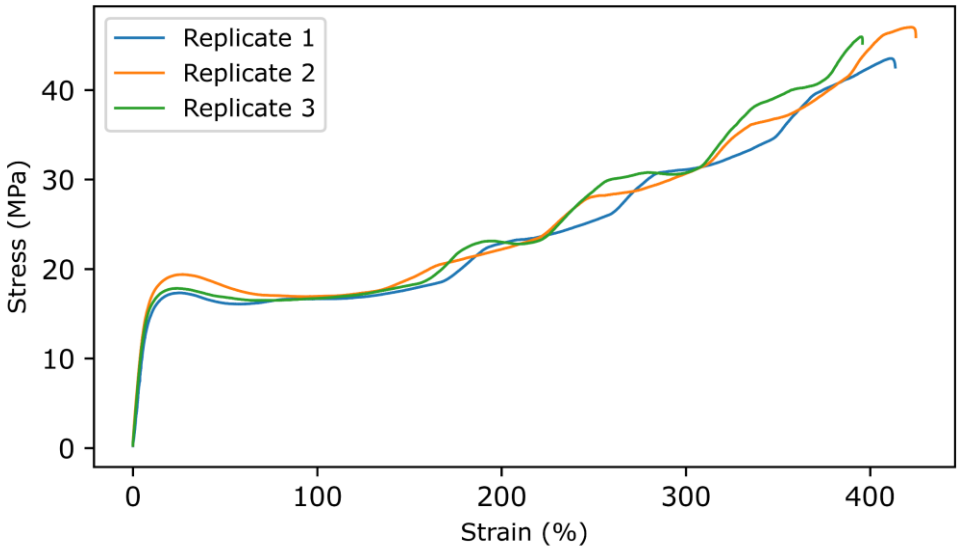

A9.40. FDCAHDO 2000 10 HDI

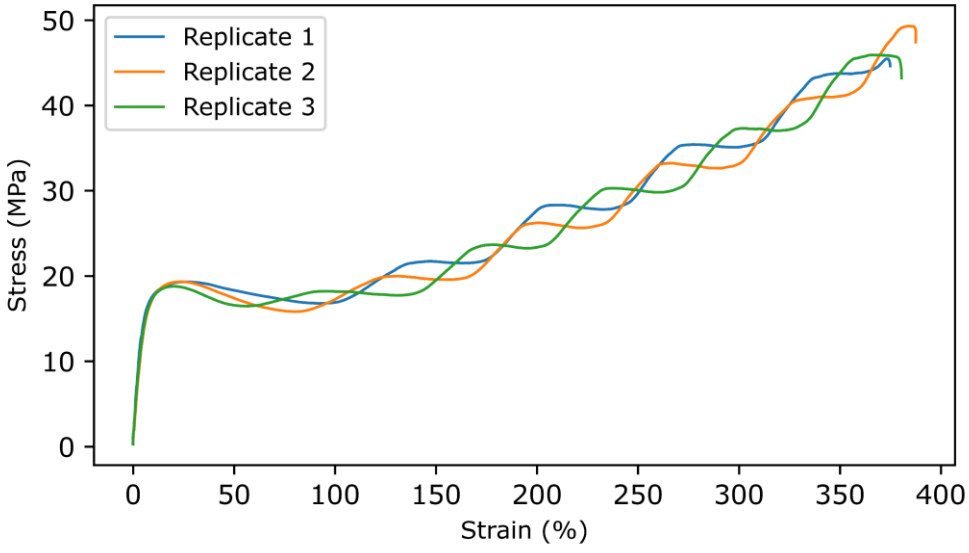

A9.41. FDCAHDO 2000 50 HDI

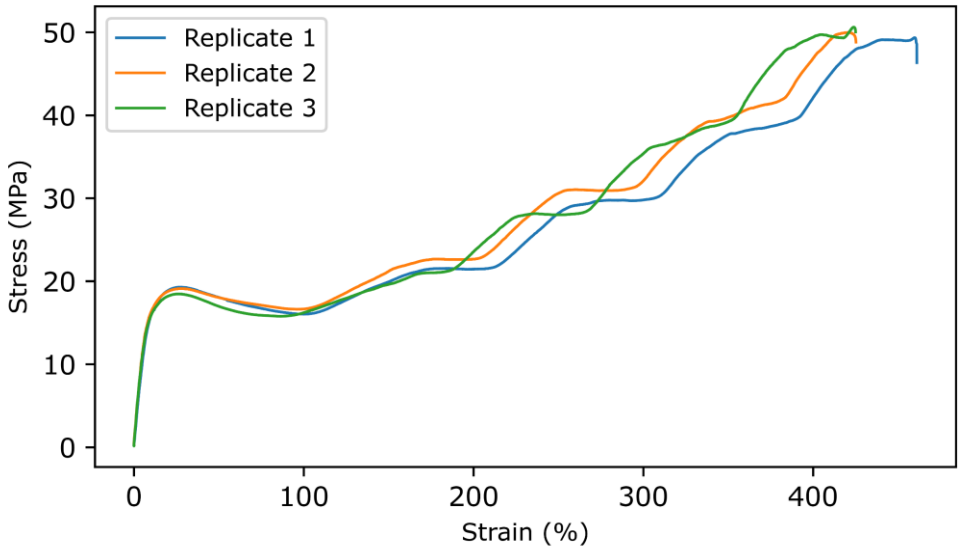

A10 Shape memory cycles of the unannealed TPUs

A10.1. IPHTAPDO 1000 10 MDI

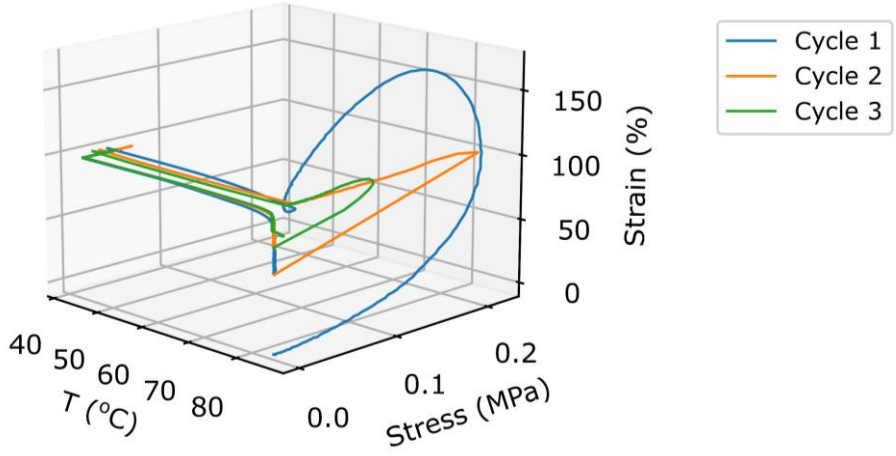

A10.2. IPHTAPDO 1000 30 MDI

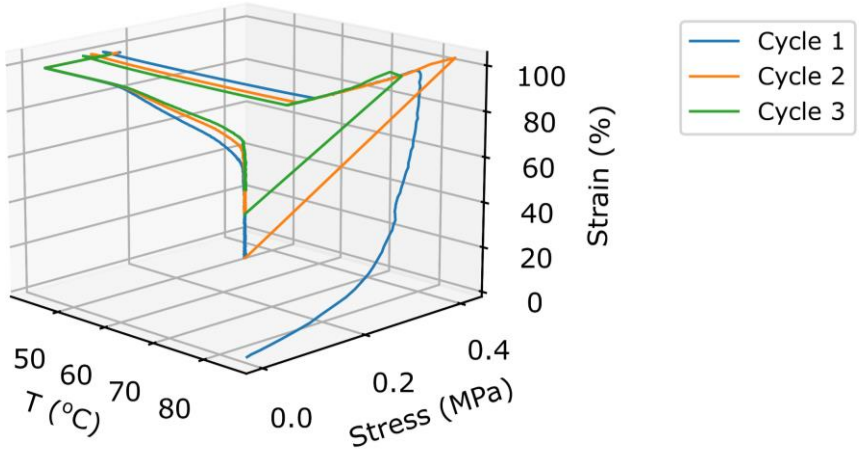

A10.3. IPHTAPDO 1000 50 MDI

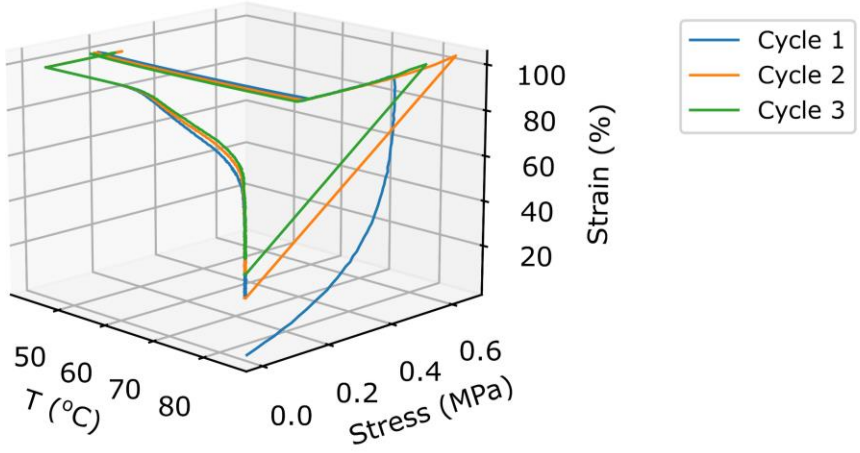

A10.4. IPHTAPDO 2000 10 MDI

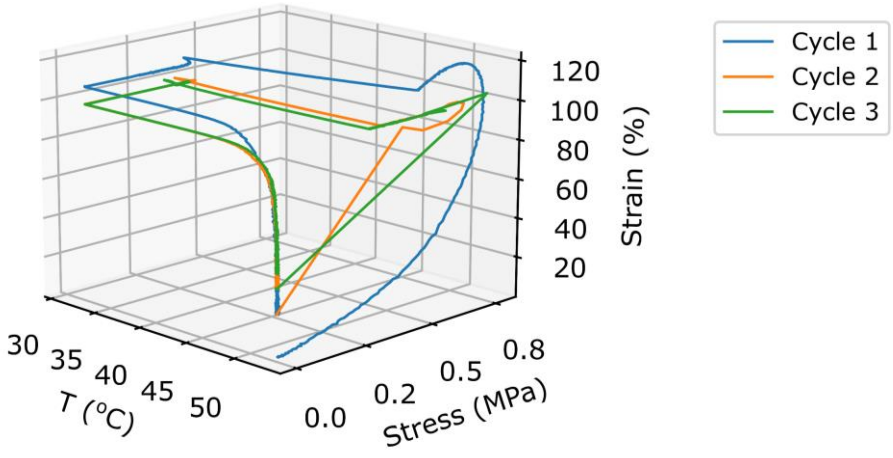

A10.5. IPHTAPDO 2000 30 MDI

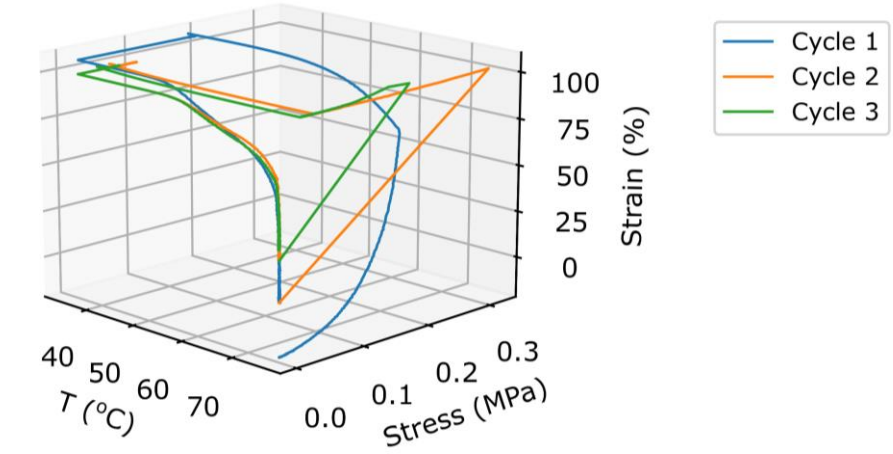

A10.6. IPHTAPDO 2000 50 MDI

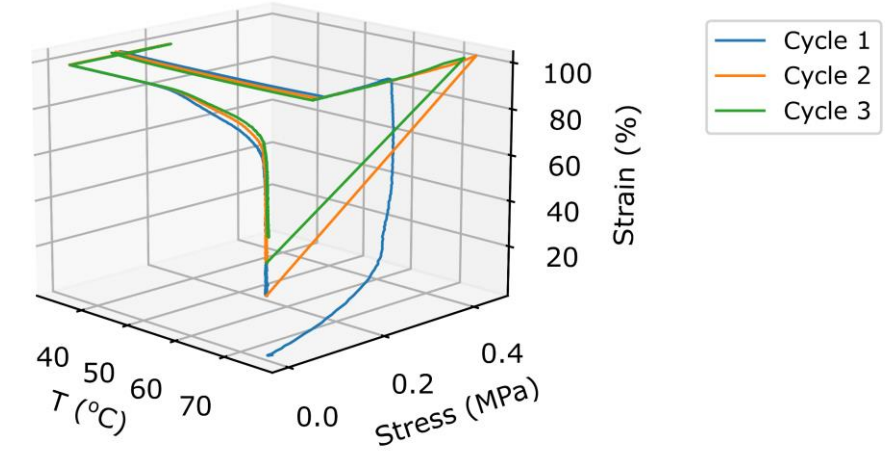

A10.7. IPHTAHDO 1000 10 MDI

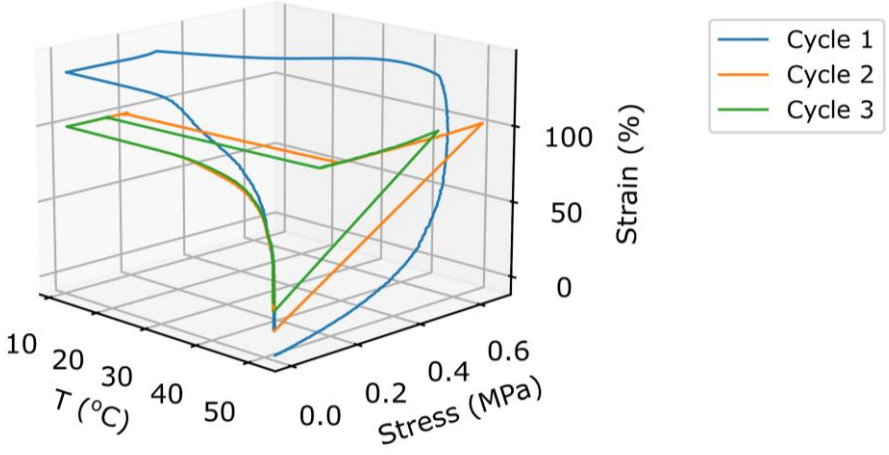

A10.8. IPHTAHDO 1000 30 MDI

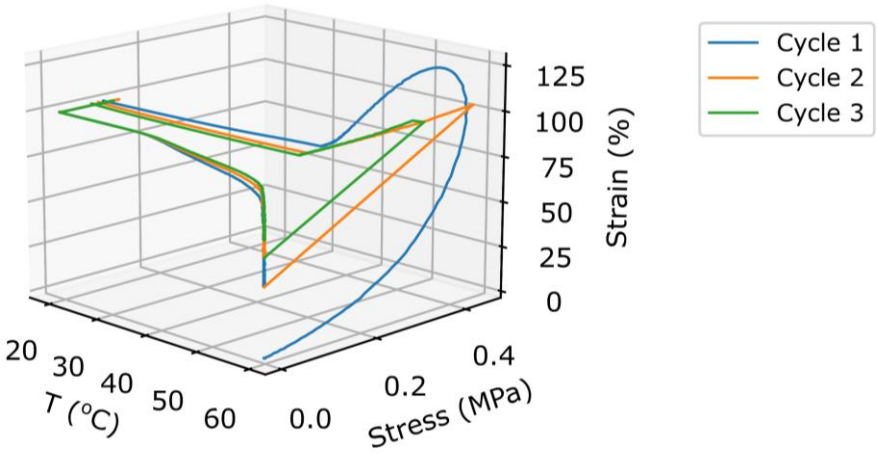

A10.9. IPHTAHDO 1000 50 MDI

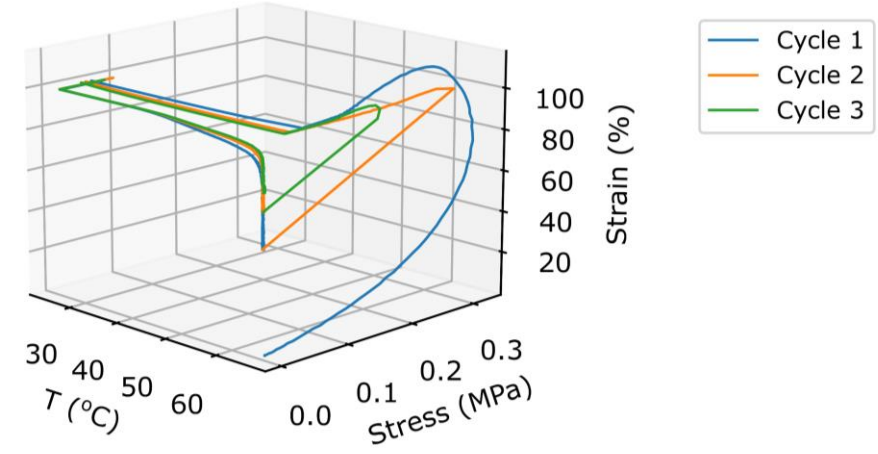

A10.10. IPHTAHDO 2000 10 MDI

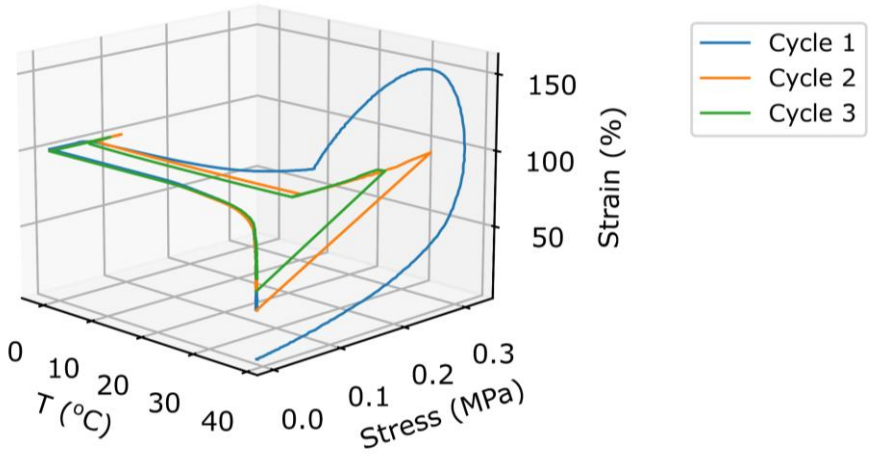

A10.11. IPHTAHDO 2000 30 MDI

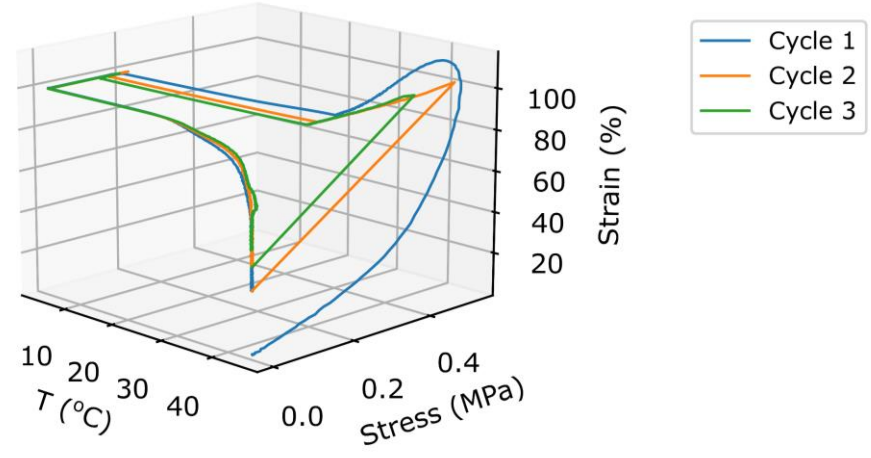

A10.12. IPHTAHDO 2000 50 MDI

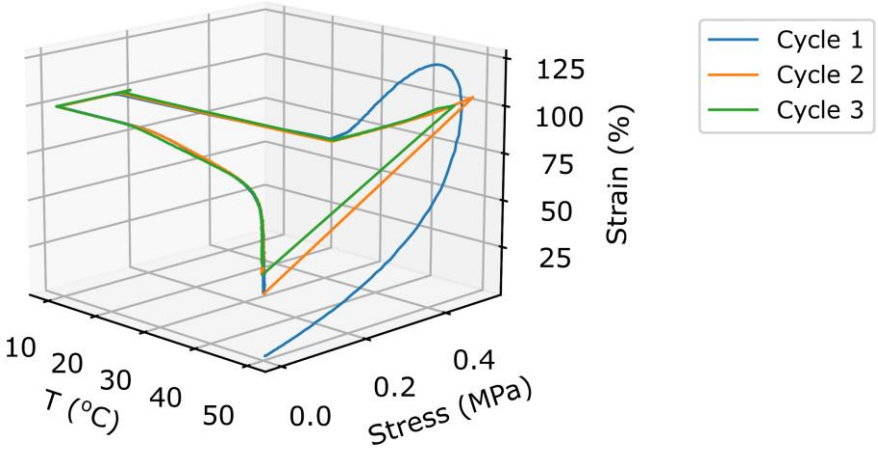

A10.13. IPHTAPDO 1000 10 HDI

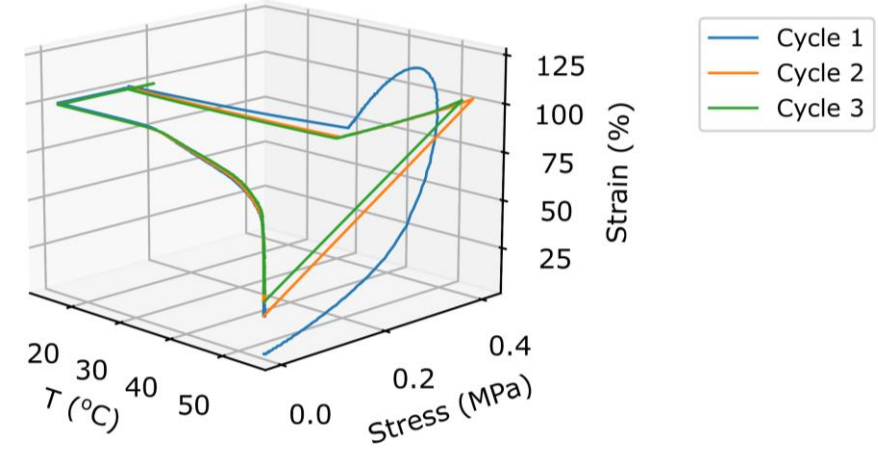

A10.14. IPHTAPDO 1000 30 HDI

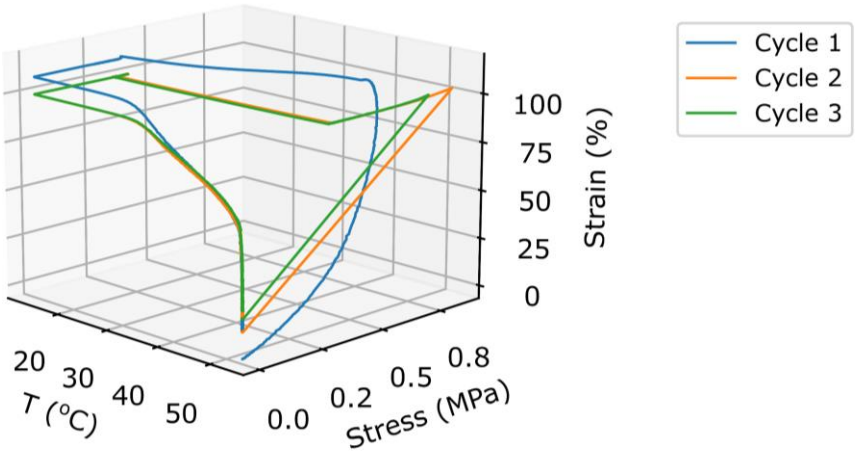

A10.15. IPHTAPDO 1000 50 HDI

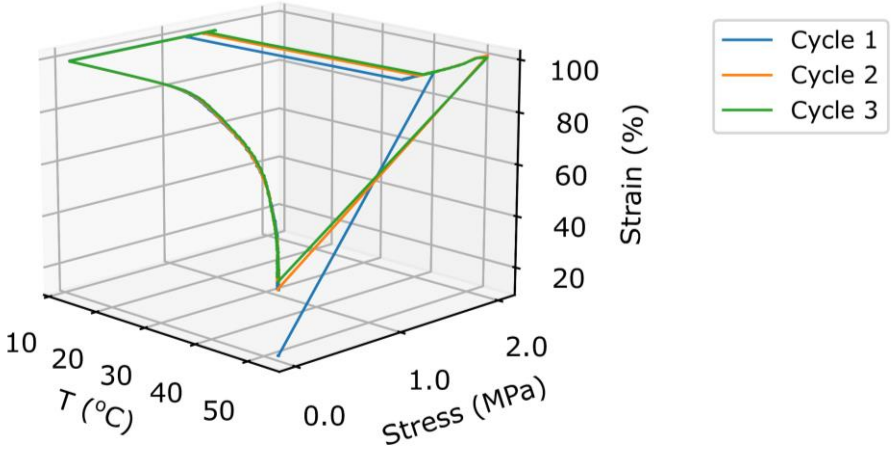

A10.16. IPHTAPDO 2000 10 HDI

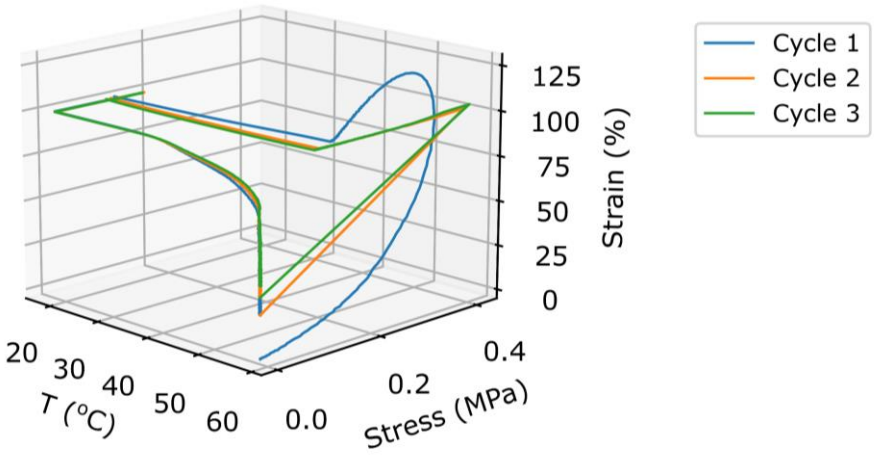

A10.17. IPHTAPDO 2000 30 HDI

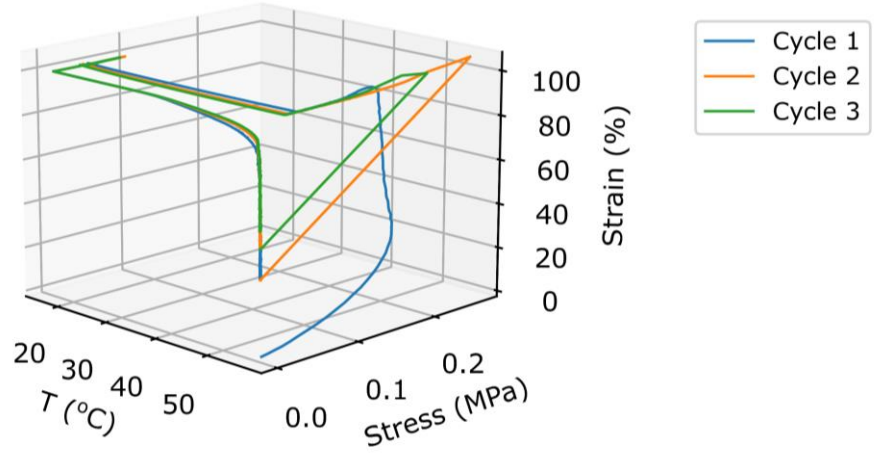

A10.18. IPHTAPDO 2000 50 HDI

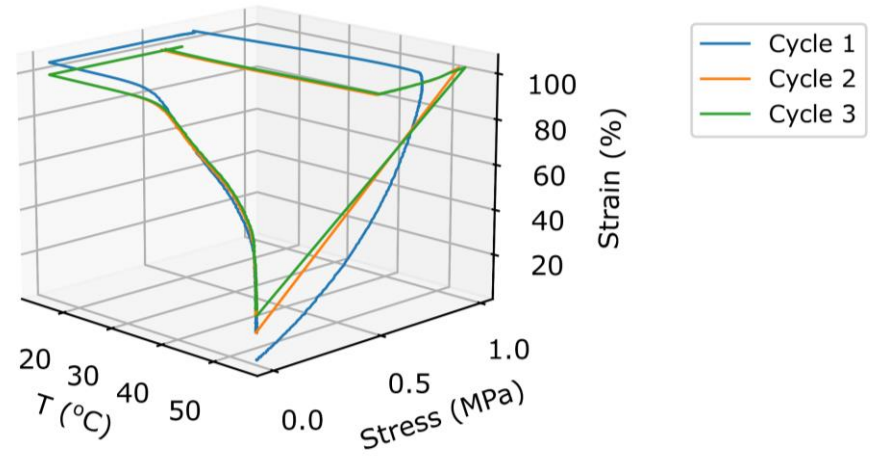

A10.19. IPHTAHDO 1000 10 HDI

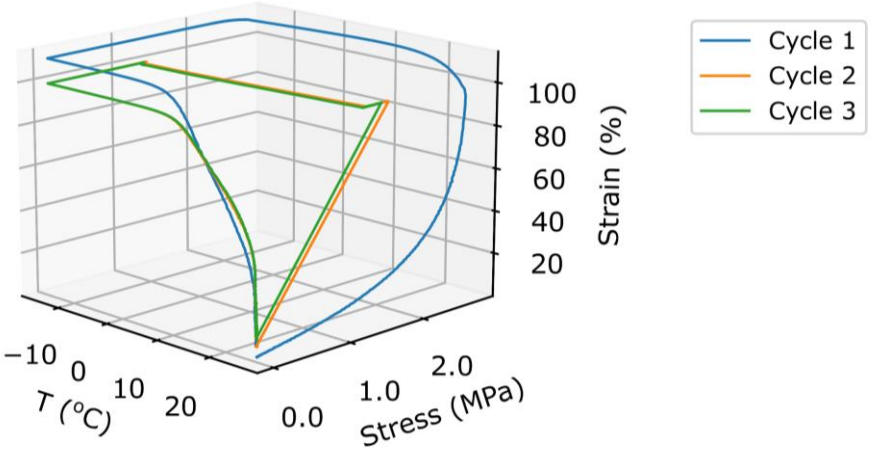

A10.20. IPHTAHDO 1000 30 HDI

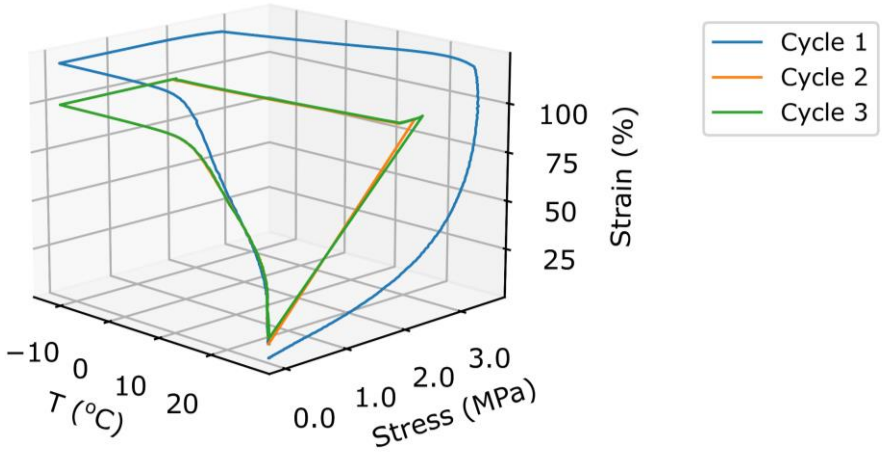

A10.21. IPHTAHDO 1000 50 HDI

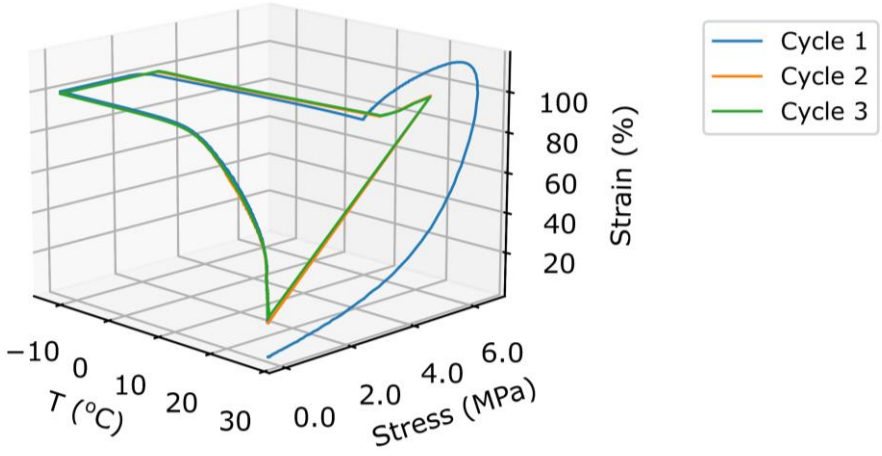

A10.22. IPHTAHDO 2000 10 HDI

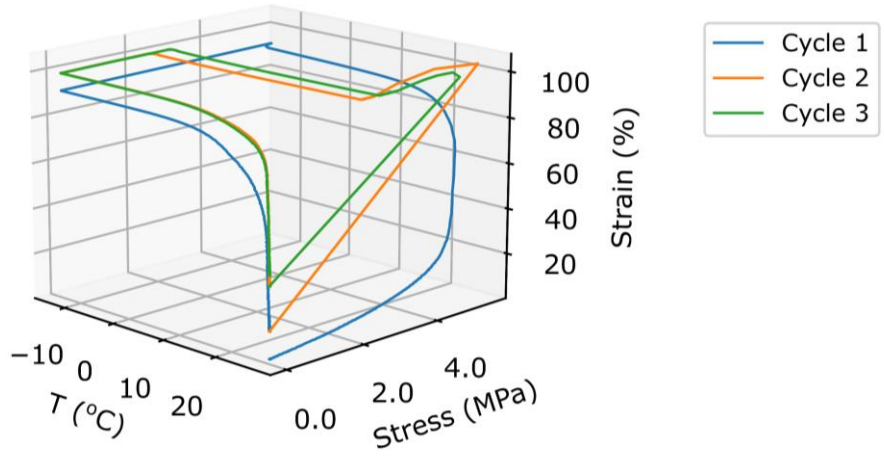

A10.23. IPHTAHDO 2000 30 HDI

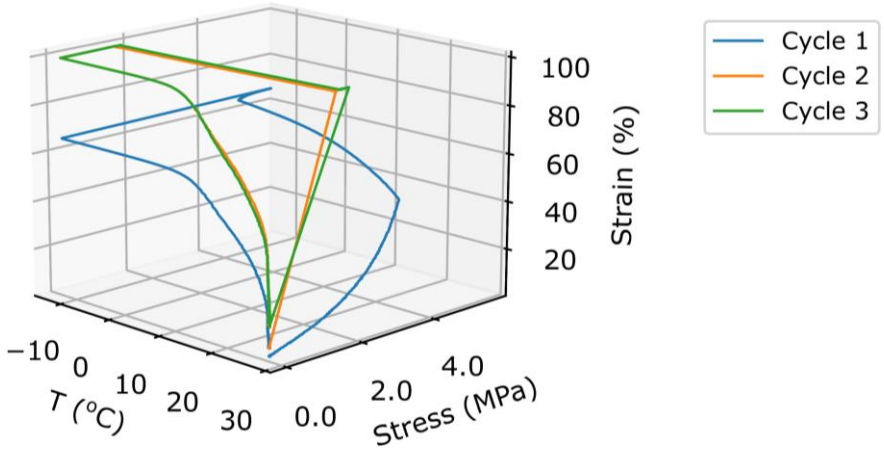

A10.24. IPHTAHDO 2000 50 HDI

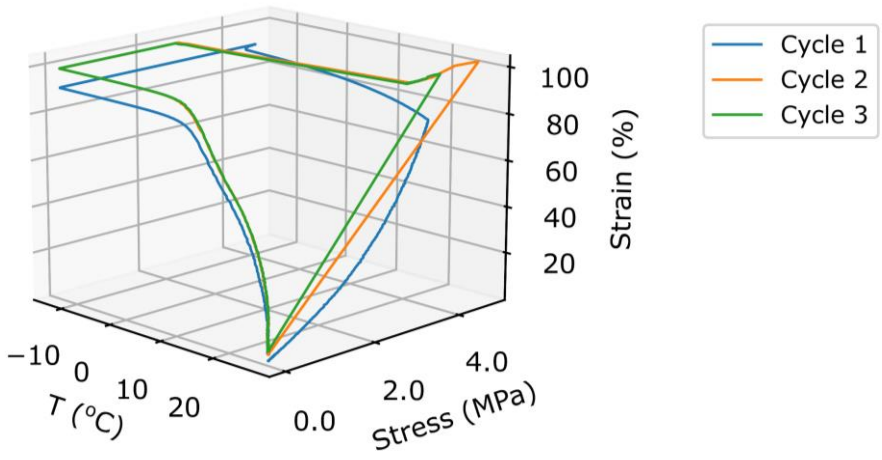

A10.25. FDCAPDO 1000 10 MDI

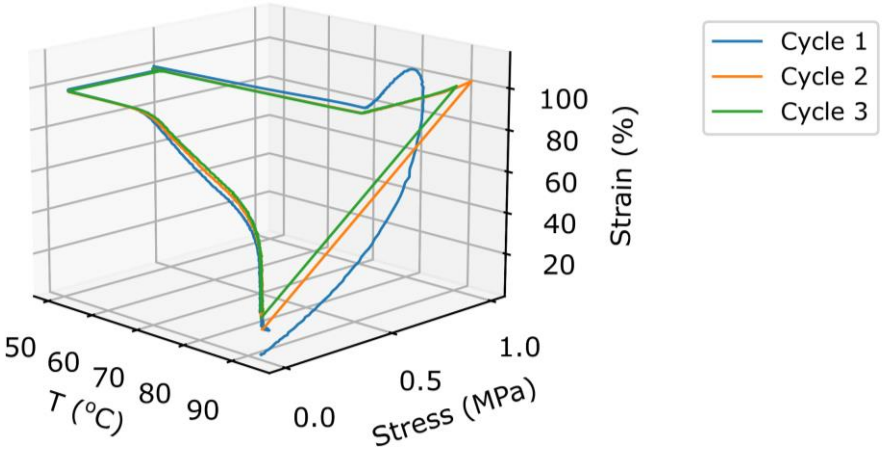

A10.26. FDCAPDO 1000 50 MDI

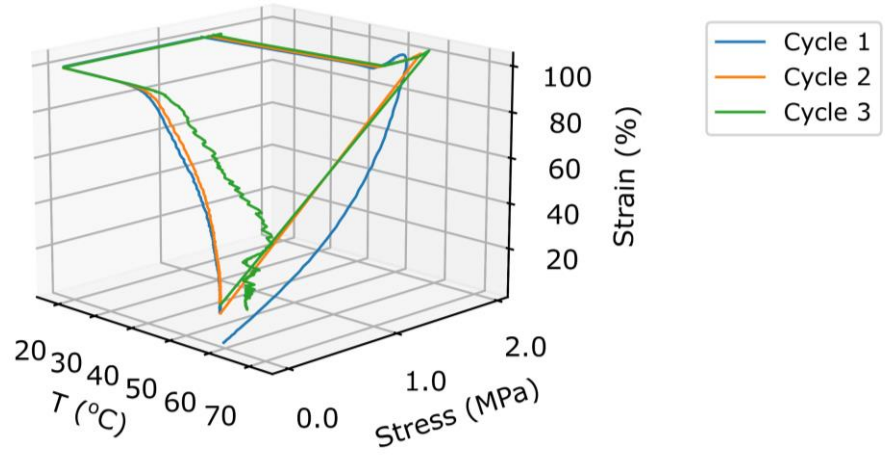

A10.27. FDCAPDO 1500 30 MDI

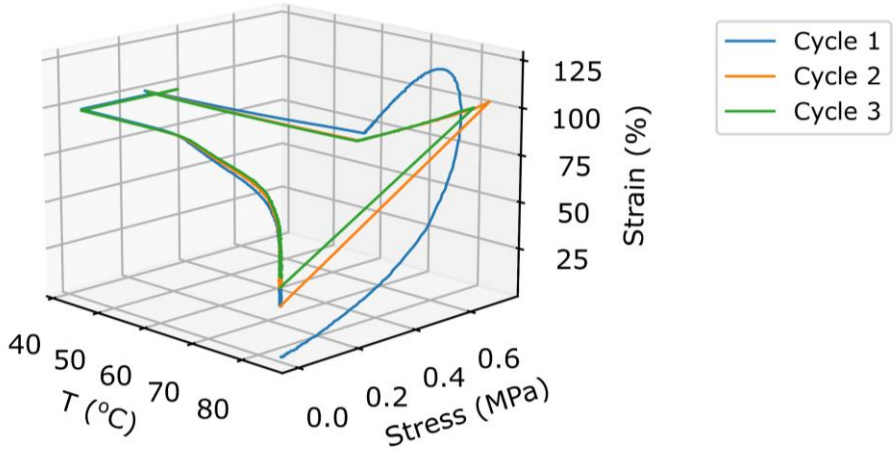

A10.28. FDCAPDO 2000 10 MDI

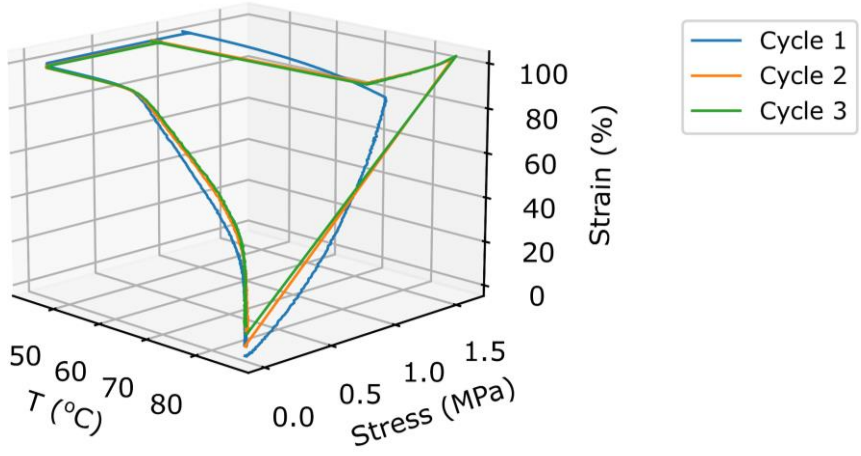

A10.29. FDCAPDO 2000 50 MDI

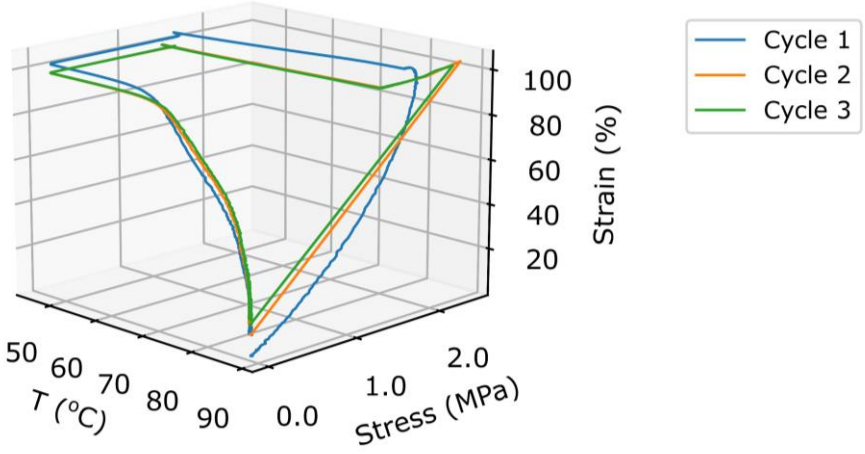

A10.30. FDCAHDO 1000 10 MDI

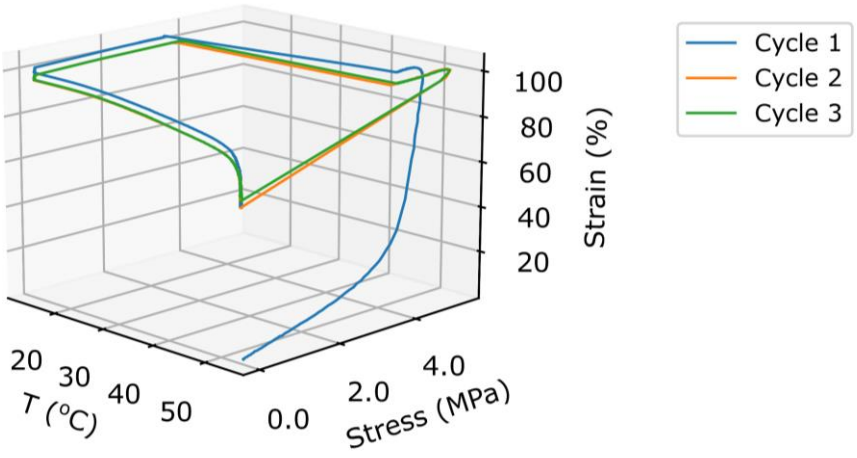

A10.31. FDCAHDO 1000 50 MDI

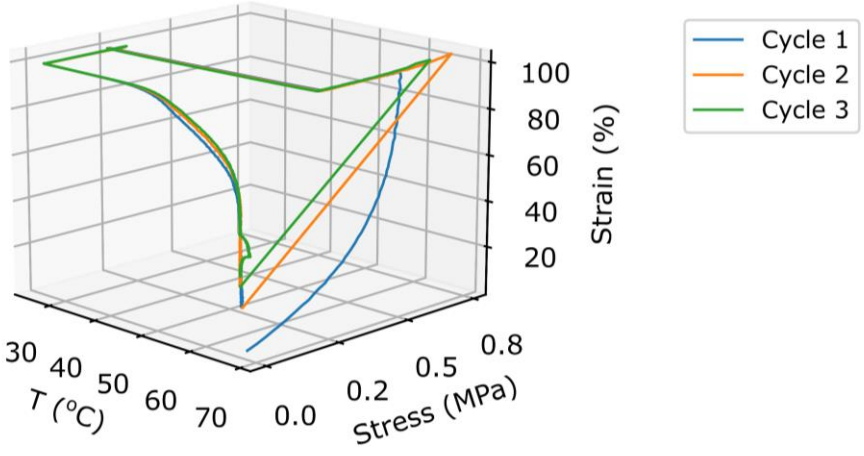

A10.32. FDCAHDO 1500 30 MDI

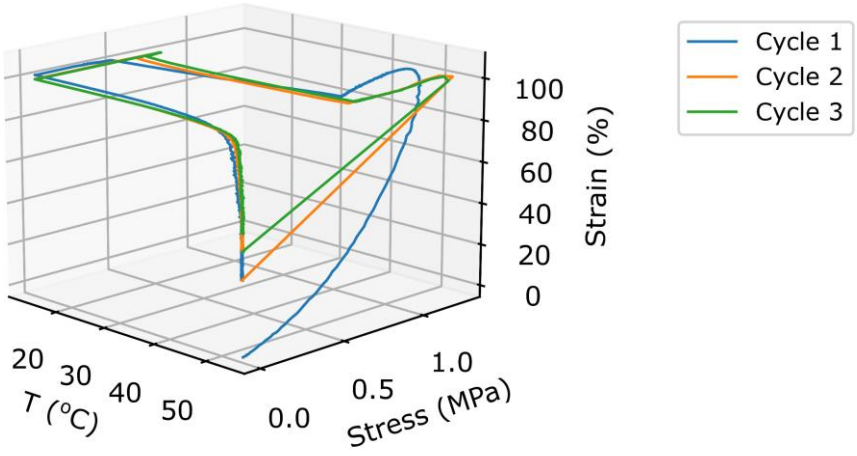

A10.33. FDCAHDO 2000 10 MDI

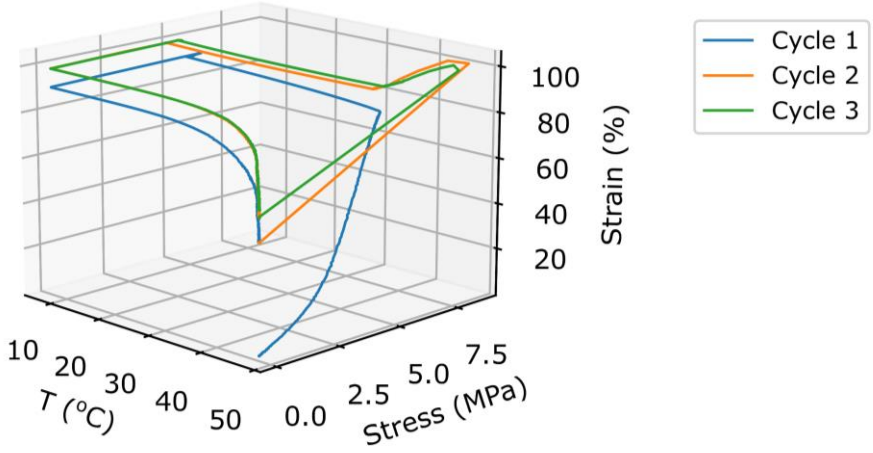

A10.34. FDCAHDO 2000 50 MDI

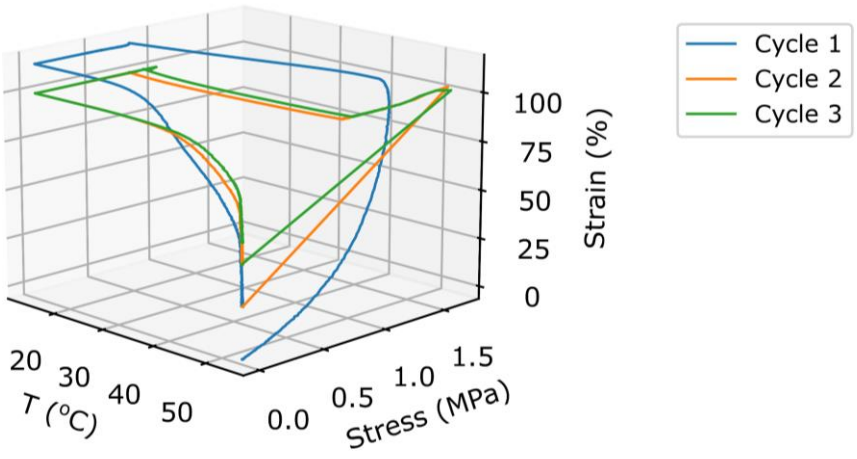

A10.35. FDCAPDO 1000 10 HDI

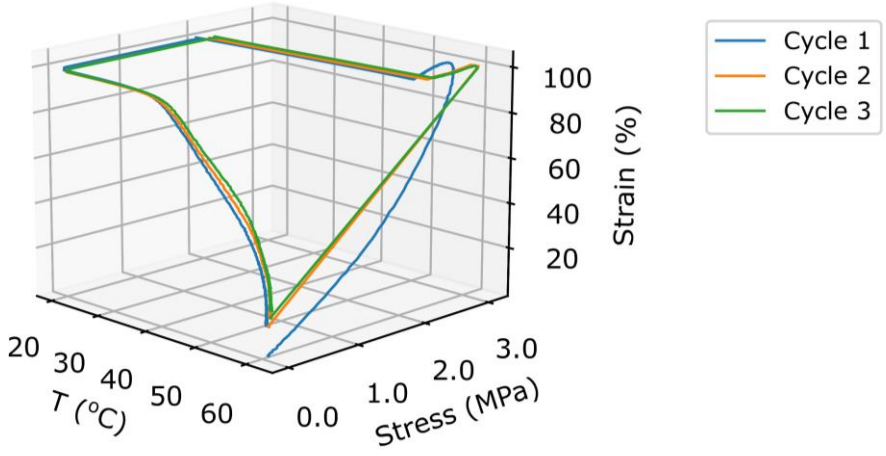

A10.36. FDCAPDO 1000 50 HDI

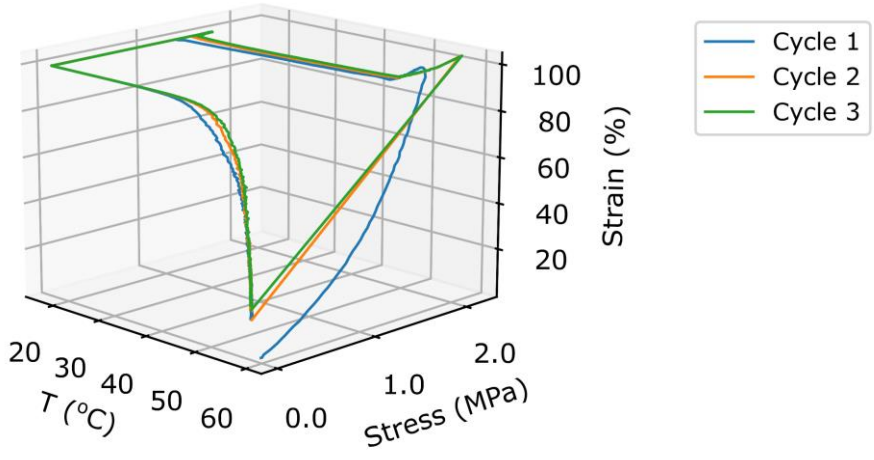

A10.37. FDCAPDO 1500 30 HDI

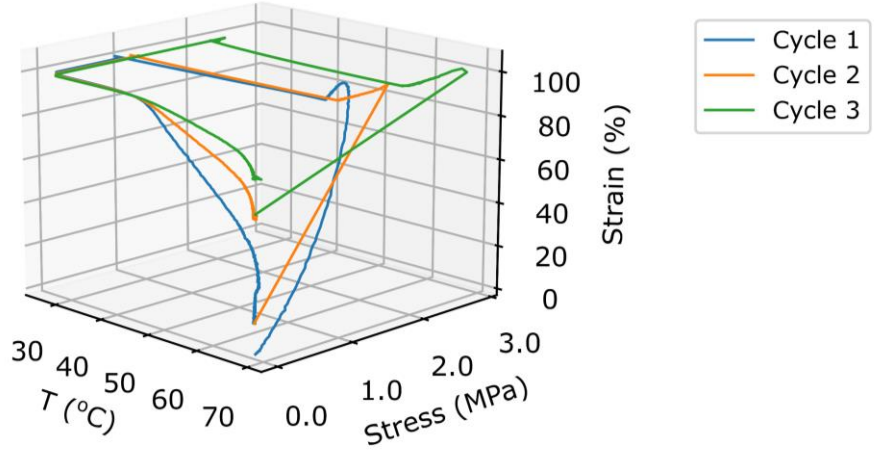

A10.38. FDCAPDO 2000 10 HDI

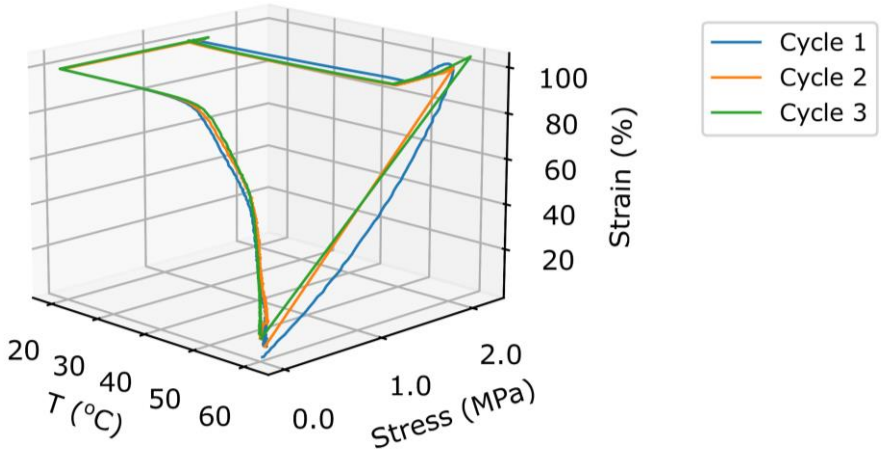

A10.39. FDCAHDO 1000 10 HDI

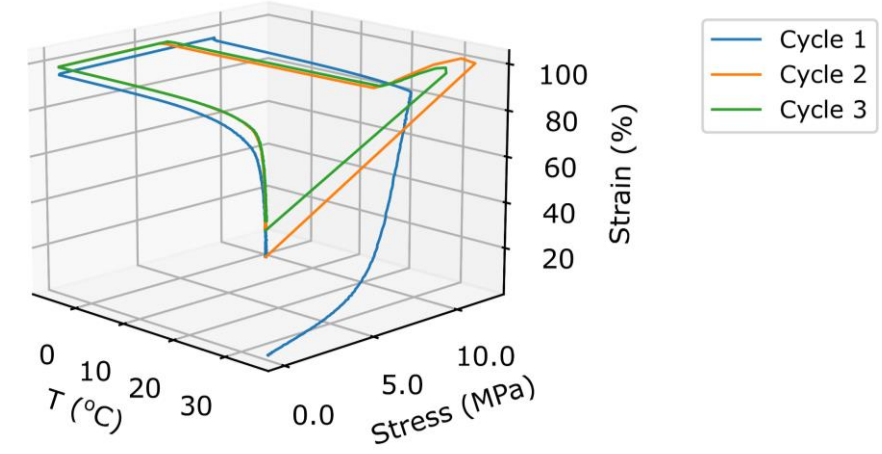

A10.40. FDCAHDO 1000 50 HDI

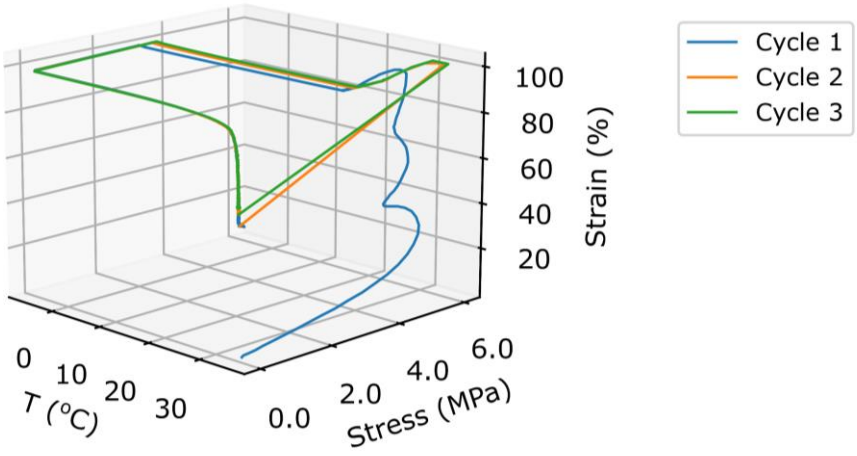

A10.41. FDCAHDO 1500 30 HDI

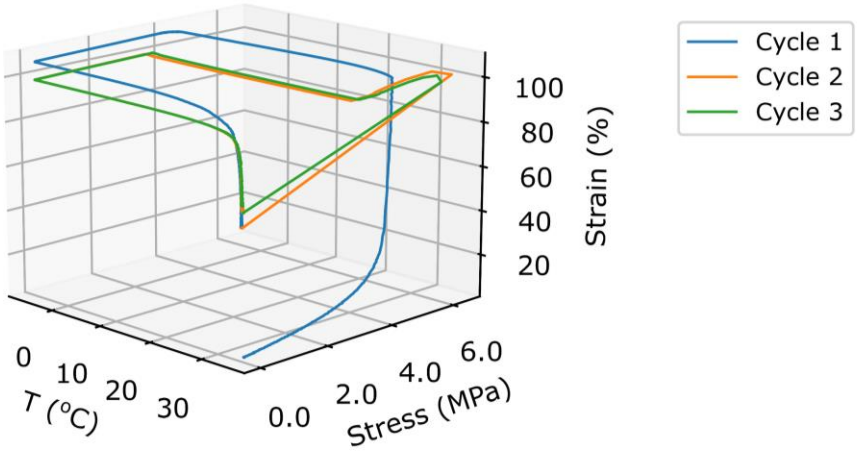

A10.42. FDCAHDO 2000 10 HDI

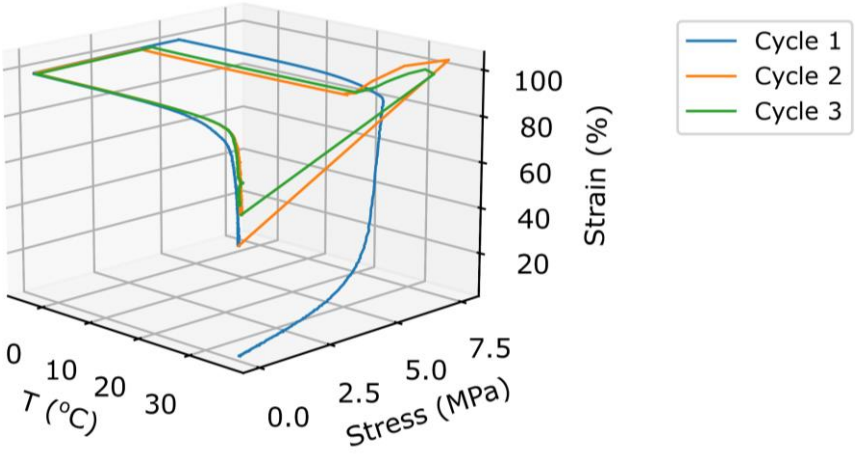

A11 Tensile testing at 20 °C above T_g of the unannealed TPUs

A11.1. IPHTAPDO 1000 10 MDI

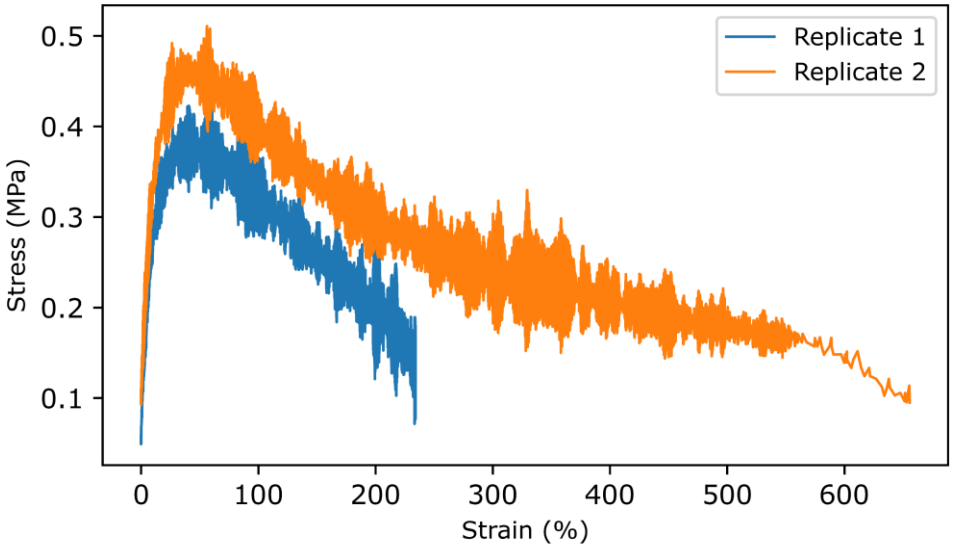

A11.2. IPHTAPDO 1000 30 MDI

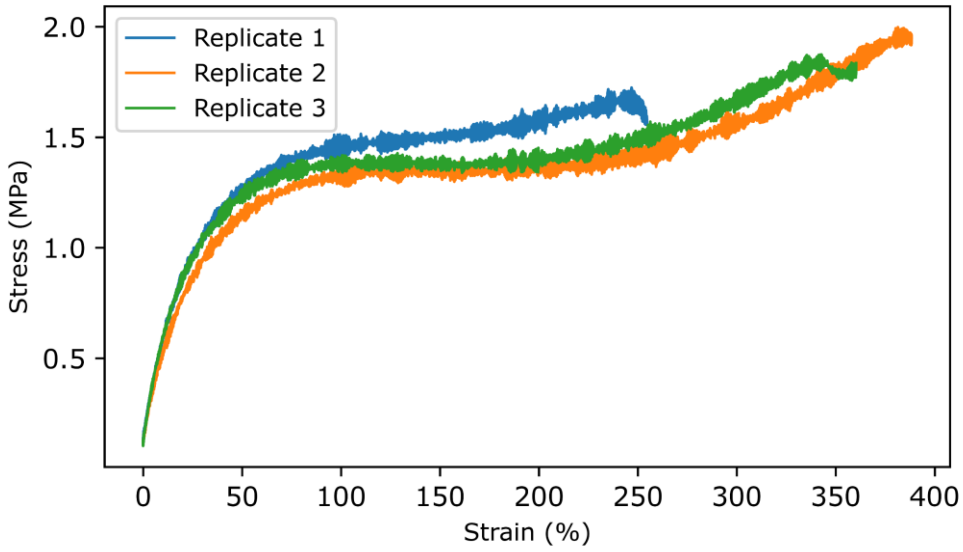

A11.3. IPHTAPDO 2000 10 MDI

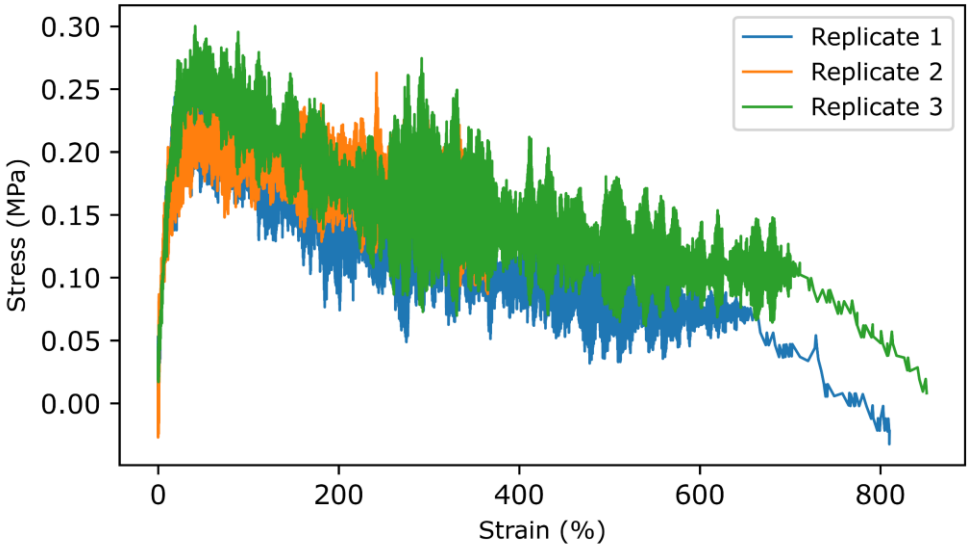

A11.4. IPHTAPDO 2000 30 MDI

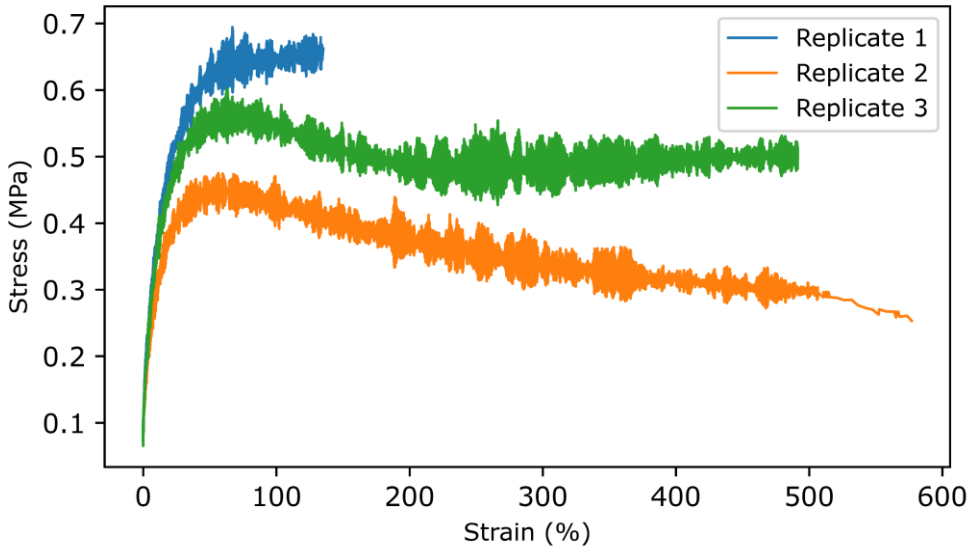

A11.5. IPHTAPDO 2000 50 MDI

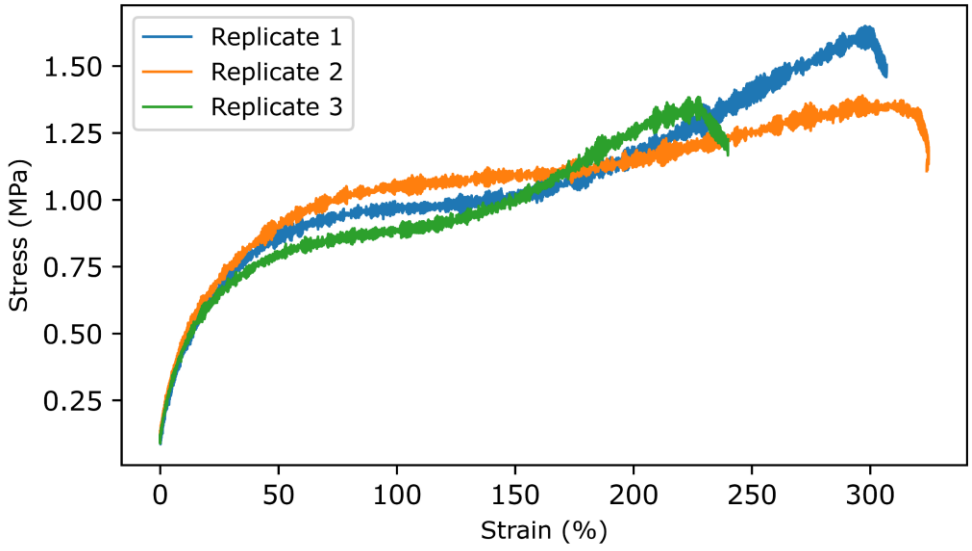

A11.6. IPHTAHDO 1000 10 MDI

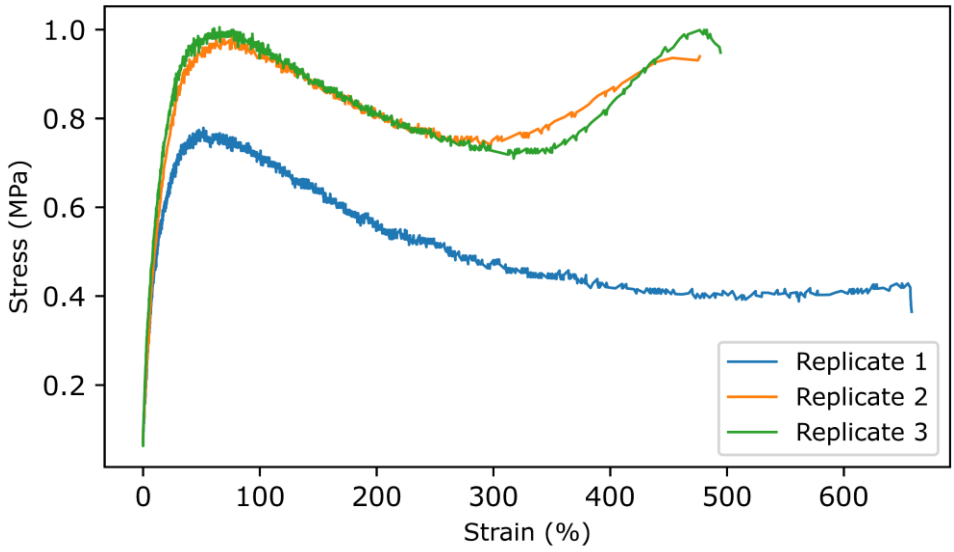

A11.7. IPHTAHDO 1000 30 MDI

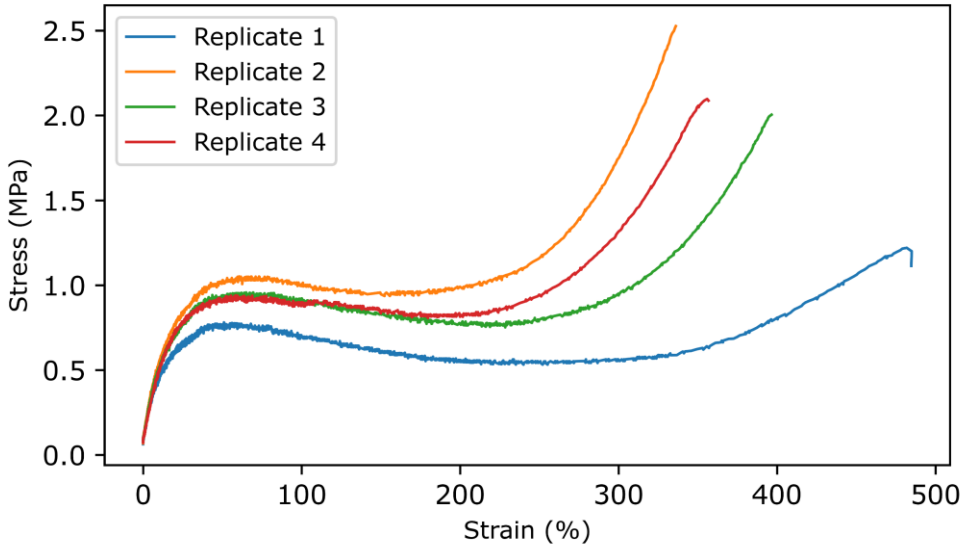

A11.8. IPHTAHDO 1000 50 MDI

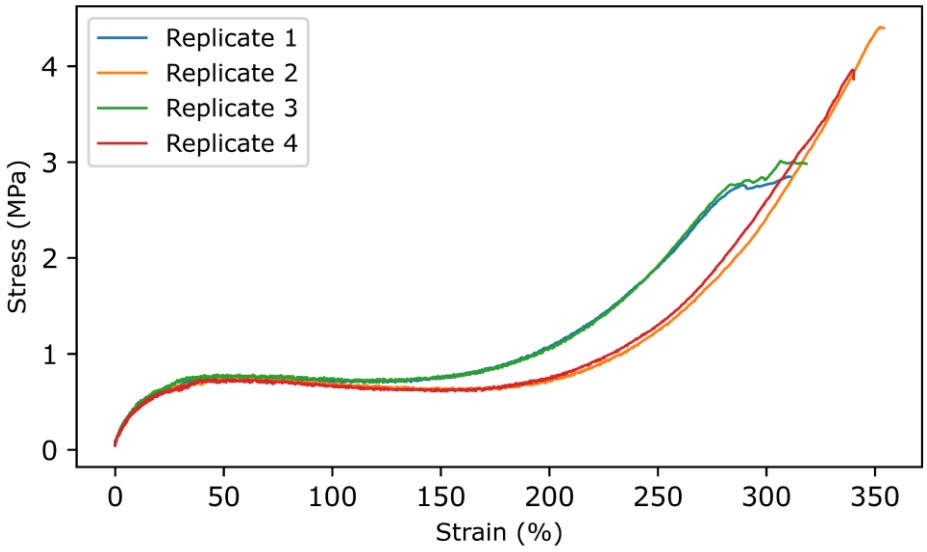

A11.9. IPHTAHDO 2000 10 MDI

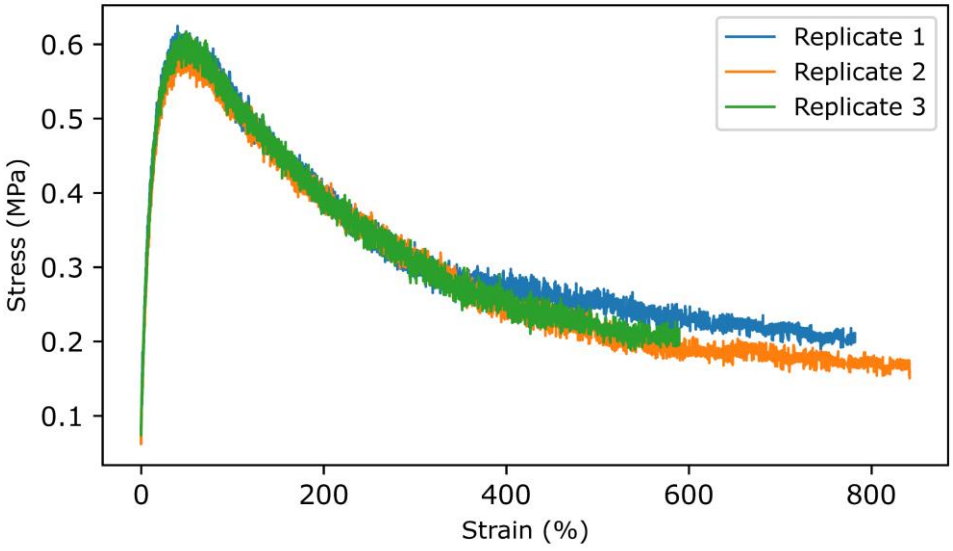

A11.10. IPHTAHDO 2000 30 MDI

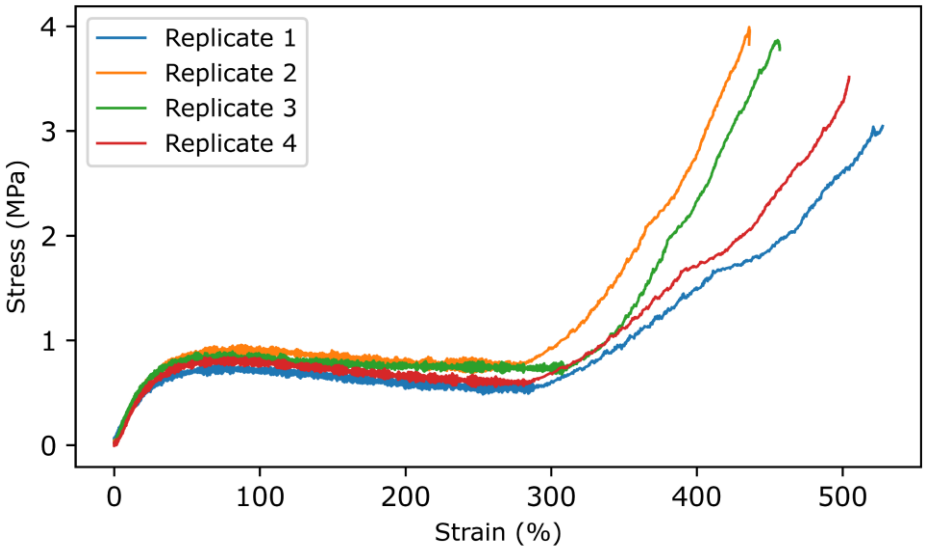

A11.11. IPHTAHDO 2000 50 MDI

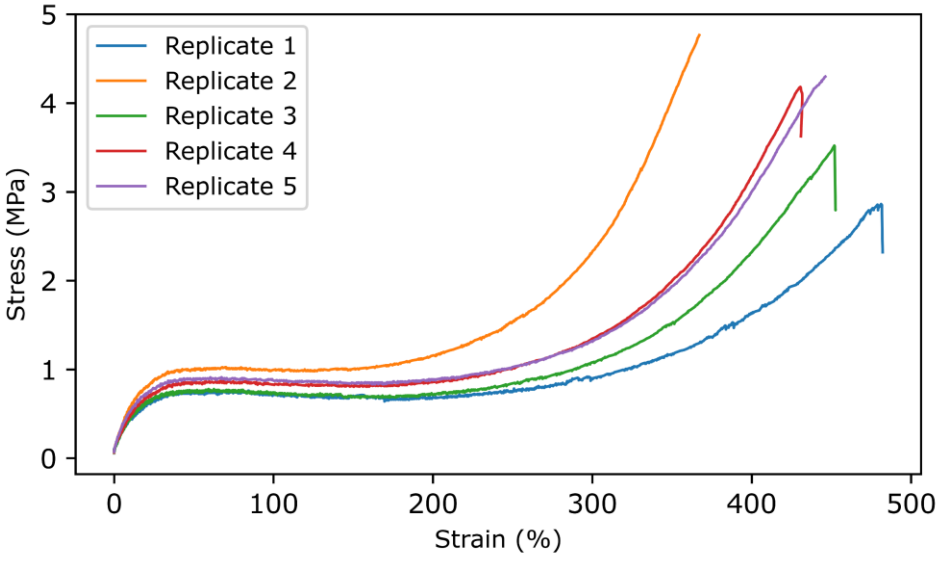

A11.12. IPHTAPDO 1000 10 HDI

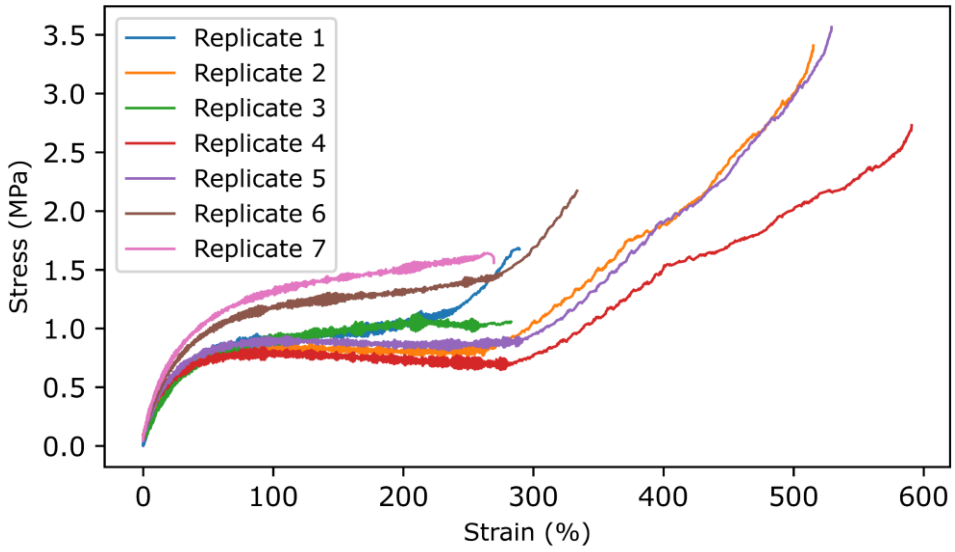

A11.13. IPHTAPDO 1000 30 HDI

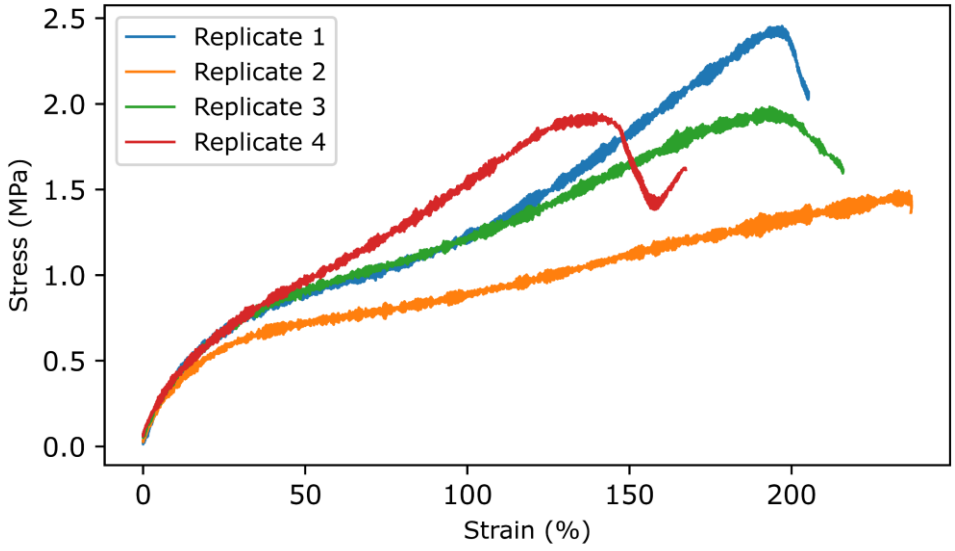

A11.14. IPHTAPDO 1000 50 HDI

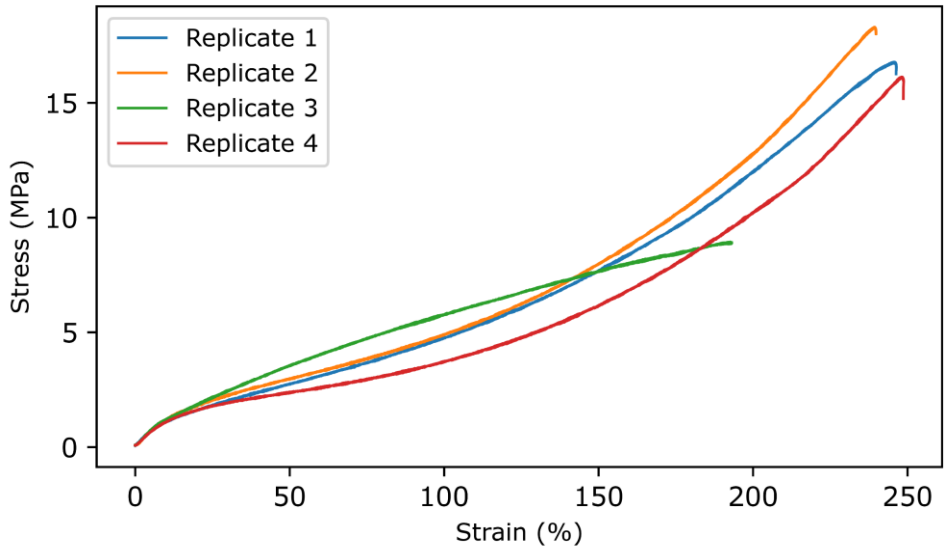

A11.15. IPHTAPDO 2000 10 HDI

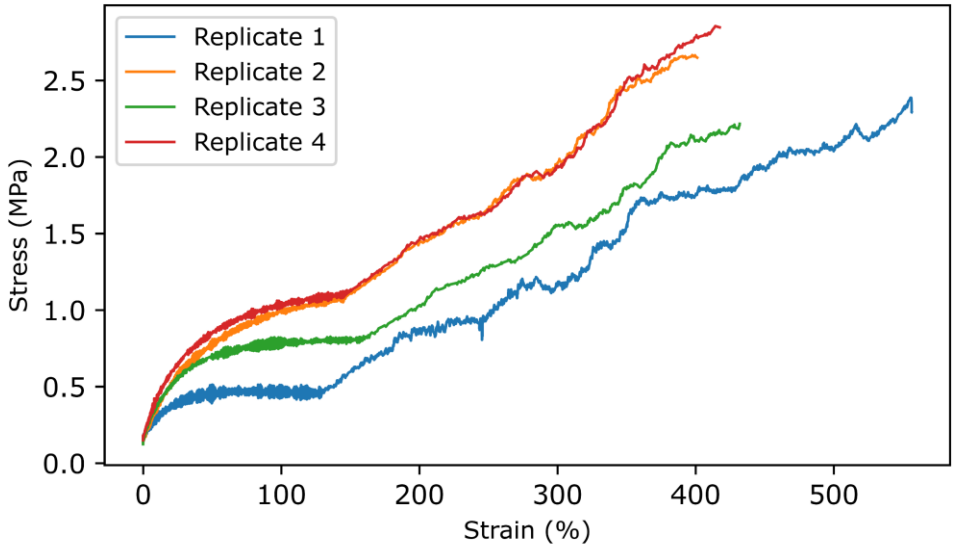

A11.16. IPHTAPDO 2000 30 HDI

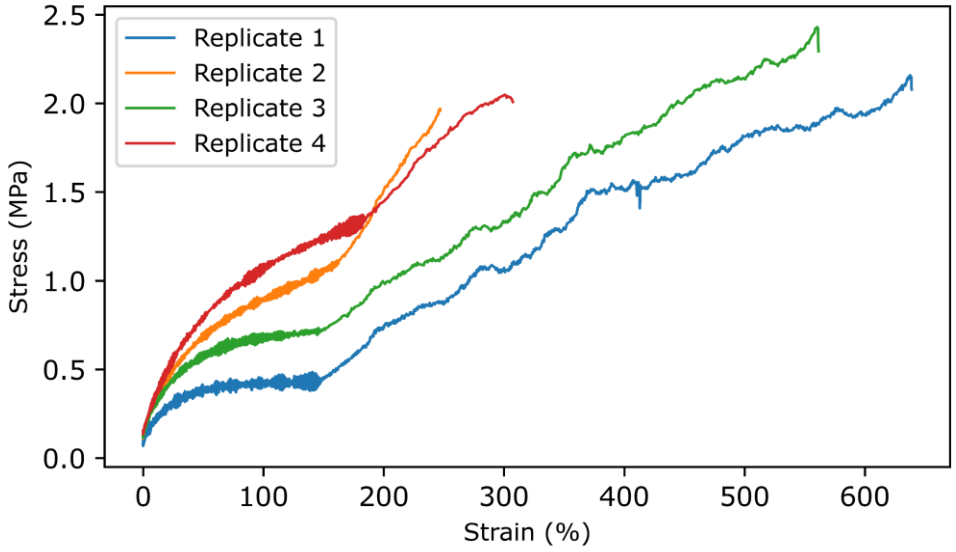

A11.17. IPHTAPDO 2000 50 HDI

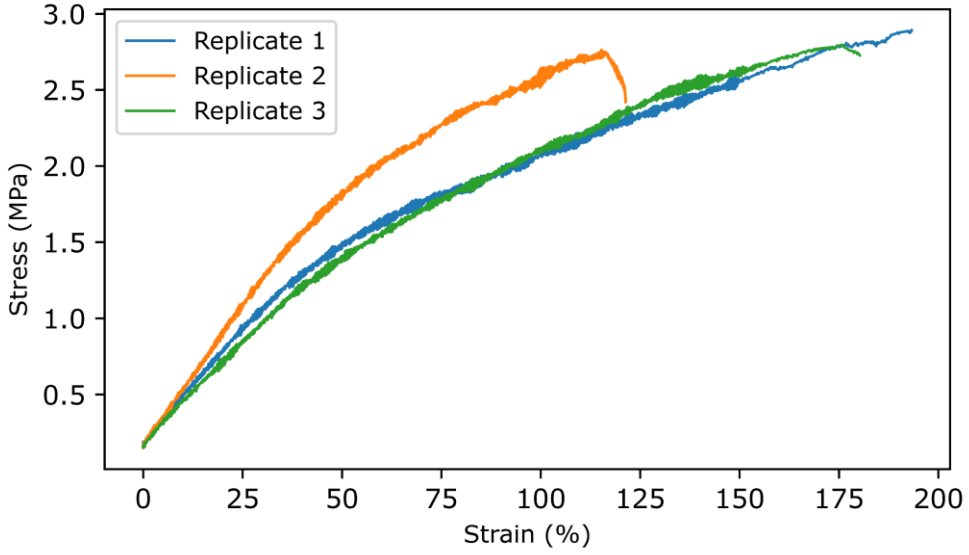

A11.18. IPHTAHDO 1000 10 HDI

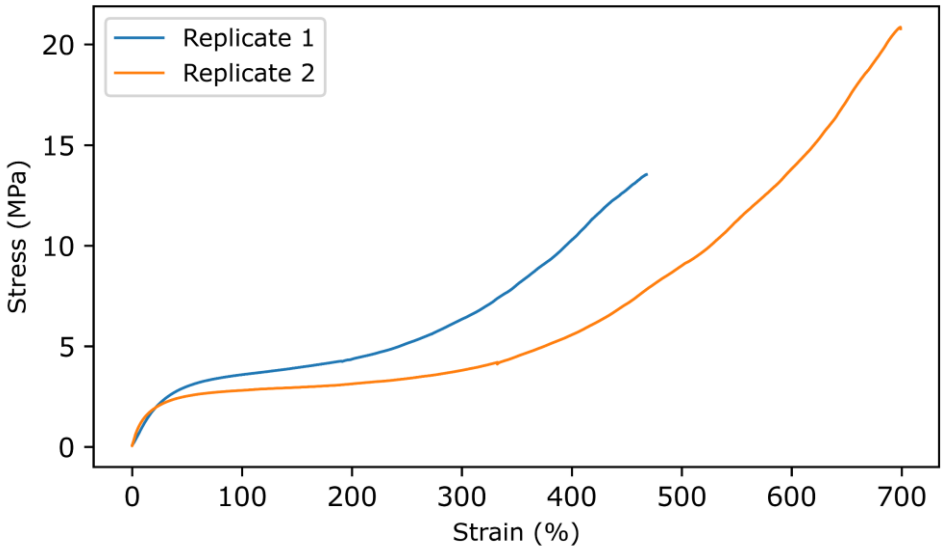

A11.19. IPHTAHDO 1000 30 HDI

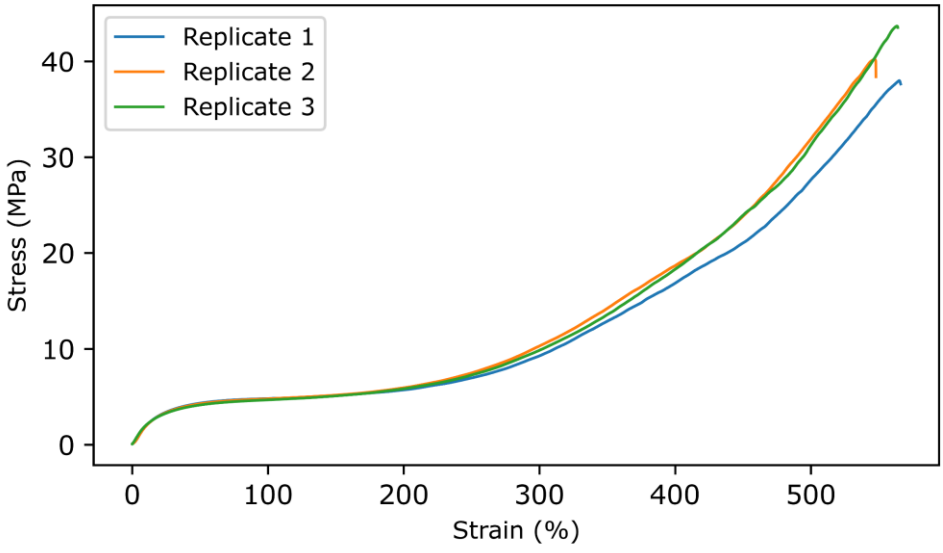

A11.20. IPHTAHDO 1000 50 HDI

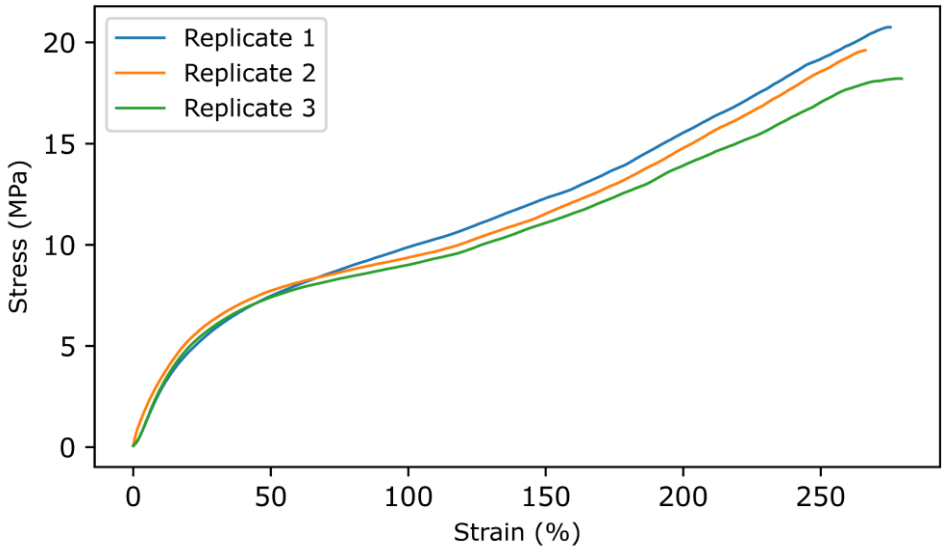

A11.21. IPHTAHDO 2000 10 HDI

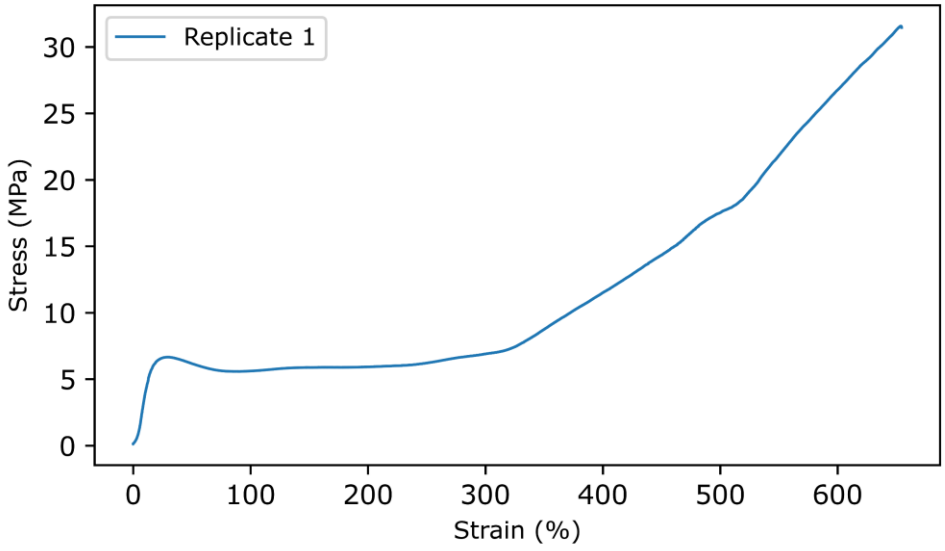

A11.22. IPHTAHDO 2000 30 HDI

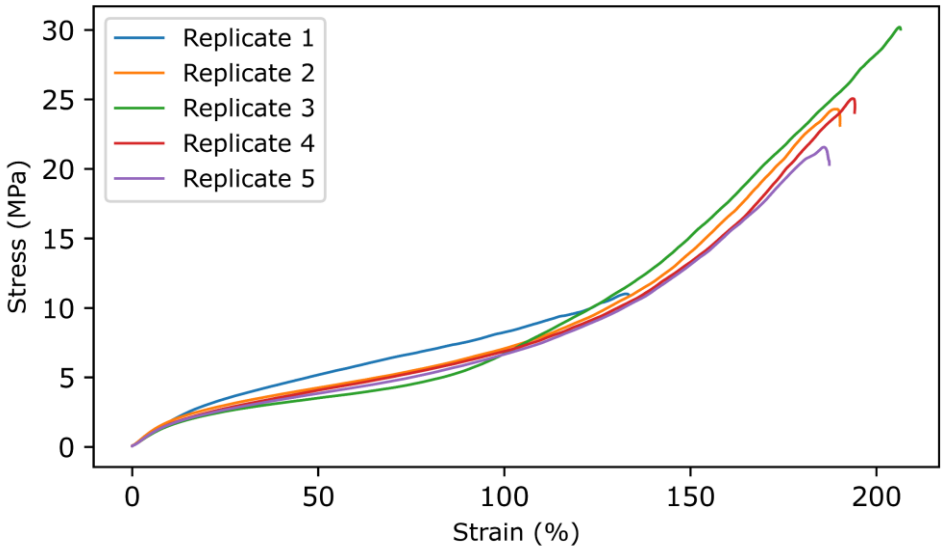

A11.23. IPHTAHDO 2000 50 HDI

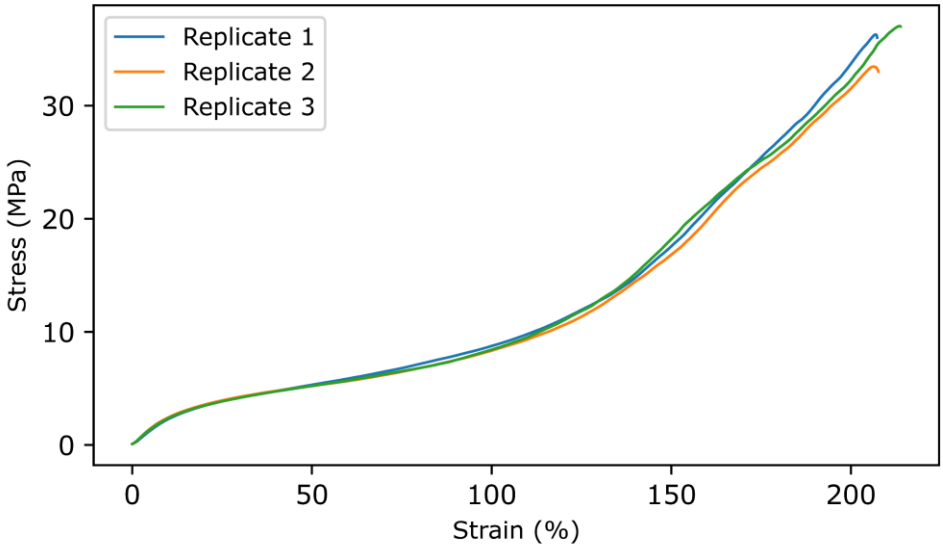

A11.24. FDCAPDO 1000 10 MDI

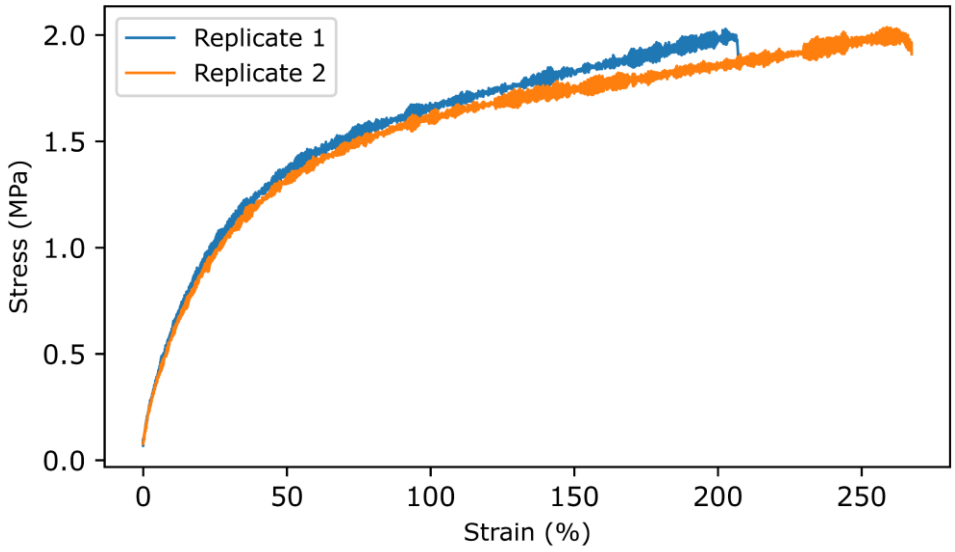

A11.25. FDCAPDO 1000 50 MDI

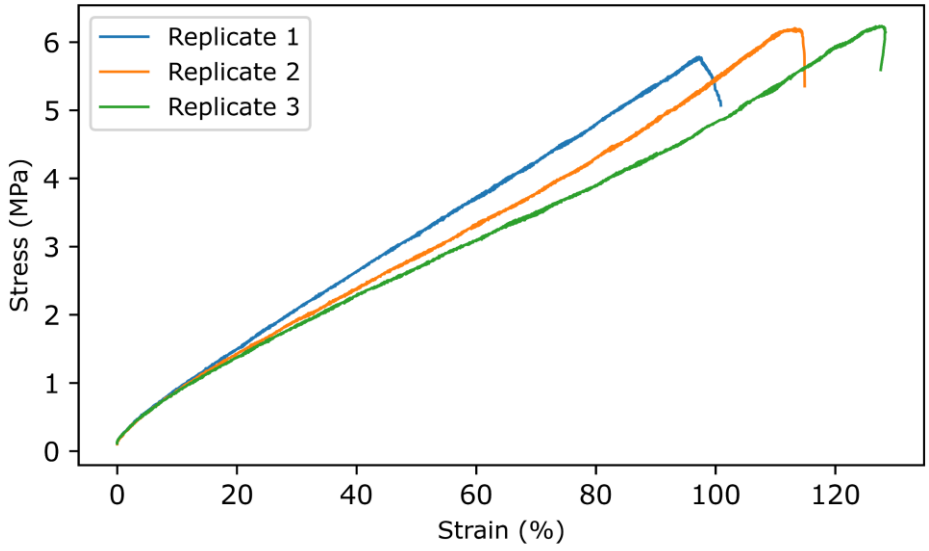

A11.26. FDCAPDO 1500 30 MDI

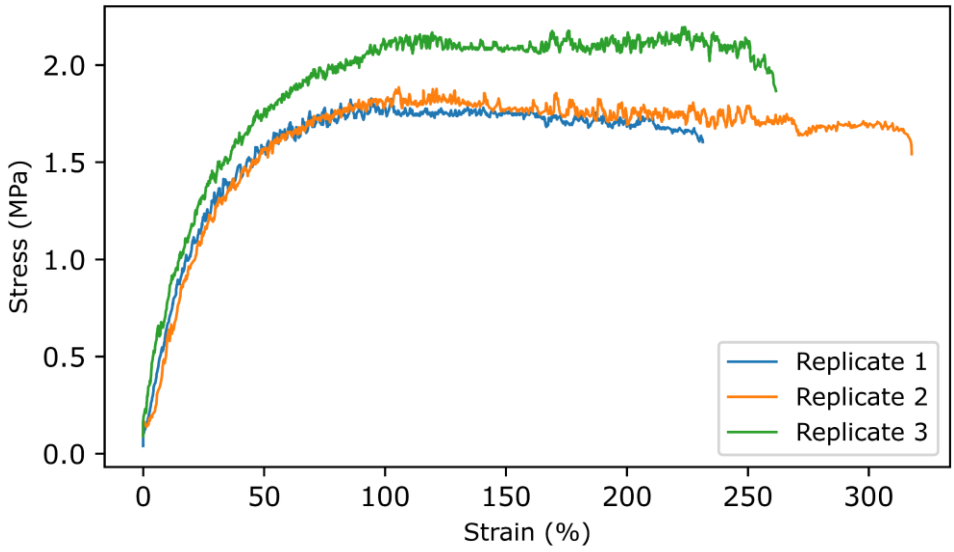

A11.27. FDCAPDO 2000 10 MDI

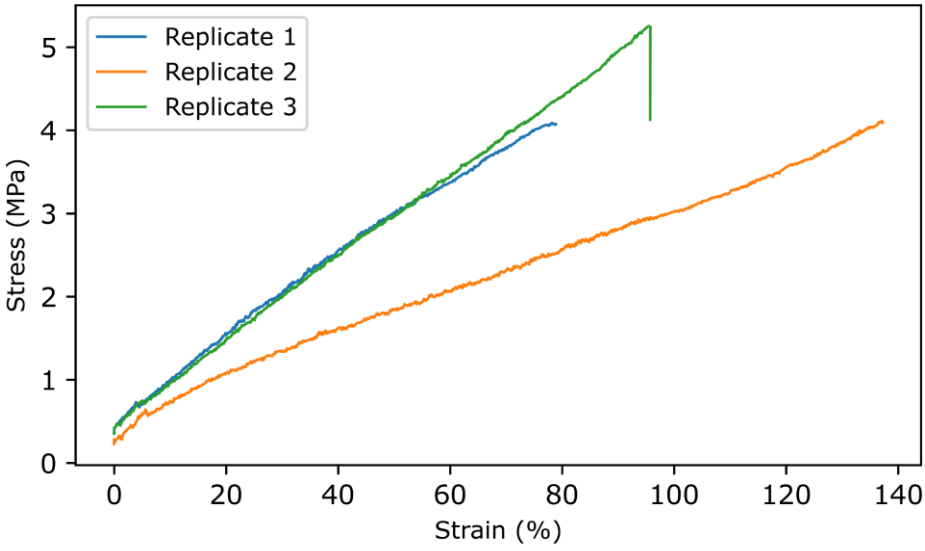

A11.28. FDCAPDO 2000 50 MDI

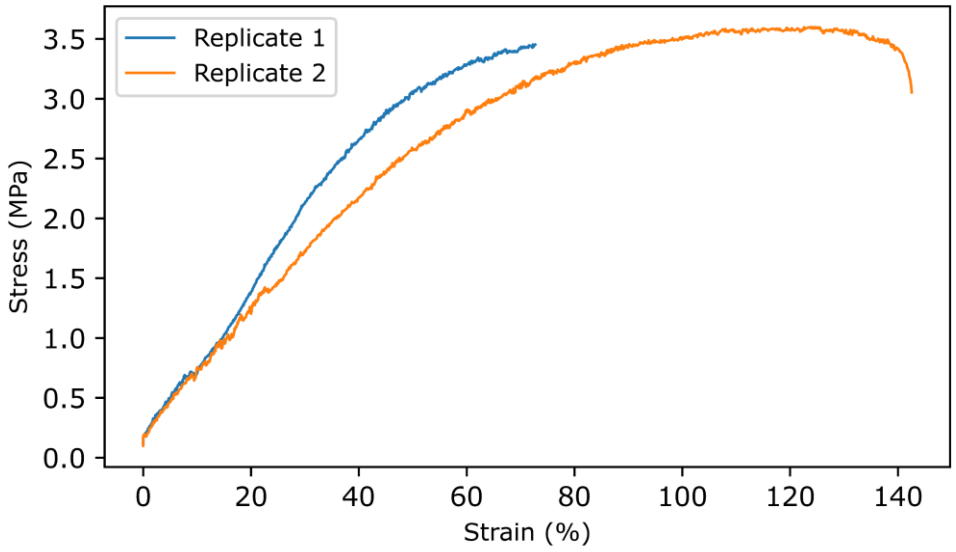

A11.29. FDCAHDO 1000 10 MDI

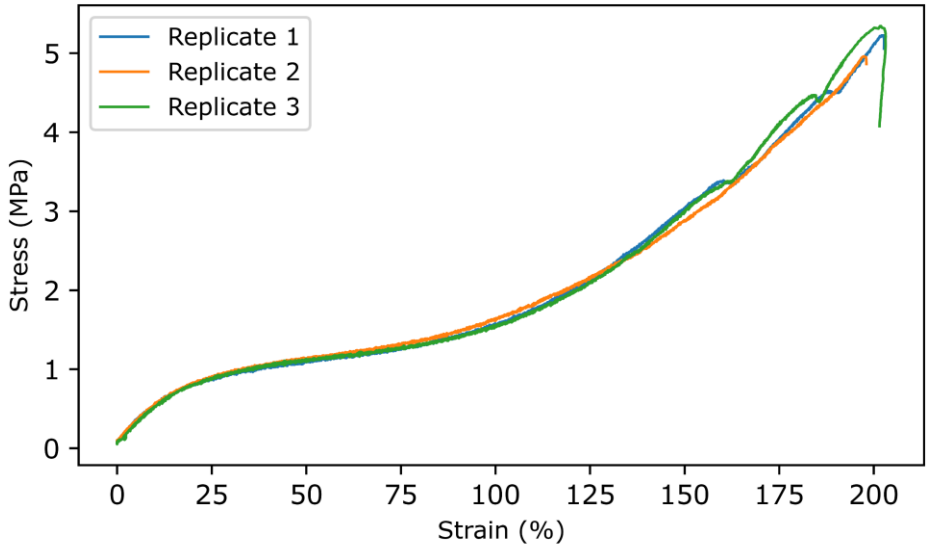

A11.30. FDCAHDO 1000 50 MDI

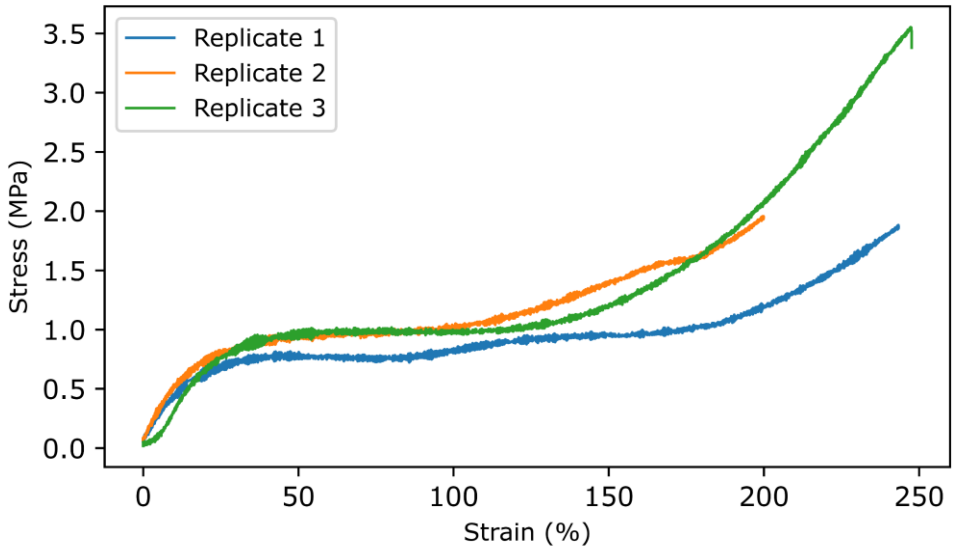

A11.31. FDCAHDO 1500 30 MDI

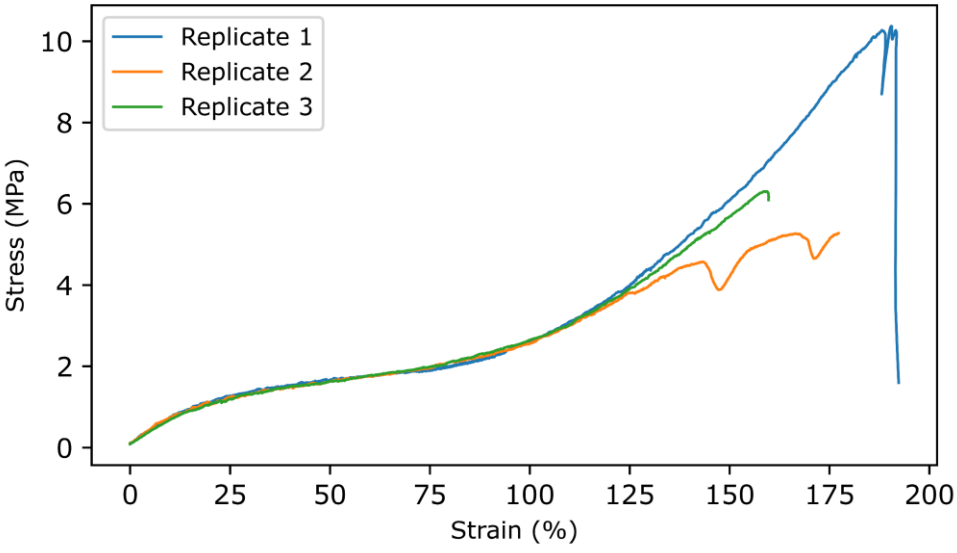

A11.32. FDCAHDO 2000 10 MDI

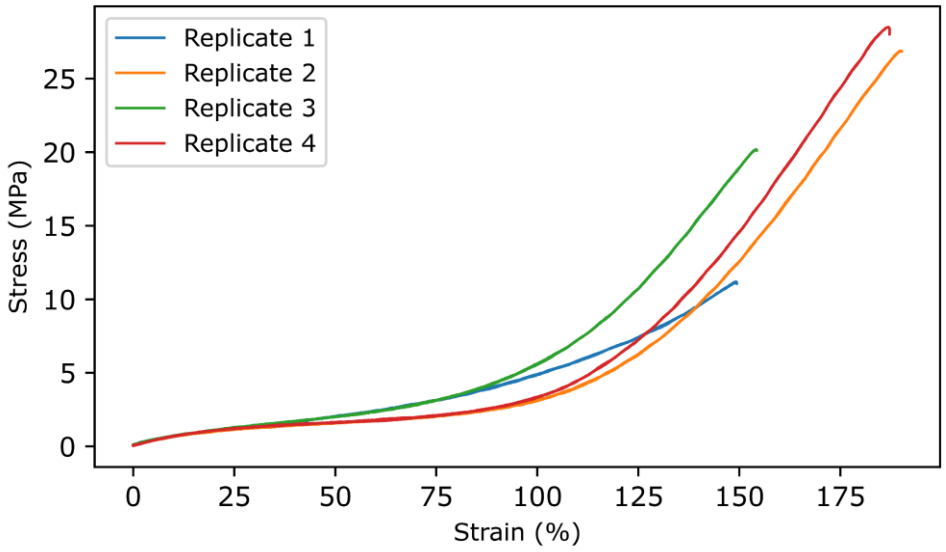

A11.33. FDCAHDO 2000 50 MDI

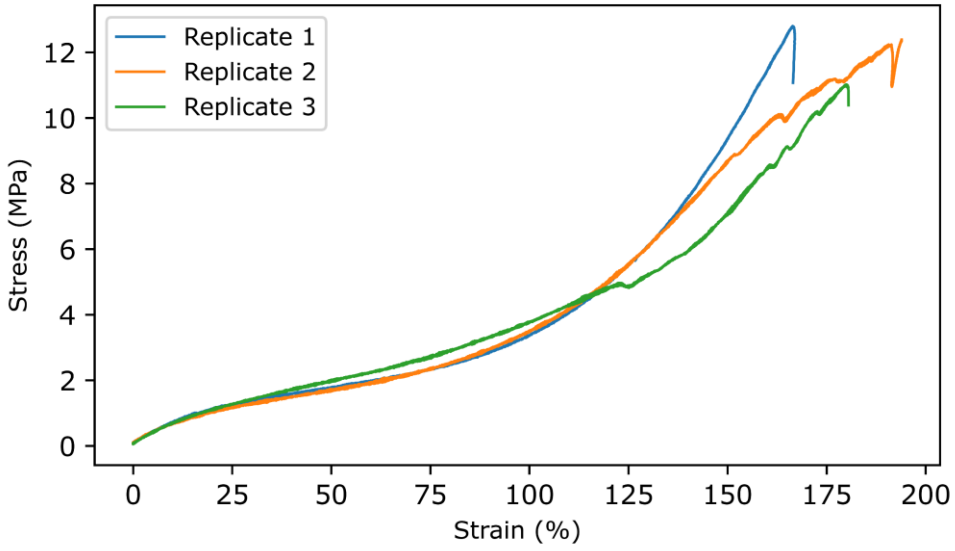

A11.34. FDCAPDO 1000 10 HDI

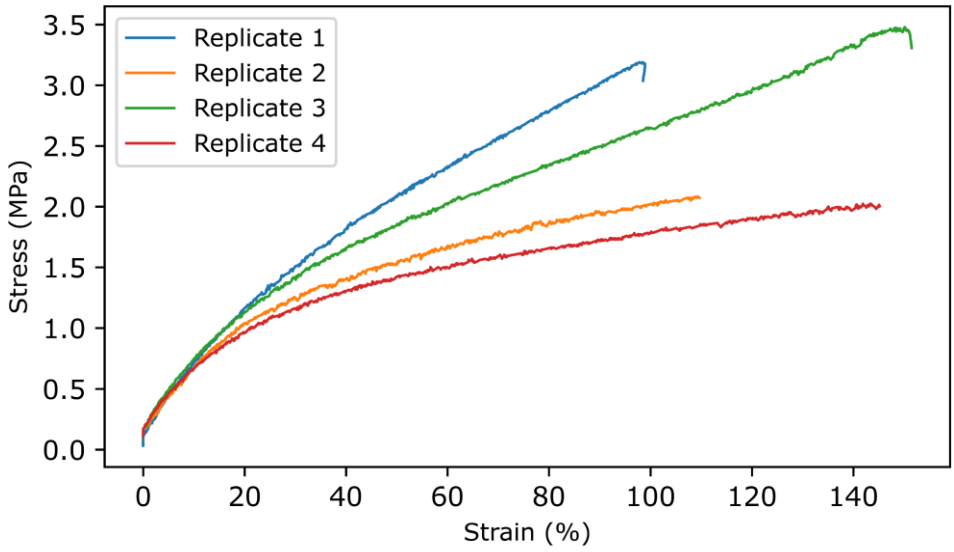

A11.35. FDCAPDO 1500 30 HDI

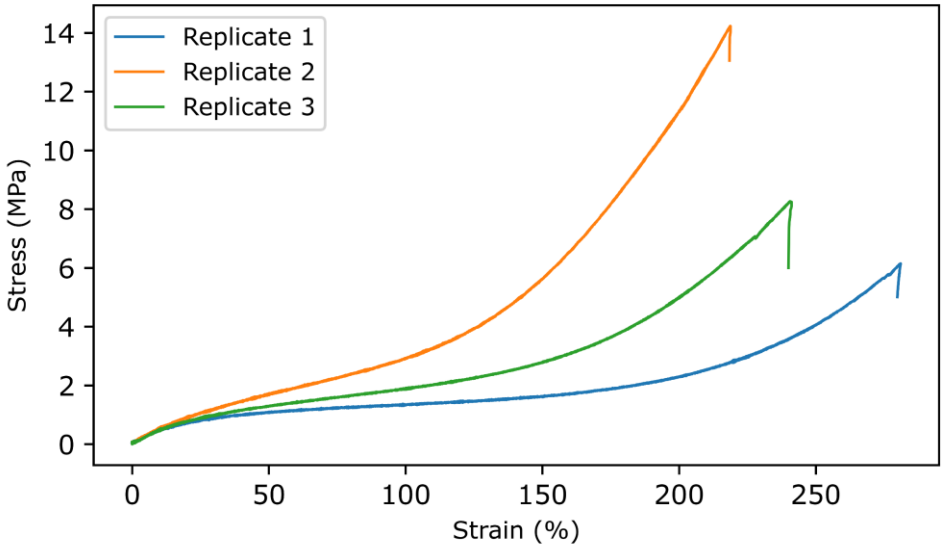

A11.36. FDCAPDO 2000 10 HDI

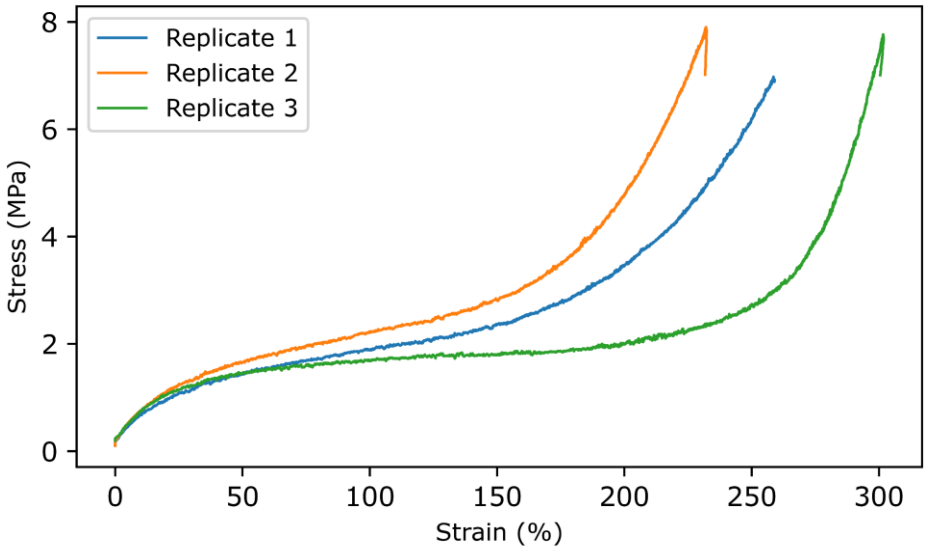

A11.37. FDCAPDO 2000 50 HDI

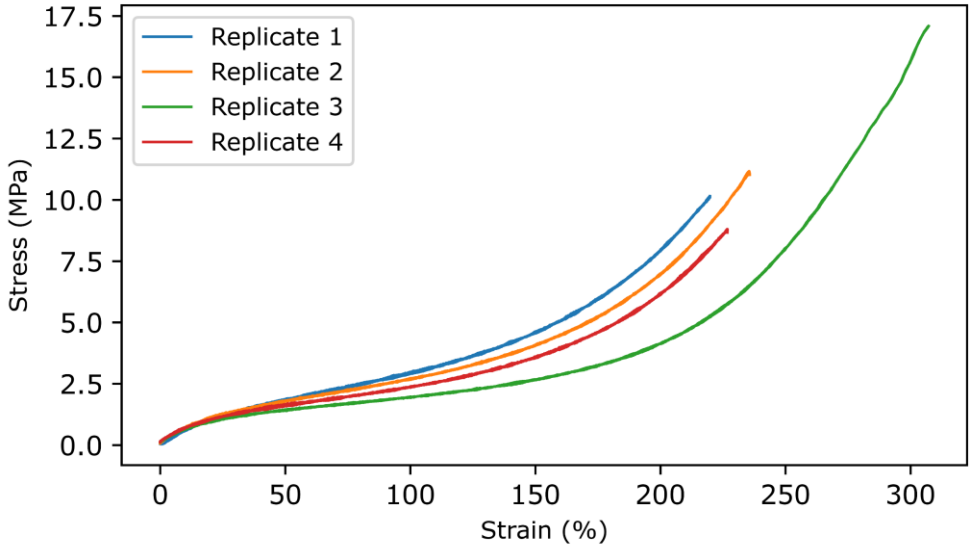

A11.38. FDCAHDO 1000 10 HDI

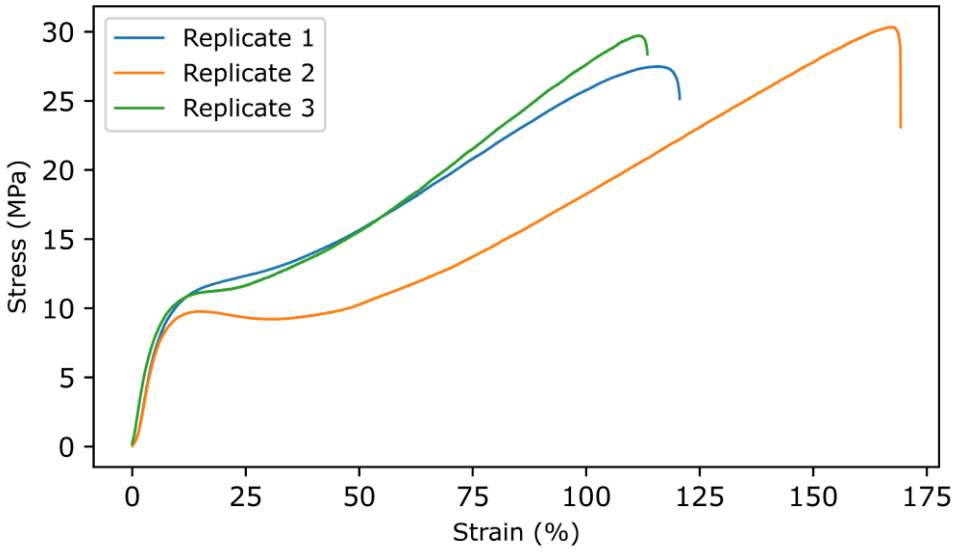

A11.39. FDCAHDO 1000 50 HDI

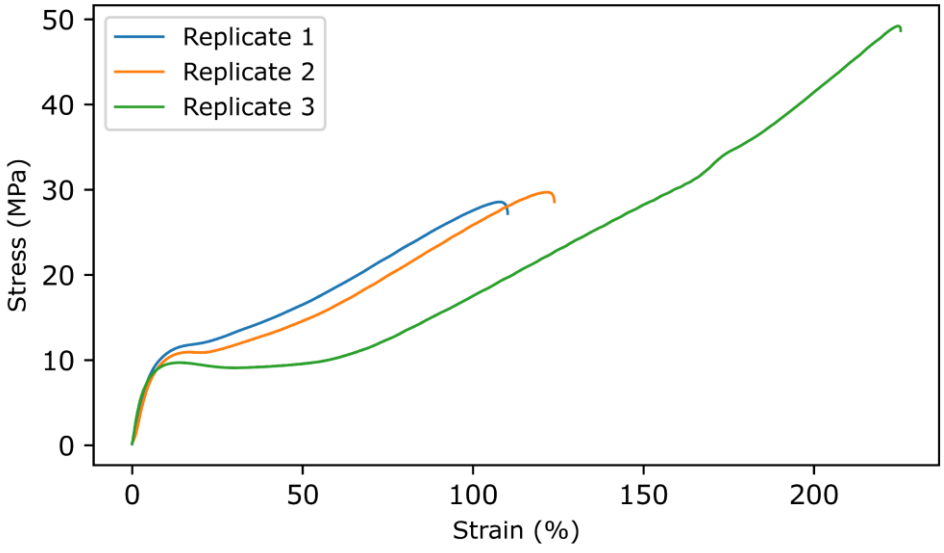

A11.40. FDCAHDO 1500 30 HDI

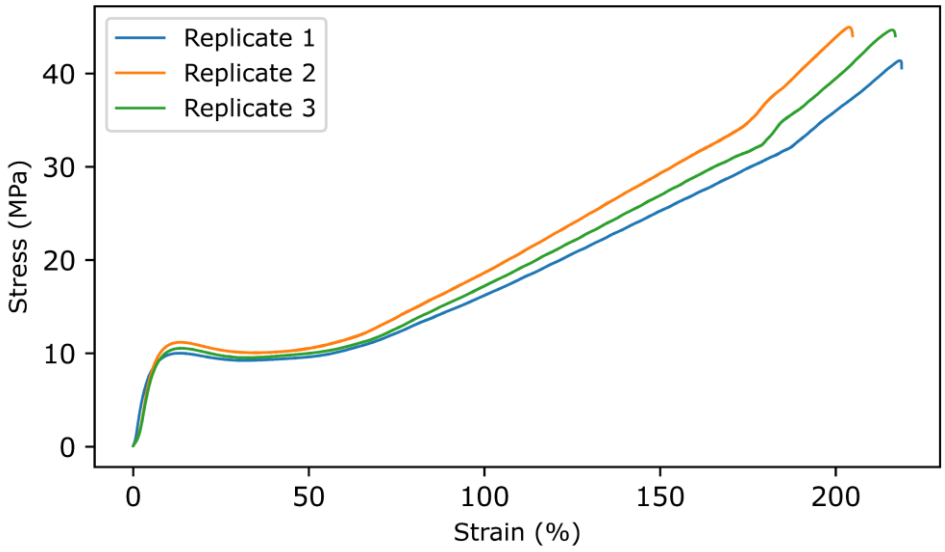

A11.41. FDCAHDO 2000 10 HDI

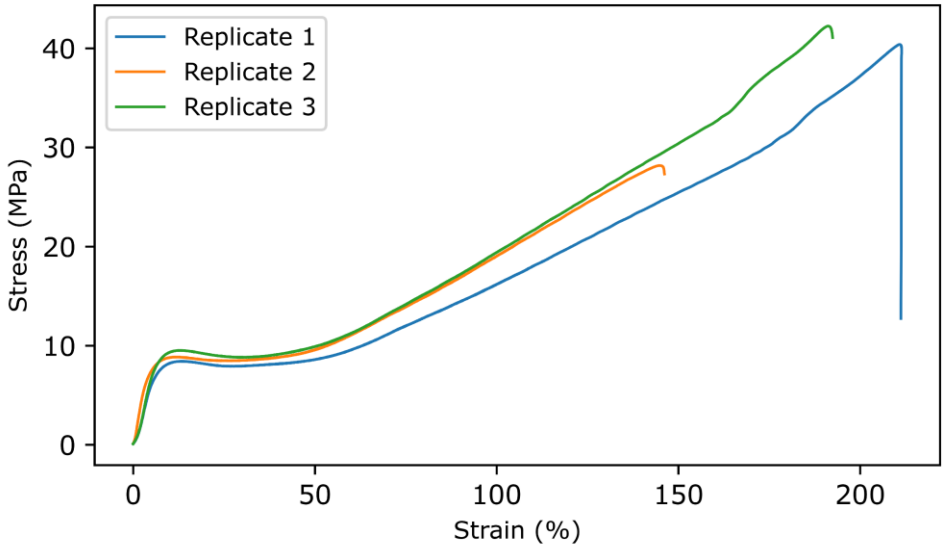

A11.42. FDCAHDO 2000 50 HDI

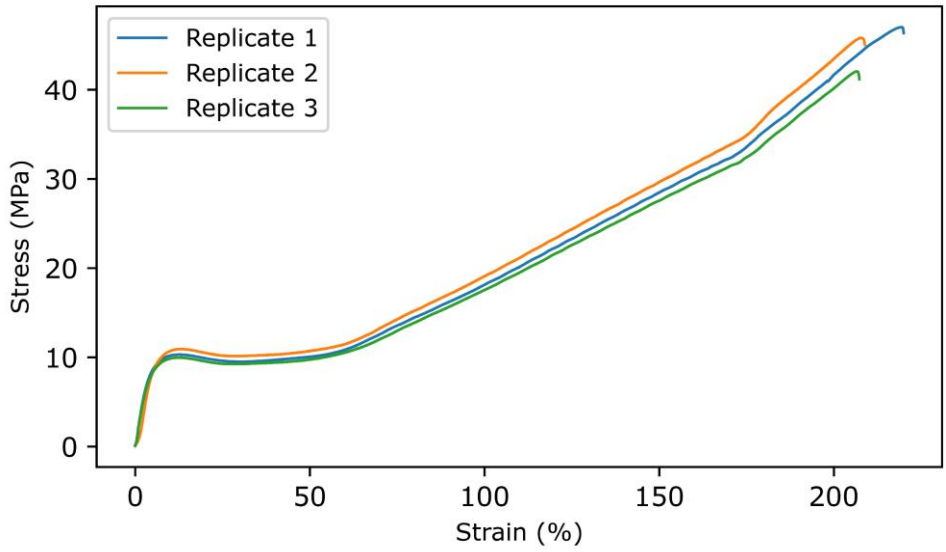

A12 Actuation strength of unannealed TPUs

A12.1. IPHTAPDO 1000 10 MDI

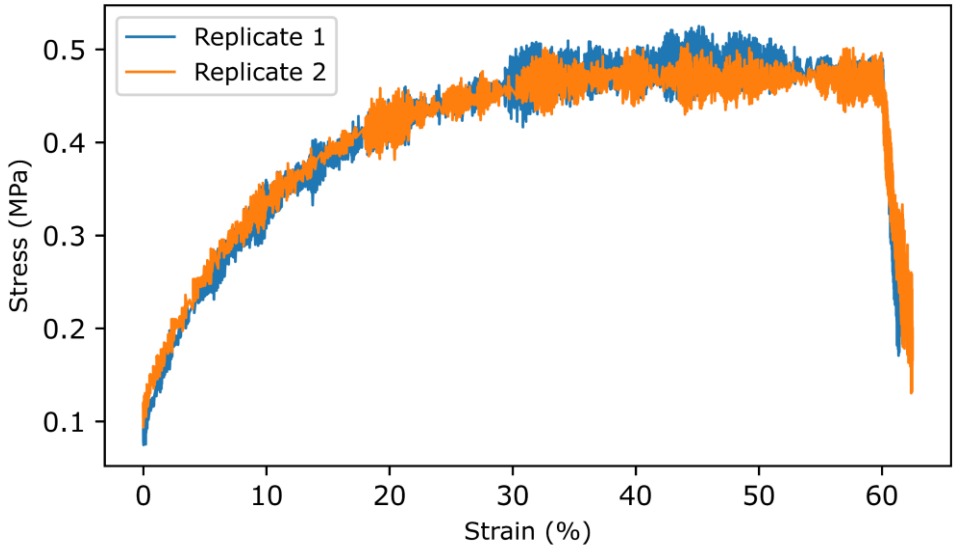

A12.2. IPHTAPDO 1000 30 MDI

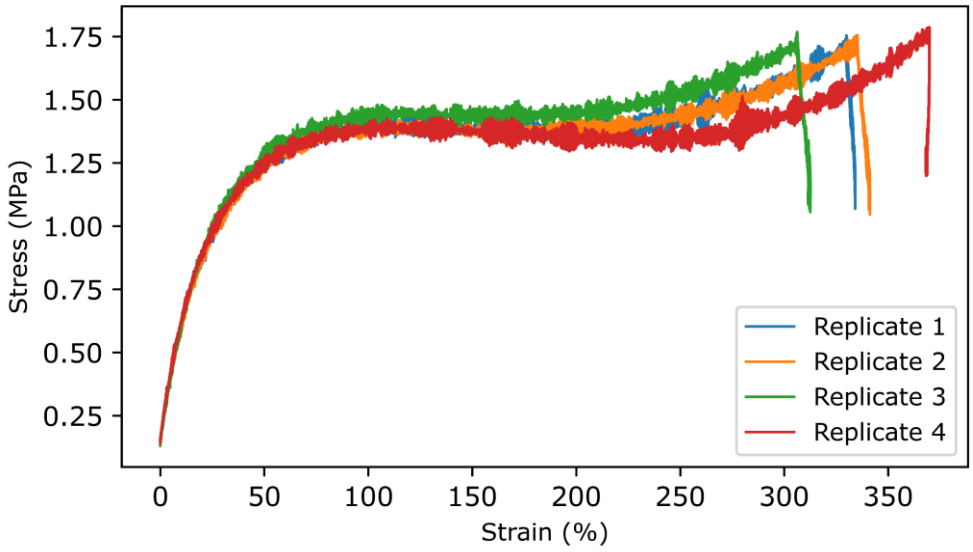

A12.3. IPHTAPDO 2000 50 MDI

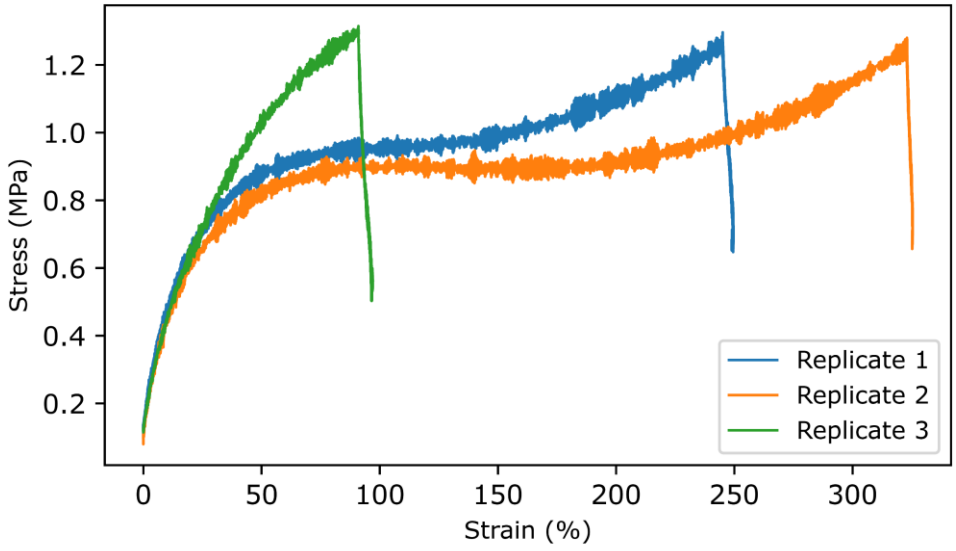

A12.4. IPHTAHDO 1000 10 MDI

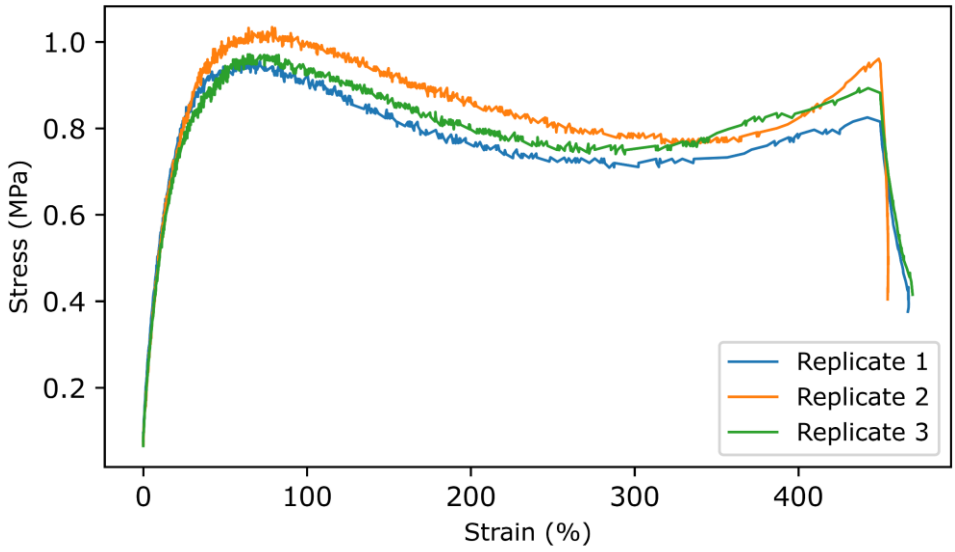

A12.5. IPHTAHDO 1000 30 MDI

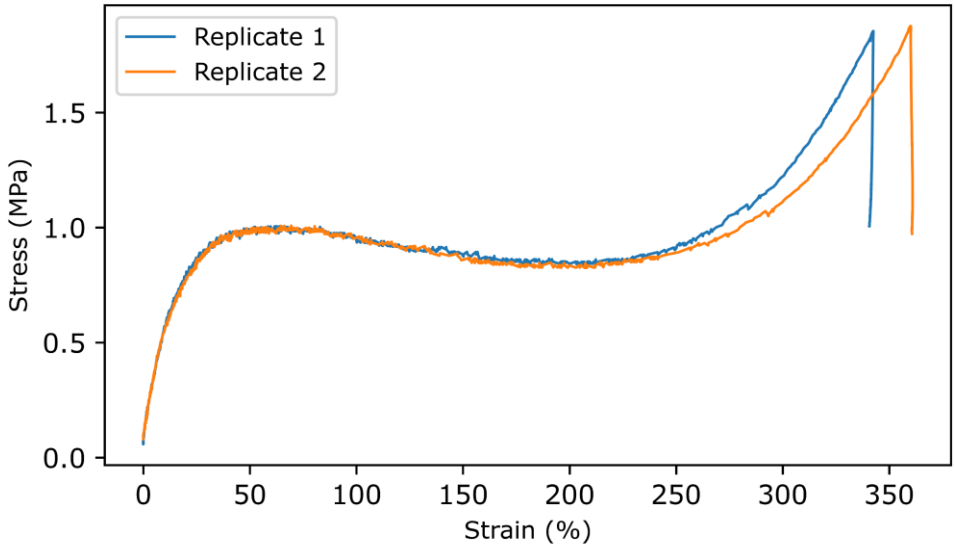

A12.6. IPHTAHDO 1000 50 MDI

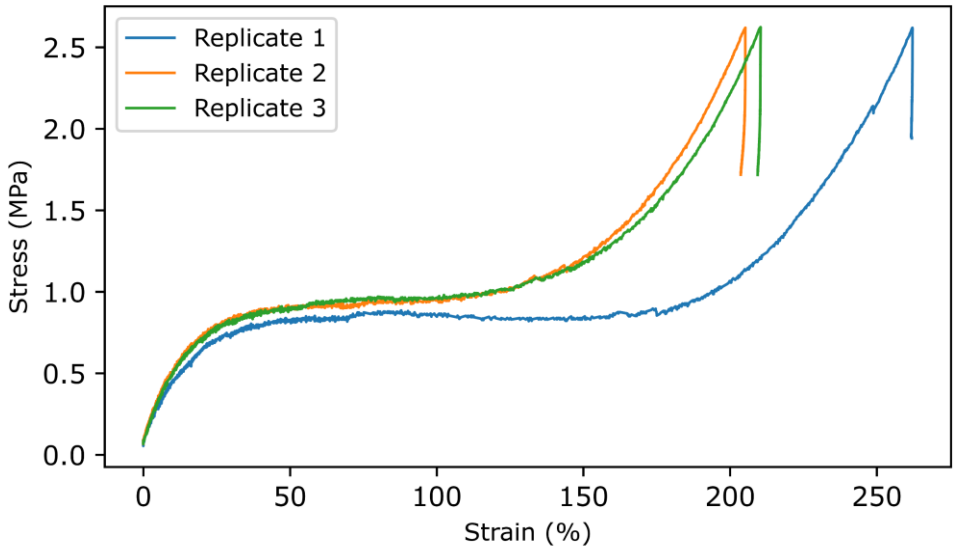

A12.7. IPHTAHDO 2000 10 MDI

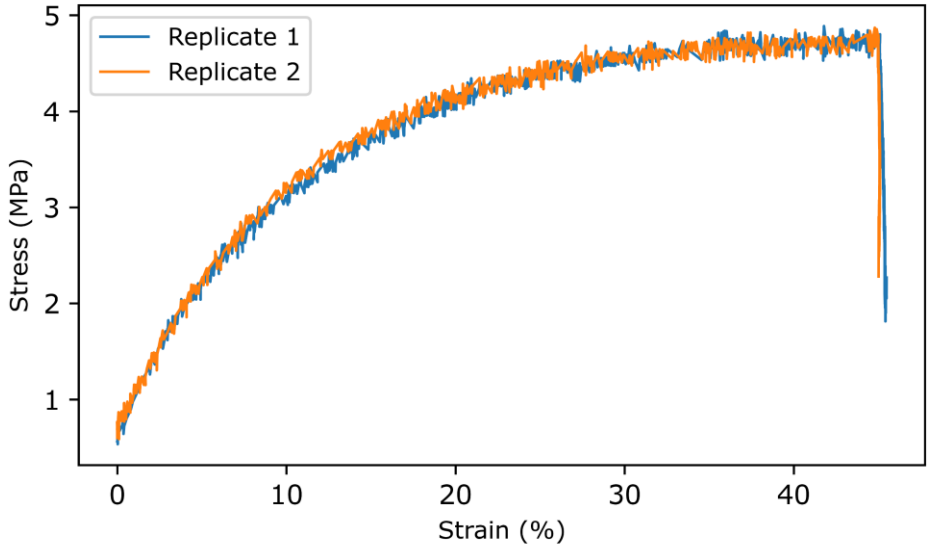

A12.8. IPHTAHDO 2000 30 MDI

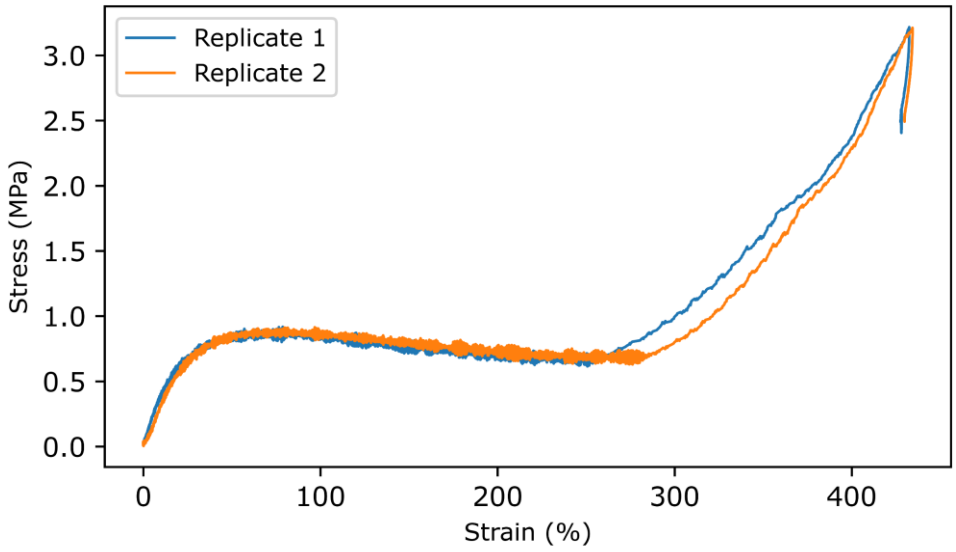

A12.9. IPHTAHDO 2000 50 MDI

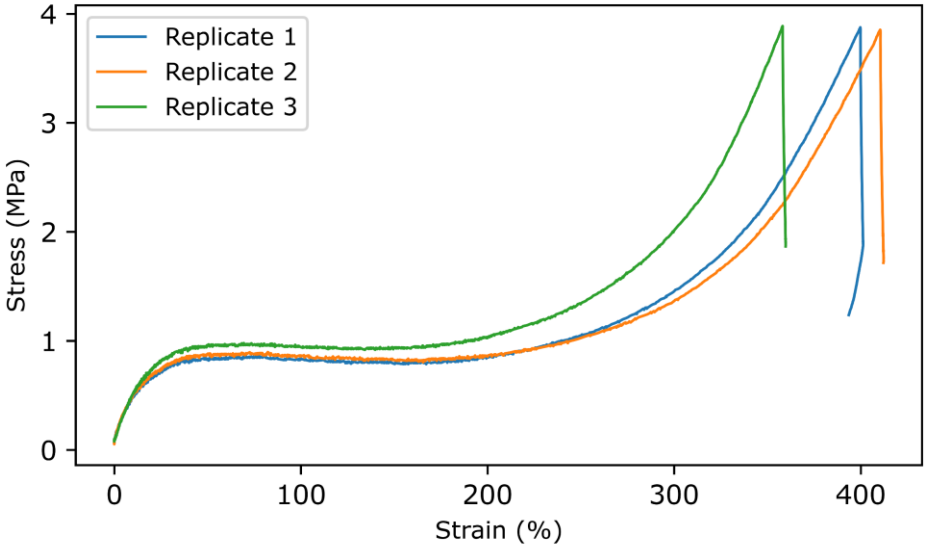

A12.10. IPHTAPDO 1000 10 HDI

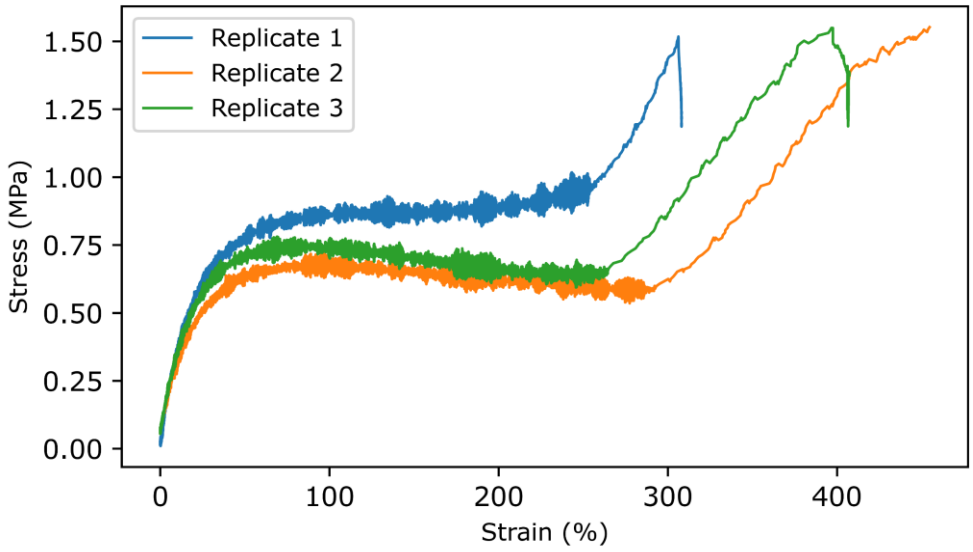

A12.11. IPHTAPDO 1000 30 HDI

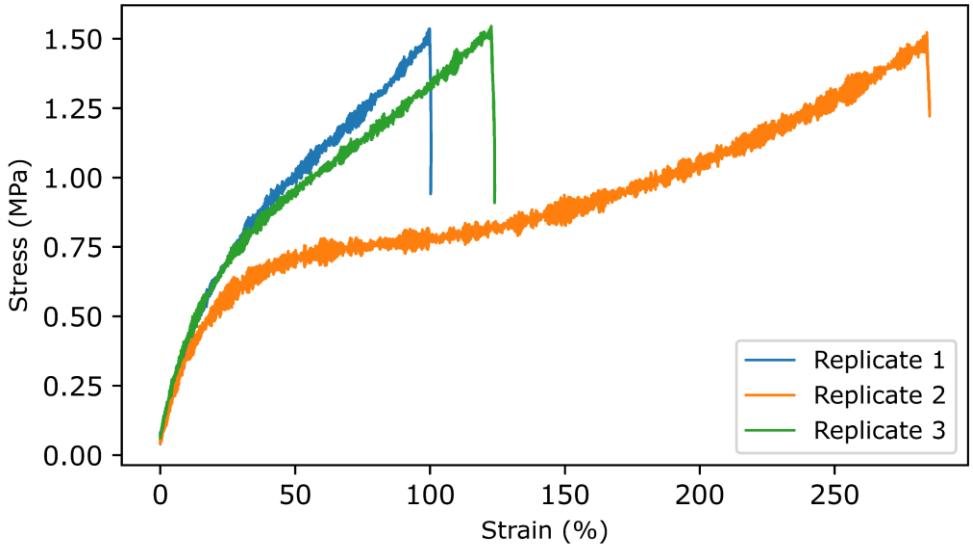

A12.12. IPHTAPDO 1000 50 HDI

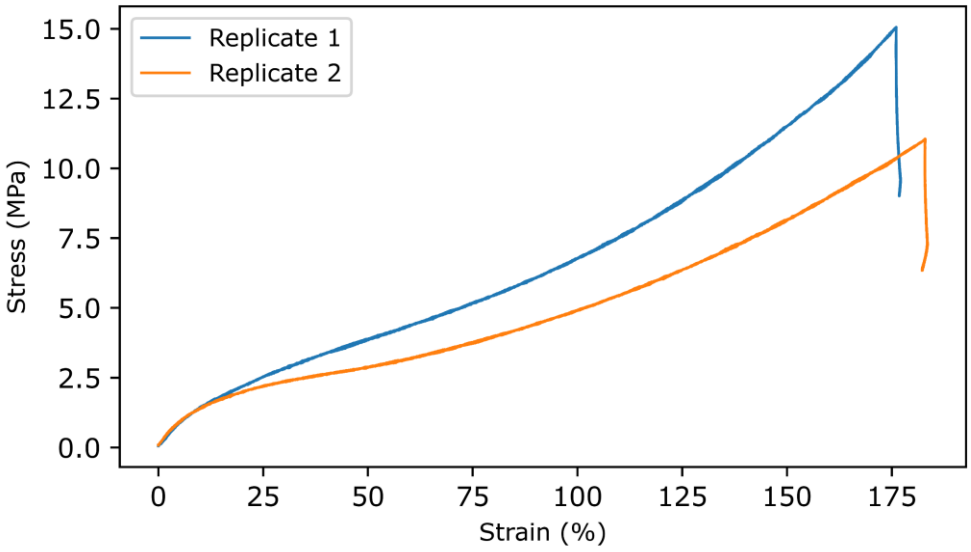

A12.13. IPHTAPDO 2000 10 HDI

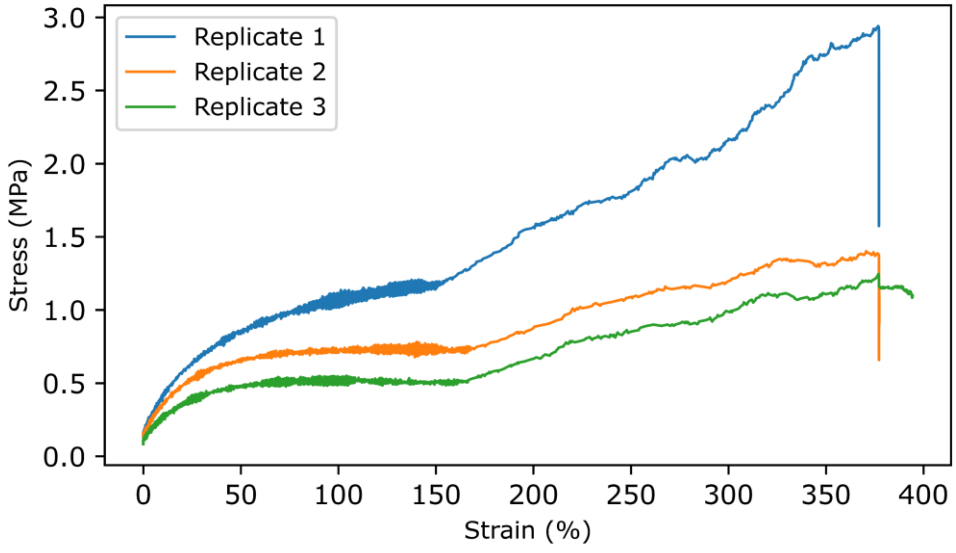

A12.14. IPHTAPDO 2000 30 HDI

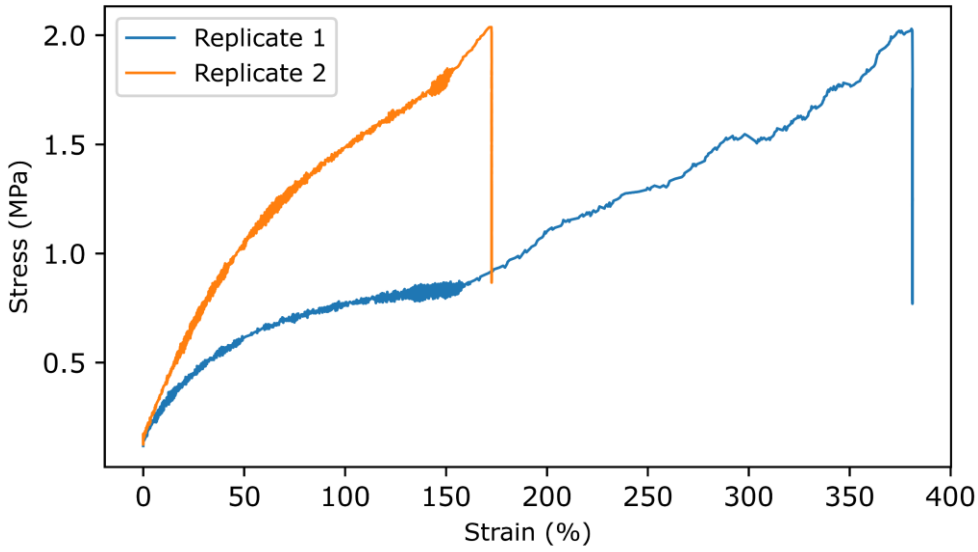

A12.15. IPHTAPDO 2000 50 HDI

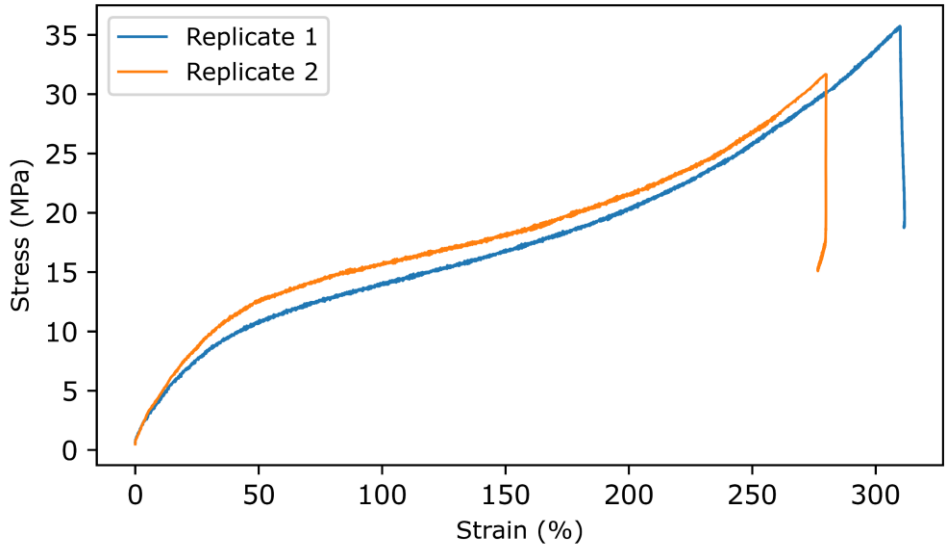

A12.16. IPHTAHDO 1000 10 HDI

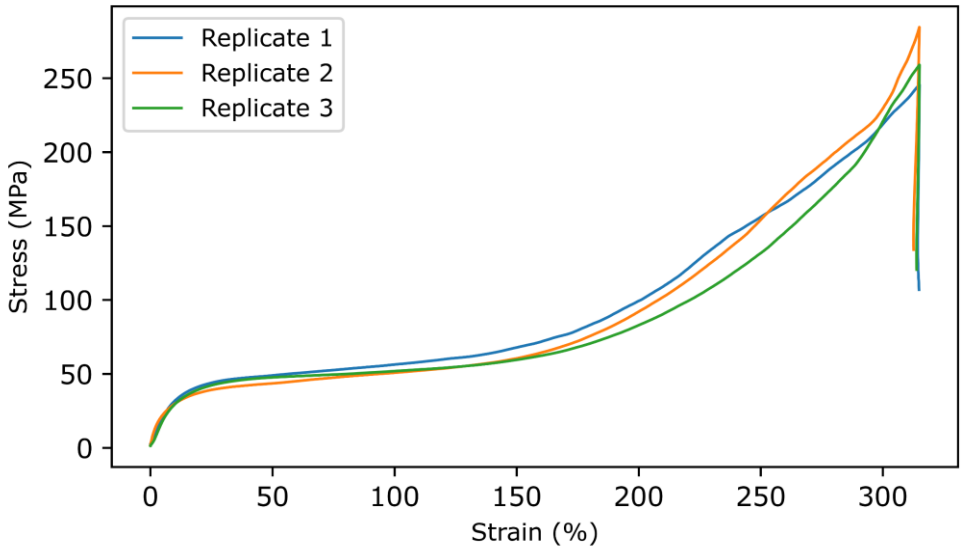

A12.17. IPHTAHDO 1000 30 HDI

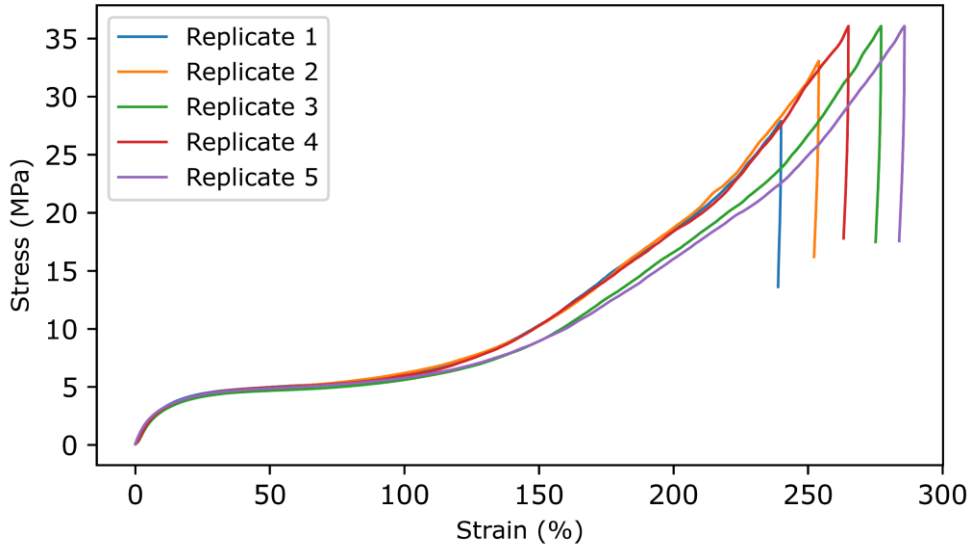

A12.18. IPHTAHDO 1000 50 HDI

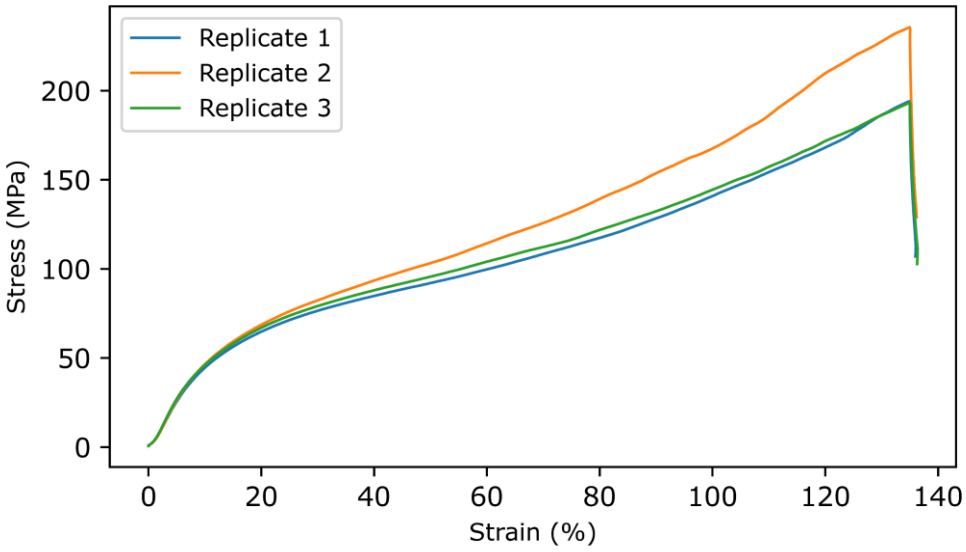

A12.19. IPHTAHDO 2000 10 HDI

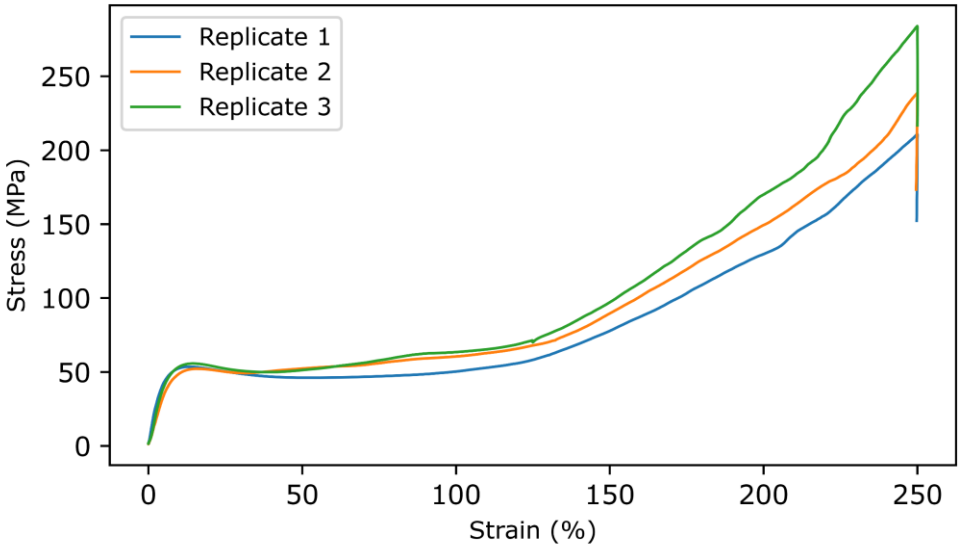

A12.20. IPHTAHDO 2000 30 HDI

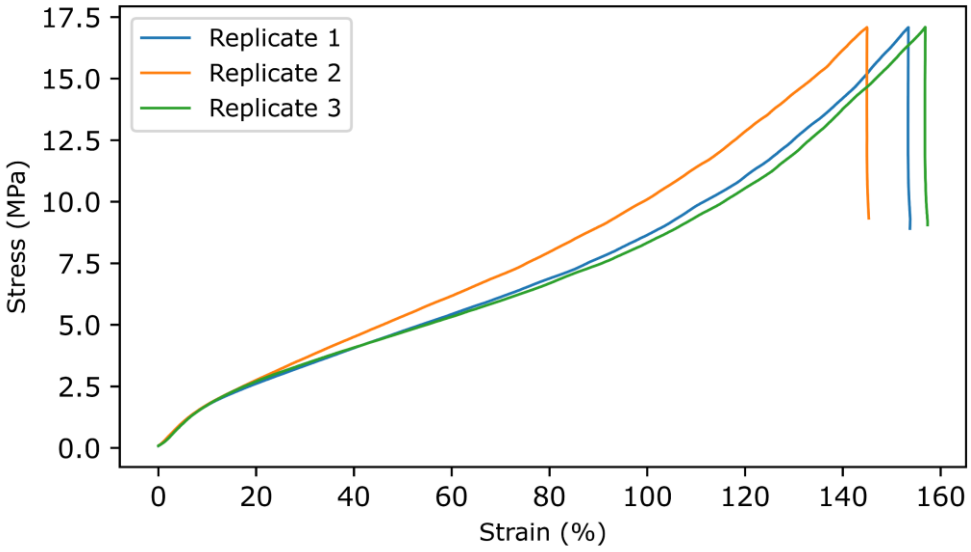

A12.21. IPHTAHDO 2000 50 HDI

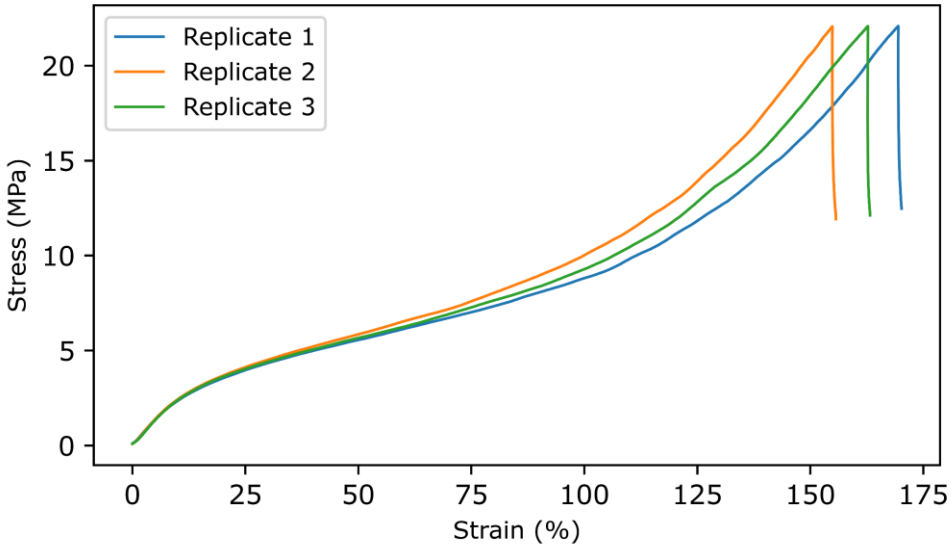

A12.22. FDCAPDO 1000 10 MDI

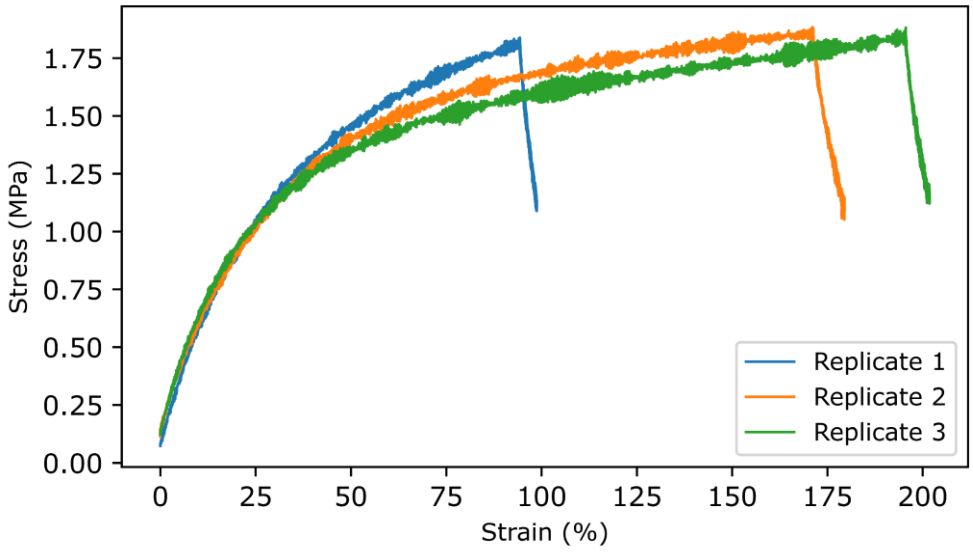

A12.23. FDCAPDO 1000 50 MDI

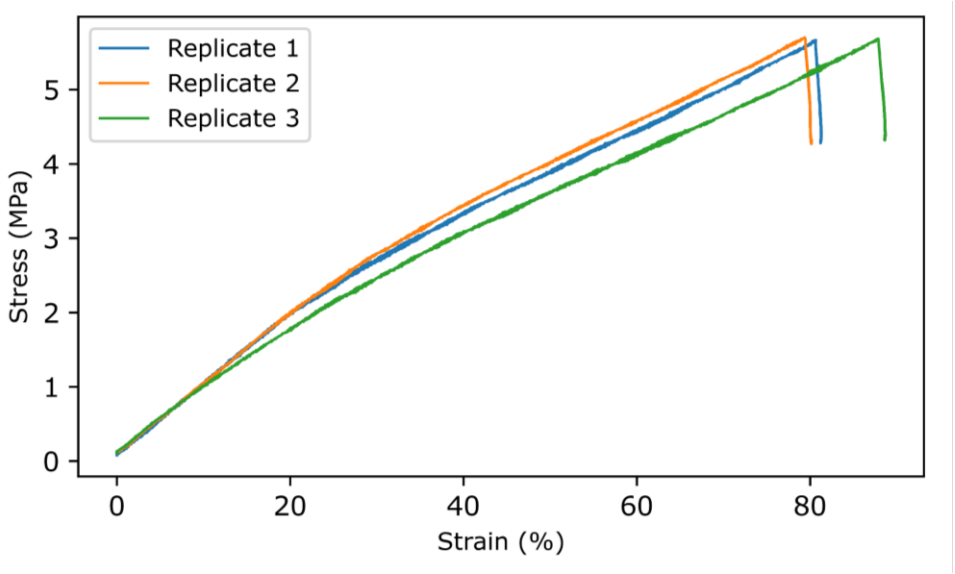

A12.24. FDCAPDO 1500 30 MDI

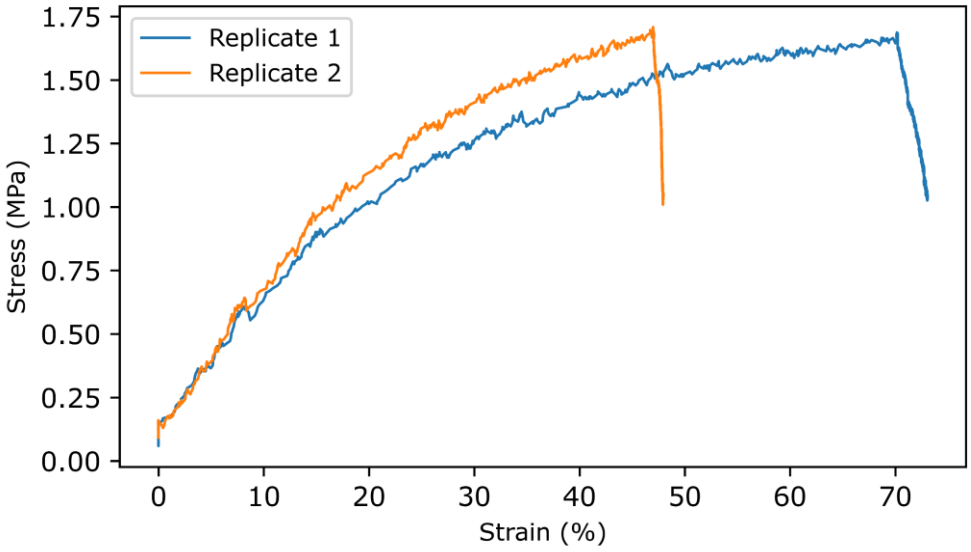

A12.25. FDCAPDO 2000 10 MDI

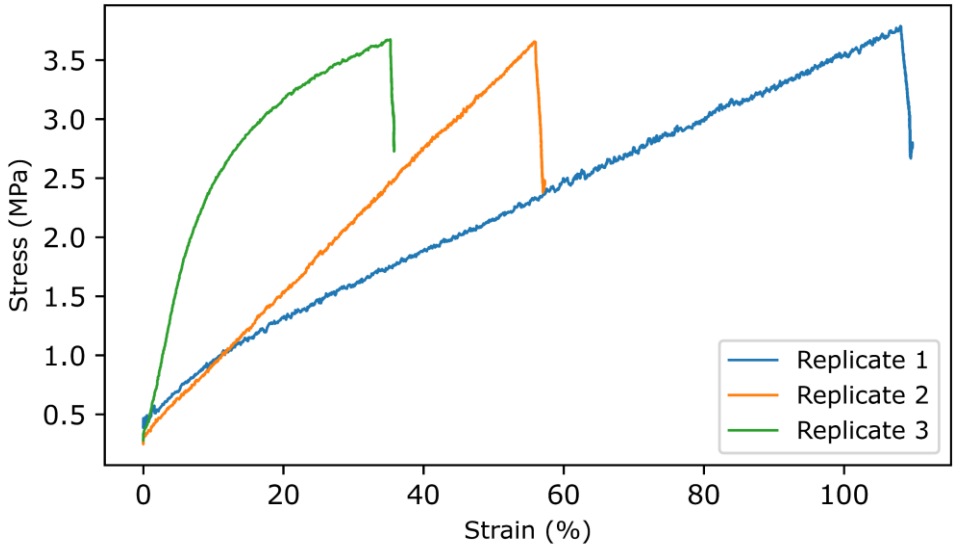

A12.26. FDCAPDO 2000 50 MDI

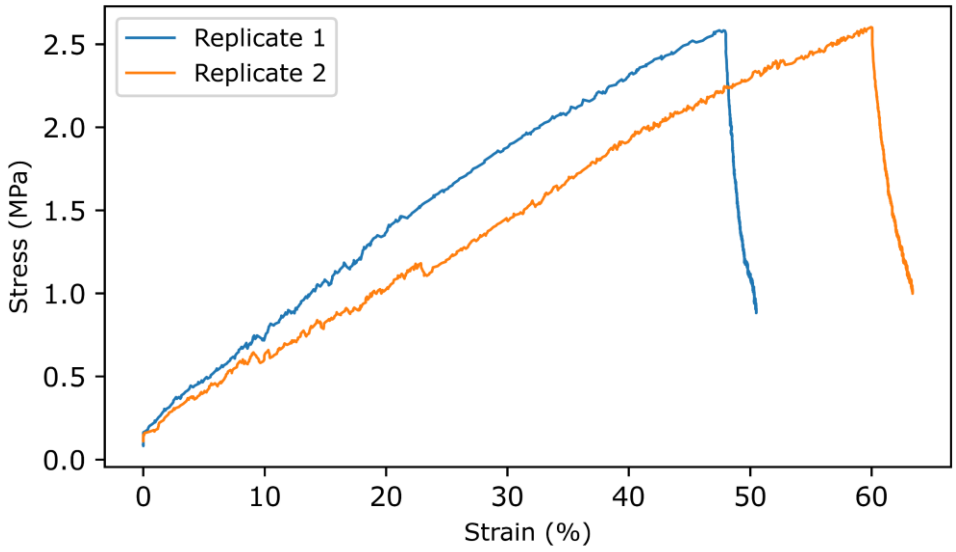

A12.27. FDCAHDO 1000 10 MDI

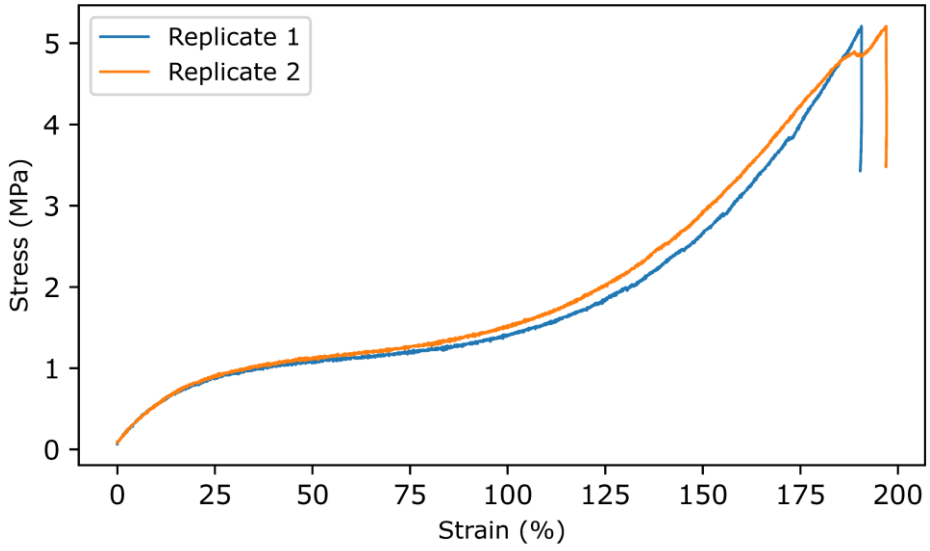

A12.28. FDCAHDO 1000 50 MDI

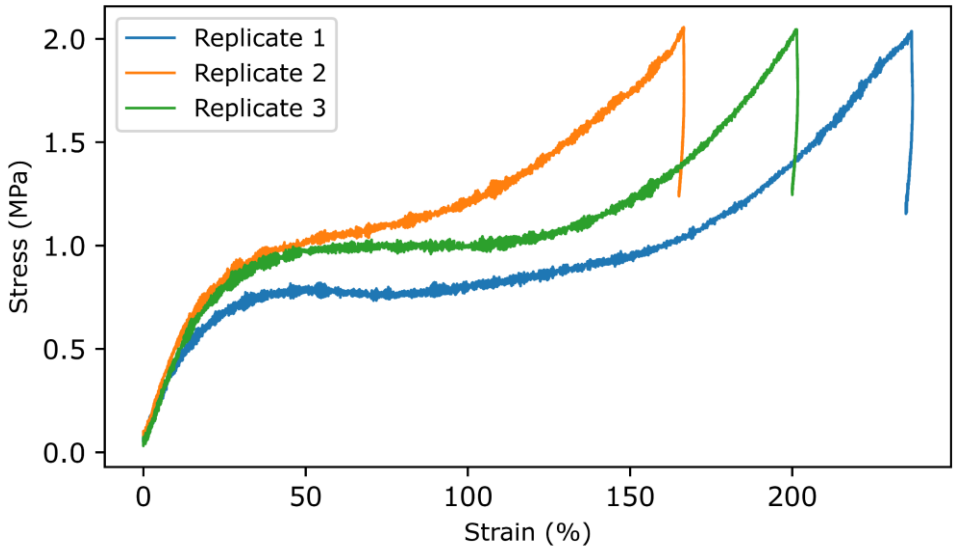

A12.29. FDCAHDO 1500 30 MDI

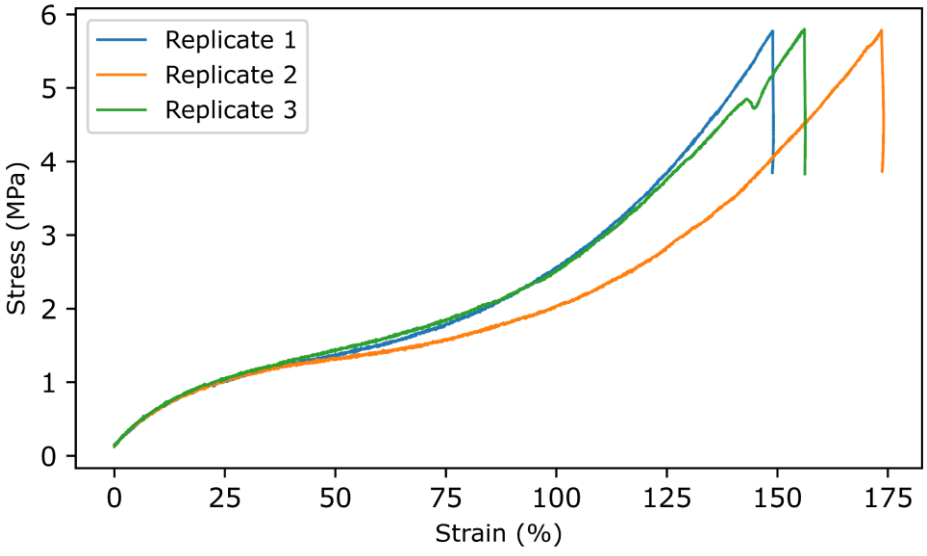

A12.30. FDCAHDO 2000 10 MDI

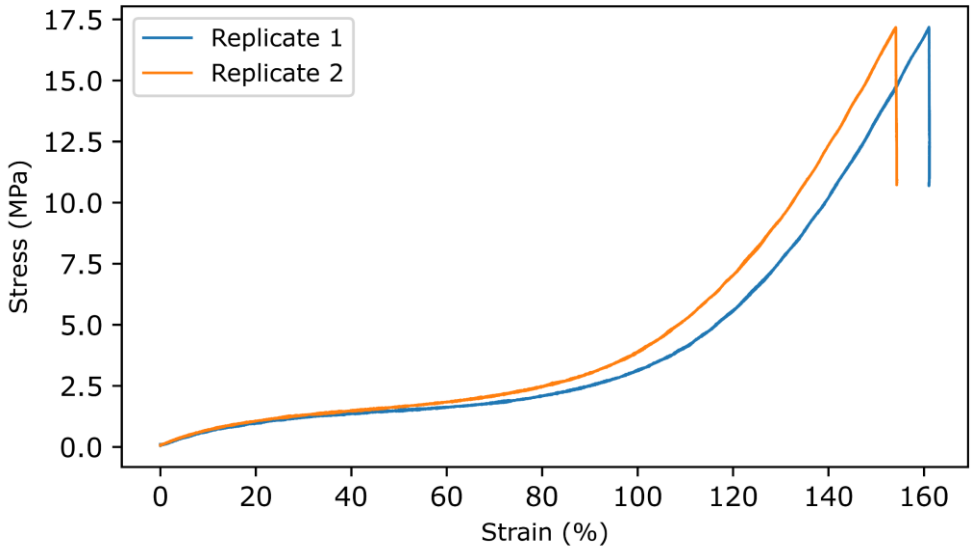

A12.31. FDCAHDO 2000 50 MDI

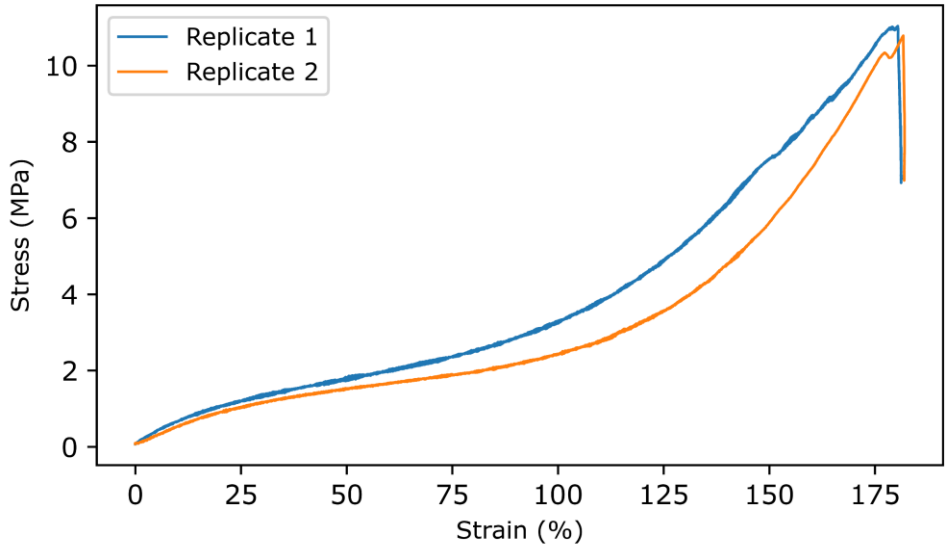

A12.32. FDCAPDO 1000 10 HDI

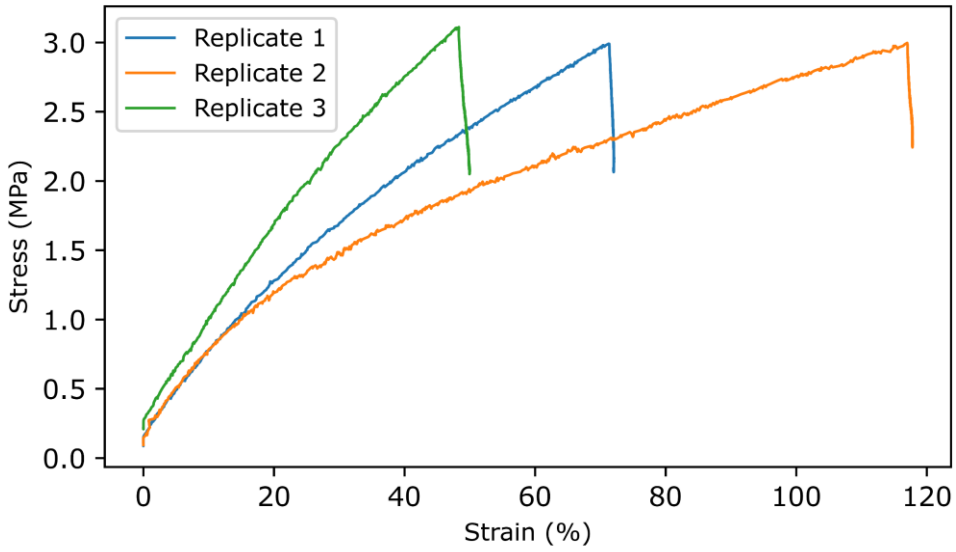

A12.33. FDCAPDO 1000 50 HDI

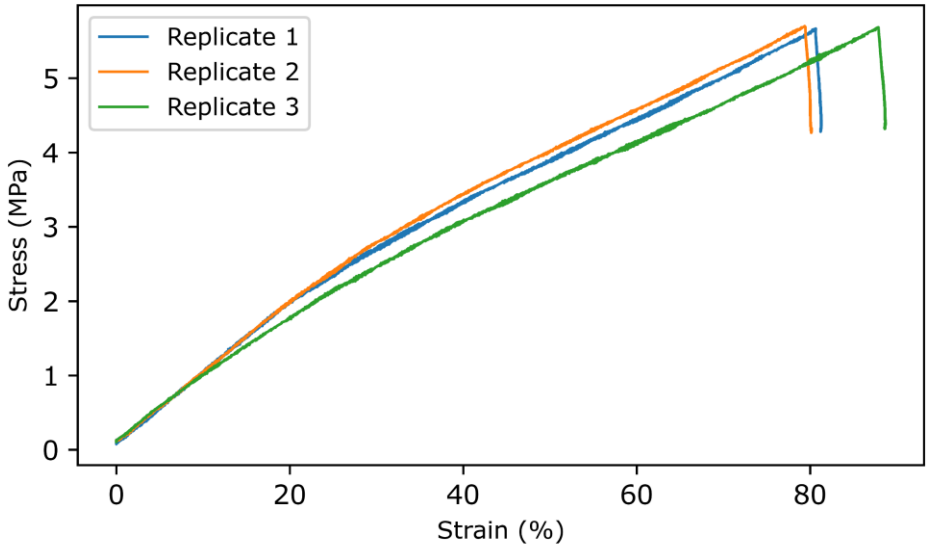

A12.34. FDCAPDO 1500 30 HDI

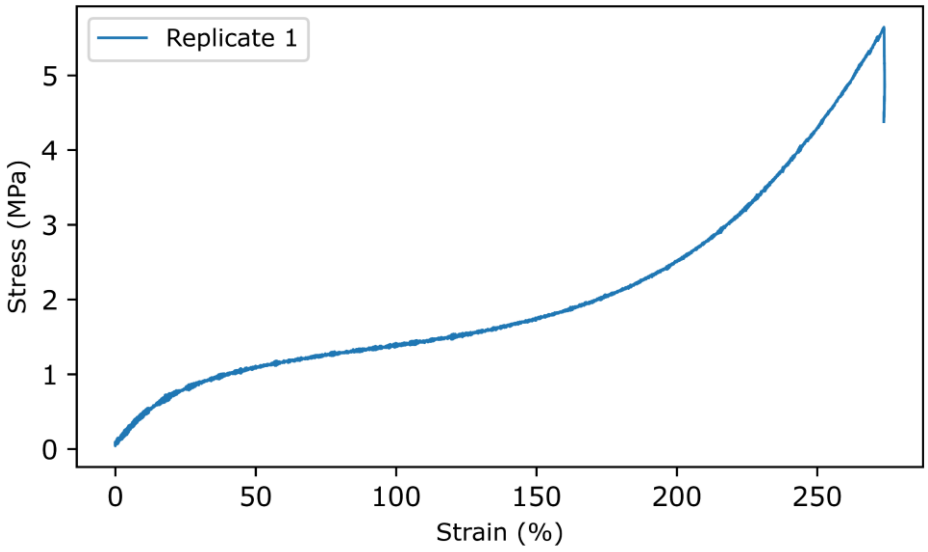

A12.35. FDCAPDO 2000 10 HDI

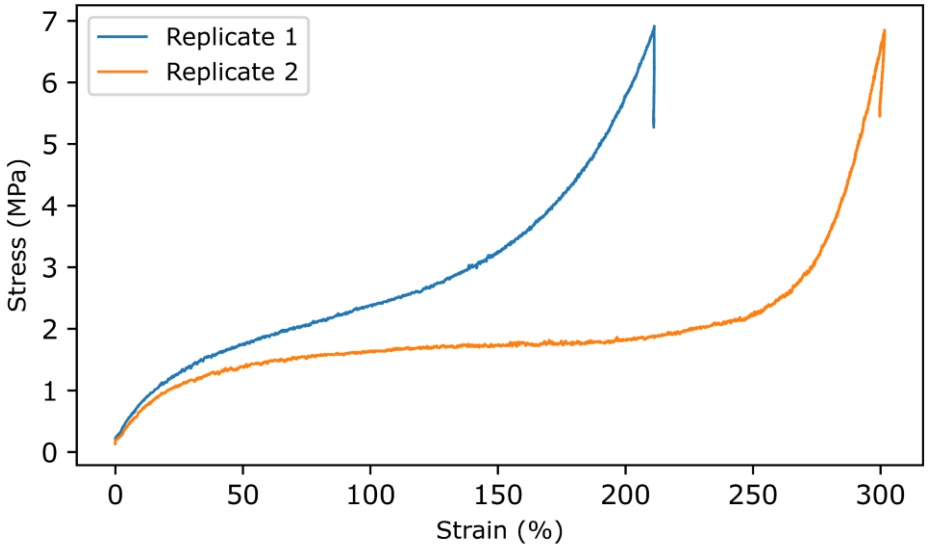

A12.36. FDCAPDO 2000 50 HDI

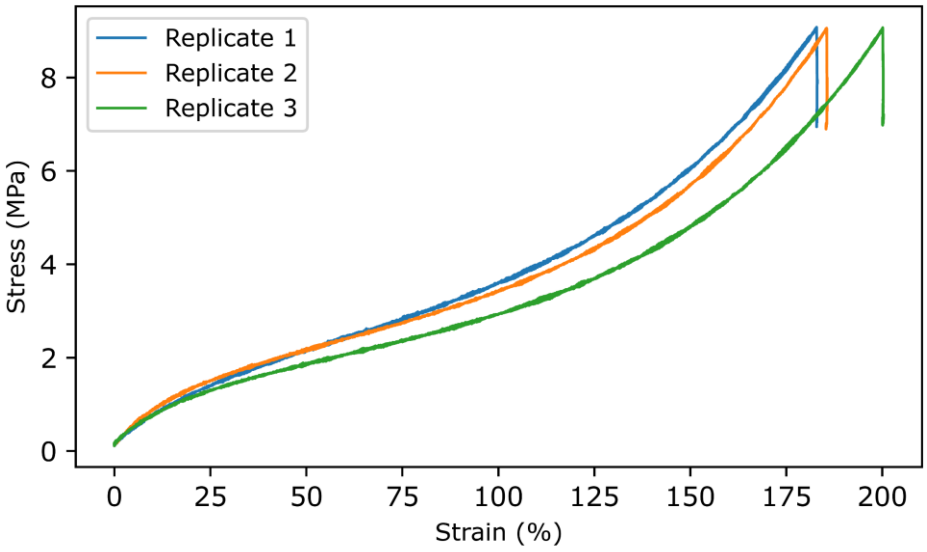

A12.37. FDCAHDO 1000 10 HDI

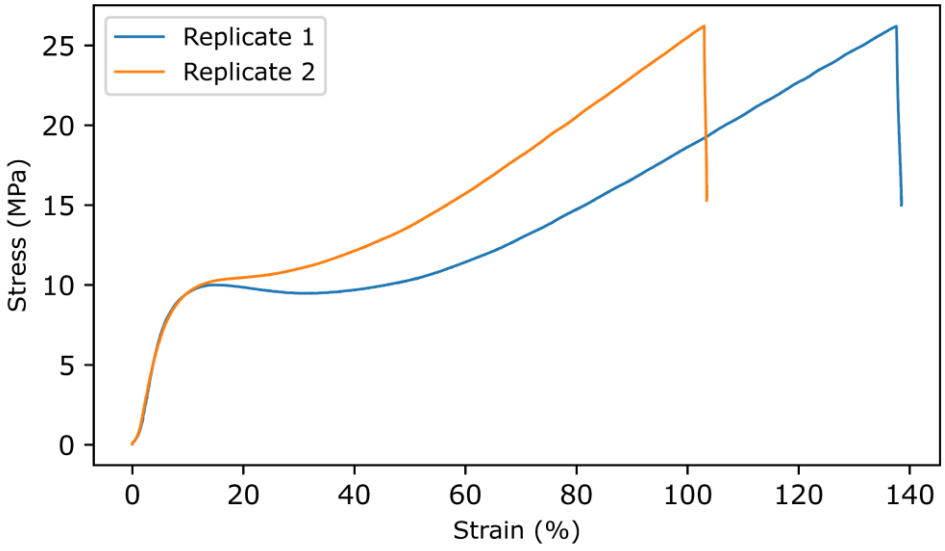

A12.38. FDCAHDO 1000 50 HDI

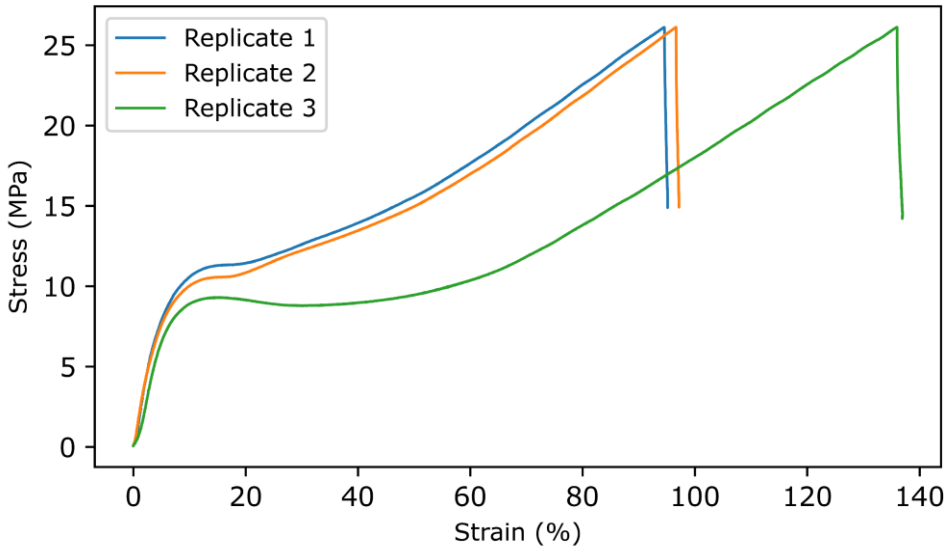

A12.39. FDCAHDO 1500 30 HDI

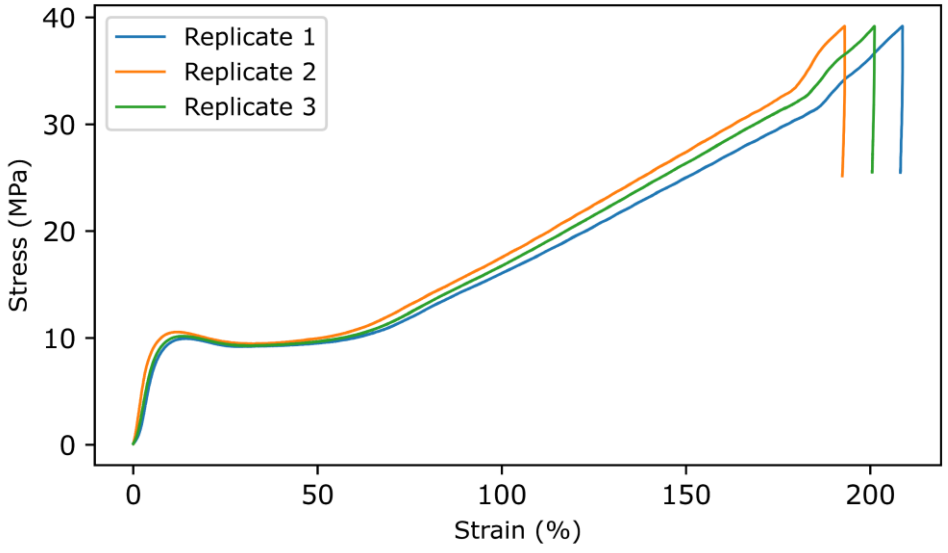

A12.40. FDCAHDO 2000 10 HDI

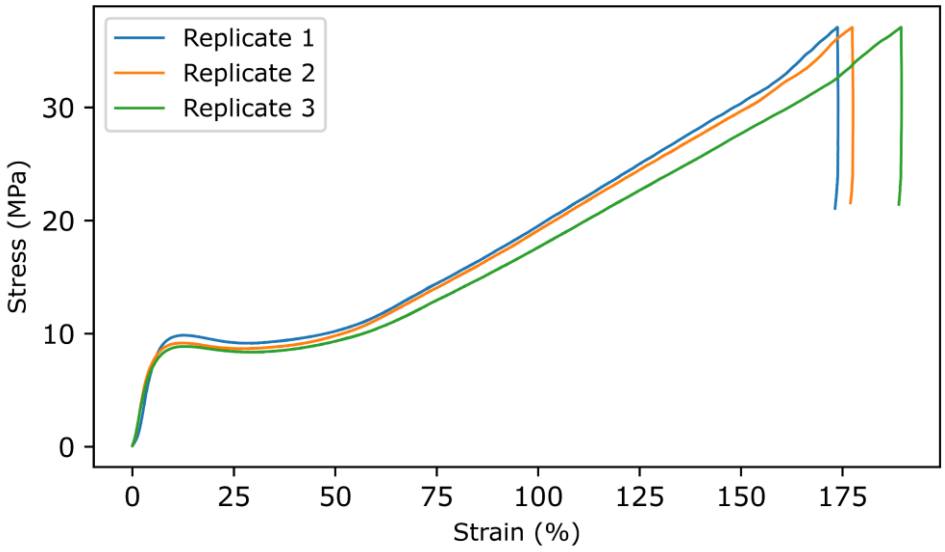

A12.41. FDCAHDO 2000 50 HDI

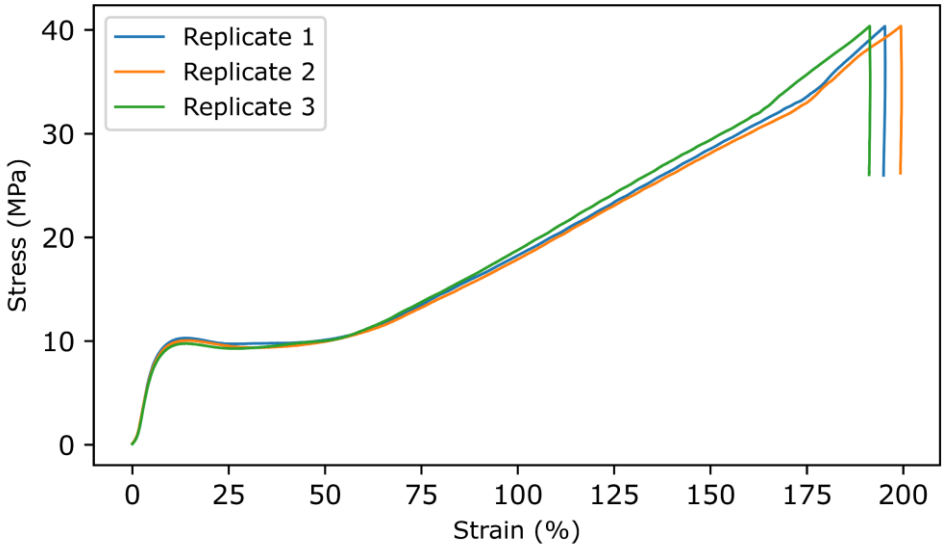

A13 SAXS annealed TPUs

A13.1. IPHTAPDO 1000 10 HDI

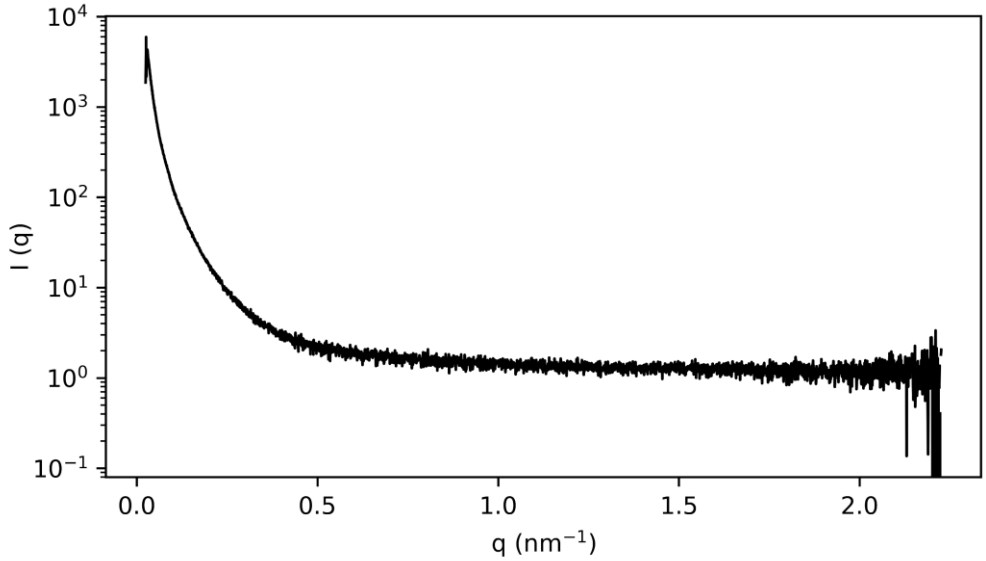

A13.2. IPHTAPDO 1000 30 HDI

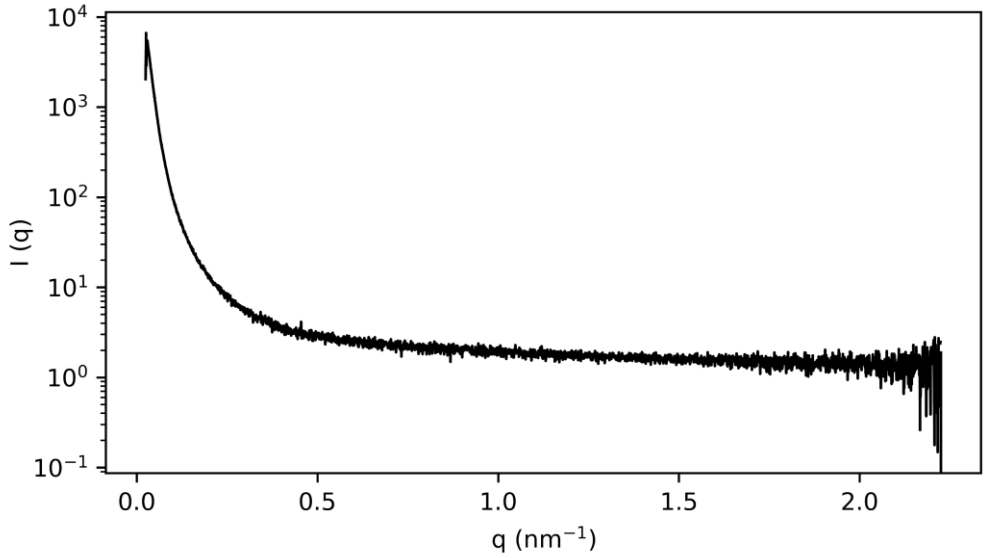

A13.3. IPHTAPDO 1000 50 HDI

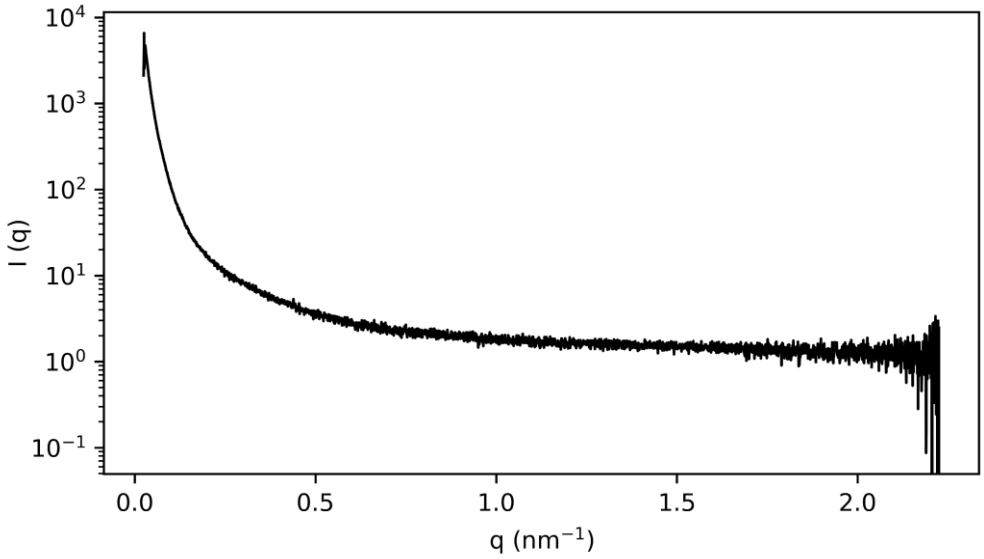

A13.4. IPHTAPDO 2000 10 HDI

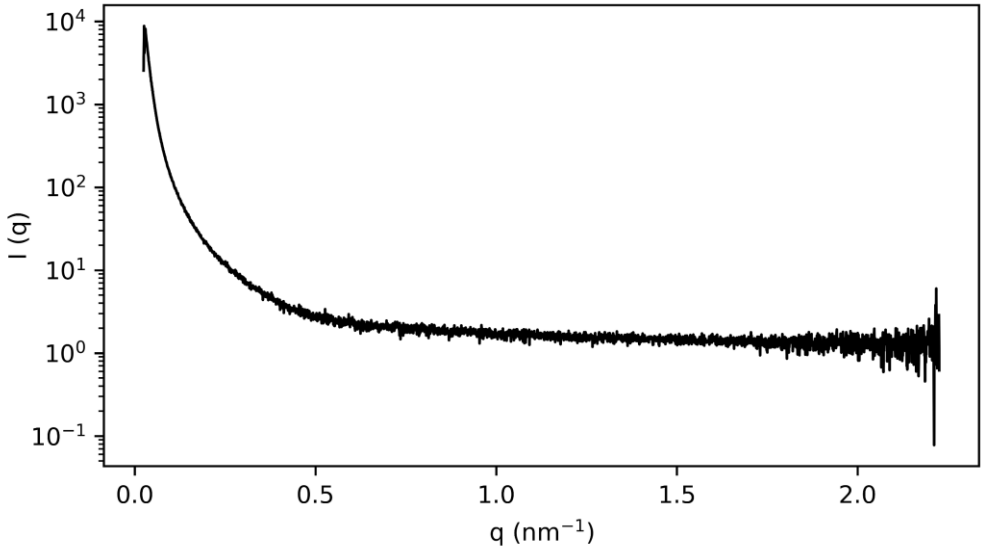

A13.5. IPHTAPDO 2000 30 HDI

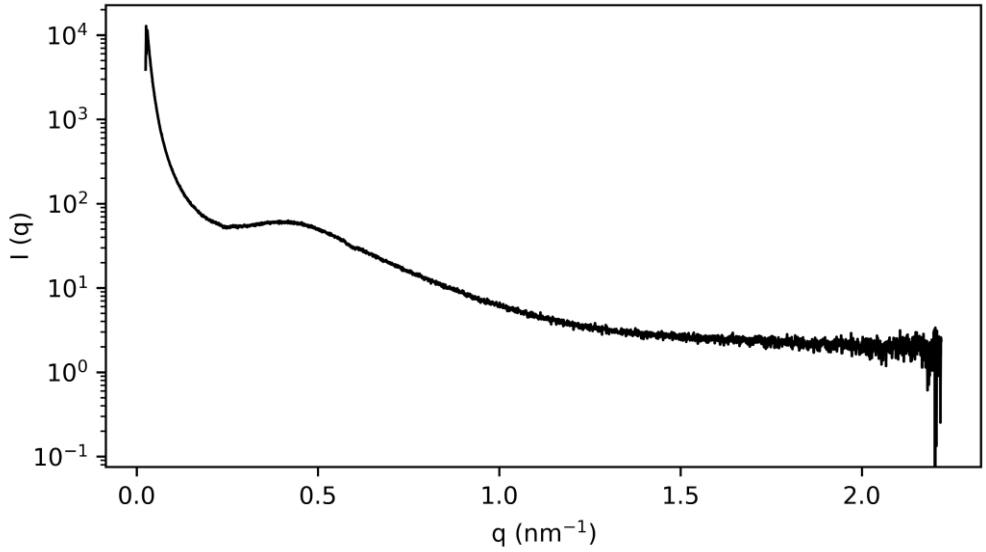

- Fitting

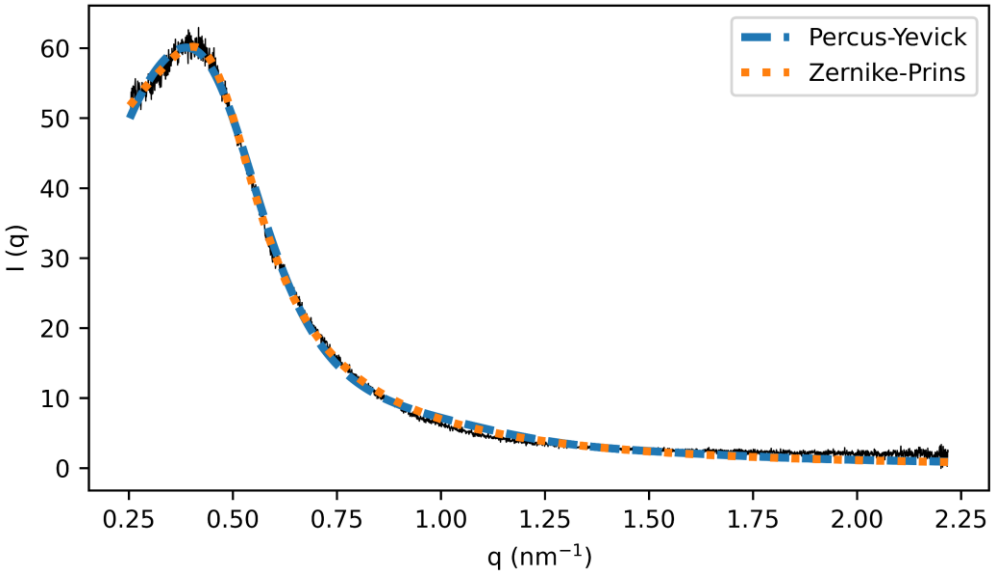

A13.6. IPHTAPDO 2000 50 HDI

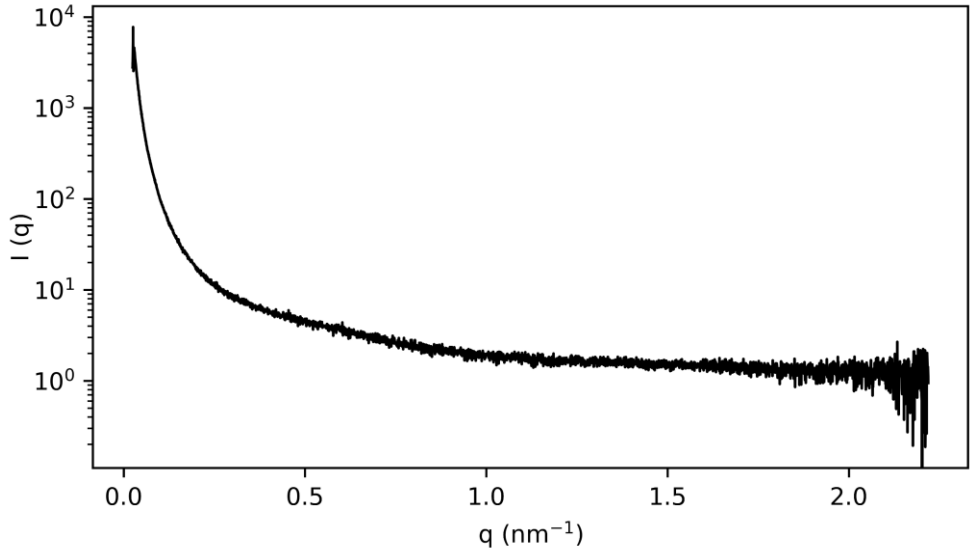

A13.7. FDCAPDO 1000 10 MDI

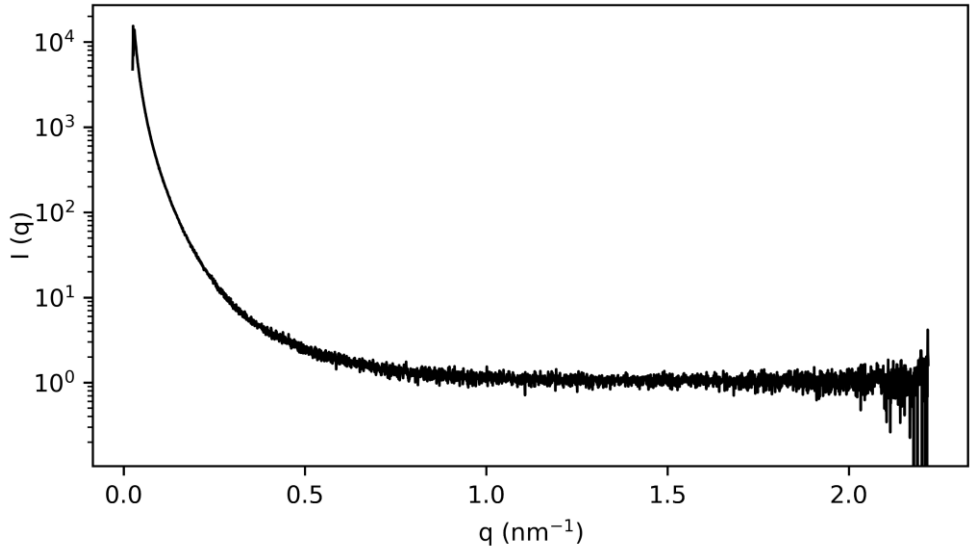

A13.8. FDCAPDO 1000 50 MDI

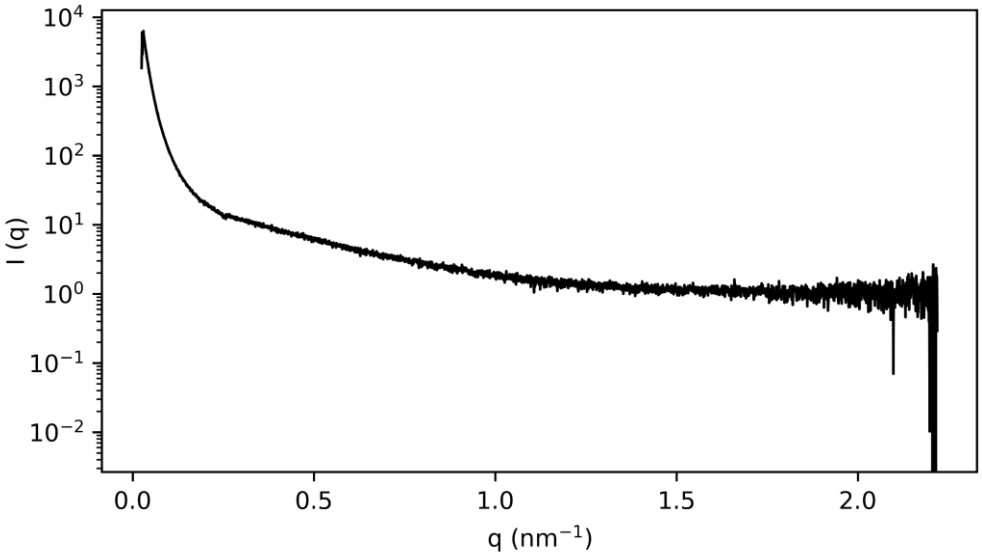

A13.9. FDCAPDO 1500 30 MDI

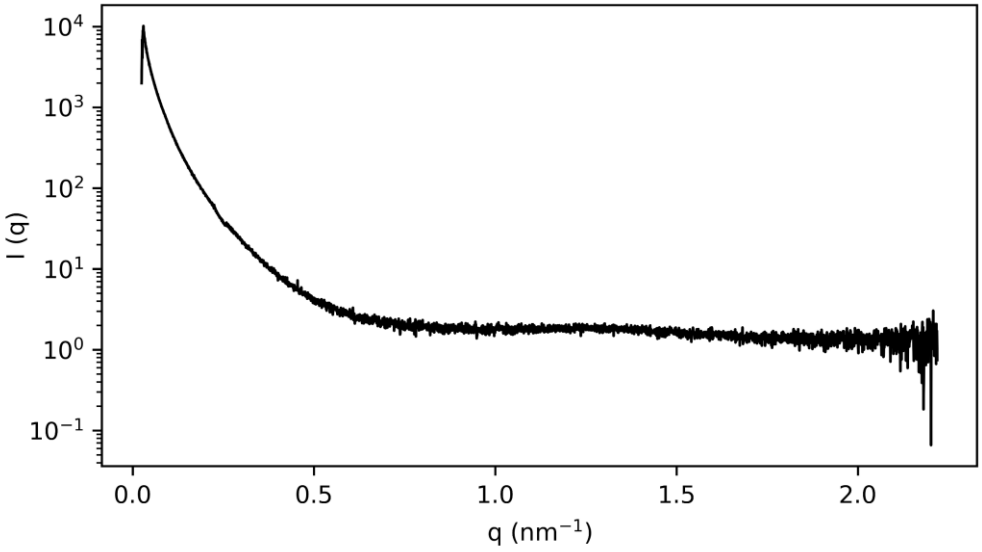

A13.10. FDCAPDO 2000 10 MDI

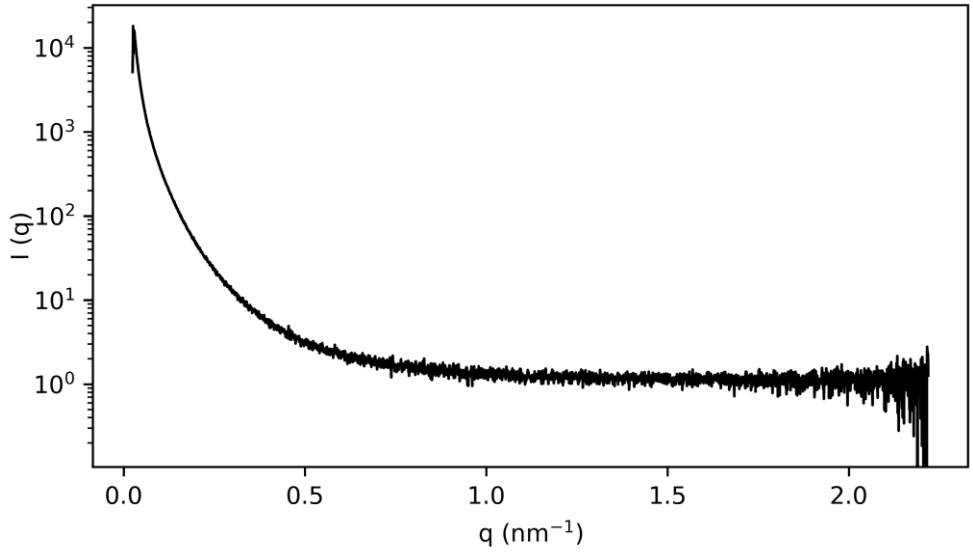

A13.11. FDCAPDO 2000 50 MDI

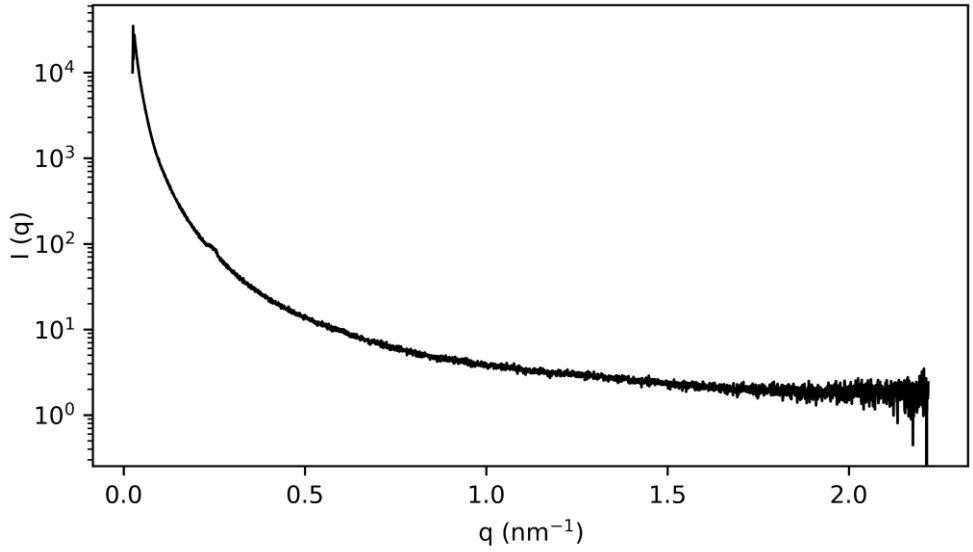

A13.12. FDCAHDO 1000 10 MDI

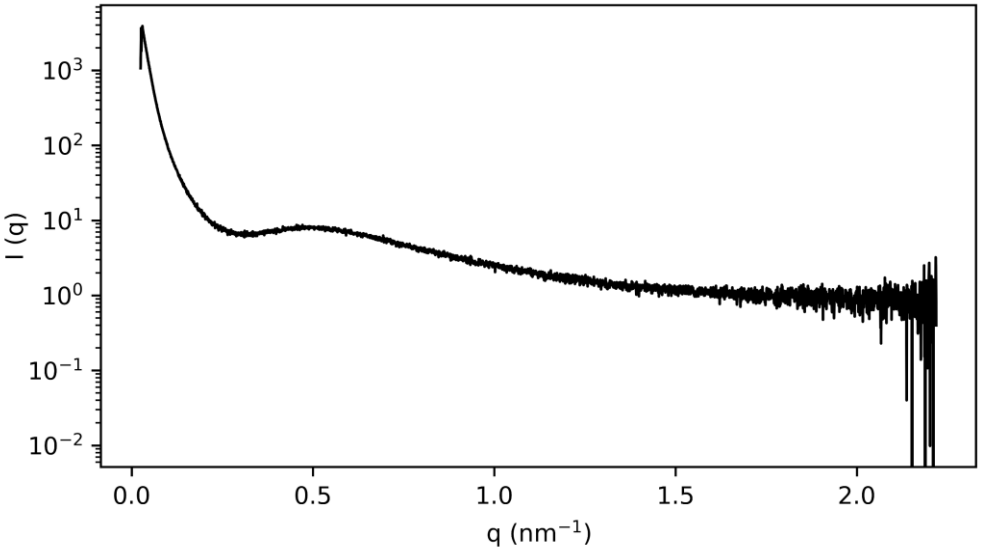

- Fitting
-

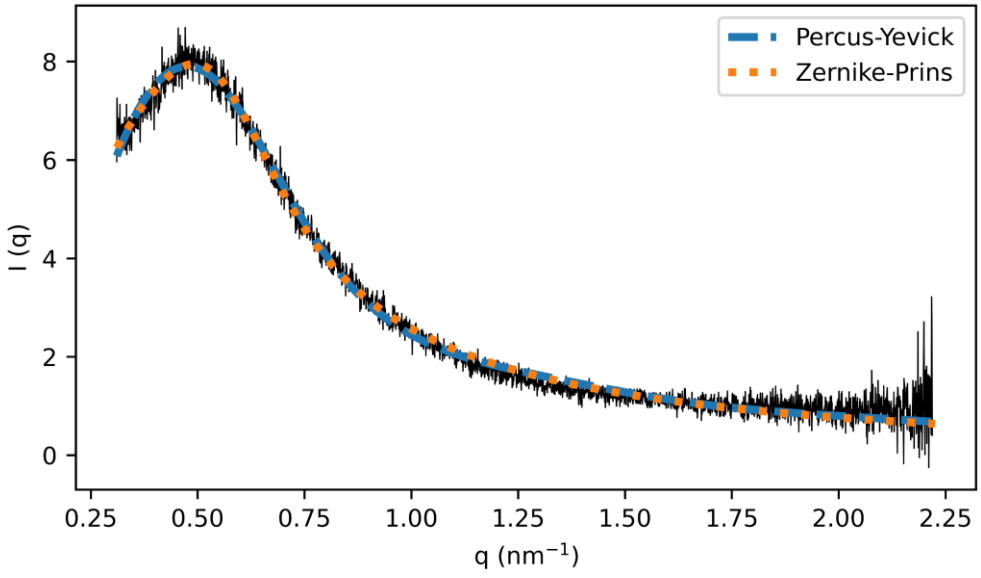

A13.13. FDCAHDO 1000 50 MDI

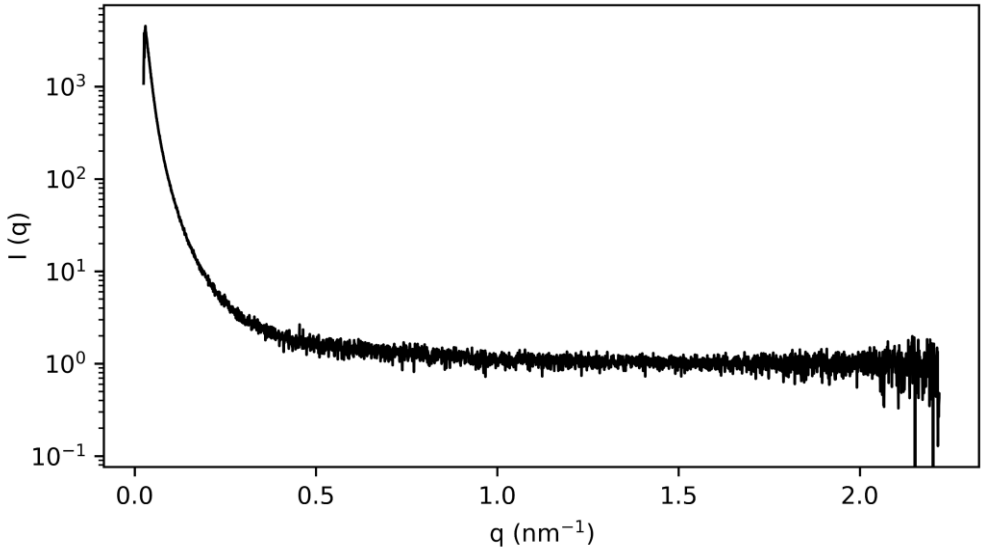

A13.14. FDCAHDO 1500 30 MDI

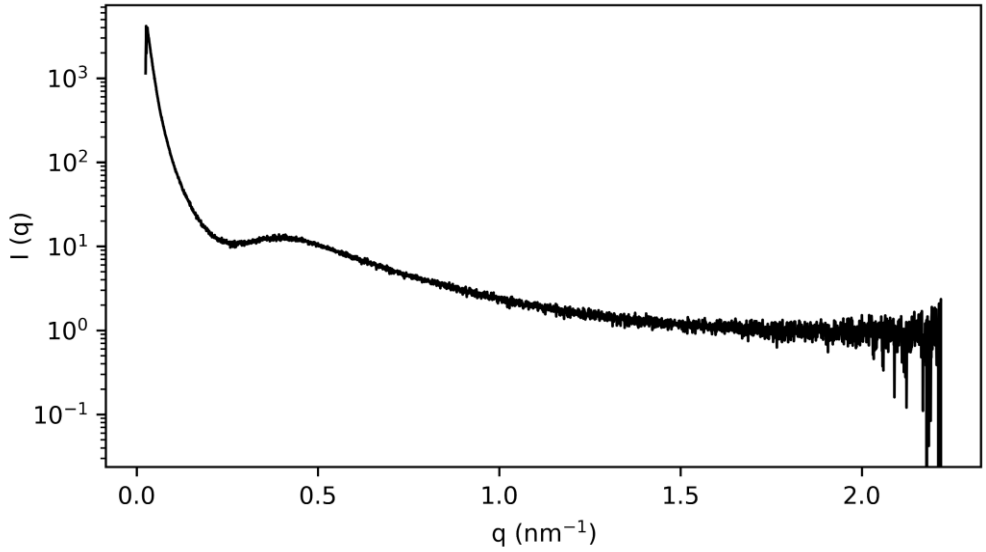

- Fitting

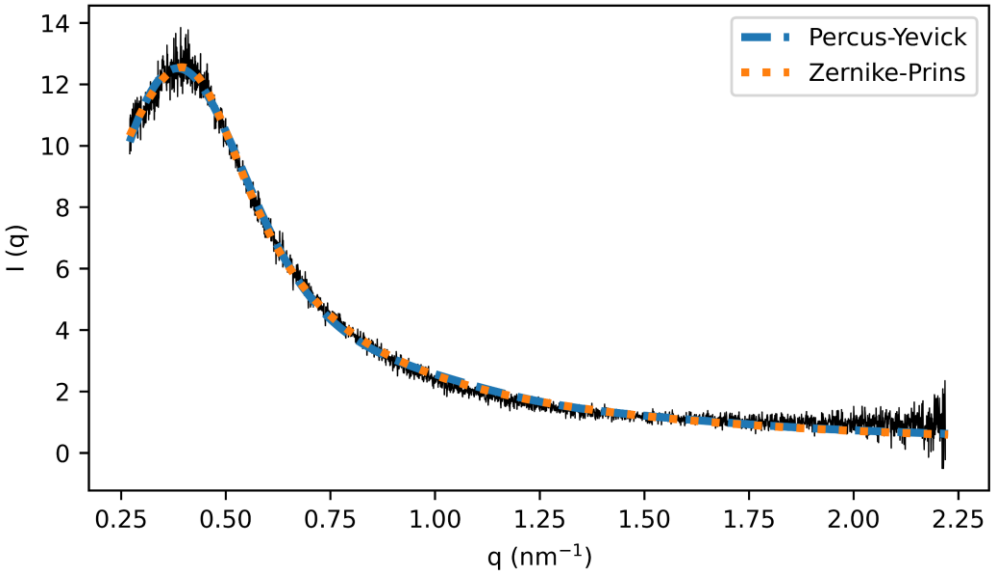

A13.15. FDCAHDO 2000 10 MDI

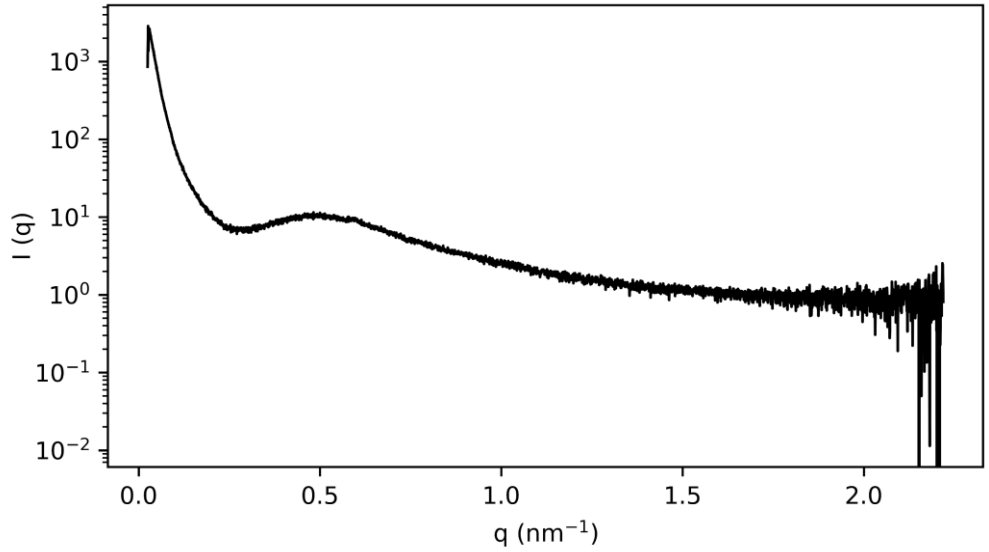

- Fitting

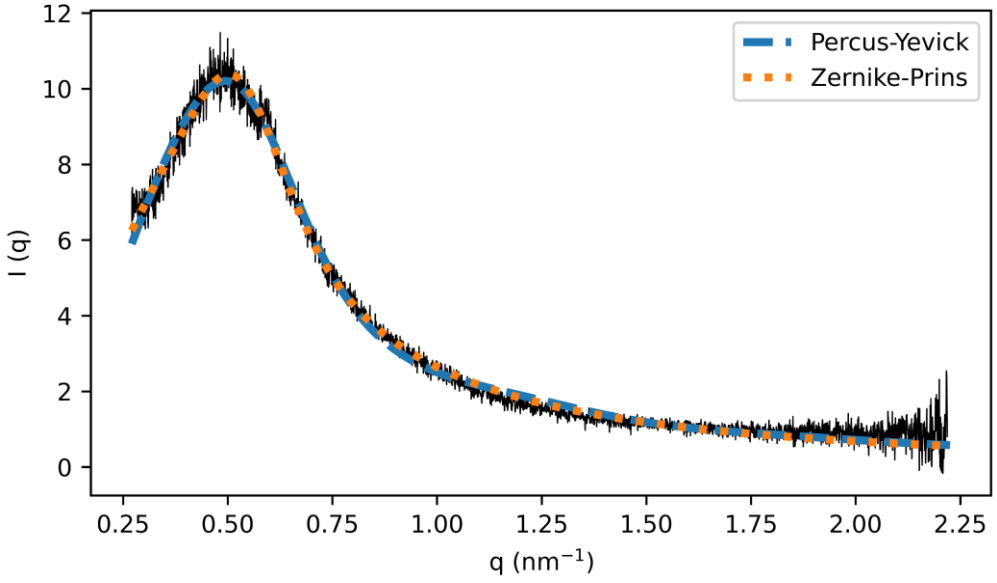

A13.16. FDCAHDO 2000 50 MDI

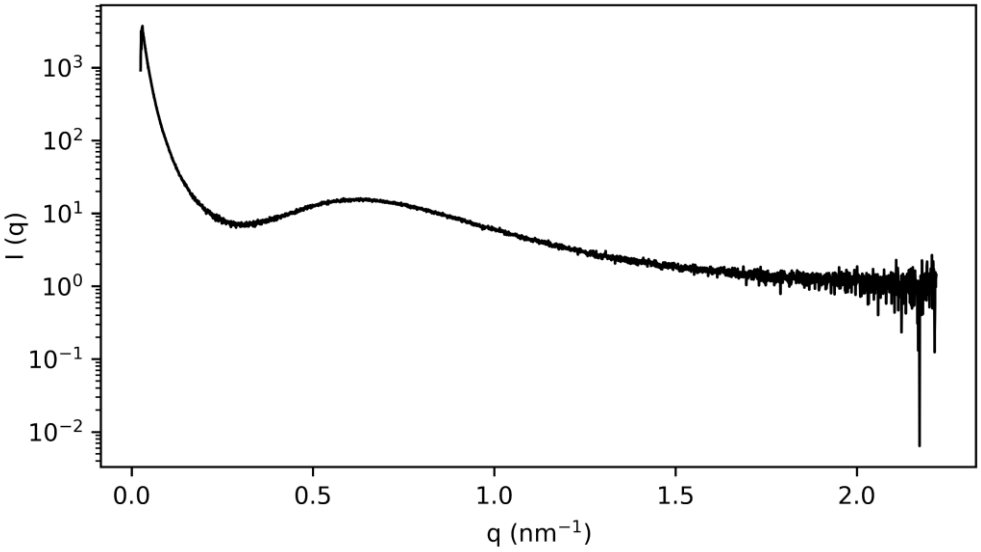

- Fitting

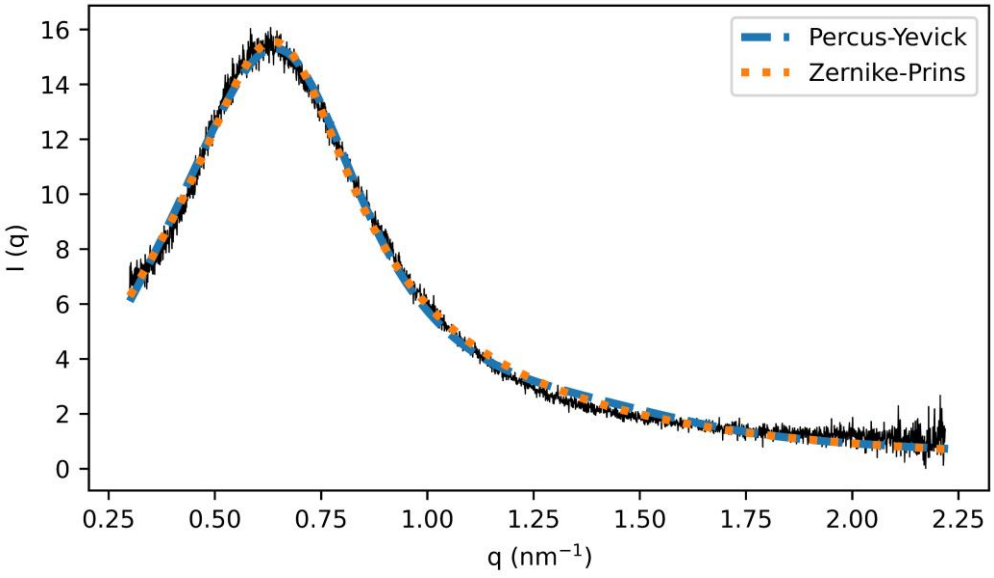

A13.17. FDCAPDO 1000 10 HDI

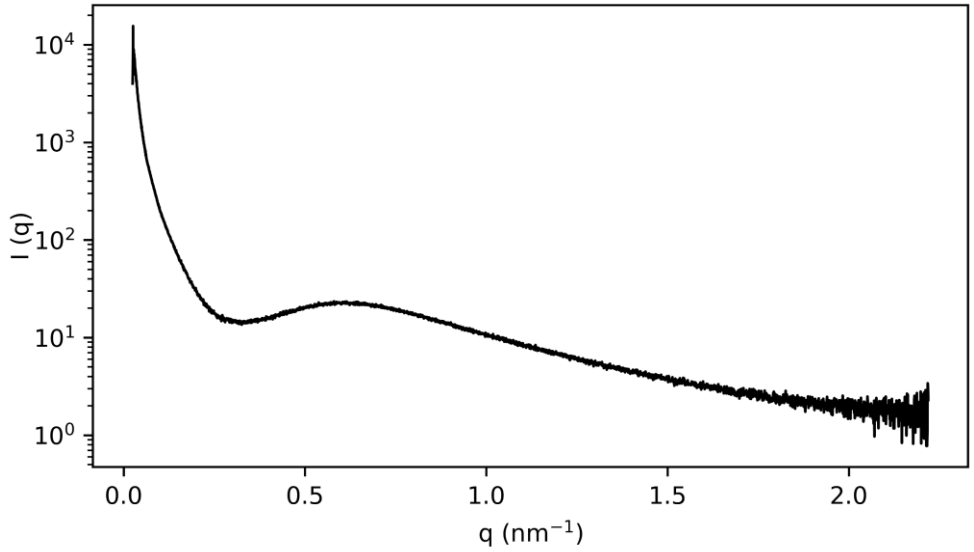

- Fitting

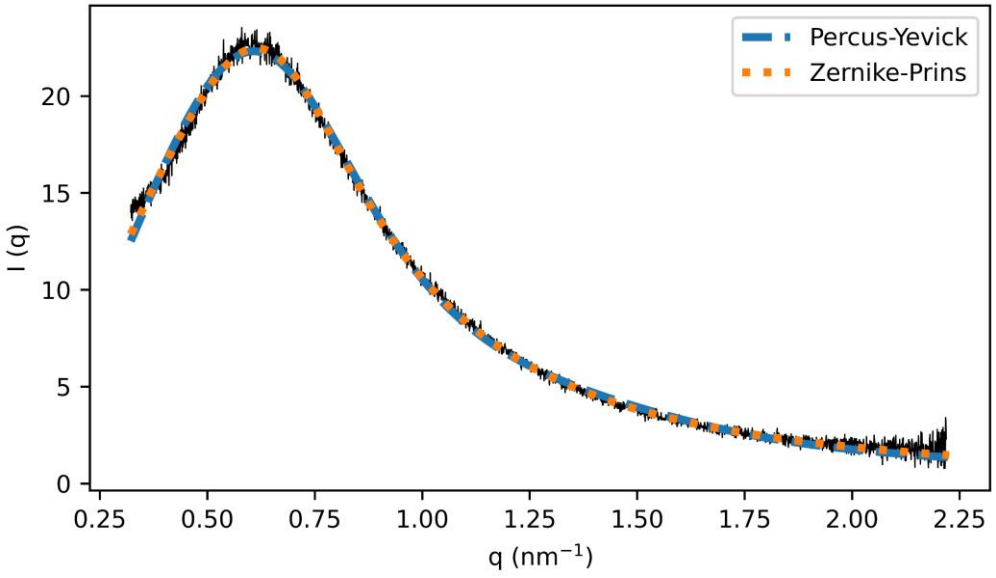

A13.18. FDCAPDO 1000 50 HDI

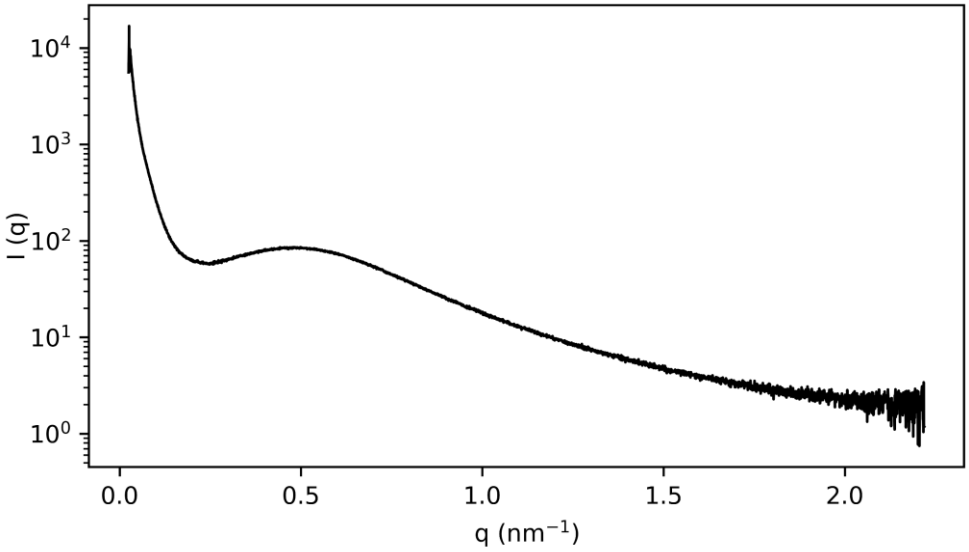

- Fitting

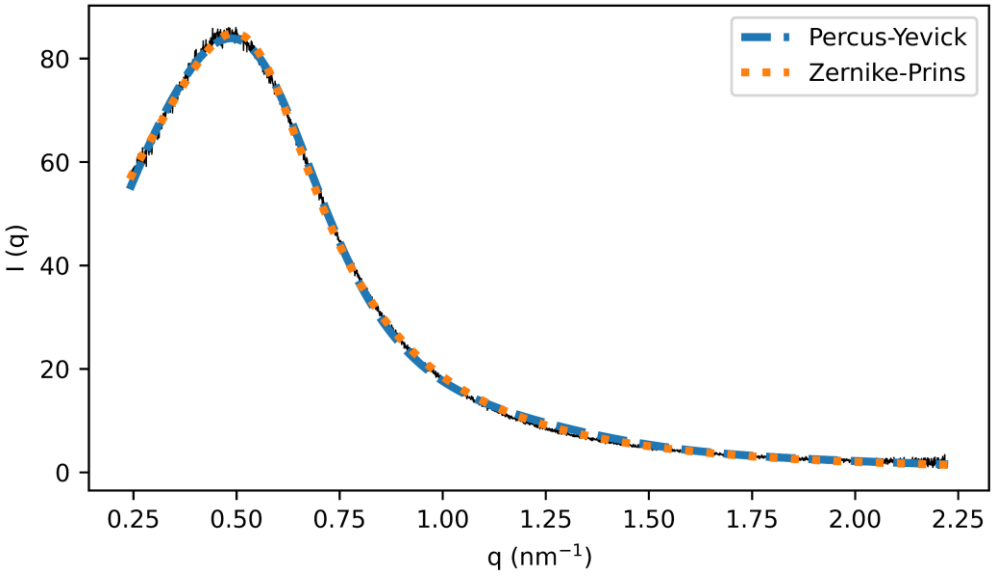

A13.19. FDCAPDO 1500 30 HDI

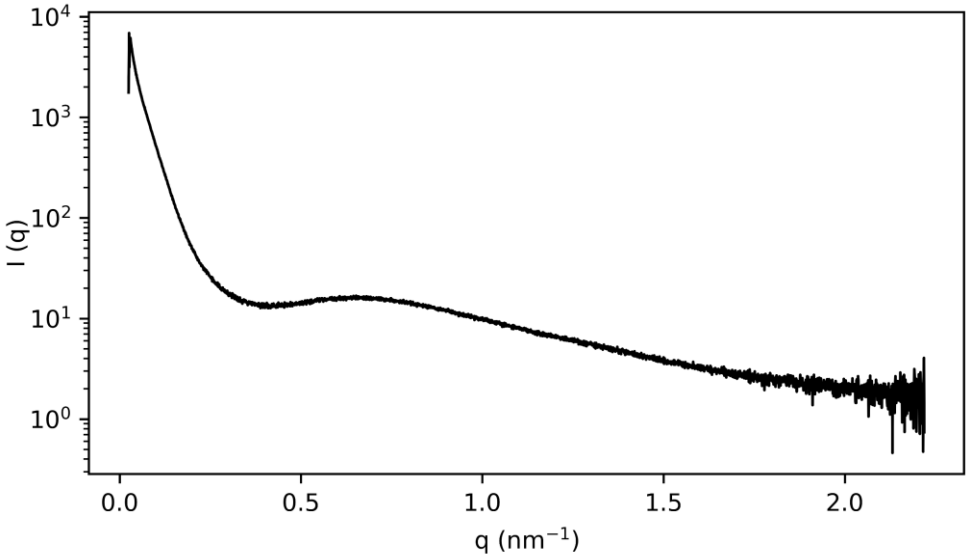

- Fitting

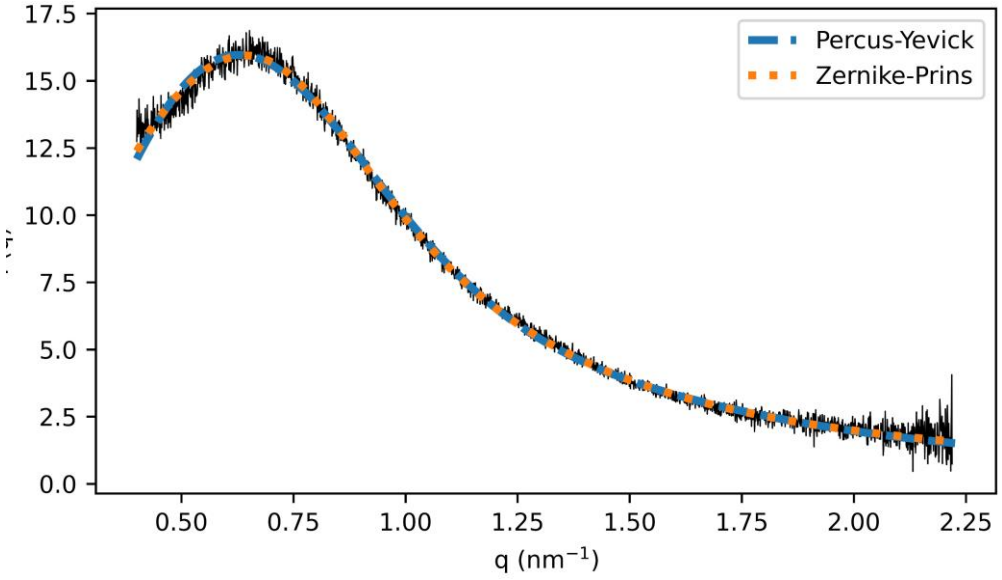

A13.20. FDCAPDO 2000 10 HDI

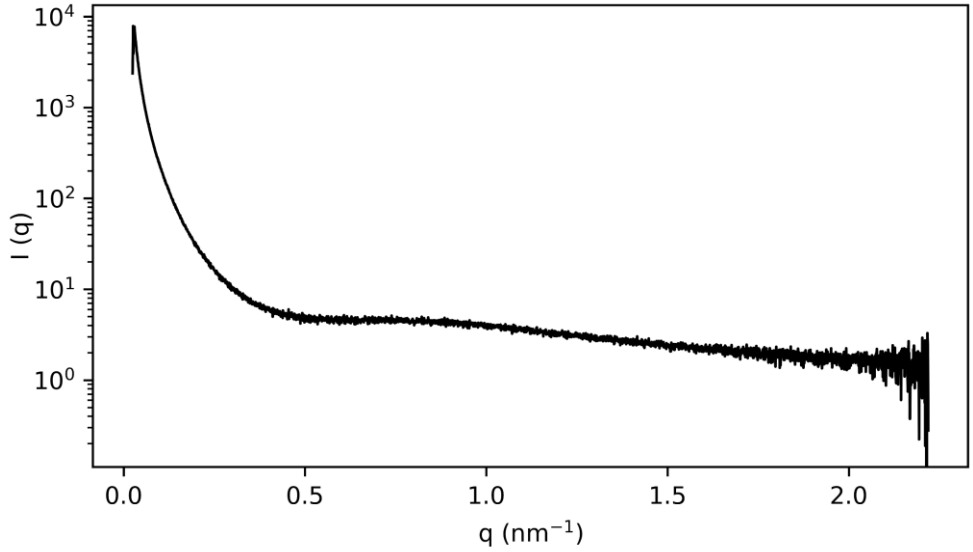

- Fitting

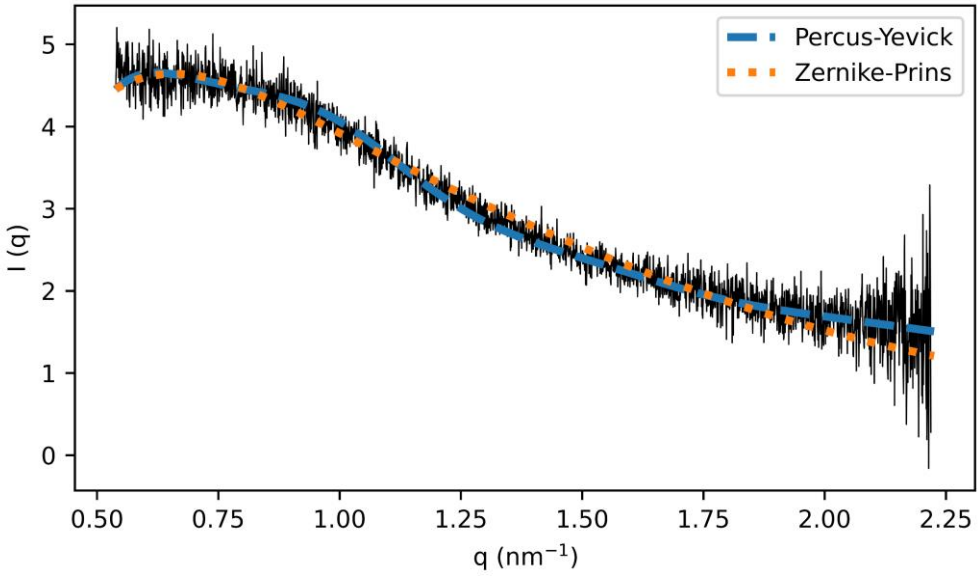

A13.21. FDCAPDO 2000 50 HDI

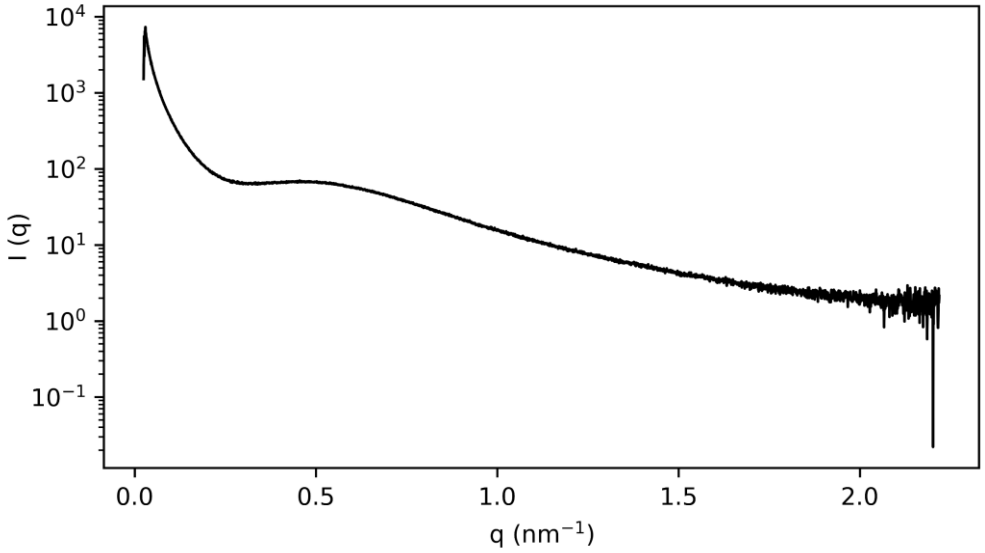

- Fitting

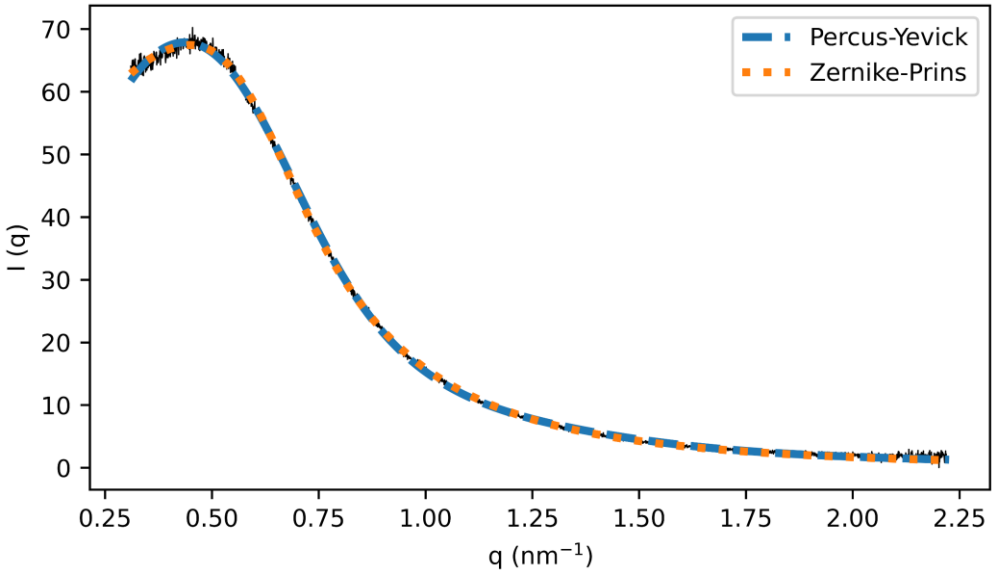

A14 WAXS annealed TPUs

A14.1. IPHTAPDO 1000 10 HDI

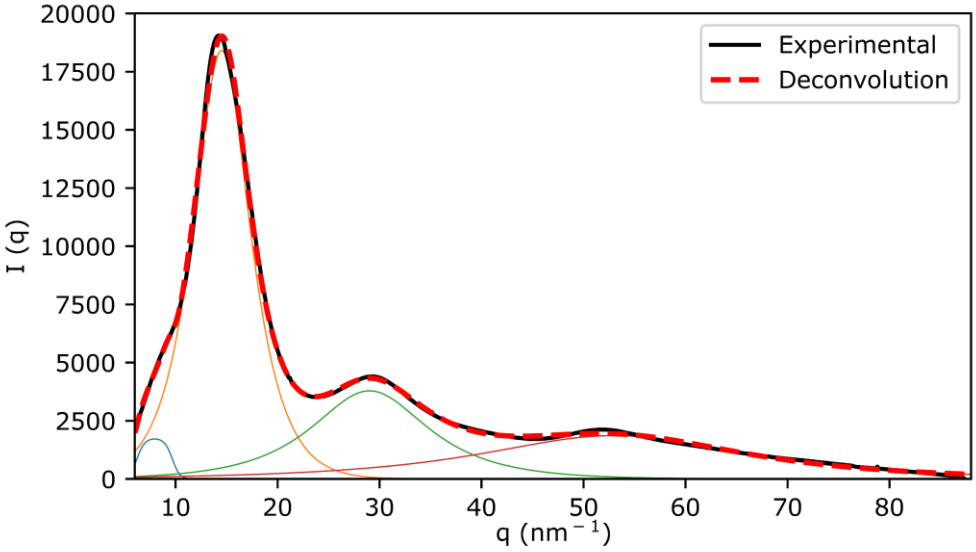

A14.2. IPHTAPDO 1000 30 HDI

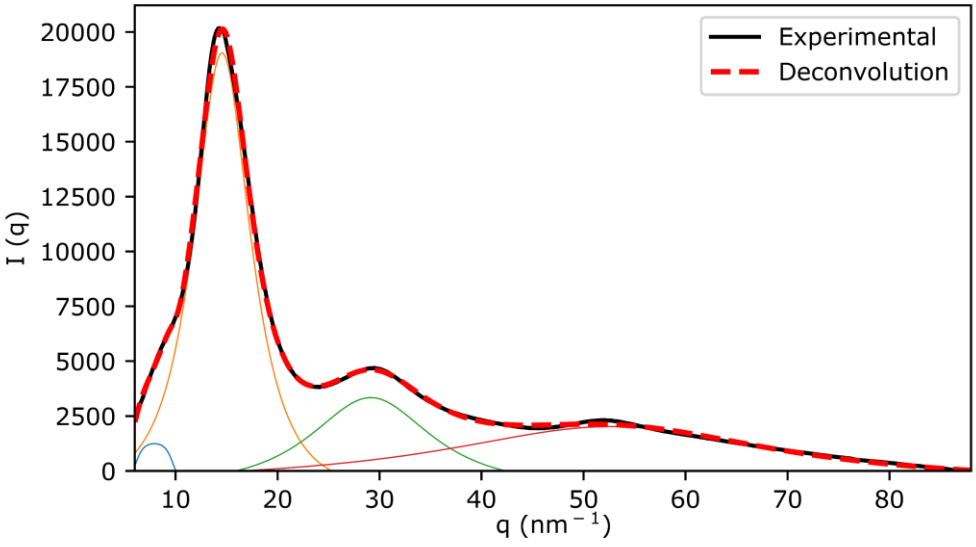

A14.3. IPHTAPDO 1000 50 HDI

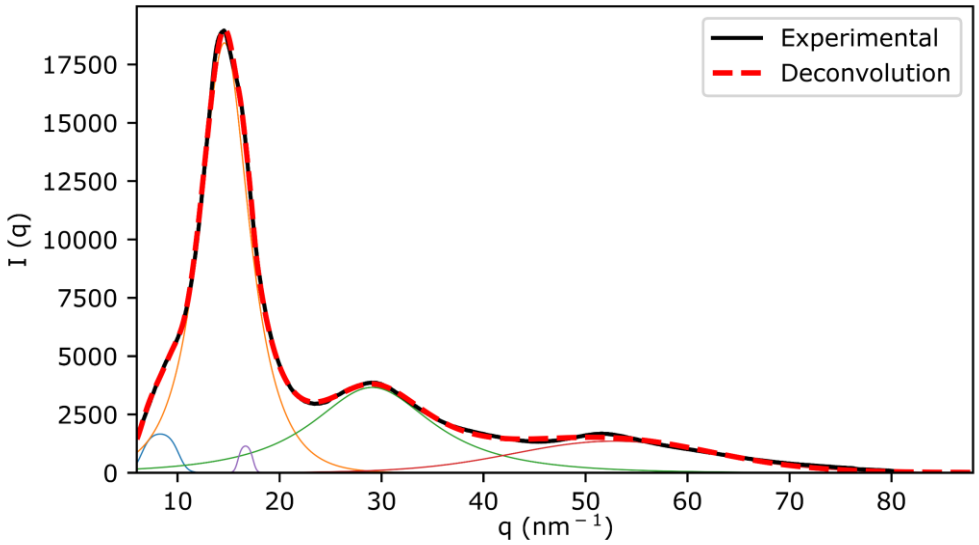

A14.4. IPHTAPDO 2000 10 HDI

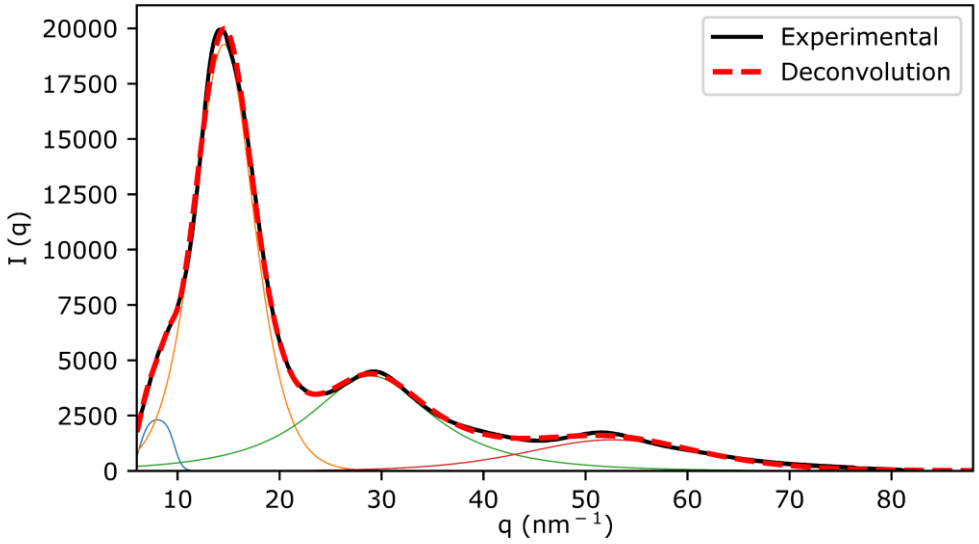

A14.5. IPHTAPDO 2000 30 HDI

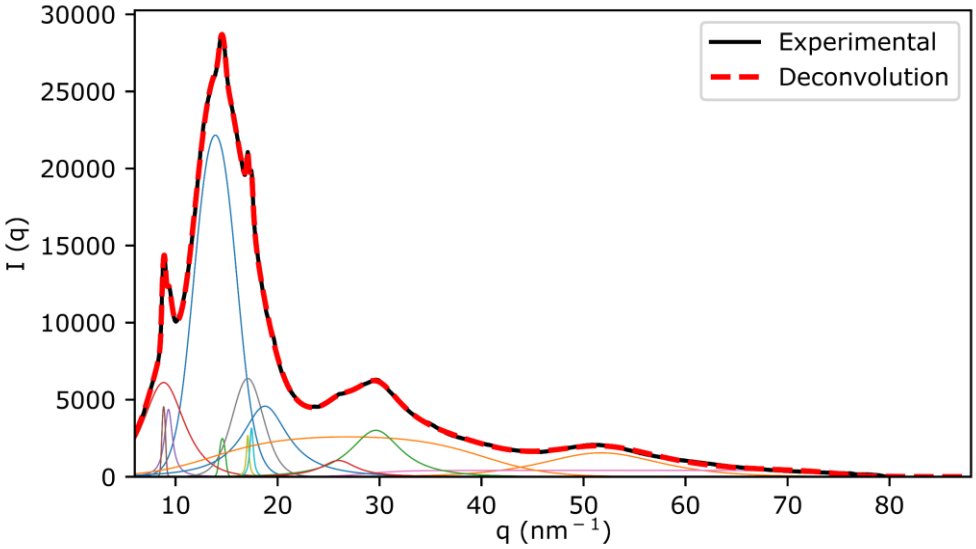

A14.6. IPHTAPDO 2000 50 HDI

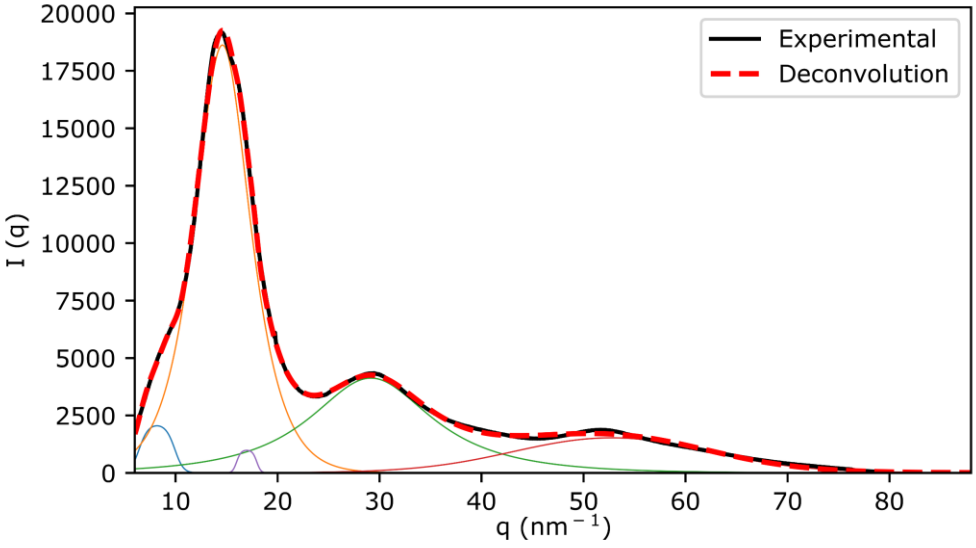

A14.7. FDCAPDO 1000 10 MDI

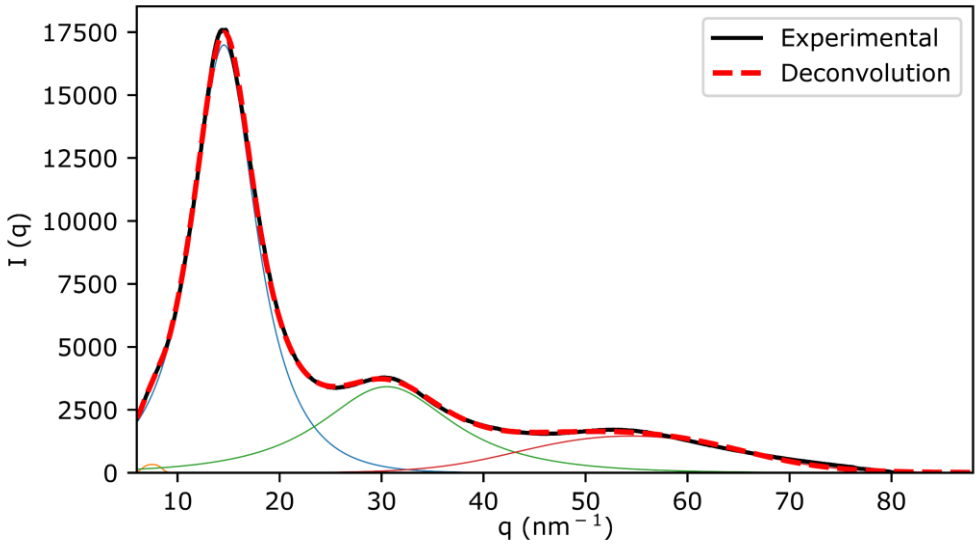

A14.8. FDCAPDO 1000 50 MDI

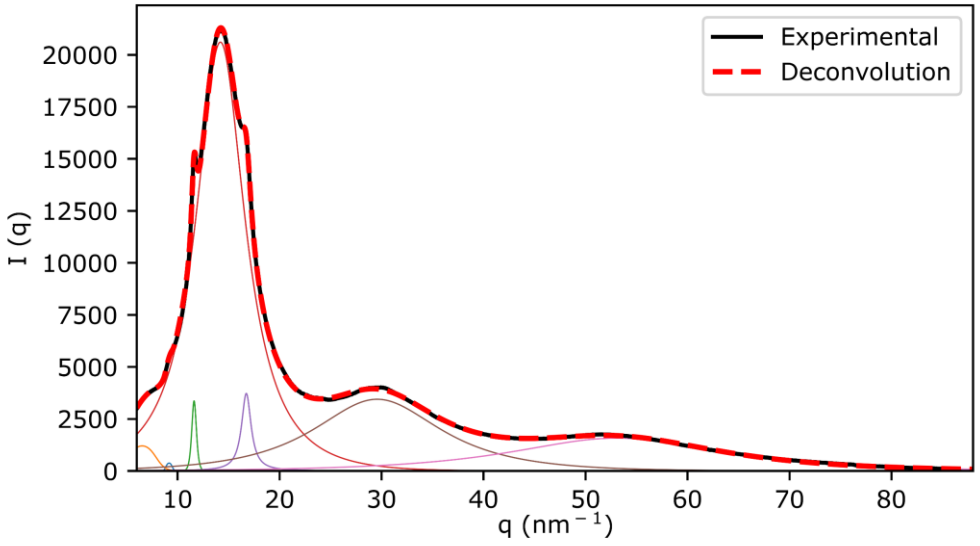

A14.9. FDCAPDO 1500 30 MDI

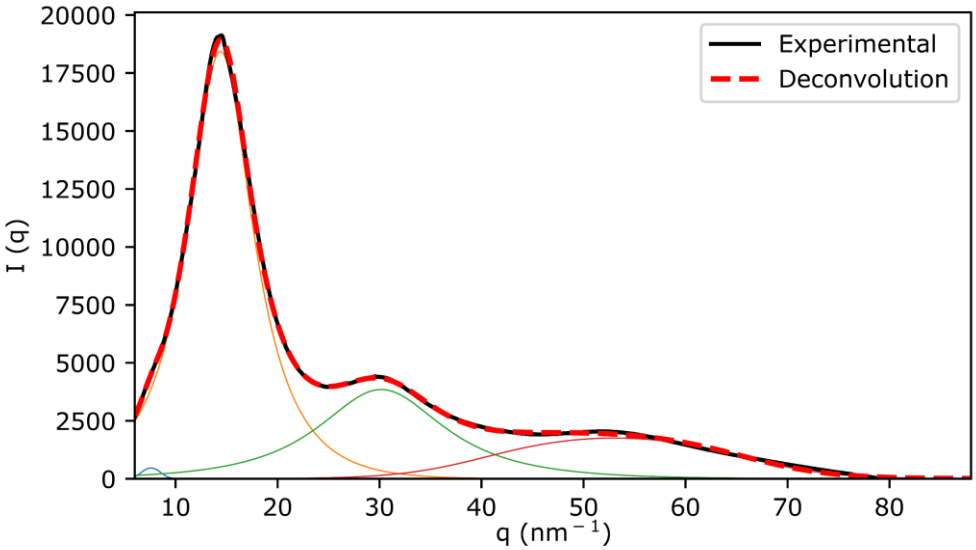

A14.10. FDCAPDO 2000 10 MDI

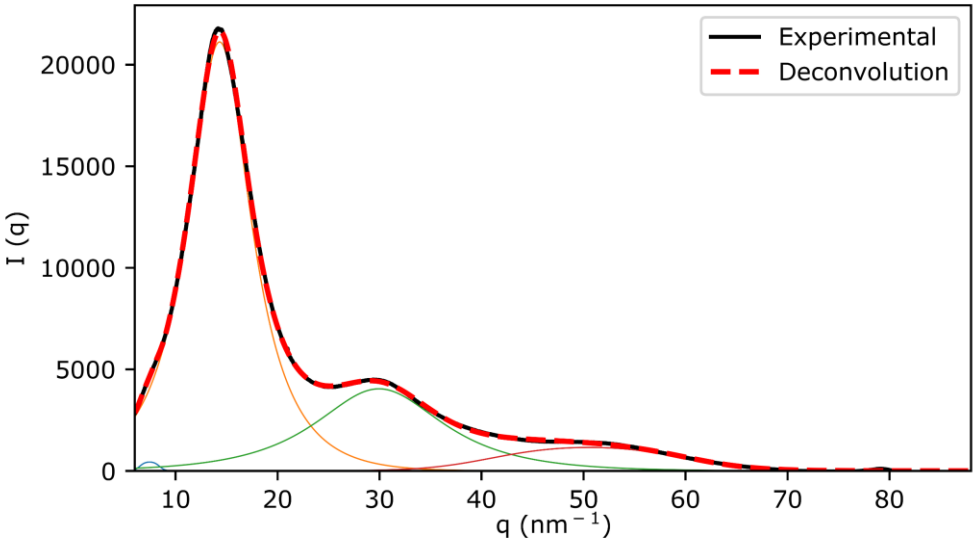

A14.11. FDCAPDO 2000 50 MDI

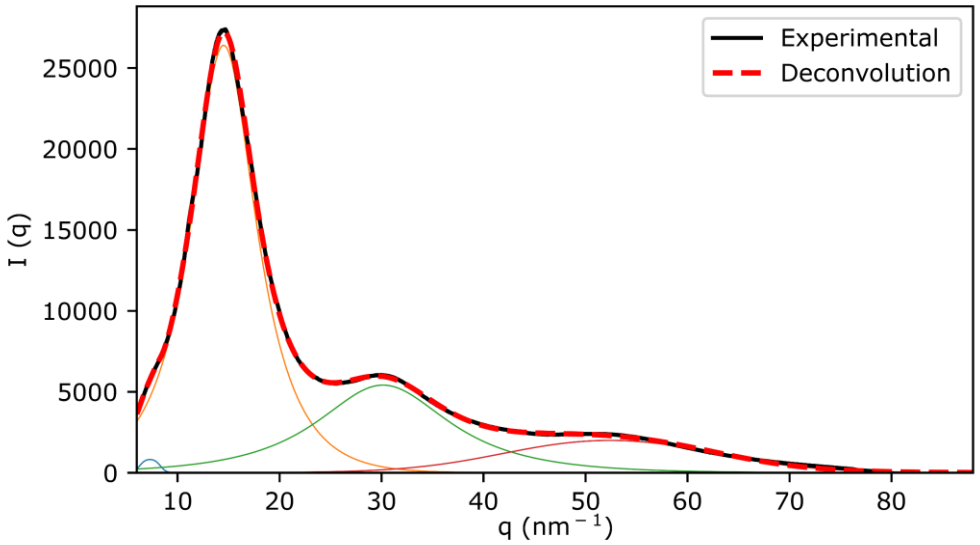

A14.12. FDCAHDO 1000 10 MDI

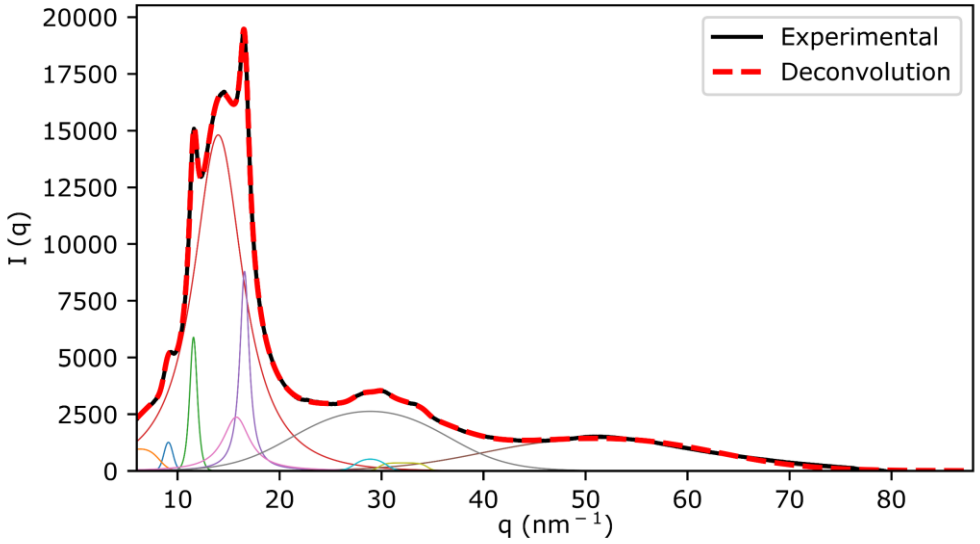

A14.13. FDCAHDO 1000 50 MDI

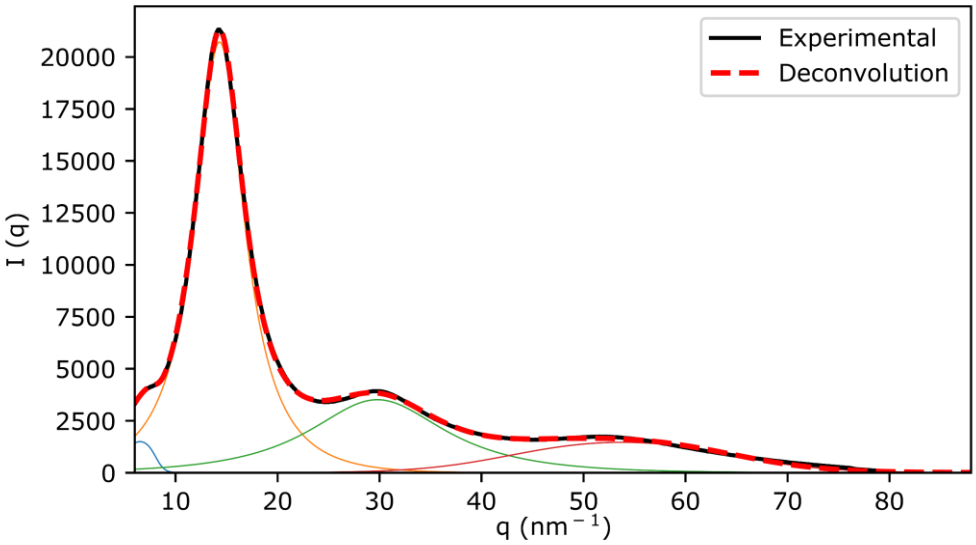

A14.14. FDCAHDO 1500 30 MDI

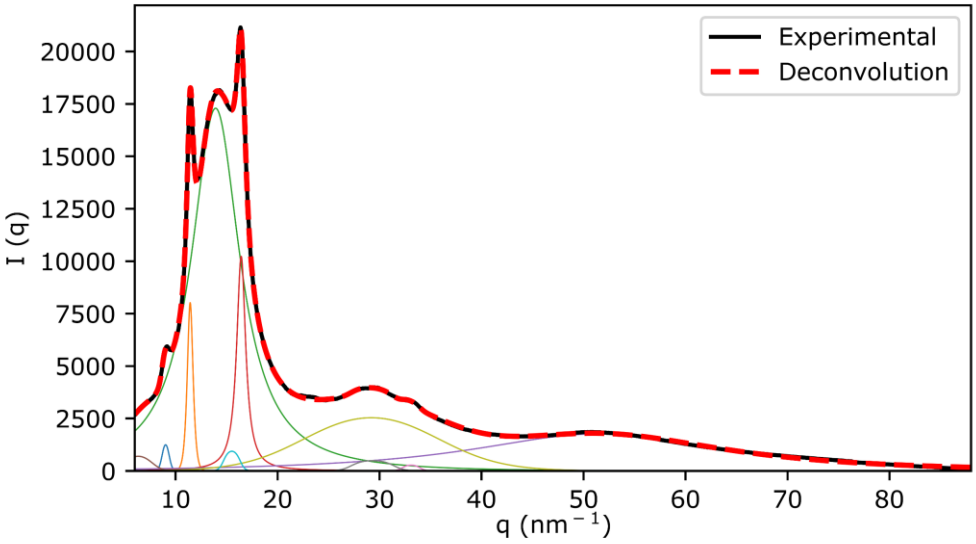

A14.15. FDCAHDO 2000 10 MDI

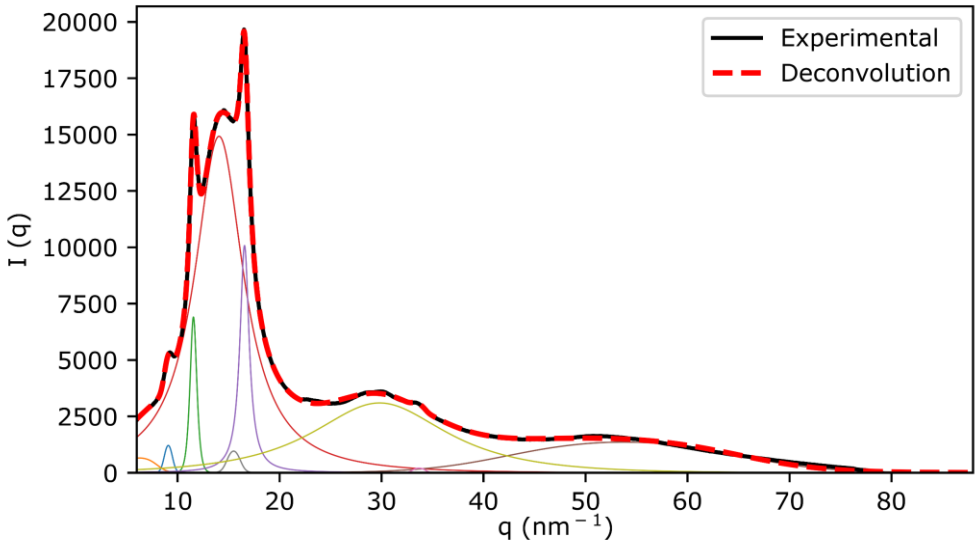

A14.16. FDCAHDO 2000 50 MDI

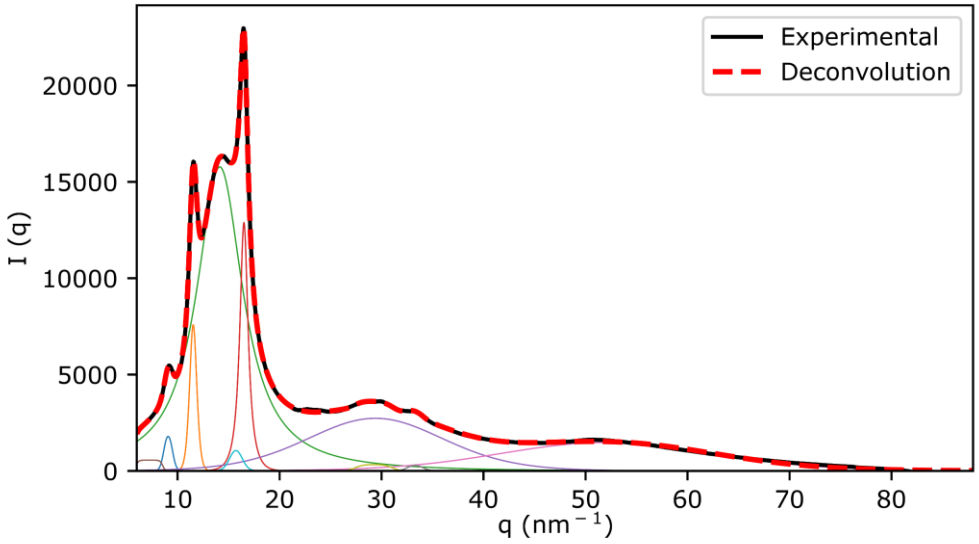

A14.17. FDCAPDO 1000 10 HDI

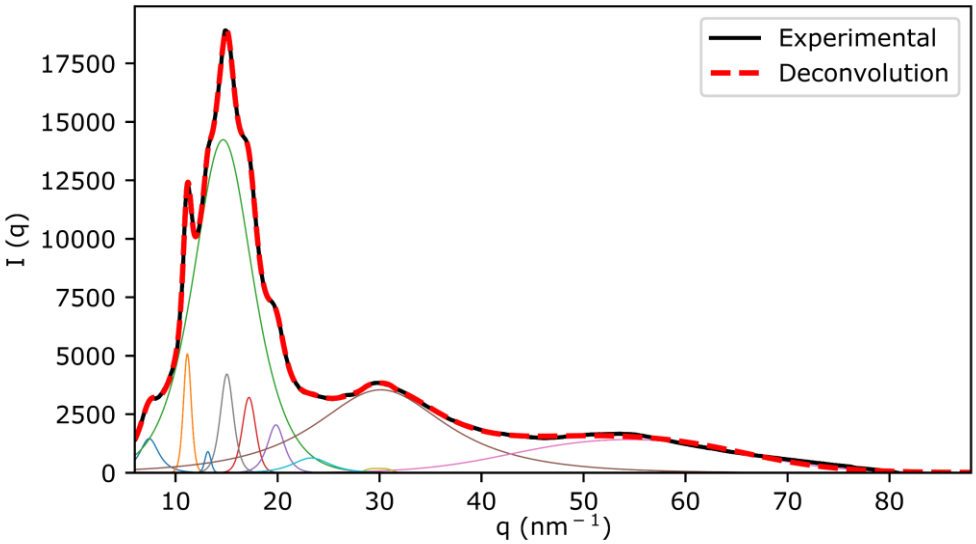

A14.18. FDCAPDO 1000 50 HDI

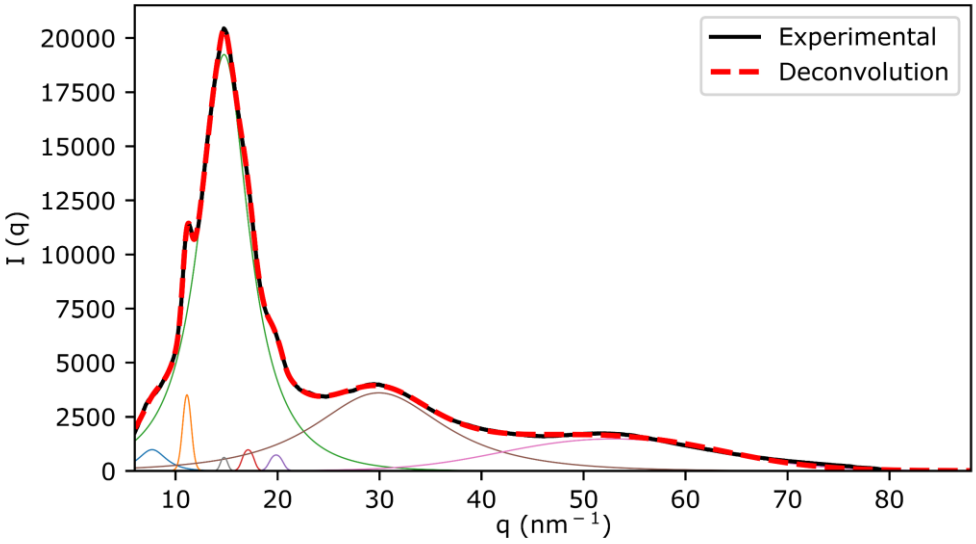

A14.19. FDCAPDO 1500 30 HDI

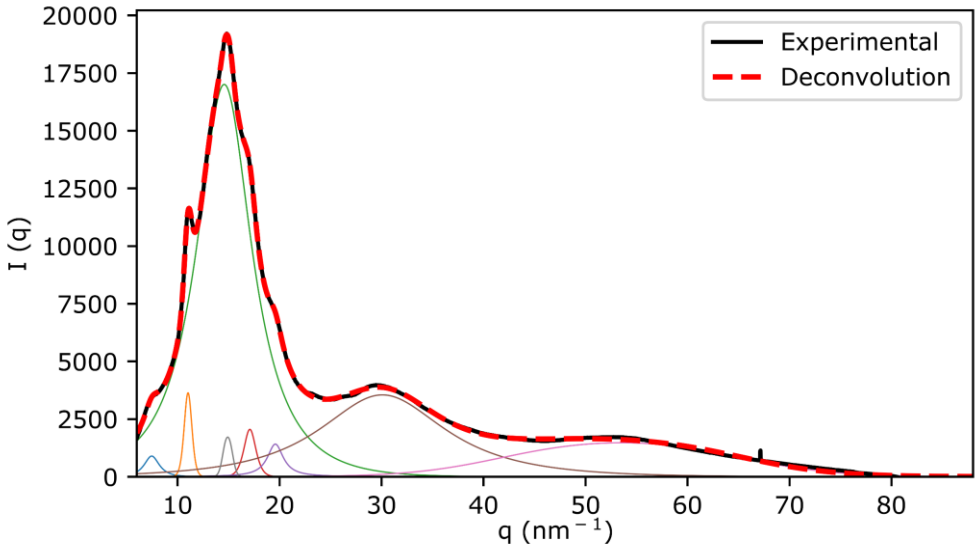

A14.20. FDCAPDO 2000 10 HDI

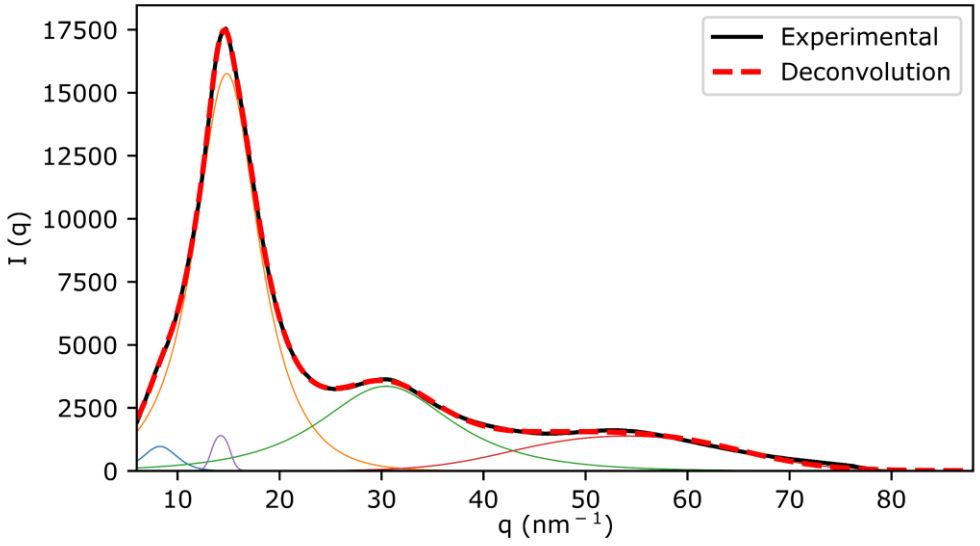

A14.21. FDCAPDO 2000 50 HDI

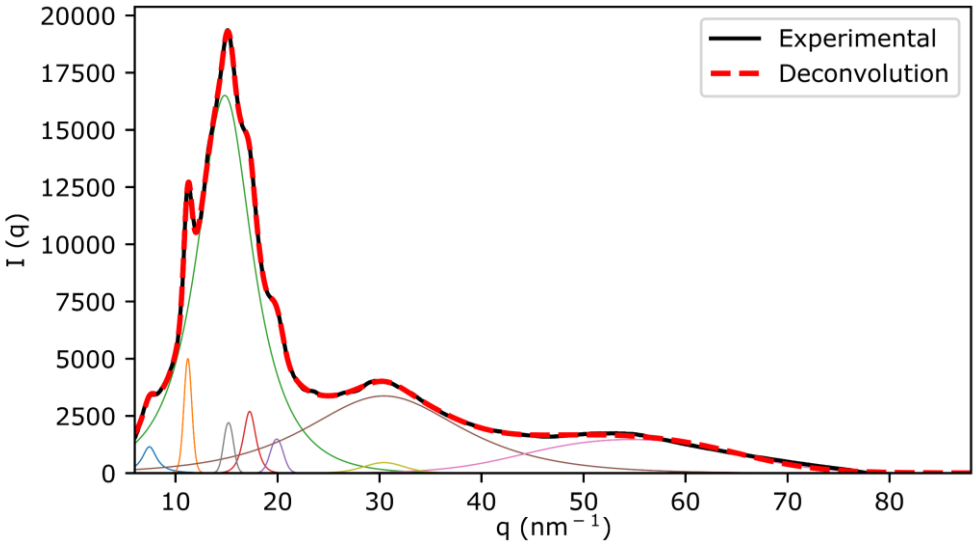

A15 Shape memory cycles of the annealed TPUs

A15.1. IPHTAPDO 1000 30 HDI

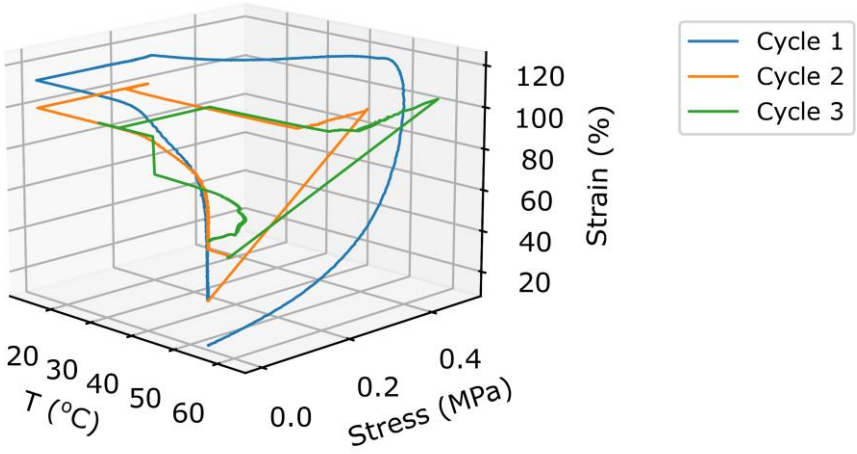

A15.2. IPHTAPDO 1000 50 HDI

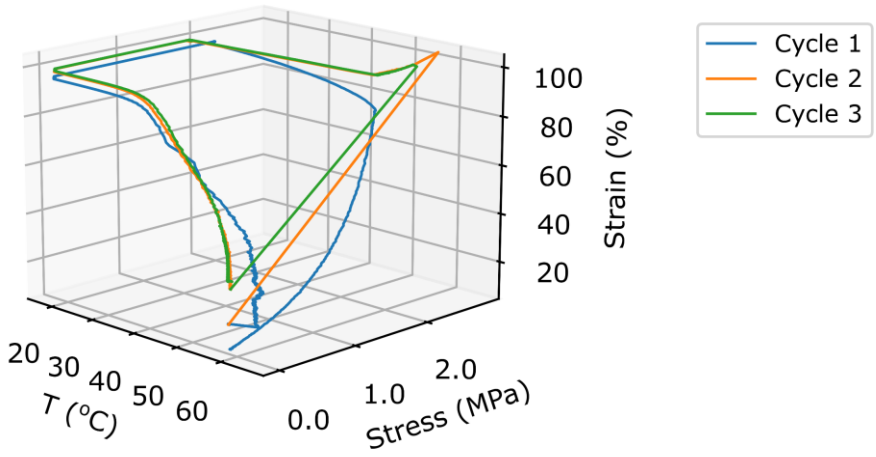

A15.3. IPHTAPDO 2000 10 HDI

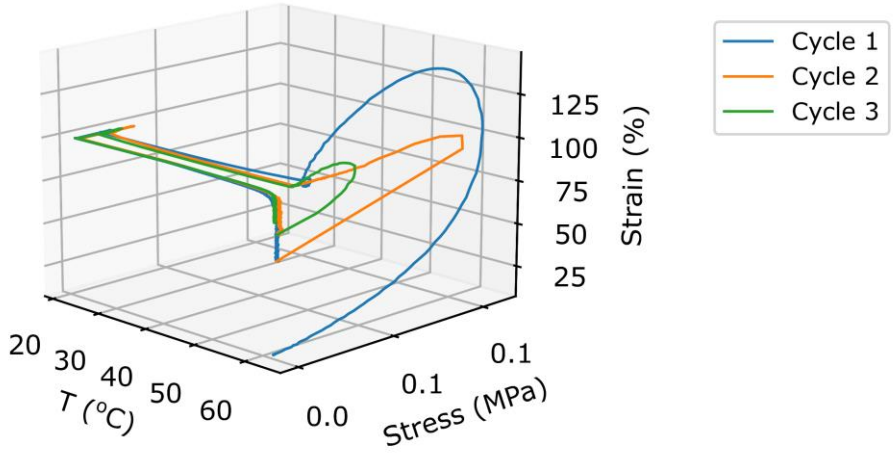

A15.4. IPHTAPDO 2000 30 HDI

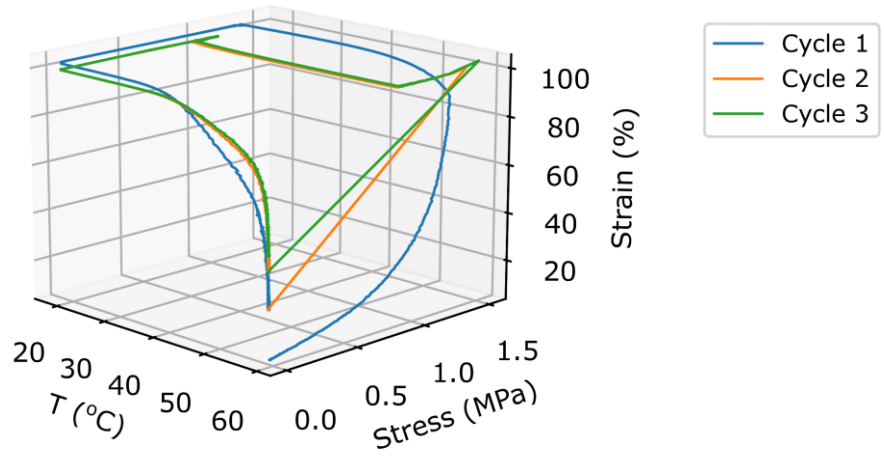

A15.5. IPHTAPDO 2000 50 HDI

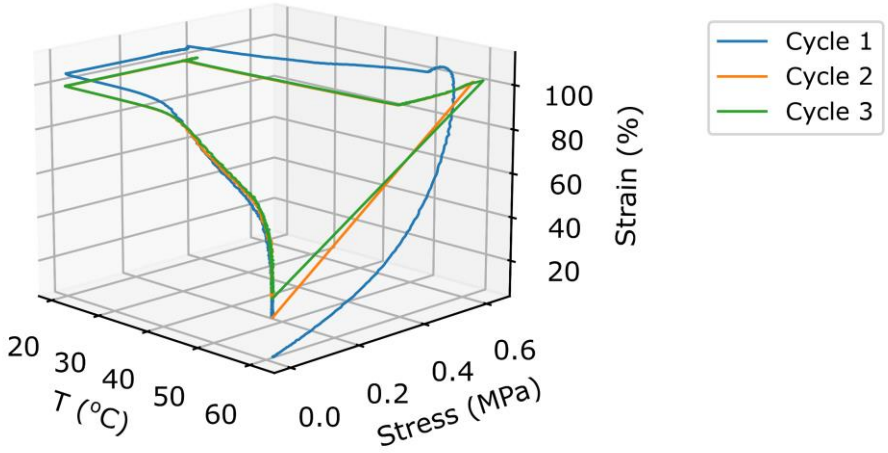

A15.6. FDCAPDO 1000 10 MDI

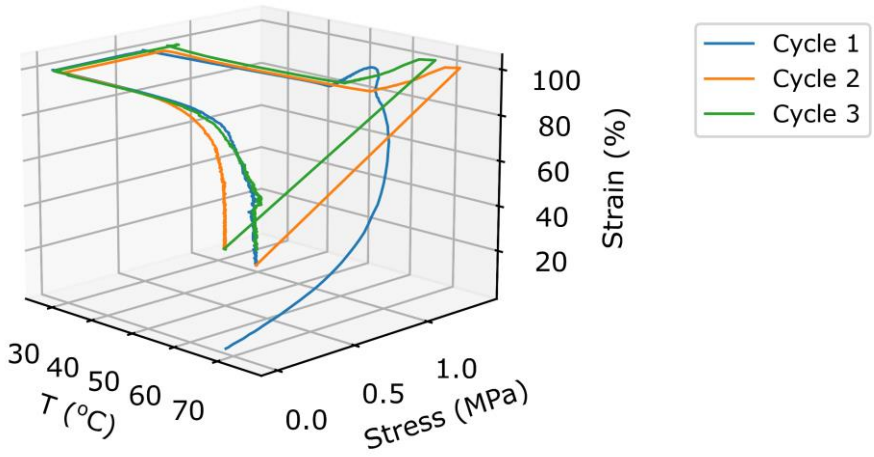

A15.7. FDCAPDO 1000 50 MDI

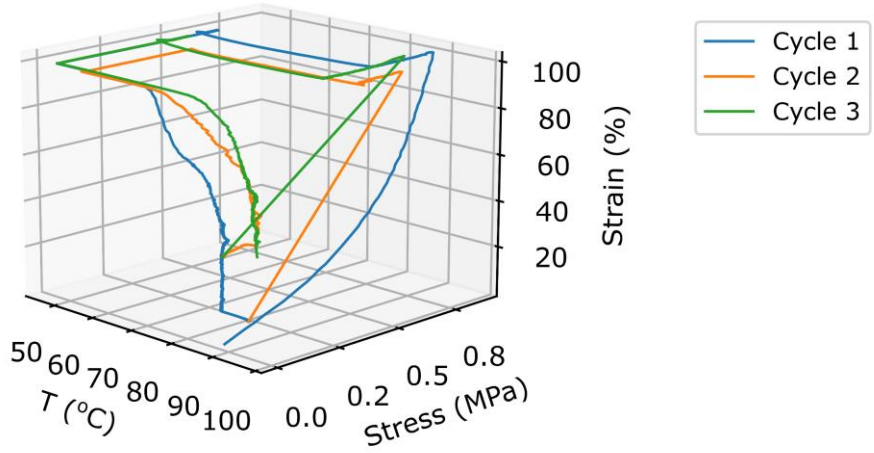

A15.8. FDCAPDO 1500 30 MDI

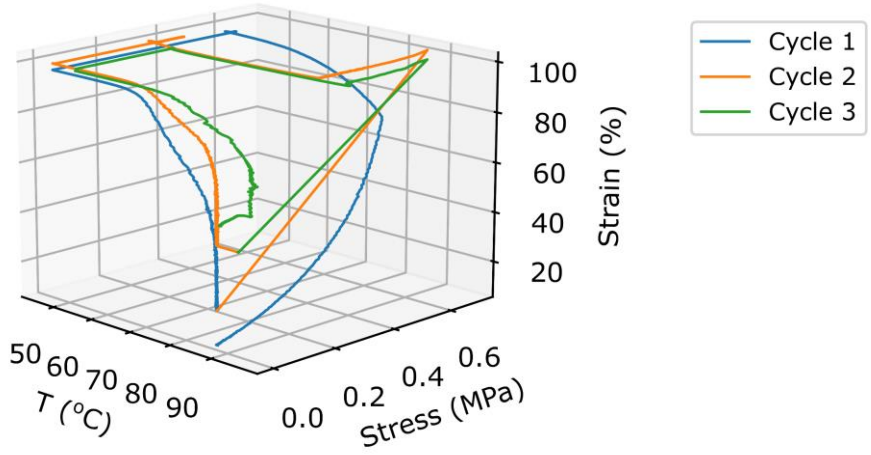

A15.9. FDCAPDO 2000 10 MDI

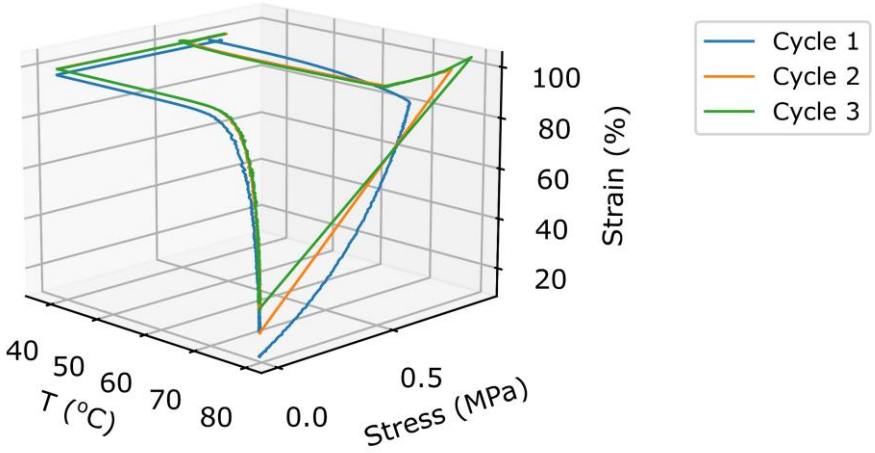

A15.10. FDCAPDO 2000 50 MDI

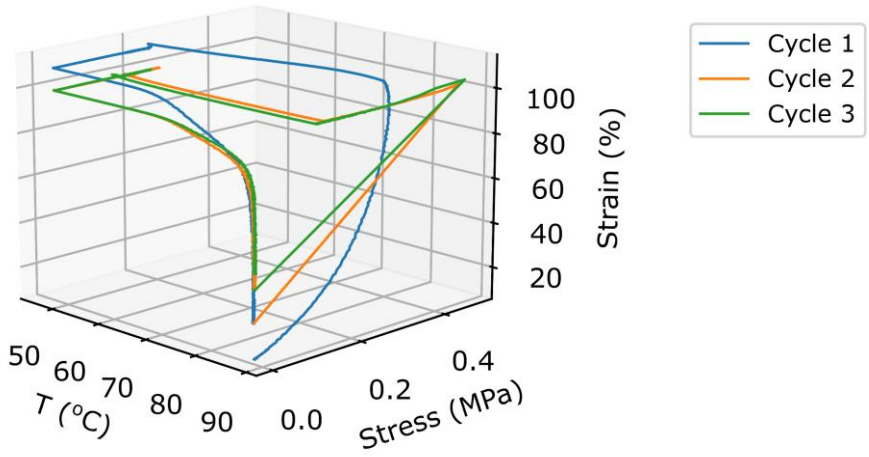

A15.11. FDCAHDO 1000 50 MDI

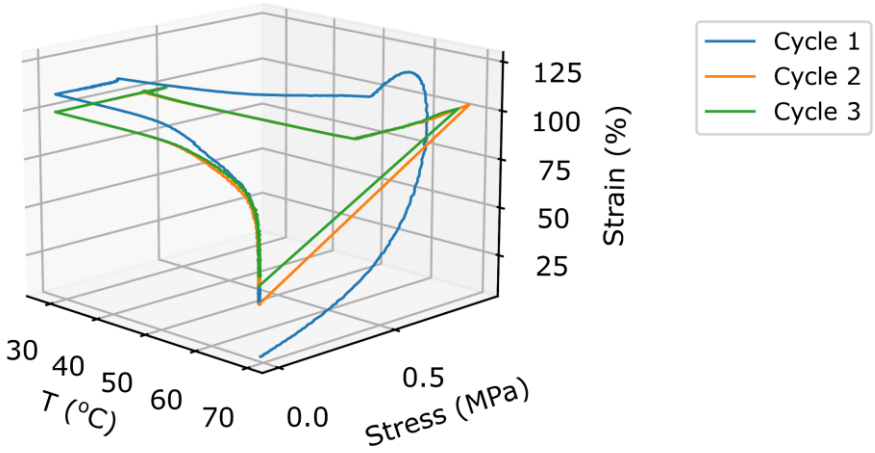

A15.12. FDCAHDO 1500 30 MDI

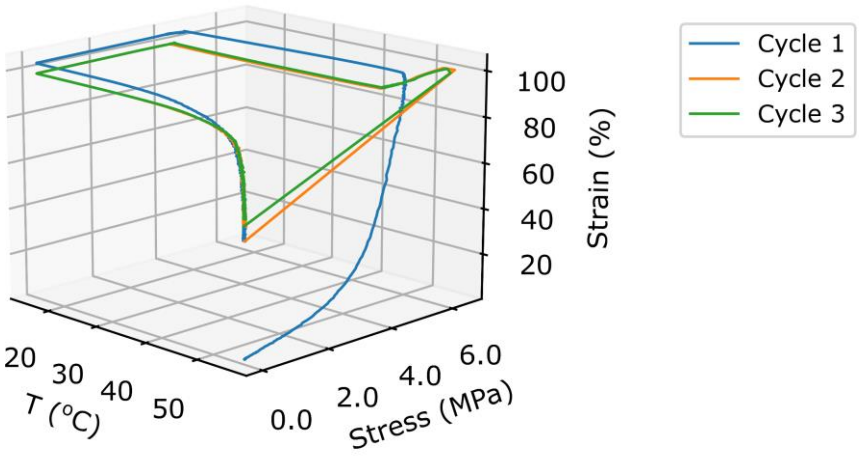

A15.13. FDCAHDO 2000 10 MDI

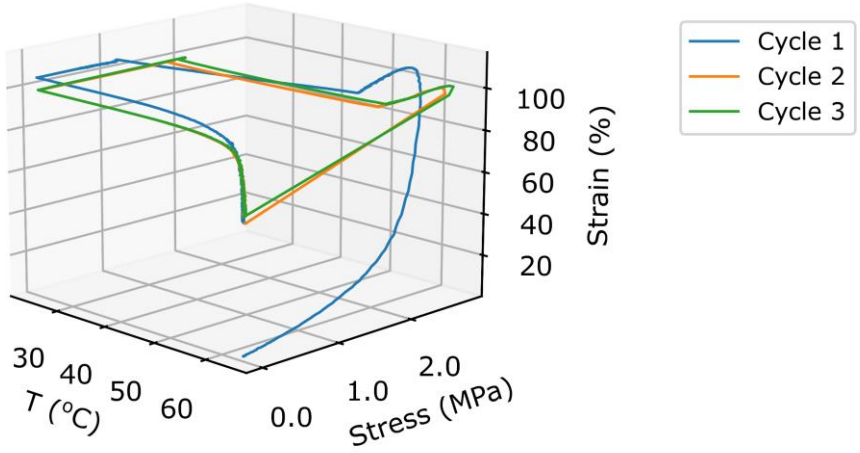

A15.14. FDCAHDO 2000 50 MDI

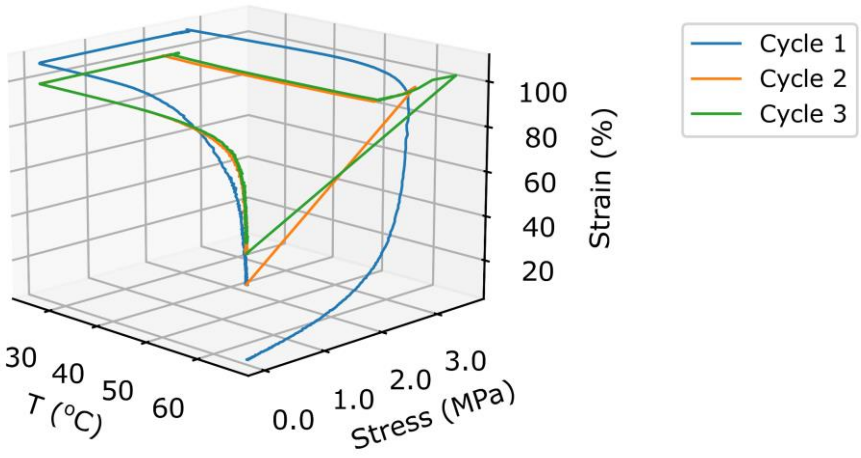

A15.15. FDCAPDO 1000 10 HDI

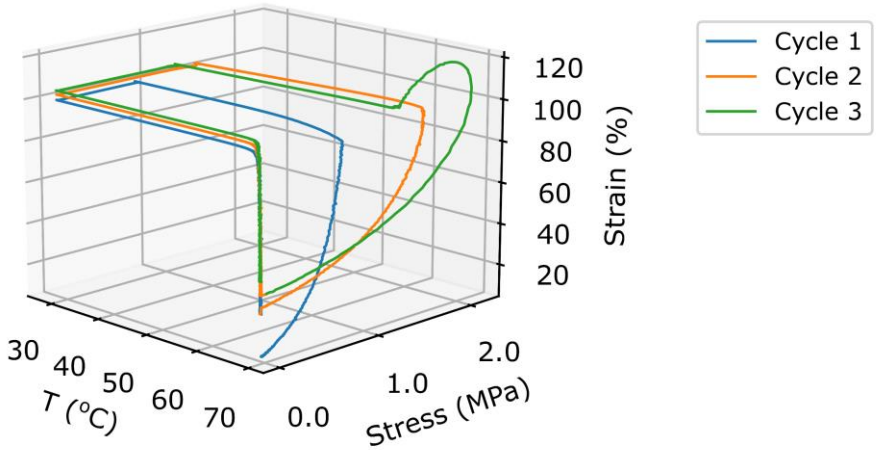

A15.16. FDCAPDO 1500 30 HDI

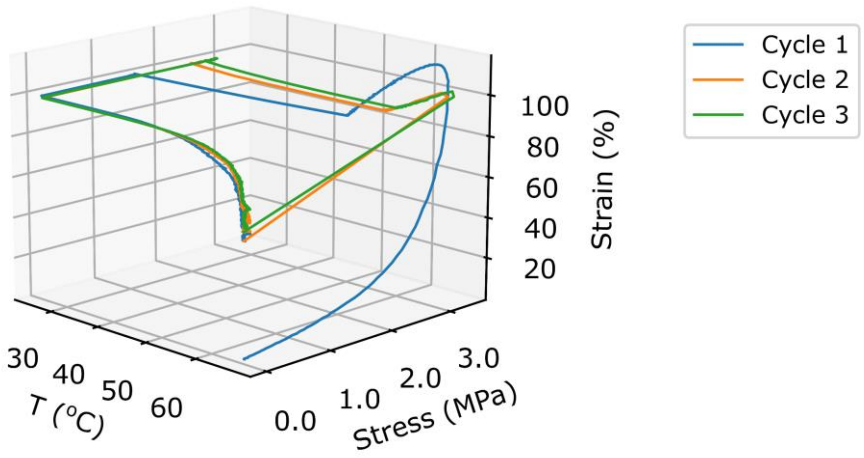

A15.17. FDCAPDO 2000 10 HDI

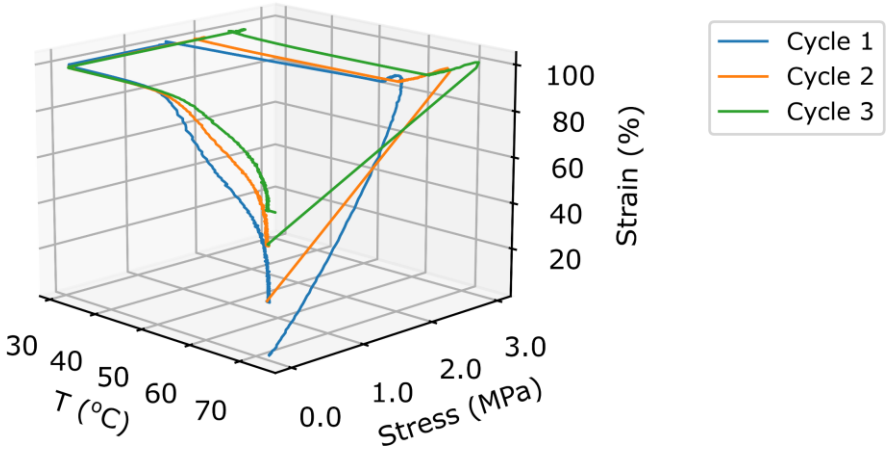

A15.18. FDCAPDO 2000 50 HDI

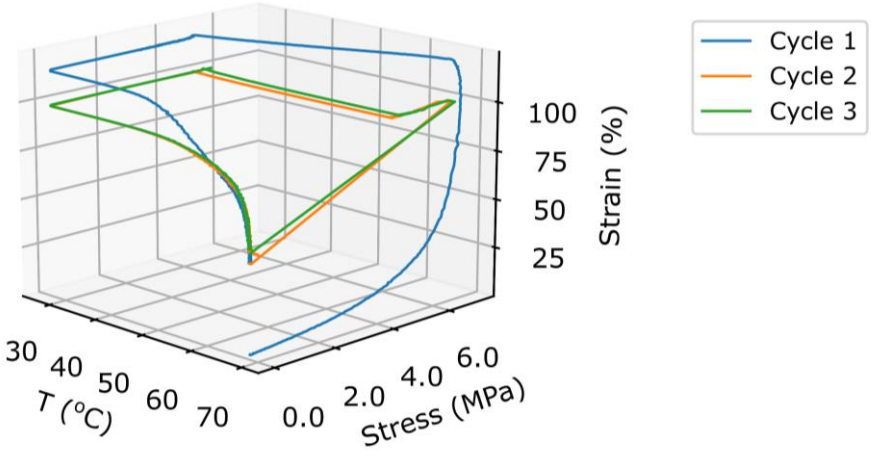

A16 Tensile testing at 20 ºC above the T_g of the annealed materials

A16.1. IPHTAPDO 1000 10 HDI

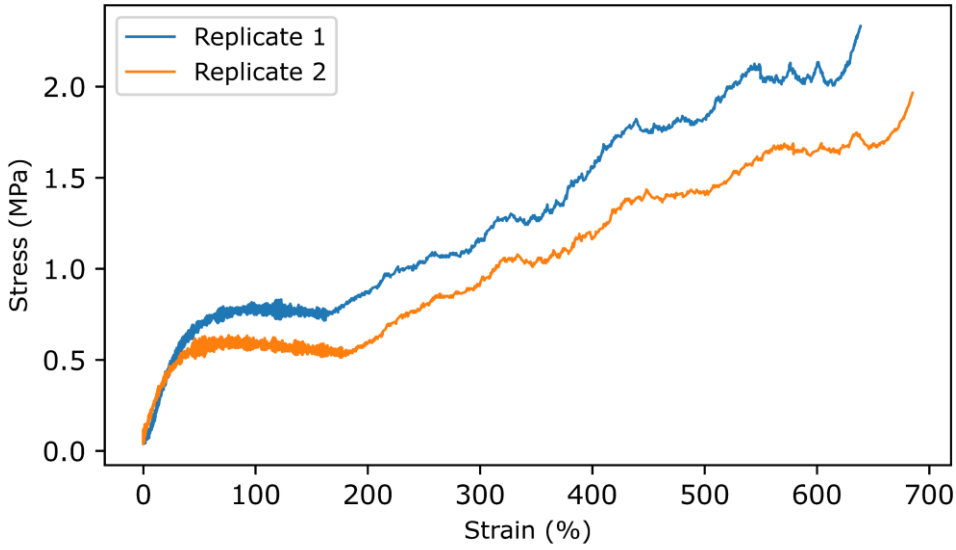

A16.2. IPHTAPDO 1000 30 HDI

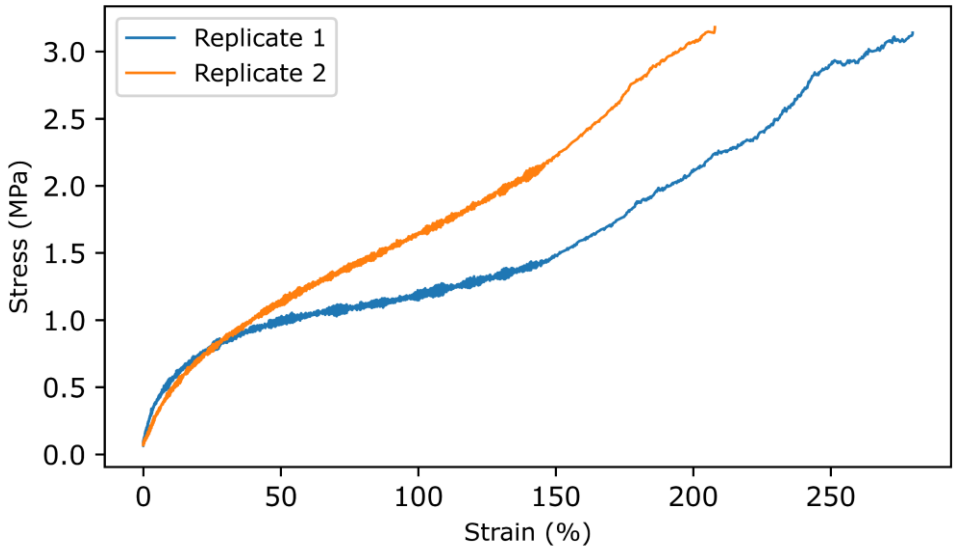

A16.3. IPHTAPDO 1000 50 HDI

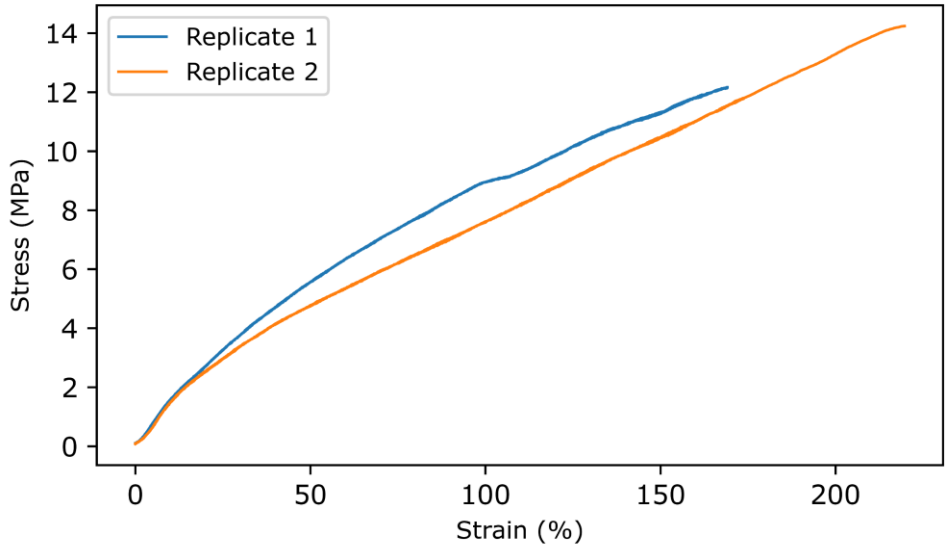

A16.4. IPHTAPDO 2000 10 HDI

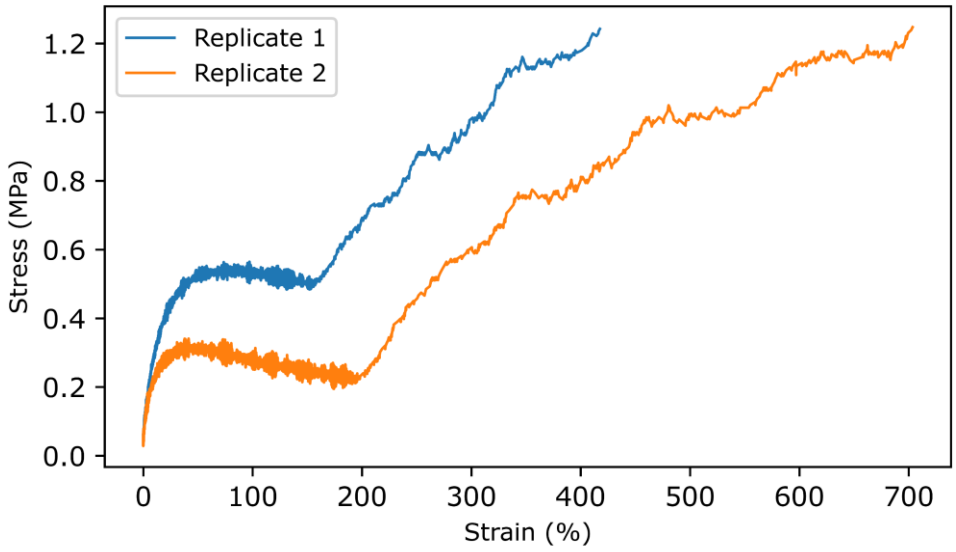

A16.5. IPHTAPDO 2000 30 HDI

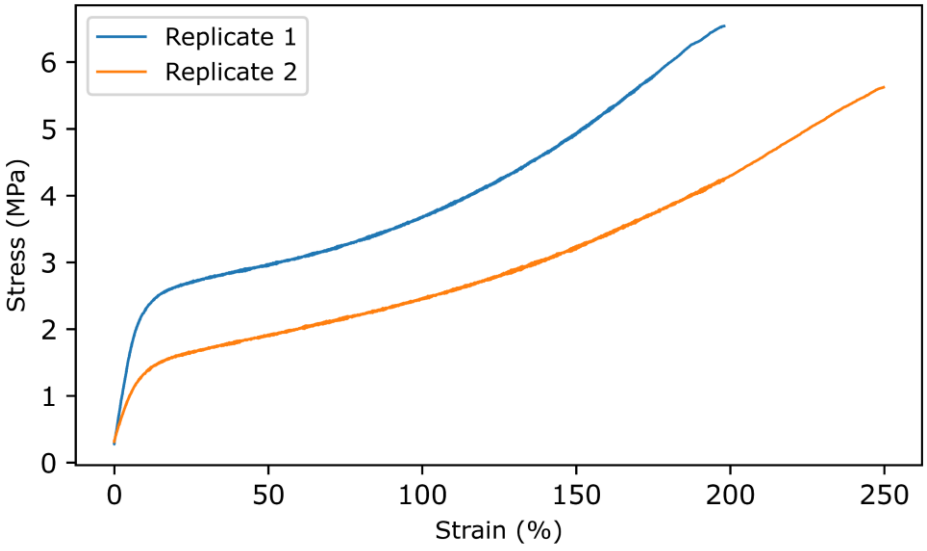

A16.6. IPHTAPDO 2000 50 HDI

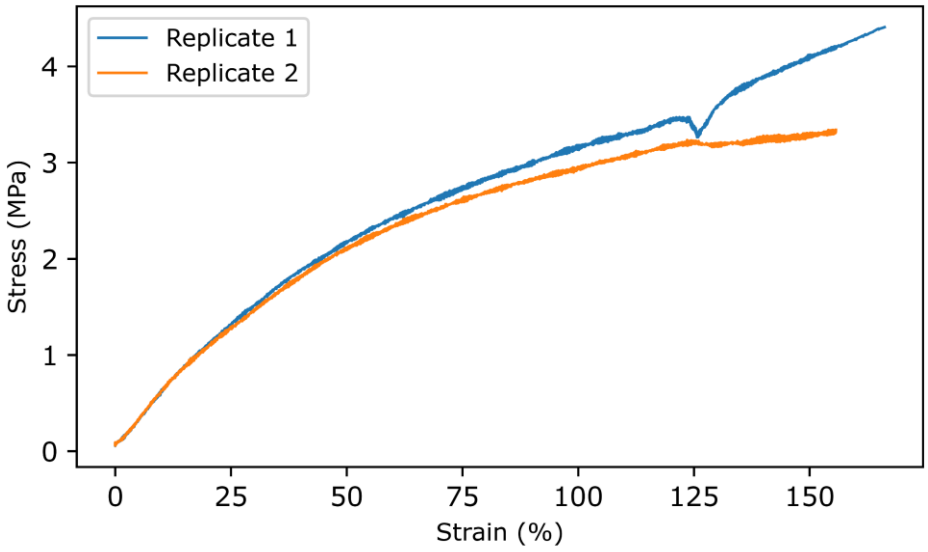

A16.7. FDCAPDO 1000 10 MDI

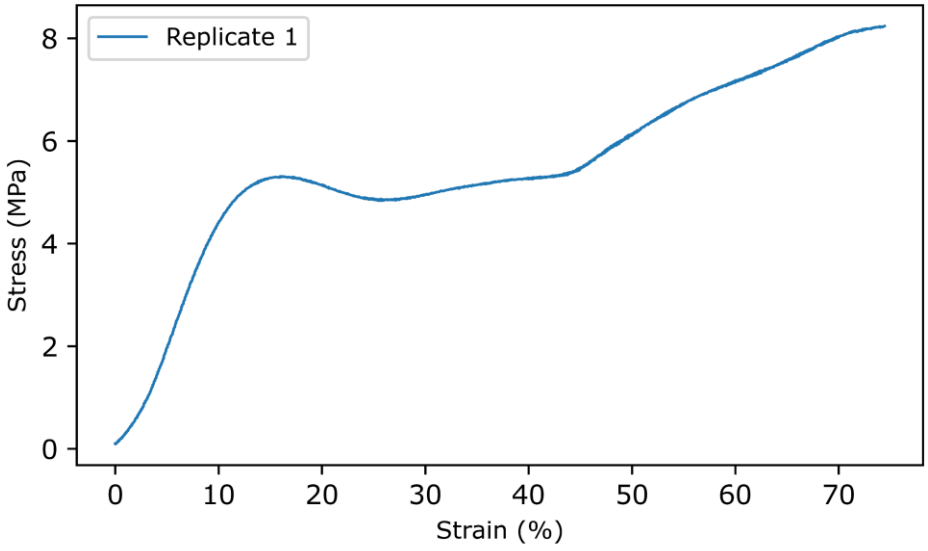

A16.8. FDCAPDO 1000 50 MDI

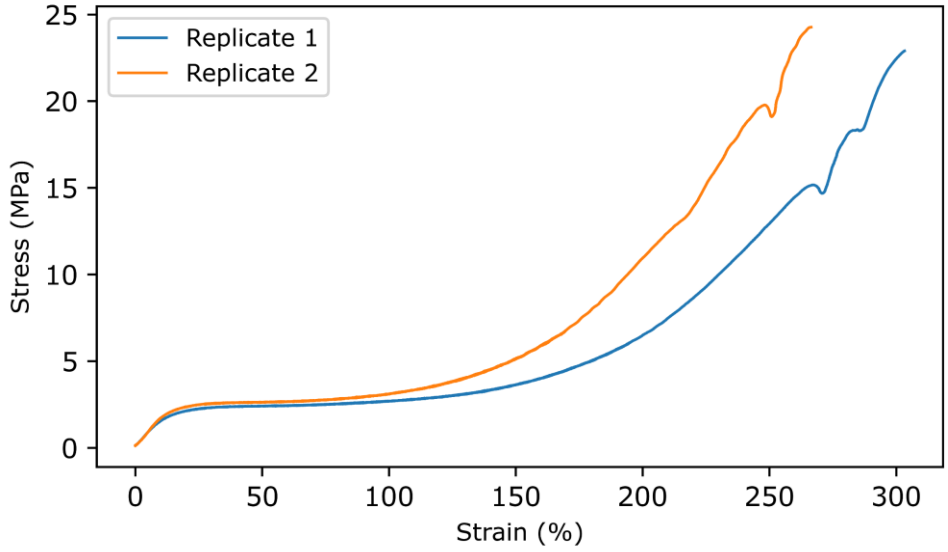

A16.9. FDCAPDO 1500 30 MDI

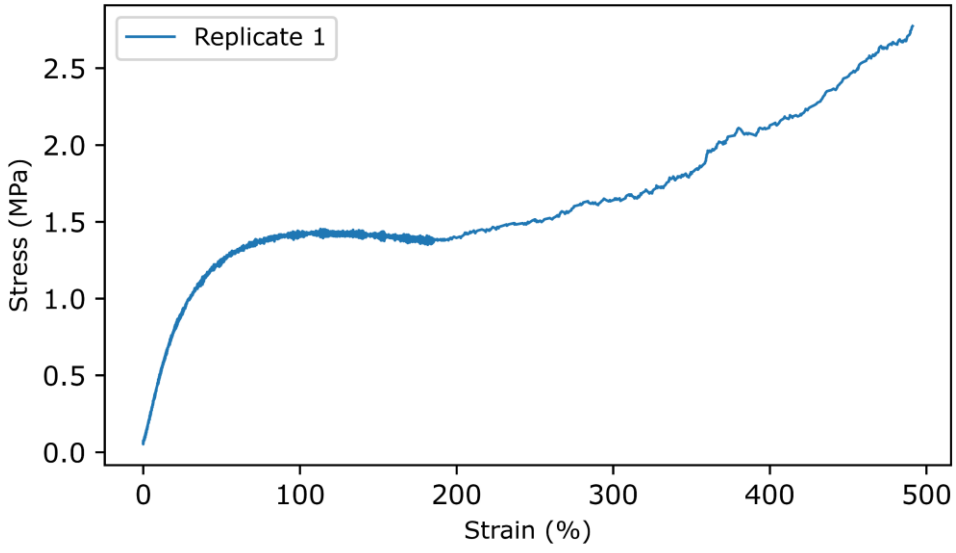

A16.10. FDCAPDO 2000 10 MDI

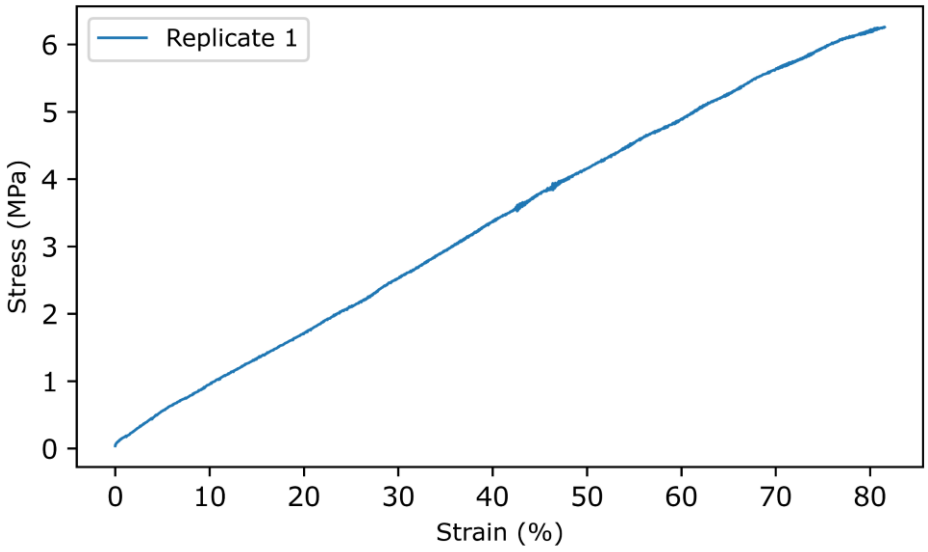

A16.11. FDCAPDO 2000 50 MDI

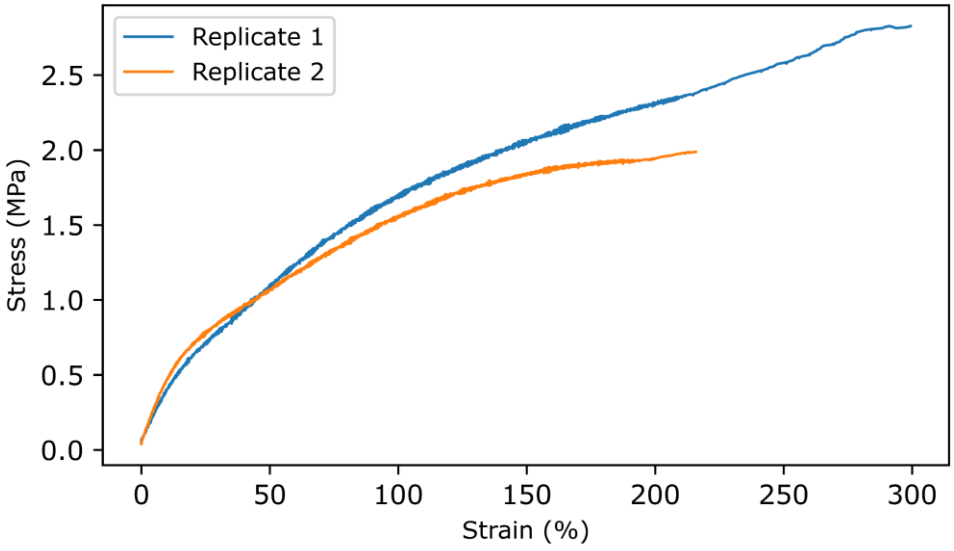

A16.12. FDCAHDO 1000 10 MDI

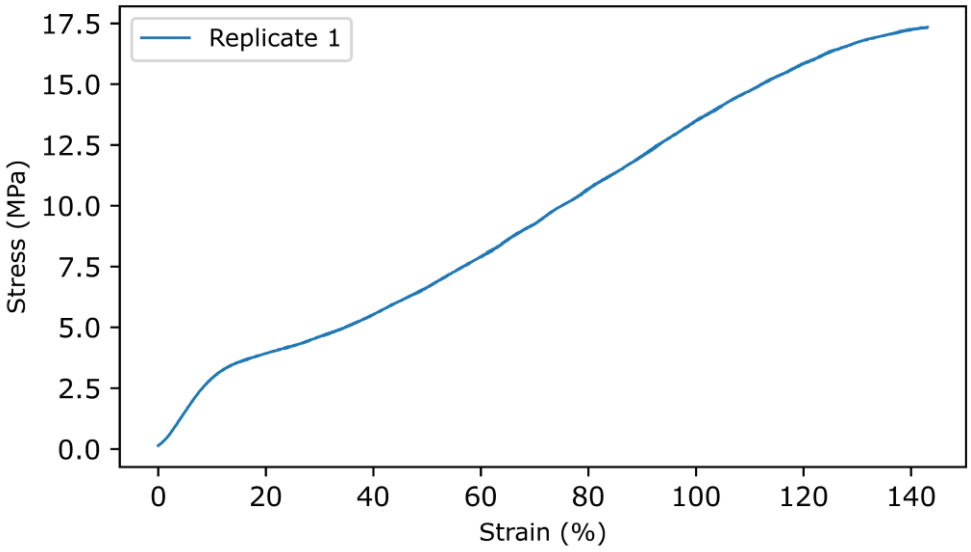

A16.13. FDCAHDO 1000 50 MDI

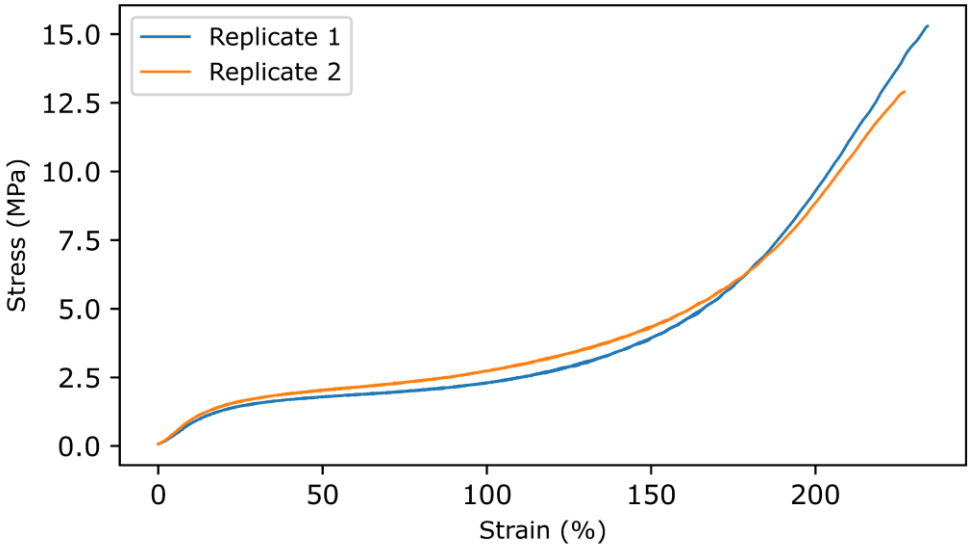

A16.14. FDCAHDO 1500 30 MDI

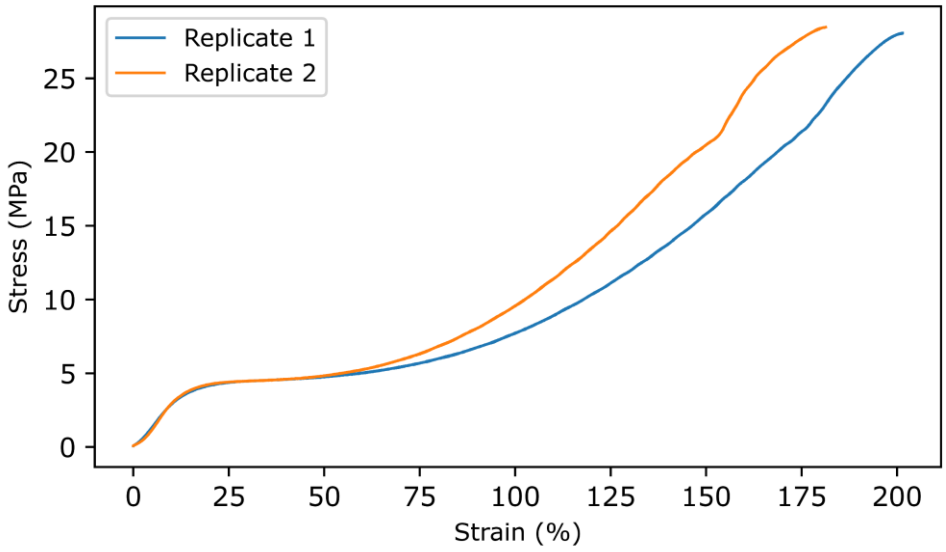

A16.15. FDCAPDO 1000 10 HDI

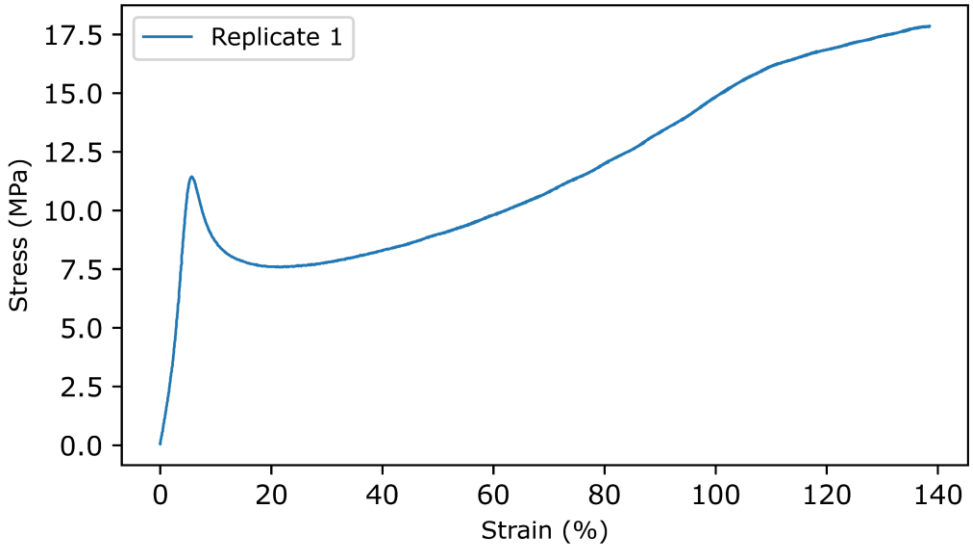

A16.16. FDCAPDO 1000 50 HDI

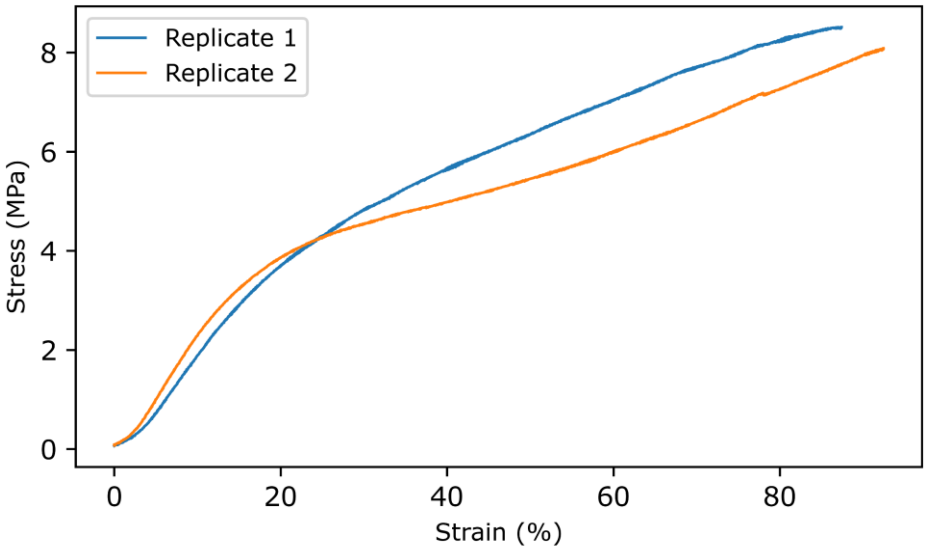

A16.17. FDCAPDO 1500 30 HDI

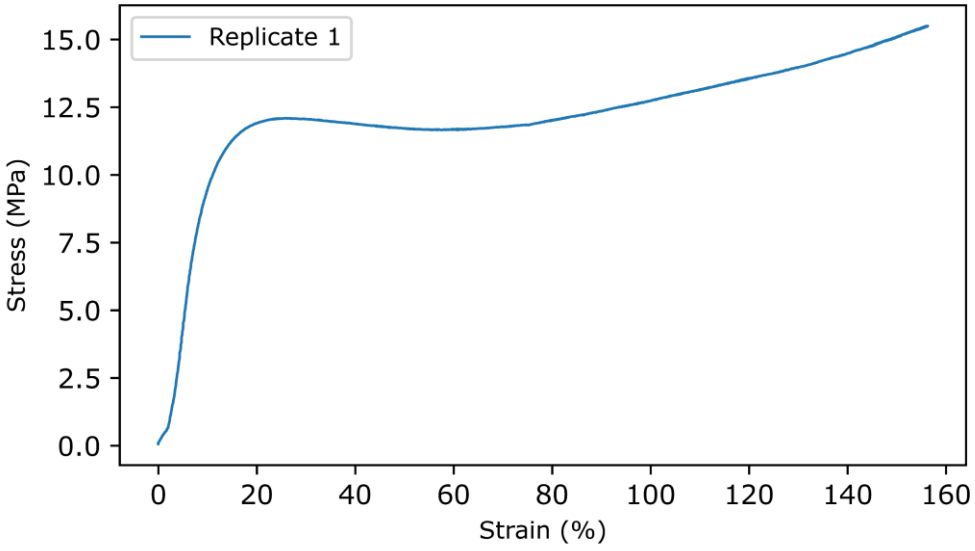

A16.18. FDCAPDO 2000 10 HDI

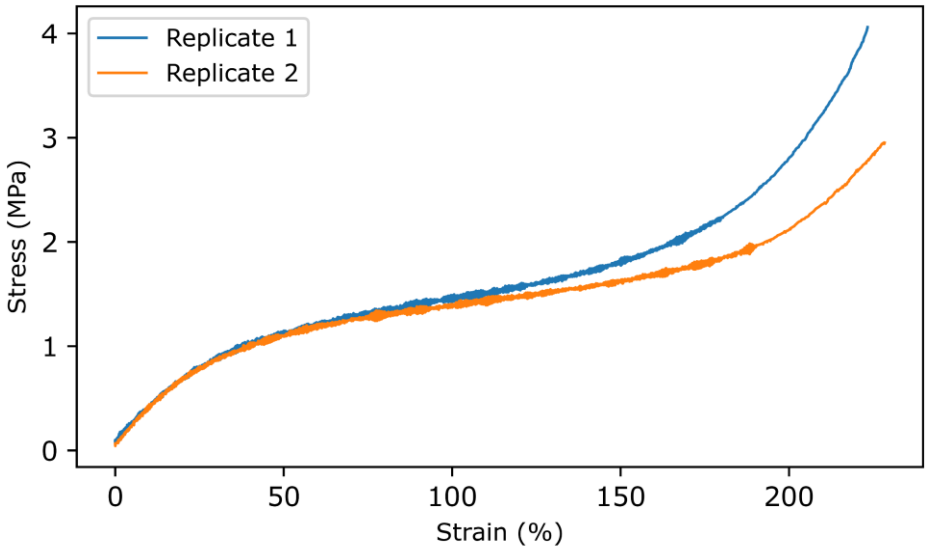

A16.19. FDCAPDO 2000 50 HDI

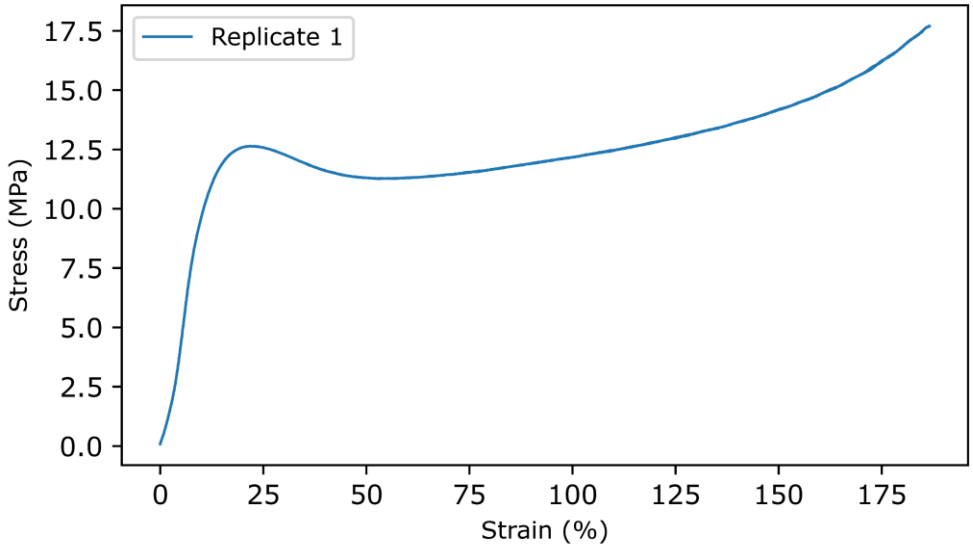

A17 Actuation strength of the annealed TPUs

A17.1. IPHTAPDO 1000 10 HDI

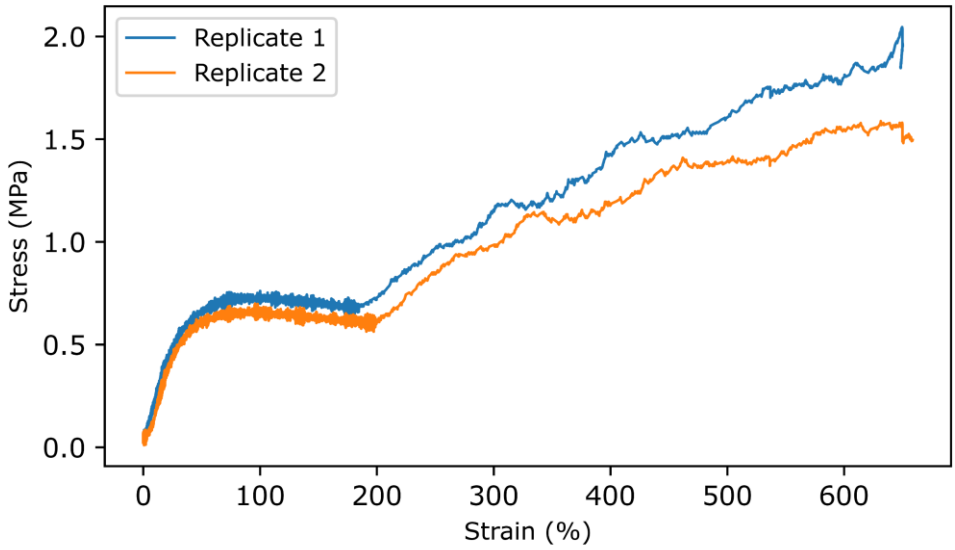

A17.2. IPHTAPDO 1000 30 HDI

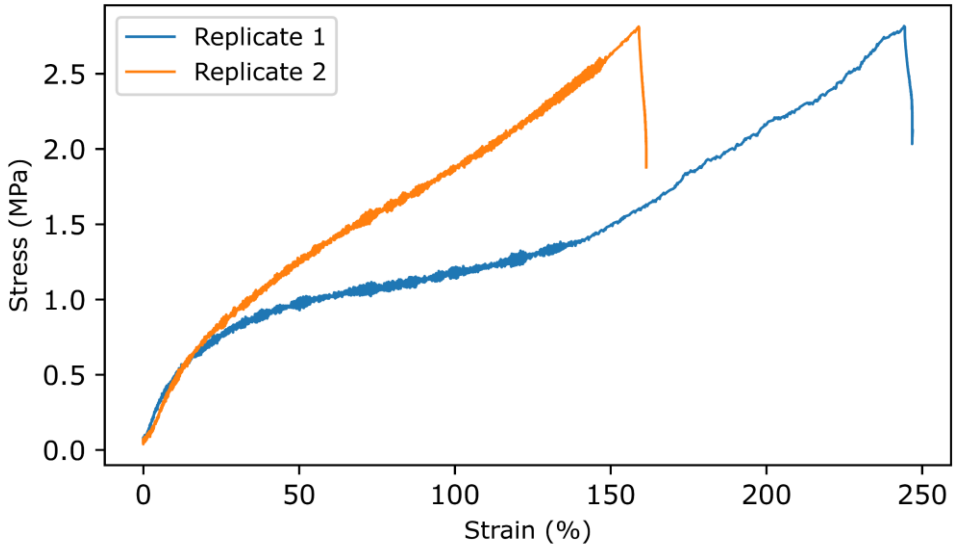

A17.3. IPHTAPDO 1000 50 HDI

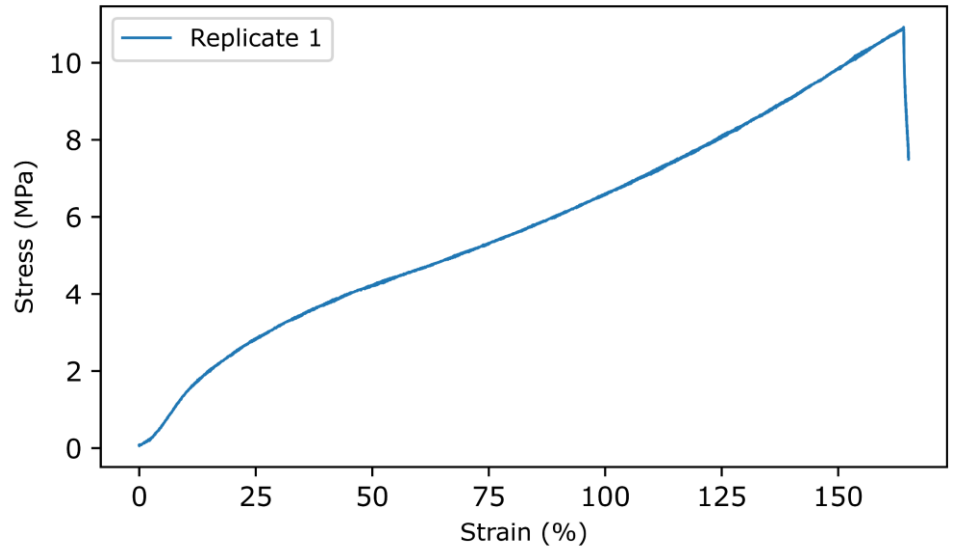

A17.4. IPHTAPDO 2000 10 HDI

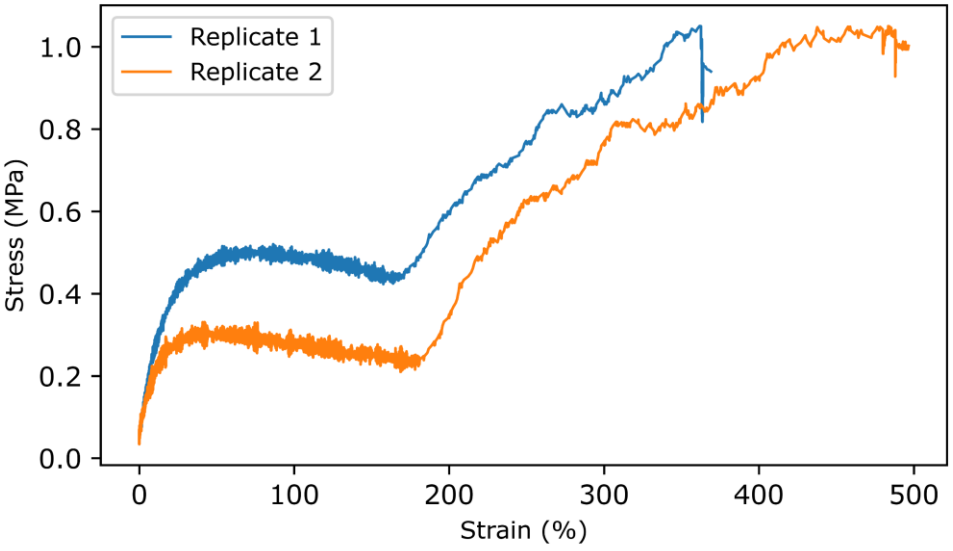

A17.5. IPHTAPDO 2000 30 HDI

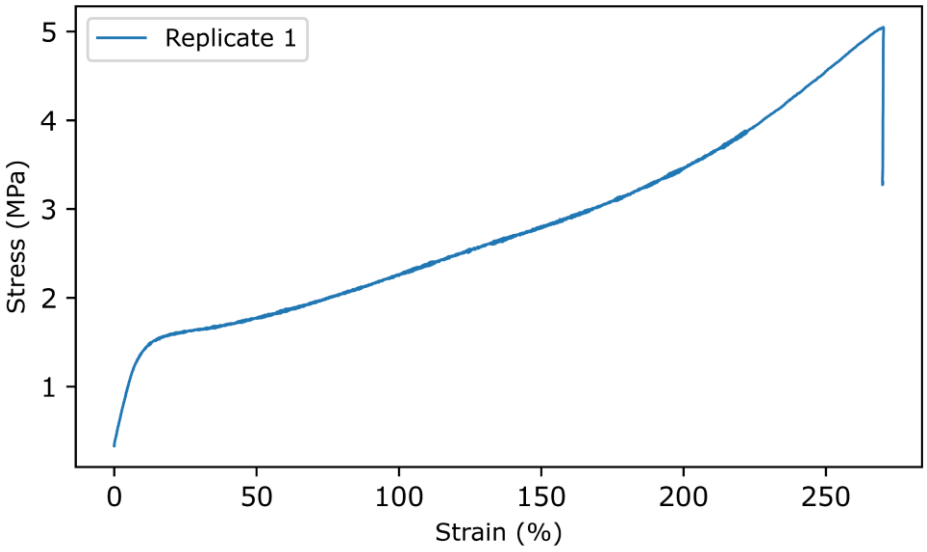

A17.6. IPHTAPDO 2000 50 HDI

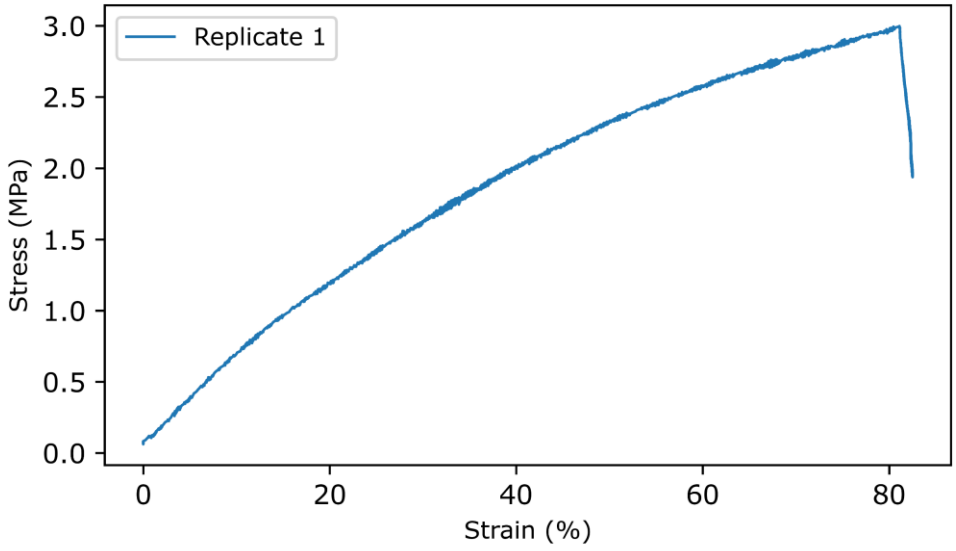

A17.7. FDCAPDO 1000 10 MDI

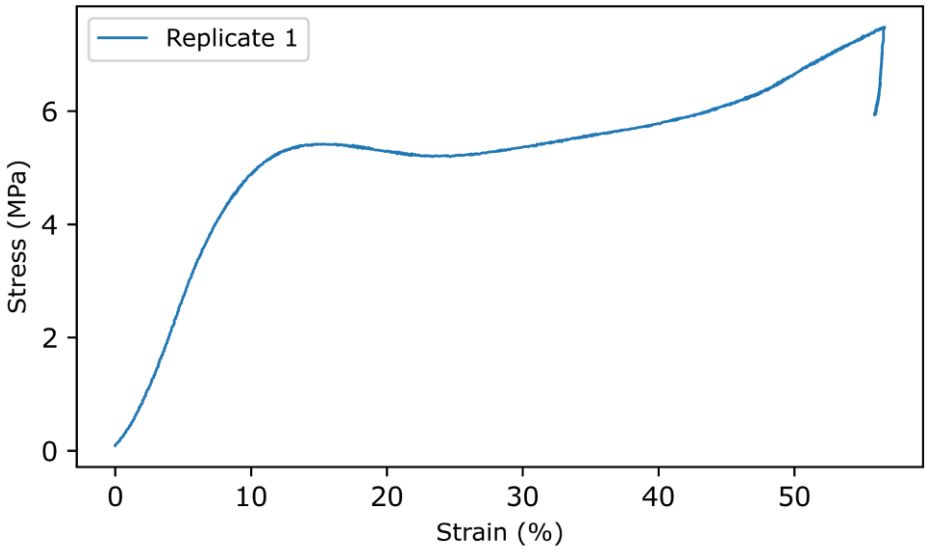

A17.8. FDCAPDO 1000 50 MDI

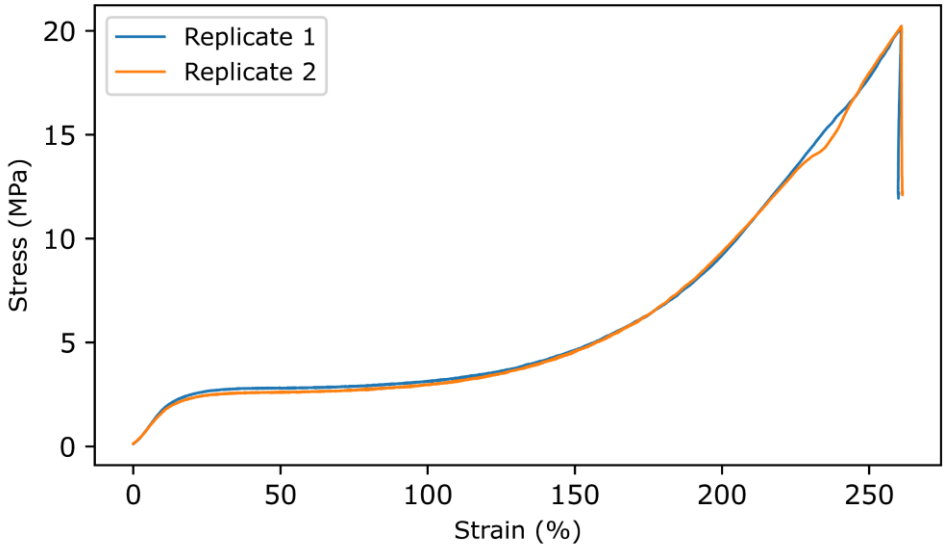

A17.9. FDCAPDO 1500 30 MDI

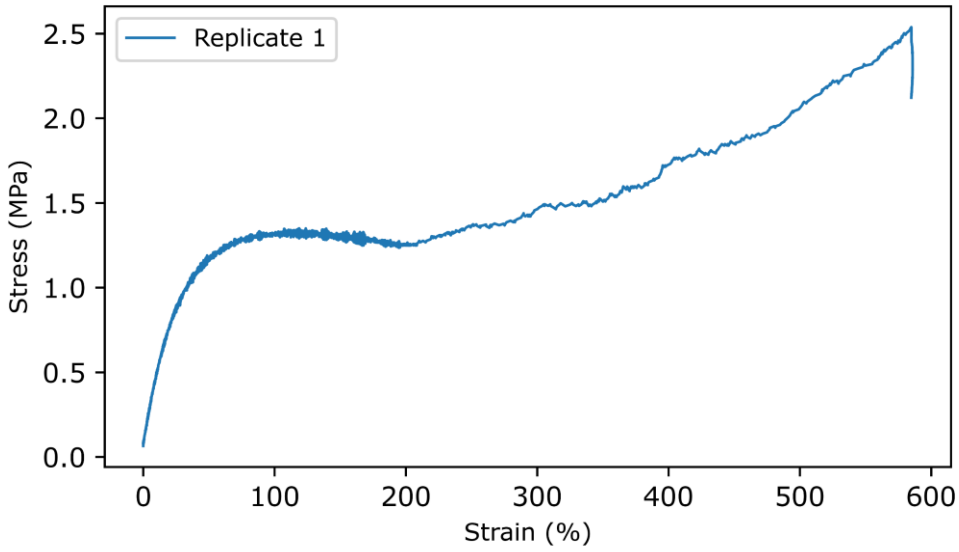

A17.10. FDCAPDO 2000 10 MDI

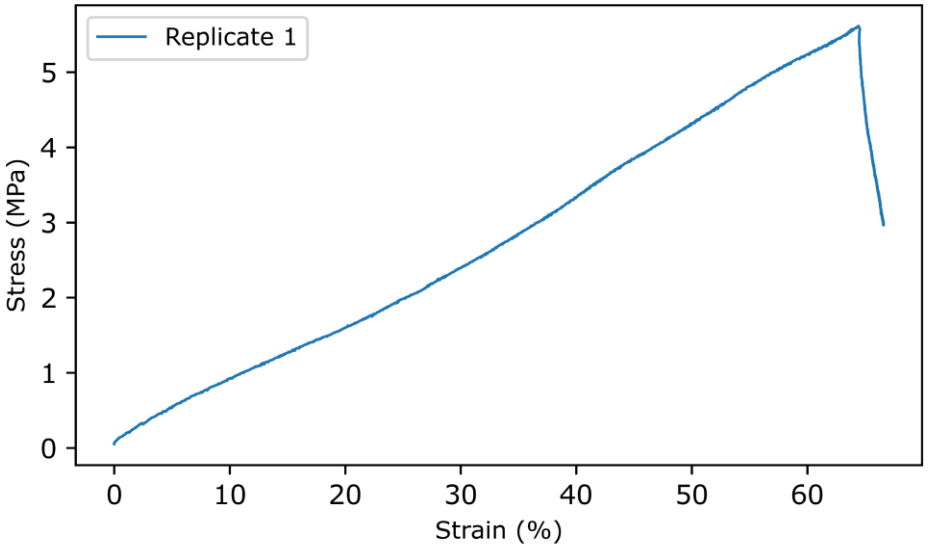

A17.11. FDCAPDO 2000 50 MDI

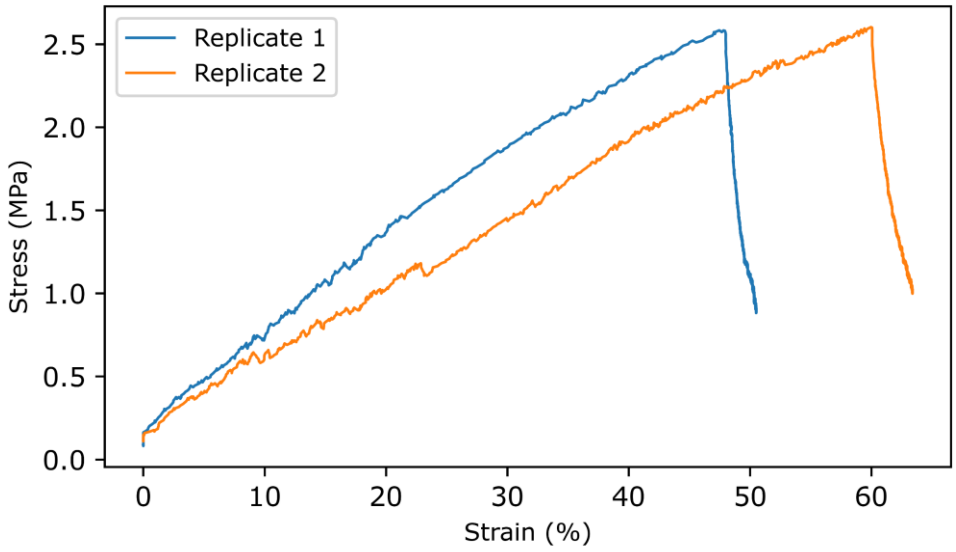

A17.12. FDCAHDO 1000 10 MDI

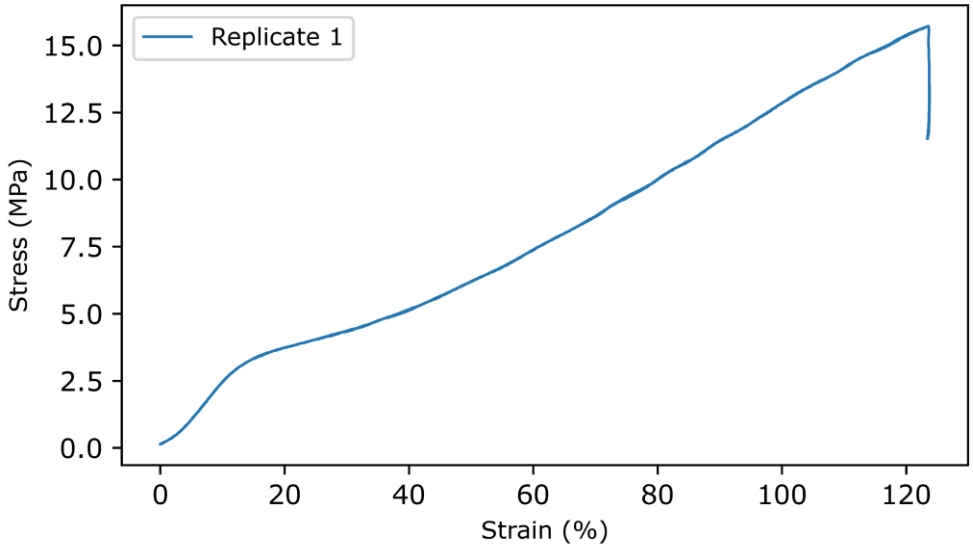

A17.13. FDCAHDO 1000 50 MDI

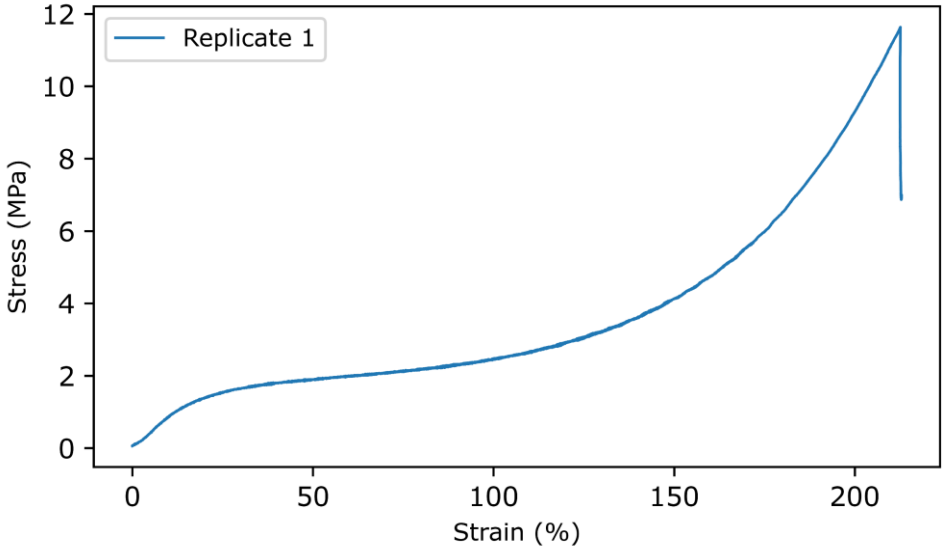

A17.14. FDCAHDO 1500 30 MDI

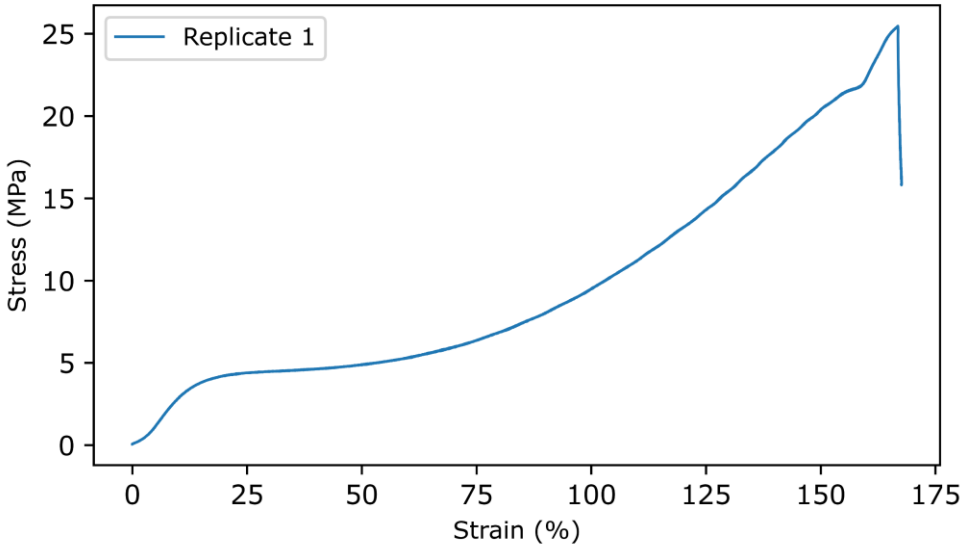

A17.15. FDCAHDO 2000 10 MDI

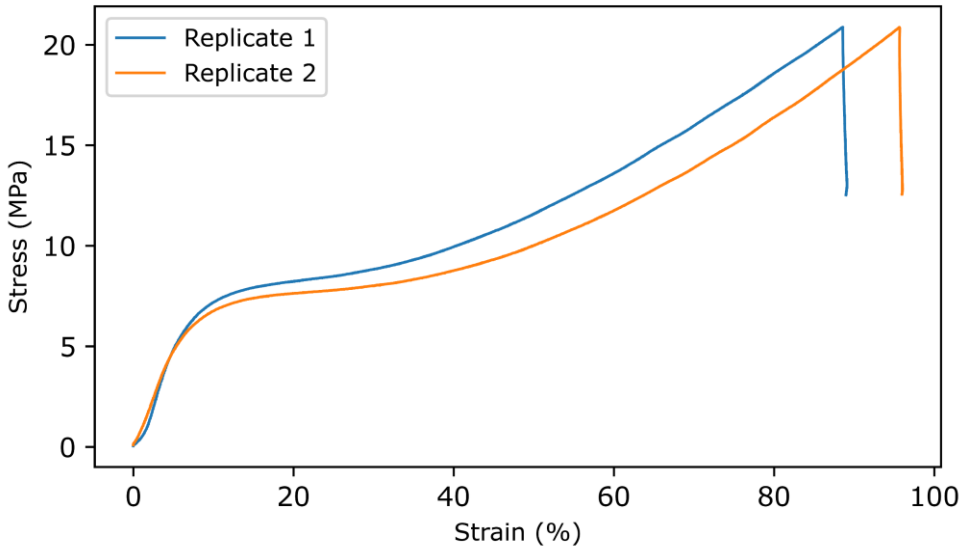

A17.16. FDCAHDO 2000 50 MDI

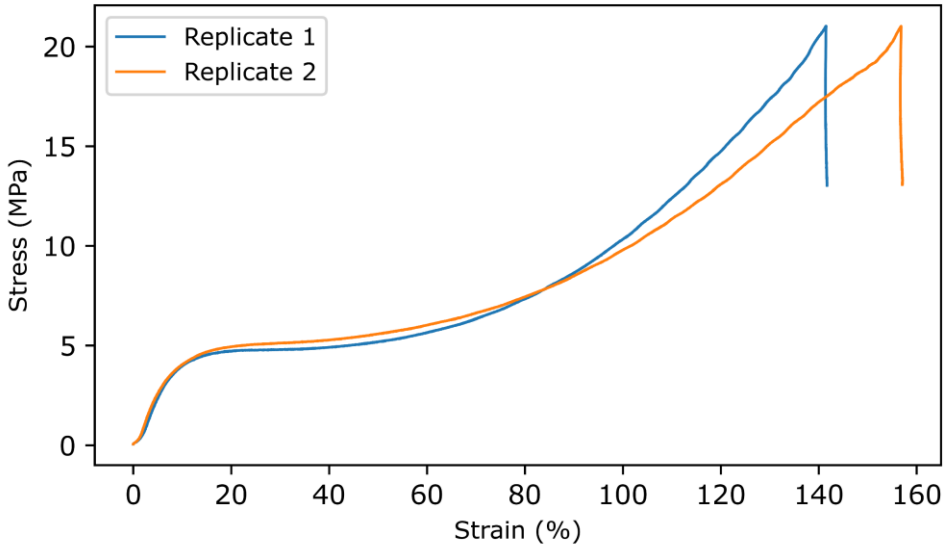

A17.17. FDCAPDO 1000 10 HDI

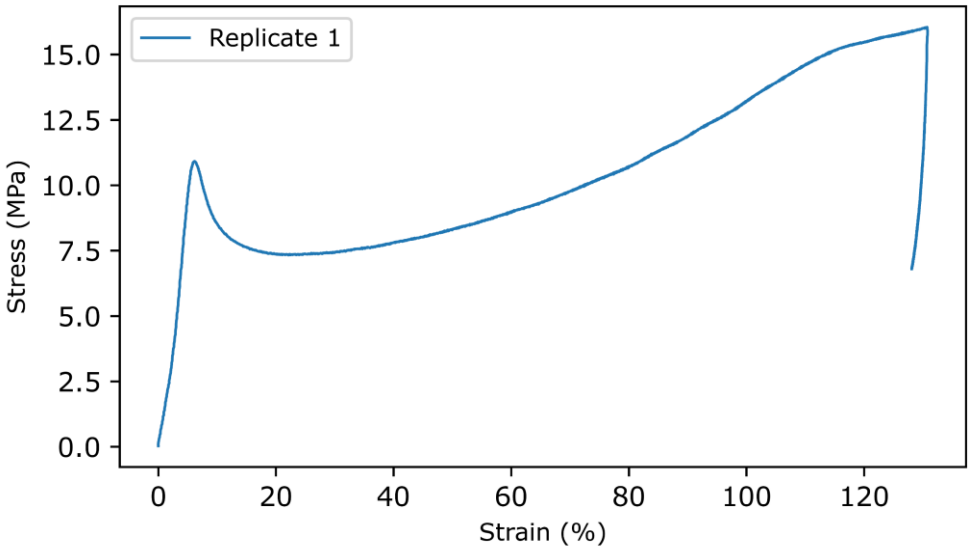

A17.18. FDCAPDO 1000 50 HDI

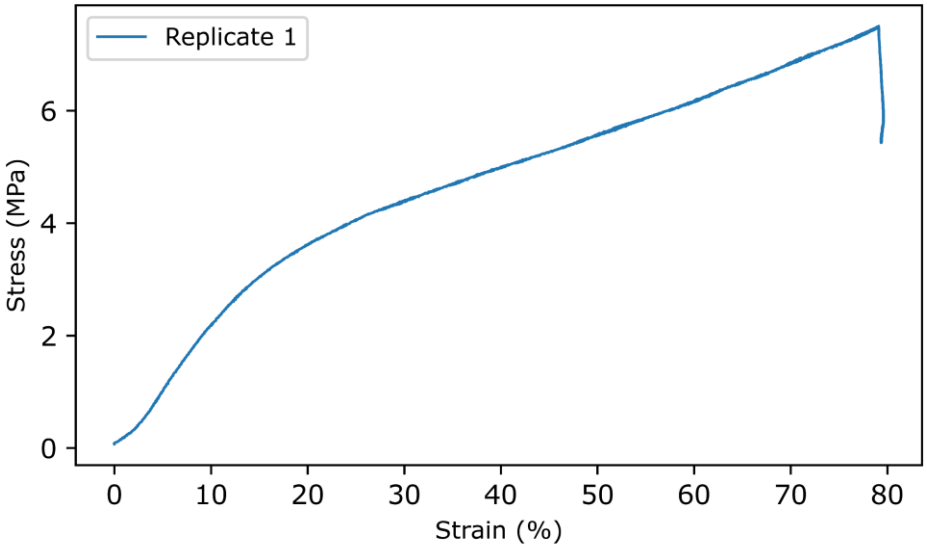

A17.19. FDCAPDO 1500 30 HDI

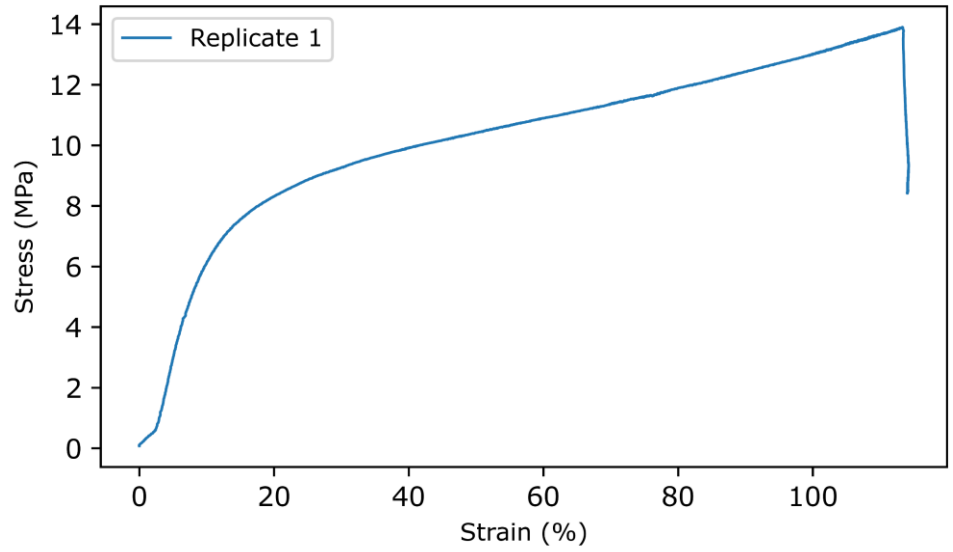

A17.20. FDCAPDO 2000 10 HDI

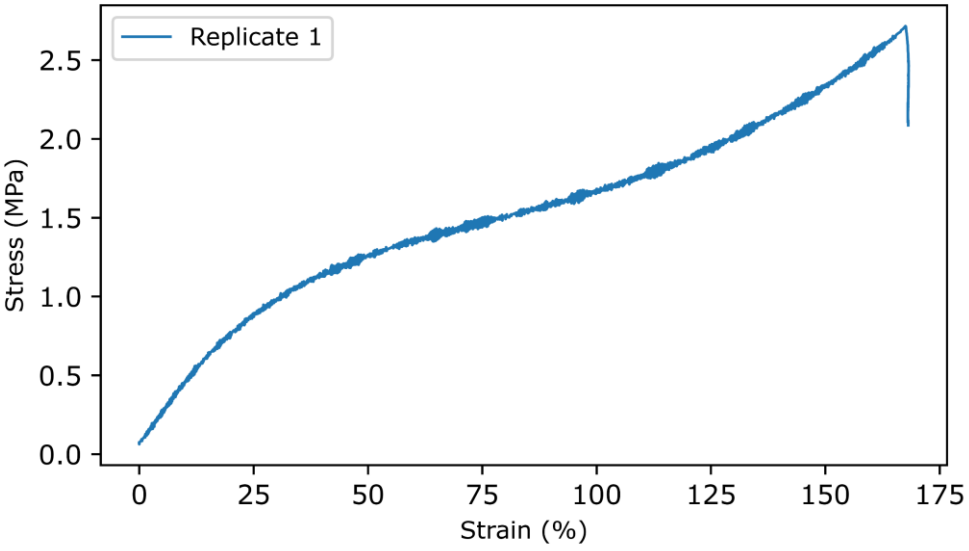

A17.21. FDCAPDO 2000 50 HDI

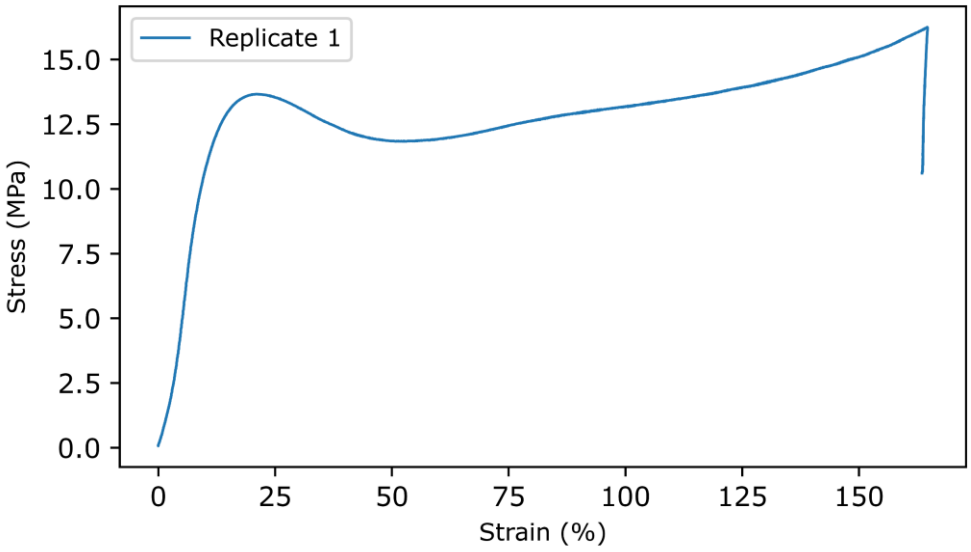

A18 Injection temperature profiles

A18.1. IPHTAMDI TPUs

	T1 (ºC)	T2 (ºC)	T3 (ºC)	T4 (ºC)
IPHTAPDO 1000 10% MDI	150	190	205	200
IPHTAPDO 1000 30% MDI	150	195	205	200
IPHTAPDO 1000 50% MDI	160	200	210	200
IPHTAPDO 2000 10% MDI	140	185	195	190
IPHTAPDO 2000 30% MDI	155	195	210	200
IPHTAPDO 2000 50% MDI	160	205	210	200
IPHTAHDO 1000 10% MDI	85	190	205	195
IPHTAHDO 1000 30% MDI	85	195	200	200
IPHTAHDO 1000 50% MDI	85	190	200	195
IPHTAHDO 2000 10% MDI	85	185	195	190
IPHTAHDO 2000 30% MDI	85	185	200	190
IPHTAHDO 2000 50% MDI	85	190	200	195

A18.2. IPHTAHDI TPUs

	T1 (ºC)	T2 (ºC)	T3 (ºC)	T4 (ºC)
IPHTAPDO 1000 10% HDI	150	220	225	220
IPHTAPDO 1000 30% HDI	160	225	230	220
IPHTAPDO 1000 50% HDI	155	225	230	220
IPHTAPDO 2000 10% HDI	160	215	225	215
IPHTAPDO 2000 30% HDI	160	225	230	225
IPHTAPDO 2000 50% HDI	155	230	235	230
IPHTAHDO 1000 10% HDI	140	215	225	220
IPHTAHDO 1000 30% HDI	140	220	230	225
IPHTAHDO 1000 50% HDI	140	210	220	215
IPHTAHDO 2000 10% HDI	140	220	225	215
IPHTAHDO 2000 30% HDI	145	215	220	210
IPHTAHDO 2000 50% HDI	140	220	230	225

A18.3. FDCAMDI TPUs

	T1 (ºC)	T2 (ºC)	T3 (ºC)	T4 (ºC)
FDCAPDO 1000 10% MDI	165	200	210	205
FDCAPDO 1000 50% MDI	165	205	215	205
FDCAPDO 1500 30% MDI	165	205	215	210
FDCAPDO 2000 10% MDI	165	210	220	215
FDCAPDO 2000 50% MDI	165	210	225	215
FDCAHDO 1000 10% MDI	165	205	215	210
FDCAHDO 1000 50% MDI	165	200	210	205
FDCAHDO 1500 30% MDI	165	210	220	215
FDCAHDO 2000 10% MDI	165	205	215	205
FDCAHDO 2000 50% MDI	165	200	220	210

A18.4. FDCAHDI TPUs

	T1 (ºC)	T2 (ºC)	T3 (ºC)	T4 (ºC)
FDCAPDO 1000 10% HDI	190	235	240	240
FDCAPDO 1000 50% HDI	190	230	235	235
FDCAPDO 1500 30% HDI	190	240	245	240
FDCAPDO 2000 10% HDI	190	235	240	235
FDCAPDO 2000 50% HDI	190	240	245	240
FDCAHDO 1000 10% HDI	190	230	235	230
FDCAHDO 1000 50% HDI	190	235	240	235
FDCAHDO 1500 30% HDI	190	225	230	225
FDCAHDO 2000 10% HDI	190	240	245	240
FDCAHDO 2000 50% HDI	190	235	240	240